Title

Performance of Ordinary C-Shaped Reinforced Concrete Structural Walls Subjected to Wind and Seismic Loading Protocols

Author

Unal, Mehmet Emre

Publication Date

2024

Peer reviewed|Thesis/dissertation

UNIVERSITY OF CALIFORNIA

Los Angeles

Performance of Ordinary C-Shaped Reinforced Concrete Structural Walls Subjected to Wind and Seismic Loading Protocols

A dissertation submitted in partial satisfaction

of the requirements for the degree Doctor of Philosophy

in Civil Engineering

by

Mehmet Emre Unal

2024

ABSTRACT OF THE DISSERTATION

Performance of Ordinary C-Shaped Reinforced Concrete Structural Walls
Subjected to Wind and Seismic Loading Protocols

by

Mehmet Emre Unal
Doctor of Philosophy in Civil Engineering
University of California, Los Angeles, 2024
Professor John Wright Wallace, Chair

The design of buildings under wind demands has traditionally been based on prescriptive code provisions such as ASCE/SEI 7, which requires the building components to stay essentially linear elastic. Recent developments in wind tunnel testing, structural analysis techniques, and performance-based design procedures led to the publication of the ASCE/SEI Prestandard for Performance-Based Wind Design (ASCE/SEI, 2019). The Prestandard allows limited inelastic behavior in ductile elements of a building's Main Wind Force Resisting System (MWFRS) under extreme wind events. However, because yielding of some building components has not historically been permitted, there is limited research available to understand the inelastic behavior of structural elements subjected to wind demands. The advantages of the performance-based wind design

(PBWD) are considered to be most impactful for the design of tall buildings, where it is very common to use coupled reinforced concrete shear wall systems as the MWFRS. Although some research has been conducted to understand the inelastic behavior of reinforced concrete and steel-reinforced concrete coupling beams, there is no published research that investigates the inelastic behavior of reinforced concrete shear walls under wind demands. To fill this gap, four reinforced concrete C-shaped structural walls have been tested in two phases under quasi-static, biaxial cyclic loading protocols simulating extreme wind events. Following the wind loading protocol, a seismic loading protocol was applied.

The design of the walls was based on the core-wall design of actual buildings that were designed and constructed in high-wind and low-seismic zones in the United States. The 5 in. thick flanges and webs of the walls were 30 in. and 75 in. long, respectively, representing approximately one-third scaled C-shaped walls of the core-walls of these buildings. The test walls were detailed as Ordinary walls based on the provisions of Chapter 11 of ACI 318-19. The test variable for the Phase-I walls (CW-1 and CW-2) was the longitudinal reinforcement ratio (ρ_l); 0.75% for CW-1 and 1.5% for CW-2. Based on the experimental results of the Phase-I walls and feedback from a Project Advisory Committee (PAC), two more walls (CW-3 and CW-4) were tested during Phase-II. The design of Phase-II walls was based on CW-2 (ρ_l=1.5%), and the test variables were the amount of confinement provided at the end zones of the flanges (flange edges) and the amount of axial load applied during the biaxial wind loading protocol.

The wind test results indicated that for the wall with the low-to-moderate reinforcement ratio (CW-1, ρ_l=0.75%), rotational ductility demands of 3.0 can be achieved without any damage (e.g., concrete spalling, bar buckling, or bar fracture) and with very small residual flexural crack widths

(around 0.1 mm). Since CW-1 failed at a rotational ductility demand of 20 during the seismic loading protocol, modest inelastic response can be allowed during extreme wind events for the walls with 0.75% or lower longitudinal reinforcement ratios. Concrete spalling was observed at the flange-web corners and the flange edges during the wind loading protocol for the walls with the higher longitudinal reinforcement ratio (1.5%). Depending on the amount of axial load applied during the biaxial load application, concrete crushing and bar buckling were also observed. Phase-II tests showed that the flange edges were more susceptible to damage than the other portions of the C-shaped walls. With moderate confinement provided at the flange edges and reduction in wall axial load during the biaxial loading (when the flange edges were under compression), bar buckling and concrete crushing were not observed during the wind loading protocols. Application of the seismic loading protocol revealed that, for the walls that did not sustain any significant damage during the wind tests, rotational ductility demands of at least 8.5 could be achieved prior to 20% loss in lateral strength.

The dissertation of Mehmet Emre Unal is approved.

Henry Burton

Kristijan Kolozvari

Thomas Sabol

John Wright Wallace, Committee Chair

University of California, Los Angeles

2024

To my mom and dad.

TABLE OF CONTENTS

LIST OF TABLES

LIST OF FIGURES

ACKNOWLEDGMENTS

The work presented in this research was supported by funding from Charles Pankow, American Concrete Institute, and Magnusson Klemencic Associates (MKA) Foundations. The project was administered by Charles Pankow Foundation as CPF Agreement RGA #01-21. Their financial support is gratefully acknowledged. This project would not have been possible without the significant in-kind support for materials and construction provided by Webcor Builders Inc. Their generous support is gratefully acknowledged. I would also like to express my gratitude for material donations and test specimen construction from Pacific Steel Group (PSG) and CalPortland. Without their support, this research could not have been completed. Any opinions, findings, and conclusions or recommendations expressed in this report are those of the authors and do not necessarily reflect the views of the funding agencies.

I would also like to express my deepest gratitude to Professor John Wallace. Without his infinite support and guidance, this research would not have been possible. I am incredibly grateful to have the opportunity to work with him and learn from him. I also could not have undertaken this journey without Professors Thomas Sabol, Kristijan Kolozvari, and Henry Burton from my defense committee, who generously provided knowledge and expertise. I am very thankful for the assistance given by Dr. Eric Ahlberg, Laboratory Manager and Principal Development Engineer in the Department of Civil and Environmental Engineering at UCLA. His extensive knowledge and expertise were vital in facilitating and conducting the experiments.

I am also very grateful to Ron Klemencic, Viral Patel, David Fields, Ian McFarlane, Sean Clifton, and Brad Malmsten from the professional advisory committee of this project. I want to extend my sincere thanks to Saman Abdullah and Sunai Kim. Their help over the years was profound for my academic journey.

Finally, I would like to thank my friends and colleagues Matias Rojas, Santiago Rodriguez Sanchez, Samul Halim, and Zafer Yilmaz, who were like a second family to me and helped me with many of the challenges I experienced over the last couple of years.

VITA

2012-2017	B.S., Civil and Environmental Engineering Bogazici University, Istanbul, Turkey
2015-2017	Student Assistant Department of Civil and Environmental Engineering Bogazici University, Istanbul, Turkey
2017-2019	M.Sc., Civil Engineering Technische Universität Dresden, Dresden, Germany
2019	Teaching Assistant Department of Civil Engineering Technische Universität Dresden, Dresden, Germany
2019-2024	Graduate Student Researcher & Teaching Assistant Department of Civil and Environmental Engineering University of California, Los Angeles, CA

1. Introduction

1.1. Background

The population of metropolitan areas worldwide is increasing rapidly due to the movement of people from rural and/or suburban areas. In many cases, these metropolitan areas are located along coastlines where extreme wind events, high seismicity, or combinations of the two exist. Figure 1-1 shows a map of the world where seismic activity is shown in yellow-red colors, and the tropical windstorm hazard is shown in green. It can be observed from the map that many fast-growing cities in the United States, such as Los Angeles, San Francisco, Seattle, Houston, Miami, and New York City, along with the other regions around the world, e.g., Philippines, Taiwan, and Indonesia are located at the regions where seismic and/or wind hazards are inevitable. This population densification has led to the construction of taller buildings, which brings its own challenges. Many of the challenges associated with designing and constructing tall buildings in high wind and seismic hazard regions are compounded by other, sometimes competing factors. Amongst these is the responsibility to society to provide efficient, affordable, and comfortable housing and work environments while simultaneously addressing the global issues of sustainability and the resiliency of our building stock (Aswegan et al., 2017).

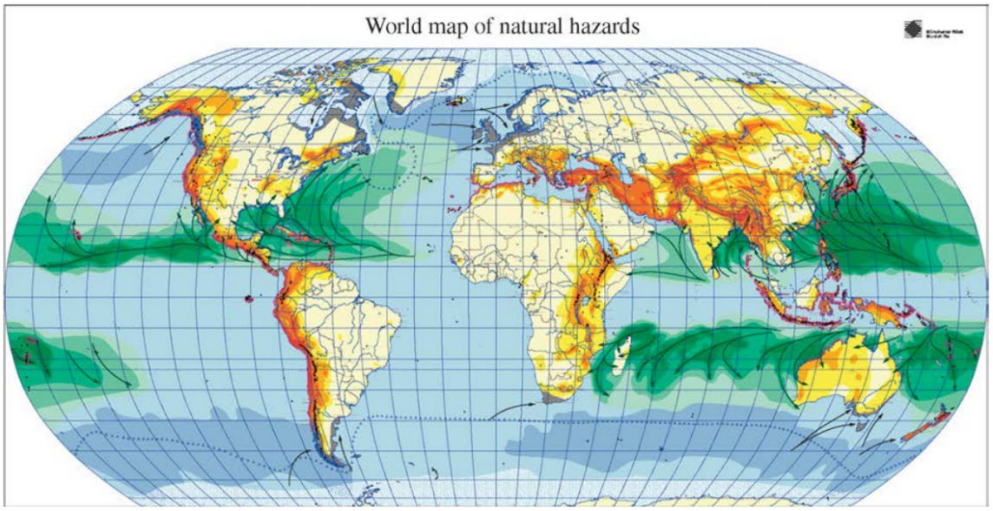

Figure 1-1: Seismic and wind hazard map (Smolka, 2006)

Prior to 1972, the design of structures for wind loading was generally governed by local authorities. In most instances, a simple horizontal (and/or vertical) pressure was prescribed to be applied to the building surfaces generating demands on the primary structural system. The primary structural system was then designed to respond within the elastic range to the combined effects of gravity and lateral loading. There was little, if any, consideration given to building displacement, story drift, or occupant comfort (Klemencic et al., 2019). Starting with ANSI A58-1 (1972), wind hazards began to be determined in a probabilistic manner where wind loading criteria were provided using wind speeds and tabulated design load parameters for various regions around the United States. With the beginning of wind tunnel studies and various editions of ASCE 7, starting with ASCE 7-88 and most recently ASCE 7-22, the characterization of wind loading on the structures has evolved remarkably. This evolution of the definition of wind loading includes changing the reference wind speed from fastest-mile to a 3-second gust, calculated using a 3-second gust measured 33 ft. (10 m) above ground in an open terrain (Exposure C category). Also, until ASCE 7-05, the mapped wind speeds were based on a 50-year mean recurrence interval

(MRI), and the load and importance factors were applied to approximate wind speeds for 300-year, 700-year, and 1700-year MRIs. With ASCE 7-10, ultimate wind speed maps for different risk categories directly representing the 300-year, 700-year, and 1700-year MRIs are introduced. Accordingly, the current ASCE 7 provisions (ASCE 7-22, 2022) provide different ultimate wind-speed maps, calculated using a 3-second gust, for 300-year, 700-year, 1700-year, and 3000-year mean recurrence intervals (MRIs) for Risk Category I, II, III, and IV buildings, respectively. In the early 1960s and 1970s, wind tunnel tests were generally used for "special" or very tall buildings. Since then, wind tunnel tests have been used by designers to improve designs using more detailed knowledge of the expected wind loads and how a building responds to those loads (Irwin et al., 2013). Although improvements have been made to characterize the wind demands, ASCE 7 requires the buildings to stay essentially linear elastic during extreme wind events. Also, the prescriptive codes have remained silent regarding drift and occupant comfort criteria as these performance parameters are viewed as serviceability-related and not matters of life safety (Klemencic et al., 2019).

Unlike the design of buildings under wind demands, significant attention has been paid to the design of structures under seismic demands. Since the mid-1990s, when performance-based seismic design (PBSD) procedures were first introduced, the seismic design of buildings has become more involved, resulting in buildings with more reliable performance. The yielding of ductile building elements/actions has long been permitted by building codes for seismic design to provide more reliable energy dissipation mechanisms. In seismic design, demands on the structural components due to the extreme loading can be managed through different energy-absorbing mechanisms such as concrete cracking, bar yielding, and deformation of specially designed structural elements. However, in some cases, the elastic demands due to wind design loads can

exceed the demands for seismic loads (which are reduced to account for ductility and damping). If this happens, due to the use of capacity design concepts for seismic design, the demands on force-controlled elements (e.g., foundation, joints, diaphragm) and/or actions (e.g., shear, anchorage) of the seismic LFRS can increase substantially. The inconsistency in design philosophy between the seismic and the wind demands results in higher cost and less efficiency by negating the benefits of the PBSD for tall buildings. Therefore, a framework for performance-based wind design (PBWD) that introduces appropriate modeling approaches, building performance objectives, and corresponding acceptance criteria is needed. According to Spence et al. (2016), the reasons for inelastic response not being contemplated in the design of wind-excited systems is most likely due to unease with the idea of a wind-excited system suffering damage under a hazard that is easily and frequently perceived as well as to the significant difficulty from a computational standpoint in modeling the inelastic response of structural systems under events that can last for several hours. With the application of performance-based engineering to the wind design, 1) a more reliable, better-performing building design that will result in the rigorous consideration of serviceability, strength, and stability can be achieved, and 2) a more efficient and effective structural design can be produced by allowing a modest amount of nonlinear response in specially designed structural elements during extreme wind events (Klemencic et al., 2019). A case study conducted by Aswegan et al. (2017) on a 60-story (approximately 900 ft. tall) reinforced concrete core wall building with buckling-restrained brace (BRB) outriggers subjected to extreme wind loading (1700-year MRI) showed that allowing inelastic rotations (as small as 0.001 radians) in the coupling beams resulted in more than 25% reduction in the BRB peak forces as opposed to the code prescriptive elastic design.

1.2. Performance-Based Wind Design Framework

In recent years, it has been realized by the civil engineering community that there is an inconsistency between the state of the practice and the state-of-the-art of wind design. Despite many improvements achieved in understanding wind loading, the code prescriptive design approach to the wind demands is to enforce elastic response under design-level loads. Prior to 2013, the effort to extend the performance-based engineering approach to wind loads was mainly conceptual and mostly focused on feasibility assessment (Bernardini et al., 2013, Bernardini et al., 2015; Ciampoli et al., 2011; Smith & Caracoglia, 2011; Spence & Gioffrè, 2012; Spence & Kareem, 2014; Spence et al., 2015). Over the last ten years, many reports have been published to create a framework for PBWD that can guide the engineers who wish to go beyond the limitations of ASCE 7 regarding wind design. In 2016, Spence et al. (2016) proposed a method specifically for multi-story wind-excited buildings in order to mitigate structural and non-structural damage and loss. In particular, the post-yield behavior of the structural system was modeled using the theory of dynamic shakedown, therefore providing a full portrait of the post-yield behavior without the need for computationally expensive non-linear finite element models. A case study was presented illustrating the practicality of the proposed PBWD framework. Their work showed that allowing limited inelasticity for elements that are specifically designed and detailed for these demands can result in better building performance relative to one designed in accordance with ASCE 7 provisions and also improve the reliability associated with the expected performance. Later, in 2016 and 2017, Larsen et al. (2016) and Aswegan et al. (2017) developed a framework for PBWD, including different performance objectives and corresponding analysis techniques and acceptance criteria. In 2023, the state-of-the-art report from the ASCE workshop was published in the "Advancement in Performance-Based Wind Design" (Scott, 2023).

All these efforts and the knowledge gained by PBSD helped result in the publication of "Prestandard for Performance-Based Wind Design" by ASCE/SEI (2019). This publication successfully comprises a method to use performance-based engineering ideas for wind loading in a similar manner to PBSD. The Prestandard benefits building owners and developers by enabling the design of more efficient buildings that meet the desired building functionality requirements and reduce property damage from wind events while meeting public safety and performance requirements. The Prestandard is permitted to be used for the design of the Main Wind Force Resisting System (MWFRS), the building envelope (including roof systems, wall cladding systems, and fenestration systems), or both. Figure 2.1 illustrates the outline of the PBWD procedure for MWFRS, where the performance objectives are separated into three different categories: 1) Occupant Comfort, 2) Operational, and 3) Continuous Occupancy, Limited Interruption.

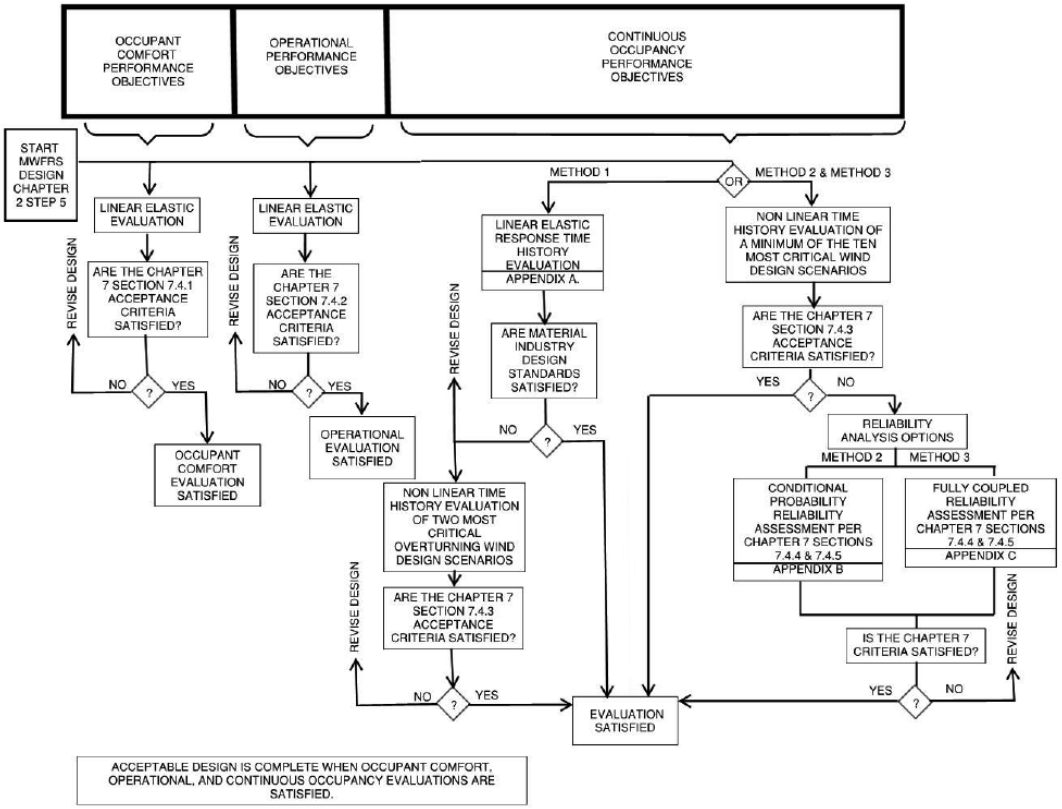

Figure 1-2: Outline of PBWD MWFRS analysis and acceptance methods for each performance objective (ASCE, 2019)

In general, the design process that will lead to an acceptable design involves 8 steps;

1) Identification of risk category, performance objectives, performance requirements, and acceptance criteria
2) Identification of wind loads
3) Conceptual design
4) Development of a MWFRS analysis model
5) Evaluation of MWFRS and Building Envelope acceptance criteria
6) Refinement of the design
7) Gain Agreement of the Peer Review Team and Authority having jurisdiction

8) Implementation of construction observation and supplemental special inspections

Figure 1-3 provides a summary of the different acceptance criteria that correspond to performance objectives that depend on the building risk category. The risk category of the building is proposed to be established based on the governing building code. IBC Section 1604.5 requires the determination of the building risk category, which is based on the consequences of building failure and/or nonperformance to the building occupants and users, and potential impacts on society. Other performance-based design guides, such as LATBSDC (2023), FEMA P-58 (2018), and FEMA P-424 (2010), express general performance objectives specific to hazards and building risk categories. With respect to wind, ASCE 7-16 (2016) risk category criteria pertain only to the basic wind speed; the standard does not address other issues, such as drift control or envelope toughness, that are necessary to achieve a desired functional level of building performance. PBWD is intended to overcome these shortcomings (ASCE, 2019). It can be seen from Figure 1-3 that for Occupant Comfort and Operational performance objectives, the MWFR system is required to remain elastic. However, for Continuous Occupancy (strength level demands), specific elements or components of the system are permitted to become inelastic. The details of these elements and corresponding acceptance criteria (for Continuous Occupancy) are explained in more detail in Chapter 7.4 of the Prestandard, where it is stated that the peak drift ratio should not exceed H/200 or H/300 (the exact ratio is left to the judgment of the designer), where H is the building height. The residual peak drift ratio is limited to H/1000 and h/1000, where h is the height of the story under consideration. The strength limits of the elements and/or actions (Force-controlled or Deformation-Controlled) are set depending on the method used during the analysis. Although linear elastic analysis is permitted for the assessment of Occupant Comfort and Operational performance objectives, for Continuous Occupancy, the Prestandard offers three different methods: Method 1) a linear elastic analysis

procedure followed by nonlinear time (response) history analysis (NLTHA), Method 2) NLTHA with a conditional reliability approach for a given scenario that is based upon FEMA P-695 studies (2009), and Method 3) NLTHA with system reliability assessment.

If Method 1 is used, then for force-controlled elements or actions (e.g., shear wall shear, moment frame column axial compression and shear, joint shear, column shear, etc.), calculated demand to capacity ratios are not allowed to exceed 1.0 where the demands are calculated according to the provisions in Chapter 6 of the Prestandard and the capacities are calculated using the appropriate material standard (e.g., ACI 318 for reinforced concrete). Therefore, using Method 1, no yielding or inelastic responses are permitted. For deformation-controlled elements or actions (e.g., shear wall flexure, column tension and flexure, coupling beams, etc.), calculated demand-to-capacity ratios are not allowed to exceed 1.25, where the demands are calculated according to the provisions in Chapter 6 of the Prestandard and the capacities are calculated according to the appropriate material standard (e.g., ACI 318) using expected material strengths with ϕ=1. Calculated deformations are required to be within predefined deformation limits (i.e., acceptance criteria). However, if Method 2 or 3 is used, the calculated demand to the capacity ratios for deformation-controlled elements of the MWFRS are not allowed to exceed 1.5, where demands are calculated per the static wind loads prescribed in ASCE 7-16 Directional Procedure and the capacities are calculated according to the appropriate material standard (e.g., ACI 318) using expected material strengths and applicable ϕ factors. Chapter 5 of the Prestandard explains how wind loads are to be determined (Step 2). For PBWD, only wind tunnel testing is allowed to determine local wind pressures and global wind-induced structural loads and responses. Wind tunnel tests are required to meet the requirements of ASCE 7-22 (Chapter 31) and ASCE 49-21 (2021).

	Occupant Comfort	Operational	Continuous Occupancy, Limited Interruption
Risk Category II Risk Category III Risk Category IV	Risk category independent	10-years MRI 25-years MRI 50-years MRI	700-years MRI 1,700-years MRI 3,000-years MRI
MWFRS	Performance Objective: The structural system shall remain elastic. The building motions and vibrations shall minimize occupant discomfort at design wind 1-month, 1-year, and 10-years MRI. Acceptance Criteria: See Section 7.2	Performance Objective: The structural system shall remain elastic. The building systems shall remain operational during the wind event for the building risk category. Acceptance Criteria: See Section 7.3	Performance Objective: Specific elements or components of the structural system shall be permitted to become inelastic. The structural system shall withstand a design wind event for the building risk category with a low probability of partial or total collapse. Acceptance Criteria: See Section 7.4
Building Envelope		Performance Objective: The building envelope shall remain attached to the structure. The building envelope shall maintain wind-driven rain resistance. Acceptance Criteria: See Section 8.3	Performance Objective: The building envelope shall remain attached to the structure. The building envelope system shall be designed to maintain wind-driven rain resistance for 25-year MRI wind events for Risk Category II and 50-year MRI wind events for Risk Category III and IV. Acceptance Criteria: See Section 8.3
Nonstructural Components and Systems		Performance Objective: Nonstructural components and systems shall remain attached and maintain wind-driven rain resistance. Acceptance Criteria: See Sections 7.3.1 and 8.4.3	Performance Objective: Nonstructural components and systems shall remain attached. Acceptance Criteria: See Sections 7.4.1 and 8.4.3

Figure 1-3: Performance objectives and acceptance criteria (ASCE, 2019)

1.3. Testing under Wind Loading Protocols

Although the knowledge obtained from the development and use of PBSD has helped in the development of PBWD there are fundamental differences between seismic and wind loads and the structural responses under these load that must be considered. Some of these differences are pointed out in the ASCE/SEI Prestandard (2019) as follows:

- While the duration of strong earthquakes rarely lasts more than 60 seconds, the duration of strong wind loads can be hours (even days for tropical storms or hurricanes).
- The responses of the along-wind and across-wind loading are significantly different. While, in general, the along-wind load has a significant mean value and can be considered force-controlled, the across-wind loading is dominated by vortex shedding, which has the potential to generate a significant dynamic response and has a near-zero mean and can be considered displacement-controlled (in a sense similar to seismic loading).
- As opposed to seismic loading, where the number of inelastic excursions is likely less than 25, due to the long duration of wind loading, hundreds or thousands of inelastic excursions may occur. Because of this larger number of cycles under wind loading, the magnitude of inelastic deformation permitted (if permitted) during the response is significantly less than for seismic loading due to low cycle fatigue.
- For most cases, during seismic excitation, the inertial forces will reduce in the nonlinear response range due to the reduction in the natural frequency of the structural system. However, for the wind loading, this is not entirely true since the reduction of natural frequency may cause greater resonance and, therefore, inertia loads unless damping increases sufficiently.

- Cyclic degradation due to a few strong cycles of earthquake loading is expected to be significantly different from that produced by a large number of cycles of wind loading.

Although considerable work has been conducted to develop a framework for PBWD, few publications in the literature focus on supporting details, such as test results of structural elements under wind loading protocols. To date, testing has focused on reinforced concrete and steel reinforced concrete coupling beams (e.g., Abdullah et al., 2020, 2021, 2022; Chou et al., 2023; Hill et al., 2023), since coupling beams are the primary components expected to undergo inelastic responses for core wall systems. Abdullah et al. (2020; 2021) published summaries of results on testing of reinforced concrete coupling beams in coupled wall systems under different wind loading protocols. The beam test specimens were designed and detailed as "ordinary" beams, i.e., the provisions for special structural walls Section 18.10.8 of ACI 318-19 were not applied. The study goals included: 1) establishing experimental evidence that limited nonlinearity in concrete coupling beams subjected to extreme wind events can be permitted and does not result in unacceptable behavior, 2) providing experimental coupling beam data to help develop modeling parameters for nonlinear dynamic analysis of coupled concrete wall systems, and 3) studying the impact of prior limited nonlinear wind demands on the post-windstorm reserve seismic capacity of concrete coupling beams in terms of strength, stiffness, ductility, energy dissipation capacity, and failure mode (Abdullah et al., 2022). To accomplish these objectives, a total of 8 different 2/3 scale concrete coupling beams were tested under quasi-static, cyclic loading protocols that represent extreme wind loading followed by a standard seismic loading protocol. The experiments were conducted in two phases; during the first phase, four beams (CB1 through CB4) were tested in Summer and Fall of 2018; for the second phase, based on the feedback from practicing engineers, another set of four beams (CB5 through CB8) were tested during Spring and Summer

2019. During the experiments, after the testing of the beams under wind loads, damage to the specimens was evaluated to assess the need for repair. It was found that the level of structural damage and concrete cracking observed were minor. Based on observed residual crack widths, the damage level of the beams was classified as "insignificant" using FEMA 306 (1998) criteria. Therefore, no repair was done. However, to evaluate the effectiveness of epoxy injection repair as a performance restoration measure, one of the beams (CB5) in Phase II testing was repaired using injected epoxy and retested using the same wind loading protocol. As noted previously, one of the main goals of the study was to assess the seismic performance of coupling beams subjected to prior (modest) inelastic deformation demands under wind loading protocols. To this end, beams were subjected to standard, quasi-static, reversed cyclic seismic loading protocols. The seismic loading protocol was initiated at the largest wind displacement demand (approximately 1.5% or 2% chord rotation) and then subjected to larger rotation demands (e.g., 3 cycles at 3% rotation and then 2 cycles at larger rotation levels) until significant strength loss was observed. Primary findings of the research included:

- Following the seismic requirements of ACI 318-19 Section 18.10.7 was not necessary to achieve acceptable performance under the applied wind loading protocols. No crushing or spalling of concrete or buckling or fracture of reinforcing bars was observed in all beam tests.
- Comparing test results for two very similar beams, a 1/2-scale RC coupling beam (referred to as CB24F-RC) tested by Naish et al. (2013) under a seismic loading protocol and CB4 tested under a wind loading protocol demonstrated that the loading protocol did not affect beam strength; however, for roughly the same ductility demand, slightly less initial stiffness and more hysteric pinching were observed under the wind loading protocol.

- Testing with a non-zero mean loading protocol resulted in higher residual rotations testing of beams with a zero mean loading protocol.
- Increasing the number of the inelastic cycles by a factor of four did not significantly affect beam behavior.
- Varying the applied wind loading protocol did not impact the reserve seismic capacity of the beams, except for the case where the entire wind loading protocol was applied more than once.
- Injecting epoxy into cracks was effective in preventing the cracks from re-opening; however, the repair was only modestly effective in restoring initial stiffness. The repair restored the initial secant stiffness values to about 150% (0.05 versus 0.033) and 115% (0.075 versus 0.065) of the values for loading at 0.15*Mpr* to 0.75*Mpr*, respectively,
- Comparing beams tested first under wind loading and then seismic loading with similar beams tested under seismic loading only in the literature showed that the application of the wind loading protocol did not significantly affect the strength, axial growth, energy dissipation capacity, deformation capacity, and failure mode. The most significant influence of the prior nonlinear wind demands was a reduction in the initial stiffness (ranging from 10% to 63%).
- Allowing limited nonlinearity with a maximum ductility demand of 1.5 in coupling beams provides a reliable mechanism to dissipate energy through concrete cracking and reinforcement yielding without compromising the strength and stability of the beam.

The advantages of performance-based wind design (PBWD) are considered to be most impactful in the design of tall buildings. It is very common for engineers to use coupled core-wall systems

for this purpose. These systems usually consist of C-shaped and/or I-shaped shear walls connected with coupling beams at the floor levels. Although there are some tests in the literature that focus on the behavior of coupling beams under wind loading protocols, there are no published studies addressing issues for structural walls.

1.4. Motivation and Objectives

To address the lack of information on the performance of coupled core walls under wind loading protocols, four C-shaped reinforced concrete shear walls were designed, constructed, and tested under wind loading protocols. The test program was conducted in two phases. Phase I consisted of testing of two walls (CW-1 and CW-2) during the Spring and Summer of 2023. Based on the experimental results and feedback from a Project Advisory Committee (PAC) that included practicing structural engineers from four engineering firms involved in the design of tall RC core wall buildings for wind loads, two more walls (CW-3 and CW-4) were constructed and tested in Phase-II during the Winter and Spring of 2024. Test objectives included:

- Assessing the performance of "Ordinary" walls, i.e., walls design and detailed according to Chapter 11 of ACI 318-19, to determine if additional design requirements are needed to achieve acceptable performance for modest inelastic demands under wind loading protocols.
- Developing a test program that included four isolated C-shaped wall tests that could adequately represent the demands on C-shaped walls as components of a core wall of buildings designed and constructed in high-wind zones in the United States.
- Testing of the four C-shaped walls under wind loading protocols.

- Investigating the test results to evaluate ACI 318-19 design requirements and to recommend new design requirements, as needed.
- Evaluating the reserve (residual) seismic capacity of C-shaped RC walls subjected to prior wind loading protocols with limited non-linear rotation demands
- Developing non-linear analytical models capable of reasonably replicating the measured test responses to advance modeling of core wall systems for PBWD.

1.5. Dissertation Outline

This dissertation is comprised of seven chapters and eight appendices. Chapter 1 includes background on the design of buildings under wind loading, recent developments in performance-based wind design, and the motivation and objectives of this research. Chapter 2 focuses on the experimental program, including test specimen design details, material property information, test setup, instrumentation, and loading protocols. The presentation of the experimental results is divided into four chapters; Chapters 3 and 4 include the test results of the first specimen tested (CW-1) under wind loading and seismic loading, respectively, and the test results of the rest of the walls (CW-2, CW-3, and CW-4) are given in Chapters 5 and 6 for the wind loading and seismic loading, respectively. Chapter 7 focuses on the details of the analytical model developed to represent the test walls and includes comparisons of analytical results with the experimental results. Summary and conclusions are given in Chapter 8. Appendices A through H include a variety of additional details on the test specimens and test results.

2. Experimental Program

2.1. General

The experimental program consisted of designing, constructing, and testing four C-shaped ordinary reinforced concrete structural walls in two phases. During Phase-I, two walls, CW-1 and CW-2, were constructed and tested during the Spring and Summer of 2023. Based on the experimental results of the Phase-I wall tests and feedback from a Project Advisory Committee (PAC), two more walls (CW-3 and CW-4) were constructed and tested in Phase-II during the Winter and Spring of 2024. This chapter provides details on test specimen design, construction materials, test setup, instrumentation and data acquisition, and test protocols.

2.2. Test Specimen Design

2.2.1. Phase-I

The design of Phase-I wall test specimens was based on a review of drawings from actual buildings that were designed and constructed in high-wind and low-seismic zones in the United States. The buildings were located in Austin (Texas), Houston (Texas), Miami (Florida), and Chicago (Illinois), with roof heights ranging from 215 ft (65.5 m) to 525 ft (160 m). The lateral force-resisting systems for the buildings mainly consisted of reinforced concrete core walls composed of C- and/or I-shaped wall segments connected with coupling beams. A review of the critical sections of the C-shaped walls used in these buildings, at the wall-foundation interface or just above the podium level where a significant decrease in floor area occurs, showed that the thickness, length, and longitudinal and transverse reinforcement ratios varied significantly. Table 2-1 summarizes the details of eleven different C-shaped walls examined from four buildings.

Table 2-1: Review of C-shaped walls

Wall Number		Section			Longitudinal Reinforcement		Transverse Reinforcement	
		Thickness (in.)	Length (ft.)	l/t	Bar size	ρ_l	Spacing (in.)	ρ_t
#1	Flanges	18	21	14.0	#6	0.0044	12	0.0029
	Web	18	29	19.3	#8	0.0081	12	0.0029
#2	Flanges	18	10	6.7	#6	0.0048	12	0.0029
	Web	12	29	29.0	#8	0.0062	12	0.0029
#3	Flanges	18	12	8.0	#5	0.0035	12	0.0029
	Web	18	19	12.7	#5	0.0032	12	0.0029
#4	Flanges	30	17	6.8	#10	0.0071	-	-
	Web	36	23	7.7	#11	0.0279	-	-
#5	Flanges	24	11	5.5	#11	0.0213	12	0.0042
	Web	24	23	11.5	#6	0.0031	-	-
#6	Flanges	18	6.5	4.3	#9	0.0086	-	-
	Web	18	6.5	4.3	#9	0.0091	12	0.0056
#7	Flanges	18	12	8.0	#11	0.0281	-	-
	Web	18	21	14.0	#11	0.0255	6	0.0111
#8	Flanges	18	9.5	6.3	#9	0.0123	12	0.0019
	Web	24	20	10.0	#5	0.0123	12	0.0022
#9	Flanges	16	10	7.5	#8	0.0101	12	0.0021
	Web	24	20	10.0	#5	0.0101	12	0.0022
#10	Flanges	30	10	4.0	#11	0.0281	4	0.01
	Web	24	22	11.0	#11	0.0030	6	0.0083
#11	Flanges	30	18	7.2	#10	0.0083	12	0.0033
	Web	24	32.5	16.2	#9	0.0073	12	0.0031
Mean	Flanges	21.6	12.5	7.1	-	0.0124	-	0.0038
	Web	21.8	22.2	13.2	-	0.0105	-	0.0046

Note: Empty cells indicate that no information was available.

Based on a review of the data in Table 2-1 and discussions with the PAC, longitudinal reinforcement ratio (ρ_l) was selected as the test variable for Phase-I wall test specimens. The longitudinal reinforcement ratios (ρ_l) for the walls in Table 2-1 range from 0.3% to 2.8%, with a mean value of 1.15%. For the first wall (CW-1), a ρ_l value of 0.75% was chosen to represent walls

with low-to-moderate longitudinal reinforcement ratios, whereas for the second wall (CW-2), the ratio was doubled to 1.5% to represent walls with moderate-to-high longitudinal reinforcement ratios. Due to test setup limitations (force demands), the use of a value greater than 1.5% was not practical. For CW-1, #3 (d_b = 0.375 in.) Grade 60 longitudinal (vertical) reinforcement was used, whereas, for CW-2, #4 (d_b = 0.5 in.) Grade 80 was used. Grade 80 longitudinal reinforcement was used because its use has become common for taller core wall buildings. Grade 60 #3 reinforcement was used for CW-1 because Grade 80 #3 is not available in the United States. Grade 60 6 mm (d_b = 0.24 in.) bars were used for transverse reinforcement.

Due to the minimum clear cover and clear spacing requirements for wall longitudinal reinforcement in ACI 318-19, a minimum practical wall thickness of 4 in. was determined for the test walls (e.g., for CW-2, with larger diameter bars). However, based on typical core wall geometry, the use of a 1.5% longitudinal reinforcement ratio and a typical gravity axial load ratio of P = $0.1A_g f_c'$, where A_g is the wall gross cross-sectional area and f_c' the specified concrete compressive strength, use of a wall thicker than approximately 5 in. was not possible due to test setup limitations. Therefore, a wall thickness of 5 in. was selected. Ratios of wall length to wall web thickness (l_w/t_w) in Table 2-1 varied from 4.3 to 29, with a mean value of 13.25. A ratio of 15 was selected for the test walls based on a review of wall tests by Abdullah (2019), resulting in a wall web length of 75 inches. Based on various considerations (e.g., coupling beam width-to-depth, span-to-depth, typical core plan geometry), a flange length of (l_f) of 30 in. was selected. The flange cross-section aspect ratio (l_f/t_f) of 6.0 for the test walls was similar to the average l_f/t_f value of 7.1 for the examined buildings. The resulting core wall geometry for the assumed test walls is shown in Figure 2-1.

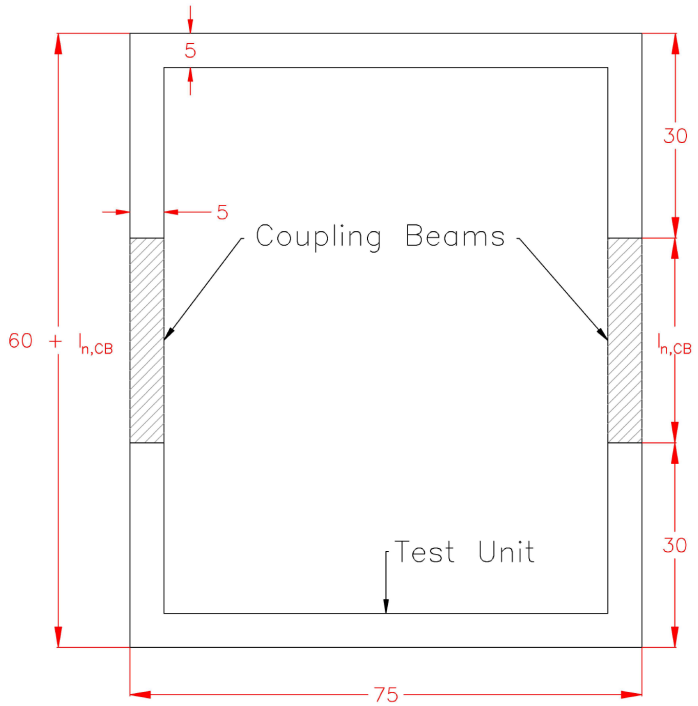

Figure 2-1: Assumed core wall system and the selected test specimen dimensions (Dimensions are in inches)

Since ASCE 7-16 requirements are based on elastic response under the design wind loads, wall detailing provisions are covered in Chapter 11 of ACI 318-19 (versus Chapter 18 for special walls). It is common practice to use a fairly uniform distribution of longitudinal reinforcement in ordinary core walls, although some concentration of boundary longitudinal reinforcement may be used for ordinary and special walls. Typical detailing at wall edges and corners for ordinary walls designed according to ACI 318-19 Chapter 11 consists of U-bars that are lapped to web horizontal reinforcement. Alternatively, a single closed tie is sometimes used at wall edges. Unlike special walls designed according to ACI 318-19 Chapter 18, for ordinary walls, lap splices of longitudinal reinforcement are permitted at critical sections because yielding of reinforcement is not expected. Therefore, longitudinal reinforcement was lap-spliced at the critical section (wall-foundation

interface) of the test walls. Figure 2-2 and Figure 2-3 show cross-sections of CW-1 and CW-2, respectively. The detailing of the flange edges and the flange-web corners are shown in Figure 2-4.

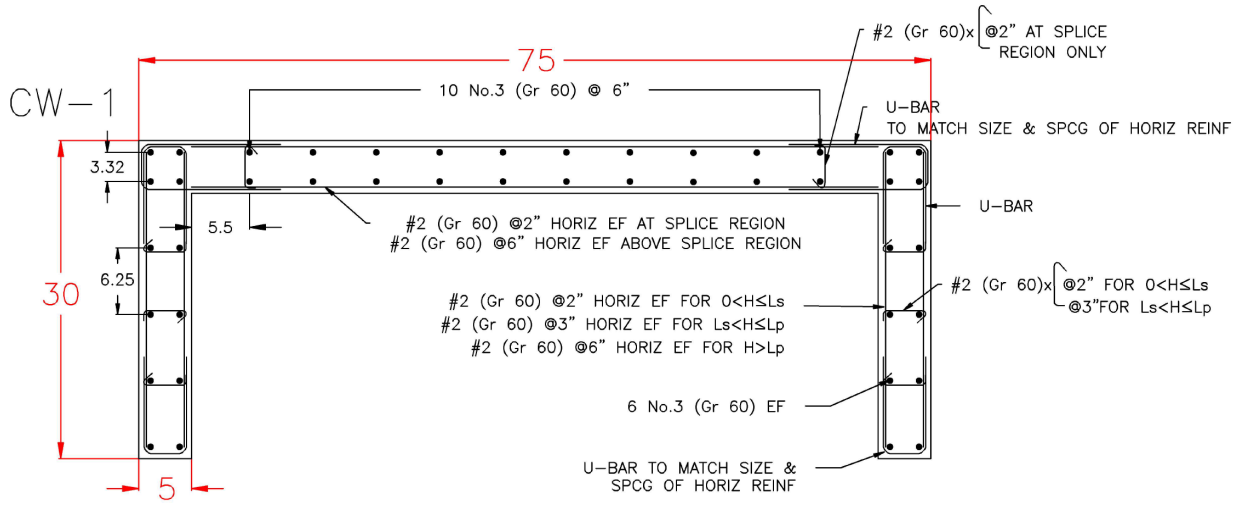

Figure 2-2: Cross-section and reinforcement of CW-1

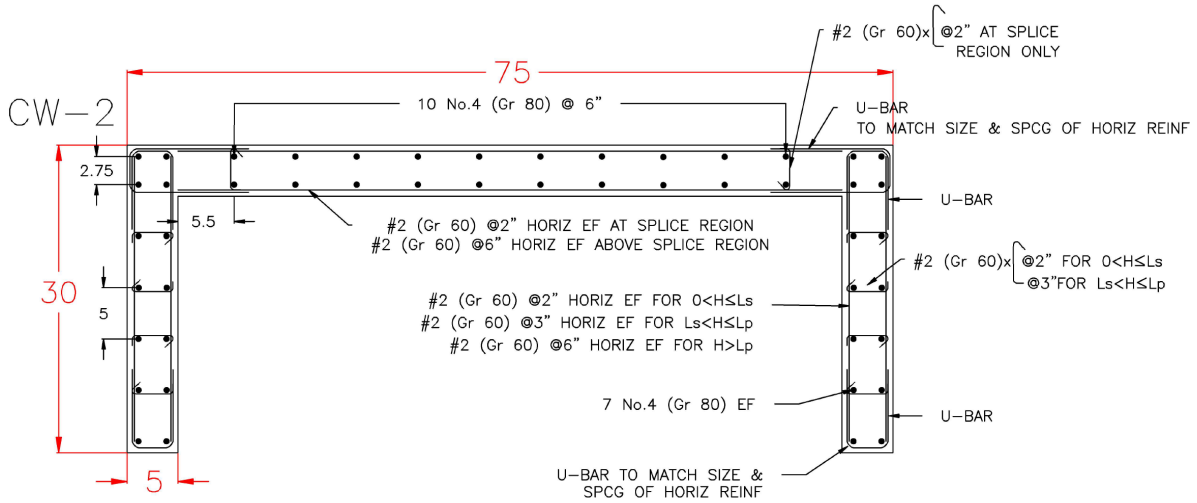

Figure 2-3: Cross-section and reinforcement of CW-2

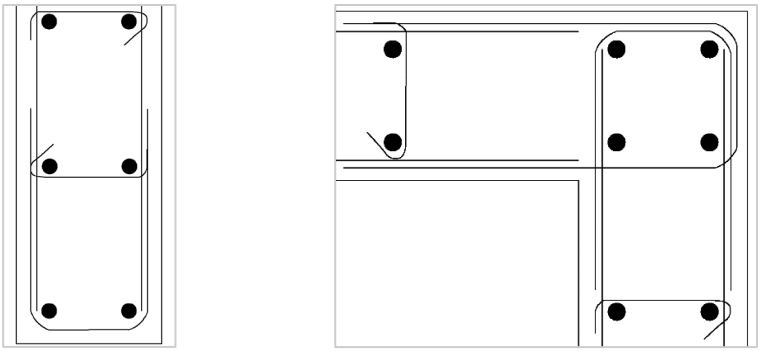

Figure 2-4: Flange edge detailing (left), Flange-Web corner detailing (right)

The behavior of lap splices under monotonic and cyclic loading has been extensively studied since the 1960s; however, there are no published studies on the behavior of lap splices under wind-loading protocols (WLPs). Although there are tests where the lap splices are subjected to inelastic cyclic loading, the loading protocol used in these tests does not reasonably represent recently used wind loading protocols (e.g., Abdullah et al. 2020) in terms of the number of cycles, the amplitude of the demands (both tensile and compressive), and the ramp-up and ramp-down behavior. Details on the WLP used in this study are described later in Section 2.6.2. Because constructing and testing C-shaped walls is rather expensive and complicated, a supplemental study was conducted to investigate the behavior of lap splices under WLPs in T-beam test specimens. The details and results of this study are reported elsewhere by Unal et al., (2024) and Halim (2024). A brief summary of the tests and the test results are provided in the following paragraphs.

Since the longitudinal reinforcement strain demands of the lap spliced rebars were higher for CW-2 (#4 Grade 80 bars) compared to CW-1 (#3 Grade 60 bars), the T-beams were designed to have the same conditions; bar size and grade, cover, thickness, and strain gradient (neutral axis depth/section depth) as CW-2. Therefore, #4 Grade 80 spliced reinforcement was used. Similarly, beams with 5 in. thick webs were constructed with clear cover of 5/8 in. to the transverse

reinforcement to match the conditions in the wall tests (Figure 2-5). The beams were designed to be 78 in. long and 10 in. deep, resulting in a span-to-depth ratio of 7.8. Top reinforcement consisted of two Grade 60 #8 longitudinal bars to prevent yielding under tension when the bottom spliced bars were subjected to high compressive strain demands (Figure 2-5). The flanges of the beams were 8.5 in. long and 2 in. deep to result in similar beam strain gradients as for the wall specimen CW-2. The test setup for the beams was designed to apply a constant moment over the spliced region. According to ACI 318-19 §11.7.3, the spacing (s) of the transverse reinforcement in cast-in-place walls should not exceed the lesser of; 3 times the wall thickness (15 in.), 18 inches (6 inches for 1/3 scaled test walls), and $l_w/5$ (75 in./5 = 15 in.). Therefore, initially, 6 in. spacing of stirrups was used for the test beams. A naming convention for each test beam was selected as B-SX-Y, where X is the spacing of the transverse reinforcement, and Y is the splice length.

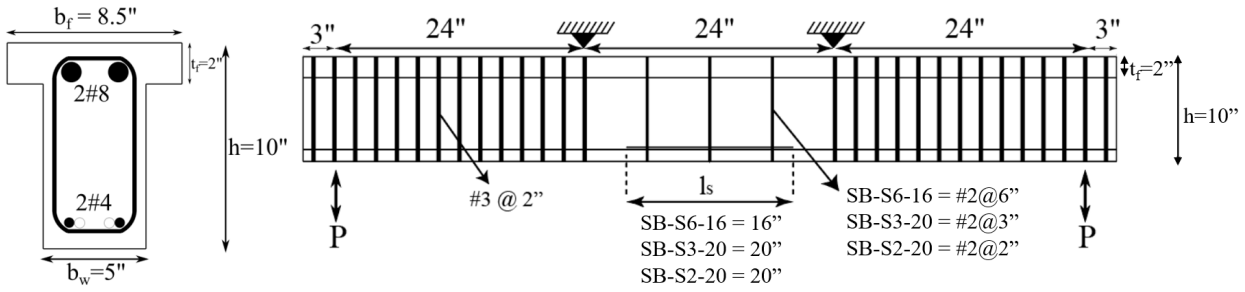

Figure 2-5: Cross-section and plan view of the T-beams

The splice lengths used in the T-beam test specimens were based on the ACI 318-19 §25.4.2.4 and §25.5.2 provisions:

$$l_s = 1.3 \times l_d \tag{2.1}$$

$$l_d = \left[\frac{3}{40}\frac{f_y}{\lambda\sqrt{f_c'}}\frac{\Psi_t\Psi_e\Psi_s\Psi_g}{\left(\frac{c_b + K_{tr}}{d_b}\right)}\right]d_b \tag{2.2}$$

where l_s is the splice length, l_d is the development length, f_y is the yield strength of the reinforcement, λ is the lightweight concrete modification factor, f_c' is the concrete compressive strength, c_b is the lesser of the distance from the center of the spliced reinforcement to the nearest concrete surface and one-half of the center-to-center spacing between longitudinal reinforcement in the same layer, K_{tr} is the transverse reinforcement index, d_b is the diameter of the spliced reinforcement, and $\Psi_t, \Psi_e, \Psi_s, \Psi_g$ are modification factors according to ACI 318-19 Table 25.4.2.5. Using Equation 2.2, l_d was computed to be 12.3 in., resulting in a splice length (Equation 2.1) of 1.3(12.3 in.) = 16.0 in.; therefore, initial T-beam tests were conducted on beams with 6 in. spacing of transverse reinforcement and a 16.0 in. splice length (i.e., B-S6-16). For B-S6-16, splice failure occurred prior to completing the WLP (see Unal et al., 2024 and Halim, 2024). Therefore, additional tests were conducted, with the primary variables being the splice length and the quantity of transverse reinforcement along the splice. The splice length was multiplied by 1.25 to account for overstrength and strain hardening of the longitudinal reinforcement, as is done in ACI 318-19 §18.10.2.3 for special walls, resulting in a splice length of $l_s = 1.25(1.3)l_d = 20$ in. The spacing of transverse reinforcement was reduced to 3 in. and 2 in. for the additional tests. Therefore, the resulting beam tests are referred to as B-S3-20 and B-S2-20. The beams were subjected to wind loading protocols that resulted in tensile and compressive strain demands for the spliced reinforcement that were the same as those expected for the outer layer of the CW-2 spliced rebars (see Halim et al., 2024). The test results showed that the lap splices failed at yield for the beam designed based on the minimum ACI 318-19 requirements (B-S6-16). The second beam (B-S3-20) failed during the WLP before reaching the peak (nonlinear) demand for the WLP. However, for the third beam (B-S2-20), the WLP was applied successfully without splice failure. It is noted that the T-beam tests represent a worst-case scenario for the wall tests since the tension

reinforcement for the beam tests consists of a single layer and, unlike the wall, where tension reinforcement consists of multiple layers (i.e., spice failure of the outer bars would not be expected to result in substantial strength loss, as it would be the T-beam tests). Therefore, splice performance in the wall tests was expected to be at least as good as the performance observed in the T-beam tests. Based on the T-beam splice tests, splice lengths for the test walls were calculated to be 10 in. and 20 in. long (l_s=1.25(1.3)l_d) for CW-1 and CW-2, respectively, with 2 in. spacing of transverse reinforcement. Similarly, seismic crossties (135-degree hook at one end, 90-degree at the other, referred to as 135-90 crossties herein) were provided around the spliced bars of the flange and the first layer web reinforcement to provide a corner of a U-bar or a crosstie for all the spliced bars with high expected tensile strain demands (longitudinal reinforcement located in the flange).

Since the wall tests were to be conducted on wall panels subjected to moment and shear at the top of the panel (versus cantilever walls, see Section 2.4), the spacing of transverse reinforcement above the splice region also needed to be determined. Models for buckling of reinforcement developed by Rodriguez et al. (1999), Moyer & Kowalsky (2003), Hilson et al. (2014), Motter et al. (2018), and Rodriguez and Iñiguez (2019) were used to determine the spacing of the transverse reinforcement above the spliced region. Based on analysis (see Appendix A), buckling of longitudinal reinforcement was expected to occur immediately above the splice in the flange during or right after the wind loading protocol was completed if a 6 in. spacing was used (the maximum spacing allowed, see prior discussion). Therefore, a 3 in. spacing of 135-90 crossties was used above the splice region within the flanges up to the height of the assumed plastic hinge length equal to one-half of the wall web length (L_p=l_w/2). Above the plastic hinge region, the spacing was increased to 6 inches, and the cross-ties were eliminated. Due to the lower strain demands for longitudinal web reinforcement, a spacing of 6 in. was used immediately above the

splice region for the wall web transverse reinforcement, and the crossties were not used. Elevation views of the flanges and web of CW-1 and CW-2 are shown in Figure 2-6 and Figure 2-7, respectively.

More detailed information on the calculation of the development length for the wall longitudinal reinforcement, including wall starter bars anchored into the footing and overlapping U-bars at wall edges and corners, can be found in Appendix B. The footings and the top caps were designed to sustain the load demands from the wall test without cracking or failure. Appendix C provides the dimensions and the reinforcement details of the footing and the top cap. Appendix D shows the fabrication of the test specimens.

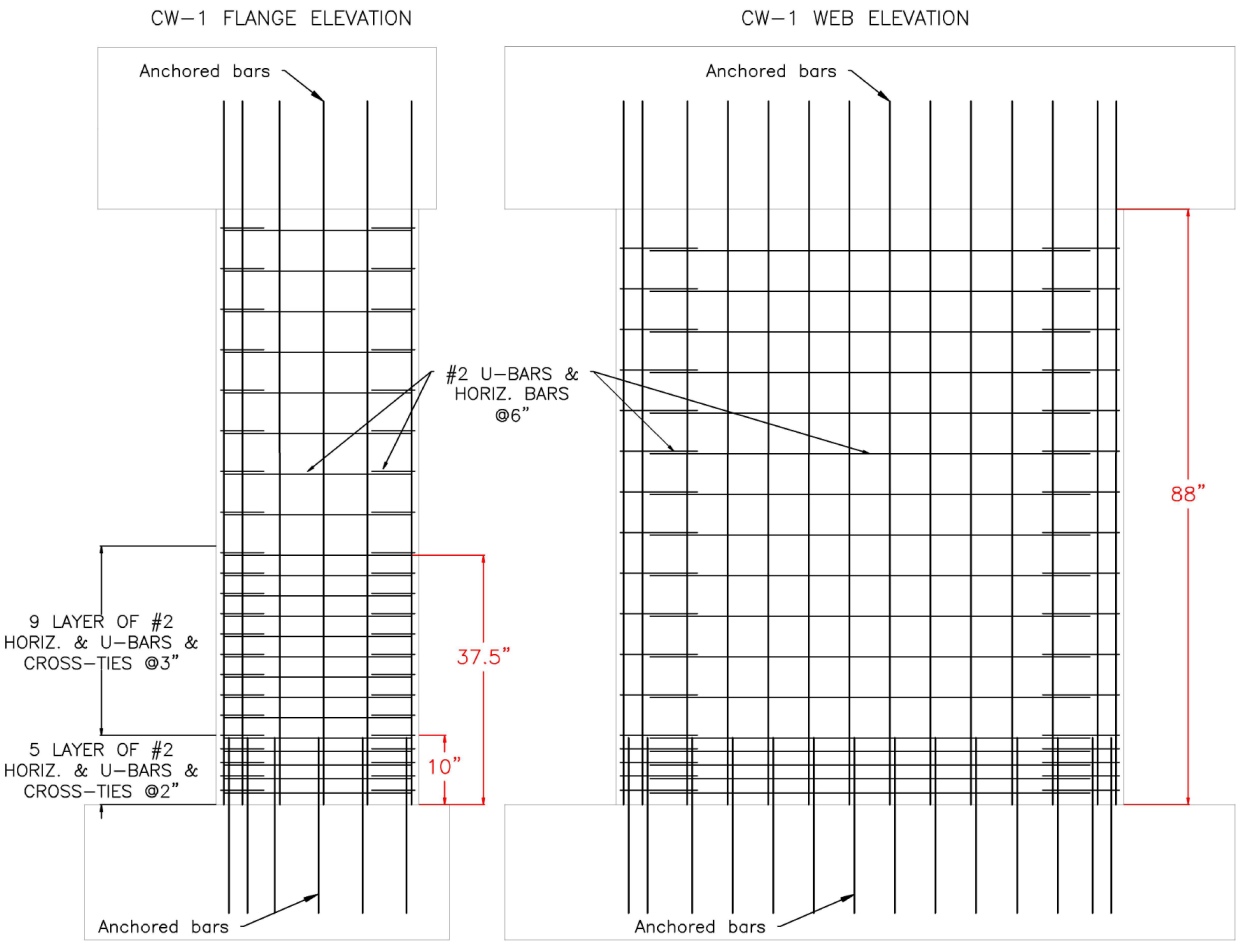

Figure 2-6: CW-1 flange and web elevations

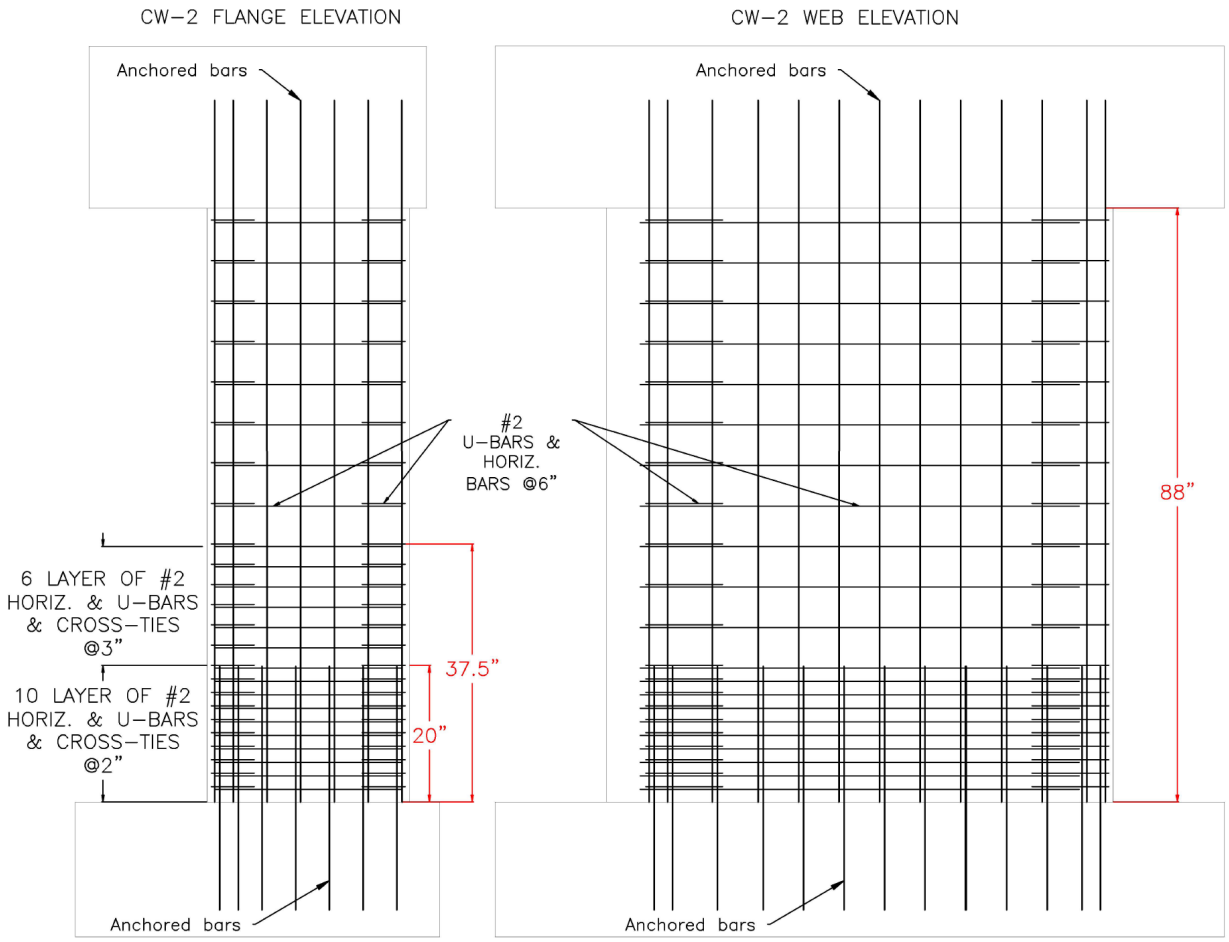

Figure 2-7: CW-2 flange and web elevations

2.2.2. Phase-II

After completing the Phase-I tests, two more C-shaped walls (CW-3 and CW-4) were constructed and tested in Phase-II of the research project. Test results from Phase-I showed that the wall with the lower longitudinal reinforcement ratio (CW-1, ρ_l = 0.75%) sustained no significant damage during the wind loading protocol, and subsequent testing of CW-1 under a seismic loading protocol resulted in substantial lateral strength loss (60%) at a plastic hinge rotation demand of 20 times yield plastic hinge rotation ($20\Theta_y$), whereas, for the WLP, the maximum rotation demands were $3\Theta_y$. Additional information on the test results for CW-1 is included in Chapters 3 and 4. Given

this excellent performance of CW-1, Phase-II tests focused on changes to CW-2 (ρ_l = 1.5%), which sustained significant damage at the flange edges during the WLP. Significant lateral strength loss (55%) was observed for CW-2 due to concrete crushing at the flange edges during the first cycle of SLP at a rotation demand of $4.5\Theta_y$. Based on the test results and the feedback from the PAC, the quantity (ρ_l of 1.5%) and distribution (uniform) of the longitudinal reinforcement was not changed.

The variables for the Phase-II tests were selected to be the axial load applied during the biaxial loading (Section 2.6) and the detailing at the flange boundaries (amount and the distribution of transverse reinforcement). Similar to the Phase-I tests, the gravity axial load applied during the in-plane lateral loading (parallel to the wall web) was held constant at 500 kips ($P_{IP} = 0.1A_g f'_c$). However, for the Phase-II tests, during the application of the biaxial loading, where the flange edges were under compression (Positions B and E, Figure 2-37), the axial load was decreased to $0.05A_g f'_c$ and $0.075A_g f'_c$ for CW-3 and CW-4, respectively, based on the range of wall axial load variation due to the presence of coupling beam shear forces over the wall height. More details regarding the gravity and the variation of the axial load during biaxial loading can be found in Section 2.6.1.

Apart from the variation of the axial load, the amount of confinement provided at the flange edges was increased for CW-3 and CW-4 compared to CW-2. A procedure similar to that developed by Wallace and Orakcal (2002) was used to calculate the length of the region where confinement should be provided at the flange boundary. This approach is also used in ACI 318-19 §18.10.6.2 for detailing the special boundary elements of structural walls. The requirements in ACI 318-19 are based on a simple displacement-based approach and an assumed compression strain limit for

unconfined concrete (ε_{cl} = 0.003, Figure 2-8) to calculate the region of the wall (*c''*, Figure 2-8) over which closely spaced transverse reinforcement is required. The approach used for this assessment is summarized in the following paragraphs.

The displacements at the top of the wall can be calculated using the curvature at the base of the wall as follows,

$$\delta_u = \theta_p h_w = (\phi_u l_p) h_w = \left(\frac{\varepsilon_{cu}}{c}\frac{l_w}{2}\right) h_w \tag{2.3}$$

$$\varepsilon_{cu} = 2\left[\frac{\delta_u}{h_w}\right]\left[\frac{c}{l_w}\right] \tag{2.4}$$

where c is the neutral axis depth computed for the concrete strain of 0.003, δ_u is the design displacement, h_w and l_w are the height and the length of the wall, respectively, ϕ_u is the ultimate curvature, Θ_p is the plastic rotations at the base of the wall, and ε_{cu} is the extreme fiber compressive strain associated with the ultimate curvature (ϕ_u). Using similar triangles (Figure 2-8), *c''* can be determined as,

$$c'' = c\left[1 - \frac{\varepsilon_{cl}}{\varepsilon_{cu}}\right] \tag{2.5}$$

By combining Equations 2.4 and 2.5, and using a value of 0.003 for ε_{cl}, the following relationship can be derived.

$$\frac{c''}{l_w} = \frac{c}{l_w} - \frac{1}{667(\delta_u/h_w)} \tag{2.6}$$

A value of 0.015 was proposed for δ_u/h_w by Wallace and Orakcal (2002) for seismic detailing of the walls; however, since the purpose of these tests is to investigate their behavior under wind demands, the use of a smaller value is appropriate. During the testing of CW-2, the plastic hinge

yield rotation ($\Theta_{y,CW2}$) was observed to be 0.003; therefore, the maximum WLP hinge rotation demand should be $3\Theta_y = 0.009$. Therefore, to reach $3\Theta_y$, the roof level drift (δ_u/h_w) can be estimated as approximately 0.01 (assuming the contribution of elastic deformations over the wall height to roof drift is small). Consequently, the wall length where confinement should be provided for test specimens CW-3 and CW-4 was calculated as:

$$c'' = c - 0.15l_w \tag{2.7}$$

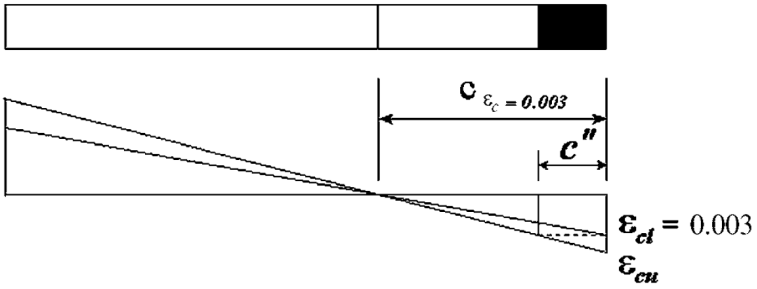

Figure 2-8: Wall strain distributions and the required length of confinement (Wallace and Orakcal, 2002)

For the calculation of $c_{\varepsilon c=0.003}$, the commercial software *CSICol* (CSI) was used. The WLP developed for the C-wall tests (see Section 2.6.2) included biaxial loading in which the walls were first displaced in the in-plane direction (parallel to the web) to specific inelastic rotation demands and then loaded in the out-of-plane direction (parallel to the flanges) to half of the probable moment capacities ($0.5M_{pr,OOP}$, calculated with $1.25f_y$ at ε_c=0.003, ACI 318-19). Therefore, the neutral axis depth at an extreme fiber concrete strain of 0.003 ($c_{\varepsilon c=0.003}$) was calculated under biaxial loading with axial loads of $0.05A_g f'_c$ and $0.075A_g f'_c$ for CW-3 and CW-4, respectively. After applying half of the probable moment capacity in the out-of-plane direction (flanges are under compression), sufficient in-plane moment demands ($M_{u,IN}$) were applied so that the resulting extreme fiber concrete strain was (ε_c) equal to 0.003. Table 2-2 summarizes the applied moment demands, the resulting neutral axis depth under biaxial loading (c_b), the distance from the extreme

compression fiber to the tension fiber ($l_{w,b}$), and the length of the flange edges that require confinement (*c"*). Results are summarized in Figure 2-9 and Figure 2-10 for CW-3 and CW-4, respectively. Based on this procedure, for CW-3, a single hoop was used to confine the region between the first two layers of flange longitudinal (vertical) reinforcement. Similarly, a longer hoop that confines the area between the first and the third layers of longitudinal (vertical) reinforcement was used, along with a 135-90 crosstie for the second layer of reinforcement for the flanges of CW-4. Figure 2-11 and Figure 2-12 show the cross-sectional details of Phase-II walls (CW-3 and CW-4, respectively), which have the same cross-section dimensions, and quantity and grade of longitudinal reinforcement as wall CW-2. The spacing of the transverse reinforcement over the splice region ($h \leq L_s$) and between the top of the splice and the height of the plastic hinge region ($L_s<h\leq L_p$) were not changed, i.e., values of 2 in. and 3 in. were used, respectively. However, above the plastic hinge region (h>Lp), the spacing was decreased from 6 in. to 4.5 in. to provide sufficient shear capacity calculated based on ACI 318-19 §11.5.4. Figure 2-13 shows the detailing provided at the flange edges of Phase-II walls.

Table 2-2: Summary of biaxial analysis

	CW-3	CW-4
Axial Load Ratio[(1)]	$0.05A_g f'_c$	$0.075A_g f'_c$
Axial Load (kips)	250	375
$M_{pr,IN}$ [(2)] (k-ft)	3516	3862
$M_{pr,OOP+y}$ [(3)] (k-ft)	1310	1330
$M_{u,IN}$ (k-ft) @ ε_c=0.003	3005	3340
$M_{u,OOP+y}$ (k-ft) @ ε_c=0.003	655	665
$M_{u,IN}$ / $M_{pr,IN}$	0.85	0.86
$M_{u,OOP+y}$ / $M_{pr,OOP+y}$	0.5	0.5
c_b [(4)] (in.)	15.1	18.9
$l_{w,b}$ [(5)] (in.)	80.0	78.6
$c_b - 0.15l_{w,b}$ (in.)	3.1	7.1

(1) Axial load ratios applied at Positions B and E (Figure 2-37)
(2) In-plane probable moment capacity calculated under the given axial load
(3) Out-of-plane probable moment capacity, flanges under compression
(4) Biaxial neutral axis depth
(5) Distance from the extreme compression fiber to the tension fiber

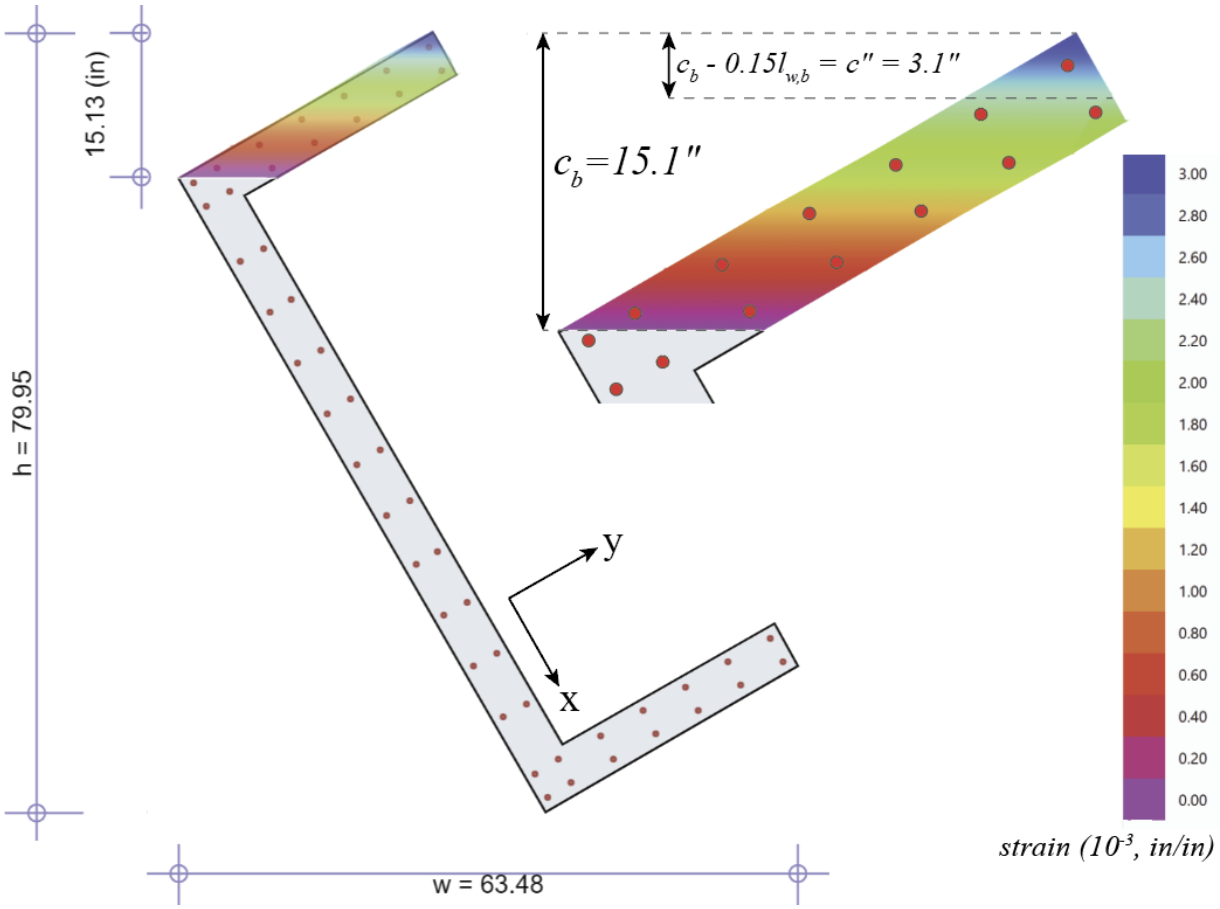

Figure 2-9: Biaxial analysis of CW-3, compressive strains, and the biaxial neutral axis depth

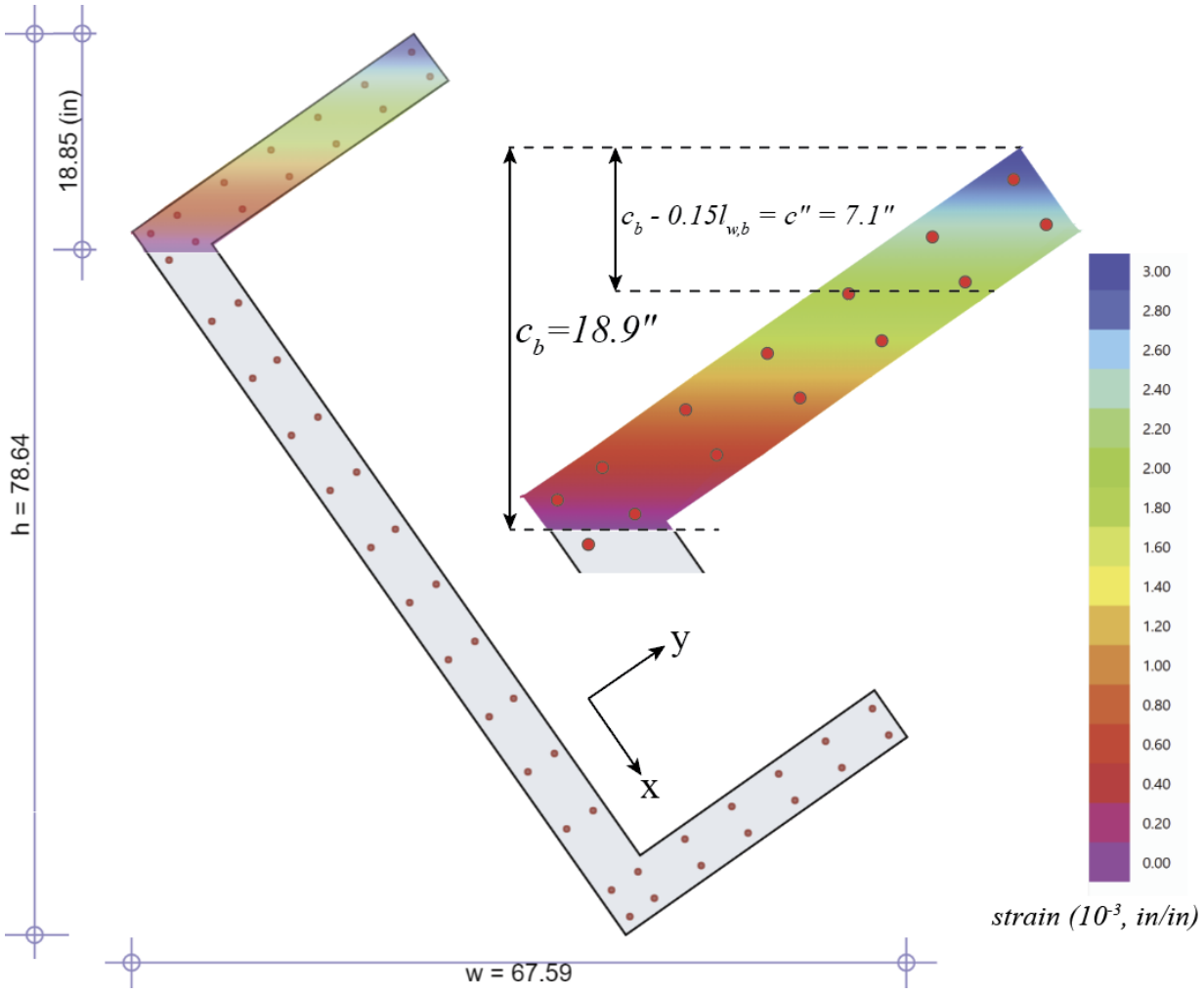

Figure 2-10: Biaxial analysis of CW-4, compressive strains, and the biaxial neutral axis depth

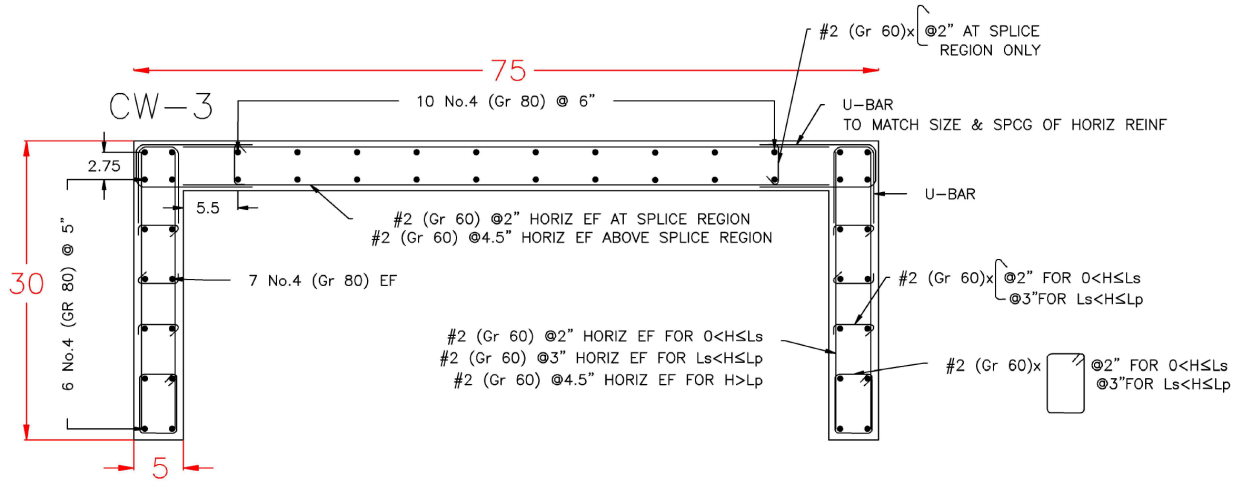

Figure 2-11: Cross-section of CW-3

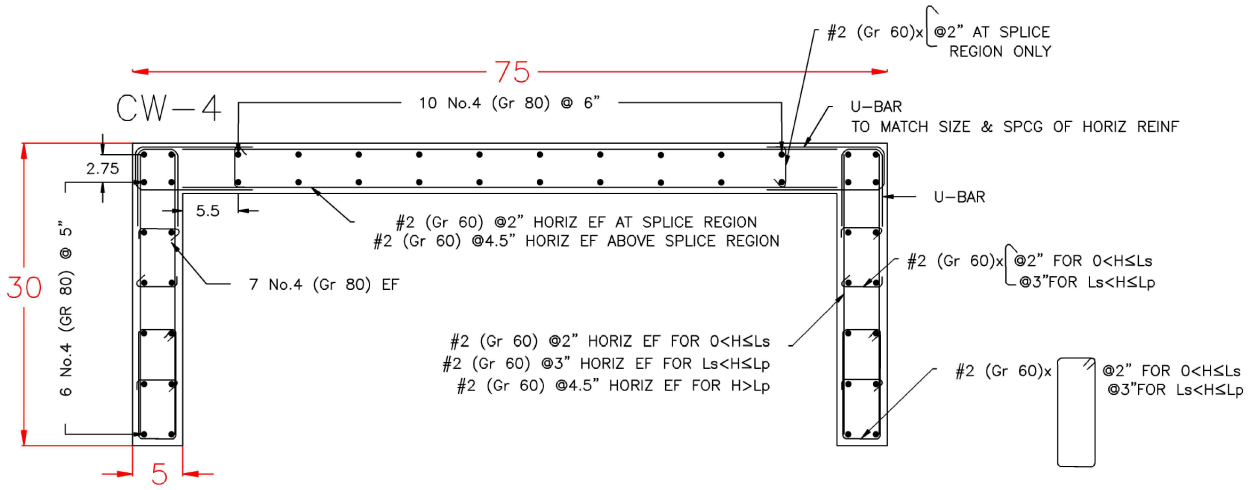

Figure 2-12: Cross-section of CW-4

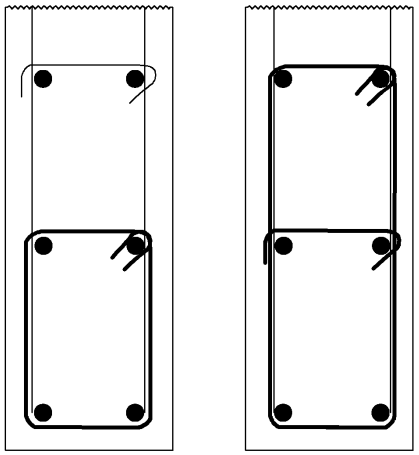

Figure 2-13: Flange edge detailing, CW-3 (left), CW-4 (right)

2.2.3. Test Matrix

The maximum shear stress in the in-plane loading direction during testing was limited to 4.25 times the square root of concrete nominal strength, i.e., $\nu_{Mpr,IN} = 4.25\sqrt{f'_c}$, for the walls with 1.5% reinforcement ratio (CW-2, CW-3, and CW-4) based on input from the PAC. The shear span ratio in the in-plane direction (SSR_{IN}) at probable moment capacity ($M_{pr,IN}$) was determined as $M_{pr,IN}$ / $V_{@Mpr,IN}(l_w)$ where $V_{@Mpr,IN}$ was calculated as the shear stress times the gross area ($\nu_{Mpr,IN}A_g$) resulting in $SSR_{IN} = 4.72$. To enable direct comparisons, the SSR_{IN} value was held constant for all test specimens. Therefore, for CW-1, a value of $2.60\sqrt{f'_c}$ was used for $\nu_{Mpr,IN}$. Similarly, the maximum shear stress in the out-of-plane direction when the flanges are under compression ($\nu_{Mpr,OOP+y}$) was limited to $3.50\sqrt{f'_c}$ at probable moment capacity ($M_{pr,OOP+y}$) based on input from PAC, which resulted in shear span ratios (SSR_{OOP}) of 4.80 and 5.75 for CW-1 and CW-2-3-4, respectively. The same SSR_{OOP} value was also used in the -y direction of the out-of-plane loading (web under compression). Therefore, $\nu_{Mpr,OOP-y}$ values were $1.77\sqrt{f'_c}$ and $2.42\sqrt{f'_c}$ for CW-1 and CW-2-3-4, respectively. Table 2-3 summarizes the test matrix of Phase-I and Phase-II tests.

Table 2-3: Test matrix

	CW-1	CW-2	CW-3	CW-4
Web Thickness, t_w (in.)	5			
Flange Thickness, t_f (in.)	5			
Web Length, l_w (in.)	30			
Flange Length, l_f (in.)	75			
Long. Reinf. Ratio, ρ_l (%)	0.75	1.5	1.5	1.5
Long. Reinf. Size	#3	#4	#4	#4
Long. Reinf. Grade	Grade 60	Grade 80	Grade 80	Grade 80
Axial load ratio (Pos. A and D)*	$0.1A_g f'_c$	$0.1A_g f'_c$	$0.1A_g f'_c$	$0.1A_g f'_c$
Axial load ratio (Pos. B and E)*	$0.1A_g f'_c$	$0.1A_g f'_c$	$0.05A_g f'_c$	$0.075A_g f'_c$
Axial load ratio (Pos. C and F)*	$0.1A_g f'_c$	$0.1A_g f'_c$	$0.1A_g f'_c$	$0.1A_g f'_c$
Reinf. Distribution	Uniform	Uniform	Uniform	Uniform
Flange Edge Detailing	Overlapping U-bars	Overlapping U-bars	Hoops	Hoops
Web Corner Detailing	Overlapping U-bars	Overlapping U-bars	Overlapping U-bars	Overlapping U-bars
Splice Length, l_s (in.)	10	20	20	20
ν_{Mpr} (Pos. A and D)*	$2.60\sqrt{f'_c}$	$4.25\sqrt{f'_c}$	$4.25\sqrt{f'_c}$	$4.25\sqrt{f'_c}$
ν_{Mpr} (Pos. B and E)*	$3.50\sqrt{f'_c}$	$3.50\sqrt{f'_c}$	$3.50\sqrt{f'_c}$	$3.50\sqrt{f'_c}$
ν_{Mpr} (Pos. C and F)*	$1.77\sqrt{f'_c}$	$2.42\sqrt{f'_c}$	$2.42\sqrt{f'_c}$	$2.42\sqrt{f'_c}$
SSR_{IN}	4.72	4.72	4.72	4.72
SSR_{OOP}	4.80	5.75	5.75	5.75

* Loading positions from Figure 2-37

2.3. Material Properties

2.3.1. Concrete

The concrete mix used for both the Phase-I and Phase-II tests was designed to have an 8000 psi strength on the day of testing, i.e., $f'_{c,expected}$ = 8000 psi. Therefore, a concrete design strength of 6000 psi mix (f'_c = 6000 psi) was used based on strength data provided by the supplier. Due to the small clear cover over longitudinal and boundary transverse reinforcement (<1 in.), a mix based on a maximum aggregate size of 3/8 in. was used. More details regarding the concrete mix can be found in Appendix E. Phase-I wall specimens (CW-1 and CW-2) were cast in February 2023. During casting, 4 in. diameter cylinder samples were collected to test the concrete strength at 7 days, 14 days, 28 days, and the day of the testing. For CW-1, testing was started approximately 120 days after concrete placement, whereas, for CW-2, testing was started approximately 210 days after concrete placement. Table 2-4 summarizes the concrete cylinder test results for CW-1 and CW-2 walls. The difference between the test day results of CW-1 and CW-2 was attributed to the fact that concrete from different trucks were used due to the total amount of concrete needed to cast the wall samples and the top caps simultaneously. Figure 2-14 shows the stress-strain curves obtained from the test day cylinder test results for CW-1 and CW-2.

Table 2-4: Concrete cylinder test results (Phase-I walls)

Sample	7 Days	14 Days	28 Days	Test Day CW-1	Test Day CW-2
1	6968 psi	8165 psi	8001 psi	7934 psi	10042 psi
2	6828 psi	8176 psi	9068 psi	7945 psi	10777 psi
3	-	-	7942 psi	8049 psi	10002 psi
4	-	-	-	-	10538 psi
Average	6898 psi	8170 psi	8337 psi	7976 psi	10340 psi

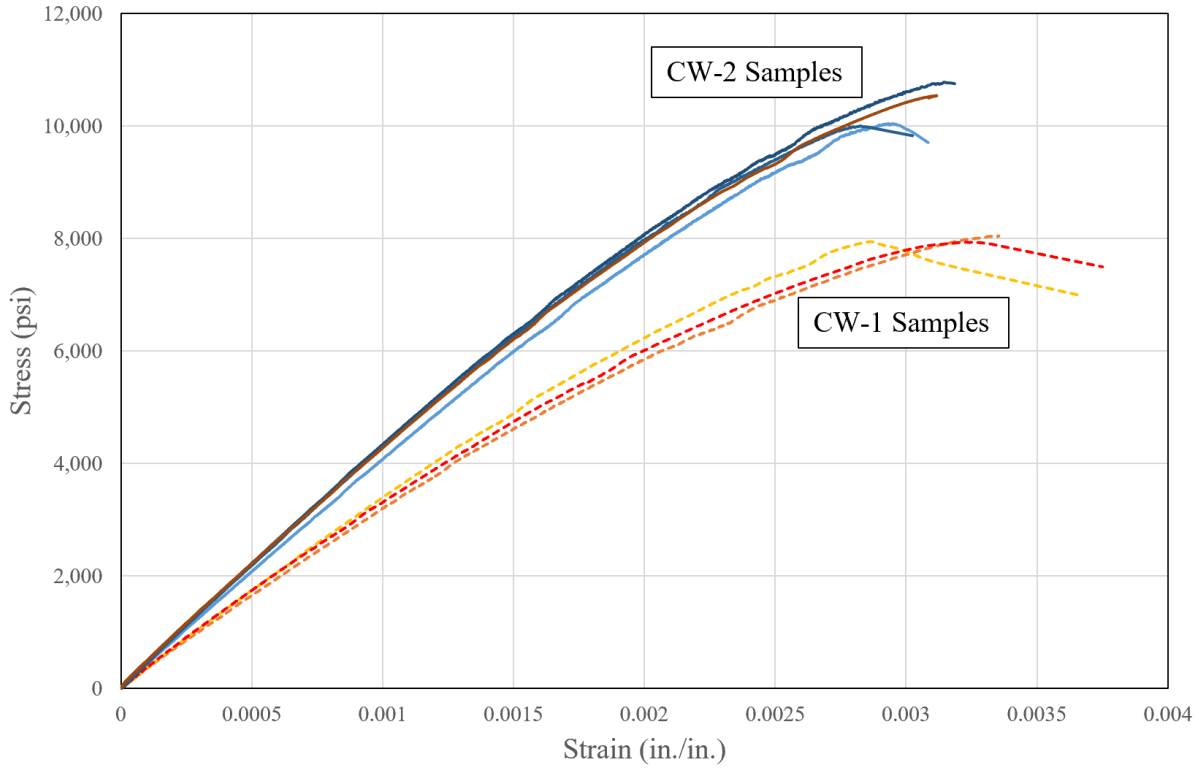

Figure 2-14: Test Day concrete stress-strain curves (Phase-I walls)

Like the Phase-I walls, concrete cylinder samples were also collected during the casting (April 2024) of Phase-II walls (CW-3 and CW-4). The samples were tested at 7 days and 28 days, and at test day, which was 28 days for CW-3 wall and 56 days for CW-4. It is noted that the cylinder tests were conducted at the beginning of testing and that testing typically required 4 to 5 days to complete. Unlike the Phase-I walls, concrete from the same truck was used to cast both test specimens. Therefore, the test day strengths of CW-3 and CW-4 were more similar to each other. Table 2-5 summarizes the cylinder test results. The stress-strain curves for the Phase-II walls were only measured at 28 days and are shown in Figure 2-15.

Table 2-5: Concrete cylinder test results (Phase-II walls)

Sample	7 Days	28 Days & Test Day CW-3	Test Day CW-4
1	7182 psi	8045 psi	7715 psi
2	6946 psi	7663 psi	8076 psi
3	6926 psi	8055 psi	8425 psi
4	-	7965 psi	8493 psi
Average	7018 psi	7932 psi	8177 psi

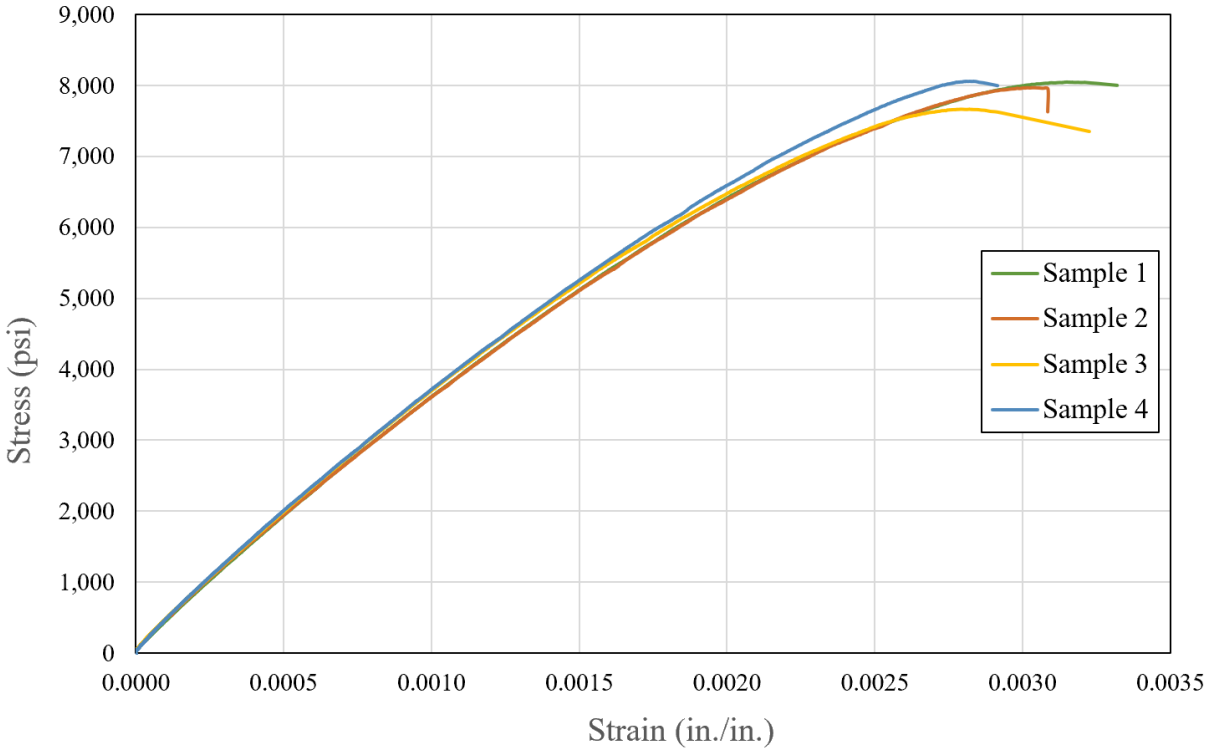

Figure 2-15: 28 Days concrete stress-strain curves (Phase-II walls)

The experimental concrete elastic modulus ($E_{c,exp}$), defined as the slope of a line drawn from zero stress to 40 percent of the compressive strength (ASTM C469), was calculated from Figures 2-14 and 2-15 and compared with the proposed values of E_c from ACI 318-19 (2019) for normal strength concrete (NSC) and ACI 363R (2010) for high strength concrete (HSC, f'_c>6000 psi) in Table 2-6. The equations for E_c for NSC and HSC are shown in Equations 2.8 and 2.9, in which the average values from Table 2-4 and Table 2-5 were used for f'_c. The comparisons between the experimentally calculated values and the values determined from Equations 2.8 and 2.9 show that, although the high-strength concrete equation recommended by ACI 363R provided a better estimate, the experimental concrete elastic moduli determined from the stress-strain relations were 27%, 16%, and 18% lower for CW-1, CW-2, and CW-3, respectively. One reason for the lower stiffness values could be the use of 3/8 in. aggregate in the mix design. The strain data was not measured for the test day cylinders of CW-4.

$$E_c = 57000\sqrt{f'_c}\ (in\ psi)\ ACI\ 318-19, NSC \tag{2.8}$$

$$E_c = 40000\sqrt{f'_c} + 10^6\ (in\ psi)\ ACI\ 369R-10, HSC \tag{2.9}$$

Table 2-6: Average concrete modulus of elasticity at the test day

	CW-1	CW-2	CW-3
E_c, ACI 318-19	5090 ksi	5796 ksi	5076 ksi
E_c, ACI 363R	4572 ksi	5067 ksi	4562 ksi
$E_{c,exp}$	3316 ksi	4260 ksi	3725 ksi

2.3.2. Reinforcement

No.3 ASTM A706 (ASTM A706/A706M-22, 2022) Grade 60 (nominal yield strength of 60 ksi) and No.4 A706 Grade 80 (nominal yield strength of 80 ksi) deformed bars were used for the longitudinal reinforcement of CW-1 and CW-2-3-4, respectively. Since deformed bars smaller than No.3 bars are not produced in the United States, 6 mm (d_b = 0.24 in.) deformed bars that were used for the transverse reinforcement of the walls were imported from Australia. Three or four samples for all the bar sizes were tested using the test setup shown in Figure 2-26 to measure the mechanical properties of the reinforcement. Figures 2-17, 2-18, and 2-19 show the stress-strain relationships of the reinforcement, and the tested material properties are summarized in Tables 2-7, 2-8, and 2-9 for #3, #4, and 6 mm bars, respectively.

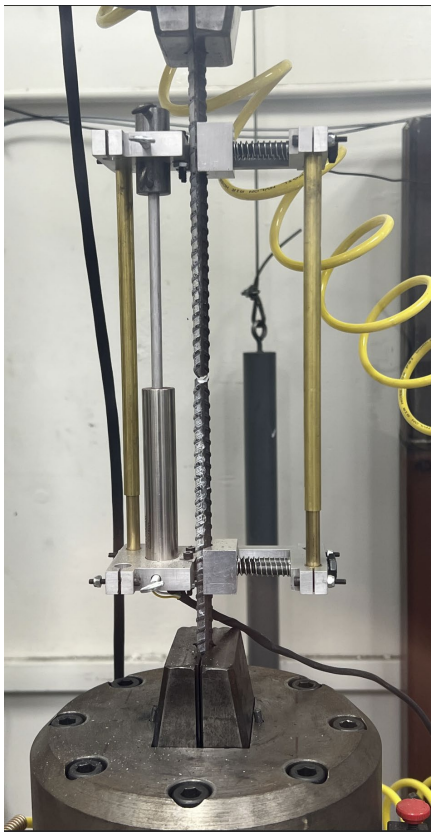

Figure 2-16: Steel reinforcement tension test setup

Table 2-7: Steel reinforcement tensile stress-strain properties of #3 Grade 60 bars

	$f_{y,test}$ (ksi)	ε_y	f_{peak} (ksi)	f_{rup} (ksi)	ε_{rup}
Sample 1	68.3	0.0024	101.5	83.3	0.10
Sample 2	71.3	0.0025	101.0	77.1	0.12
Sample 3	75.6	0.0026	106.5	87.8	0.16
Average	71.7	0.0025	103	82.7	0.13

Table 2-8: Steel reinforcement tensile stress-strain properties of #4 Grade 80 bars

	$f_{y,test}$ (ksi)	$\varepsilon_{y,test}$	$f_{u,test}$ (ksi)	$f_{rup,test}$ (ksi)	$\varepsilon_{rup,test}$
Sample 1	85.3	0.0029	109.7	78.5	0.16
Sample 2	85.0	0.0029	109.7	78.1	0.15
Sample 3	84.5	0.0029	110.0	79.2	0.14
Sample 4	84.5	0.0029	111.0	81.8	0.16
Average	84.8	0.0029	110.1	79.4	0.15

Table 2-9: Steel reinforcement tensile stress-strain properties of 6 mm deformed bars

	$f_{y,test}$ (ksi)	$\varepsilon_{y,test}$	$f_{u,test}$ (ksi)	$f_{rup,test}$ (ksi)	$\varepsilon_{rup,test}$
Sample 1	70.0	0.0024	76.9	58.7	0.04
Sample 2	67.0	0.0023	74.7	56.6	0.11
Sample 3	69.0	0.0024	77.2	58.5	0.06
Sample 4	68.8	0.0024	77.0	61.8	0.06
Average	68.7	0.0024	76.5	58.9	0.07

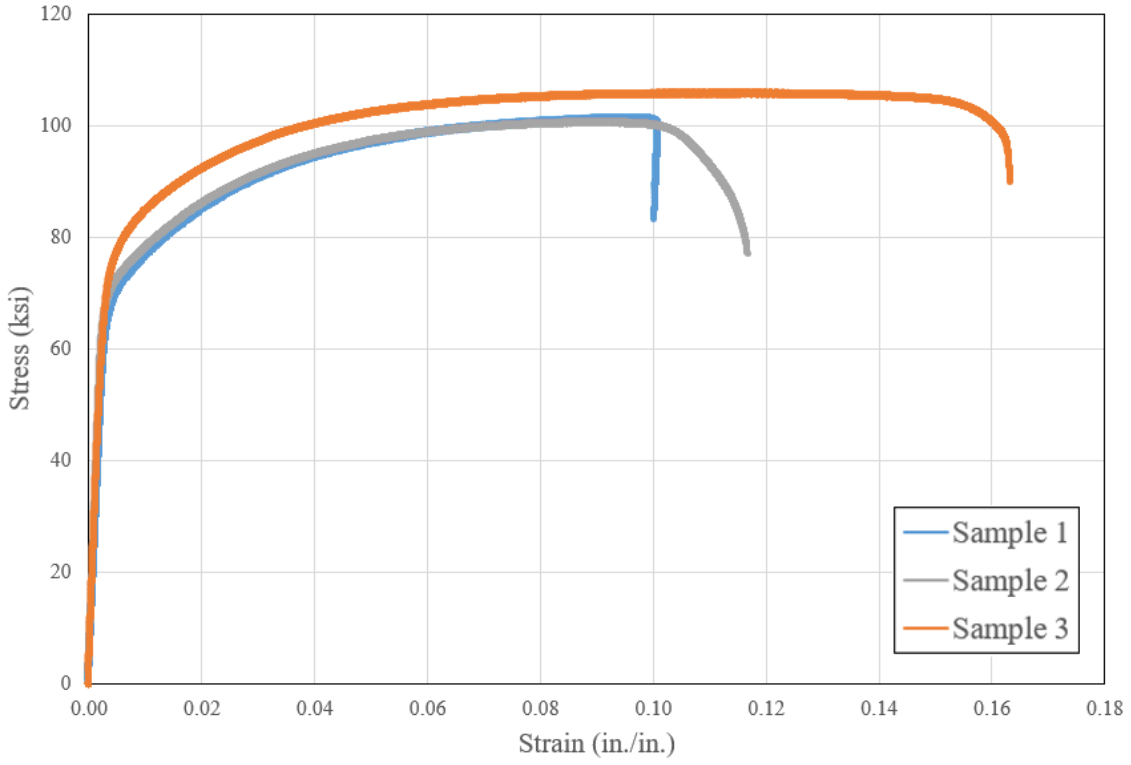

Figure 2-17: Steel reinforcement tensile stress-strain relationship of #3 Grade 60 bars

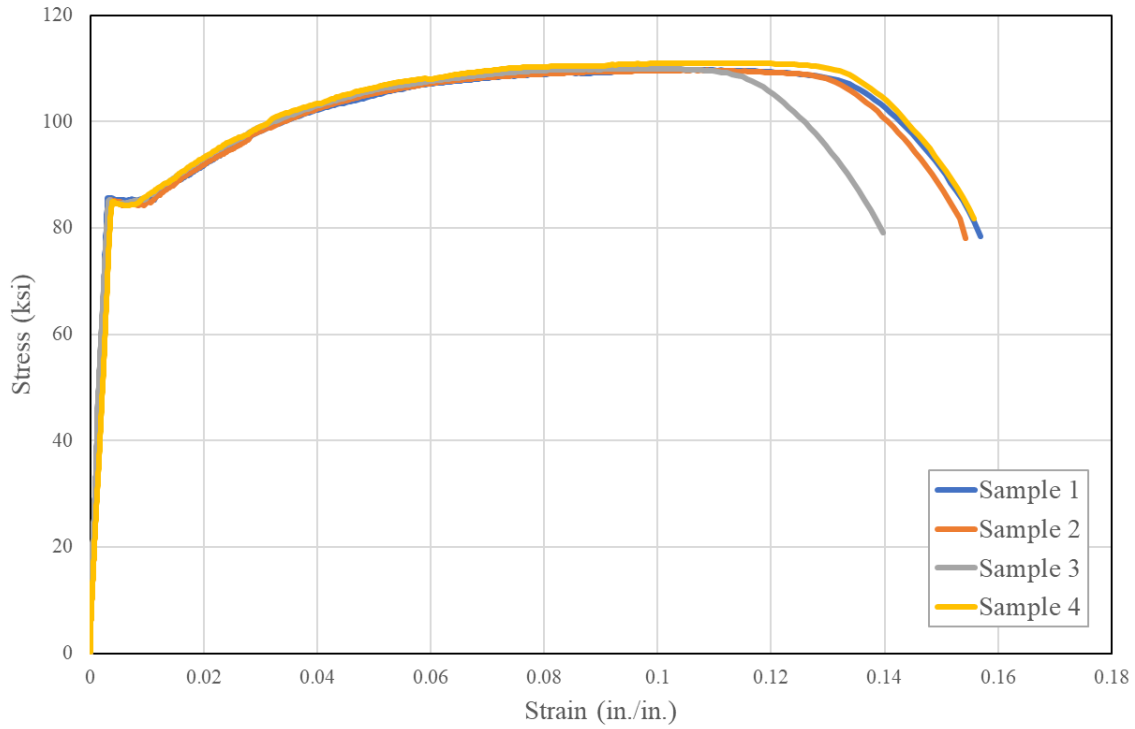

Figure 2-18: Steel reinforcement tensile stress-strain relationship of #4 Grade 80 bars

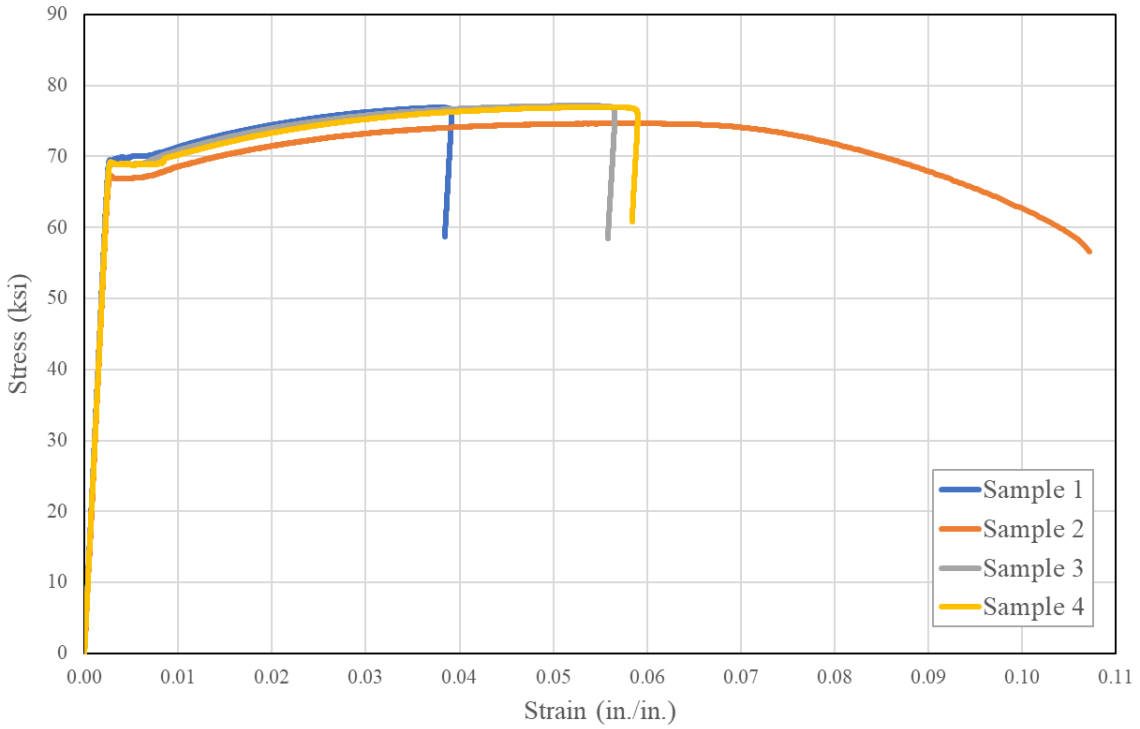

Figure 2-19: Steel reinforcement tensile stress-strain relationship of 6 mm deformed bars

2.4. Test Setup

The test setup used for the experiments (see Figure 2-20) was capable of applying both moments and shear at the top of the wall in both the in-plane (x-dir., parallel to the web) and in the out-of-plane directions (y-dir., parallel to the flanges). The in-plane moments were applied using the two vertical actuators (Actuators 2 and 3, Figure 2-21), and in-plane shear was applied using a horizontal actuator (Actuator 1). These actuators were connected to a structural steel loading beam that the specimens were attached to through the top cap using high-strength post-tensioning Dywidag bars. The specimens were attached to the steel beam at the centroid of the top cap, which was also aligned with the center of mass of the walls. Using these three actuators and the shear span ratio (SSR) of 4.72 (Table 2-3), the moment demand at the top of each wall (88 in. above the footing) when the base of the wall reaches the probable moment capacity (M_{pr}) can be calculated as:

$$M_{base} = M_{pr} = SSR \times V \times L_w$$

$$M_{top} = M_{base} - V \times 88\ in. = M_{base} - \frac{M_{base}}{4.72 \times 75\ in.} \times 88\ in. \tag{2.10}$$

$$M_{top} = 0.75 M_{base} = 0.75 M_{pr}$$

Whereas two horizontal actuators (Actuators 4 and 5, Figure 2-22) were used to apply out-of-plane (OOP) shear loads, one vertical actuator (Actuator 6) was used for the OOP moment application (at the top of the specimen). Applying the in-plane shear loads through the center of the mass of the C-shaped specimens resulted in eccentric loading with the shear center of the C-shaped specimens. Actuators 4 and 5 also resisted the torsional moment demands during the in-plane loading, which resulted from this eccentricity. The gravity axial load was applied through four 125

kips capacity (each) hydraulic jacks located at the top of the top cap. These jacks were connected to the strong floor through steel spreader beams (Figure 2-23).

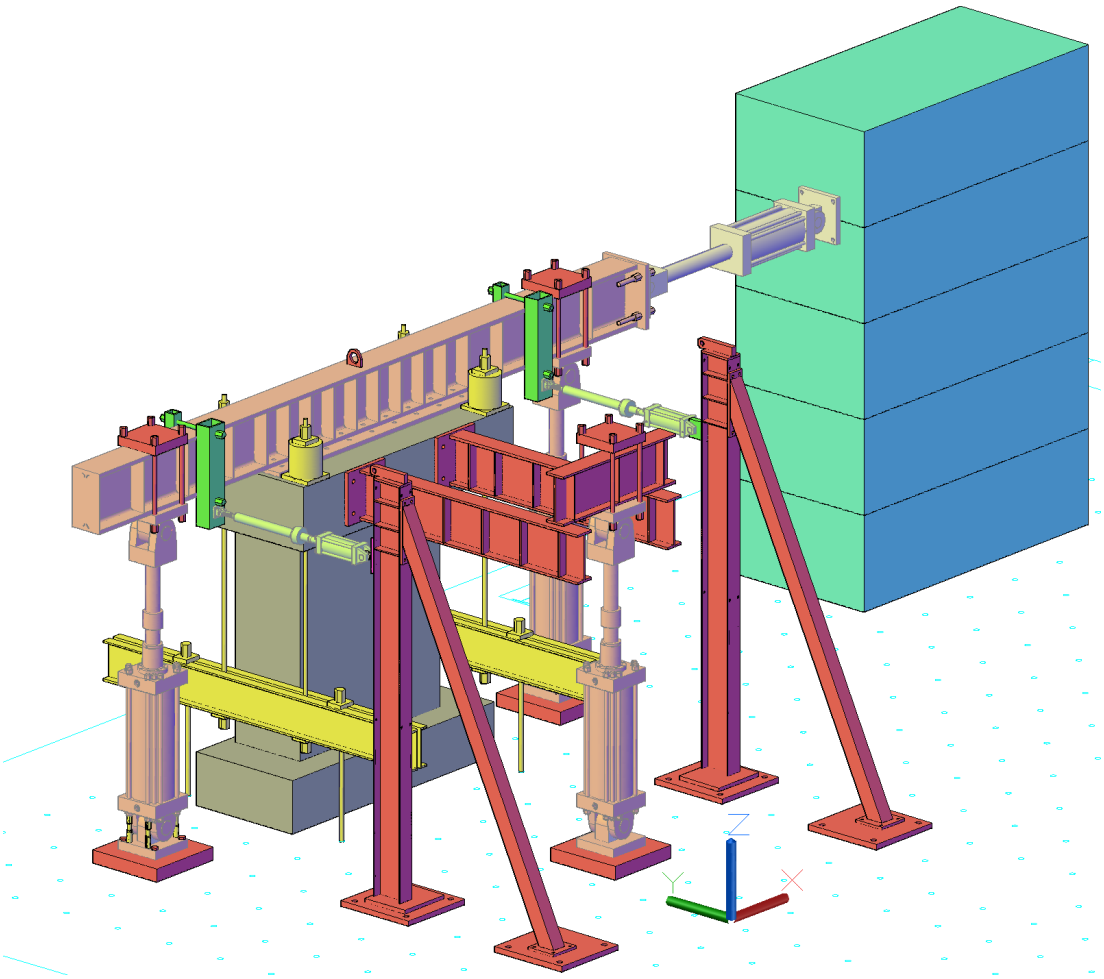

Figure 2-20: Isometric view of the test setup

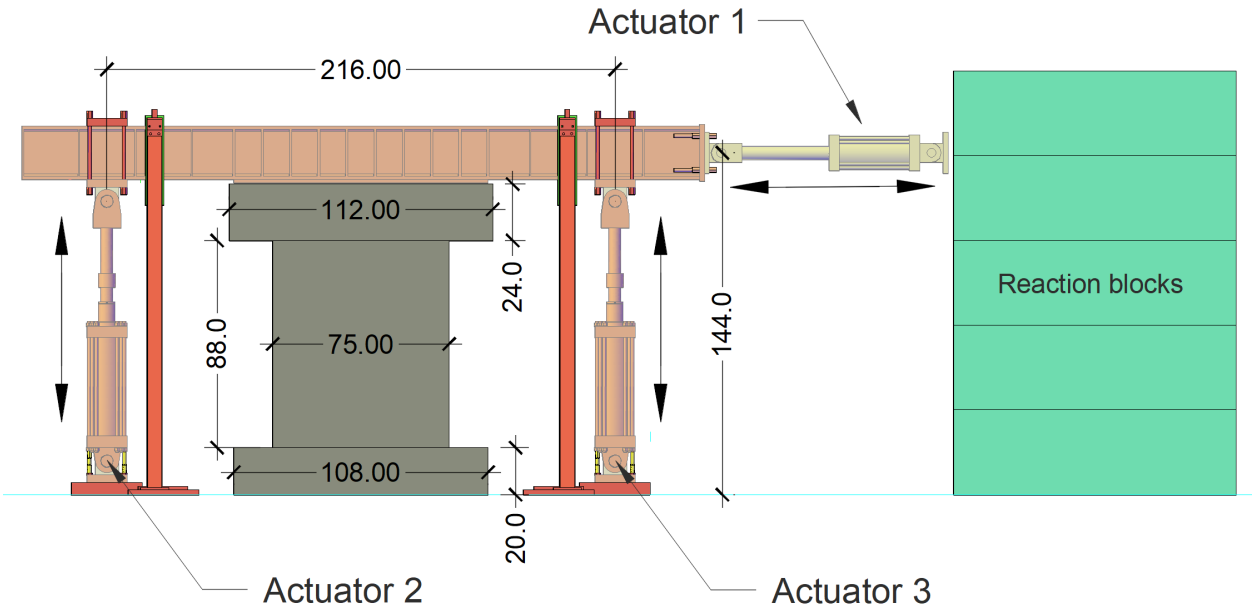

Figure 2-21: In-plane loading actuators only (Dimensions are in inches)

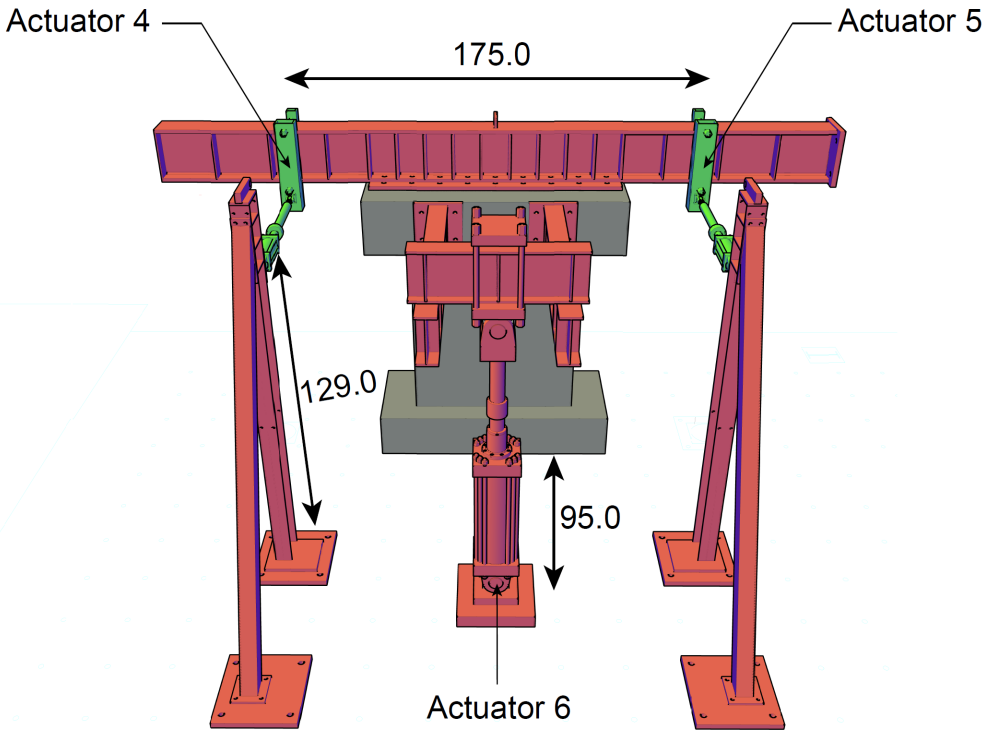

Figure 2-22: Out-of-plane loading actuators only (Dimensions are in inches)

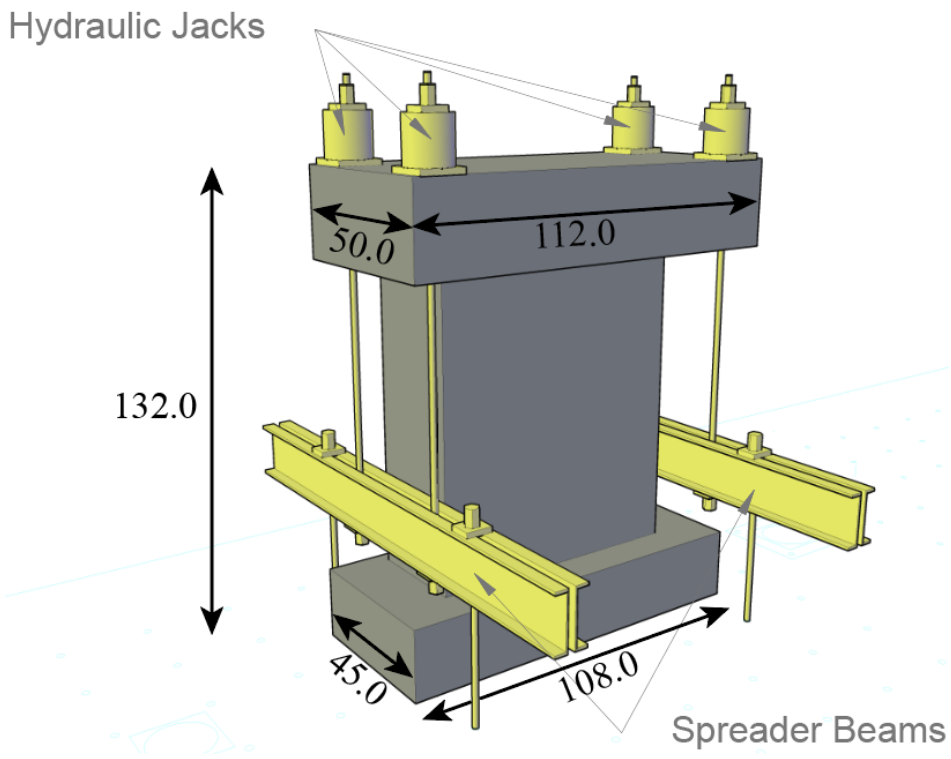

Figure 2-23: Axial load application (Dimensions are inches)

2.5. Instrumentation

2.5.1. Linear Variable Differential Transformers (LVDTs)

Each test specimen was instrumented with more than 60 linear variable differential transformers (LVDTs). For Phase-I walls (CW-1 and CW-2), 62 LVDTs were used. This number was increased to 65 and 67 for CW-3 and CW-4, respectively. The LVDTs were used to measure the wall flexural deformations, shear deformations, slip-extension at the wall-footing interface, shear sliding displacements, lateral displacements both in the in-plane and out-of-plane directions of the wall, top cap, and the footing, and the uplift of the footing from the laboratory strong floor. Also, four LVDTs (control sensors) were used to calculate the plastic hinge rotations to control the test displacement demands. Table 2-10 summarizes the total number of LVDTs used. Figures 2-24,

2-25, and 2-26 illustrate the locations of these LVDTs. Figure 2-27 shows the distances of the control sensors from the concrete surface both in the x- and y-directions. A range of values is given due to slight differences in the exact locations of the LVDTs between the walls. Similarly, Figure 2-28 shows the locations of the vertical LVDTs with respect to the flange edges and the web corners, and the horizontal distances to the concrete surface. The range of values represents the differences due to different walls and also the different layers of LVDTs along the height of the wall.

Table 2-10: Total number of LVDTs

	Total # of LVDTs
Flexural deformations	26[(1)]
Shear deformations	10
Slip-Extension	6
Lateral displacements	10
Shear Sliding displacements	2
Footing uplift	4[(2)]
Plastic hinge rotations	4

[(1)] 30 for CW-3 and 32 for CW-4
[(2)] 3 for CW-3 and CW-4

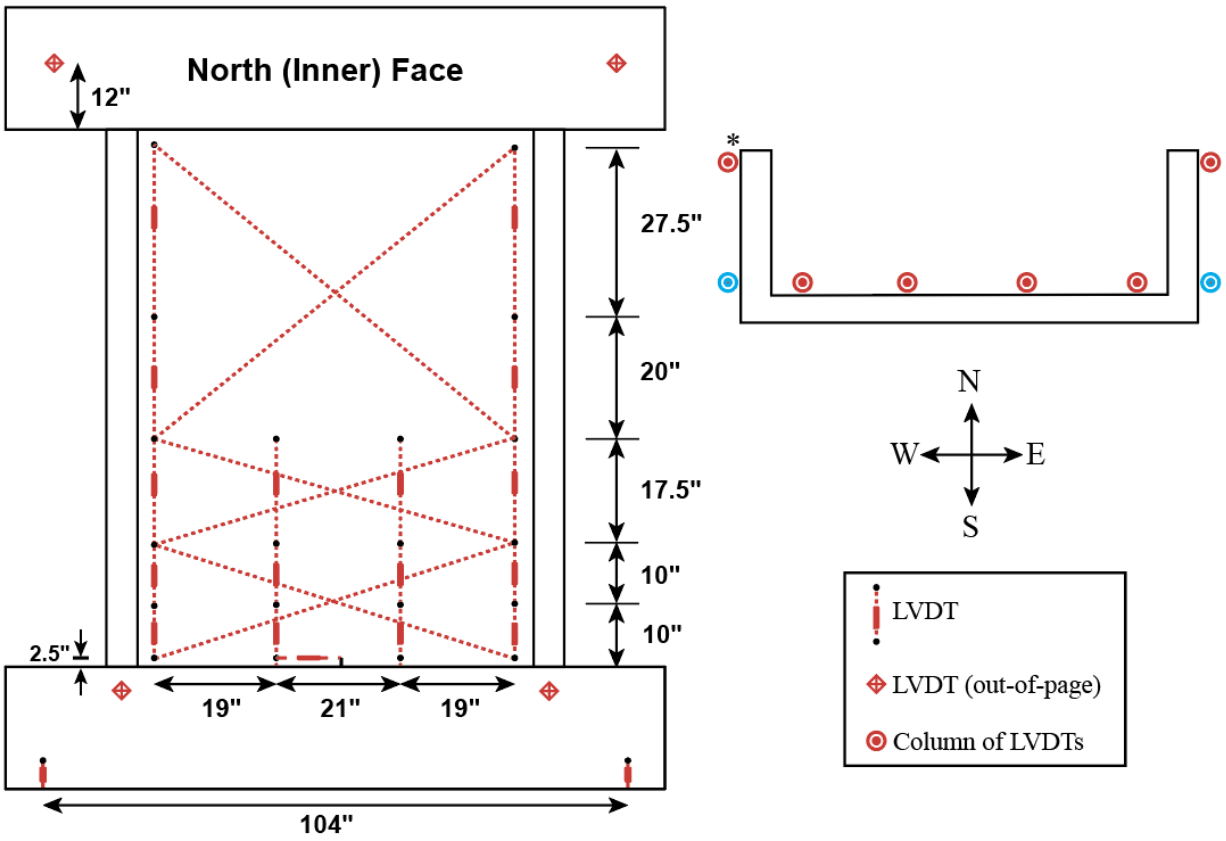

Figure 2-24: LVDT layout (Web inner surface)

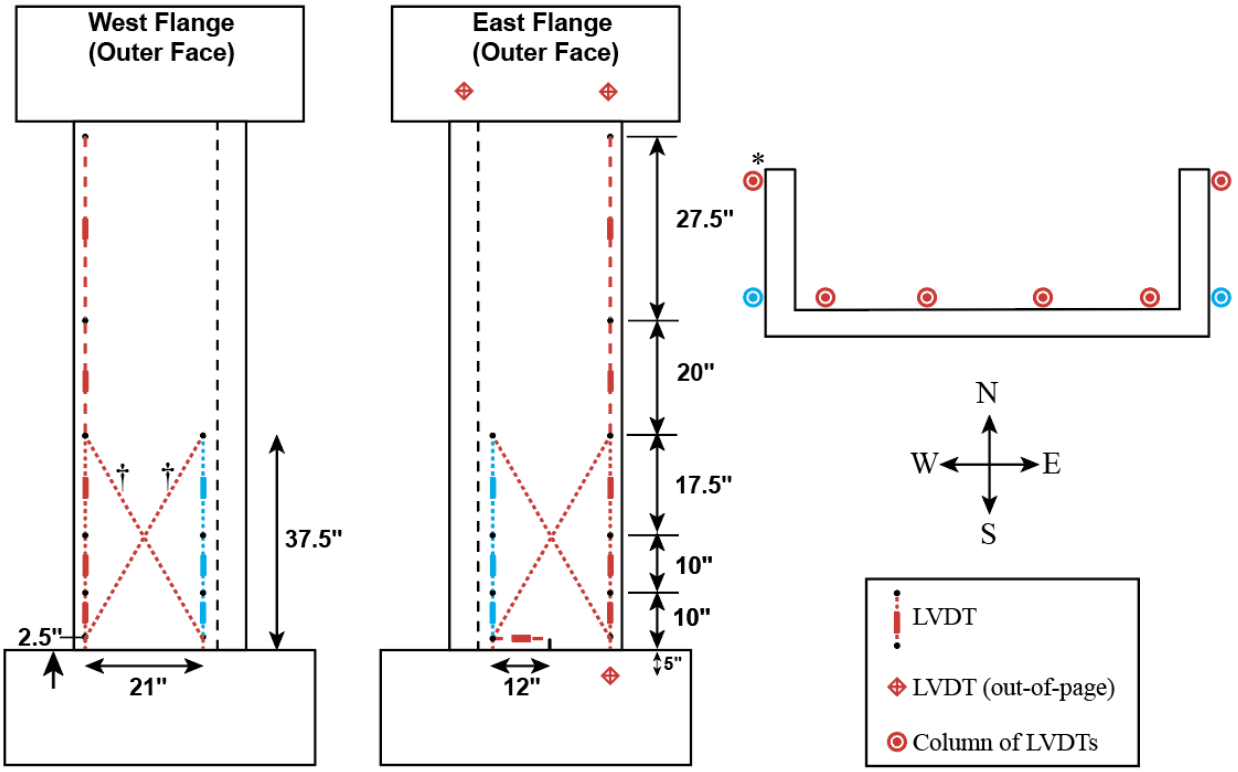

* This column of LVDTs for CW-1 was located in the inside face of the west flange

† These diagonal LVDTs were attached to the inside face of the west flange

These column of LVDTs were only used for Phase-II walls

Figure 2-25: LVDT layout (flange outer surfaces)

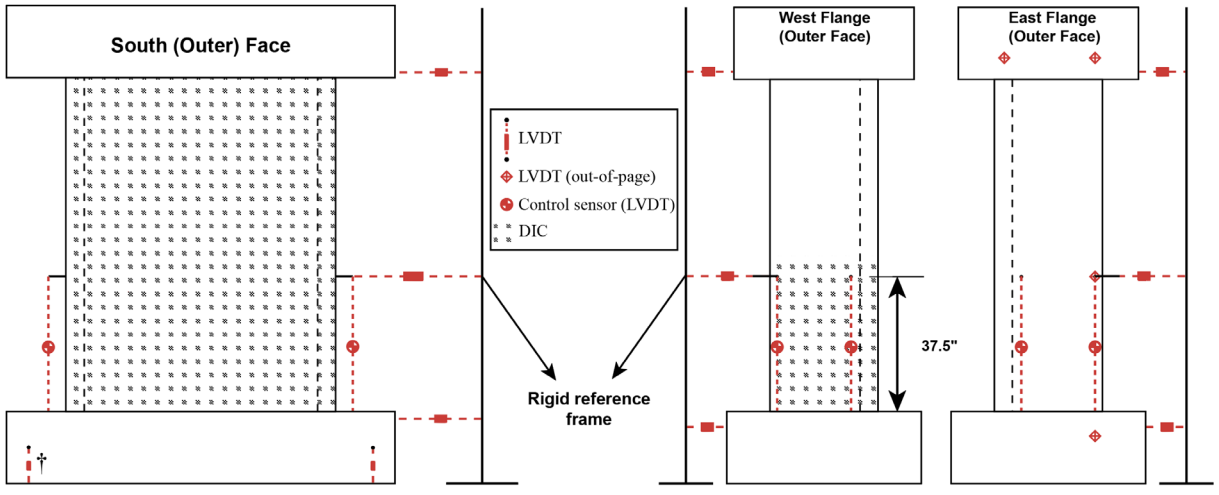

† Only used for CW-1 and CW-2

Figure 2-26: LVDT layout (control sensors and lateral displacements)

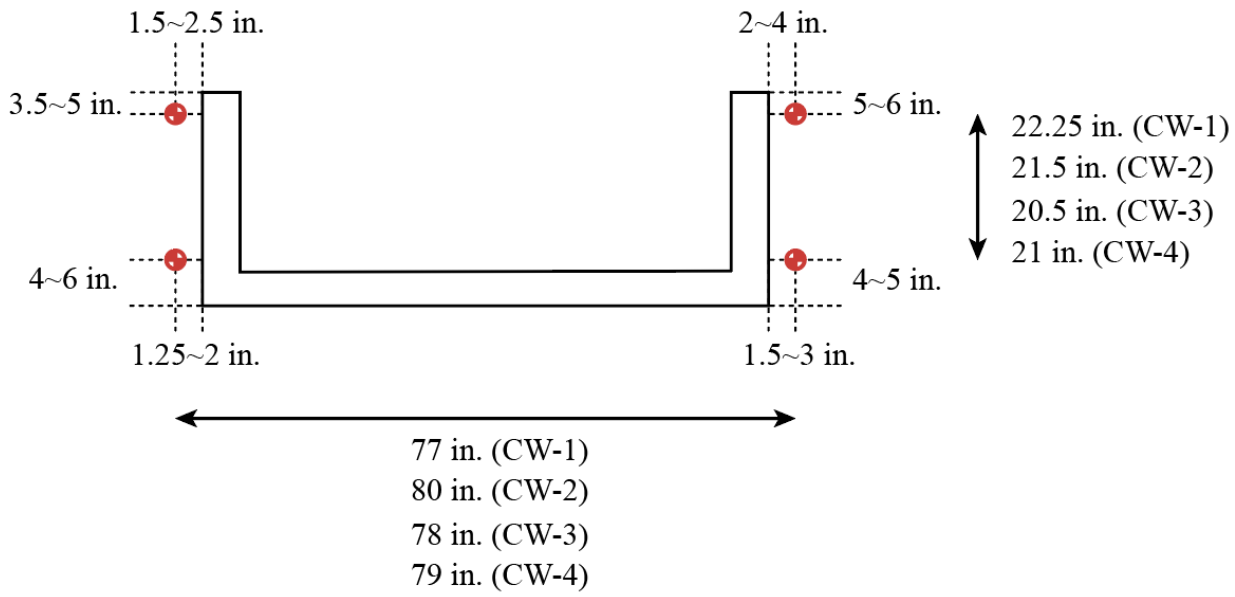

Figure 2-27: Distances of the control sensors from the concrete surface, flange edges, and the flange-web corners

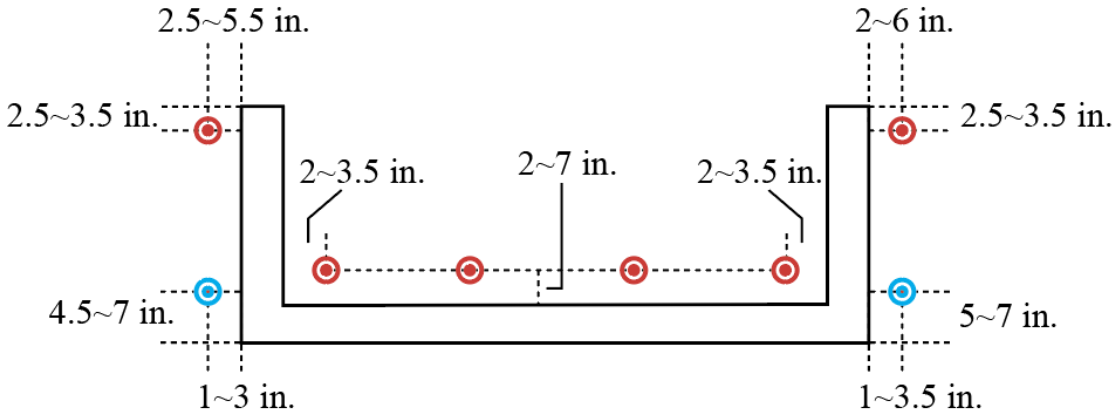

Figure 2-28: Distance of the vertical LVDTs from the concrete surface, flange edges, and the flange-web corners

2.5.2. Strain Gauges

For Phase-I walls, 32 strain gauges were used for each wall at various locations to measure the strains of longitudinal reinforcement, U-bars, cross-ties, and transverse reinforcement for the flanges and the web. After the Phase-I experiments, it was found that most of the strain gauges mounted on the 6 mm rebars were not functioning correctly. Therefore, for the Phase-II specimens, the number of strain gauges was decreased to 13. Figure 2-29 through Figure 2-32 illustrate the locations of the strain gauges for Phase-I and Phase-II walls.

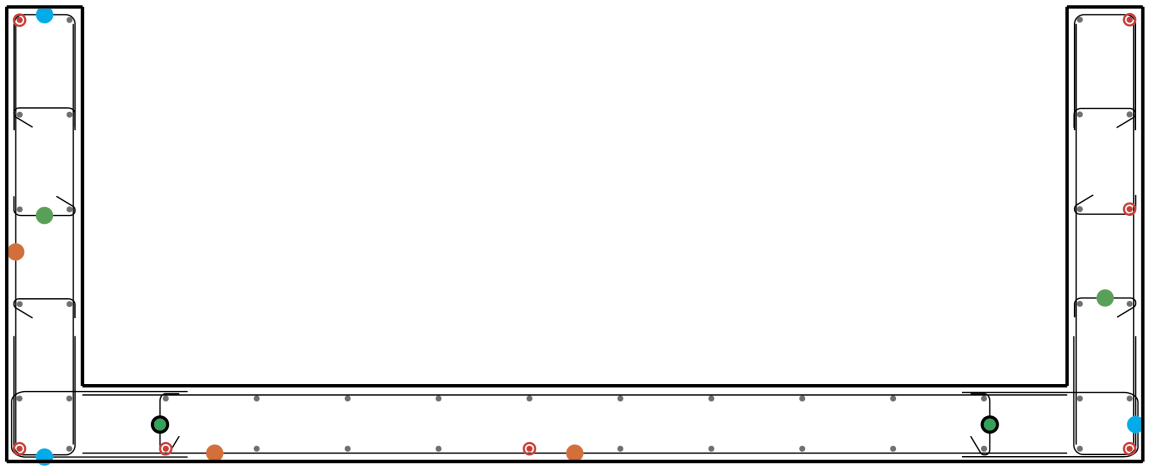

Figure 2-29: CW-1 strain gauge layout

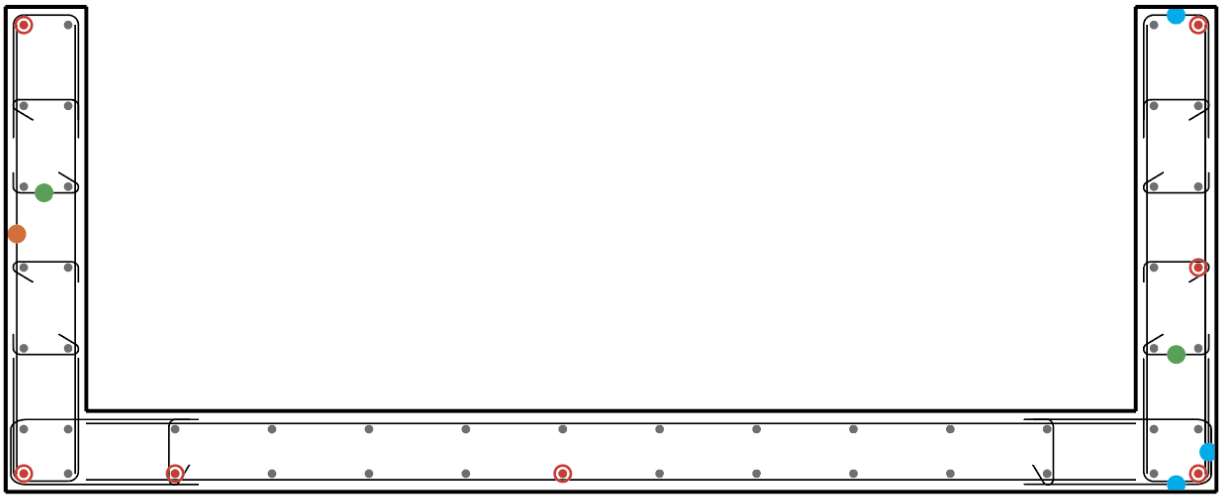

Strain gauges at the longitudinal rebars, 3” and 21” above the footing (also at 37.5” for the 4 corner bars)

Strain gauges at the U-bars, 10” and 20” above the footing

Strain gauges at flange cross-ties, 10”, 14” and 20” above the footing

Strain gauges at the transverse reinforcement, 10” and 20” above the footing

Figure 2-30: CW-2 strain gauge layout

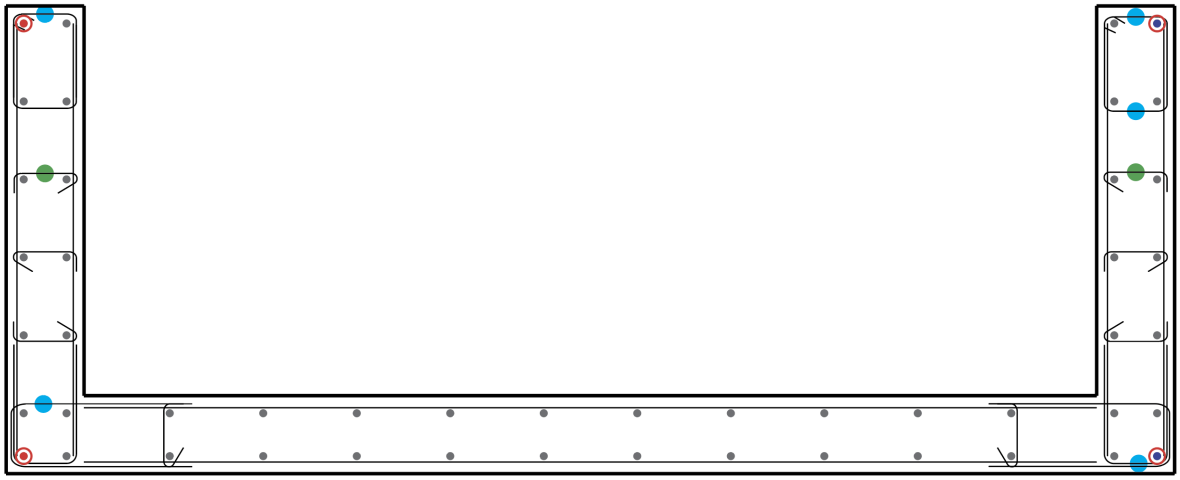

Strain gauges at the west flange longitudinal rebars, 3” and 21” above the footing

Strain gauges at the east flange longitudinal rebars, 21” above the footing

Strain gauges at the hoops, 5” above the footing

Strain gauges at flange cross-ties, 5” above the footing

Figure 2-31: CW-3 strain gauge layout

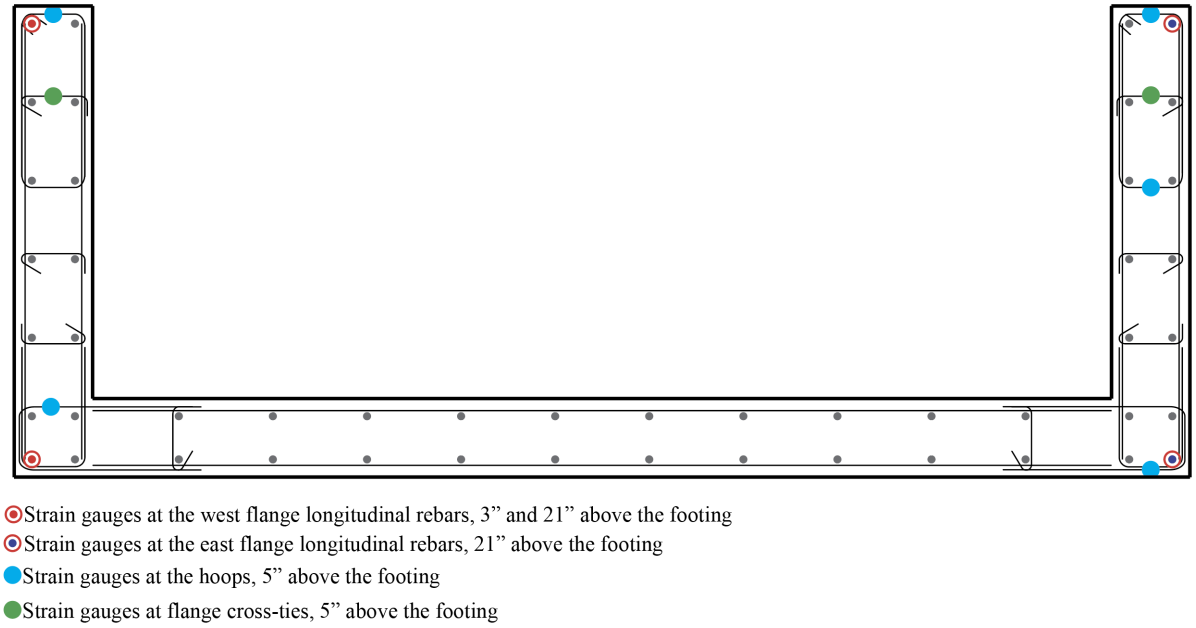

Figure 2-32: CW-4 strain gauge layout

2.5.3. Digital Image Correlation (DIC)

Digital image correlation (DIC) is a method to calculate the surface displacements of a solid object by tracking a pattern in a sequence of images. By using DIC, the surface displacements and the strains of the test specimens were calculated using a series of pictures and an open-source software called DICe. Although this method does not require any physical instrumentation attached to the test specimen, which makes it more advantageous compared to LVDTs, it is highly dependent on the surface damage of the specimens. After the cover spalling, the displacements obtained by this method are not reliable.

The outer surfaces of the web and the west flange of each specimen were painted with random patterns of black shapes (Figure 2-33). The painting was done to keep the size of each random shape to be at least 5-by-5 pixels and a maximum of 15-by-15 pixels to be able to get the maximum amount of information from surface cracking and displacements. Three high-resolution cameras

were used to take the DIC images while testing the Phase-I walls. While two cameras were used to take pictures of the web of the specimens, the other one was used for the west flange. For Phase-II, only one camera was used per web and flange (Figure 2-34).

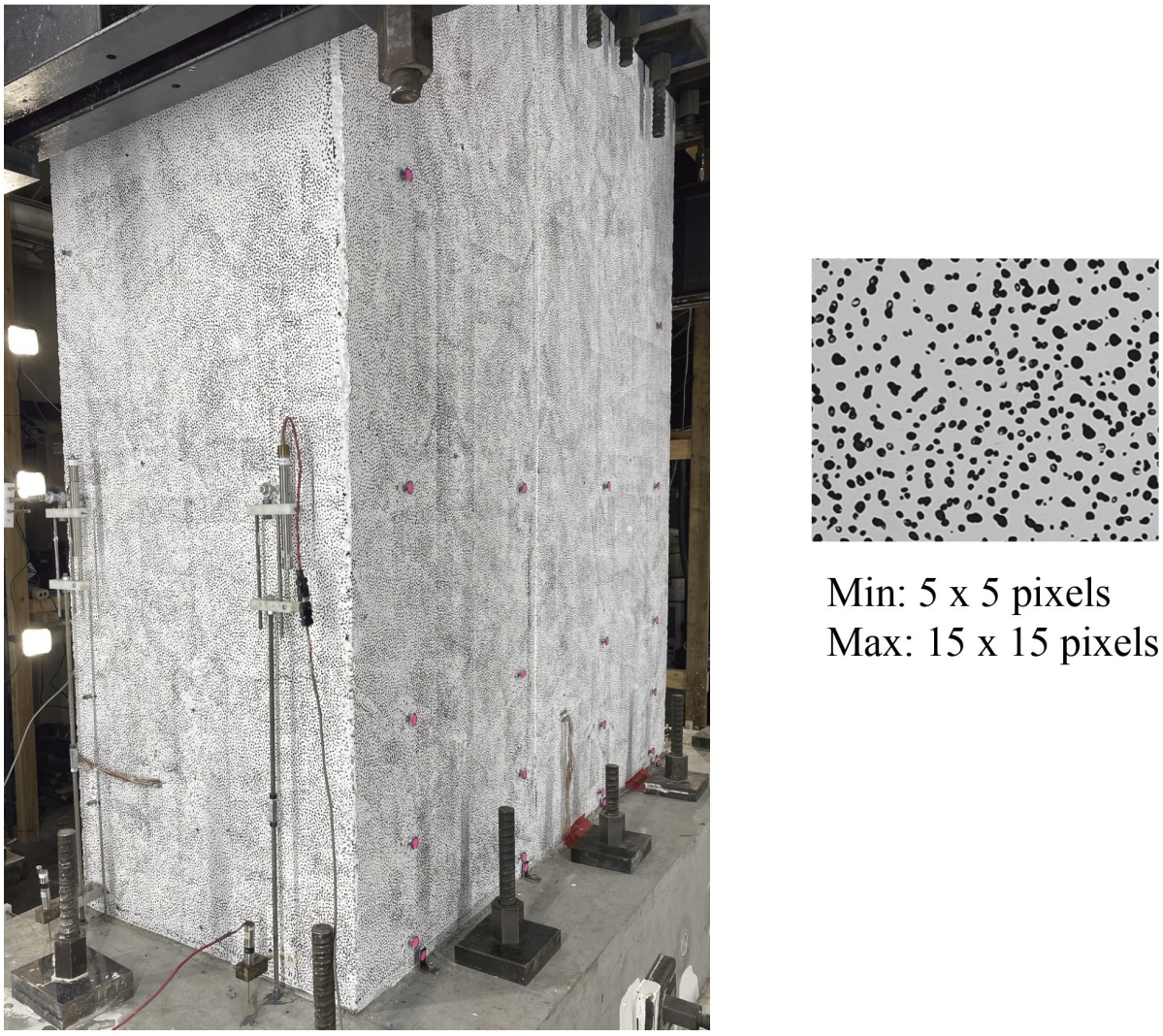

Figure 2-33: Digital image correlation pattern

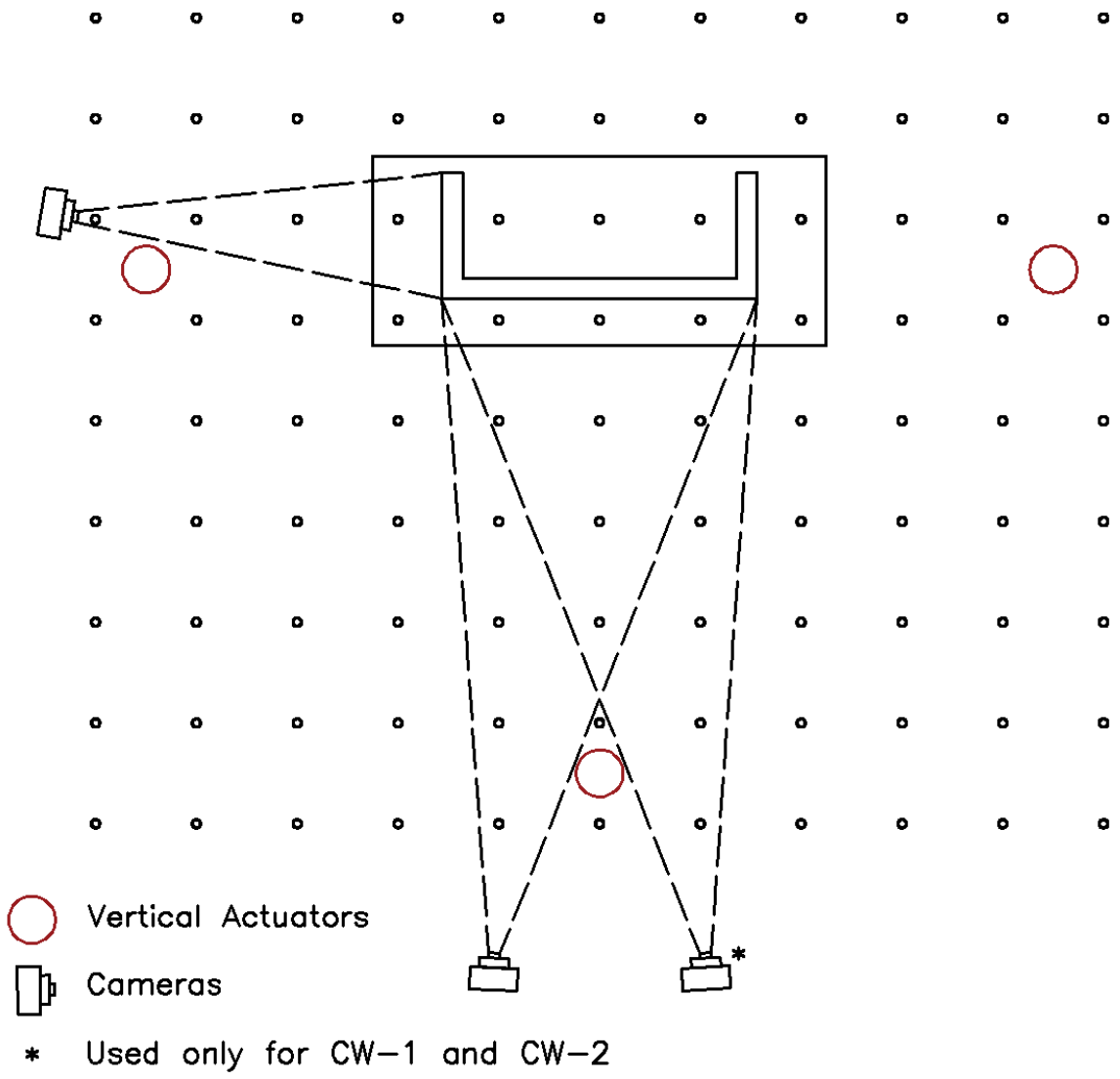

Figure 2-34: DIC cameras and their line of sight

2.6. Loading Protocols

2.6.1. Axial Load

An axial load of $0.1A_g f'_c$ = 500 kips (f'_c = 8 ksi), was applied to each test wall to represent gravity axial loads. This value was selected based on the review of drawings for actual buildings used to design the test specimens (see Section 2.2.1), as well as simple calculations. Depending on the typical floor design of the buildings and the load combinations selected, the gravity loads on the C-shaped walls were found to range from $0.05A_g f'_c$ to $0.12A_g f'_c$.

For the Phase-I specimens, the axial load was held constant at 500 kips throughout each test, i.e., for both in-plane and out-of-plane loading. However, for the Phase-II specimens, while an axial load of 500 kips was applied during in-plane loading, for the out-of-plane loading, if the web was under tension (positions B and E, Figure 2-37), the axial load was decreased to $0.05A_g f'_c$ and $0.075A_g f'_c$ for CW-3 and CW-4, respectively. This variation of axial load during the OOP bending was introduced to create more realistic test conditions, where the axial load on the wall would vary due to coupling beam shear forces developed during a wind event. As shown in Figure 2-35, for the left pier, where the bending results in compression on the flange edges and tension at the web, the coupling beam shear forces apply tensile axial loads on the wall. On the other hand, for the right pier, if the web is under compression and the flange edges are under tension, axial load increases. To create similar conditions during the test, the gravity axial load was decreased at loading positions B and E. Due to the test setup capacities, the axial load was not increased but kept constant at $0.1A_g f'_c$ at loading positions C and F (flange in tension). The variation in axial load due to the coupling beam shear forces was studied by analyzing five different C-shaped walls from two buildings. Analysis showed that the variation could range from $\pm 0.03A_g f'_c$ to $\pm 0.1A_g f'_c$

under strength level wind loads. Therefore, for CW-3, the axial loads were decreased by $0.05A_g f'_c$ to represent an average value from the analysis. For CW-4, the variation was chosen as $0.025A_g f'_c$ to represent a worst-case scenario (highest flange in compression condition for coupled C-shaped walls.

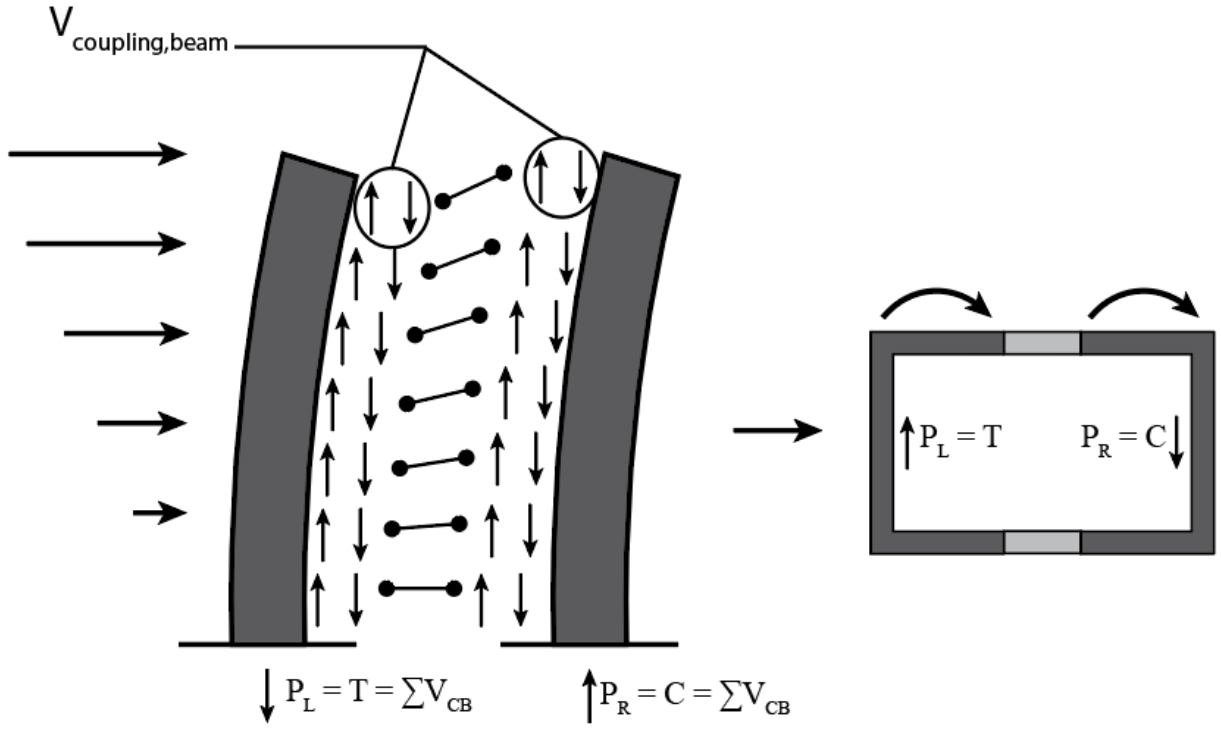

Figure 2-35: Distribution of axial load to wall piers

2.6.2. Wind Loading Protocol

The wind loading protocol (WLP) used was similar to the one developed and used by Abdullah et al. (2020) for the testing of reinforced concrete coupling beams (Figure 2-36). This loading protocol was developed using the results of a nonlinear response history analysis of a 58-story building with a coupled core wall lateral force-resisting system subjected to loading histories recorded from wind tunnel tests. The demands at the core wall were reviewed, and the number of times the demands exceeded a certain fraction of the peak demand in the positive and negative

directions was counted and averaged. Peak demand was selected as 1.5 times the yield rotation of the coupling beams, whereas the demands at other load levels were chosen as 15, 40, and 75% of the coupling beam probable moment capacity (M_{pr}). Due to the force-based nature of the wind events, the elastic cycles were applied under force-control. However, the inelastic demands after the yielding of the beams were applied under displacement-control. To represent an approaching and then passing wind event, the loading was increased in ramp-up and then decreased in the ramp-down portion of the loading protocol. More information regarding the details of the original loading protocol can be found in Abdullah et al. (2020).

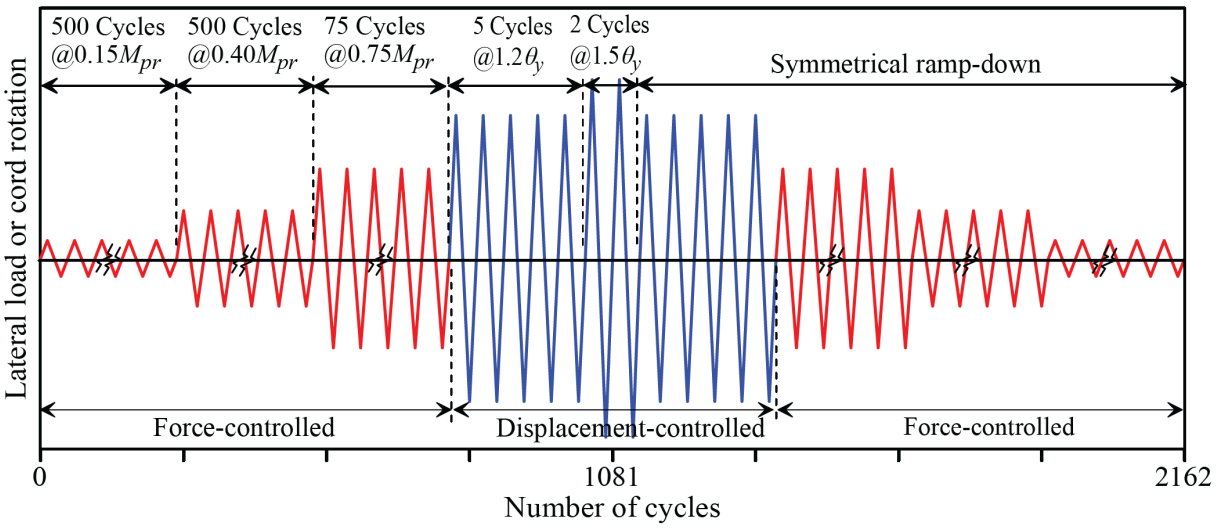

Figure 2-36: Original wind loading protocol developed by Abdullah et al. (2020)

The wind-loading protocol used for the testing of C-shaped walls (Figure 2-38) was similar to the one shown in Figure 2-36 with the following differences:

1. 500 cycles at $0.15M_{pr}$ force demands were not applied because, at a gravity axial loading of $0.1A_g f'_c$ = 500 kips, wall strain demands on the cross-section would be in compression.

2. Instead of applying 75 cycles under force-control at $0.75M_{pr}$, the protocol was modified to apply 30 cycles under displacement-control at $0.7M_{pr}$ force demands. The moment demand of $0.75M_{pr}$ was found to result in tension strain demands slightly greater than the first yield of the wall longitudinal reinforcement of test specimens; therefore, a value of $0.7M_{pr}$ was used (which corresponded to the first yield). Since the yielding of the outer level of the flange reinforcement was expected at this level, the loading was changed to displacement-controlled, and the number of cycles was decreased to 30.
3. The maximum rotation demands were increased to 3 times the plastic hinge effective yield rotations ($3\Theta_y$). Plastic hinge rotations were determined during the experiments using control sensors located between the wall-foundation interface and a height of $l_w/2 = 37.5$" above the wall-foundation interface (Figure 2-26).
4. The number of cycles at inelastic rotation demands of $1.5\Theta_y$ was increased to 3 from 2.
5. 2 additional cycles of loading were applied at $2.0\Theta_y$, $2.5\Theta_y$, and $3.0\Theta_y$.

The loading for 500 cycles at $0.4M_{pr}$ and 30 cycles at $0.7M_{pr}$ was applied as uni-directional loading only (parallel to the web, Positions A and D, Figure 2-37). However, for the inelastic cycles ($1.2\Theta_y$, $1.5\Theta_y$, $2.0\Theta_y$, $2.5\Theta_y$, and $3.0\Theta_y$), biaxial loading was applied. As shown in Figure 2-37, the wall specimens were first pushed in the in-plane directions to the specified rotation demands, and then while holding the in-plane rotations constant, they were pushed in the out-of-plane (OOP) directions (parallel to the flanges, Positions B, C, E, and F). The force demands in the OOP directions were chosen as half of the probable moment capacities ($0.5M_{pr,OOP}$). These moment capacities were calculated assuming a monotonic loading in the +y and -y directions separately under the given axial load demands (see Table 2-3).

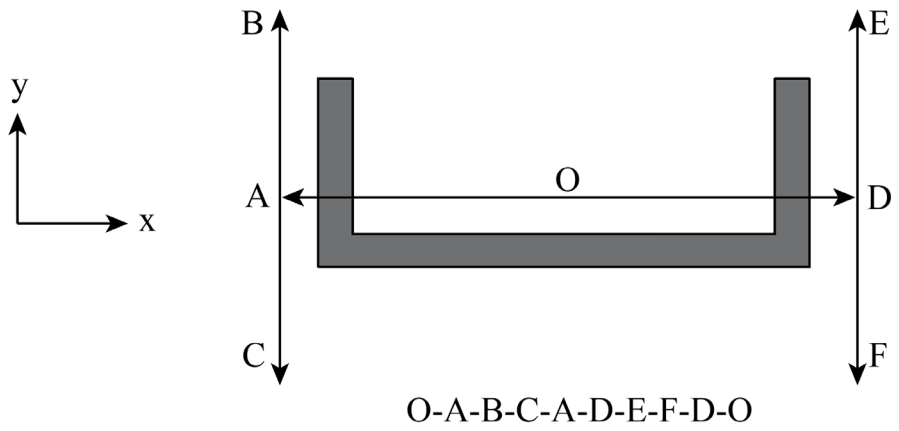

Figure 2-37: Biaxial loading scheme

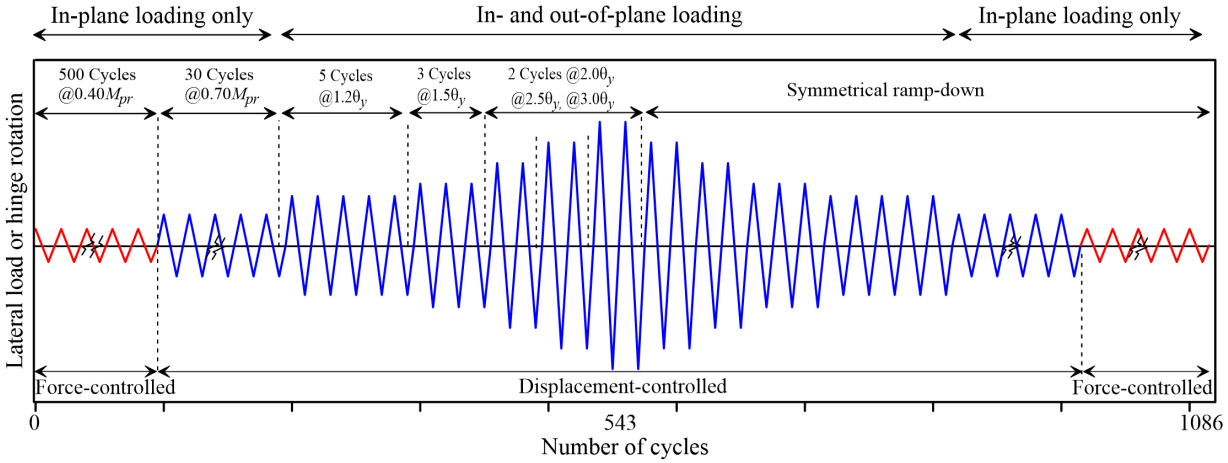

Figure 2-38: Wind loading protocol for wall specimens

2.6.3. Seismic Loading Protocol

After the wind loading protocol was completed, a seismic loading protocol (SLP) was applied to each test specimen. For walls CW-1, CW-2, and CW-3, the SLP was applied in the in-plane direction only (uni-directional loading) and the axial load was kept constant at $0.1A_g f'_c = 500$ kips. Figure 2-39 shows the SLP applied to CW-1 where 3 cycles at $5\Theta_y$, $7.5\Theta_y$, and $10\Theta_y$, and 2 cycles

were applied at $15\Theta_y$ and $20\Theta_y$ before the failure occurred. For CW-2, failure (strength loss) was observed during the first cycle at $4.5\Theta_y$, whereas for CW-3, 3 cycles were applied at $4.5\Theta_y$ before failure was observed after the first half cycle to $6.0\Theta_y$ (Figure 2-40). The damage state of CW-4 after application of the WLP was similar to CW-3; therefore, instead of applying only in-plane loading (as was done for CW-3), a biaxial loading protocol, similar to that used for the WLP, was applied as SLP for CW-4. The SLP for CW-4 consisted of applying two cycles at $2.0\Theta_y$ and $3.0\Theta_y$, and one cycle at $4.5\Theta_y$ prior to failure (Figure 2-41). However, as opposed to WLP, the axial load during the application of OOP loading was not decreased but kept constant at $0.1A_g f'_c$.

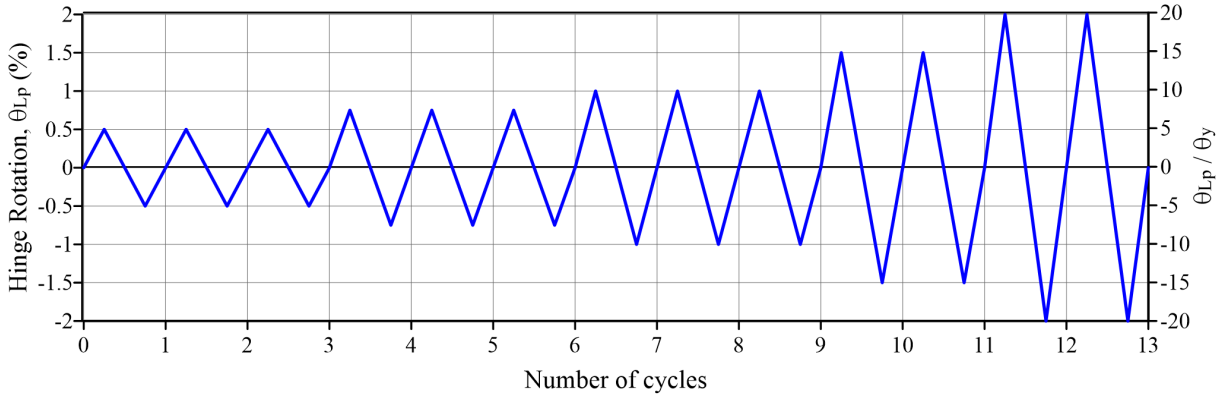

Figure 2-39: Seismic loading protocol for CW-1 (in-plane only)

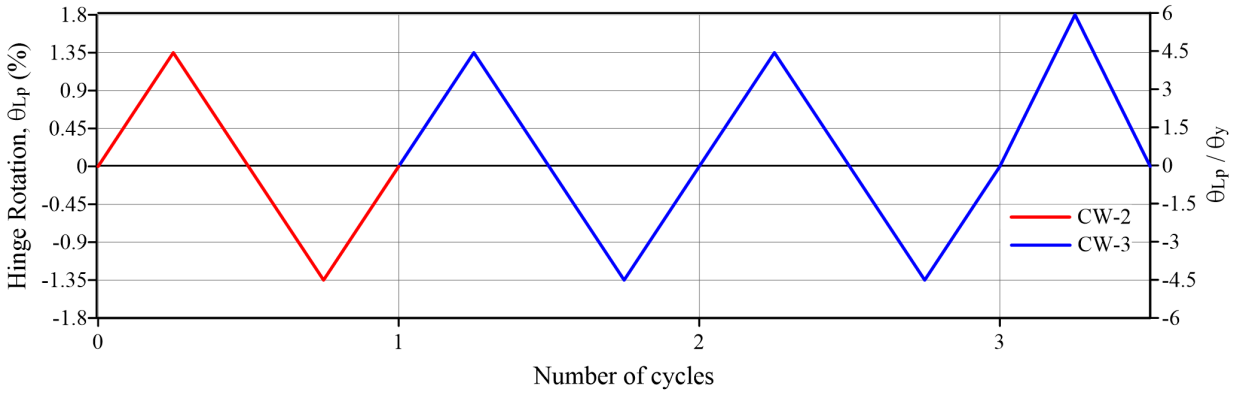

Figure 2-40: Seismic loading protocol for CW-2 and CW-3 (in-plane only)

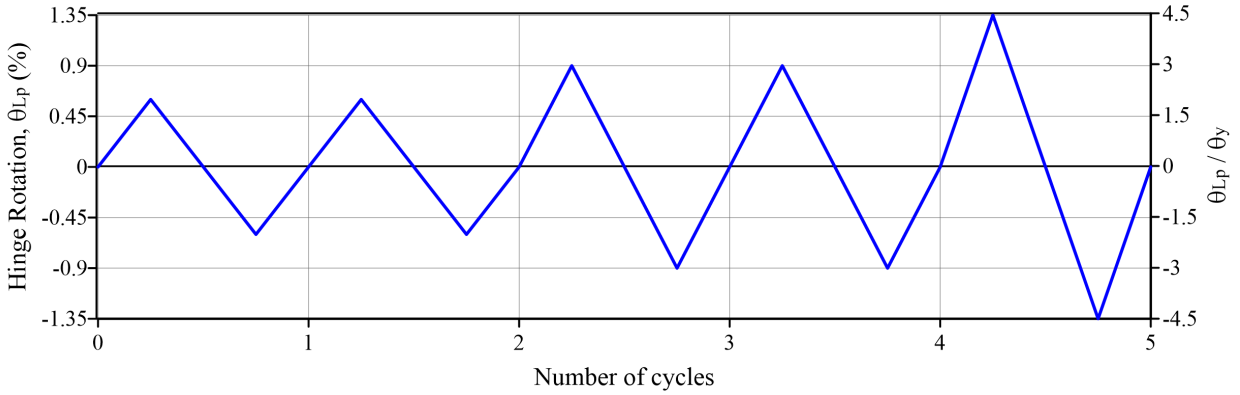

Figure 2-41: Seismic loading protocol for CW-4 (biaxial loading with constant 0.1$A_g f'_c$ axial load)

3. Experimental Wind Test Results and Discussion (CW-1)

3.1 General

This chapter focuses on the experimental results of the lightly reinforced wall specimen (ρ_l = 0.75%), CW-1, under the wind loading protocol explained in section 2.6.2. The probable moment capacity of the specimen in the in-plane ($M_{pr,IP}$, calculated with $1.25f_y$ at ε_c=0.003, ACI 318-19), and +y and -y out-of-plane ($M_{pr,OOP+y}$, $M_{pr,OOP-y}$) directions were calculated under a monotonic loading assumption using an elasto-plastic rebar behavior with $1.25f_y$ rebar strength (75 ksi), f'_c of 8 ksi, and 500 kips axial load. Figure 3-1 shows the analytical in-plane moment-curvature diagram with the calculated $M_{pr,IP}$ value of 2565 k-ft. The effective yield rotation (Θ_y) was observed to be 0.1% during the experiments. Detailed analysis done after the tests (Appendix F) resulted in a slightly higher Θ_y value of 0.11%, which was lower than the total predicted yield rotation (flexural + slip, $\Theta_{y,t,a} = \Theta_{y,f,a} + \Theta_{y,s,a}$) value of 0.14% (see Appendix F and Appendix G). Accordingly, the moment and the rotation demands are summarized in Table 3-1 for the ramp-up and the ramp-down portions of the WLP separately. During the ramp-up portion of the loading protocol, on average, the in-plane moment values were approximately 90% of the $M_{pr,IP}$. Therefore, in the OOP directions, 0.45% of probable moment capacities were applied, 0.5(0.9) = 0.45. However, during ramp-down loading, due to the displacement-controlled nature of the loading protocol, lower in-plane moment values were applied to the specimen. These in-plane moment demands were 56% of the $M_{pr,IP}$ at $1.2\Theta_y$ demands (1450 k-ft / 2565 k-ft = 0.56), during $2.5\Theta_y$ demands, it was 85% (2155 k-ft / 2565 k-ft = 0.84). Therefore, on average, 37% of the OOP M_{pr} demands were applied during the ramp-down period, 0.5(0.75) = 0.375.

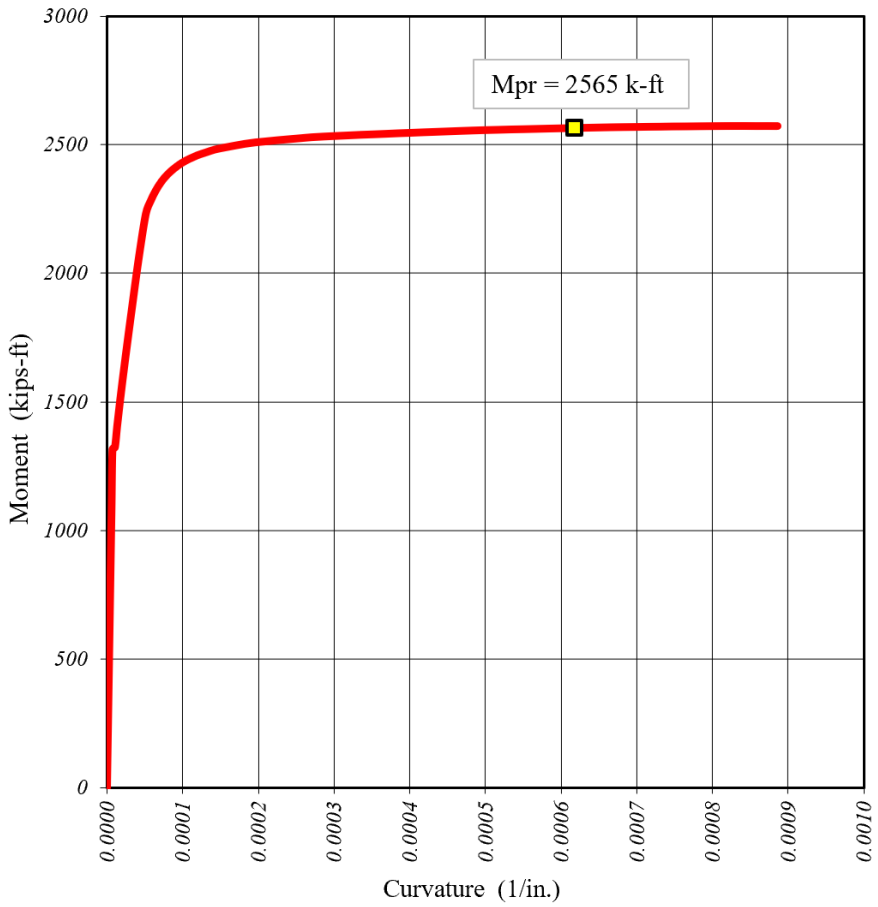

Figure 3-1: CW-1 monotonic in-plane moment-curvature diagram with $f_s = 1.25f_y$

Table 3-1: Applied WLP demands for CW-1

Load Step		In-plane Demands		Out-of-plane Demands	
		Base moment, $M_{b,IP}$ (k-ft)	Hinge rotation, $\Theta_{Lp,IP}$ (%)	Base moment, $M_{b,OOP+y}$ (k-ft)	Base moment, $M_{b,OOP-y}$ (k-ft)
Ramp-Up	$0.4M_{pr}$	±1026	±0.024	-	-
	$0.7M_{pr}$	±1795	±0.09	-	-
	$1.2\Theta_y$	±2000	±0.12	+530	-260
	$1.5\Theta_y$	±1960	±0.15		
	$2.0\Theta_y$	±2220	±0.20		
	$2.5\Theta_y$	±2350	±0.25		
	$3.0\Theta_y$	±2420	±0.30		
Ramp-Down	$2.5\Theta_y$	±2155	±0.25	+480	-200
	$2.0\Theta_y$	±1900	±0.20		
	$1.5\Theta_y$	±1650	±0.15		
	$1.2\Theta_y$	±1450	±0.12		
	$0.7M_{pr}$	±1320	±0.09	-	-
	$0.4M_{pr}$	±1026	±0.05	-	-

Notes:

- Moment values given for the first cycle at each rotation demands
- In-plane probable moment capacity, $M_{pr,IP}$ = ±2565 k-ft
- +y OOP probable moment capacity, $M_{pr,OOP+y}$ = +1126 k-ft
- -y OOP probable moment capacity, $M_{pr,OOP-y}$ = -570 k-ft
- Effective plastic hinge yield rotation, Θ_y = ±0.1%

3.2 Observed Damage

The cracking moment of the wall was estimated to be -1330 k-ft under the negative (Pos. A) and +1440 k-ft under the positive (Pos. D) in-plane moments demands. These values were estimated from the moment-hinge rotation response of the wall, where a significant change in the slope of the response occurred. These values corresponded to 52% and 56% of the in-plane probable moment capacities ($M_{pr,IP}$). Accordingly, no cracking was observed during the 500 cycles at $0.4M_{pr}$ moment demands. Digital image correlation (DIC) analysis was completed after the 30 cycles at $0.7M_{pr}$ moment demands, during which the hairline cracks become visible. The results of the DIC analysis indicate cracking in the web at the peak moment ($0.7M_{pr}$) of the last cycles at positions A and D, as shown in Figure 3-2 and Figure 3-3, respectively. The cracking was mainly concentrated right above the splice region (10 in. < h < 15 in.) at this loading step. DIC analysis was also done at the peak moment demands of the second cycle of the $3.0\Theta_y$ rotation demands for the loading at positions A (Figure 3-4) and D (Figure 3-5). These figures show a mostly uniform distribution of the cracks along the height of the wall, with the biggest cracks opening right above the splice region and the wall-footing interface. No new cracking was observed during the ramp-down portion of the WLP. After the completion of the WLP, the wall specimen CW-1 showed no damage (e.g., no concrete spalling, concrete crushing, bar buckling, or bar fracture), and only minor cracking was observed over the splice length. Figures 3-6, 3-7, and 3-8 show the cracking pattern of the specimen after WLP, which reveals a nearly uniform distribution of the horizontal flexural cracks within the flanges and diagonal tension (shear) cracks at the web. The residual flexural crack widths within the flanges were measured to be 0.1 mm, and no residual diagonal web cracks were visible. The strain gauges attached to the outer layer of the flange vertical reinforcement

(Figure 2-25) right above the splice region (h = 11in.) revealed that the yielding of the reinforcement occurred, on average, at 70% of the in-plane probable moment capacity (Table 3-2).

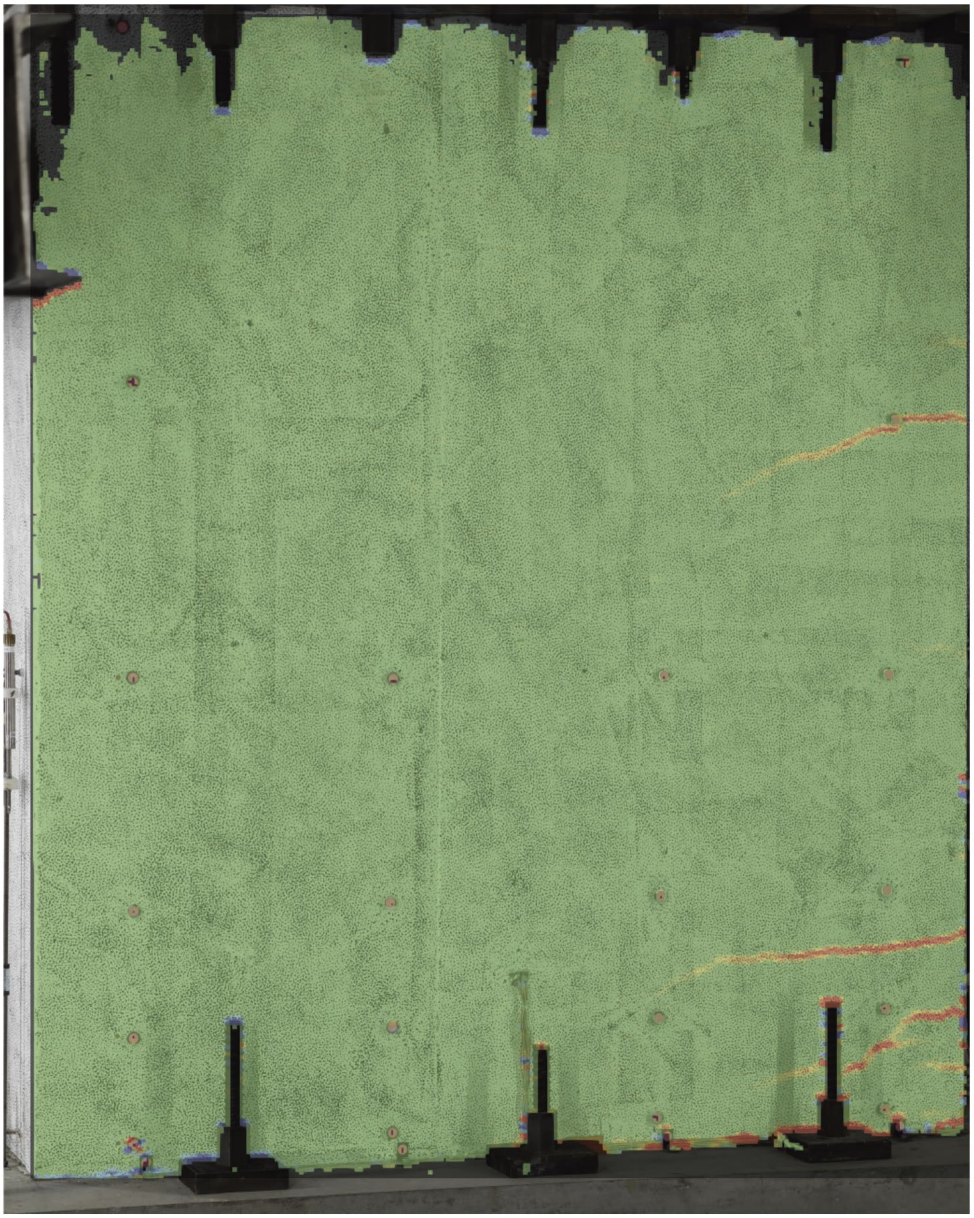

Figure 3-2: Crack pattern of the web obtained from DIC for CW-1 at the peak moment of the last cycle of $0.7M_{pr}$ moment demands under negative moment (Pos. A)

Figure 3-3: Crack pattern of the web obtained from DIC for CW-1 at the peak moment of the last cycle of $0.7M_{pr}$ moment demands under positive moment (Pos. D)

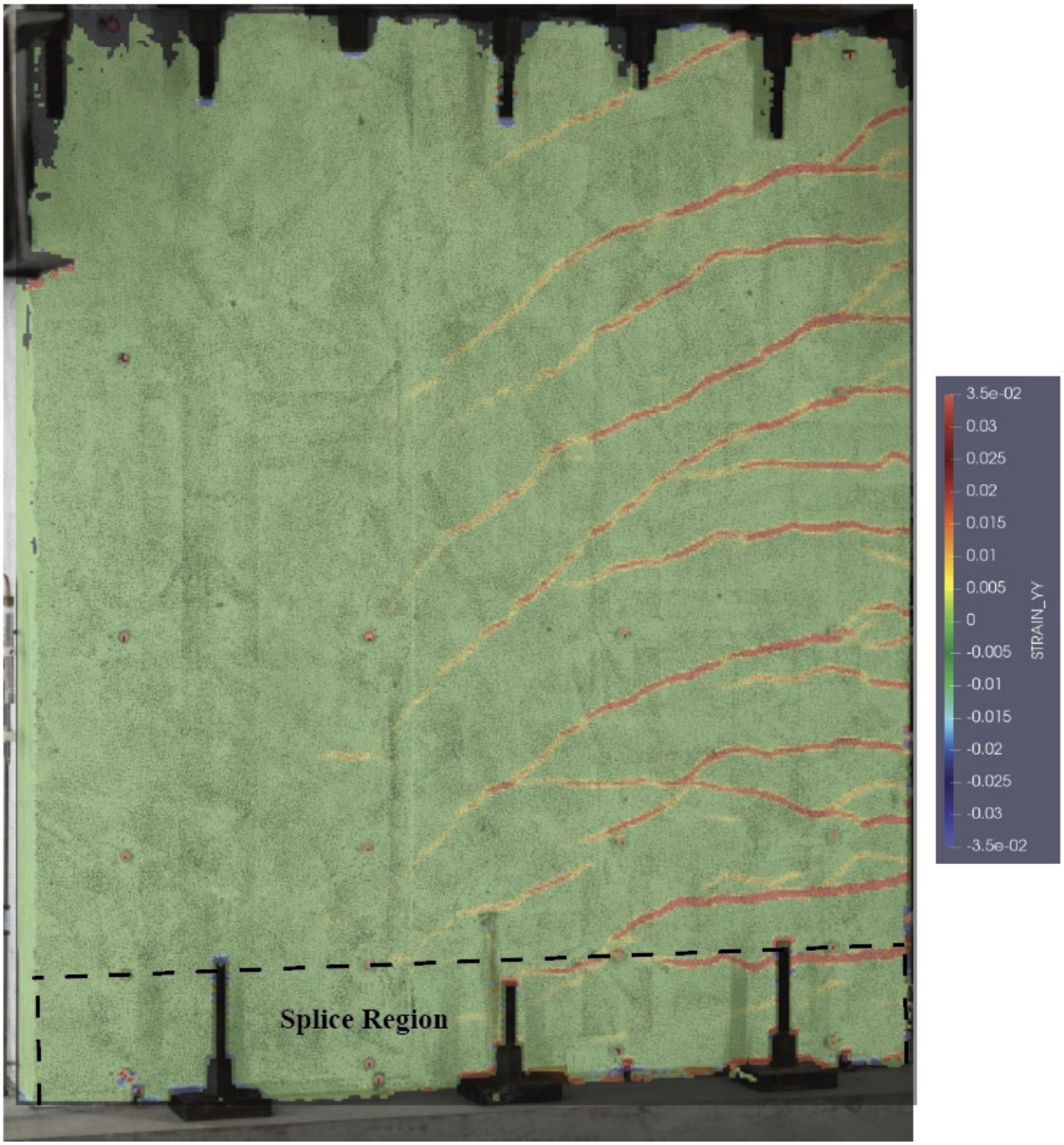

Figure 3-4: Crack pattern of the web obtained from DIC for CW-1 at the peak moment of the second cycle of $3.0\Theta_y$ rotation demands under negative moment (Pos. A)

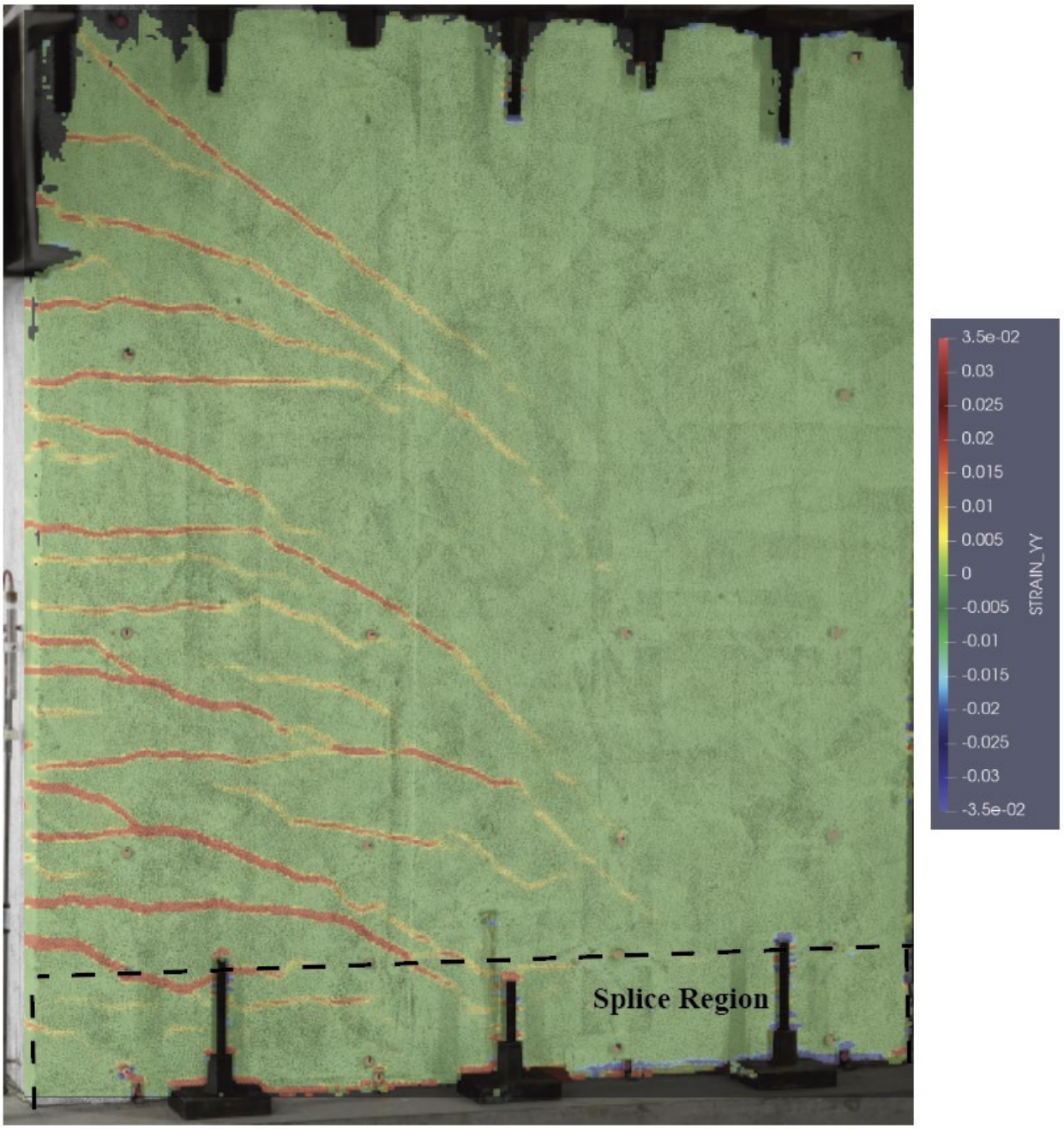

Figure 3-5: Crack pattern of the web obtained from DIC for CW-1 at the peak moment of the second cycle of $3.0\Theta_y$ rotation demands under negative moment (Pos. D)

Figure 3-6: Cracking condition of CW-1 at the end of WLP (Inside surfaces of the web and flanges)

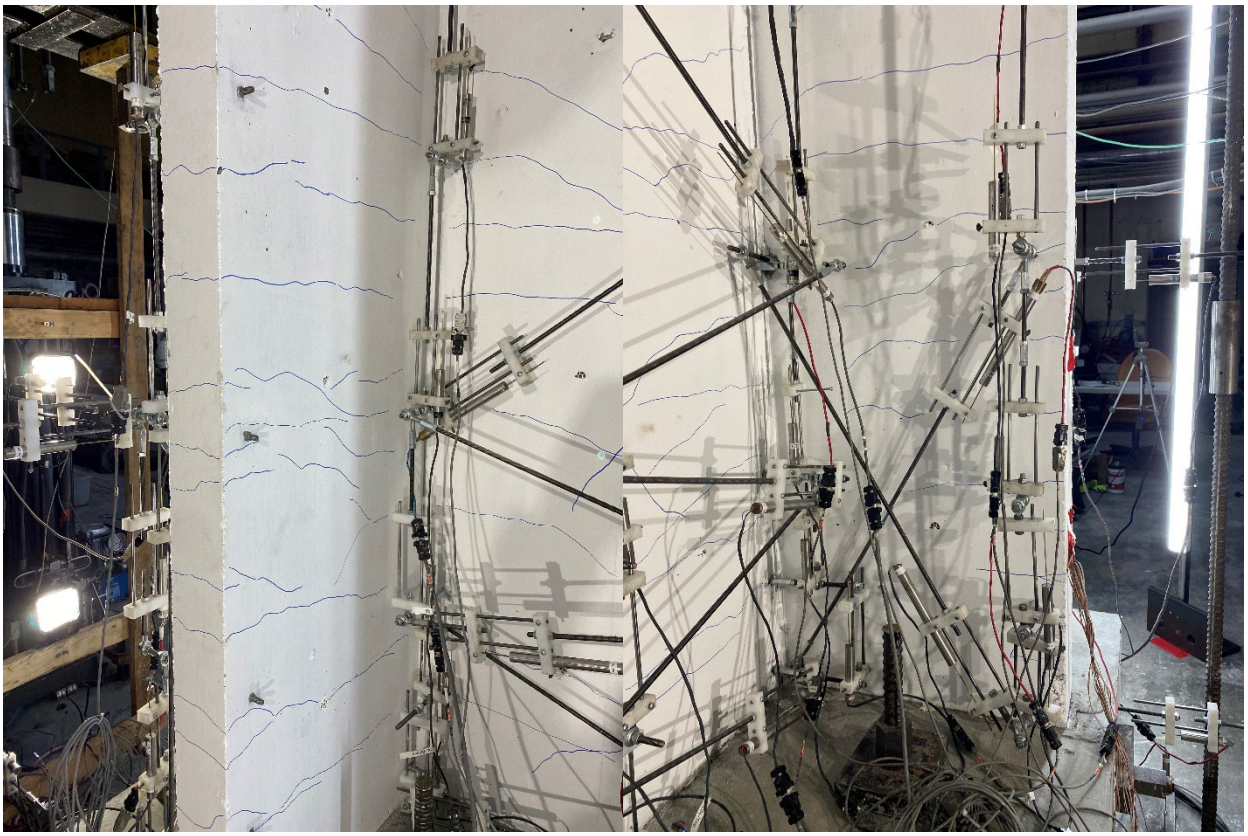

Figure 3-7: Cracking condition of CW-1 at the end of WLP (Inside surfaces of the east flange (left) and west flange (right))

Figure 3-8: Cracking condition of CW-1 at the end of WLP (Outside surface of the East flange)

Table 3-2: In-plane rotation and moment demands at first yield of outer layer of flange longitudinal reinforcement above the splice (h=11in.)

	In-plane Rot. (%)	In-plane moment (k-ft) M_{IP}	Load Step / Position	M_{IP} / $M_{pr,IP}$
West Flange Edge	+0.088	+1795	$0.7M_{pr}$ / Pos. D	0.70
West Flange Corner	+0.095	+1841	$1.2\Theta_y$ / Pos. D	0.72
East Flange Edge	-0.065	-1568	$0.7M_{pr}$ / Pos. A	0.61
East Flange Center	-0.088	-1774	$0.7M_{pr}$ / Pos. A	0.69
East Flange Corner	-0.11	-1956	$1.2\Theta_y$ / Pos. A	0.76

3.3 Load-Deformation Responses

3.3.1 Base Moment-Hinge Rotation Responses

The plastic hinge rotations were measured during the experiment by using the four LVDTs attached to the four corners of the specimen on the outside surfaces of the flanges (Figure 3-9). The LVDTs were attached to the footing on one end and to the wall at the plastic hinge height ($L_p = l_w/2$) at the other end. Therefore, the measured rotations included the rebar slip/extension at the wall-footing interface. The readings from LVDTs attached to the same flange were averaged to calculate the average in-plane hinge rotations.

$$\theta_{Lp,IP} = \frac{\frac{\delta_{NW} + \delta_{SW}}{2} - \frac{\delta_{NE} + \delta_{SE}}{2}}{L_w + \frac{l_{NW} + l_{SW}}{2} + \frac{l_{NE} + l_{SE}}{2}} \tag{3.1}$$

where δ_{NW}, δ_{SW}, δ_{NE}, and δ_{SE} are the displacements of the LVDTs, and l_{NW}, l_{SW}, l_{NE}, and l_{SE} are the distance from the concrete surface to the LVDTs attached to the northwest, southwest,

northeast, and southeast corners (Figure 2-27), respectively. Similarly, the plastic hinge rotations in the out-of-plane direction were calculated as:

$$\theta_{Lp,OOP} = \frac{\frac{\delta_{SW} + \delta_{SE}}{2} - \frac{\delta_{NW} + \delta_{NE}}{2}}{\frac{d_W + d_E}{2}} \tag{3.2}$$

where d_W and d_E are the distances between the LVDTs attached to the west and east flanges (Figure 2-27), respectively.

Figure 3-10 shows the in-plane base moment versus hinge rotation response of the wall specimen CW-1 under the WLP. As mentioned in Section 2.6.2, the WLP was developed to keep the in-plane rotations constant during the OOP load application. However, slight variations were observed in the IP rotations during the OOP load application due to the flexibility of the test setup. As expected, the IP moment values decreased during the OOP bending. During ramp-up, the slope of the moment-rotation response changed at every first and second cycle of each loading stage. This is because new cracks developed, and the existing cracks propagated further during the ramp-up for the first two cycles of each loading stage. Generally, no change in the wall stiffness was observed after the first two cycles. Similarly, during ramp-down loading, the lateral stiffness was unchanged, i.e., the slope of the moment-rotation response did not change. This was because no new cracks were observed during ramp-down loading. The in-plane moment-hinge rotation response was also compared with the predicted response (details are in Appendix F); the comparisons showed that the predicted response matched the experimental results well. The predicted initial stiffness was found to be slightly higher than the stiffness determined from experimental measurements, which was due to the slip/extension deformations that were not included in the predicted response. The

OOP base moment versus the OOP hinge rotation response of the wall specimen is shown in Figure 3-11. This response was not predicted, unlike IP moment-hinge rotation response, by using the analytical monotonic moment-curvature behavior of the wall because of the biaxial loading protocol. However, more complex analytical models were used in Chapter 7 for predicting the biaxial cyclic behavior of the specimens.

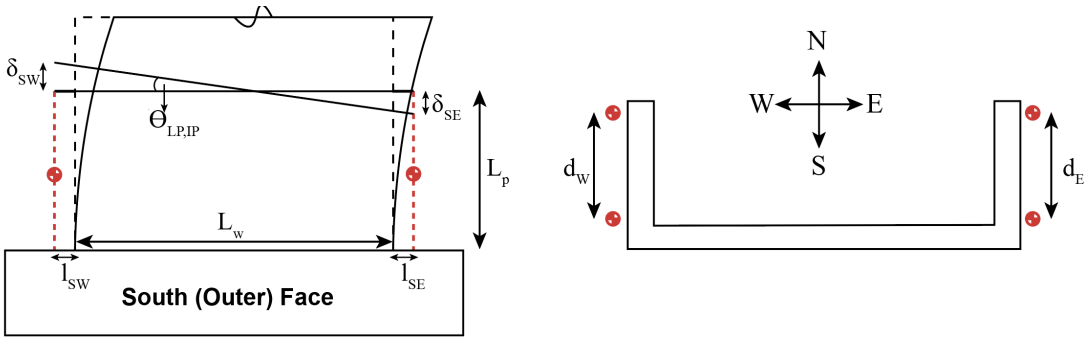

Figure 3-9: LVDT layout for in-plane hinge rotation measurements

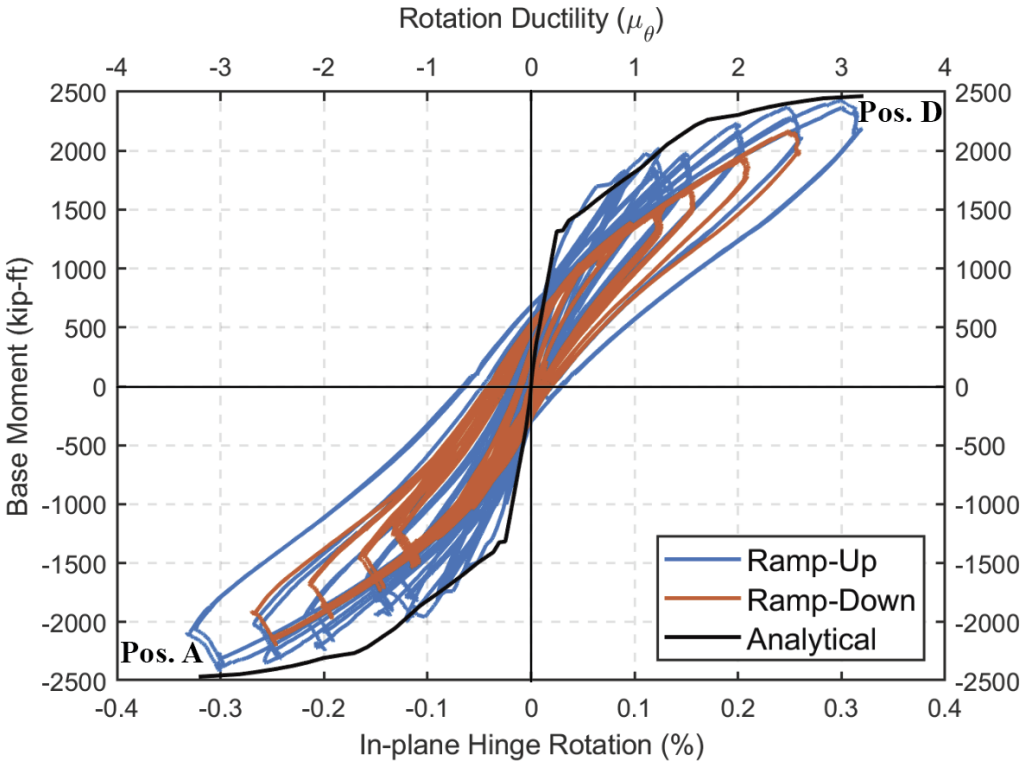

Figure 3-10: In-plane moment-hinge rotation of CW-1 under WLP

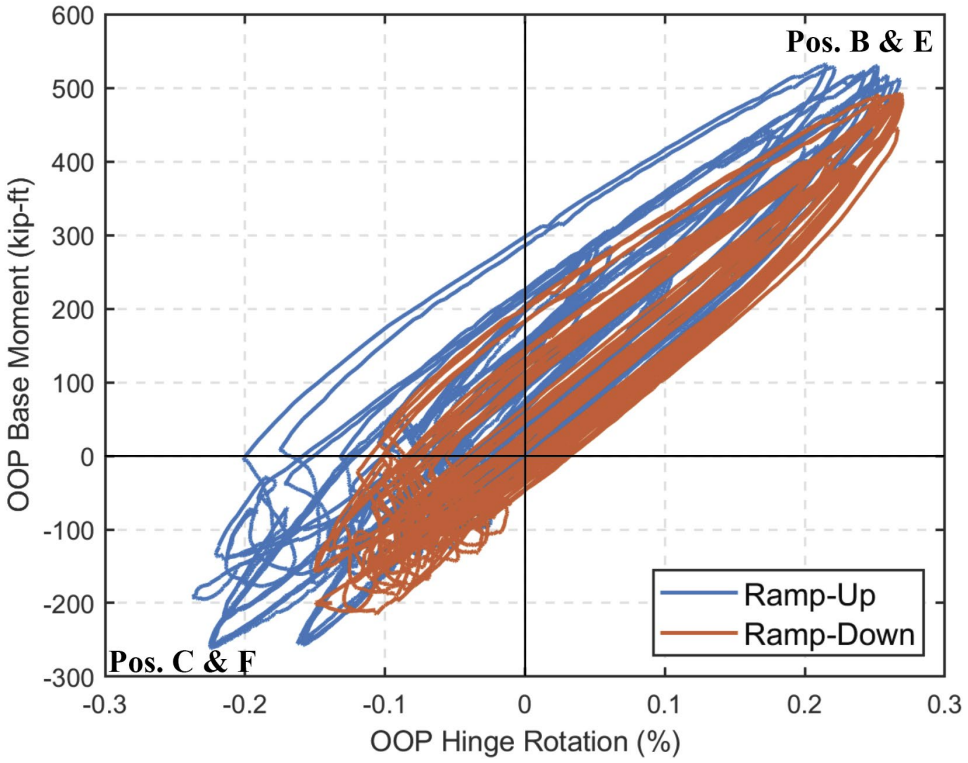

Figure 3-11: Out-of-plane moment-hinge rotation of CW-1 under WLP

3.3.2 Moment-Curvature Responses

The in-plane moment-curvature response over the height of the wall during the WLP was measured using layers of LVDTs attached to the inner surface of the west flange, to the web (4 columns of LVDTs), and to the outer surface of the east flange (Figure 2-24 and Figure 2-25). The LVDTs at Layer 1 spanned between 2 in. and 10 in. above the footing (2-10 in.). Similarly, dimensions were 10-20 in., 20-37.5 in., 37.5-57 in., and 57-85 in. for Layers 2, 3, 4, and 5, respectively. The average curvatures over the plastic hinge length (ϕ_{Lp}) were calculated by using the hinge rotation LVDTs shown in Figure 3-9 (spanning between 0-37.5 in.) and the LVDTs attached at the base (0-2 in.) at the four corners of the wall. These LVDTs were used to estimate the slip/extension deformations at the wall-footing interface. For the calculation of ϕ_{Lp}, the displacement values recorded using the

slip/extension LVDTs were subtracted from the hinge rotation LVDT readings. The results are shown in Figure 3-12, where the moment values were calculated as the average in-plane moment demand over the height of the layer. Curvature ductility (μ_ϕ) shown in Figure 3-12 was calculated by dividing the curvature values by the yield curvature (ϕ_y), which was determined using the approach explained in Appendix F. The results showed that, whereas the average curvature ductility over L_p was 3.2, the peak μ_ϕ value of 4.75 was measured at the base of the wall (Layer 1) at the maximum moment demands during the $3\Theta_y$ load step. The higher μ_ϕ values of 4.75 and 4 for Layers 1 (2-10 in.) and 2 (10-20 in.) were due to the concentration of large cracks at the end of the splice region (h=10 in.). Curvature ductility of 2 was measured above the hinge region (Layers 4 and 5). The experimental results were also compared with the predicted moment-curvature response (see Appendix F). The predicted values matched well for the overall response (Figure 3-12a) and during the inelastic cycles. However, over the splice region, the experimental results showed a significantly stiffer response than predicted. This was attributed to the fact that the LVDT measurements are dependent on the level of deformation, with greater errors for lower loading levels and the larger quantity of longitudinal reinforcement over the splice region.

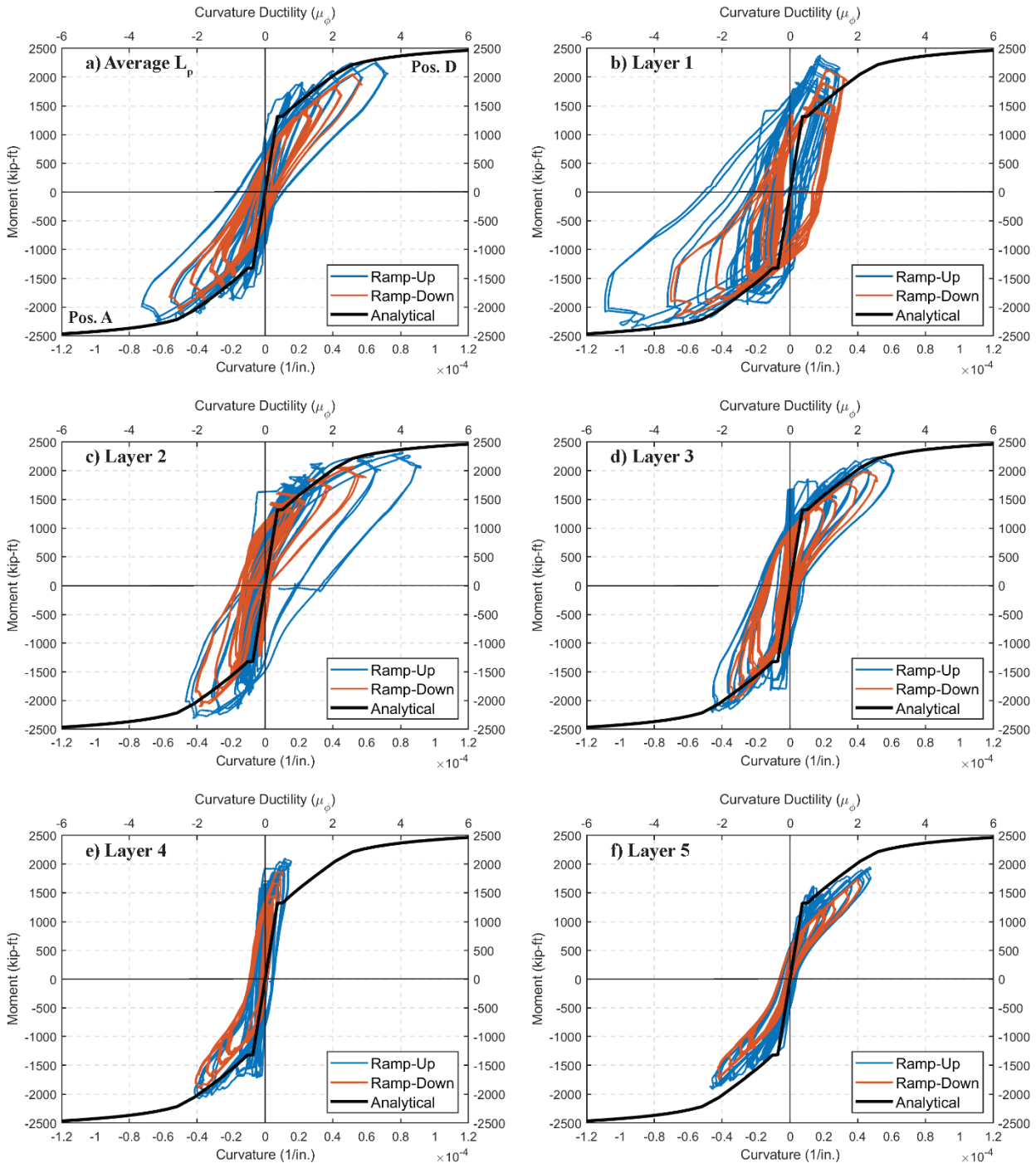

Figure 3-12: Moment-Curvature response of CW-1 during WLP

3.3.3 Base Shear-Lateral Displacement Responses

The in-plane lateral displacements of the test specimens were measured using the two LVDTs attached to the northeast and southeast corners of the top block and connected to a reference frame on the east side of the wall (Figure 2-25). Figure 3-13 shows the base shear versus drift ratio response calculated as the total displacements of the LVDTs divided by the distance from the LVDT mounting point to the base of the wall for the northeast (Figure 3-13a) and the southeast (Figure 3-13b) LVDTs. The readings from the two LVDTs were averaged to measure the average in-plane lateral displacements at the top of the wall (Figure 3-14). The lateral displacements at the top of the wall due to the sliding and the rotation of the bottom block were not included in Figure 3-13 and Figure 3-14. Displacement ductility (μ_Δ) was also calculated by dividing the drift ratios by the drift ratio at effective yield, which was measured to be 0.15%. The maximum average μ_Δ values of +2.3 and -2.43 were measured at the $3.0\Theta_y$ hinge rotation demands before the out-of-plane load application (positions D and A). The out-of-plane lateral displacements were also measured with the two LVDTs attached to the mid-height of the top block at the northeast and northwest corners. Similar to the IP drift ratios, the OOP drift ratios from the two LVDTs were calculated individually (Figure 3-15a and Figure 3-15b) and also averaged (Figure 3-16).

The total in-plane lateral displacement (δ_{tot}) of the wall can be expressed as the sum of the flexural and shear deformations over the wall height. Flexural deformations include the curvature/rotation of the wall ($\delta_{f,wall}$), and the deformations due to the slip/extension at the wall-footing interface (δ_{slip}). Shear deformations include the pure translation (shear distortion) along the height of the wall ($\delta_{s,wall}$), the shear sliding along the wall footing interface ($\delta_{s,slide,wall}$), and also the shear

sliding of the bottom block along the laboratory floor ($\delta_{s,slide,block}$). The lateral displacements due to the rotation of the bottom block were found to be negligible.

$$\delta_{tot} = \delta_{f,wall} + \delta_{f,slip} + \delta_{s,wall} + \delta_{s,slide,wall} + \delta_{s,slide,block} \quad (3.3)$$

The flexural, slip/extension, and shear sliding deformations were measured directly using the LVDTs attached to the wall and the bottom block. The wall shear deformations ($\delta_{s,wall}$) were calculated using two different approaches. For the first approach, any deformation not associated with flexure, slip/extension, or shear sliding was attributed to shear distortion (Equation G.18); Appendix G includes detailed information. For the second approach, the diagonal LVDTs attached to the inner surface of the web (Figure 2-24) were used directly (Equation G.19). Figure 3-17 shows the base shear-drift ratio response of each displacement component during the ramp-up and ramp-down portions of the WLP. The relative contributions of each displacement component were also calculated at various hinge rotation levels, for loading in both in-plane directions. The total lateral displacement at the top of the wall due to the shear sliding of the wall ($\delta_{s,slide,wall}$) and the bottom block ($\delta_{s,slide,block}$) were approximately 3% and 4% during the positive (Pos. D) and negative (Pos. A) in-plane loading, respectively. The relative contributions of wall flexural ($\delta_{f,wall}$), base slip/extension (δ_{slip}), and shear ($\delta_{s,wall}$) deformations are shown in Figure 3-18 for the ramp-up and the ramp-down portions of the loading protocol, except for the $0.4M_{pr}$ load step, where, due to the low level of deformations, the LVDT readings were not reliable. The slip/extension deformations (δ_{slip}) comprised about 30% of the total displacement at $0.7M_{pr}$ load step, where the first yield of the bars was observed. After yielding, δ_{slip} contribution decreased gradually to 13% and 18% at $3.0\Theta_y$ rotation demands in the positive and negative directions, respectively. Similarly, the contribution of the shear deformations ($\delta_{s,wall}$), calculated using Equation G.18, decreased with increasing

hinge deformations, with the highest values of approximately 60% (Pos. D) and 40% (Pos. A) at $0.7M_{pr}$ moment demands. The contribution of $\delta_{s,wall}$ was also calculated using Equation G.19 and shown in Figure 3-18 for the negative loading only; some of the diagonal LVDTs were malfunctioning during positive loading. The comparison of $\delta_{s,wall}$ contribution calculated with Equations G.18 and G.19 showed very similar results during the inelastic load steps of the ramp-up portion with the values ranging from 30% at $1.2\Theta_y$ to 24% at $3.0\Theta_y$. The effect of wall curvature/rotations on the top displacement was ranging from 25-30% at $0.7M_{pr}$ to 45%-55% at $3.0\Theta_y$. It should be noted here that the test walls represented approximately the bottom 2 stories of a 12-story cantilever core wall. For a cantilever wall, the flexural drift ratios due to plastic hinge rotations within the plastic hinge region are mostly constant along the height of the wall, whereas shear deformations (pure translation) decrease up the height of the wall. Therefore, the percent contribution of the shear deformations to the drift ratios at the top of a cantilever wall is expected to be smaller than the values shown in Figure 3-18.

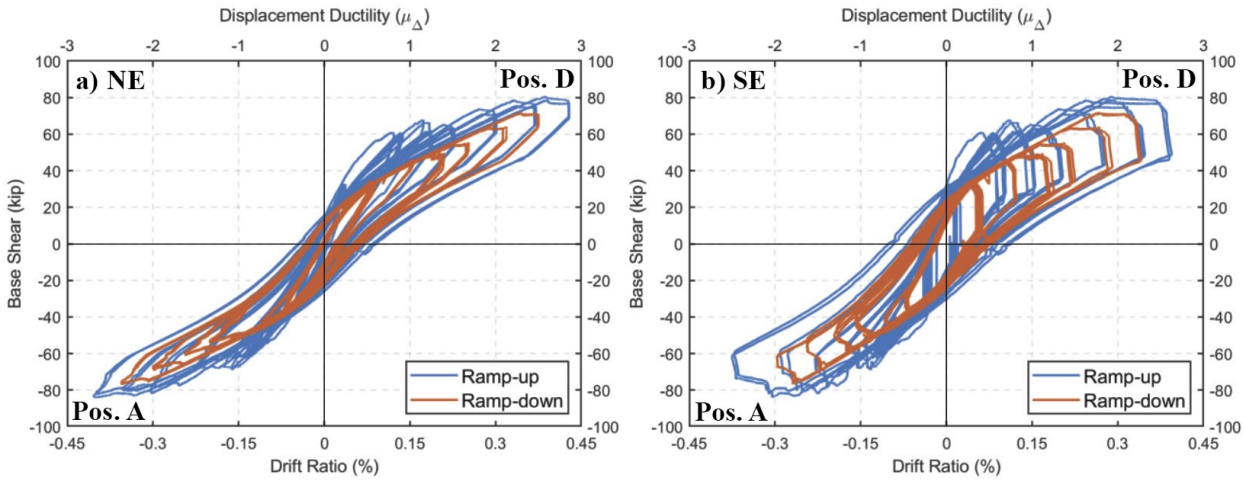

Figure 3-13: In-plane base shear-drift ratio response of CW-1 recorded a) at the NE b) at the SE corners of the top block under WLP

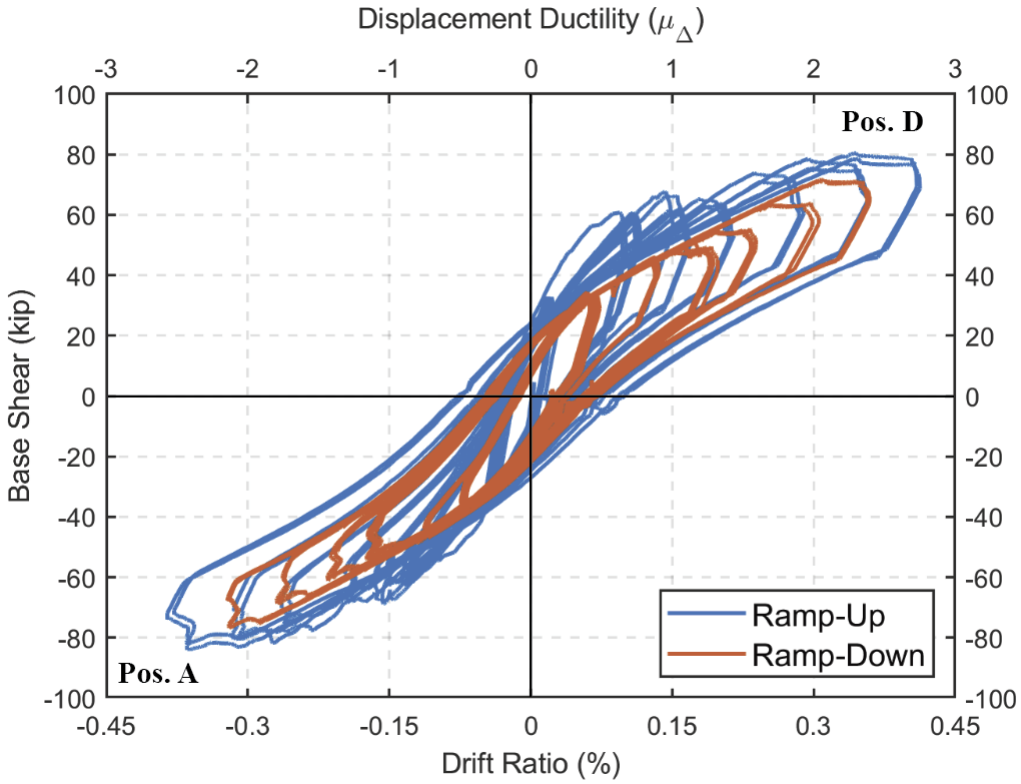

Figure 3-14: In-plane base shear-average drift ratio response of CW-1 under WLP

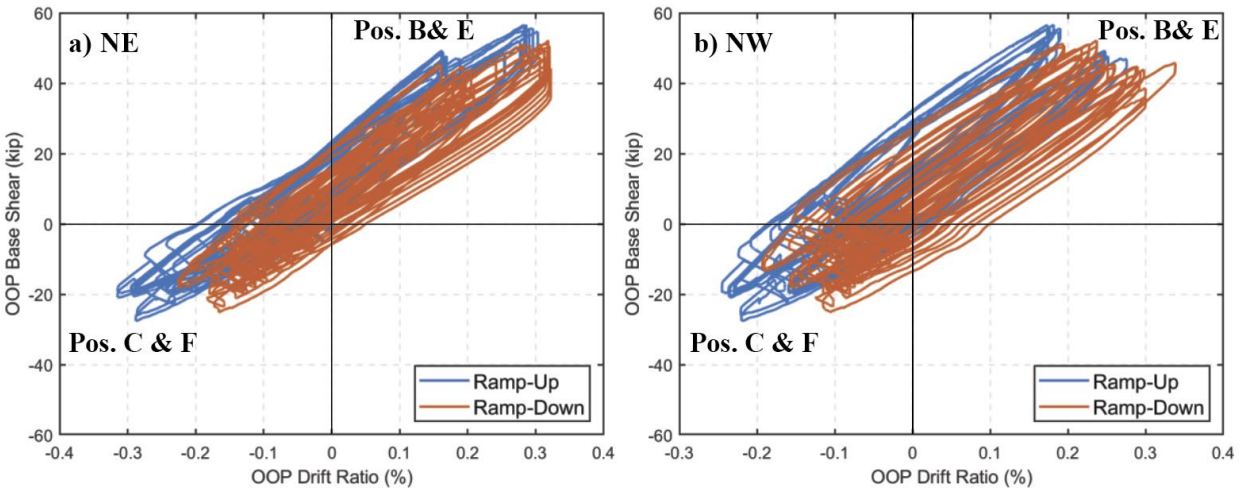

Figure 3-15: Out-of-plane base shear-drift ratio response of CW-1 recorded a) at the NE b) at the NW corners of the top block under WLP

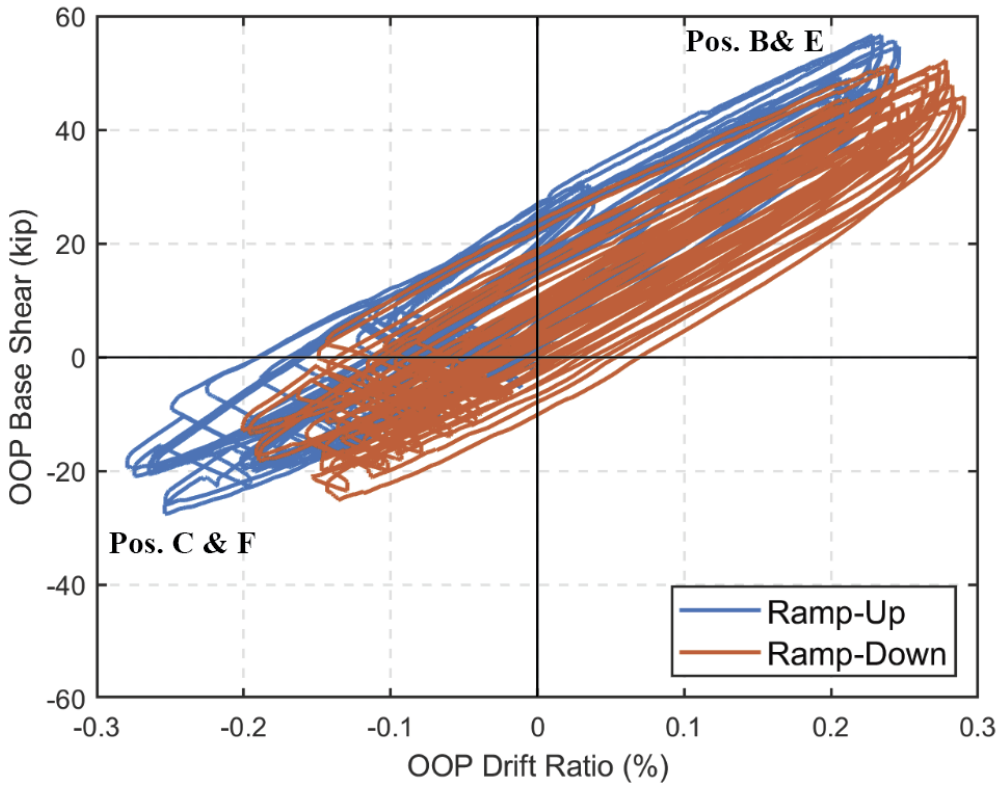

Figure 3-16: Out-of-plane base shear-average drift ratio response of CW-1 under WLP

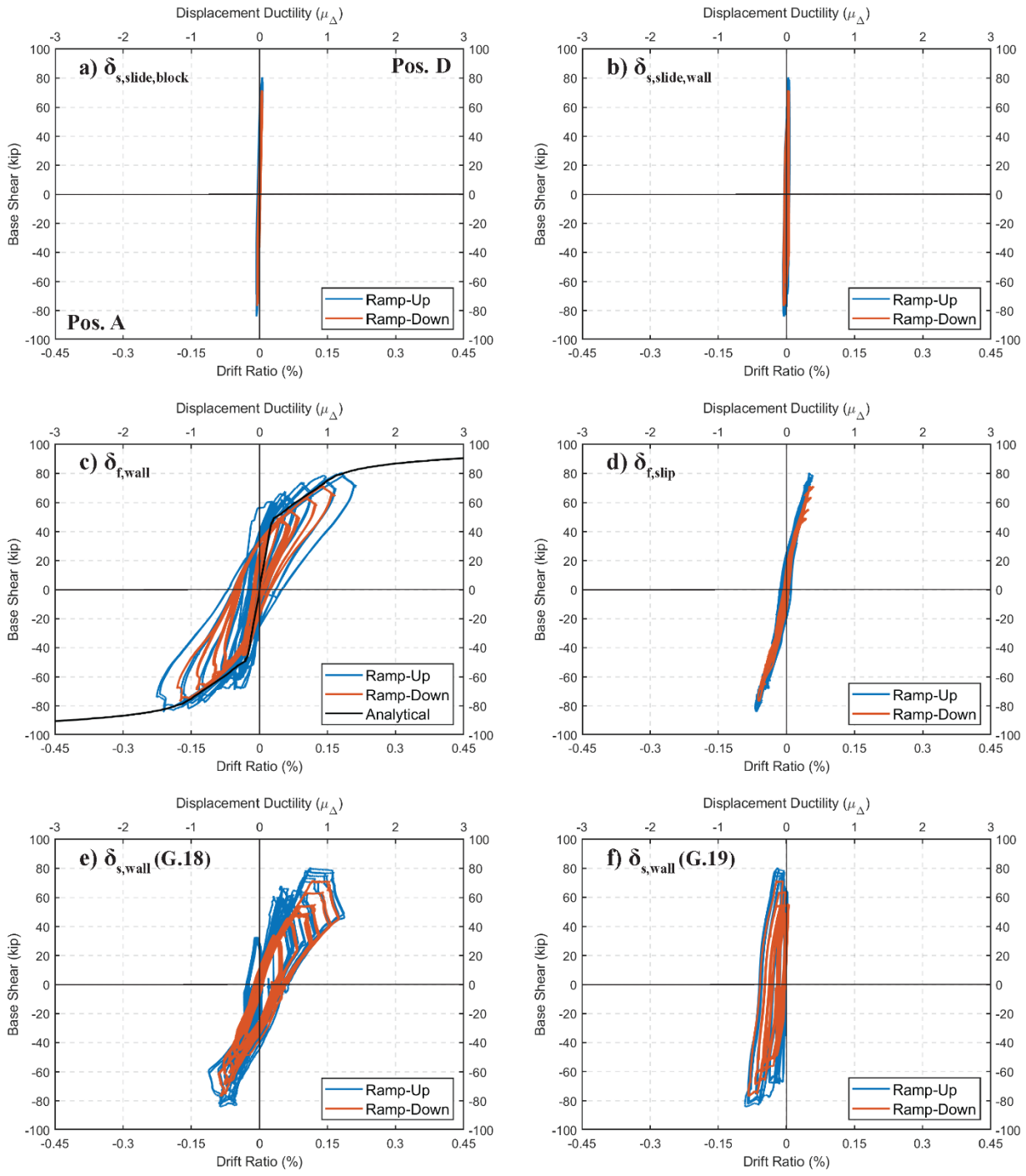

Figure 3-17: Different components of in-plane base shear-drift ratio response of CW-1 under WLP

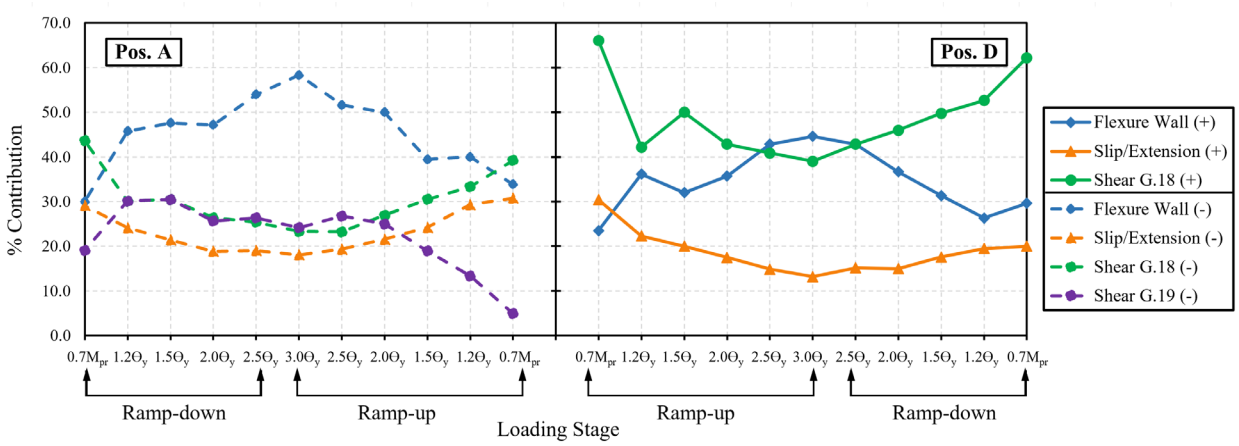

Figure 3-18: Contributions of flexure, slip/extension, and shear deformations to the lateral displacement for CW-1 during WLP

3.3.4 Torsional Response

As mentioned in Section 2.4, the out-of-plane horizontal actuators, Actuators 4 and 5 (Figure 2-22), which were used to apply the out-of-plane horizontal load, were also used to prevent the specimens from twisting during both the in-plane and out-of-plane loading. However, due to the flexibility of the test setup and possibly due to deformations at the support of Actuator 5 to the out-of-plane bracing (connected to the test setup on the east side of the specimen), torsion was observed during the testing. The torsional rotations (θ_T) at the top of the wall were calculated using the two LVDTs attached at the mid-height of the top block (Figure 2-24) on the northeast and northwest sides as follows:

$$\theta_T = \frac{\delta_{NW} - \delta_{NE}}{d_{NE-NW}} \tag{3.4}$$

where δ_{NE} and δ_{NW} are the displacement recordings of the northeast and northwest LVDTs, and $d_{NE\text{-}NW}$ is the horizontal distance between the two. The in-plane hinge rotation versus torsional rotation of the specimen during the WLP is shown in Figure 3-19b. The figure shows that during

the positive in-plane loading direction (Pos. O-D, Figure 2-37), when the west flange was under tension and the east flange was under compression, torsional rotations were minimal. Similarly, the application of OOP loading from this position, D-E-F, resulted in small torsional rotations. However, during negative in-plane loading (O-A), when the east flange was under tension and the west flange was under compression, and the OOP loading from Pos. A (A-B-C) resulted in significant torsional rotations, especially during the OOP loading. This behavior can also be observed by comparing the IP hinge rotation versus OOP hinge rotation response of the west and east flanges separately (Figure 3-19a). The comparison shows that during the in-plane loading (O-A-D-O) both flanges had some OOP rotations. For loading D-E-F, similar amounts of OOP rotations were applied to both of the flanges; therefore, small torsional rotations were observed in this direction. However, for loading A-B-C, the amount of OOP rotation applied to the east flange (flange under tension) was significantly higher than the OOP rotation applied to the west flange (flange under compression); therefore, significant torsional rotations were observed in this direction. The high torsional rotations that occurred when the east flange was under tension resulted in higher tensile strains at the edge of the east flange than at the corner of the flange. Therefore, yielding of the longitudinal reinforcement located at the edge of the flange occurred at $0.61M_{pr}$ moment demands, whereas the longitudinal reinforcement located at the corner of the east flange yielded at $0.76M_{pr}$ demands (Table 3-2). It can also be observed from Figure 3-19a and Figure 3-19b that, with the increasing in-plane rotation demands, the residual OOP rotations of both the east and west flanges and the torsional rotations increased. During the in-plane loading to the $3\Theta_y$ hinge rotation demands, the west flange had approximately -0.15%, and the east flange had approximately -0.25% residual out-of-plane rotations. Moreover, due to these differences between the flanges, there was a -0.1% torsional rotation demand at the top of the wall. Therefore,

the actual loading protocol applied to the specimen during the in-plane loading (O-A-D-O) resulted in in-plane, out-of-plane, and torsional demands on the specimen.

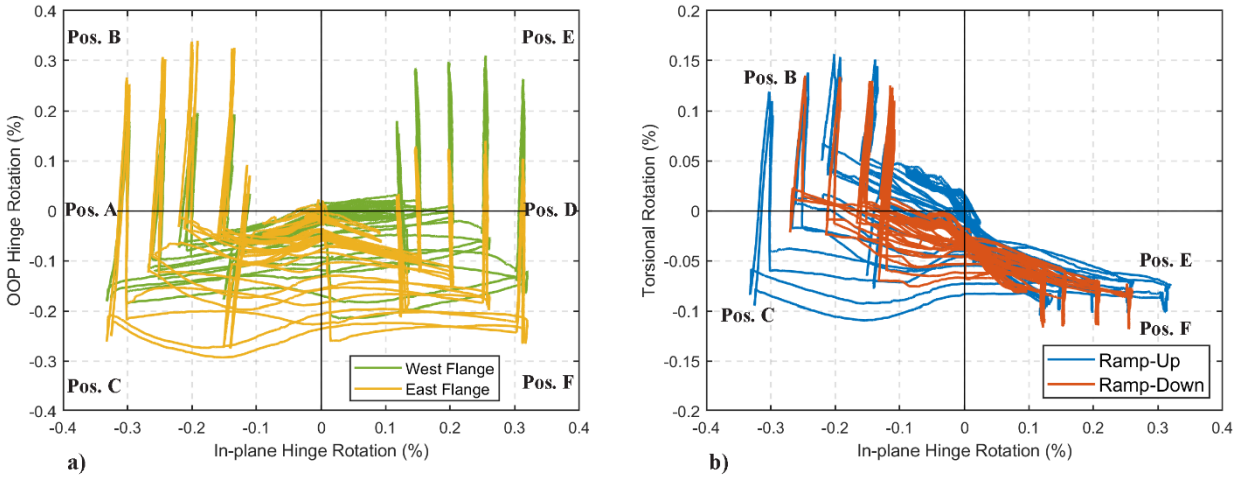

Figure 3-19: a) IP versus OOP hinge rotation of the East and West flange, b) IP Rotation versus Torsional rotation responses of CW-1 during WLP

3.3.5 Local Responses

The axial strains along the edges of the flanges were calculated using the LVDTs placed at the outside face of the east flange edge and the inside face of the west flange edge. Figure 3-20 and Figure 3-21 show the results for the ramp-up cycles of the WLP for the in-plane only loading (Pos. A and D) and for the biaxial loading (Pos. B, C, E, and F) for the east flange and the west flange, respectively. The highest tensile strain measured at the base (2-10 in.) of the east flange (Layer 1, Figure 2-24 and Figure G-1) was 0.0067 at $3\Theta_y$ hinge rotation demands at loading position A. With the application of the OOP bending in the -y direction (Pos. C), the tensile strain increased to 0.0092. Since the LVDTs were mounted to the inside surface, the tensile strains measured at the west flange were smaller compared to the east flange. For the east flange, the big crack opening above the splice region (l_s=10 in.) was inside the region for Layer 1 LVDT instrumented (2-10 in.),

whereas, for the west flange, the crack was inside Layer 2 LVDT region (10-20 in.). Therefore, the highest tensile strains, 0.0055 at Pos. D and 0.0065 at Pos. F, were measured at Layer 2 for the west flange, instead of Layer 1. The strain measurements at Layer 1 (splice region) were much lower, which was consistent with the level of damage observed in the splice region, which was mostly only minor hairline cracks. The highest compressive strain demands at the base of the east flange edge were -0.00097 at Pos. D and -0.0022 at Pos. E. Similar to the tensile strains, the compressive strains recorded with the west flange LVDTs were also smaller compared to the east flange. In fact, since the neutral axis depth after yielding was less than the thickness of the flange (5 in.), the west flange LVDTs were under tensile strain demands at the base of the wall.

The axial strain profiles along the length of the wall web under the in-plane loading only (Pos. A and D) at different hinge rotation demands are shown Figure 3-23 and Figure 3-24 for Layer 1 and Layer 2, respectively. The x-axis values in these figures show the exact location of the LVDTs attached to the wall surface, and the grey dashed lines show the location of the flanges. For example, the LVDTs attached to the inner surface of the west flange at Layer 1 were 3 in. away from the concrete surface; therefore, the x-axis value for these LVDTs was 8 in. (t_f + 3 in.). Similarly, the LVDTs attached to the outer surface of the east flange at Layer 1 were 5 in. away from the concrete surface; therefore, the axis value for these LVDTs was 80 in. (l_w + 5 in., Figure 3-22). A linear line was fitted to the data shown in Figure 3-23 and Figure 3-24 to estimate the concrete tensile and compressive strain demands at the west (x = 0 in.) and east (x = 75 in.) flanges. The strain demands given in Table 3-3 shows that the maximum tensile strain demands at the base of the wall measured at $3\Theta_y$ in-plane hinge rotation demands were 0.005 on average, and the maximum compressive strain demands were -0.0008 on average.

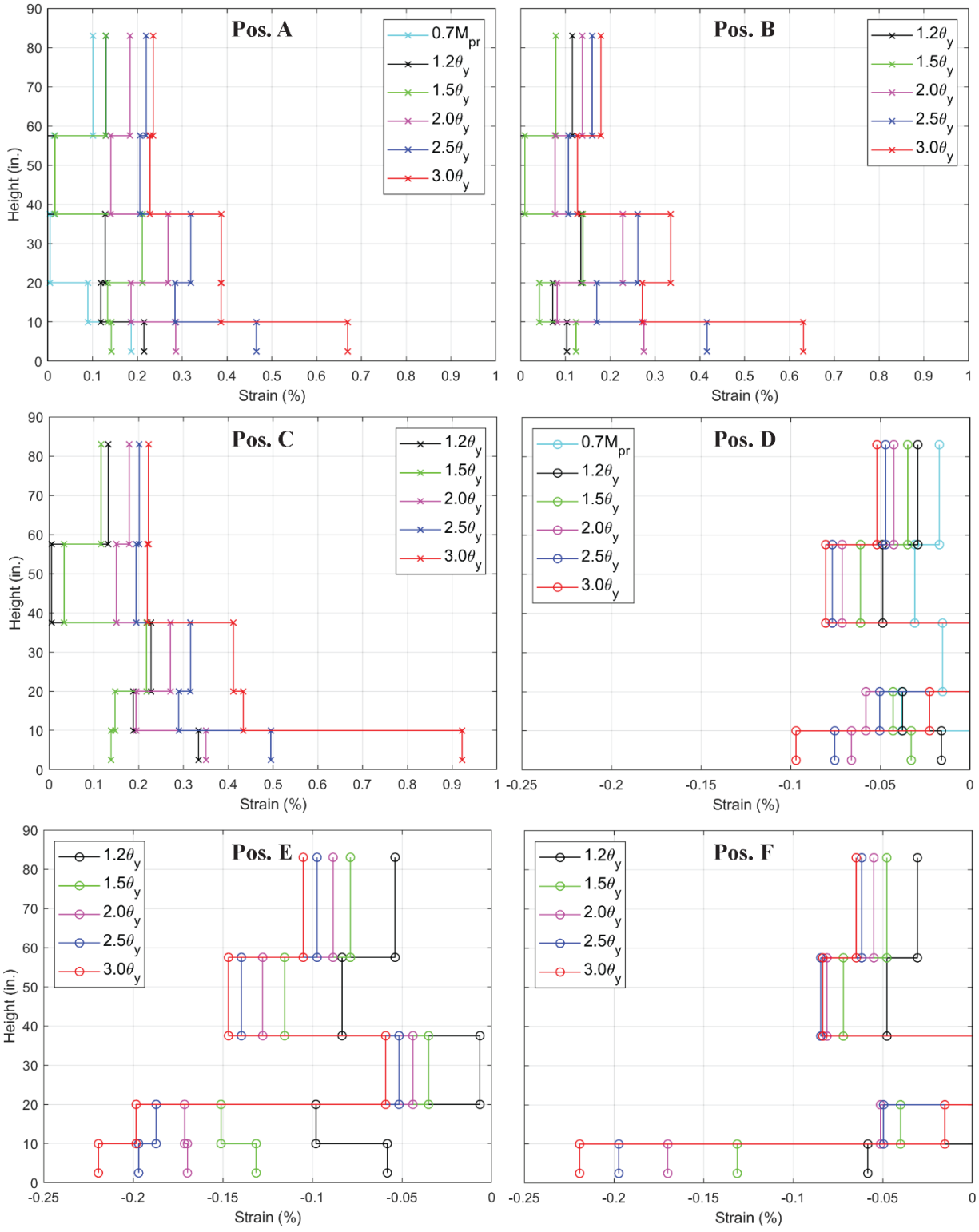

Figure 3-20: Axial strain profiles along the height of the edge of the East flange at different loading positions during WLP, CW-1

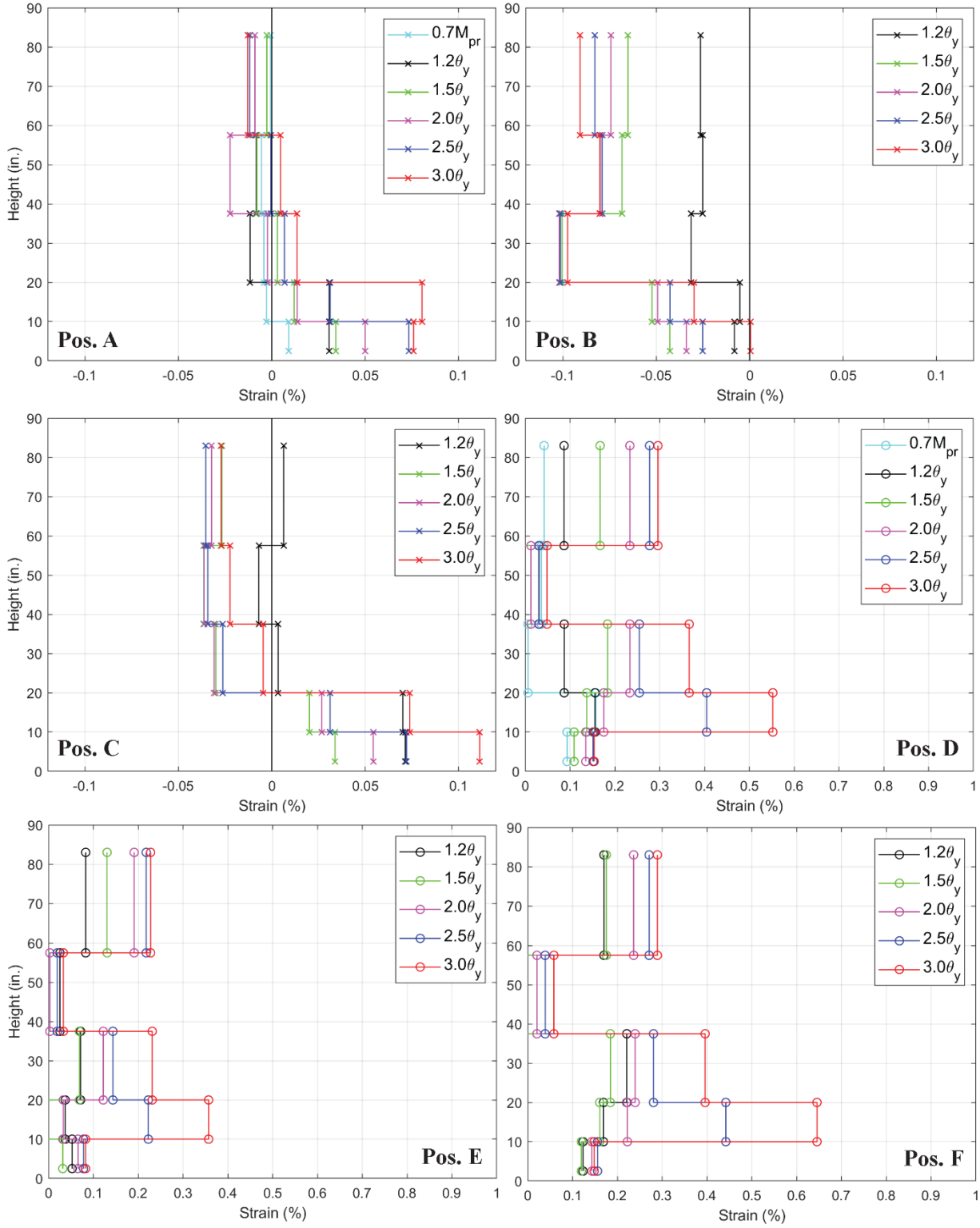

Figure 3-21: Axial strain profiles along the height of the edge of the West flange at different loading positions during WLP, CW-1

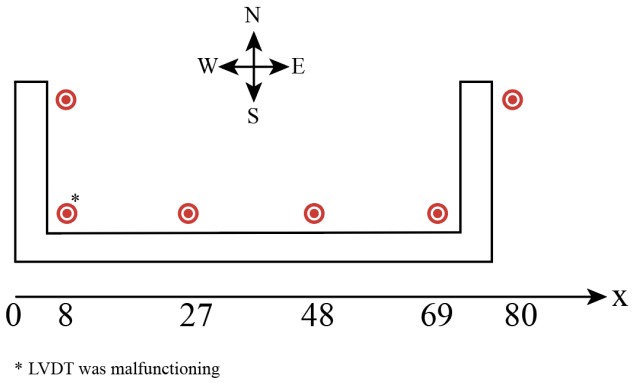

Figure 3-22: Locations of the LVDTs along the length of the web

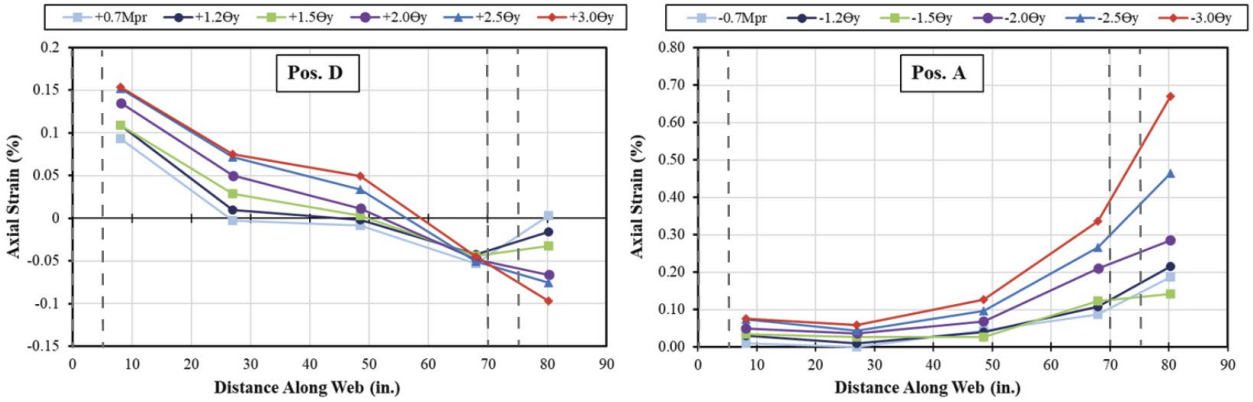

Figure 3-23: Axial strain profiles obtained from Layer 1 LVDTs

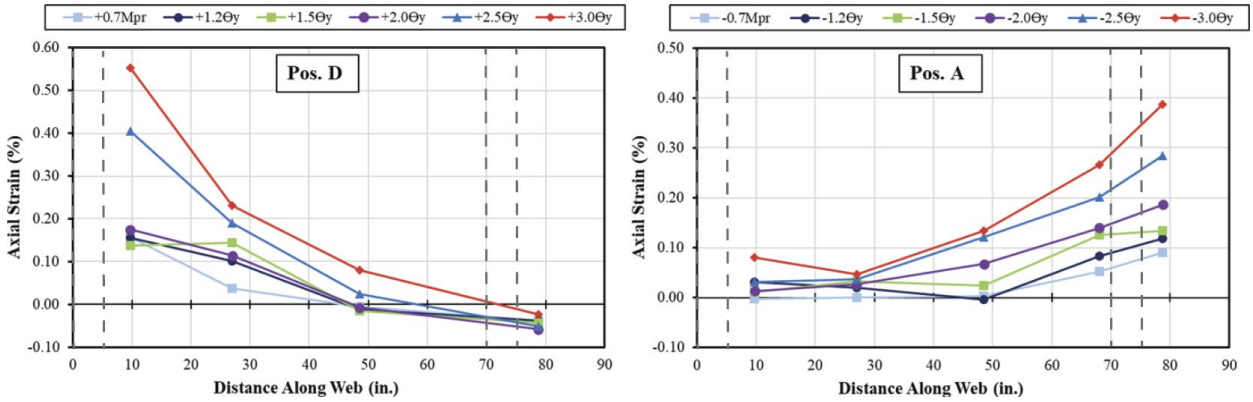

Figure 3-24: Axial strain profiles obtained from Layer 2 LVDTs

Table 3-3: Estimated maximum strain demands at $3\Theta_y$

LVDT Layers	Pos. A		Pos. D	
	West Flange	East Flange	East Flange	West Flange
	Compression	Tension	Compression	Tension
Layer 1	-0.066%	0.18%	-0.098%	0.47%
Layer 2	-0.054%	0.53%	-0.028%	0.31%

3.4 Lateral Stiffness

The effective flexural stiffness (EI_{eff}) of the specimen was calculated using Equations 3.5 and 3.6 based on the free body diagram shown in Figure 3-25.

$$EI_{eff} = \frac{M_{top}L_p + F_{top}L_pH - \frac{1}{2}F_{top}L_p^2}{\theta_{LP,IP}} \tag{3.5}$$

$$EI_{eff} = \frac{M_bL_p - \frac{1}{2}V_bL_p^2}{\theta_{LP,IP}} \tag{3.6}$$

The stiffness values, including rotations due to the reinforcement slip/extension at the base of the wall, were determined using the plastic hinge rotations measured over L_p ($l_w/2$). Figure 3-26 present the EI_{eff} values normalized with the concrete modulus of elasticity (E_c) times the gross section moment of inertia (I_g) at different rotation demands during the ramp-up portion of the WLP. The E_c value was calculated based on the ACI 318-19 provisions (Equation 2.8). Figure 3-26 shows that the effective stiffness values at the cracking moment were $0.61E_cI_g$ and $0.58E_cI_g$ for loading in the positive and negative in-plane directions, respectively. At first yield of the extreme layer flange bars ($M_b \approx 0.7M_{pr}$), EI_{eff} values of $0.36E_cI_g$ and $0.35E_cI_g$ were calculated.

The EI_{eff} values were also calculated without including the slip/extension rotations and are shown in Figure 3-26. The stiffness values were significantly higher when the slip/extension rotations were excluded from the measured hinge rotations (Figure 3-26). At the first yield, EI_{eff} values of $0.7E_cI_g$ were calculated. As shown in Figure 3-18, at first yield, both the slip/extension and flexural rotations (curvatures) comprised about 30% of the total displacement at the top of the wall. Therefore, when the slip/extension rotations were not included in the stiffness calculations, the EI_{eff} values doubled ($0.35E_cI_g$ versus $0.7E_cI_g$). At the cracking moment, the stiffness values calculated were not reliable because the measured deformations were small.

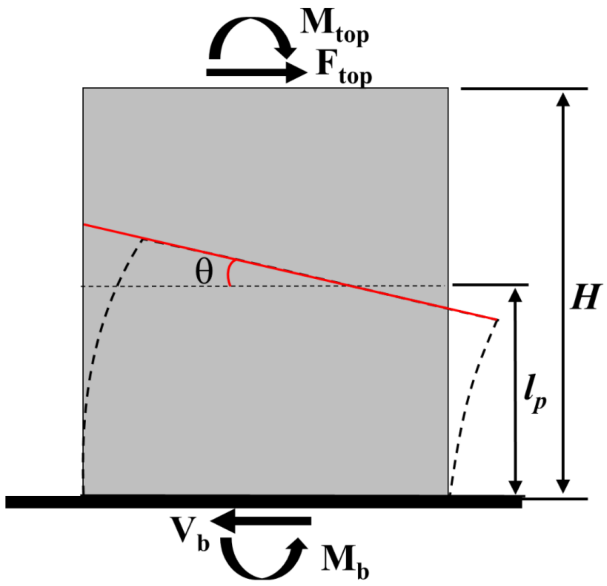

Figure 3-25: Free body diagram of wall panel

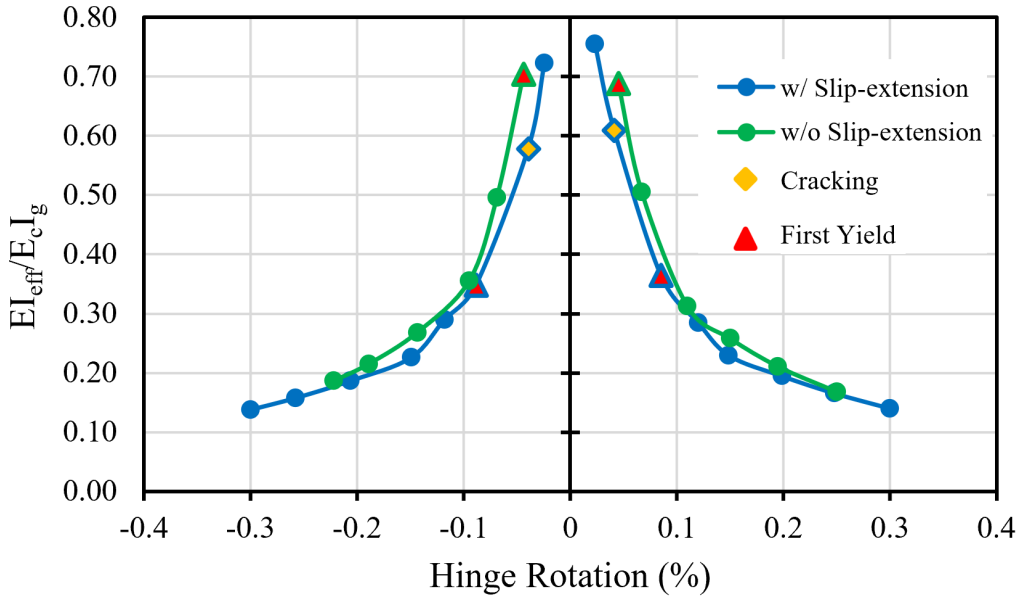

Figure 3-26: Normalized effective flexural stiffness (EI_{eff}/E_cI_g)

3.5 Vertical Growth

The vertical growth at the top of the specimen was calculated using the vertical line of LVDTs attached at the flange edges. The readings from the east and west flanges were averaged to calculate the vertical growth in between the flanges, shown as X in Figure 3-27, which was approximately 20 in. from the center of mass of the wall (shown as C). The in-plane hinge rotation versus vertical growth response during the ramp-up and ramp-down portions of the WLP is shown in Figure 3-28, where the vertical lines were due to the application of OOP loading. At $-3\Theta_y$ hinge rotation demand (east flange under tension), the vertical growth was measured as 0.15 in., which was slightly higher than the loading in the positive direction (west flange under tension, 0.13 in.). The difference was because the LVDTs for the west flange were attached to the inside surface, lower tensile displacement demands were observed than those for the east flange (where LVDTs were attached to the outside surface). At the end of the ramp-up cycles, the residual vertical (axial) growth was

approximately 0.05 in. (0.13% of L_p). However, no residual growth was observed after the application of the ramp-down cycles.

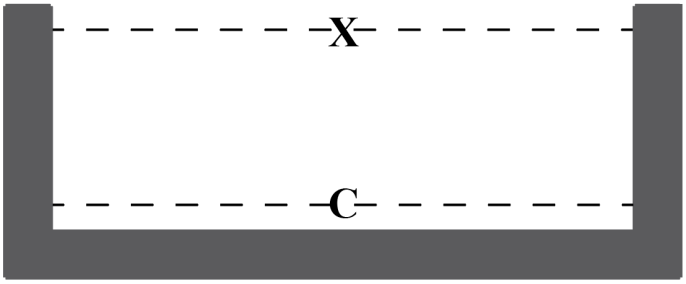

Figure 3-27: Center of mass of the wall (C) and the location where the vertical growth was measured (X)

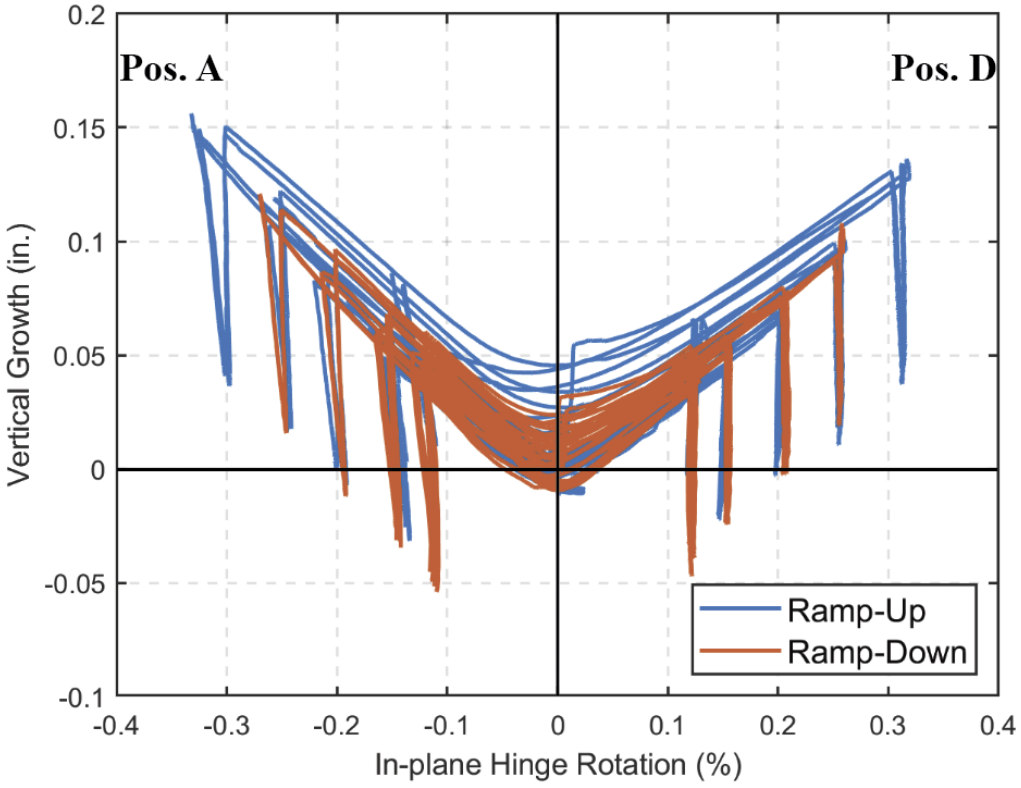

Figure 3-28: IP hinge rotation-vertical growth response of CW-1 during WLP

3.6 Impact of Lap Splices

As mentioned in Section 3.2, no damage was observed in the splice region of either the flanges or the web of the specimen. No cracks were visible during the maximum rotation demands ($3\Theta_y$) to the naked eye, and the DIC analysis showed only small hairline cracks over the splice region (Figure 3-4 and Figure 3-5). Similarly, the LVDTs attached to the edge of the west flange within the splice region showed that the tensile strains were approximately 25% of the strains measured above the splice region. Therefore, the added longitudinal reinforcement over the splice region stiffened and strengthened the splice region, resulting in a shifting of the plastic hinge to the region above the splice region. The assumed plastic hinge length was changed to $L_p=l_w/2+L_s$ (37.5+10 = 47.5 in.) from $l_w/2$ (37.5 in.), and the hinge rotations were recalculated. The LVDTs attached to the fourth layer (37.5-57.5 in., Figure G-1) were used for the more extended hinge rotation calculations. Assuming a constant strain distribution over Layer 4 (20 in. long), the vertical displacement over the first 10 in. of the layer was calculated and added to the values measured by the LVDTs previously used for the hinge rotation calculation (0-37.5 in.). Figure 3-29 shows the base moment in-plane hinge rotation ($L_p=l_w/2+L_s$) response of CW-1 under WLP, where the rotation ductility was calculated using the effective yield hinge rotation value of 0.11% (Appendix F). The increased hinge region did not result in big differences for the elastic portion of the loading protocol, i.e., the curvatures were very small at Layer 4 during these cycles, compared to Figure 3-10 ($L_p=l_w/2$). A 10% increase was observed in the negative direction at the maximum rotation demands, i.e., $3\Theta_y$ and $3.3\Theta_y$ with $L_p=l_w/2$ and $L_p=l_w/2+L_s$, respectively. Since vertical LVDTs were attached to the inside face of the west flange, in the positive direction (west flange under tension) the change was smaller ($3.1\Theta_y$).

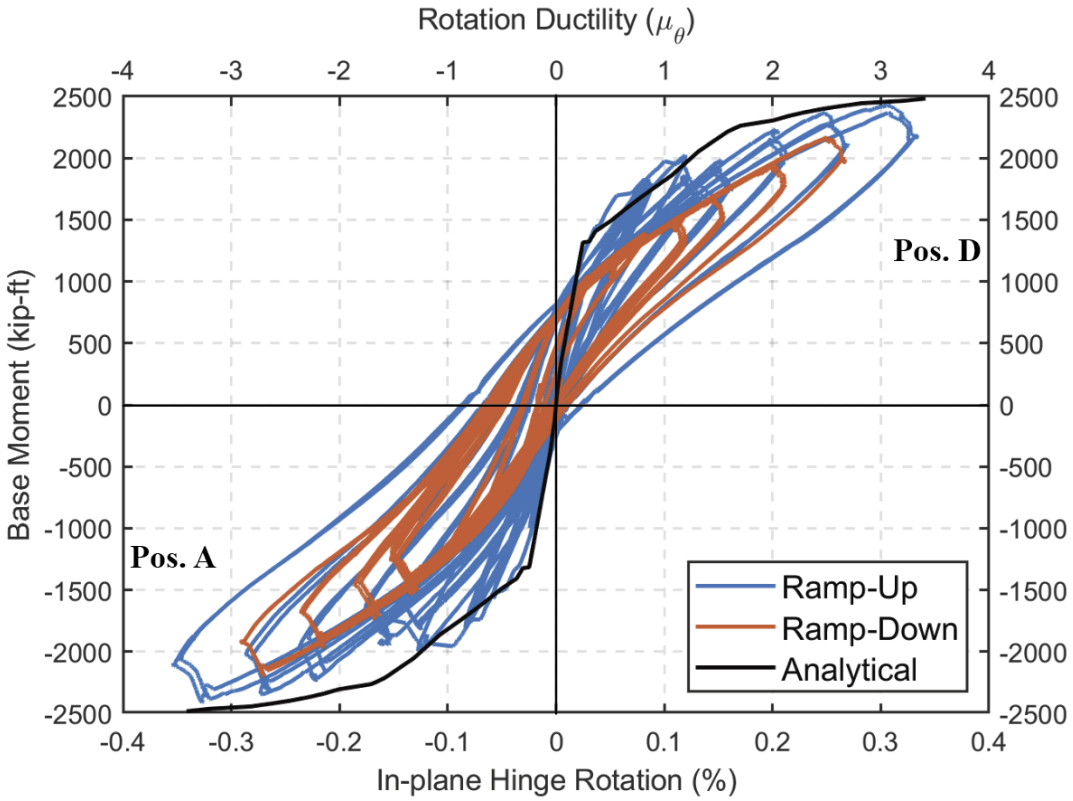

Figure 3-29: In-plane moment-hinge rotation ($L_p=l_w/2+L_s$) of CW-1 under WLP

4. Experimental Seismic Test Results and Discussion (CW-1)

4.1 General

This chapter summarizes the experimental results of CW-1 under the seismic loading protocol (SLP, Figure 2-39) applied after the completion of WLP. The loading was applied under displacement-control (uniaxial loading, in-plane only) with 3 cycles at $5\Theta_y$, $7.5\Theta_y$, and $10\Theta_y$, 2 cycles at $15\Theta_y$, and 1.5 cycles $20\Theta_y$ hinge rotation demands before failure occurred at the second half cycles at $20\Theta_y$ rotation demands. Table 4-1 shows the applied moment (at the first cycle) and hinge rotation demands during the SLP. Around 0.8% hinge rotation demands, a change in the slope of the moment-rotation response of the specimen was observed in both -x and +x directions. This change was due to the small stroke capacity of the hydraulic jacks used to apply the gravity axial loads (Figure 2-23). Because of the vertical growth of the wall, around 0.8% rotation demands, the stroke of the jacks located above the flange that was under tension was reached. After the stroke limit was reached, any increase in the vertical growth was resisted by the high-strength Dywidag bars used to connect the jacks to the laboratory strong floor. Therefore, higher lateral forces were required to apply the hinge rotation demands shown in Table 4-1.

Table 4-1: Applied in-plane base moment and hinge rotation demands during SLP, CW-1

Load Step	Positive x-direction		Negative x-direction	
	Base moment, $M_{b,IP}$ (k-ft)	Hinge rotation, $\Theta_{Lp,IP}$ (%)	Base moment, $M_{b,IP}$ (k-ft)	Hinge rotation, $\Theta_{Lp,IP}$ (%)
$5.0\Theta_y$	2620	0.5	-2607	-0.5
$7.5\Theta_y$	2881	0.75	-2952	-0.75
$10\Theta_y$	3261	1.0	-3048	-1.0
$15\Theta_y$	3651	1.5	-3301	-1.5
$20\Theta_y$	3693	2.0	-3233	-2.0

4.2 Observed Damage

No damage (i.e., concrete spalling, concrete crushing, bar buckling, or bar rupture) was observed during the $5\Theta_y$, $7.5\Theta_y$, and $10\Theta_y$ rotation demands. Minor cover spalling and a vertical crack above the wall-foundation interface at the corner of the west flange were observed during the first cycle to $-15\Theta_y$ (-1.5%) demand at -1.37%. At the end of the two cycles at $15\Theta_y$ demands, the vertical crack elongated to approximately 17 in. above the footing, and some more cover spalling was observed (Figure 4-1); however, for the east flange, no damage was observed (Figure 4-2). During the first cycle to -2.0% rotation demands, more cover crushing and spalling occurred, and the two corner bars located at the outer layer of the west flange buckled above the splice region. Cover spalling was observed at the east flange corner above the splice region during this cycle. Loading in the other direction to +2.0% rotation demands resulted in cover crushing at the corner and buckling of the outer layer corner bars above the splice region at the east flange. A strength loss of

15% was measured at the peak hinge rotation demand of the second cycle to -20Θ_y rotation demands. At the peak rotation demand of -2.0%, sudden concrete core crushing occurred along the total length of the west flange above the splice region, which resulted in bar buckling and rupture of almost all the longitudinal reinforcement (inside and outside layers) of the west flange. Flexural capacity suddenly dropped by 61%, and the axial load dropped to 295 kips ($0.06A_g f'_c$) from 500 kips ($0.1A_g f'_c$). Figures 4-5, 4-6, and 4-7 show the damage state of the wall after the test. DIC analysis was also completed for the 20Θ_y rotation demands for the loading both in the -x and +x directions (Figures 4-8, 4-9, and 4-10). The comparison between the results shown in Figure 4-8 and Figure 4-10 showed that, during the first cycle at -2.0% rotation demand, crack widths started growing approximately 7 in. away from the concrete surface above the splice region (left side of Figure 4-10), whereas for the second cycle at -2.0% rotation demand, due to longitudinal reinforcement buckling and concrete crushing that occurred during the previous cycle, the neutral axis depth increased to 15-20 in. The high axial tensile strains, up to 15%, shown in these figures were due to the crack opening and were very localized.

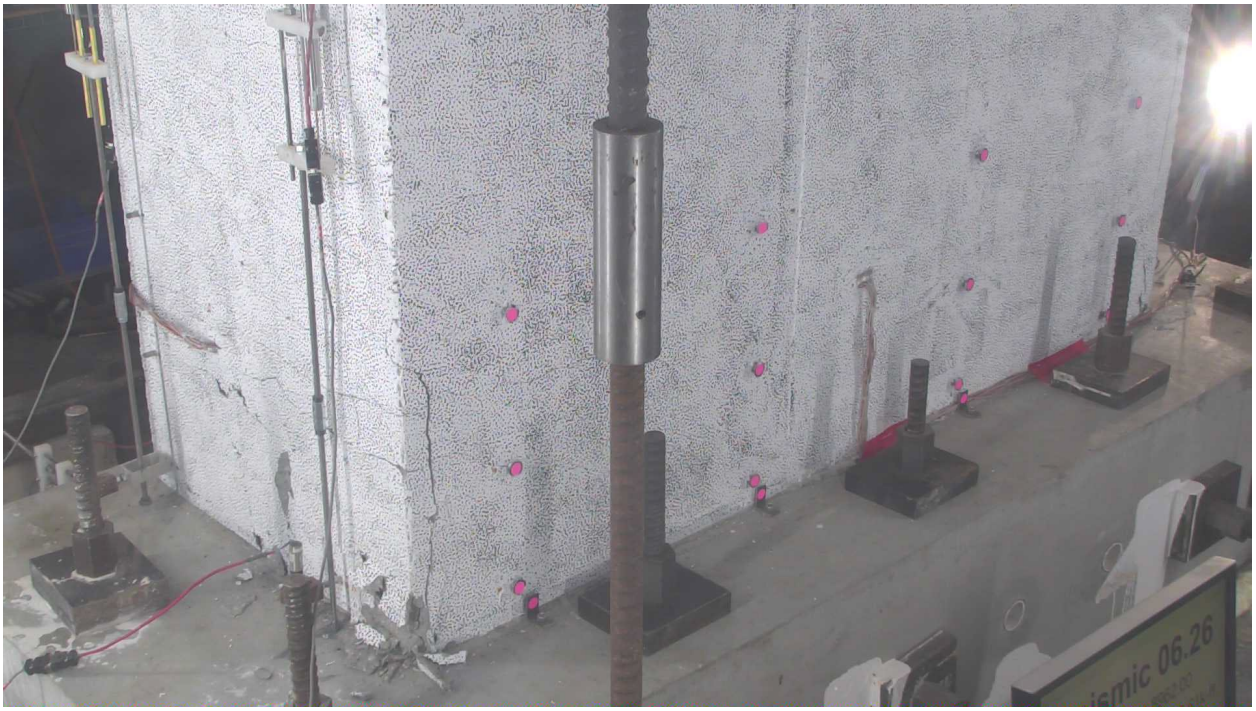

Figure 4-1: Damage state of the West flange and the web after two cycles at 1.5% hinge rotation demands (at zero loads)

Figure 4-2: Damage state of the East flange and the web after two cycles at 1.5% hinge rotation demands (at zero loads)

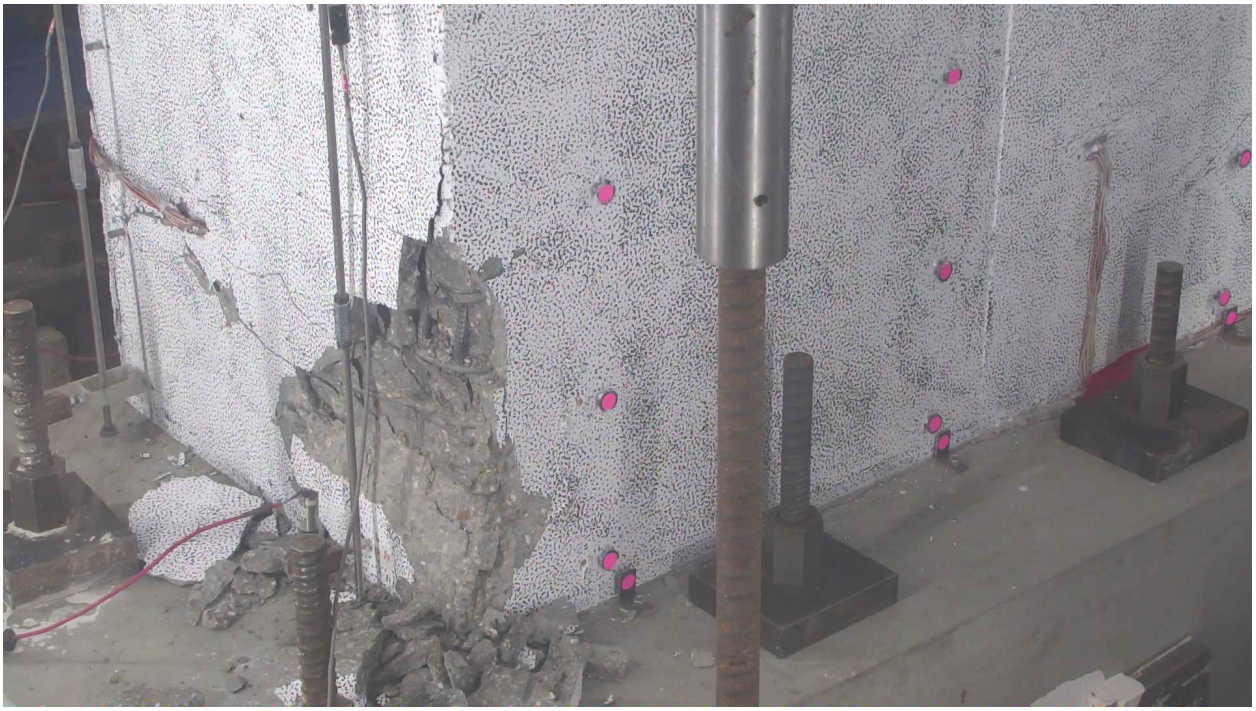

Figure 4-3: Damage state of the West flange and the web after the first cycle at 2.0% hinge rotation demands (at zero loads)

Figure 4-4: Damage state of the East flange and the web after the first cycle at 2.0% hinge rotation demands (at zero loads)

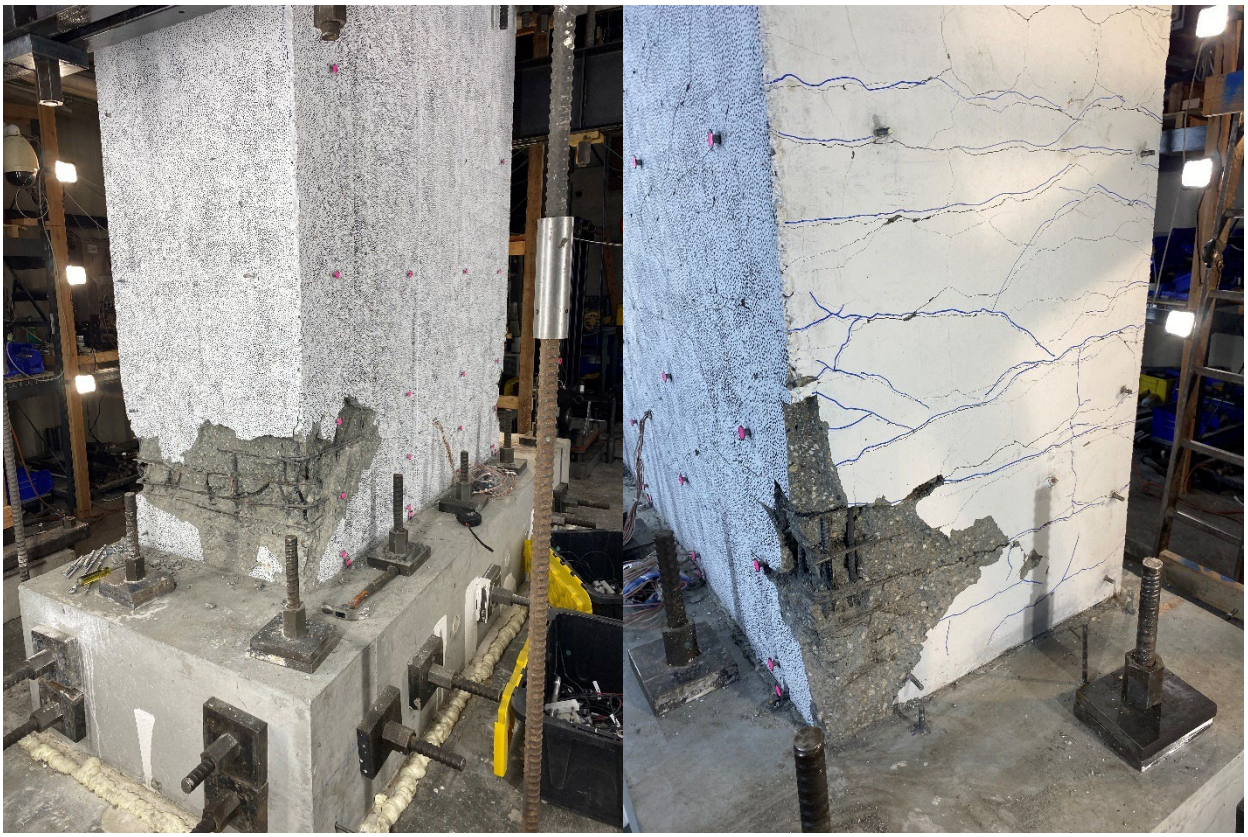

Figure 4-5: Damage state of the West flange (left) and the East flange (right) after the test

Figure 4-6: West flange close-up pictures after the test

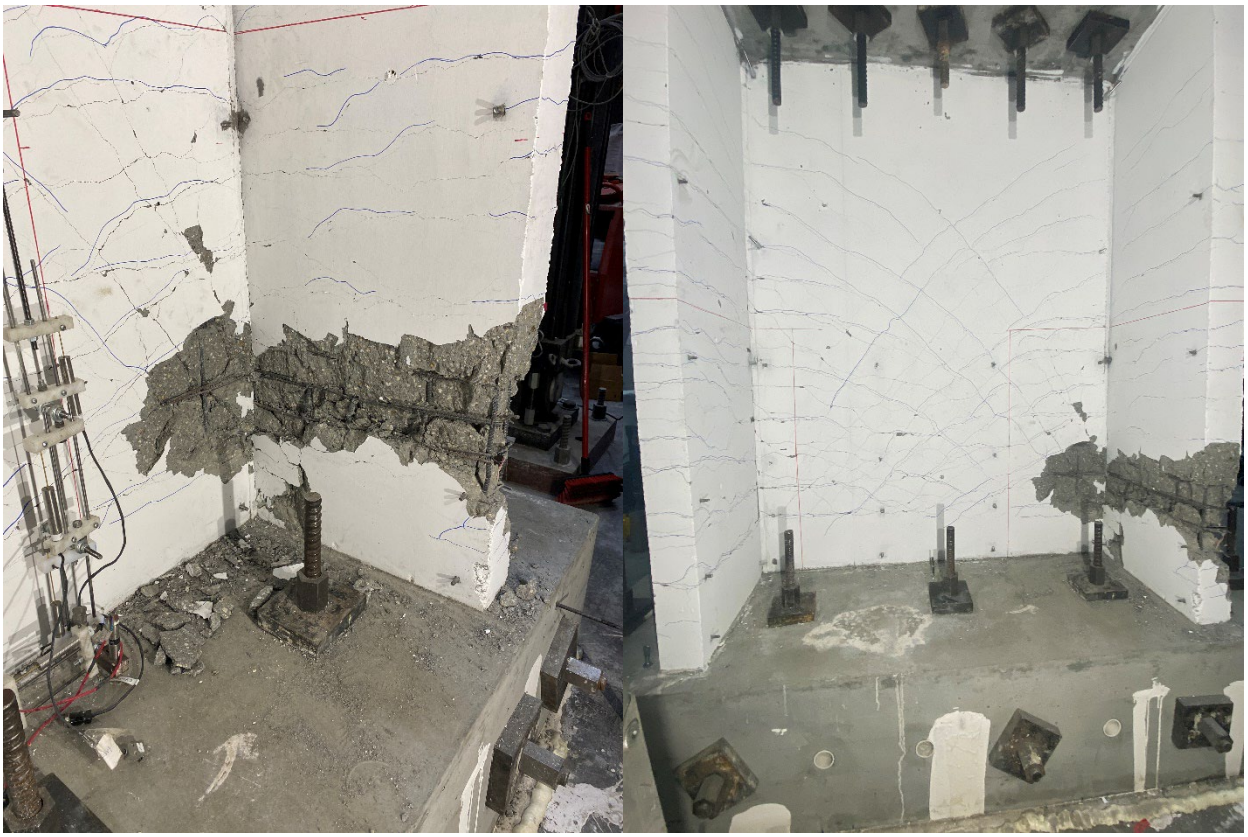

Figure 4-7: Inside surface of West flange (left) and the web (right), after the test

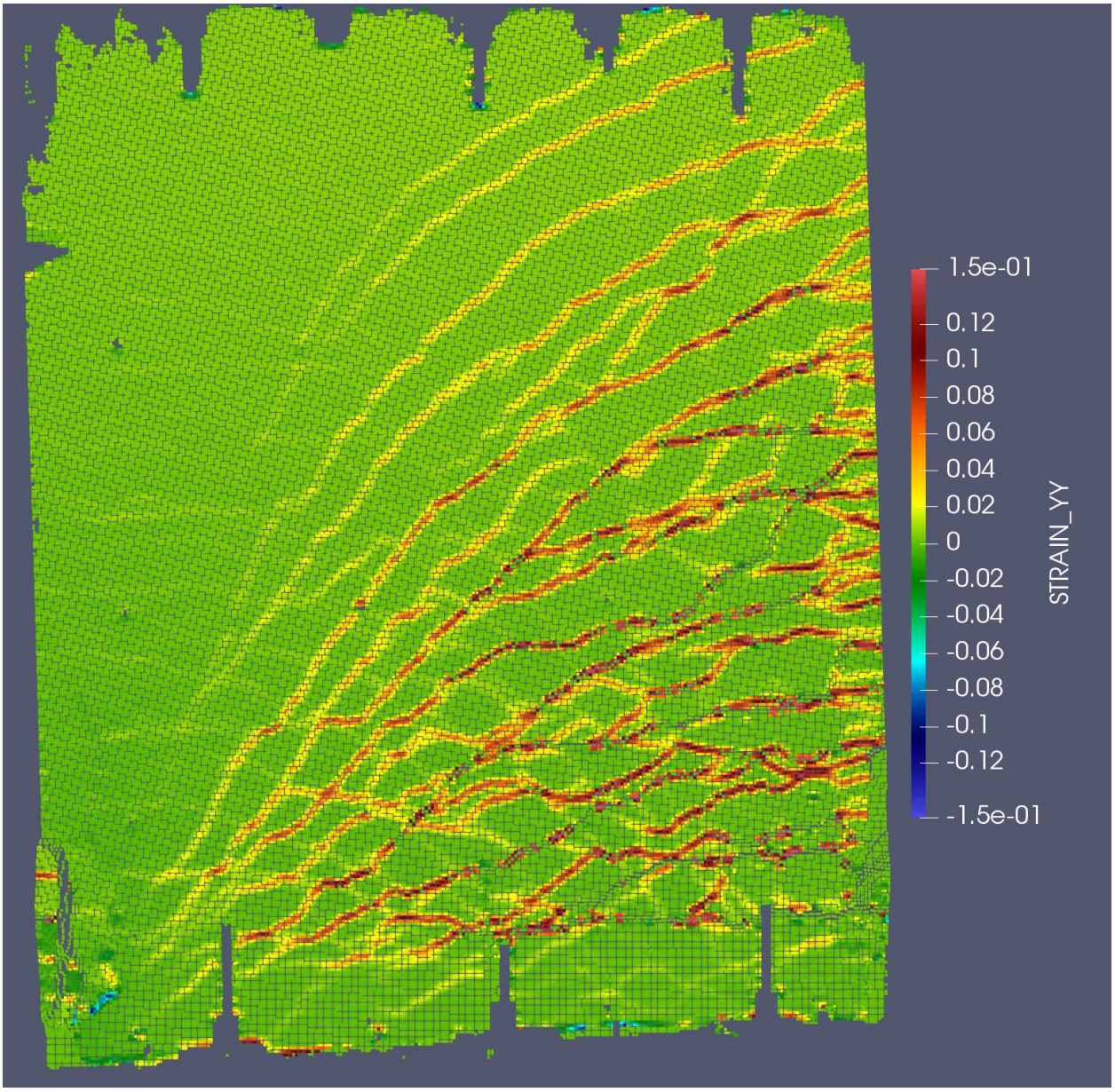

Figure 4-8: DIC analysis results at -2.0% rotation demands (first cycle)

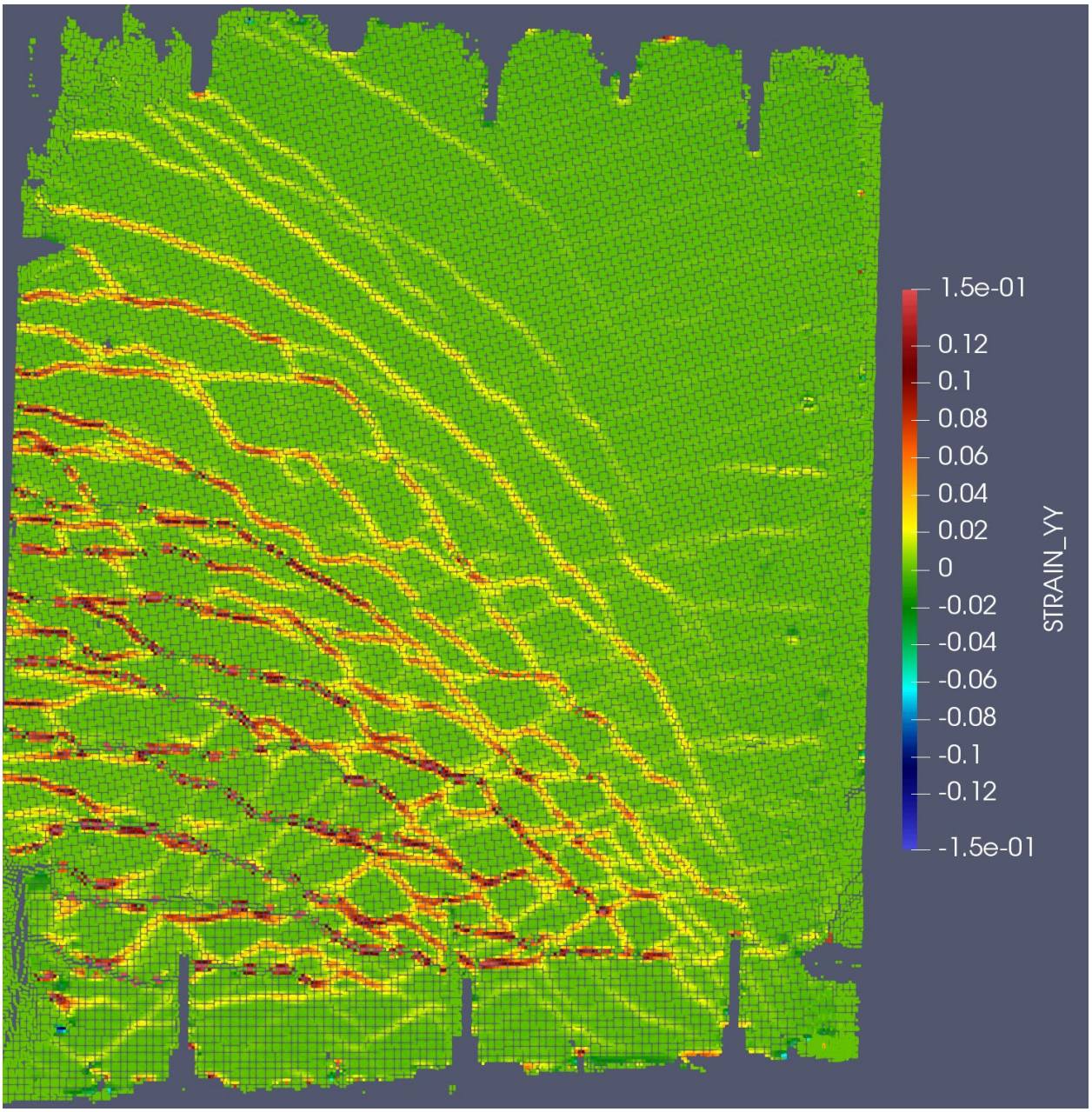

Figure 4-9: DIC analysis results at +2.0% rotation demands (first cycle)

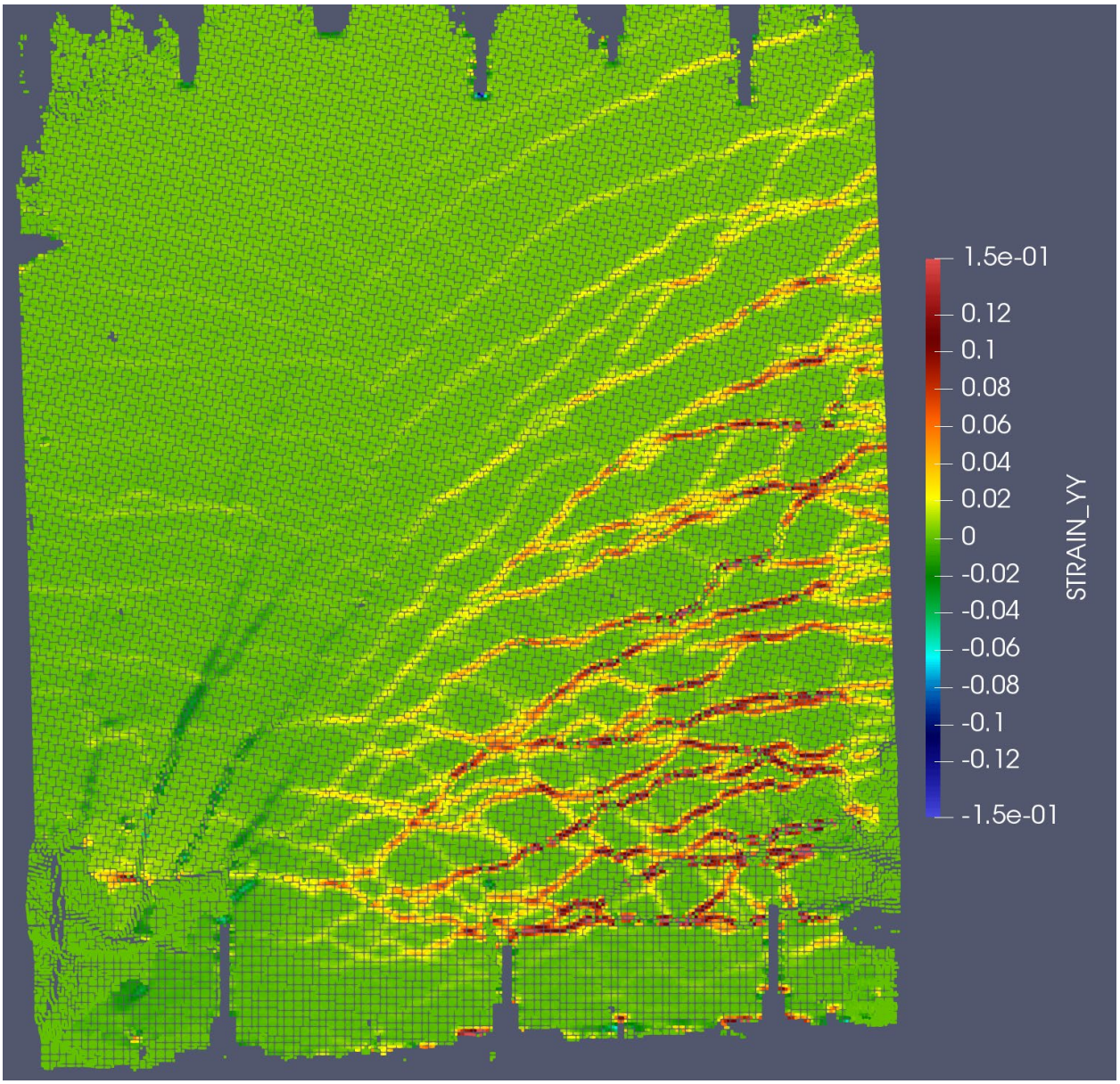

Figure 4-10: DIC analysis results at -2.0% rotation demands (second cycle)

4.3 Load-Deformation Responses

4.3.1 Base Moment-Hinge Rotation Response

The base moment-plastic hinge rotation response of CW-1 under the SLP is shown in Figure 4-11. The WLP results and the analytical prediction are also included for comparison. As mentioned in Section 4.1, since the stroke capacity of the hydraulic jacks used to apply the axial loads were reached under hinge rotation demands of around 0.8%, a change in the slope of moment-hinge rotation response occurred in both the positive and the negative in-plane loading. This change resulted in higher force demands recorded using the load cells attached to the vertical and horizontal actuators. It should be noted here that the change in the slope was not due to the behavior of the test specimen, i.e., the lateral stiffness of the test wall was not affected. After completing the SLP, test specimen CW-1 was repaired and tested again by Rodriguez Sanchez et al. (2024). The repair procedure included replacing the concrete and the reinforcements (both longitudinal and transverse) up to a height of 44 in. along the flanges and for some portions of the web (Figure 4-12). The longitudinal reinforcement in the repaired wall was coupled at 44 in. above the wall-foundation interface. The starter bars anchored to the footing were not replaced. A similar loading protocol that was applied to CW-1 was used for the repaired wall (RCW-1); however, the stroke issue with the axial jacks was addressed by using jacks with longer strokes. The moment–rotation relations for CW-1 and RCW-1 are compared in Figure 4-13 and reveal that the analytical prediction matched very well with the response of the repaired wall. The repaired wall, similar to CW-1, failed at -2% hinge rotation demands due to bar buckling/concrete crushing above the splice region. However, unlike CW-1, only a half cycle at $20\Theta_y$ was applied before the failure occurred.

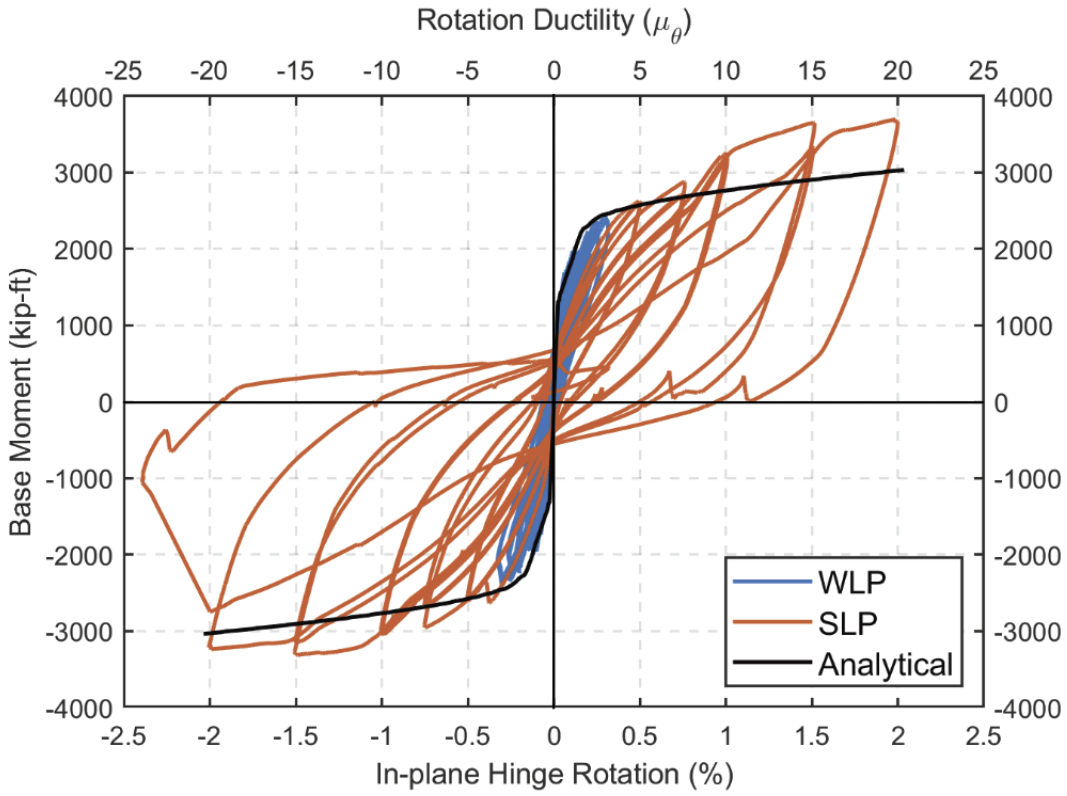

Figure 4-11: In-plane moment-hinge rotation response of CW-1, WLP & SLP

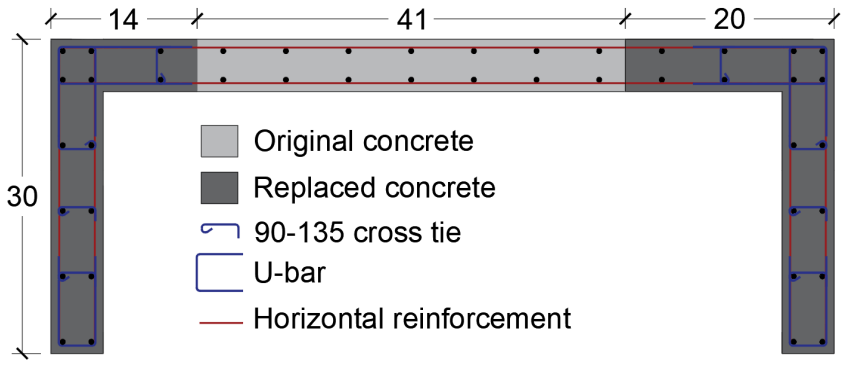

Figure 4-12: Repair scheme of CW-1 (Rodriguez Sanchez et al., 2024)

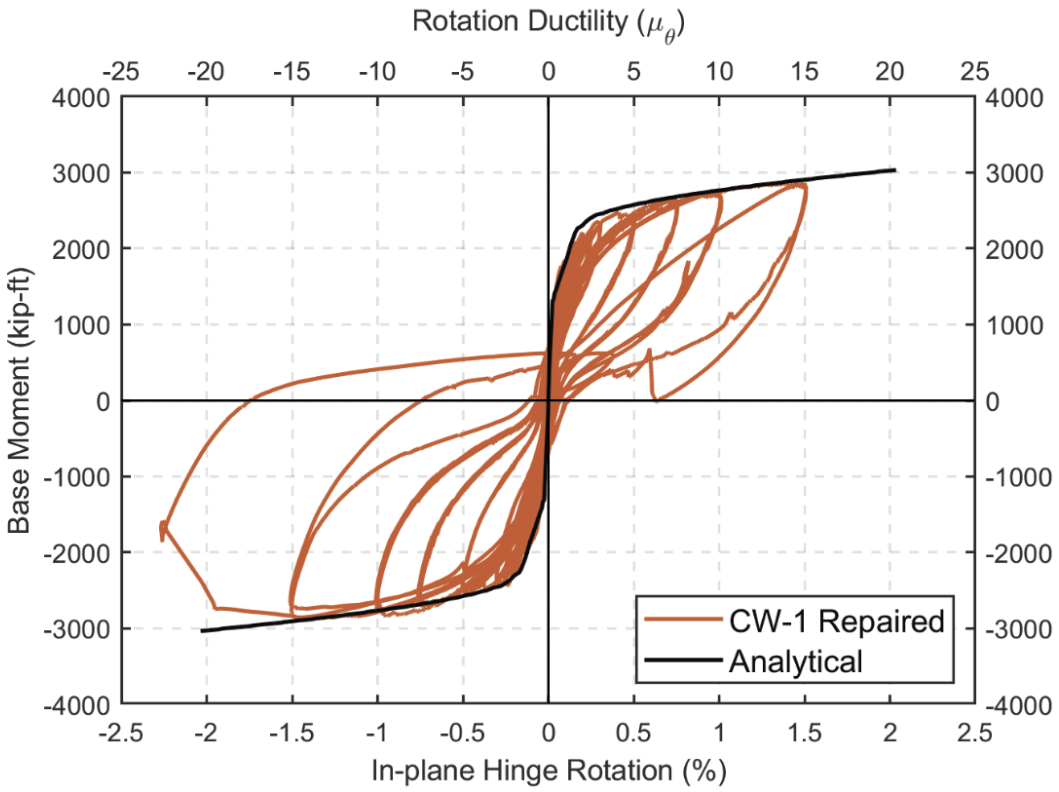

Figure 4-13: In-plane moment-hinge rotation response of RCW-1

4.3.2 Moment-Curvature Responses

The curvatures calculated using the layers of the LVDTs attached to the flange edges are shown in Figure 4-14. The average curvature ductility measured over the plastic hinge height (L_p) was found to be 22.5 and 25.0 at 2% and -2% rotation demands, respectively. Similar to the WLP, the highest curvatures were recorded at the layer where a large crack immediately above the splice region occurred (Layer 1 for the East flange and Layer 2 for the West flange). At these layers, curvature ductility of 30 was reached before the failure occurred. With increasing height, the curvature ductility decreased to 21.0, 15.0, and 10.0 on average for layers 3, 4, and 5, respectively.

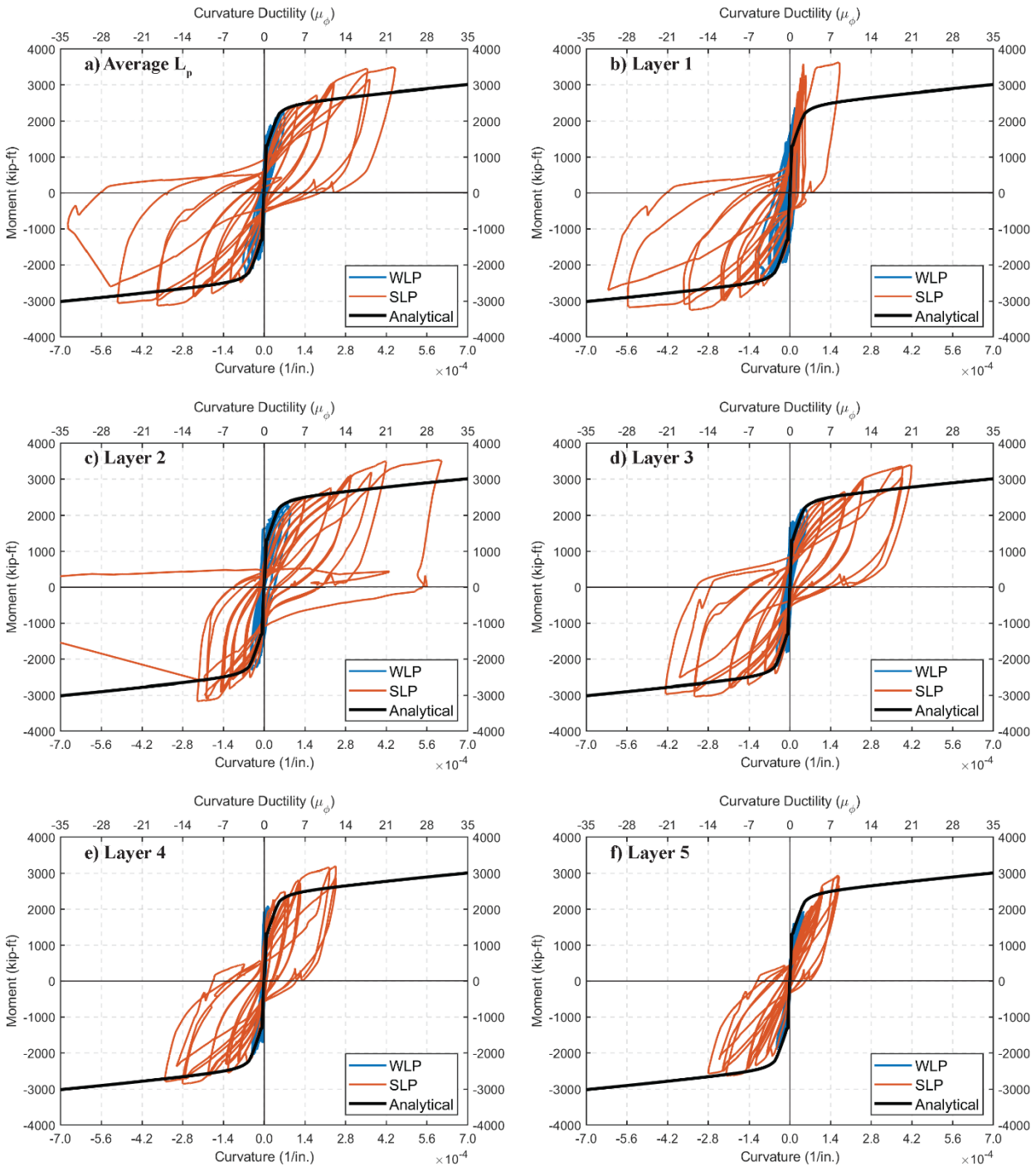

Figure 4-14: Moment-Curvature response of CW-1, WLP & SLP

4.3.3 Base Shear-Lateral Displacement Responses

The base shear-drift ratio response of the wall under the WLP and SLP is shown in Figure 4-15. For rotation demands less than 2.0%, the drift ratios were found to be mostly symmetric for the loading in the positive and negative in-plane directions. However, since the hinge rotations were controlled during the experiments rather than the drift ratios, at the first cycle of -2% hinge rotation demand, a drift ratio of -2.78% was recorded, whereas, for the loading to +2% hinge rotation demand, the drift ratio was 2.25%. The lower drift ratio at the +2% hinge rotation demand was due to damage (i.e., bar buckling, cover crushing, and cover spalling) that occurred at the east flange when the flange was under compression at the previous cycle (-2% hinge rotation demands). Similarly, because of the damage occurring at the east flange under +2% hinge rotation demands, at the second cycle to -2% rotation demands (failure point), the drift ratio was lower than the previous cycle (-2.78% versus 2.6%). Therefore, the maximum drift ratio recorded during the test was 2.78%, which resulted in an estimated displacement ductility value of 18.5.

The base shear-drift ratio responses due to flexural and shear (Equation 3.3) deformations are shown in Figure 4-16. The shear sliding along the wall-footing interface ($\delta_{s,slide,wall}$), and also the shear sliding of the bottom foundation block along the laboratory floor ($\delta_{s,slide,block}$) were found to be significantly smaller (less than 1% of the total displacement) during the SLP compared to the flexural ($\delta_{f,wall}$), shear ($\delta_{s,wall}$), and slip/extension ($\delta_{f,slip}$) deformations; therefore, they are not included in Figure 4-16. The percent contributions of $\delta_{f,wall}$, $\delta_{s,wall}$, and $\delta_{f,slip}$ are shown in Figure 4-17 for the SLP and for the ramp-up portion of the WLP. The values shown in Figure 4-17 were calculated at the peak demands of the first cycle at each load step. With increasing hinge rotation demands, the contribution of the slip/extension deformations decreased to approximately

6% at 2% rotation demands from 30% at first yield ($0.7M_{pr}$ moment demands). In the positive loading direction, shear deformations (calculated with Equation G.18) accounted for approximately 25% of the total deformation at the top of the wall. Accordingly, the contribution of flexural deformations was 60% to 65%. In the negative direction, however, the percent contribution of the flexural deformations gradually increased to 65% at $-7.5\Theta_y$ hinge rotation demands and decreased afterward to 55% at $-20\Theta_y$ hinge rotation demands (-2%). The comparison between the shear deformations calculated using Equation G.18 and G.19 resulted in similar values for the rotation demands between $-2.0\Theta_y$ and $-10\Theta_y$ with an average contribution of 25%. However, due to the decrease in the contribution of the flexural deformations after $-7.5\Theta_y$ rotation demands, the contribution of the shear deformations calculated using Equation G.18 increased to 40%. It should be noted that the differences between the positive and the negative loading directions were possibly caused by the fact that after some damage started to accumulate in the wall, although the same rotation demands were applied in the opposite directions, due to the damage that mostly occurred at the west flange, different behaviors were observed.

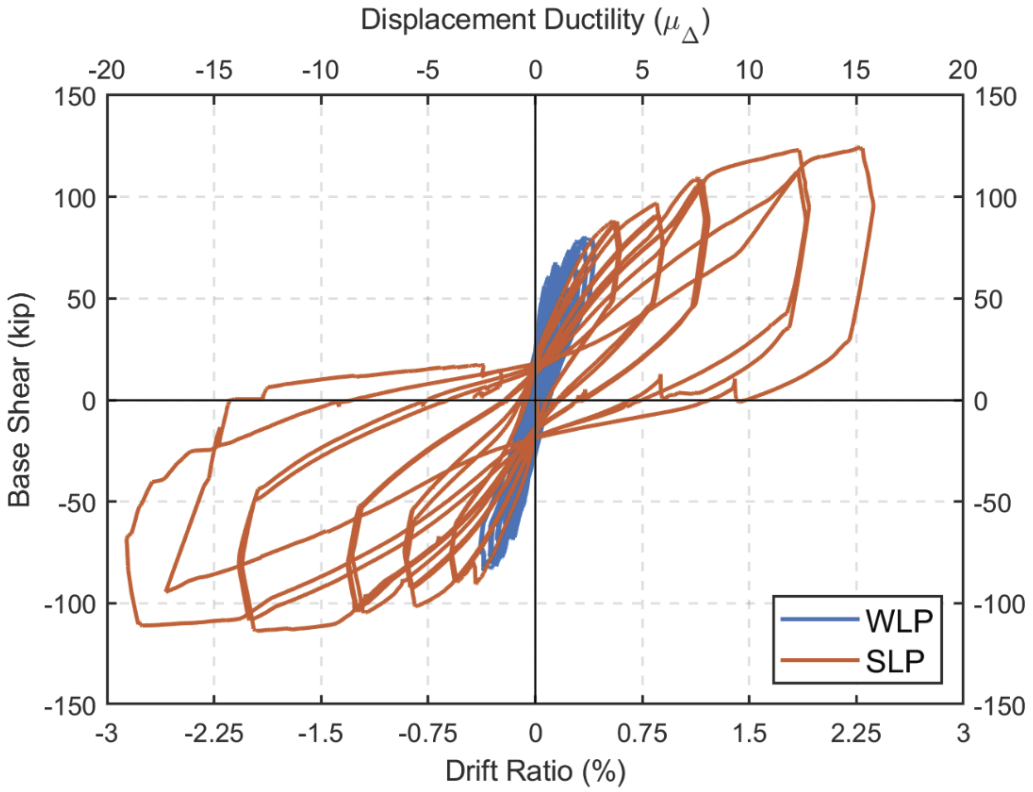

Figure 4-15: In-plane base shear-drift ratio response of CW-1, WLP& SLP

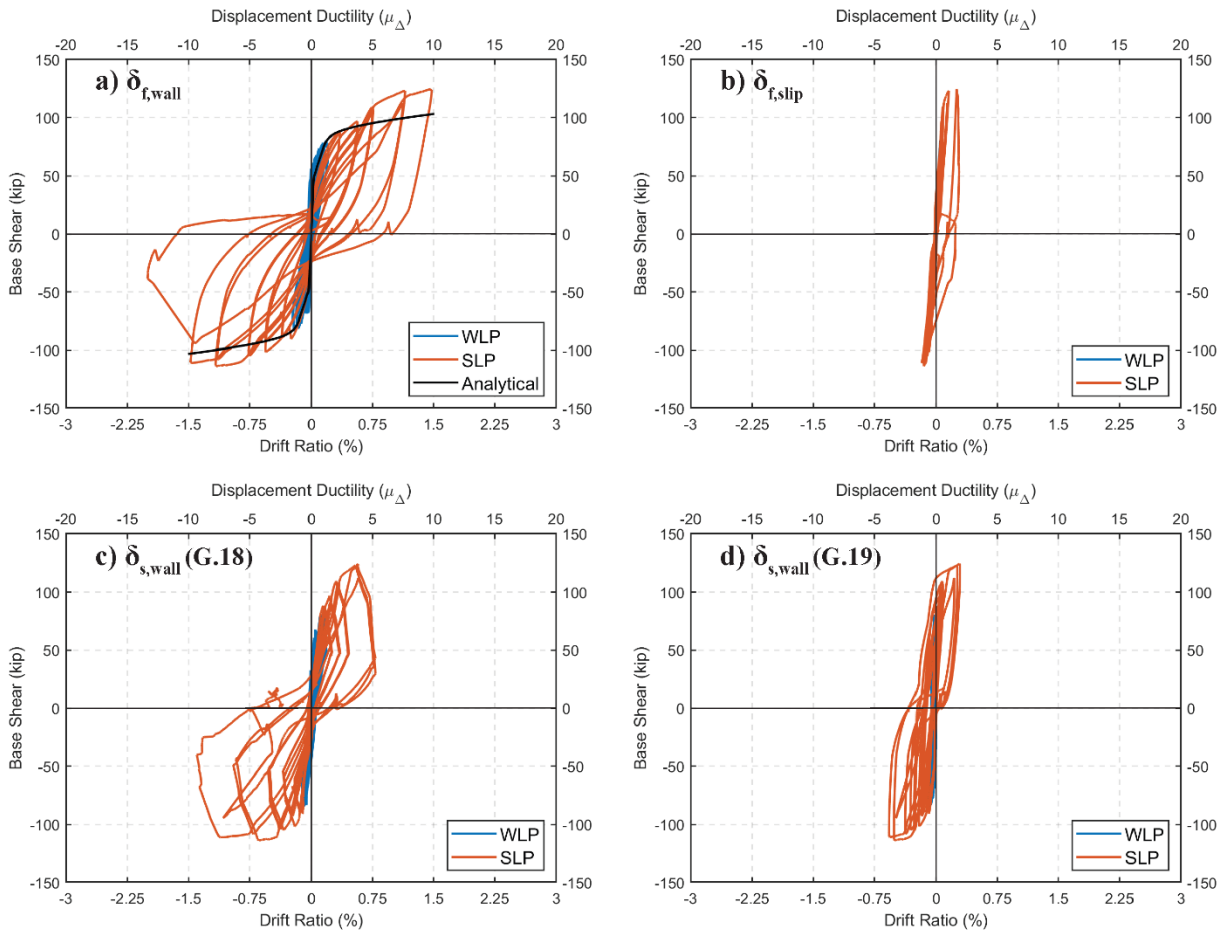

Figure 4-16: Different components of in-plane base shear-drift ratio response of CW-1, WLP & SLP

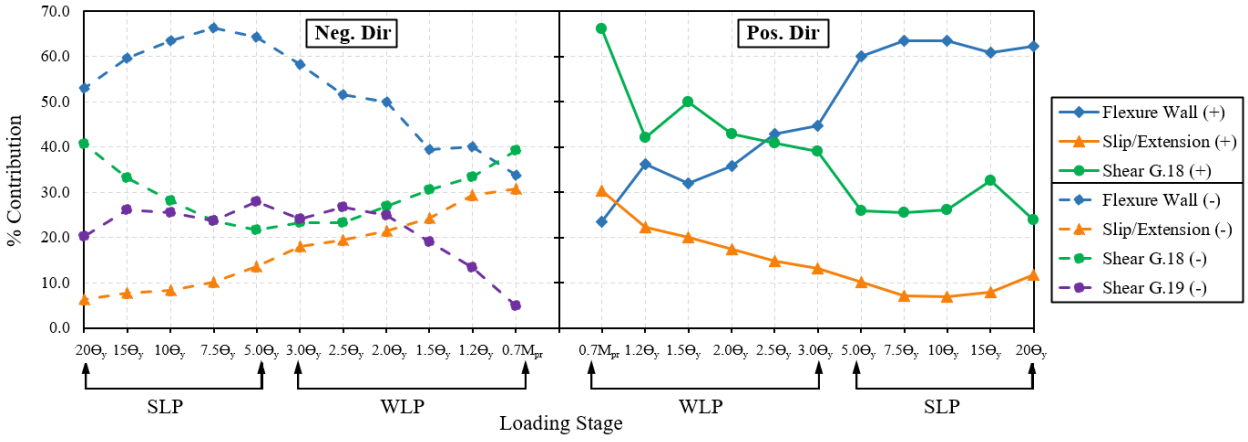

Figure 4-17: Contributions of flexure, slip/extension, and shear deformations to the lateral displacement for CW-1, WLP & SLP

4.3.4 Torsional Response

Figure 4-18 shows the in-plane versus out-of-plane hinge rotation responses of the East and the West flanges during the WLP and SLP. During the positive in-plane loading (west flange was under tension), positive (+y loading direction), and negative (+y loading direction), OOP rotations were recorded for the west and the east flanges, respectively. This behavior resulted in higher tensile strain demands at the flange-web corner of the tension flange (west flange) and higher compressive strain demands at the corner of the compression flange (east flange). Similar behavior was observed for the negative in-plane loading. Higher tension and compression resulted in earlier cover crushing and the bar buckling at the outside corners at the web-flange intersection compared to flange edges (furthest from the web).

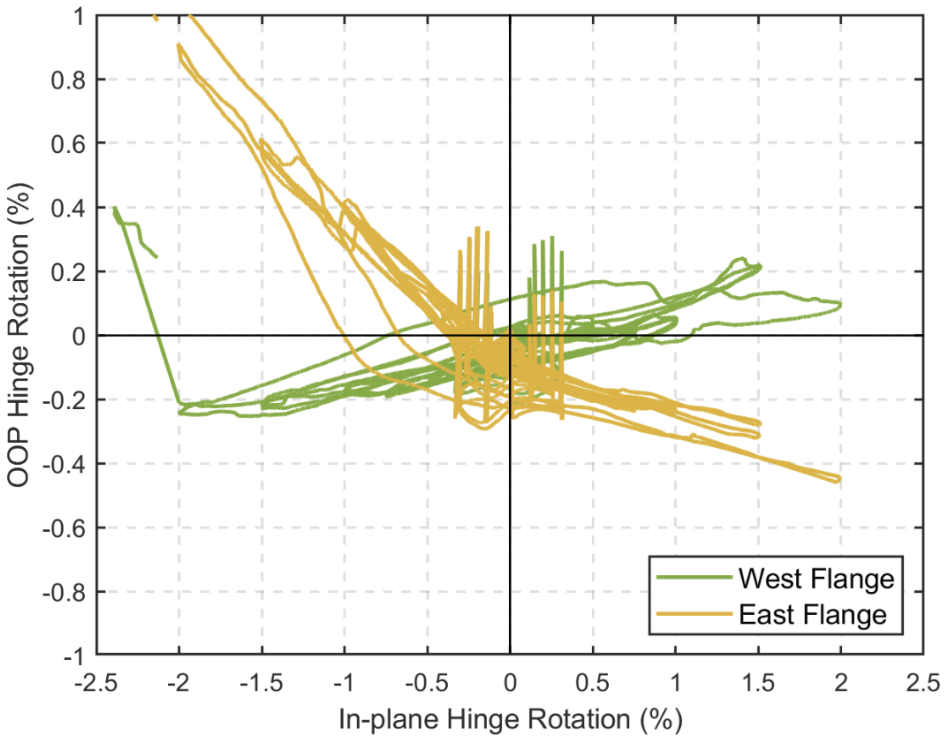

Figure 4-18: IP versus OOP hinge rotation responses of the East and West flanges of CW-1, WLP & SLP

4.3.5 Local Responses

Axial strains were measured using vertical LVDTs attached to the east (on the outer surface) and to the west (on the inner surface) flanges, as shown in Figure 4-19 and Figure 4-20, respectively. The strain values shown in these figures were measured during the first cycle of each load step. The maximum tensile strain measured at the east flange LVDTs was 5.2% at Layer 1 at -2% hinge rotation demands (-20Θ_y), whereas for the west flange, a maximum strain of 3.9% was measured at Layer 2 (above the splice region) at 2% hinge rotation demands. The tensile strains at the splice region measured using the Layer 1 west flange LVDT, 0.1% to 0.15% for hinge rotation demands less than 2%, were significantly lower than those measured above the splice region. However, an increase in the tensile strains to 0.85% at the splice region was observed at 2% hinge rotation demands. The compressive strain demand at the east flange Layer 1 LVDT was as high as -0.9% (-0.009 in./in.) at 2% hinge rotation demands. However, it should be noted here that, given the neutral axis depth, since the LVDTs were located a couple of inches away from the concrete surface (Figure 2-28), the measured LVDT strains overestimate the actual strains at the concrete surface by as much as 100%. It should also be mentioned that the torsional rotations resulted in tension at the east flange edge, which would cause lower compressive strain demands compared to a test where no torsional rotations exist during the in-plane loading.

During the loading in the negative in-plane direction (the west flange was under compression), the LVDTs attached to the inner surface of the west flange were mostly under tension. This was due to the fact that first, the neutral axis depth was inside the west flange, and second, the torsion observed during the in-plane loading resulted in tension at the west flange edge under loading in the negative direction. The axial strain profiles along the length of the wall are given in Figure 4-21 and Figure 4-22 for Layer 1 and Layer 2 LVDTs, respectively, where the grey dashed lines

show the location of the flanges. These figures show that, for the C-shaped test specimens, due to observed torsion and the shear lag effects, plane sections do not remain plane, i.e., the distribution of the strains along the length of the web is not uniform. This behavior of the flanged walls might play an important role in the modeling of these walls, i.e., models with plane section assumptions might underestimate the concrete strains.

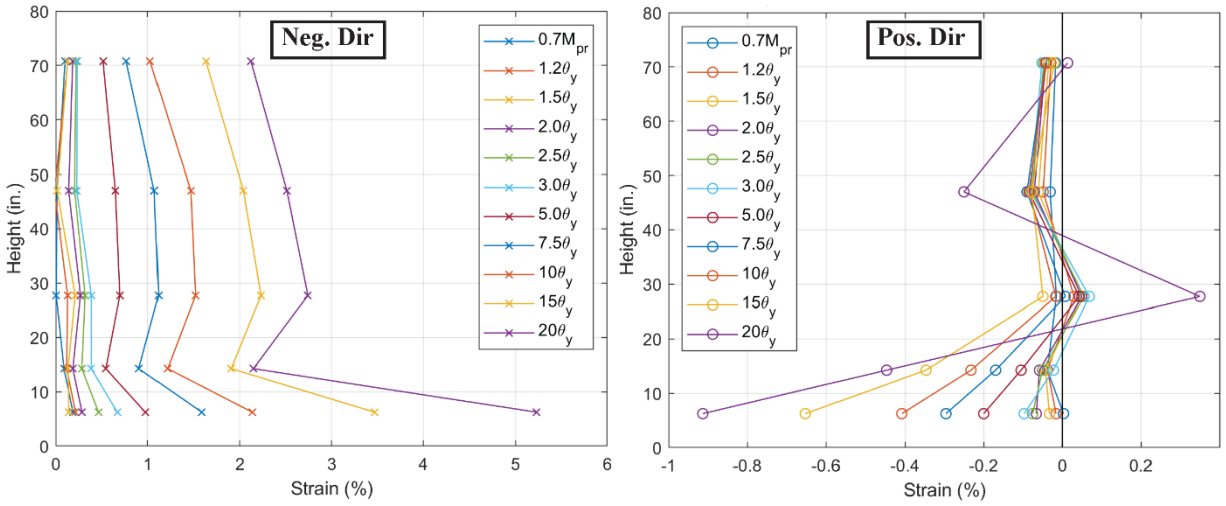

Figure 4-19: Axial strain profiles along the height of the edge of the East flange at the negative (left) and positive (right) in-plane loading, WLP & SLP

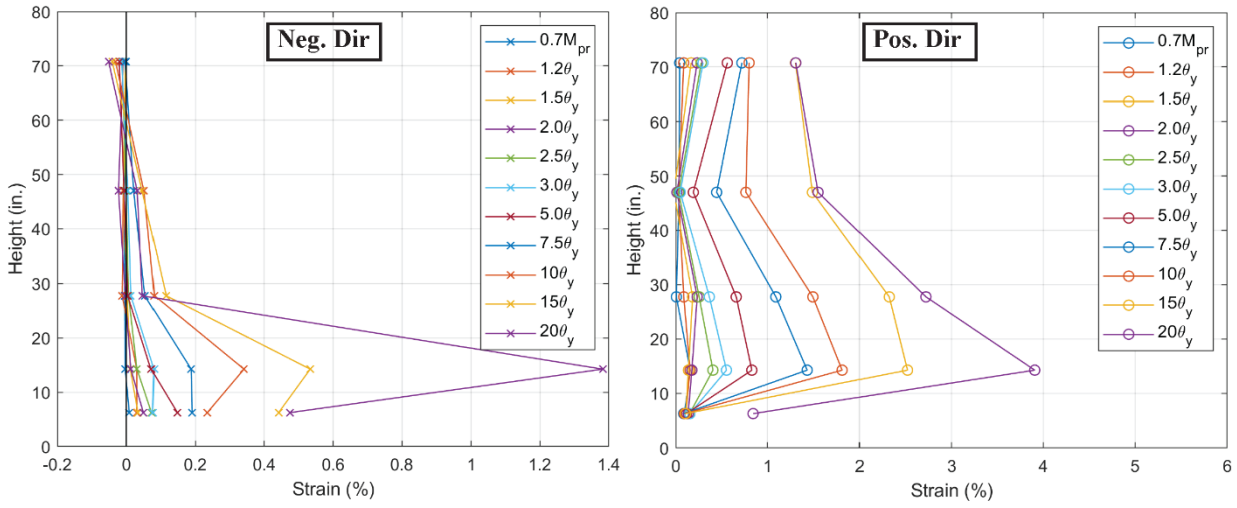

Figure 4-20: Axial strain profiles along the height of the edge of the West flange at the negative (left) and positive (right) in-plane loading, WLP & SLP

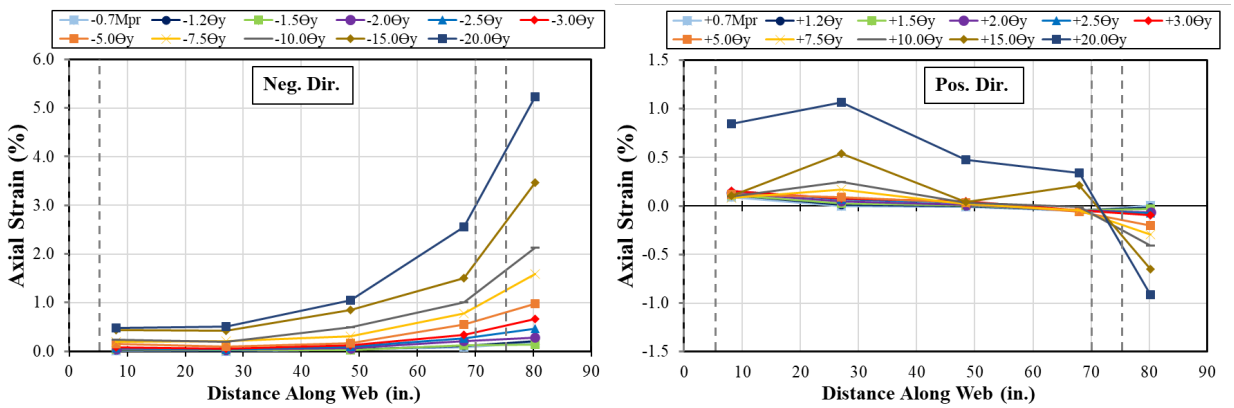

Figure 4-21: Axial strain profiles obtained from Layer 1 LVDTs, WLP & SLP

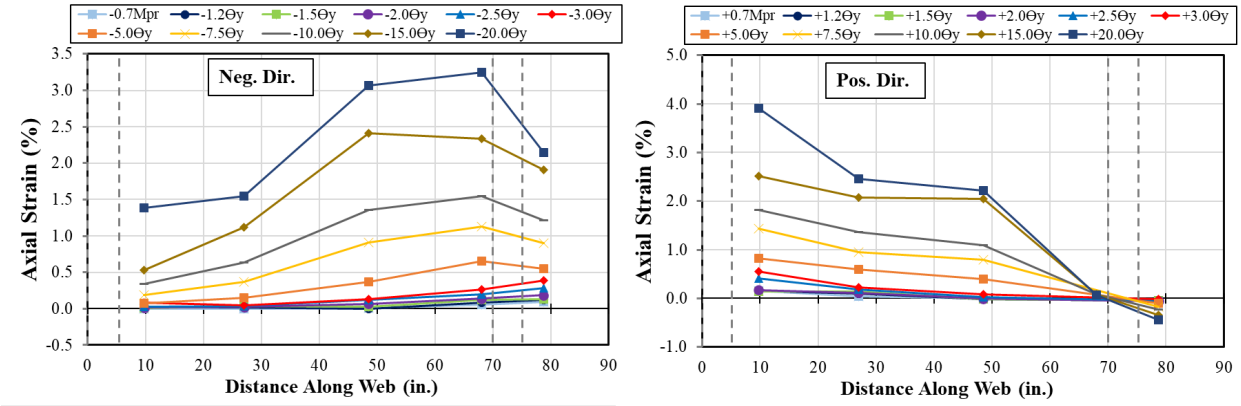

Figure 4-22: Axial strain profiles obtained from Layer 2 LVDTs, WLP & SLP

4.4 Axial Load History

The axial load history of CW-1 during the SLP is shown in Figure 4-23. The axial load was not kept constant for CW-1 during the SLP. The axial load decreased during the unloading and increased during the loading. Therefore, at the maximum rotation demands for each load step, the axial load at the specimen was around 500 kips ($0.1A_g f'_c$), whereas at zero lateral loads, the axial load was as low as 150 kips. This variation in axial load resulted in higher residual hinge rotations

for CW-1 than RCW-1, where the axial load was almost kept constant at 500 kips during the loading and unloading (Figure 4-24). The effect of variation of axial load on the pinching behaviors of CW-1 and RCW-1 can be observed by comparing base moment-hinge rotation responses of the two tests, Figure 4-11 versus Figure 4-13.

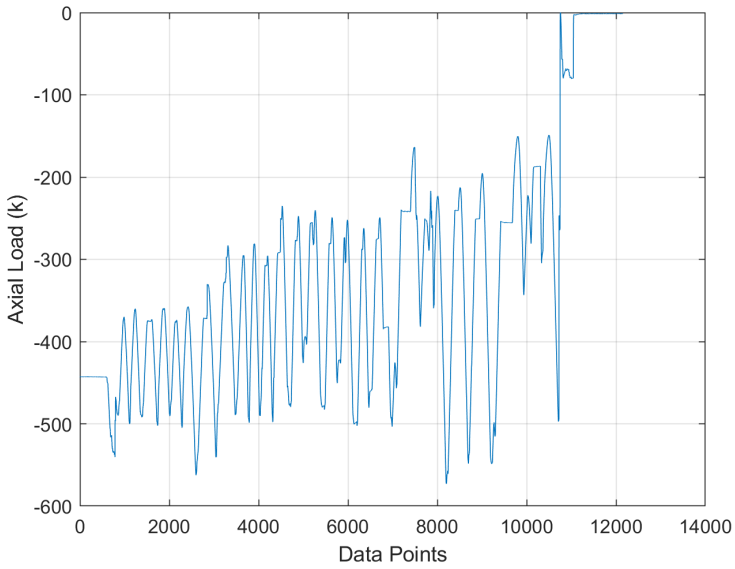

Figure 4-23: Axial load history of CW-1 during SLP

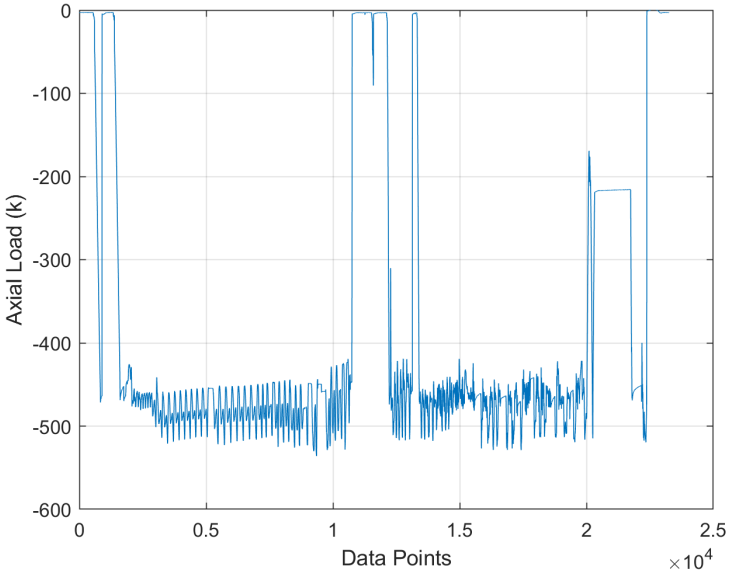

Figure 4-24: Axial load history of RCW-1

4.5 Vertical Growth

The vertical growth of CW-1 during the WLP and SLP is shown in Figure 4-25. At $20\Theta_y$ hinge rotation demands, the maximum vertical growth was 1.04 in. and 0.93 in. in the negative and positive directions, respectively. The maximum residual vertical growth under zero loading was around 0.3 in. (0.8% of L_p).

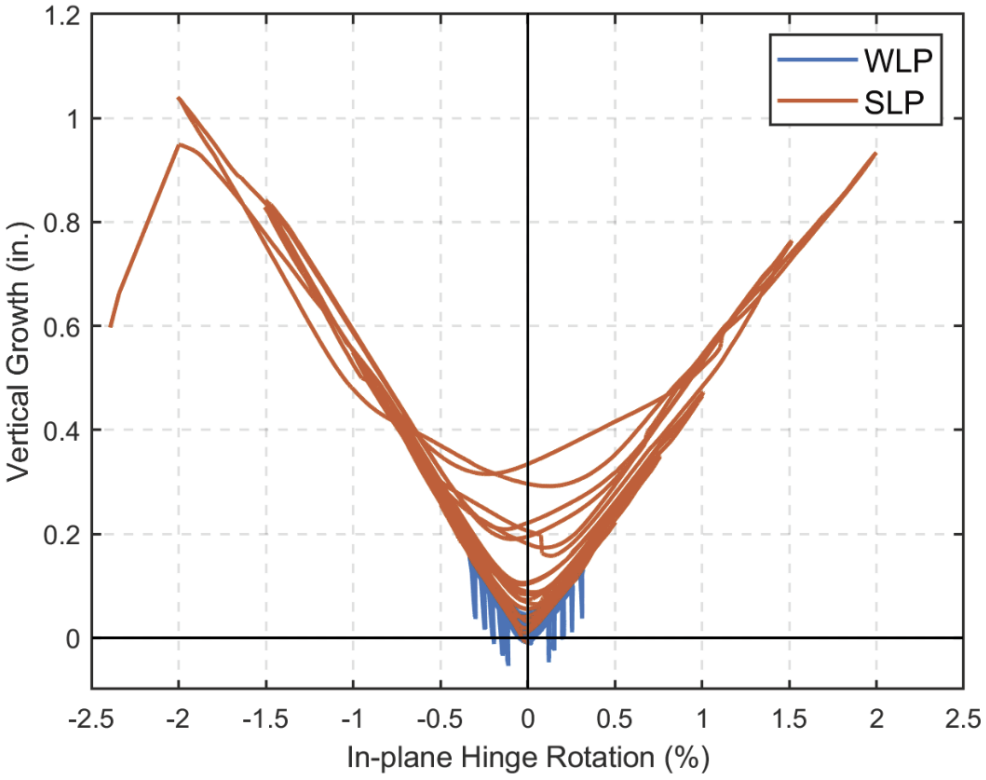

Figure 4-25: IP hinge rotation-vertical growth response of CW-1 during WLP and SLP

4.6 Impact of Lap Splices

Given that minor damage and very low tensile strains were observed in the splice region of the wall, the hinge rotations of CW-1 under SLP calculated assuming a longer hinge region ($L_p=l_w/2+L_s$) is shown in Figure 4-26. Comparison between the Figure 4-26 and Figure 4-11, where the plastic hinge length was taken as $L_p=l_w/2$, resulted in approximately 15% and 17.5% higher hinge rotation demands at the maximum ($20\Theta_y$ versus $23.5\Theta_y$) hinge rotation demands.

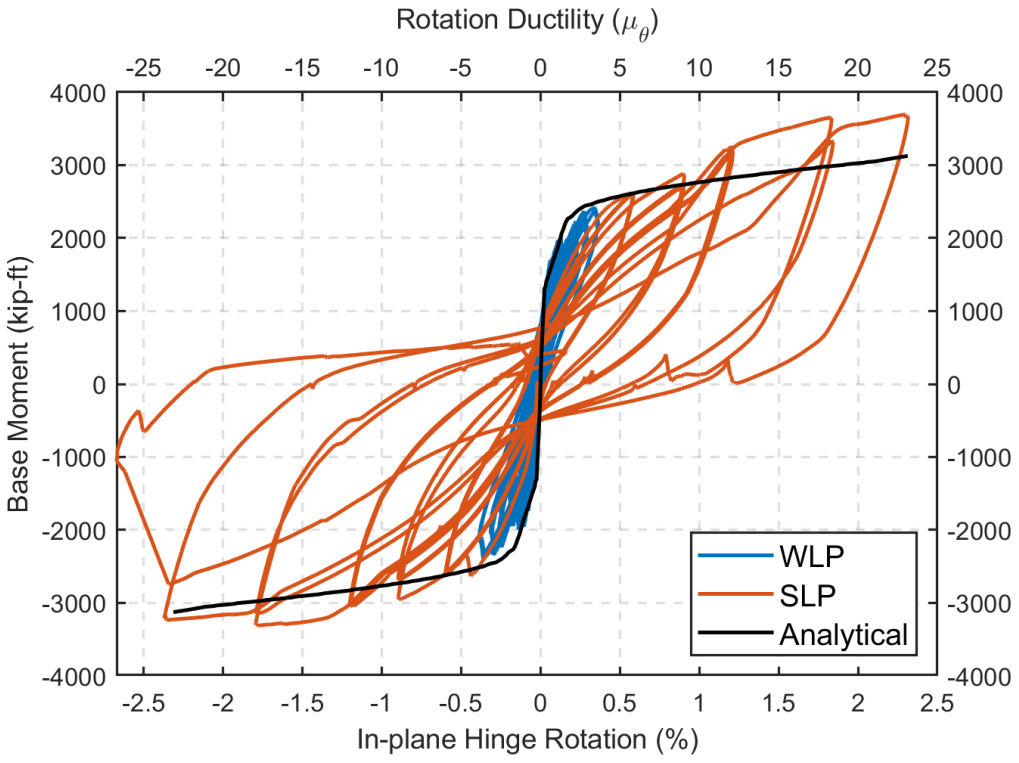

Figure 4-26: In-plane moment-hinge rotation ($L_p=l_w/2+L_s$) of CW-1 under WLP and SLP

5. Experimental Wind Test Results and Discussion (CW-2, CW-3 and CW-4)

5.1 General

This chapter focuses on the experimental results of the specimens with higher longitudinal reinforcement ratio (ρ_l = 1.5%, CW-2, CW-3, and CW-4) under the wind loading protocol (WLP). The effective yield hinge rotation was estimated to be 0.3% during the testing of CW-2; therefore, hinge rotation demands for the loading protocol were based on a hinge yield rotation of 0.3% for all the specimens. However, a detailed analysis done after the tests showed that the actual effective yield hinge rotation was approximately 0.25% ($\Theta_{y,exp}$, Appendix F), which is the same as the analytically predicted effective yield rotation value (flexural (Appendix F) + slip (Appendix G), $\Theta_{y,t,a} = \Theta_{y,f,a} + \Theta_{y,s,a}$ = 0.22% + 0.3% = 0.25%). Therefore, higher hinge rotation demands were applied to the specimens than the WLP shown in Figure 2-38. For example, at $3\Theta_y$ hinge rotation demands, 0.9% hinge rotation was applied, resulting in $3.6\Theta_{y,exp}$. Table 5-1 shows the applied hinge rotation demands in percent values and in terms of $\Theta_{y,exp}$. The hinge rotation values for the elastic cycles and the moment demands for the inelastic cycles were slightly different for each wall; values given in Table 5-1 represent an average for all three specimens. The in-plane probable moment capacity ($M_{pr,IP}$) of the specimens calculated using $1.25f_y$ at ε_c of 0.003 was calculated to be 4203 kip-ft (Figure 5-1). The out-of-plane probable moment capacity in the +y direction ($M_{pr,OOP+y}$), where the flange edges are under compression, is slightly different for different specimens due to the variation of axial loads applied at positions B and E during the loading protocol; 1352 kip-ft for CW-2 ($P_{OOP+y}=0.1A_g f'_c$), 1310 kip-ft for CW-3 ($P_{OOP+y}=0.05A_g f'_c$), and 1330 kip-ft for CW-4 ($P_{OOP+y}=0.075A_g f'_c$). In the -y direction, the probable moment capacity was calculated to be 935 kip-ft ($P_{OOP-y}=0.1A_g f'_c$). Unlike CW-1, for CW-2, CW-3, and CW-4, the same moment demands applied in the OOP direction ($0.5M_{pr,OOP}$) during ramp-up were also used during ramp-down,

except for the cases where a significant stiffness reduction was observed in the OOP direction, in which case the loading was changed to displacement-control.

Table 5-1: Applied in-plane moment and hinge rotation demands

Load Step		Base moment, $M_{b,IP}$ (k-ft)	Hinge rotation, $\Theta_{Lp,IP}$ (%)	$\Theta_{Lp,IP}/\Theta_{y,exp}$
Ramp-Up	$0.4M_{pr}^*$	±1681	±0.05	-
	$0.7M_{pr}^*$	±2942	±0.16	-
	$1.2\Theta_y$	±3900	±0.36	1.44
	$1.5\Theta_y$	±3750	±0.45	1.80
	$2.0\Theta_y$	±4050	±0.60	2.40
	$2.5\Theta_y$	±4150	±0.75	3.00
	$3.0\Theta_y$	±4250	±0.90	3.60
Ramp-Down	$2.5\Theta_y$	±3800	±0.75	3.00
	$2.0\Theta_y$	±3400	±0.60	2.40
	$1.5\Theta_y$	±2900	±0.45	1.80
	$1.2\Theta_y$	±2500	±0.36	1.44
	$0.7M_{pr}$	±1400	±0.09	-
	$0.4M_{pr}$	±1681	±0.25	-

Notes:

* Lower moment values (90% of the given values) were applied to CW-3 due to a configuration error in the test setup.

- Moment values are given for the first cycle at each rotation demands

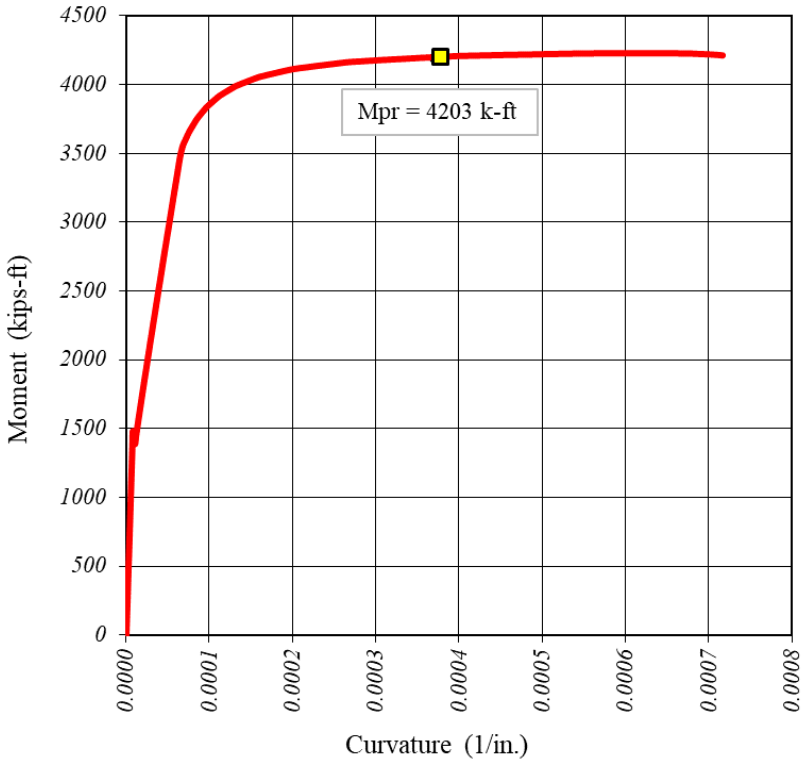

Figure 5-1: CW-2-3-4 monotonic in-plane moment-curvature diagram with $f_s = 1.25f_y$

5.2 Observed Damage

5.2.1 CW-2

The cracking moment of CW-2 was estimated to be -1363 k-ft under negative (Pos. A) and +1394 k-ft under positive (Pos. D) loading. These values were estimated using the base moment-hinge rotation response from each test, where a significant change in the slope was observed. These values correspond to 32.4% and 33.2% of the in-plane probable moment capacities ($M_{pr,IP}$). Figure 5-2 and Figure 5-3 show the DIC analysis results at the maximum moment demands during the last cycle of $0.4M_{pr}$ moment demand load step for Pos. A and Pos. D, respectively. First yield of the outer layer of flange longitudinal reinforcement was determined using strain gauge data for gauges attached to longitudinal reinforcement at different locations (Figure 2-30). Table 5-2 shows

the base moment demands at first yield of the flange longitudinal reinforcement immediately above the splices (h=21.5 in.) and at the plastic hinge height (h=L_p=37.5 in.). Similar to CW-1, first yield of the flange longitudinal reinforcement was around 0.65 to 0.7$M_{pr,IP}$ base moment demands with some variation along the length of the flange, i.e., yielding of the bars at flange edges and at the flange-web corners was observed at different moment demands. Given the shallow moment gradient over the test specimen height (Figure G-1), yielding at h=L_p=37.5 in. was also observed around 0.65 to 0.7$M_{pr,IP}$ in-plane base moment demands.

After the completion of the ramp-up cycles, some damage was observed at the west flange. Figure 5-4 shows the cover spalling at the base of the west flange edge and the corner. No damage, i.e., cover spalling, concrete crushing, bar buckling, or bar rupture, was observed at the east flange or within the web. Some vertical cracks existed at the east flange edge and east flange corner. A more significant amount of damage was observed during ramp-down loading. When the inelastic ramp-down cycles were completed, cover spalling was observed at both corners of the specimen, minor cover crushing occurred at the base of the west flange edge, and longitudinal reinforcement buckling and core crushing were observed at the base of the east flange edge. The cover spalling was more extensive at the east flange edge compared to the west flange, exposing the vertical bars at the wall-foundation interface and at around 19 in. above the interface. Figures 5-5, 5-6, and 5-7 show the damage state of CW-2 after the completion of inelastic ramp-down cycles. Although no additional damage was observed at the web or flange corners during the elastic ramp-down cycles at 0.4M_{pr} moment demands (500 cycles under force-control), more concrete crushing was observed at the flange edges, especially for the east flange. At the end of the 500 cycles, at the base of the east flange edge, the core concrete was completely crushed between the first two layers of vertical reinforcement, or for a distance of approximately 7 in. along the flange (23% of the flange length).

The cover was lost at the east flange edge, exposing the first layer of longitudinal reinforcement up to a height of approximately 8 in. above the wall-footing interface. The concrete cover on the outside surface of the east flange near the wall-footing interface was lost, and all outer layer longitudinal reinforcement was visible. Buckling of longitudinal reinforcement was observed for the first layer of bars at the east flange edge; however, no bar fracture was observed. Figures 5-8, 5-9, and 5-10 show the damage state of CW-2 after the wind loading protocol was completed.

Table 5-2: Base moment demands at first yield of flange longitudinal reinforcement, CW-2

Flange	Moment Demand	Flange Edge		Flange Corner		Flange Center
		h=21.5 in.	h=37.5 in.	h=21.5 in.	h=37.5 in.	h=21.5 in.
East Flange	Base Moment (M_{IP}) k-ft	-2652	-2725	-2871	-2692	-2692
	M_{IP} / $M_{pr,IP}$	0.63	0.65	0.68	0.64	0.64
West Flange	Base Moment (M_{IP}) k-ft	2718	2659	2554	2961	-
	M_{IP} / $M_{pr,IP}$	0.65	0.63	0.61	0.70	-

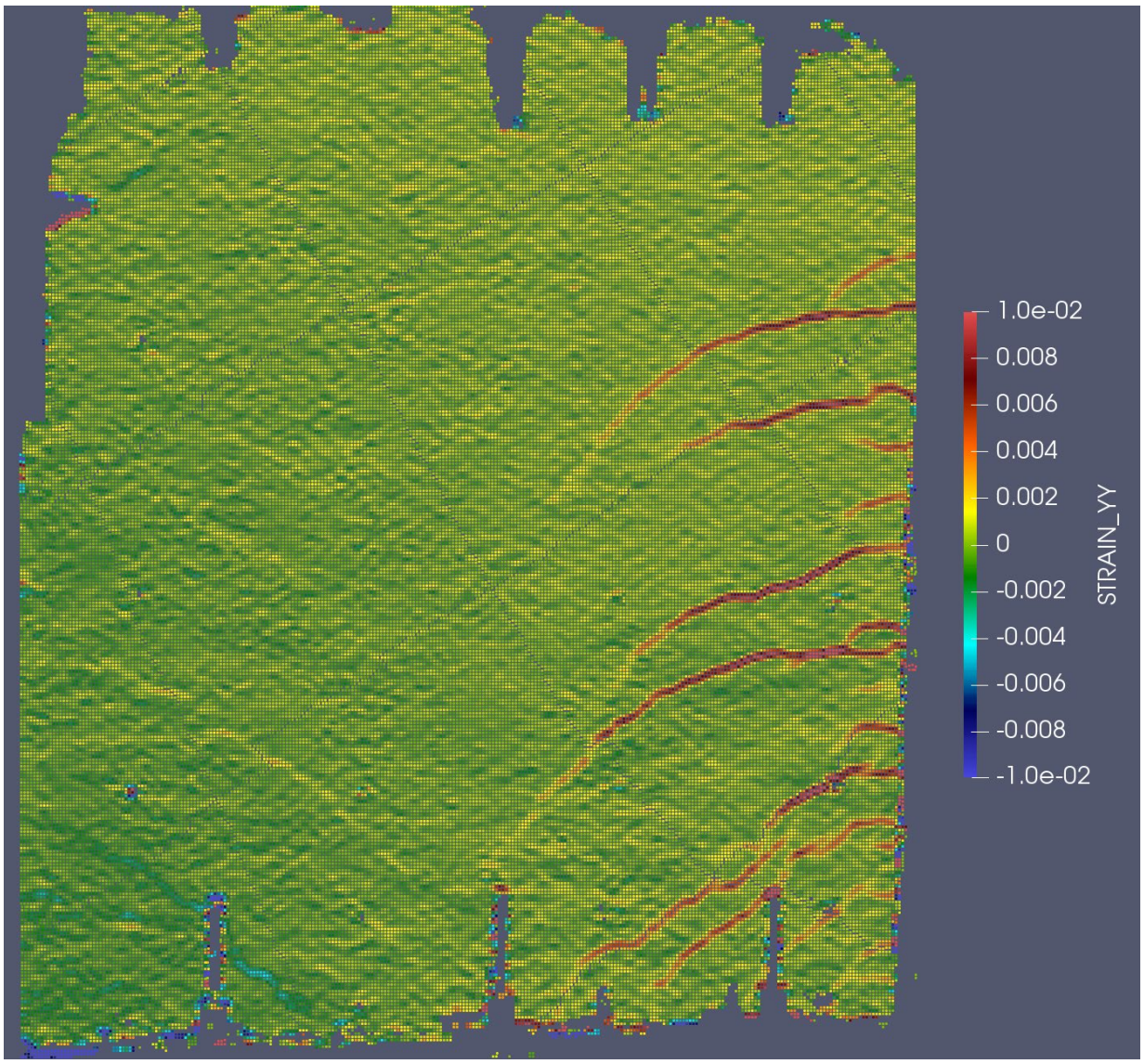

Figure 5-2: DIC analysis results at the last cycle of 0.4M_{pr} demands at Pos. A, CW-2

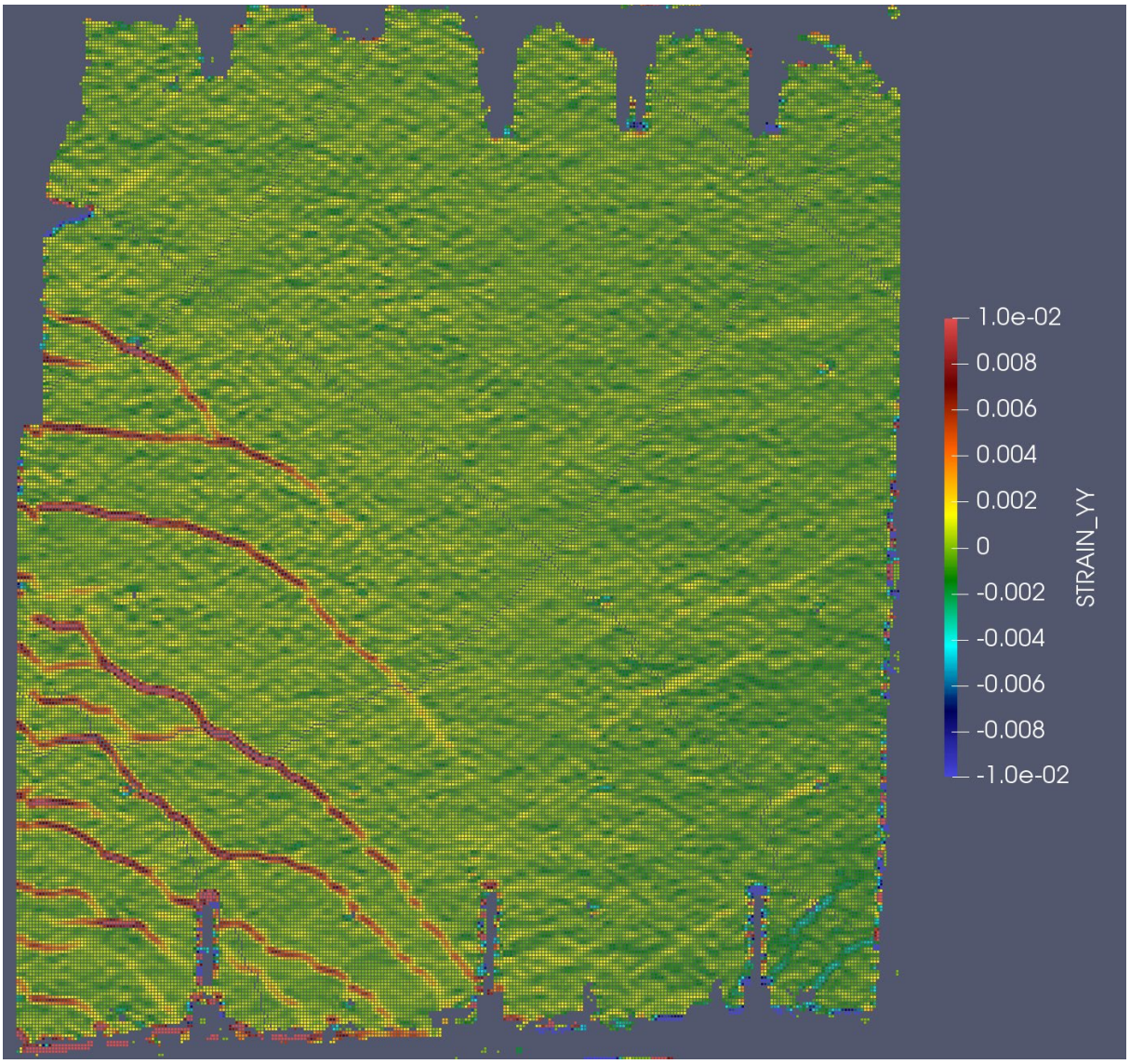

Figure 5-3: DIC analysis results at the last cycle of 0.4M_{pr} demands at Pos. D, CW-2

Figure 5-4: West flange corner (left), West flange edge (right) after the ramp-up loading of WLP, CW-2

Figure 5-5: East flange edge (left), West flange edge (right) after inelastic ramp-down cycles of WLP, CW-2

Figure 5-6: East flange after inelastic ramp-down cycles of WLP, CW-2

Figure 5-7: West flange after inelastic ramp-down cycles of WLP, CW-2

Figure 5-8: West flange after the completion of WLP, CW-2

Figure 5-9: East flange edge after the completion of WLP, CW-2

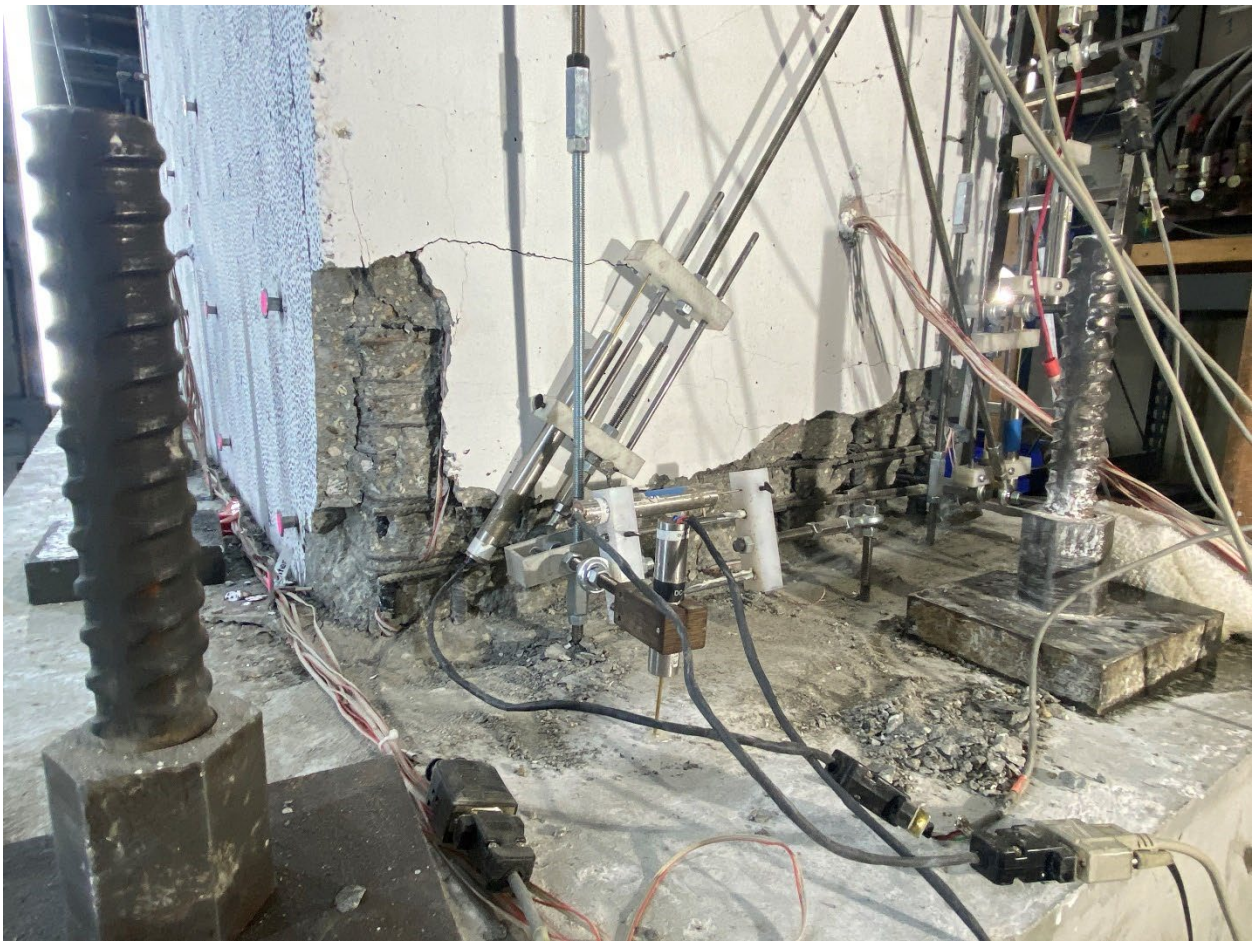

Figure 5-10: East flange after the completion of WLP, CW-2

5.2.2 CW-3

Due to a configuration error in the test control setup, the 500 cycles were applied at ±1500 k-ft ($0.36M_{pr,IP}$) base moment demands instead of at $0.4M_{pr,IP}$. Similarly, the base moment demand was $0.63M_{pr,IP}$ for the 30 cycles at $0.7M_{pr,IP}$. The cracking moment of CW-3 was estimated to be around +1750 k-ft (42% of $M_{pr,IP}$) and -1678 k-ft (40% of $M_{pr,IP}$) by observing a significant change in the slope of base moment-hinge rotation response of the wall, which occurred after the application of 500 cycles at $0.36M_{pr,IP}$. The DIC analysis showed cracking pattern a very similar to CW-2 (Figure 5-2 and Figure 5-3). During the concrete casting of the specimen, the strain gauges attached to the

east flange longitudinal reinforcement (Figure 2-31) were damaged. Therefore, only the strain gauges attached to the west flange longitudinal reinforcement (Figure 2-31) at 21 in. above the footing were used to estimate the base moment at first yield. The strain gauges attached to the outer layer flange edge and flange-web corner vertical reinforcement showed that they yielded simultaneously at $0.69M_{pr,IP}$ in-plane base moment demand.

After all the ramp-up cycles (elastic and inelastic), CW-3 showed no significant damage (e.g., no concrete spalling, concrete crushing, bar buckling, or bar fracture). Vertical cracks formed at the web-flange corners and at the east flange edge, but cover spalling was not observed. After the application of the ramp-down cycles, cover spalling (up to 7 in. above the footing) and minor concrete crushing occurred at the base of the east flange edge, exposing the first outer layer of vertical reinforcement at the base (Figure 5-11). Similarly, cover spalling up to 9 in. and 20 in. above the footing was observed at the east and west flange corners (Figure 5-12).

Figure 5-11: East flange edge after the completion of WLP, CW-3

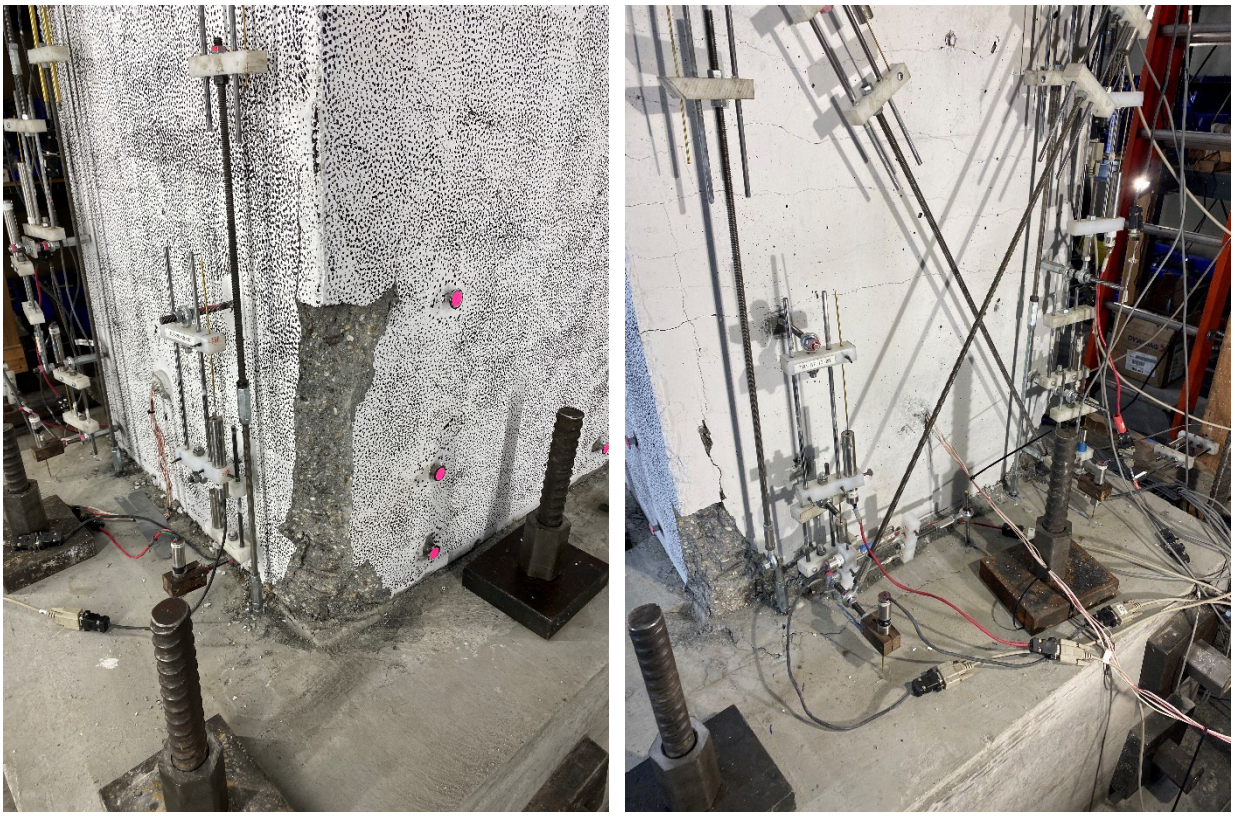

Figure 5-12: East flange (left) and West flange (right) after the completion of WLP, CW-3

5.2.3 CW-4

The cracking moment of CW-4 was estimated to be -1410 k-ft and +1530 k-ft under negative (Pos. A) and positive (Pos. D) moments, respectively. These values were estimated using the base moment-hinge rotation response of the specimen, where a significant change in the slope was observed. These values corresponded to 33.5% and 36.4% of the in-plane probable moment capacities ($M_{pr,IP}$). Using the strain gauges attached to the flange longitudinal reinforcement at 21 in. above the footing, first yield of the east flange corner reinforcement was determined to be at -2795 k-ft base moment ($0.66M_{pr,IP}$). For the west flange edge and west flange-web corner vertical reinforcement, first yield was estimated to occur at +2890 k-ft ($0.69M_{pr,IP}$) base moment demands.

The strain gauge attached to the east flange edge vertical reinforcement was damaged during the construction.

After the ramp-up loading, no damage was observed at the east flange edge, whereas for the west flange edge, cover spalling occurred at up to 3 in. above the wall-footing interface, and buckling of the outer layer of longitudinal reinforcement was observed (Figure 5-13). Cover spalling was observed up to 22 in. and 7 in. above the wall-footing interface at the west and east flange-web corners, respectively (Figure 5-14). During the inelastic ramp-down cycles, no additional damage was observed at the flange-web corners and for the west flange edge. However, concrete crushing, buckling, and fracture of the outer layer vertical reinforcement occurred at the base of the east flange edge (Figure 5-15). The elastic ramp-down cycles did not cause any additional damage to the wall.

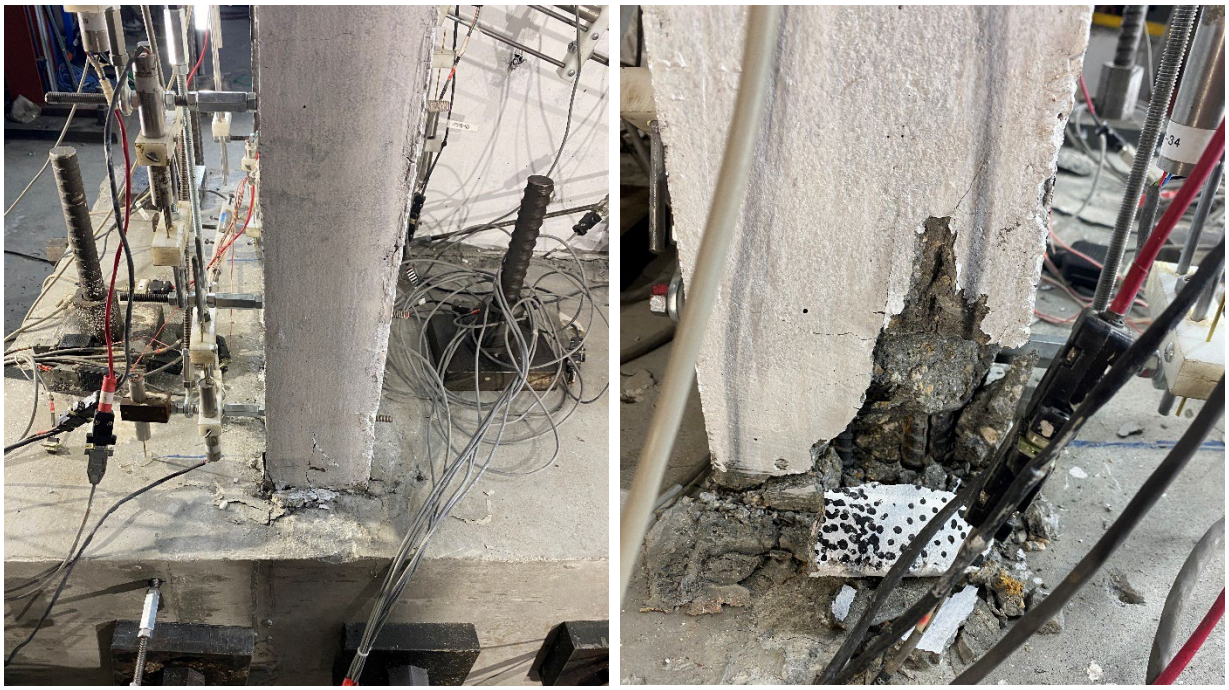

Figure 5-13: East flange edge (left) and West flange edge (right) after the ramp-up loading of WLP, CW-4

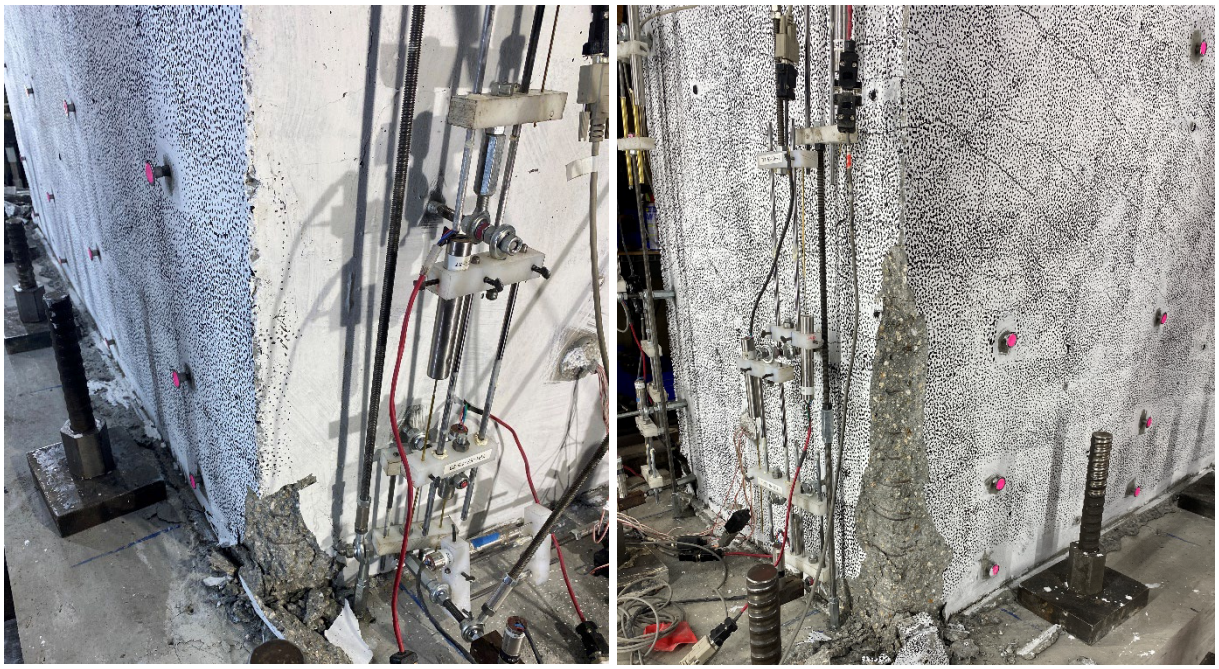

Figure 5-14: East flange corner (left) and West flange corner (right) after the ramp-up loading of WLP, CW-4

Figure 5-15: East flange edge after the inelastic ramp-down cycles of WLP, CW-4

5.3 Load-Deformation Responses

5.3.1 Base Moment-Hinge Rotation Responses

The plastic hinge ($L_p=l_w/2$) rotations (IP and OOP) were computed using the four LVDTs attached to the four corners of the specimens (Figure 2-27 and Figure 3-9) and using Equations 3.1 and 3.2. Figure 5-16 plots the in-plane base moment-hinge rotation responses of CW-2, CW-3, and CW-4 during the WLP. Values of rotation ductility shown in Figure 5-16 were calculated based on using $\Theta_{y,exp}$ = 0.25%. The responses of the three walls, for ramp-up loading only, are also plotted together in Figure 5-16(d) for comparison. As expected, since the cross-sectional dimensions, longitudinal

reinforcement ratio, diameter and grade of the longitudinal reinforcement, and axial load applied during the in-plane loading were all the same for these walls, the in-plane base moment-hinge rotation responses for the three walls are very similar to each other. No strength loss was observed during the WLP for any of the walls, although, at the maximum rotation demands ($3.6\Theta_{y,exp}$), the base moment values for CW-2 were slightly lower (3.3% and 4.4% at Pos. D and Pos. A, respectively) than CW-3 and CW-4, possibly due to the more significant damage that was observed for CW-2. The analytical prediction (Appendix F) for the in-plane base moment-hinge rotation response is also plotted in Figure 5-16, showing that the predicted response matches very closely with the experimental results for flexural stiffness (uncracked and cracked), yield moment, and post-yield responses. Since more damage was observed in all three walls during the ramp-down cycles, the in-plane base moment-hinge rotation responses during the inelastic and elastic ramp-down cycles are compared in Figure 5-17. The comparison indicates that, for the inelastic ramp-down loading (under displacement-control), CW-2 had lower base moment demands (6.8%, 11.1%, 11.5%, and 12.4% at $3.0\Theta_{y,exp}$, $2.4\Theta_{y,exp}$, $1.8\Theta_{y,exp}$, $1.4\Theta_{y,exp}$ hinge rotation demands, respectively) in the negative loading direction than CW-3 and CW-4. For the elastic ramp-down cycles (under force-control), CW-2 had 24.5% and 45.5% more in-plane rotation demands than CW-3 and CW-4, respectively, in the positive in-plane loading direction. In the negative direction, the hinge rotation demands were similar (around 10% difference). It should be noted that, due to the high level of hinge rotation demands (approximately equal to $\Theta_{y,exp}$) during the ramp-down loading at $0.4M_{pr}$ moment demands, the number of cycles was decreased to 250 from 500 for CW-3 and CW-4.

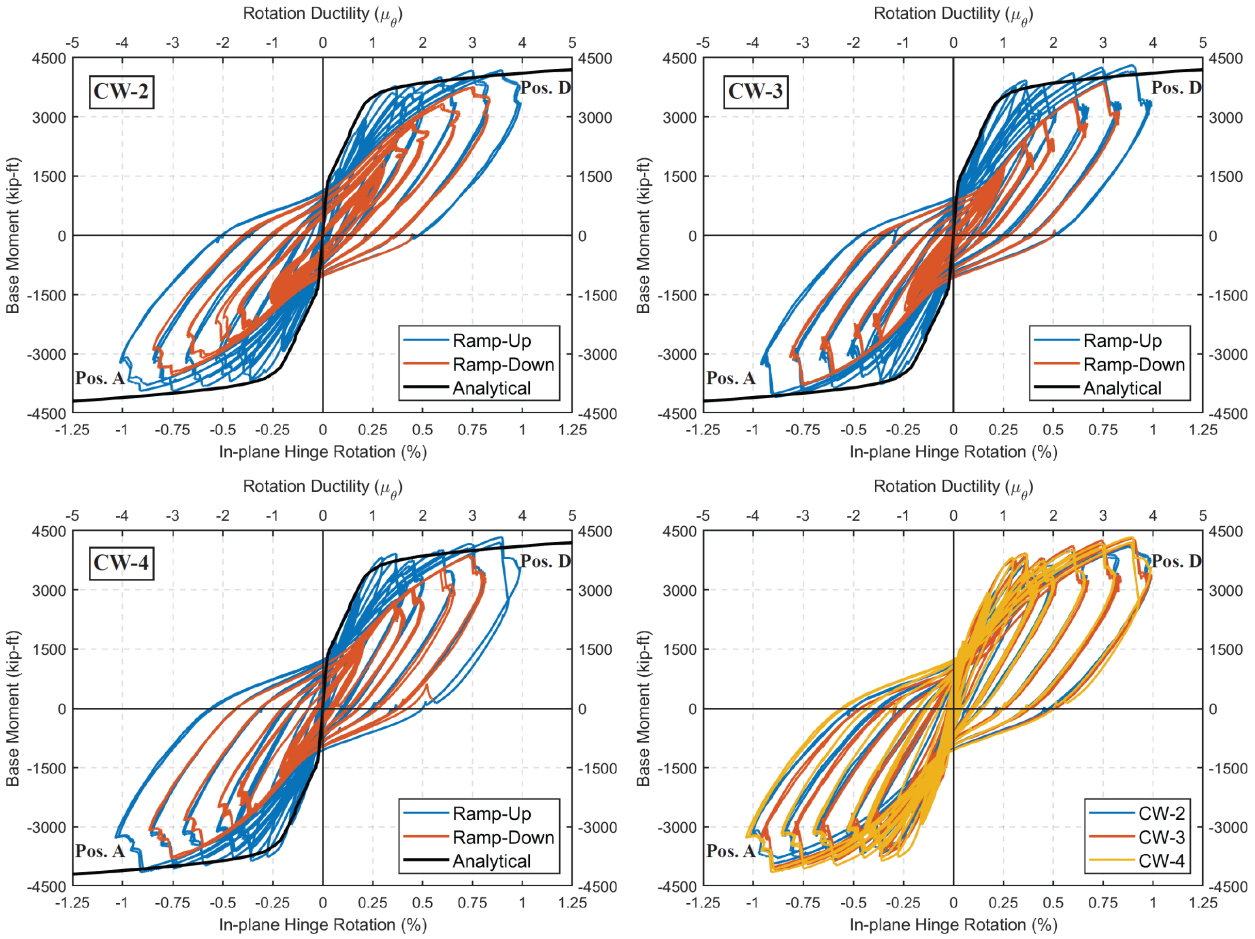

Figure 5-16: In-plane moment-hinge rotation responses during WLP (only the ramp-up cycles are shown for the bottom right figure)

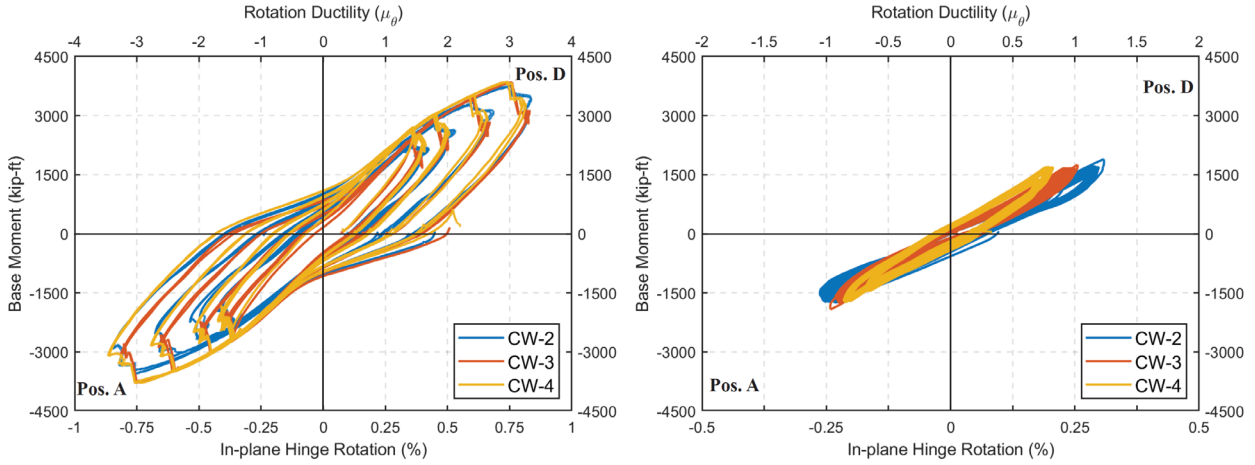

Figure 5-17: In-plane moment-hinge rotation responses during the inelastic ramp-down (left) and elastic ramp-down (right) cycles of WLP

The out-of-plane base moment-hinge rotation responses during the WLP are shown in Figure 5-18(a) – (c) for CW-2, CW-3, and CW-4, respectively, and also plotted for the ramp-up cycles for all three tests in Figure 5-18. During the ramp-up loading, loading was applied under force-control in both the negative and positive directions for all three specimens. Almost no stiffness degradation was observed for CW-3 ($P_{OOP+y}=0.05A_g f'_c$) during the ramp-up loading at Pos. B and E (flange edges were under compression), whereas for CW-2 ($P_{OOP+y}=0.10A_g f'_c$) and CW-4 ($P_{OOP+y}=0.075A_g f'_c$), the OOP hinge rotations increased from around 0.25% to 0.45% and 0.6% for CW-2 and CW-4, respectively. This behavior was consistent with the damage progression observed at the flange edges for CW-2 and CW-4. On the other hand, in the negative direction (Pos. C and F, web corners were under compression), stiffness degradation was observed for all four of the specimens, with the lowest degradation observed for CW-3. Similar responses were expected in the negative direction since the axial load was identical for the negative direction, $P_{OOP-y}=0.10A_g f'_c$, and the damage that occurred at the flange-web corners was very similar for all the specimens.

Figure 5-19 shows the OOP base moment-hinge rotation responses of the walls during the inelastic ramp-down loading. CW-3 experienced a more significant stiffness reduction in the negative direction compared to the ramp-up cycles. Therefore, the loading was changed from force- to displacement-control, and OOP hinge rotations of -0.5% were applied instead of OOP moment values of $0.5M_{pr,OOP-y}$. For CW-4, loads were applied under force-control during the ramp-down loading, and no significant stiffness degradation was observed in either direction (+y and -y). Unlike CW-3 and CW-4, CW-2 experienced significant damage at the east flange edge. Approximately 23% of the east flange core concrete was crushed at the end of the ramp-down cycles (Section 5.2.1). Therefore, in the positive y direction, a significant degree of stiffness

degradation was observed at the start of the ramp-down cycles; therefore, the loading was done under displacement-control instead of force-control. OOP hinge rotations of +0.5% were applied for the ramp-down cycles, and at the end of the inelastic ramp-down cycles, the OOP base moments decreased to 230 k-ft from 675 k-ft (66% strength loss). Figure 5-20 shows the OOP base moment-hinge rotation responses, calculated using the LVDTs shown in Figure 2-27 and Figure 3-9, for the east and west flanges under ramp-down loading separately. Figure 5-20 reveals that the strength loss observed in the positive direction during the ramp-down loading for CW-2 was mainly due to the damage that occurred at the east flange edge.

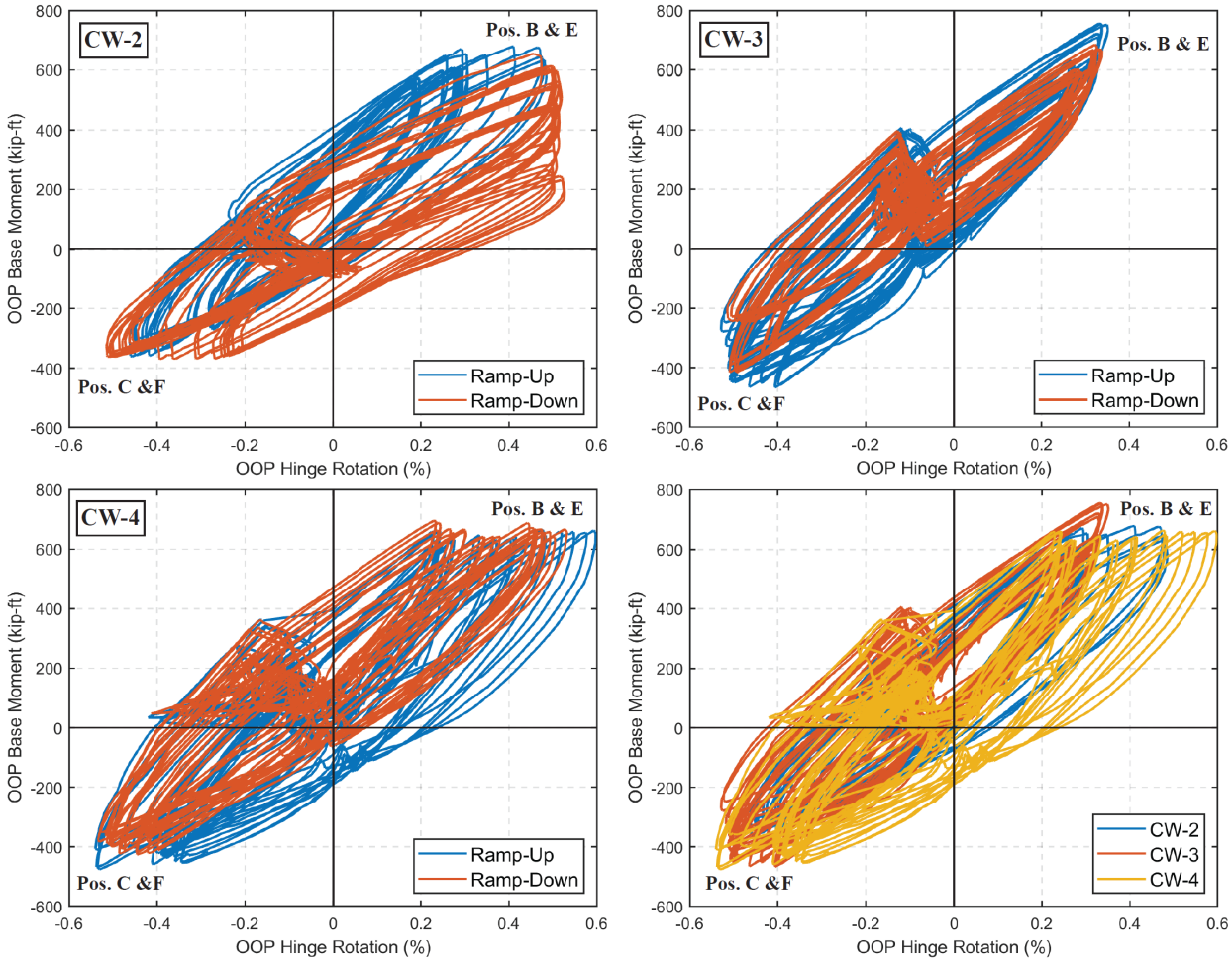

Figure 5-18: OOP moment-hinge rotation responses during WLP (only the ramp-up cycles are shown for the bottom right figure)

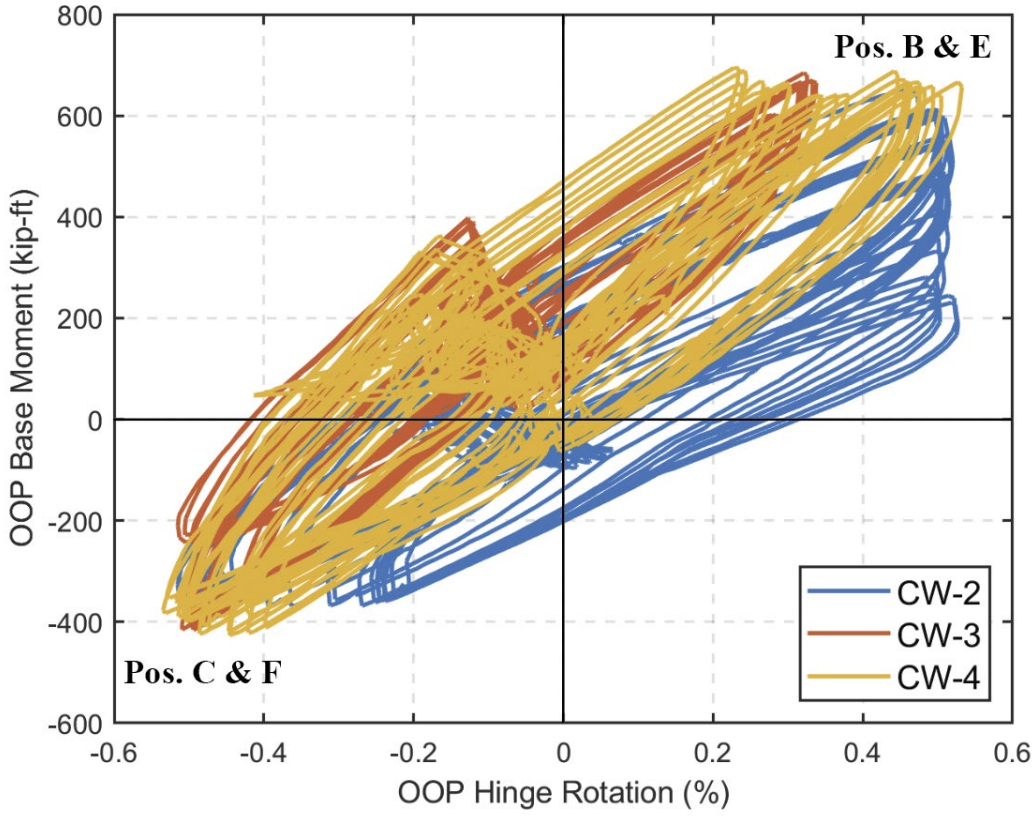

Figure 5-19: OOP moment-hinge rotation responses during the inelastic ramp-down cycles of WLP

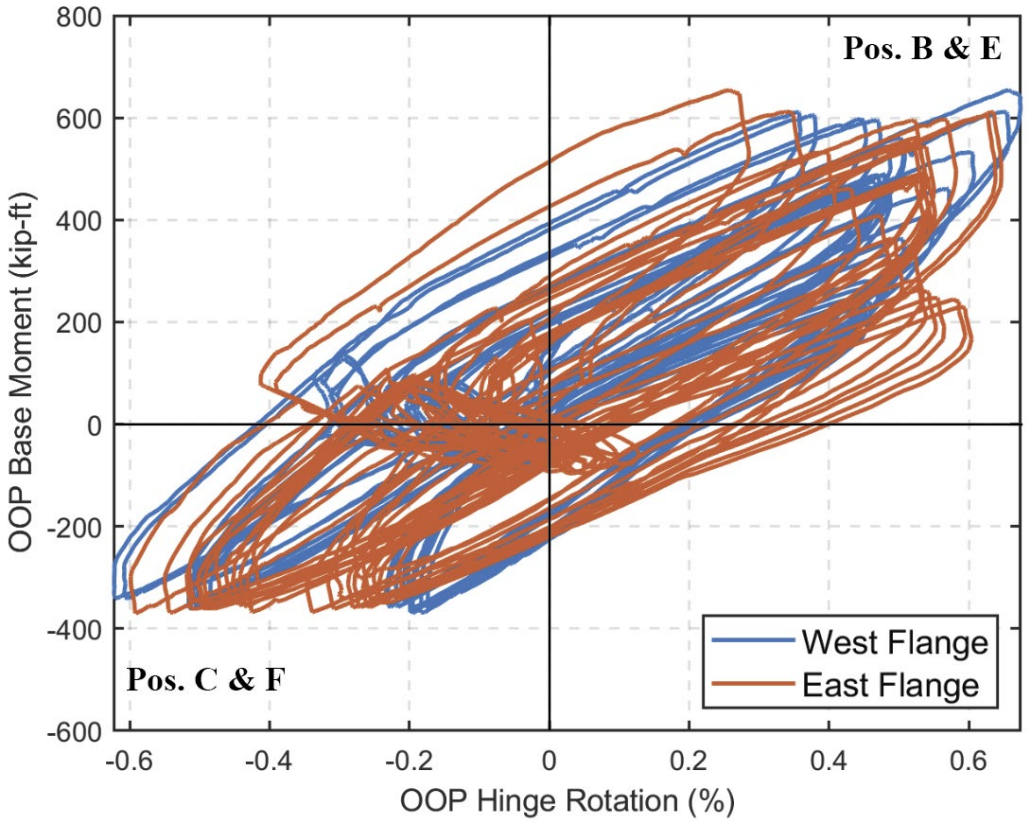

Figure 5-20: OOP moment-hinge rotation response of CW-2 flanges during the inelastic ramp-down cycles of WLP

5.3.2 Moment-Curvature Responses

Curvature values for each wall were calculated using the column of LVDTs attached over the wall height at various locations (Figure 2-24 and Figure G-1). For CW-2, there were no LVDTs attached at the flange-web corners; therefore, only the Group 1 LVDTs shown in Figure 5-21 were used for the curvature calculations. For Phase II wall tests (CW-3 and CW-4), additional LVDTs were used on the outer surface of the flange-web corners (Figure 5-21); therefore, both the Group 1 and Group 2 LVDTs were used to compute curvature values for CW-3 and CW-4. Figure 5-22 shows the moment-curvature responses calculated at different layers and the average curvature over L_p (l_w/2) calculated using the control sensor LVDTs (Figure 2-27). For CW-2, the biggest curvatures were

observed at Layers 3 (20-37.5 in.) and 4 (37.5-57.5 in.), with curvature ductility values ($\mu\varphi$) of 4.4 in the negative direction at Layer 3 and μ_ϕ=4.0 in the positive direction at Layer 4. The curvature values within the splice region (l_s=20 in.) were considerably lower compared to Layers 3 and 4. In Layer 1 (2-10 in.), μ_ϕ of 0.8 and 2.4 was observed in the positive and negative directions, respectively. For Layer 2 (10-20 in.), the curvature ductility values (-2.75 and +3.0) were higher than Layer 1 but lower than Layers 3 and 4. The analytically predicted moment-curvature response was also plotted in Figure 5-22. The predicted response matched well for the layers above the splice region. For the splice region, the stiffness was higher due to the higher amount of longitudinal reinforcement. Figures 5-23 and 5-24 show the moment-curvature responses of CW-3, and Figures 5-25 and 5-26 show the moment-curvature responses of CW-4. The curvature responses of Phase-II walls were very similar to each other, i.e., for Layer 1, the μ_ϕ was less than 1.0 in both directions, and the highest curvature ductility values were measured at Layers 3 and 4, with μ_ϕ ranging from 4.0 to 5.0. The curvature values calculated using Group 1 and Group 2 LVDTs resulted in similar results in most cases. In general, Group 2 LVDTs showed larger curvature values relative to Group 1, which was due to the fact that higher tensile and compressive strain demands were measured at the flange-web corners than at flange edges (Section 5.3.5).

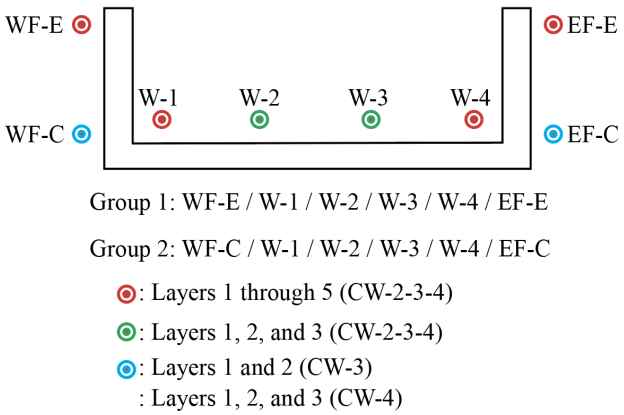

Figure 5-21: LVDT groups used for curvature calculations

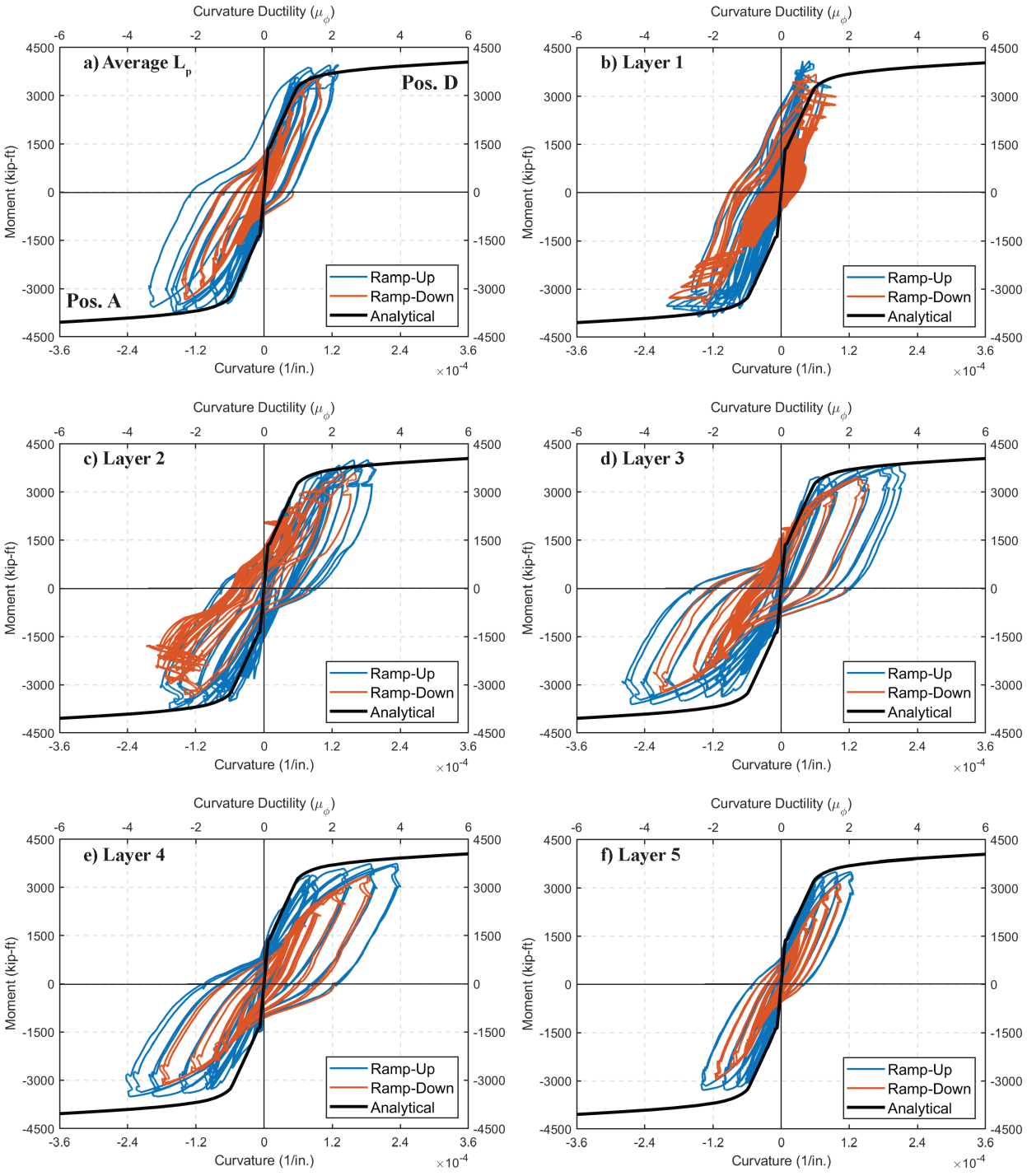

Figure 5-22: Moment-Curvature responses of CW-2 during WLP

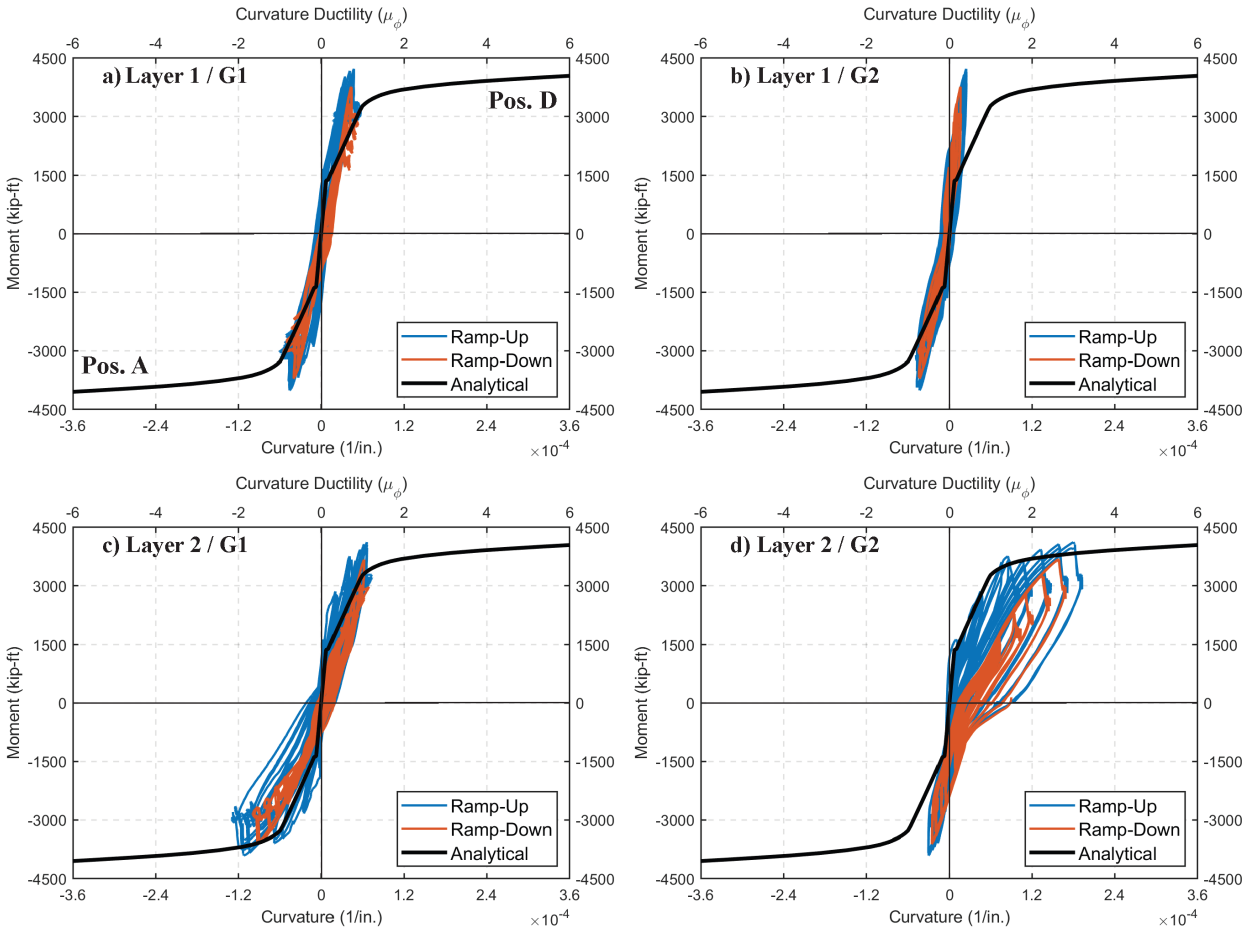

Figure 5-23: Moment-Curvature responses at Layers 1 and 2 of CW-3 during WLP

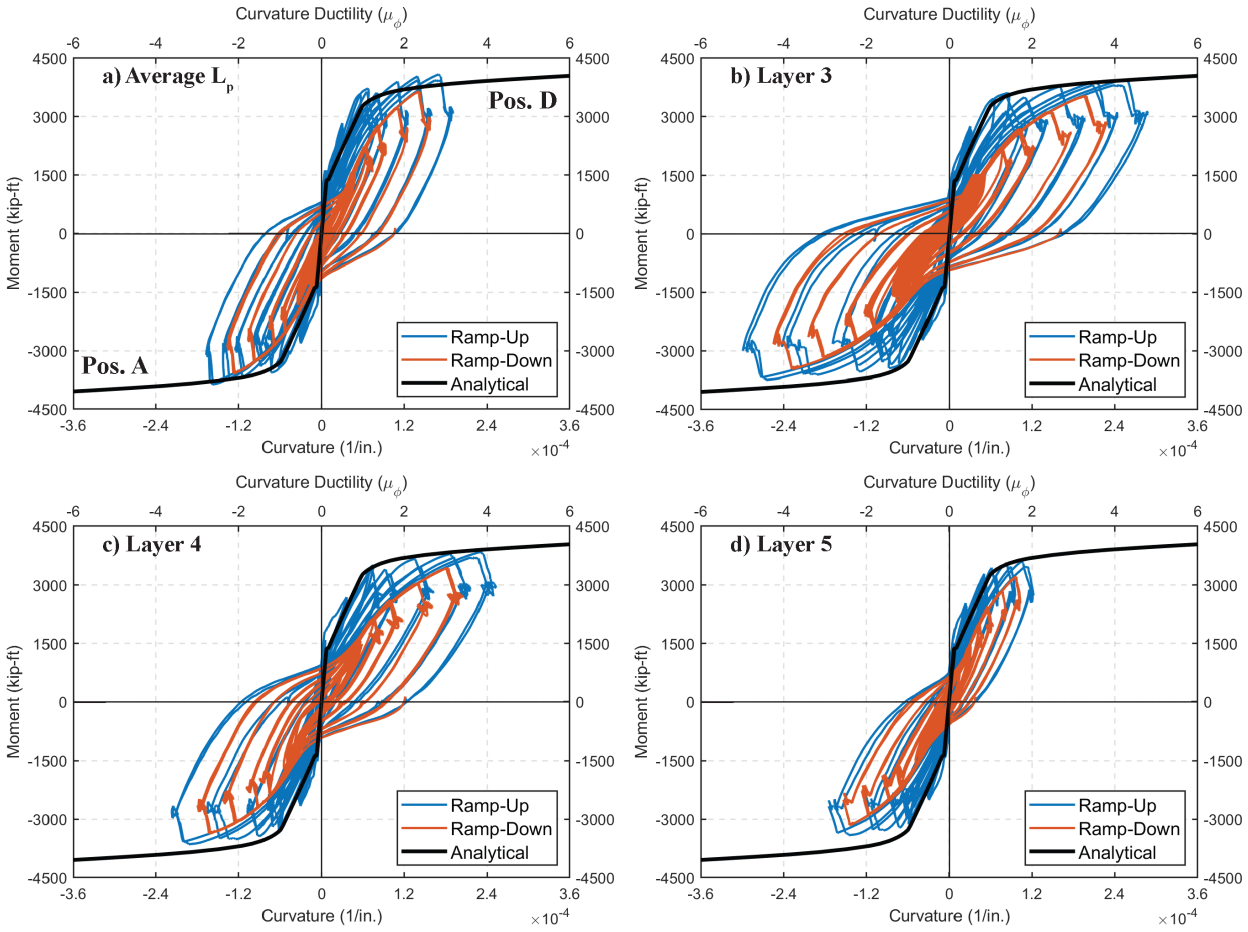

Figure 5-24: Moment-Curvature responses at L_p and Layers 3, 4, and 5 of CW-3 during WLP

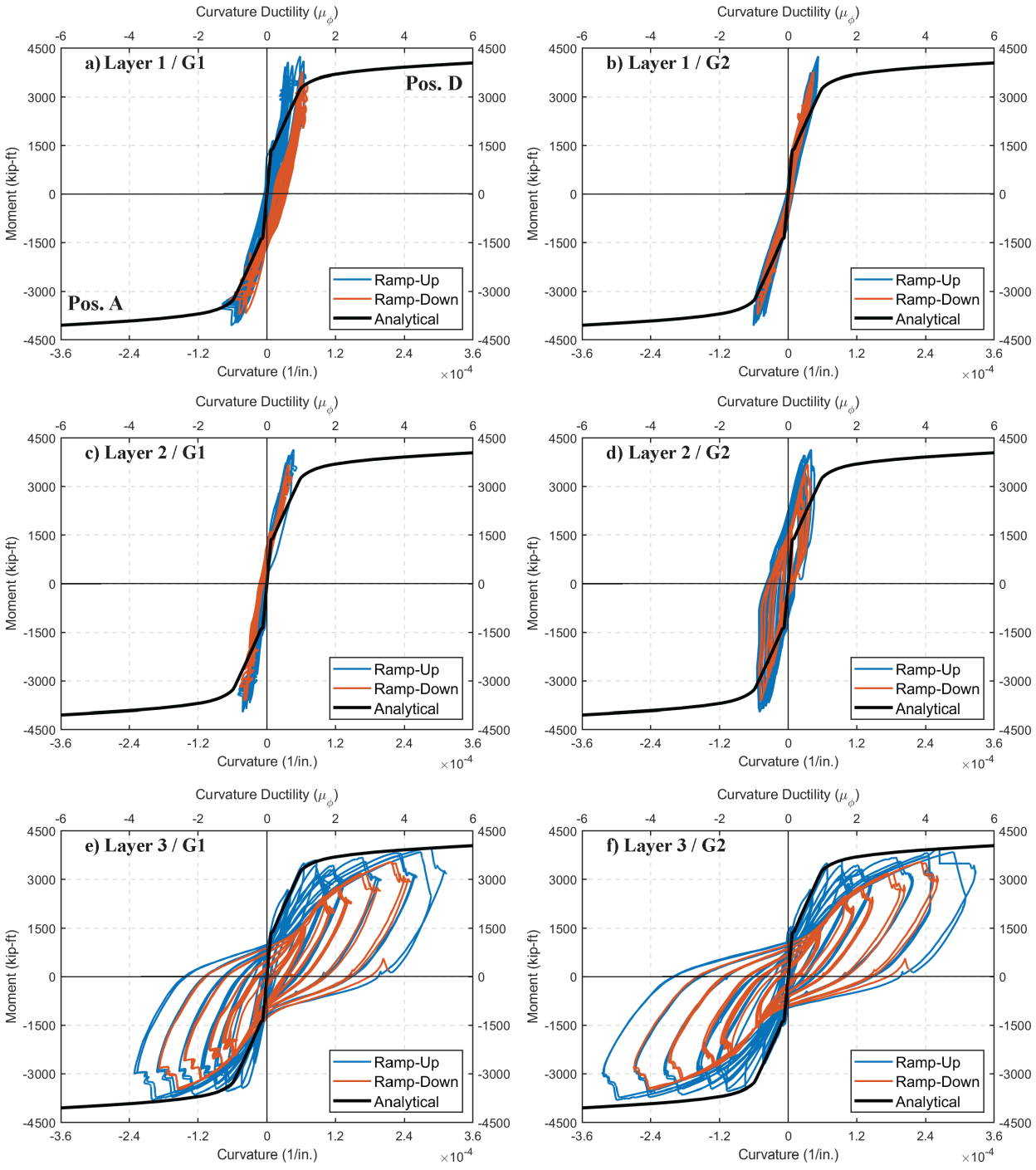

Figure 5-25: Moment-Curvature responses at Layers 1, 2, and 3 of CW-4 during WLP

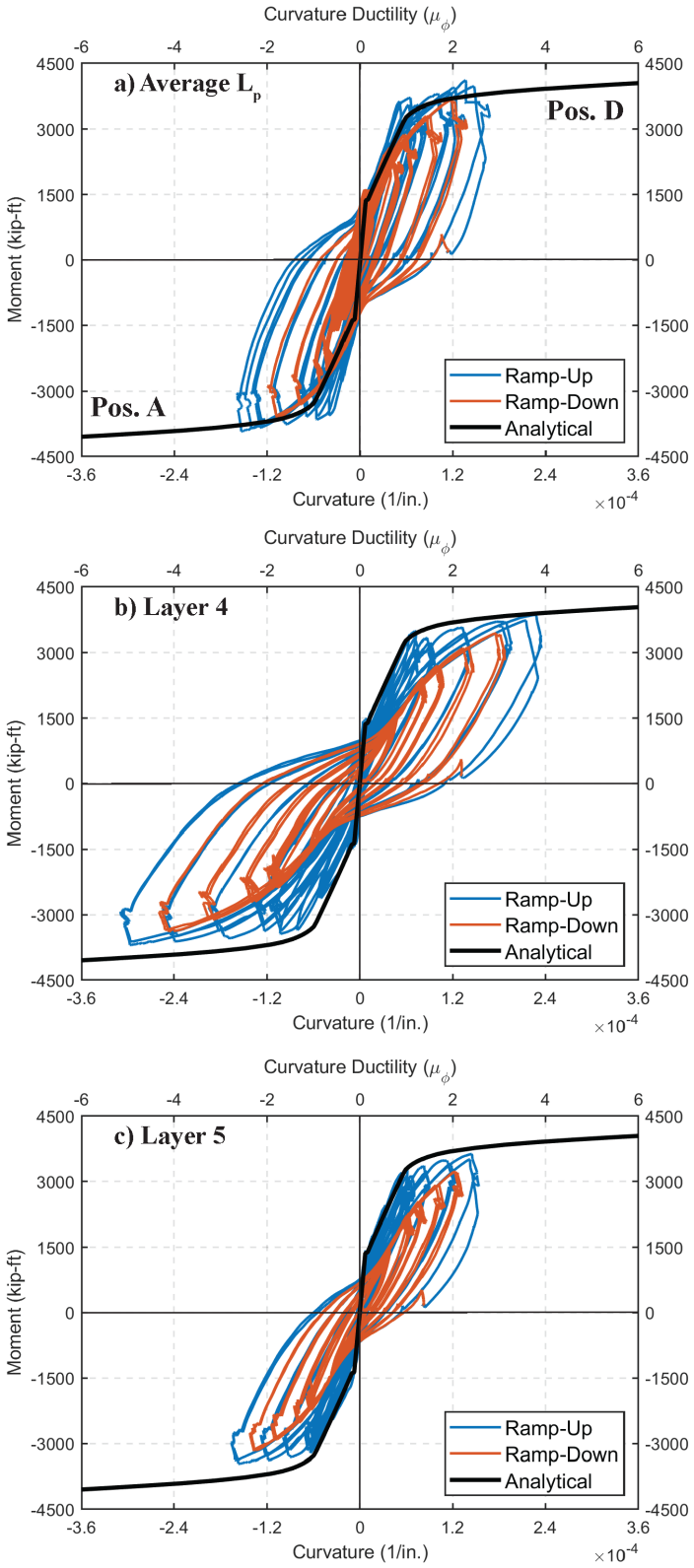

Figure 5-26: Moment-Curvature responses at L_p, and Layers 4 and 5 of CW-3 during WLP

5.3.3 Base Shear-Lateral Displacement Responses

In-plane (IP) drift ratios were measured using the two horizontal LVDTs attached to the northeast and southeast corners of the top block. Figure 5-27 shows the IP drift ratios computed for each of the two LVDTs for CW-2, CW-3, and CW-4 during the WLP. The lateral displacements at the top of the wall due to sliding and rotation of the bottom foundation block were excluded. For all specimens, in both the positive and negative in-plane directions, the drift ratios were higher at the northeast corner compared to the southeast corner. The drift ratios at the northeast corner were approximately 30% higher for CW-2 and CW-3 in the positive direction and 23% higher for CW-2 in the negative direction at the maximum rotation demands. The differences were smaller for CW-4 in both directions (approximately 3%) and for CW-3 in the negative direction (approximately 10%). The differences in the drift ratios were observed due to the torsion that occurred during in-plane loading. The readings from the two LVDTs were averaged to calculate the average in-plane drift ratios. The average drift ratios for all specimens during the WLP are shown in Figure 5-28, where the displacement ductility values were calculated using an effective yield drift ratio of 0.4% in both the positive and negative directions. The average in-plane drift ratios during ramp-up loading for all three specimens were also plotted together in Figure 5-28 for comparison. The highest drift ratio measured in the positive direction, +1.92%, was for CW-4 at the maximum rotation demand, whereas for CW-2 and CW-3, it was +1.61% and +1.64%. In the negative loading direction, CW-4 had -2.10%, and CW-2 and CW-3 had -1.75% and -1.53% drift ratio demands, respectively. The in-plane drift ratio demands during the ramp-up loading are summarized in Table 5-3. Different drift ratios were measured for the different walls because the in-plane rotation demands were controlled during the testing, not the drift ratios. Due to the different amounts of damage that occurred over the hinge region for different walls, different drift

ratios were observed. At the maximum hinge rotation demands of the WLP, the in-plane hinge rotation demand was 0.9%, whereas the in-plane drift ratios were significantly higher than these values, ranging from 1.5% to 2.1%. This difference was due to the high curvature/rotation demands that occurred above the assumed hinge region (Layers 4 and 5, Figures 5-22 through 5-26). For the hinge region, lower curvature values were computed for the splice region (l_s = 20 in.), which accounted for 53.3% of the plastic hinge length (L_p = 37.5 in.) but only 22.7% of the total wall height (88 in.). Therefore, at 0.9% hinge rotation demands, the drift ratios were approximately 1.7 and 2.33 times larger. The results suggest that overlapping longitudinal reinforcement stiffens and strengthens the splice region such that inelastic curvatures spread over a greater height.

The drift ratios in the out-of-plane (OOP) direction were measured using the two LVDTs attached to the northeast and northwest corners of the top block; computed drift ratios using these LVDTs are shown in Figure 5-29 for the ramp-up and ramp-down loading of the WLP. Average drift ratios using the readings from the two LVDTs were also calculated and shown in Figure 5-30. In the negative OOP direction (web-flange corners were under compression), no strength loss was observed for any of the specimens; however, some stiffness reduction was observed, i.e., the drift ratios increased from around -0.5% to around -1.0%, mainly during the ramp-up loading. In the positive OOP direction (flange edges were under compression), given the lower amount of damage that occurred to CW-3 relative to CW-2 and CW-4, which was due to the lower level of applied axial load ($P_{OOP+y}=0.05A_g f'_c$), no stiffness degradation or strength loss was observed for CW-3. For CW-4 ($P_{OOP+y}=0.075A_g f'_c$), similar to CW-3, no strength loss was observed, but stiffness reduction occurred, i.e., the drift ratios increased from around +0.25% to 0.5%. For CW-2 ($P_{OOP+y}=0.10A_g f'_c$), the drift ratios increased from around +0.25% to 0.5% during the ramp-up

cycles. During the ramp-down loading, a significant amount of strength loss was observed, i.e., the base shear decreased to 15 kips from 54 kips (72% reduction).

Table 5-3: Drift ratios at the top of the walls during the ramp-up loading of WLP

Load Step		Hinge rotation, $\Theta_{Lp,IP}$ (%)	Top Drift Ratio (%)		
		CW-2-3-4	CW-2	CW-3	CW-4
Pos. Dir (Pos. D)	$0.4M_{pr}$	+0.05	+0.13	+0.032	+0.14
	$0.7M_{pr}$	+0.19	+0.41	+0.22	+0.40
	$1.2\Theta_y$	+0.36	+0.68	+0.63	+0.76
	$1.5\Theta_y$	+0.45	+0.81	+0.86	+0.91
	$2.0\Theta_y$	+0.60	+1.06	+1.10	+1.19
	$2.5\Theta_y$	+0.75	+1.32	+1.37	+1.56
	$3.0\Theta_y$	+0.90	+1.61	+1.64	+1.92
Neg. Dir (Pos. A)	$0.4M_{pr}$	-0.06	-0.17	-0.15	-0.17
	$0.7M_{pr}$	-0.19	-0.40	-0.40	-0.45
	$1.2\Theta_y$	-0.36	-0.64	-0.67	-0.87
	$1.5\Theta_y$	-0.45	-0.80	-0.77	-1.03
	$2.0\Theta_y$	-0.60	-1.06	-0.95	-1.33
	$2.5\Theta_y$	-0.75	-1.37	-1.20	-1.69
	$3.0\Theta_y$	-0.90	-1.75	-1.53	-2.10

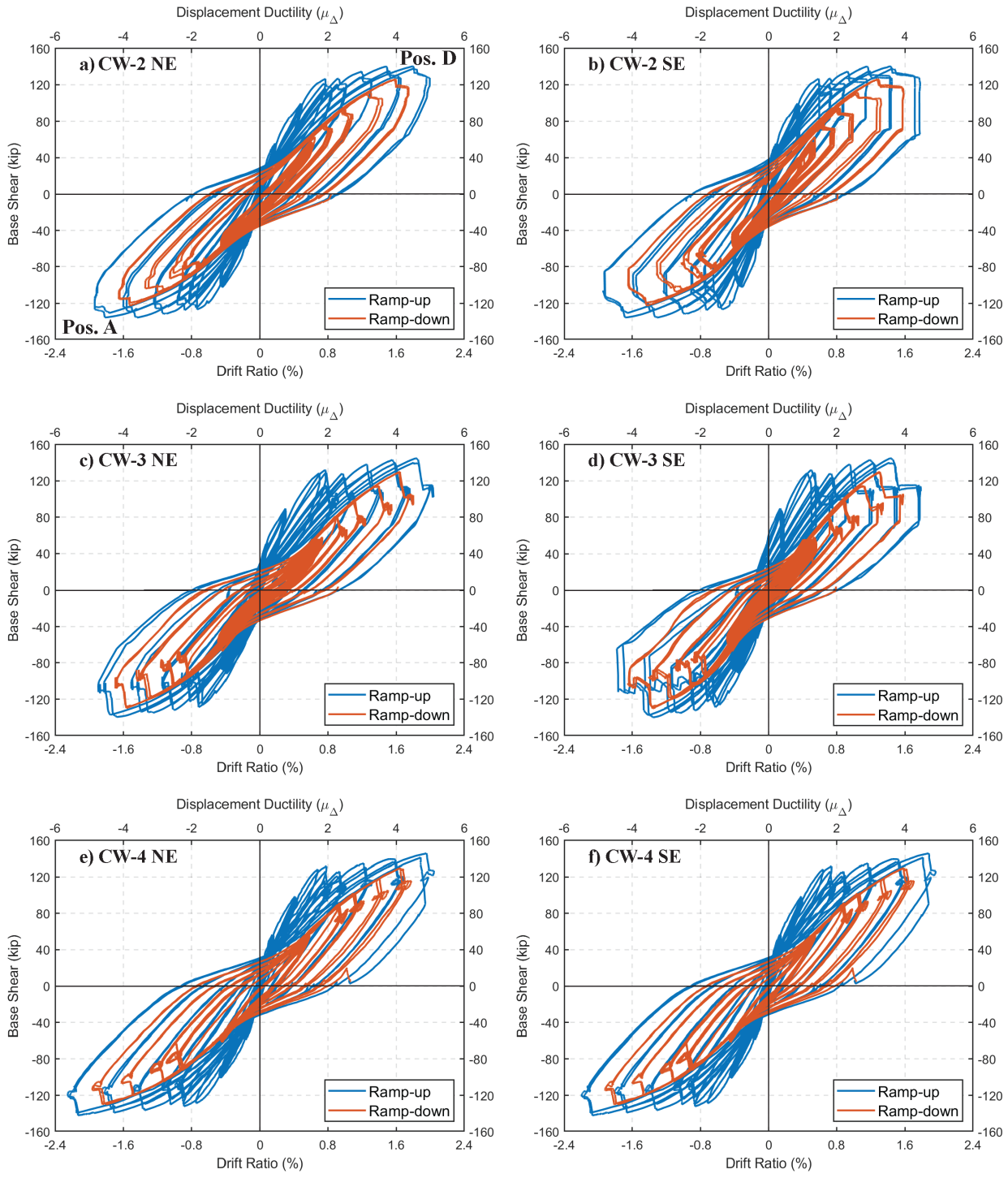

Figure 5-27: In-plane base shear-drift ratio responses measured at the NE, and SE corners of the top block under WLP

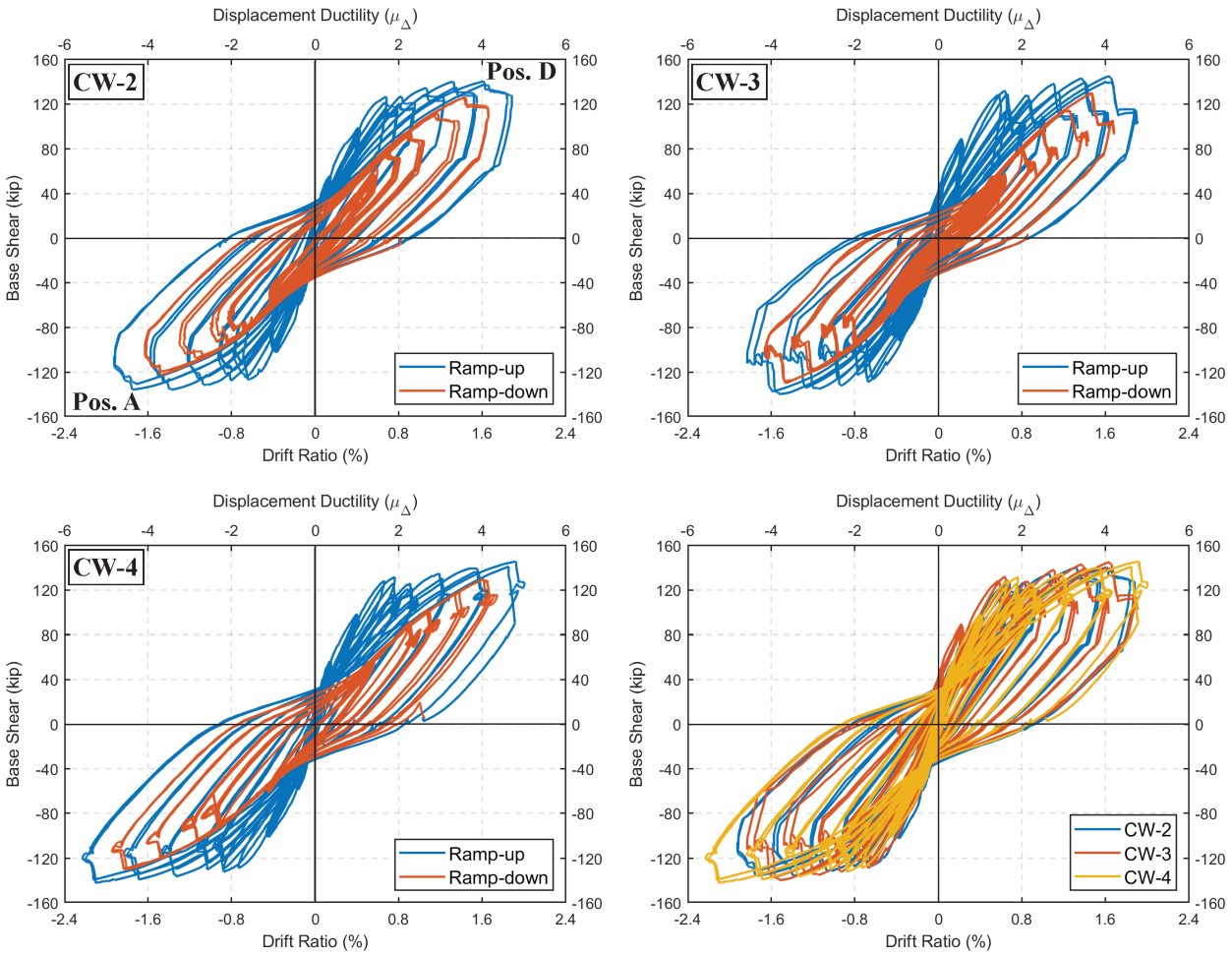

Figure 5-28: Average In-plane base shear-drift ratio responses under WLP

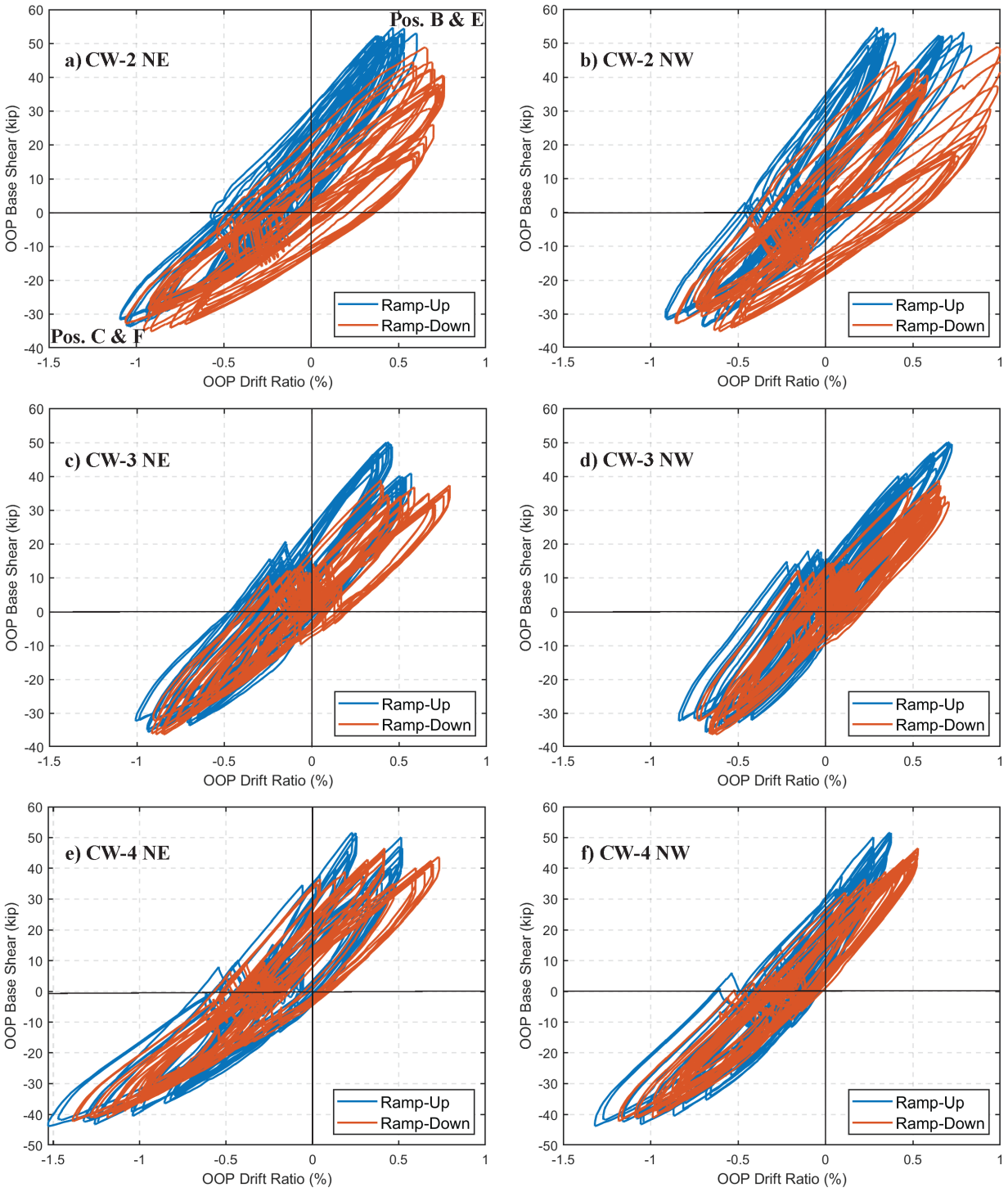

Figure 5-29: Out-of-plane base shear-drift ratio responses measured at the NE, and NW corners of the top block under WLP

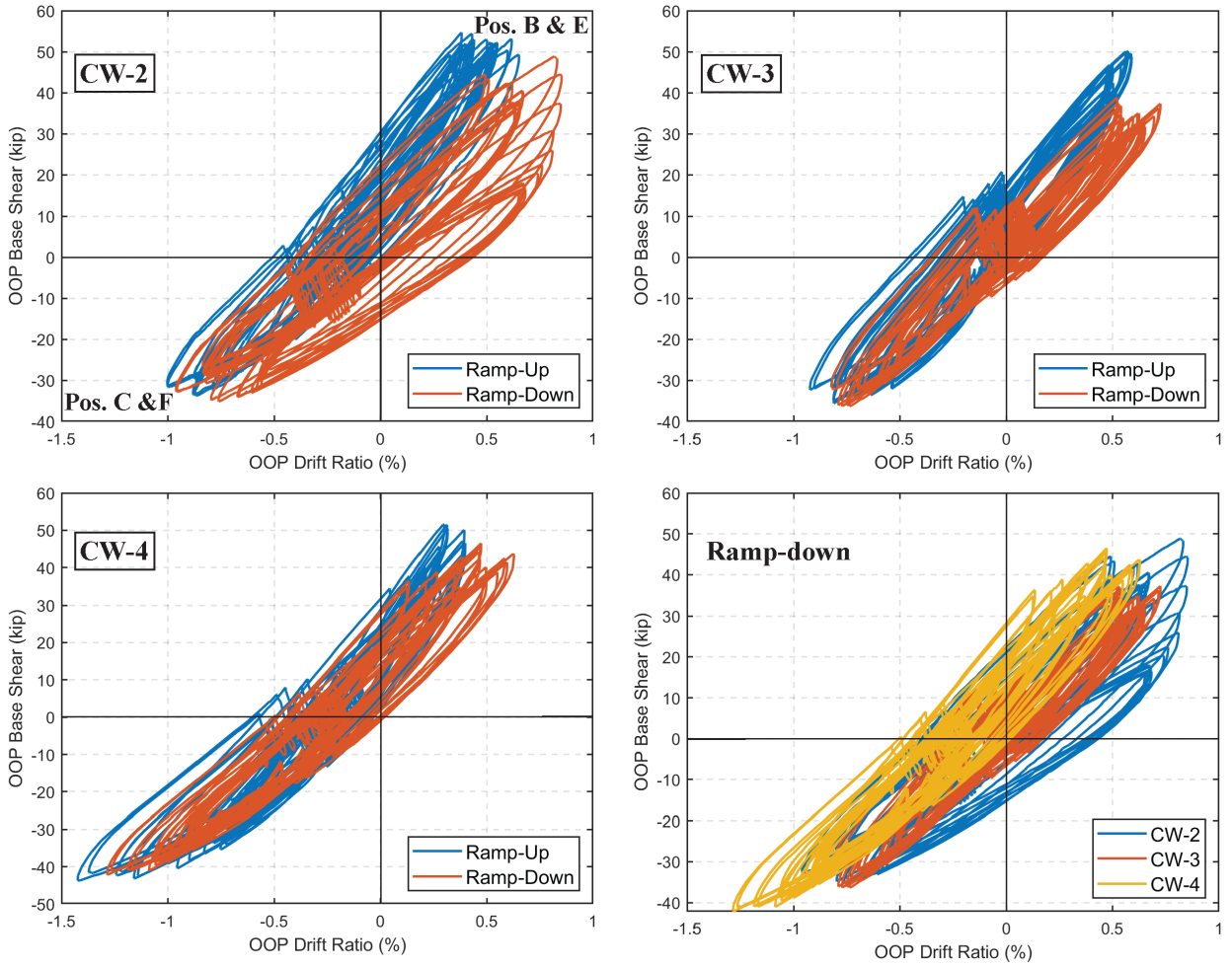

Figure 5-30: Average out-of-plane base shear-drift ratio responses under WLP

As mentioned in Section 3.3.3, the total in-plane lateral displacement (δ_{tot}) of the wall can be expressed as the sum of the flexural and shear deformations over the wall height (Equation 3.3). Flexural deformations include the curvature/rotation of the wall ($\delta_{f,wall}$) and the deformations due to the slip/extension at the wall-footing interface (δ_{slip}). Shear deformations include the pure translation (shear distortion) along the height of the wall ($\delta_{s,wall}$), the shear sliding along the wall footing interface ($\delta_{s,slide,wall}$), and also the shear sliding of the bottom block along the laboratory floor ($\delta_{s,slide,block}$). The lateral displacements due to the rotation of the bottom block were found to be negligible. The details regarding the displacement calculations due to $\delta_{f,wall}$, δ_{slip}, and

$\delta_{s,wall}$ are given in Appendix G. $\delta_{s,slide,wall}$ and $\delta_{s,slide,block}$ were measured directly using LVDTs. Figures 5-31, 5-32, and 5-33 show the base shear-drift ratio responses for the different deformation components for CW-2, CW-3, and CW-4, respectively, during the ramp-up and ramp-down loading of the WLP. The percent contributions of flexural, shear, and slip/extension deformations to the lateral displacement at the top of each wall are shown in Figures 5-34, 5-35, and 5-36 for CW-2, CW-3, and CW-4, respectively. The average contributions from (negative and positive values) CW-2, CW-3, and CW-4 are also shown in Figure 5-37. While the contributions of the shear sliding of the wall and bottom block are not given in these figures, in total, these items contributed approximately 5%, 6%, and 3%, on average, to the total lateral displacement for CW-2, CW-3, and CW-4, respectively. The slip/extension deformations at the base of the wall contributed approximately 10% and 20% of the total displacement, on average, at first yield ($0.7M_{pr}$) and at the maximum rotation demands ($3\Theta_y$), respectively. In general, the contribution of the slip/extension stayed constant after $1.2\Theta_y$ rotation demands. The lateral displacements due to flexural deformations were around 30 to 35% of the total displacements at the first yield; however, with increasing displacement demands, this contribution increased to 50%, 45%, and 40% for CW-2, CW-3, and CW-4, respectively. There was a greater variation for the lateral displacement contribution of the shear deformations calculated using Equation G.18. Generally, shear deformations accounted for around 50% to 60% of the total top displacement at first yield and decreased to 30% to 40% at the maximum displacement demands. When the lateral displacements due to shear deformations were calculated using Equation G.18, the percent contributions were lower, with values around 20% to 30%. As mentioned in Section 3.3.3, the flexural drift ratios due to plastic hinge rotations are mostly constant along the height of a wall, whereas shear deformations (pure translation) decrease up the height of the wall; therefore, the percent

contribution of the shear deformations to the drift ratios at the top of a cantilever wall is expected to be much smaller than the values given here.

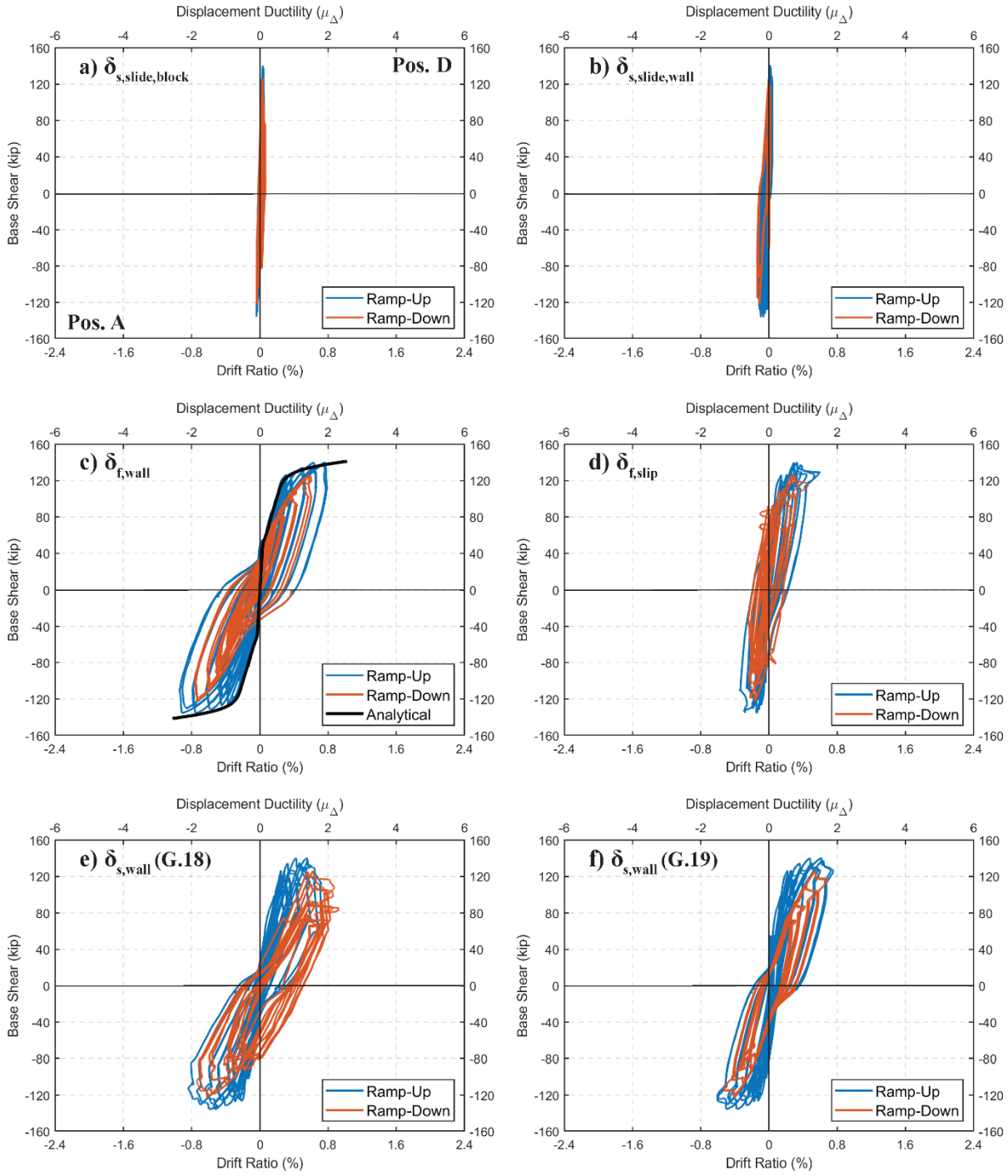

Figure 5-31: Different components of in-plane base shear-drift ratio response of CW-2 under WLP

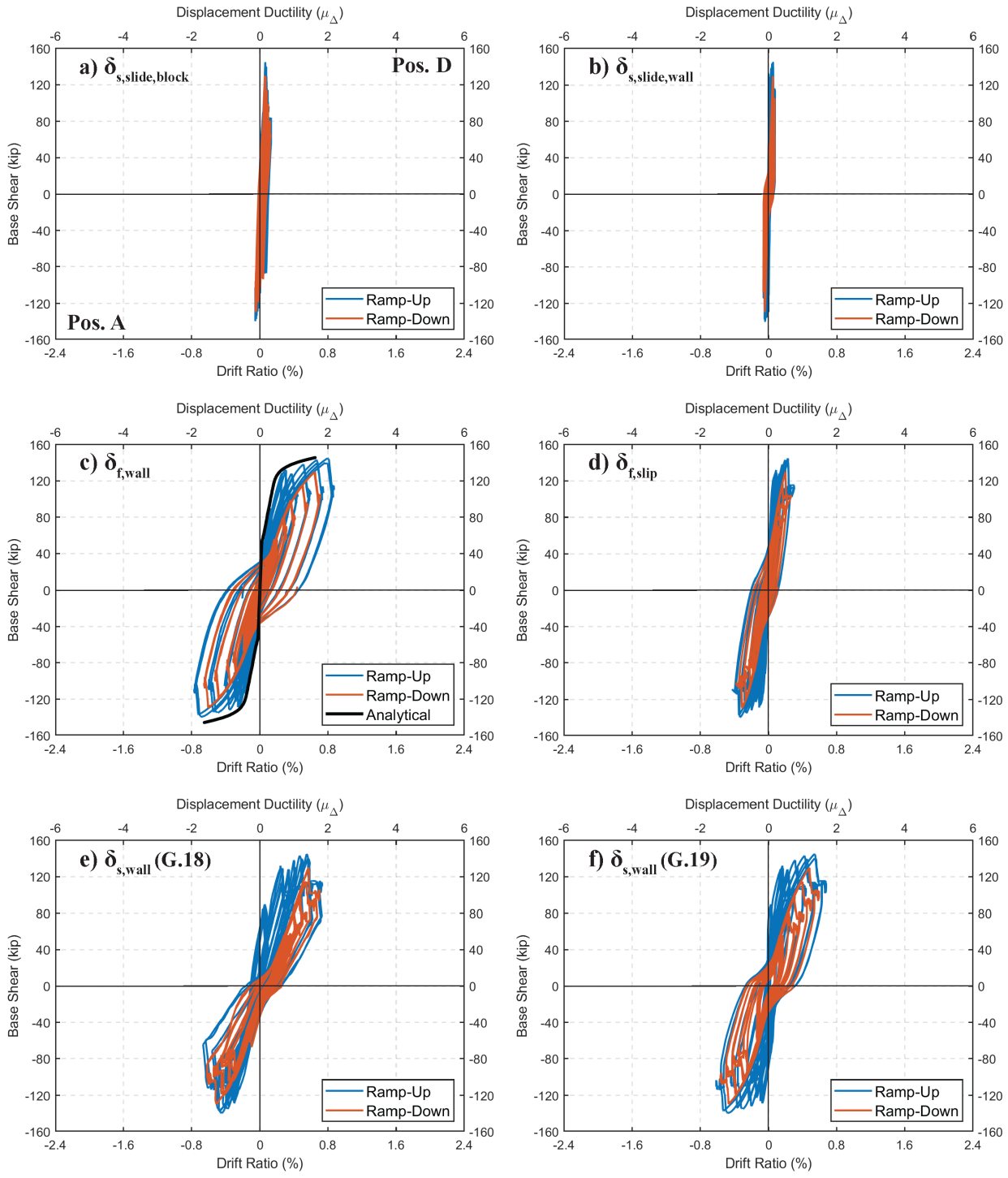

Figure 5-32: Different components of in-plane base shear-drift ratio response of CW-3 under WLP

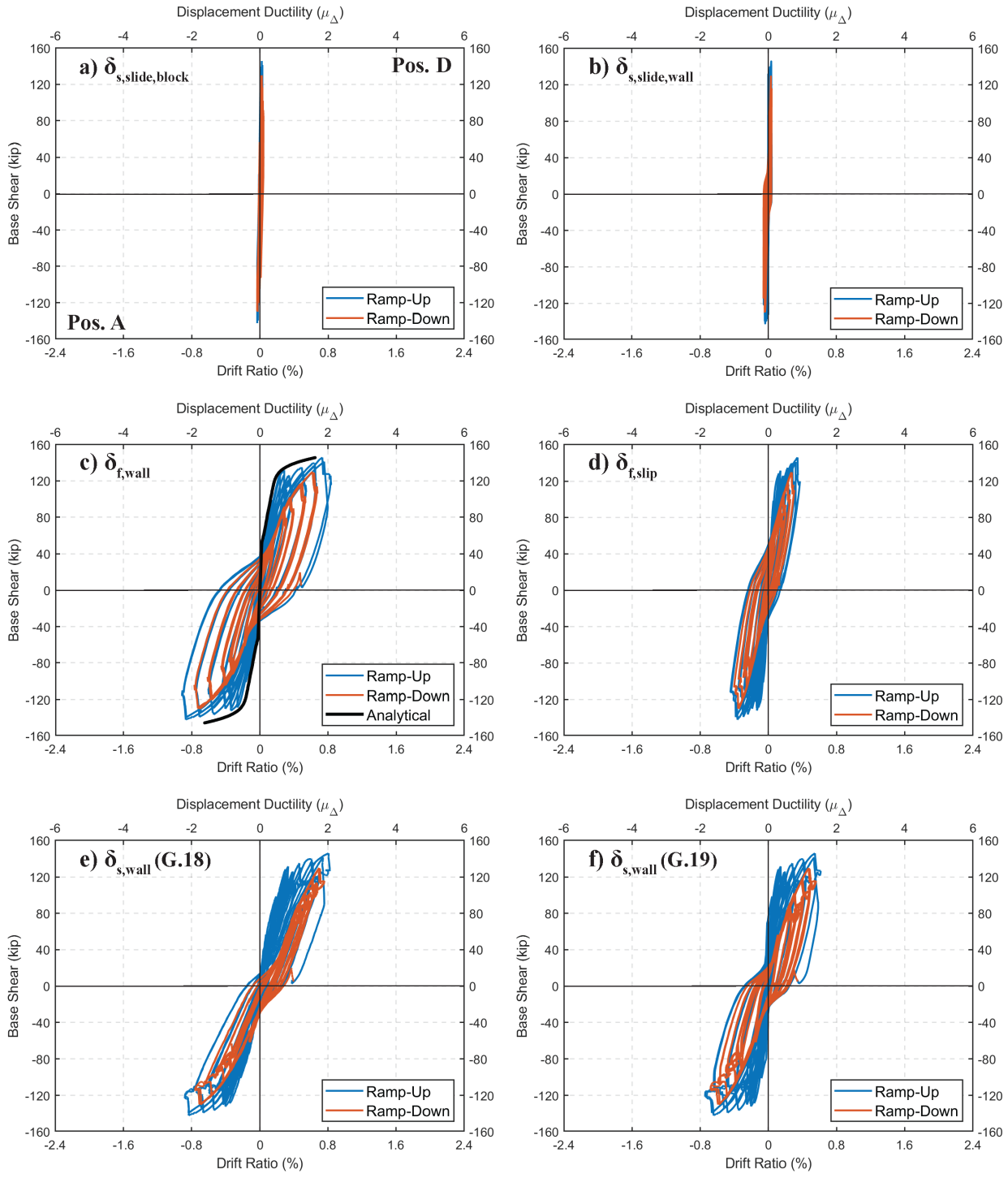

Figure 5-33: Different components of in-plane base shear-drift ratio response of CW-4 under WLP

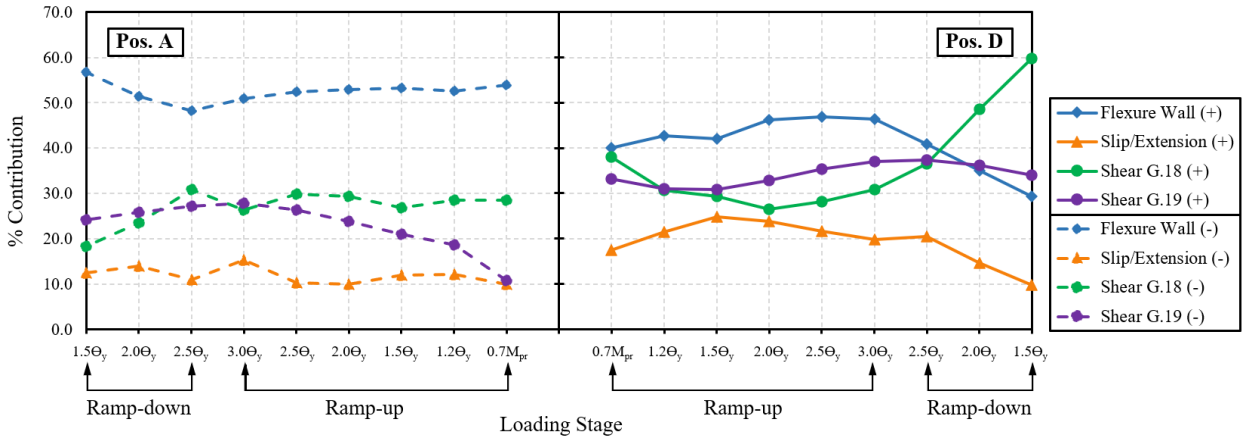

Figure 5-34: Contributions of flexure, slip/extension, and shear deformations to the lateral displacement for CW-2 during WLP

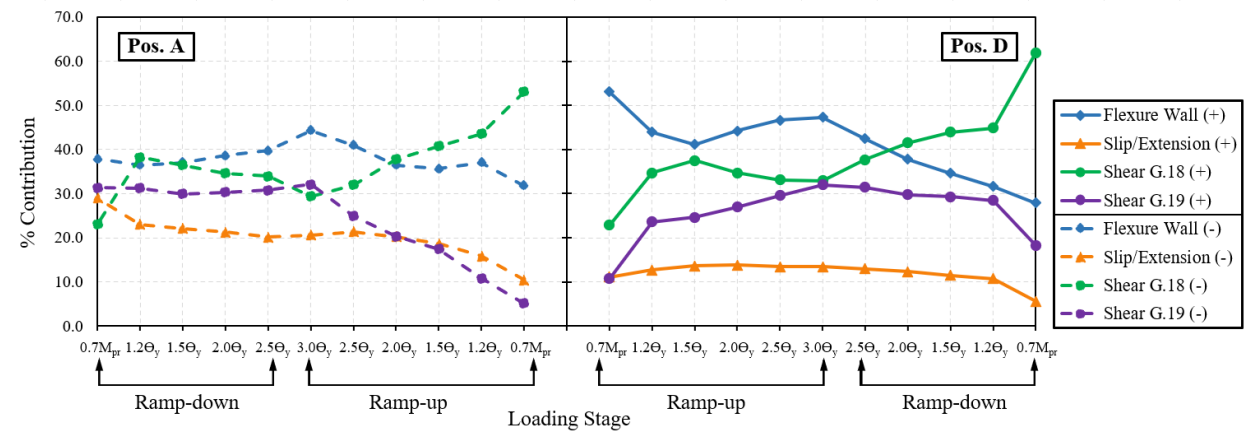

Figure 5-35: Contributions of flexure, slip/extension, and shear deformations to the lateral displacement for CW-3 during WLP

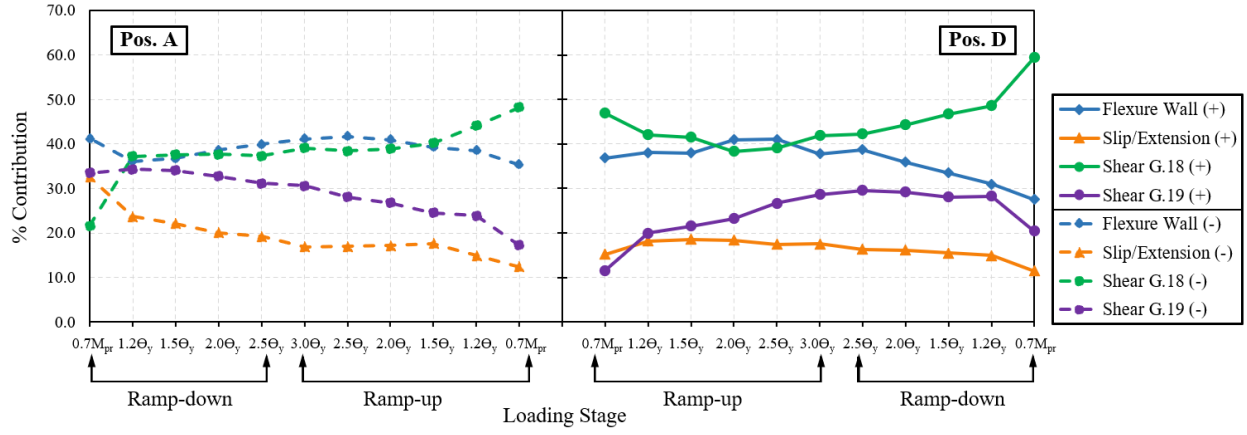

Figure 5-36: Contributions of flexure, slip/extension, and shear deformations to the lateral displacement for CW-4 during WLP

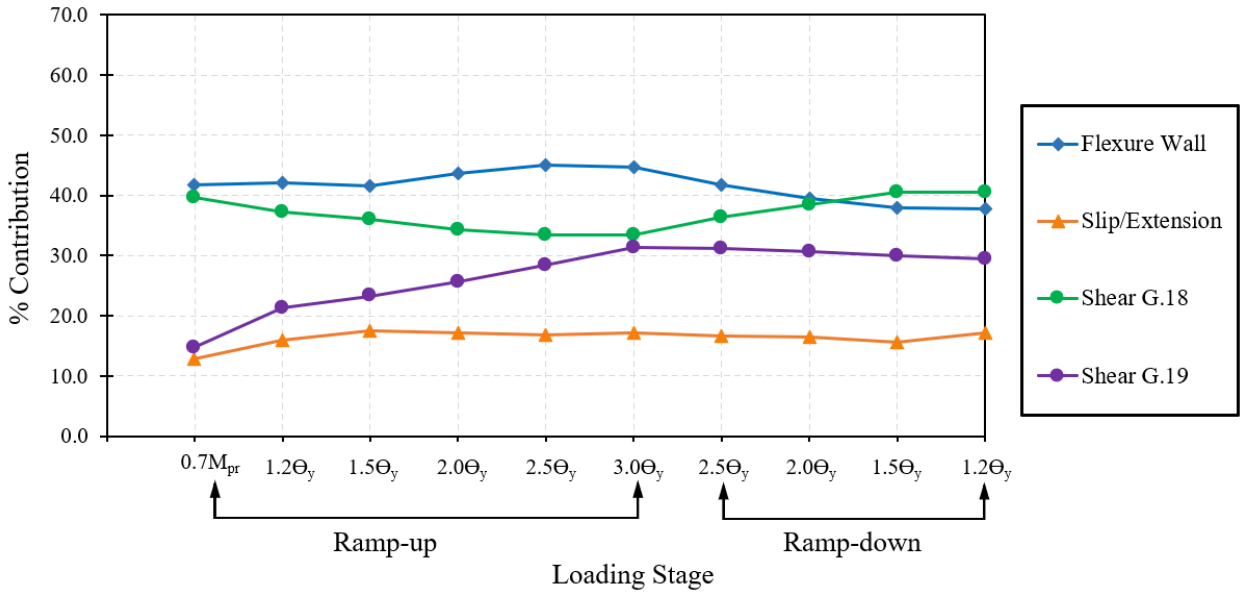

Figure 5-37: Average contributions of flexure, slip/extension, and shear deformations to the lateral displacement

5.3.4 Torsional Responses

Torsional rotations during the WLP, calculated using Equation 3.4, are shown in Figures 5-38b, 5-39b, and 5-40b for CW-2, CW-3, and CW-4, respectively. The torsional responses of the specimens were similar to each other both during the ramp-up and ramp-down loading; in general, there was a change in the torsional rotations during the in-plane loading, with the values ranging around -0.45% to +0.2%. This torsional behavior of the specimens during the in-plane loading can also be observed in Figures 5-38a, 5-39a, and 5-40a, which show the IP versus OOP rotation responses of the east and west flanges individually. The torsional rotations resulted in higher compressive strain demands at the flange-web corners than at the flange edge for the flange that was under compression. Similarly, torsional rotations resulted in higher tensile strain demands at the flange-web corners for the flange that was under tension. This behavior caused concrete cover crushing and spalling at the flange-web corners sooner than the flange edges for all the specimens

(Section 5.2), possibly delaying concrete crushing and longitudinal reinforcement buckling observed at the flange edges.

During the application of biaxial loading, almost no changes in the torsional rotations were observed when loading was in the positive in-plane direction (Pos. E and F). However, there was a significant change in the torsional rotation demands during the OOP loading for negative in-plane rotation demands (Pos. B and C, the east flange was under tension). This behavior was mainly due to the flexibility of the support for the horizontal actuator used in the OOP direction attached to the steel loading beam on the east side of the specimen (Actuator 5). The higher torsion rotations occurred at Pos. B and C of the loading protocol resulted in higher positive OOP rotation demands at the east flange (flange that was under tension) and higher negative OOP rotation demands at the west flange (flange that was under compression). This behavior resulted in concrete spalling over a greater height (approximately up to 20 in. above the footing) for the west flange corner compared to the east flange corner (spalling up to 7 in. above the footing).

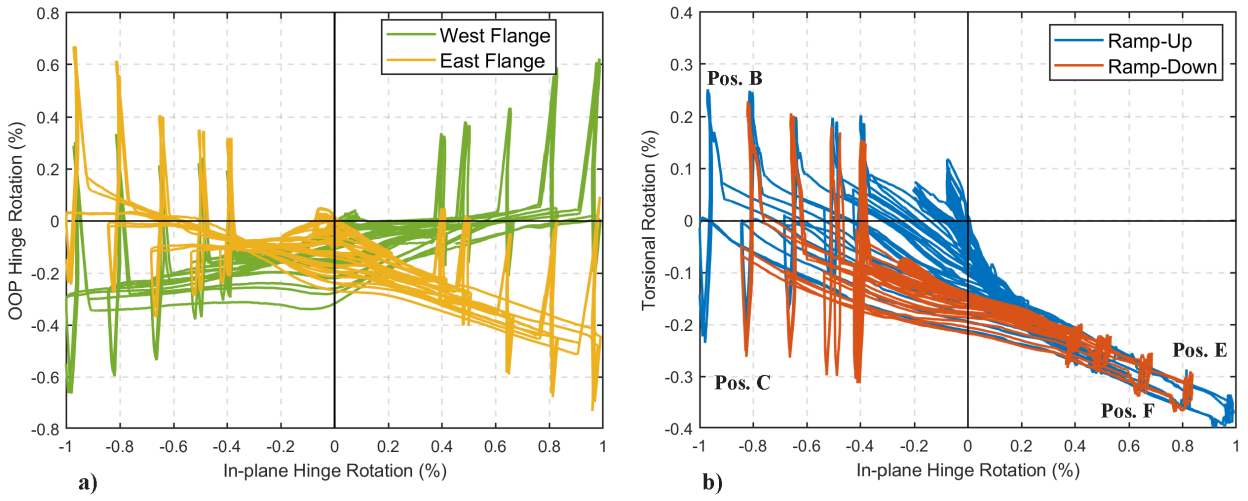

Figure 5-38: a) IP versus OOP hinge rotation of the East and West flange, b) IP Rotation versus Torsional rotation responses of CW-2 during WLP

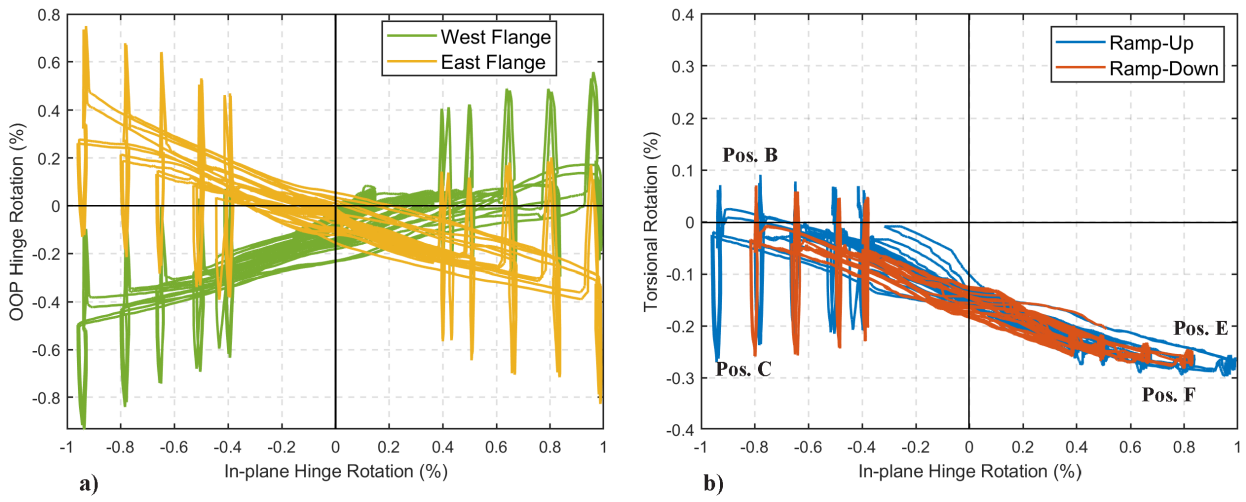

Figure 5-39: a) IP versus OOP hinge rotation of the East and West flange, b) IP Rotation versus Torsional rotation responses of CW-3 during WLP

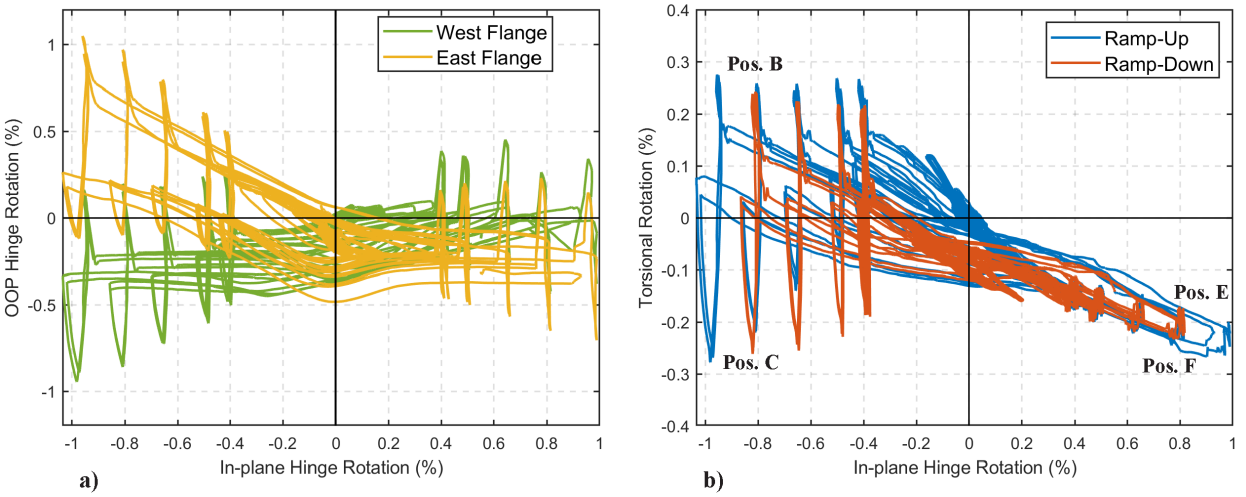

Figure 5-40: a) IP versus OOP hinge rotation of the East and West flange, b) IP Rotation versus Torsional rotation responses of CW-4 during WLP

5.3.5 Local Responses

Axial strains were measured using columns of LVDTs attached at the flange edges, at the inside surface of the web, and at the flange-web corners for CW-3 and CW-4 (Figures 2-24, 2-25, and 5-21). Figure 5-41 and Figure 5-42 show the axial strain distribution along the height of the east and west flange edges of CW-2, respectively, during the ramp-up loading of WLP at different loading positions. The highest tensile strains were measured as 1.88% and 1.77% for the east and west flanges, respectively, at Layer 4 (37.5-57.5 in.) for both flanges during the in-plane loading (Pos. A and D). With the application of the biaxial loading, the tensile strains at the flange edges at Layer 4 increased to 1.93% and 1.87% for the east flange (at Pos. C) and west flange (at Pos. F), respectively. The effect of biaxial loading on the tensile strains along the flange edges was more significant for the Layer 1 LVDTs than the other layers, i.e., the tensile strains, for flanges, increased from around 0.65% to 0.9% (approximately 40% increase) for Layer 1 with the application of OOP loading. The Layer 1 LVDTs (2-10 in.) had the lowest tensile strains for both flanges due to the splice(0-20 in.), which appeared to strengthen and stiffen this region. For the east flange, the tensile strains were also low for Layer 2 (10-20 in.) compared to the other layers, whereas for the west flange, Layer 2 LVDTs had higher tensile strains than Layer 3 LVDTs, possibly because of a large crack that occurred at the end of the splice that was within the Layer 2 LVDT anchor rod (versus within Layer 3).

During positive in-plane (Pos. D, the east flange was under compression) ramp-up loading, the east flange Layer 1 LVDTs were under tension. This was due to the torsion that occurred during in-plane loading, i.e., during the in-plane loading, the east flange had negative OOP rotations (Figure 5-38a) which resulted in tension at the base of the east flange edge. Figure 5-43 shows the in-plane versus out-of-plane rotation response of the east flange during the ramp-up and ramp-

down loading. The figure shows that, during positive in-plane ramp-up loading, the east flange had negative OOP rotations, which was consistent with the tensile strain reading at the east flange edge Layer 1 LVDTs and with the fact that no damage occurred at the east flange during ramp-up loading. However, during ramp-down loading, less torsion was observed, and the east flange had higher positive OOP rotations during the positive IP loading (Figure 5-43), which resulted in higher compressive strain values at the east flange edge during ramp-down loading (Figure H-1). At the $+2\Theta_y$ IP hinge rotation ramp-down load step (Pos. D), Layer 1 LVDTs at the east flange edge recorded -0.006 compressive strain demands, and with the application of the OOP loading (Pos. E), the compressive strain demands increased to -0.015 (Figure H-1). At the $+1.5\Theta_y$ and $+1.2\Theta_y$ ramp-down load steps, the compressive strain demands at Pos. D (in-plane loading only) were -0.01 and -0.012, respectively, and these values increased to -0.025 and -0.029 with the application of OOP loading (Pos. E, Figure H-1). These high compressive strain values observed during the ramp-down loading for the east flange edge Layer 1 LVDTs were consistent with the significant amount of damage (concrete core crushing) that occurred during the ramp-down loading at the east flange edge (Section 5.2.1).

Unlike the east flange, torsional responses were less pronounced when the west flange was under compression (negative IP loading, Pos. A). During negative IP ramp-up loading, the west flange had lower negative OOP rotation demands (around -0.002, Figure 5-38a) than the east flange, which resulted in compressive strain demands of -0.0068 at Pos. A at $-3.0\Theta_y$ IP hinge rotation load step for the west flange edge Layer 1 LVDTs. With the application of the OOP loading (Pos. B), the compressive strain demands increased to around -0.011. The higher compressive strain demands measured within the Layer 1 west flange edge LVDTs were consistent with the damage that occurred at the base of the west flange edge during the ramp-up loading. During the ramp-

down loading at Pos. B, the compressive strain demands at the west flange Layer 1 LVDTs were around -0.01 to -0.013 (Figure H-2), which resulted in more damage at the west flange edge during the ramp-down loading (Section 5.2.1).

Figure 5-44 shows the effect of biaxial loading on the flange edge compressive strains by comparing the Layer 1 and Layer 2 LVDT readings during the ramp-up loading at Pos. A and Pos. B for the west flange, and at Pos. D and Pos. E for the east flange. In general, the application of $0.5M_{pr,OOP+y}$ OOP moment demands resulted in the compressive strain demands increasing by a factor of approximately 2.0 during the lower IP hinge rotation demands ($1.2\Theta_y$ and $1.5\Theta_y$), and by approximately factors of 1.5 and 1.6 during the higher IP rotation demands ($2.5\Theta_y$ and $3.0\Theta_y$).

Figure 5-45 and Figure 5-46 show the axial strain profiles along the length of the wall using the Group 1 LVDTs (Figure 5-21) for the Layer 1 and Layer 2 LVDTs, respectively, during the ramp-up loading. The grey dashed lines in these figures represent the location of the flanges. Because of the lower tensile strains over the splice region, the distribution of the strains along the wall length were not linear for the Layer 1 LVDTs. However, for the Layer 2 LVDTs, higher tensile strains were computed for the web and flange edge LVDTs, which resulted in a more linear distribution than for Layer 1. To estimate the strains at the concrete surfaces (LVDTs were attached a couple of inches away from the concrete surfaces, Figure 2-28), a neutral axis depth of 13 in. was assumed at Layer 1. This value was selected using the analytical moment-curvature predictions which matched the experimental results very well (see Section 5.3.2 and also Figure 5-46). The neutral axis depth at Layer 2 was estimated to be around 11 in. at the maximum IP hinge rotation demands at both Pos. A and Pos. D from Figure 5-46. Given that the curvatures were smaller within Layer 1 than within Layer 2 (Figure 5-22), a higher neutral axis depth value was expected at Layer 1.

Also, the neutral axis depth was found to be 15 in. at the curvature values observed from Layer 1 using an analytical (monotonic) moment-curvature analysis. Therefore, a value of 13 in. was selected for the strain predictions. The Layer 1 LVDTs were attached approximately 3.5 in. away from the concrete surfaces, by assuming a neutral axis depth of 13 in., the compressive strain values at the concrete surfaces were estimated to be 0.79 of the LVDT readings (13/(13+3.5)=0.79), and the tensile strain values were estimated to be 0.95 of the LVDT strains (62/(62+3.5)=0.95). Therefore, the maximum compressive strains at the concrete surfaces were estimated to be -0.53% for the west flange edge during the in-plane only ramp-up loading and around -1.0% during the ramp-down loading for the west and the east flanges. The compressive strains during biaxial (IP + OOP) loading were not estimated using this procedure because, under the biaxial loading, the neutral axis orientation was diagonal (not parallel to the flanges).

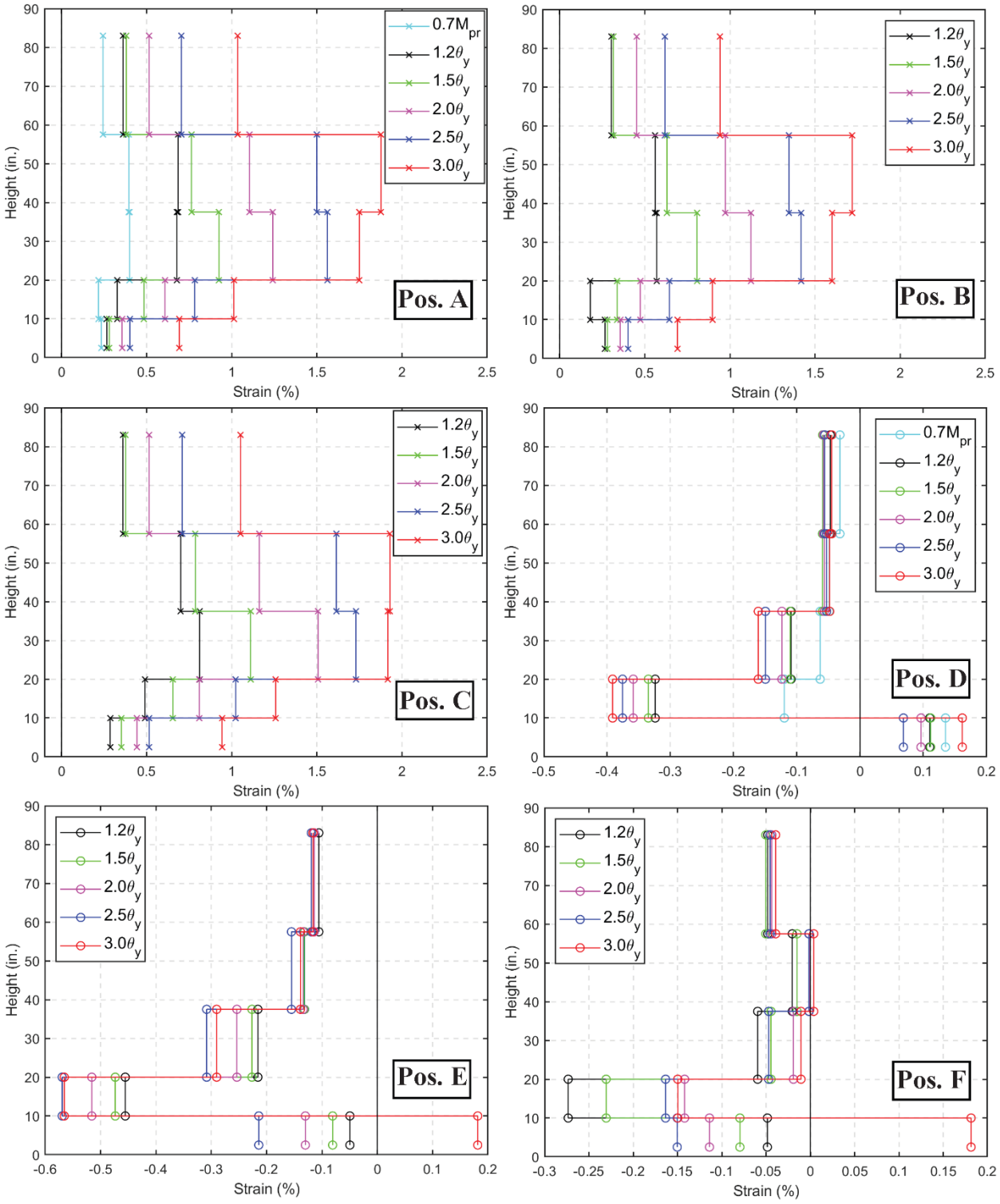

Figure 5-41: Axial strain profiles along the height of the edge of the East flange at different loading positions during the ramp-up loading of WLP, CW-2

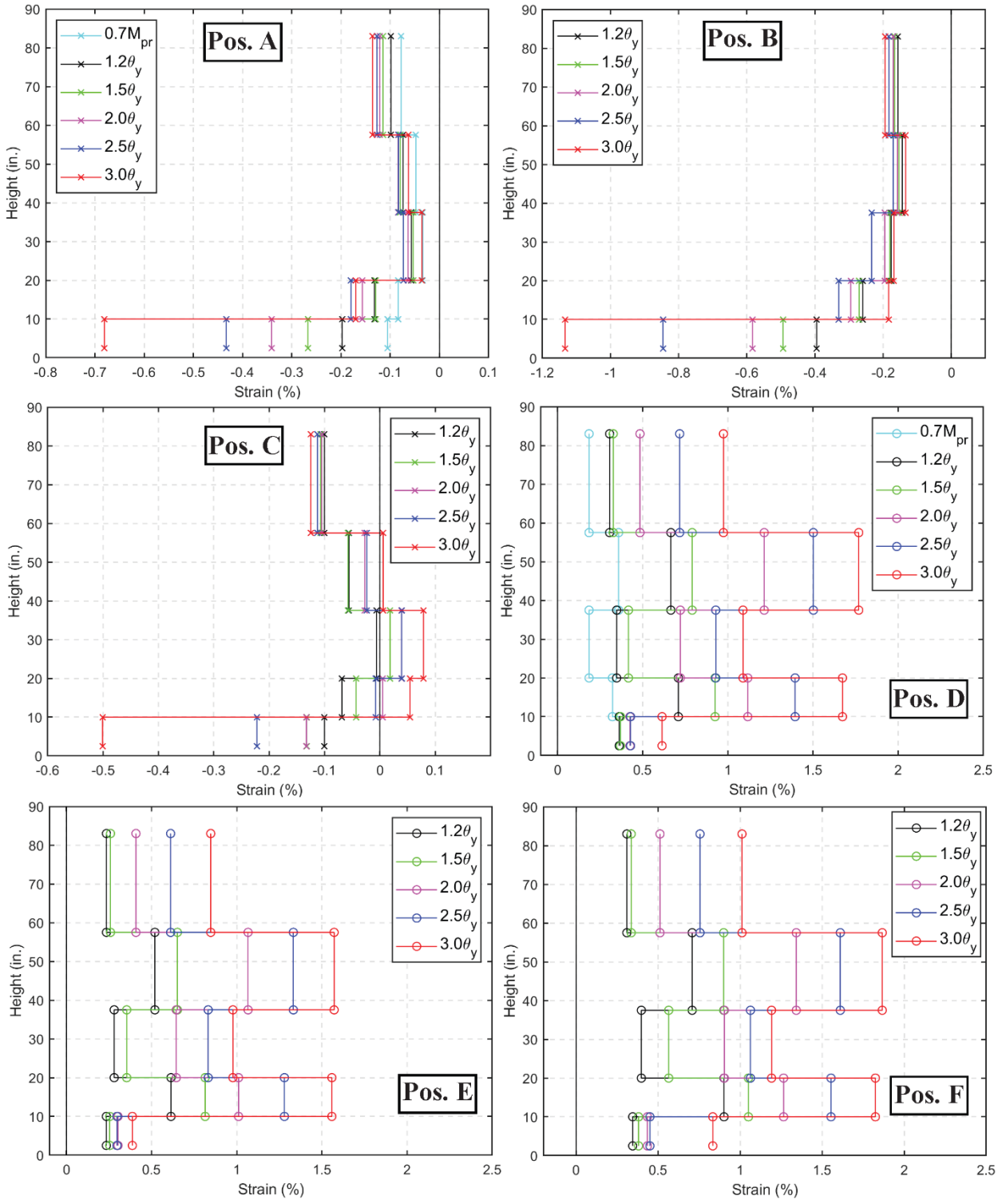

Figure 5-42: Axial strain profiles along the height of the edge of the West flange at different loading positions during the ramp-up loading of WLP, CW-2

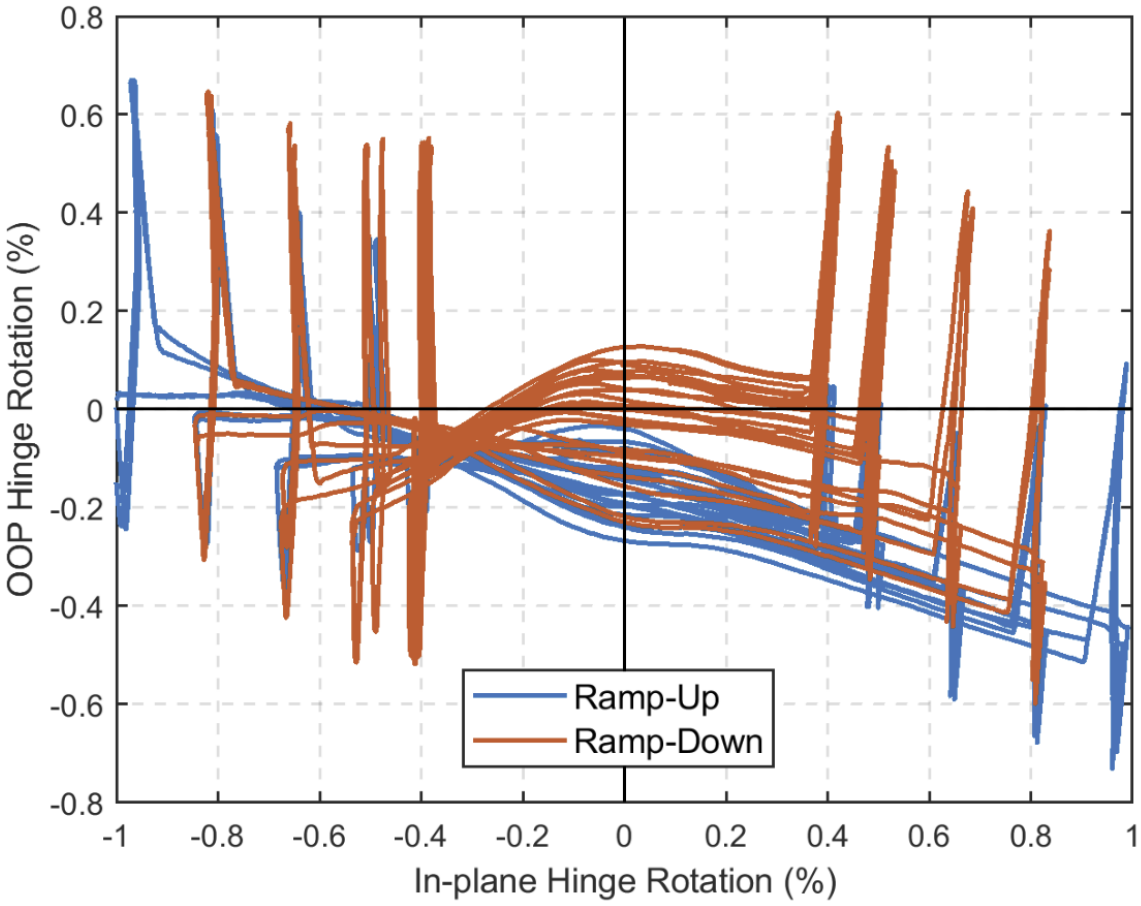

Figure 5-43: IP – OOP hinge rotation response of the east flange of CW-2

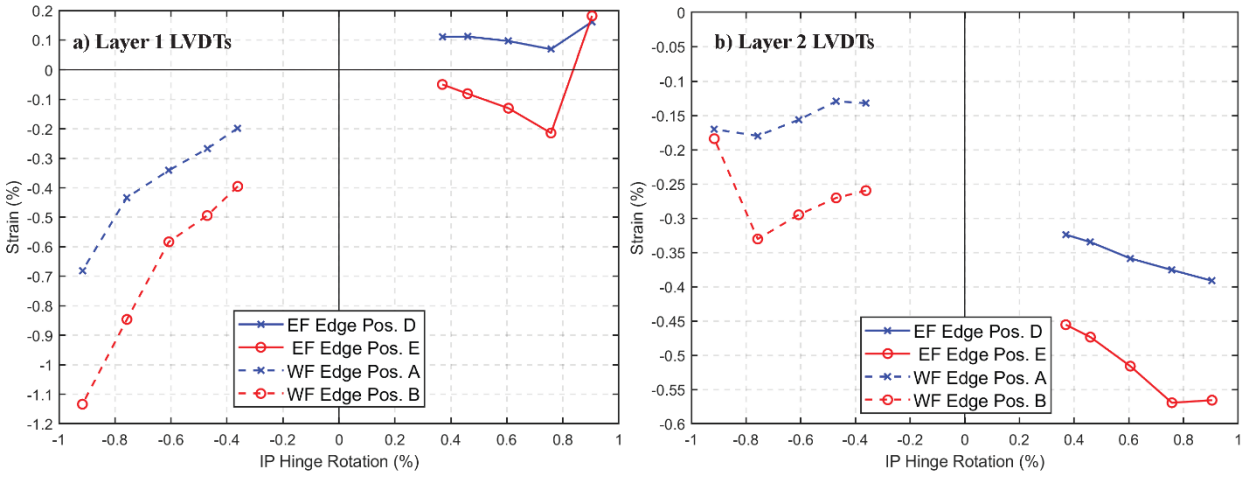

Figure 5-44: Comparison of compressive strains at different loading positions during the ramp-up loading of WLP for the first- and second-layer flange edge LVDTs, CW-2

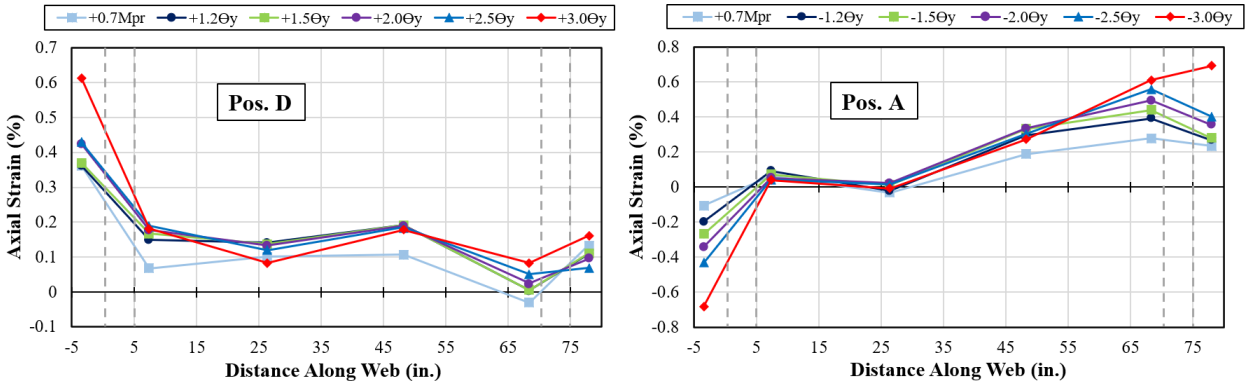

Figure 5-45: Axial strain profiles obtained from Layer 1 LVDTs (Group 1), CW-2

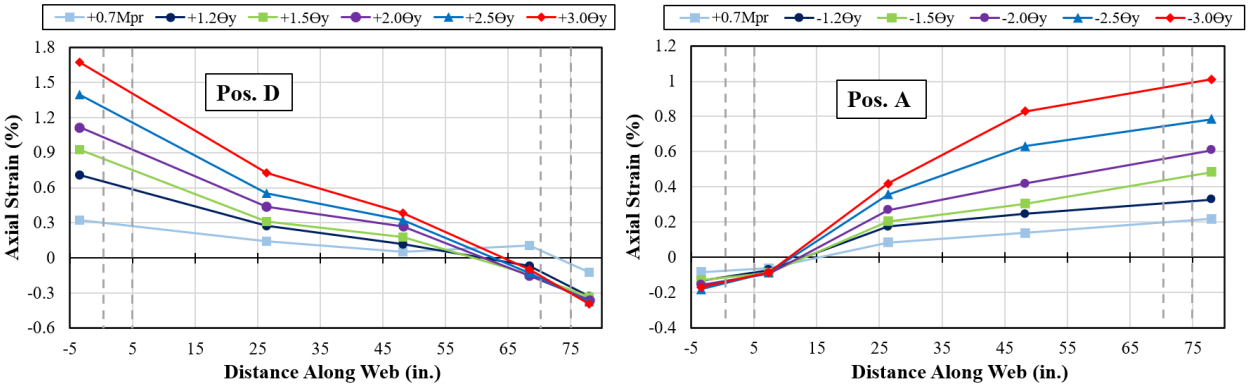

Figure 5-46: Axial strain profiles obtained from Layer 2 LVDTs (Group 1), CW-2

Figure 5-47 and Figure 5-48 show the axial strain profiles for CW-3 along the height of the east and the west flange edges, respectively, during the ramp-up loading of the WLP. Similar to CW-2, the highest tensile strains were measured at the Layer 3 LVDTs with values around 1.5% and 1.8% during the in-plane loading for the east (at Pos. A) and the west flange (at Pos. D), respectively. Application of the biaxial (IP + OOP) loading increased the Layer 3 tensile strains to 1.9% and 2.1% for the east (at Pos. C) and the west flange (at Pos. F), respectively. For the west flange edge, both Layer 1 (2-10 in.) and Layer 2 (10-20 in.) LVDTs had very small tensile strain values (around

0.1%), whereas, for the east flange edge, the Layer 2 LVDTs had higher tensile strain values, possibly due to the localized cracking at the end of the splices (L_s = 20 in.) that occurred inside the Layer 2 LVDTs anchor points.

The compressive strain demands measured at the east and west flange edges during the in-plane ramp-up loading were similar. The highest compressive strains during the in-plane loading were measured at Pos. D (-0.0041) within Layer 1 for the east flange, and at Pos. A (-0.0036) within Layer 2 for the west flange. The west flange Layer 1 LVDTs had slightly lower compressive strain demands (-0.0034) than Layer 2 LVDTs, possibly because of the higher negative OOP rotations observed at the west flange during the in-plane loading than the east flange (Figure 5-39a), i.e., higher negative OOP rotations observed during the in-plane loading decreased the compressive strain demands within Layer 1 (the same behavior was also observed for the east flange of CW-2). The application of the biaxial loading, after decreasing the axial load from $0.1A_g f'_c$ to $0.05A_g f'_c$, increased the maximum compressive strain demands at the flange edges to -0.0057 and -0.0046 for the east (at Pos. E) and the west (at Pos. B) flanges, respectively. Unlike CW-2, a gradual decrease was observed in the strain demands during the ramp-down loading (Figure H-3 and Figure H-4). However, although no significant damage was observed at the flange edges at the end of the WLP (Section 5.2.2), the higher compressive strain demands measured during the ramp-down loading (ranging from -0.005 to -0.0035, Figure H-3) resulted in concrete cover spalling and some minor core crushing at the base of the east flange edge.

Figure 5-49 shows the effects of biaxial loading and the variation of the axial load on the compression strains measured within Layer 1 and Layer 2 flange edge LVDTs by comparing the strains at different in-plane rotations during the ramp-up loading of the WLP. Similar to CW-2, at

lower inelastic in-plane hinge rotation demands, the biaxial load application increased the compressive strains at the flange edges by approximately a factor of 2.0. With increasing IP rotation demands, the OOP loading only increased compressive strain demands for the west and east flanges by factors of 1.3 and 1.4, respectively. For CW-3, additional LVDTs were used at Layers 1 and 2 at the flange-web corners (attached approximately 7 in. to the north of the corners, Figure 2-28). The compressive strains measured at these LVDTs were compared to those measured from the LVDTs attached to flange edges in Figure 5-51. The comparison shows that the compressive strains at the flange edges and the flange-web corners during the in-plane-only ramp-up loading of the WLP were similar to each other. In general, the corner compressive strains were slightly higher than those at the flange edges. The effect of OOP loading on the corner compressive strain is shown in Figure 5-50 by comparing the strains measured at Pos. A with the strains measured at Pos. C for the west flange and by comparing the strains measured at Pos. D with the strains measured at Pos. F for the east flange. Depending on the IP hinge rotation demands, the OOP loading increased the corner compressive strain demands from around 5% to 15%.

Figure 5-52 and Figure 5-53 show the axial strain profiles along the length of the wall by using either the Group 1 or Group 2 LVDTs (Figure 5-21). Similar to CW-2, for the Layer 1 LVDTs, since the tensile strains were very small in the splice region, a linear distribution of the strains was not observed. Unlike Layer 1, higher tensile strains were measured at Layer 2, which resulted in a more linear distribution. By assuming a neutral axis depth of 13 in. at the maximum IP hinge rotation demands, the compressive strains at the concrete surface can be estimated to be 0.91of the compressive strains measured at the west flange Layer 1 corner LVDTs, and 0.81 of the west flange edge LVDTs, i.e., the corner LVDT was 1.25 in. away from the concrete surface (13/(13+1.25)=0.91) and the flange edge LVDT was 3 in. away from the concrete surface

(13/(13+3)=0.81). Therefore, the maximum concrete compressive strains during in-plane loading at the west flange-web corner and west flange edge can be estimated as -0.0032 and -0.0028, respectively. Similarly, the LVDT attached east flange-web corner at Layer 1 was 2.25 in. away from the concrete surface and the one attached to the east flange edge was 4 in. away from the concrete surface; therefore, east flange concrete strains can be estimated as 0.85 (13/(13+2.25)=0.85) and 0.76 (13/(13+4)=0.76) of the Layer 1 LVDT strains. This resulted in compressive strains of -0.0036 and -0.0031 for Layer 1 at the east flange-web corner and east flange edge, respectively.

Although both the axial load and the IP rotation demands were the same for CW-2 and CW-3 during in-plane loading, i.e., $0.1A_g f'_c$ axial load and the IP hinge rotation demands given in Table 5-1, the compressive strain demands measured at the flange edges during the maximum IP rotation demands were significantly higher for CW-2 (-0.0068 at the west flange Layer 1 LVDT) than CW-3 (-0.0034 at the west flange Layer 1 LVDT). This difference occurred because more significant damage occurred at the flange edges during the OOP loading for CW-2, and the damage (i.e., cover spalling and core crushing) caused the compressive strains to increase significantly. This behavior can be seen by comparing Figure 5-44 with Figure 5-49; for CW-3 the slope of the IP rotation versus the compressive strain curve is more linear, whereas for CW-2 west flange edge Layer 1 LVDTs, after around -0.008 IP hinge rotation, a significant change in the slope was observed. This change occurred after concrete crushing initiated at the west flange edge.

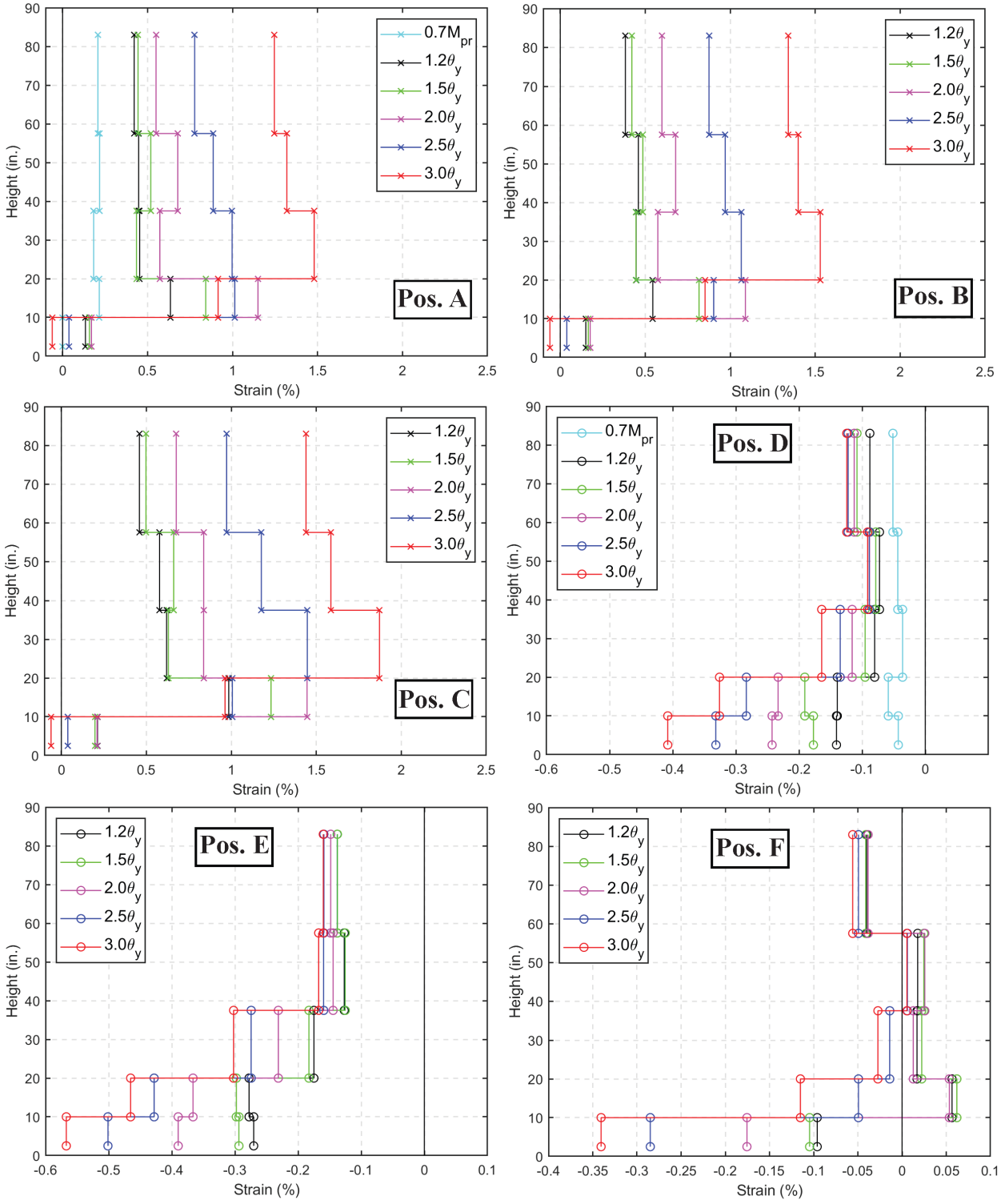

Figure 5-47: Axial strain profiles along the height of the edge of the East flange at different loading positions during the ramp-up loading of WLP, CW-3

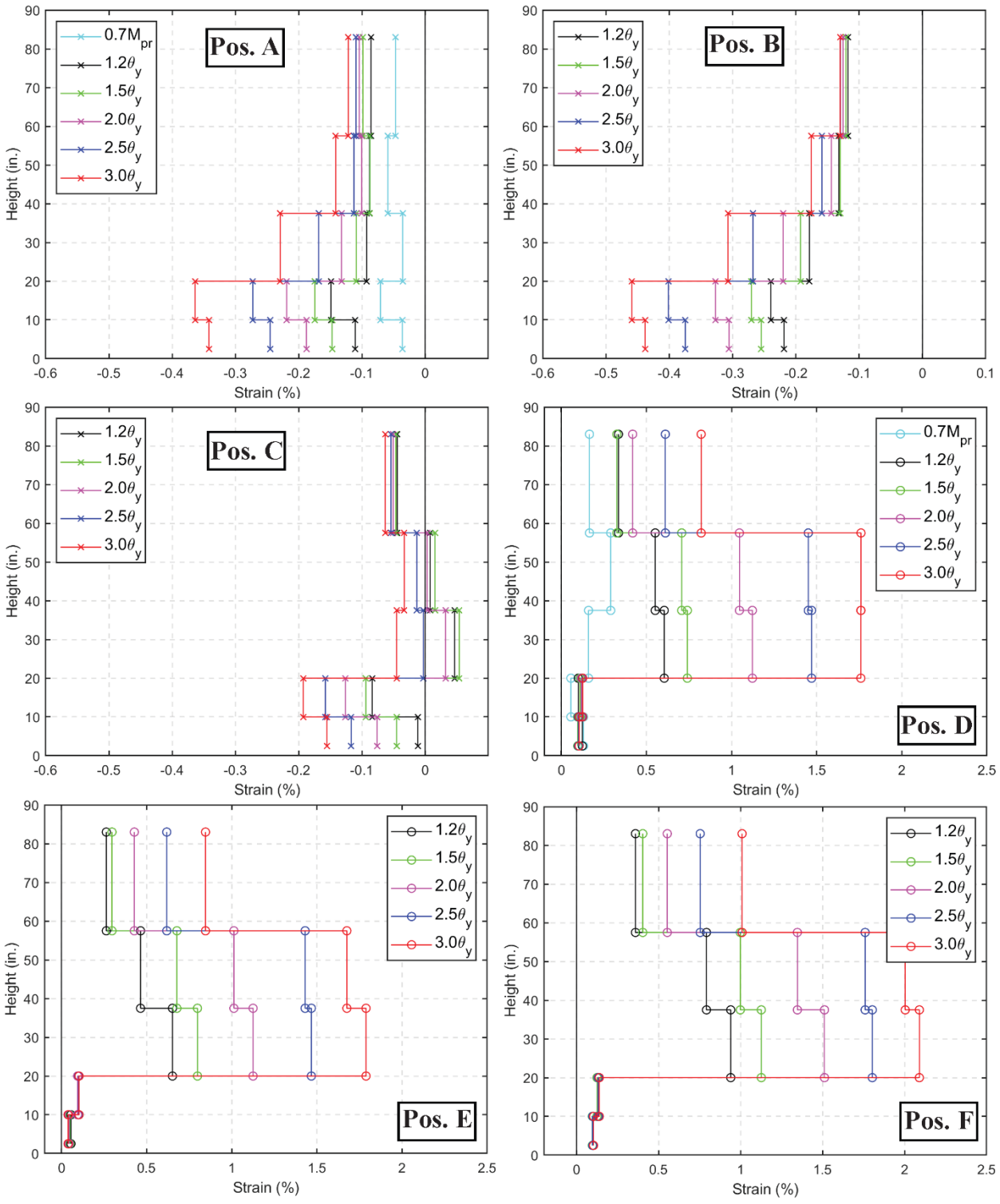

Figure 5-48: Axial strain profiles along the height of the edge of the West flange at different loading positions during the ramp-up loading of WLP, CW-3

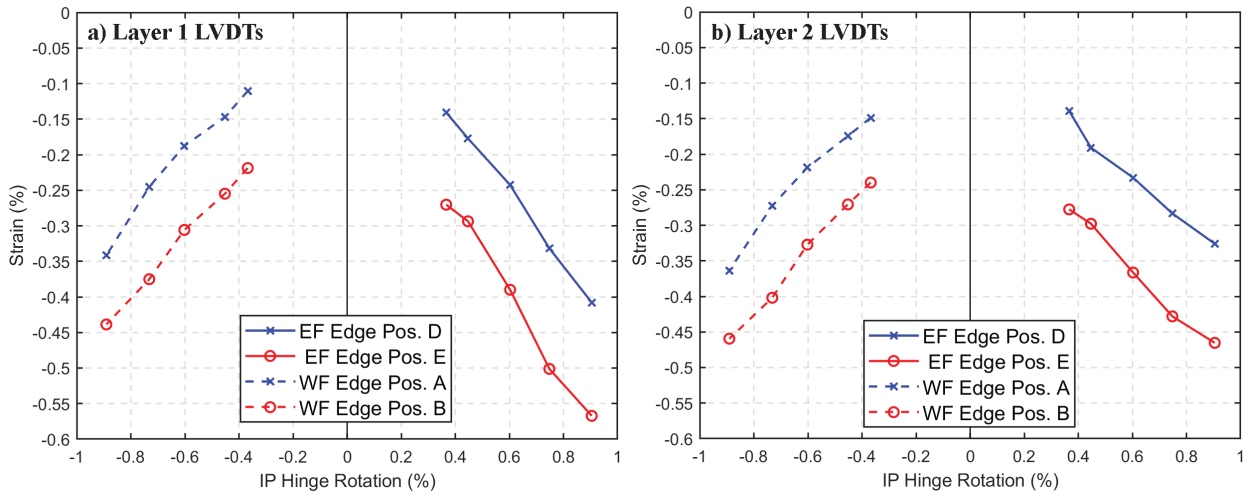

Figure 5-49: Comparison of compressive strains at different loading positions during the ramp-up loading of WLP for the first- and second-layer flange edge LVDTs, CW-3

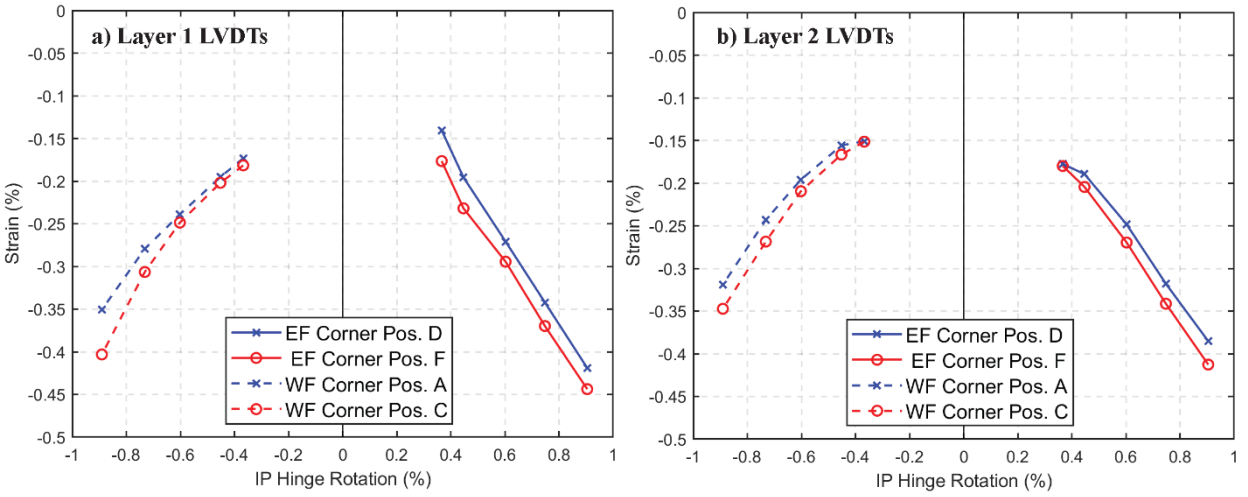

Figure 5-50: Comparison of compressive strains at different loading positions during the ramp-up loading of WLP for the first- and second-layer corner LVDTs, CW-3

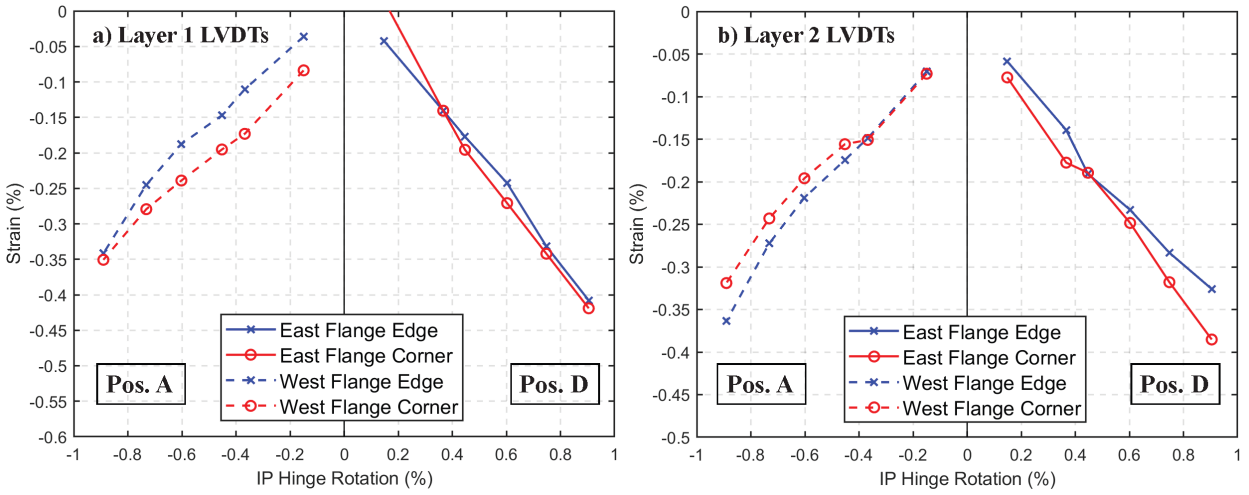

Figure 5-51: Comparison of compressive strains at the flange edges and corners during the ramp-up loading of WLP for the first- and second-layer LVDTs, CW-3

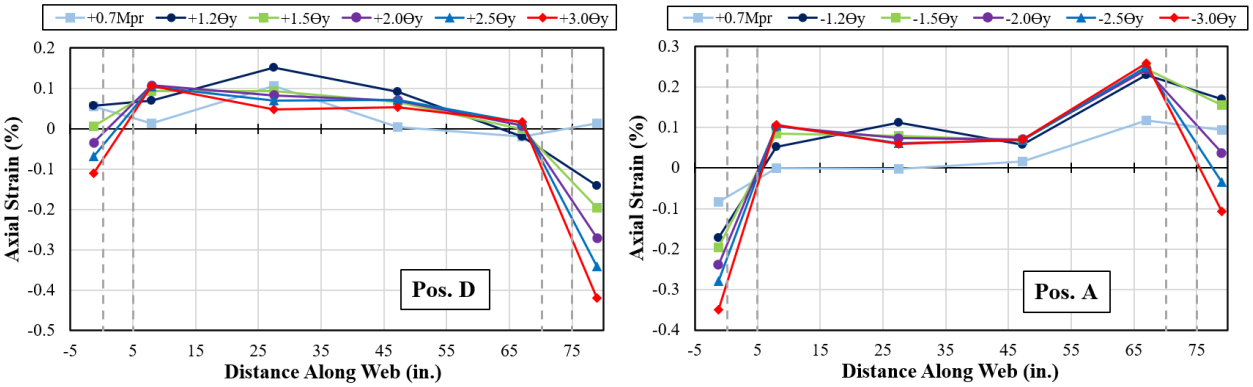

Figure 5-52: Axial strain profiles obtained from Layer 1 LVDTs (Group 2), CW-3

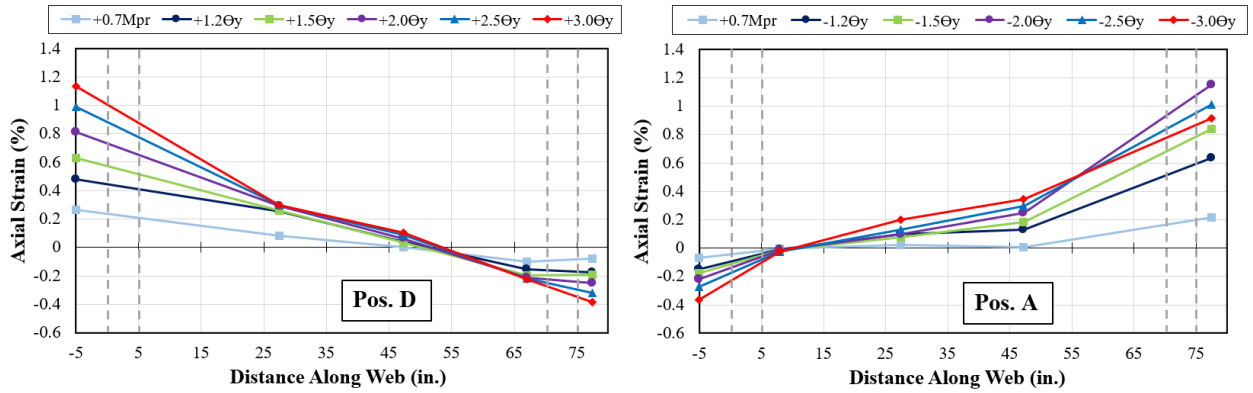

Figure 5-53: Axial strain profiles obtained from Layer 2 LVDTs (Group 2 at Pos. D and Group 1 at Pos. A), CW-3

Figures 5-54 and 5-55 show the axial strain profiles computed at the east and west flange edges of CW-4, respectively, during the ramp-up loading of the WLP. At the maximum in-plane hinge rotation demands, the highest tensile strains were around 0.025 and 0.019 at the Layer 4 east flange and Layer 3 west flange edge LVDTs, respectively. Applying OOP moment demands increased the tensile strains to 0.027 and 0.023, respectively, for the east and west flanges. For CW-4, the tensile strain demands at the splice region LVDTs (Layers 1 and 2) were very small (around 0.001 to 0.002).

The maximum compressive strain demands during the ramp-up loading at Pos. A and at Pos. D were -0.0036 and -00031 for the Layer 1 west and east flange edge LVDTs, respectively. Applying the OOP bending moments after decreasing the axial load to $0.075A_g f'_c$ resulted in compressive strains of -0.0057 and -0.0045 for the west flange (at Pos. B) and the east flange (at Pos. E). The higher compressive strain demands measured at the west flange edge Layer 1 LVDT were consistent with the greater level of damage observed at the base of the west flange edge compared to the east flange edge (Figure 5-13). During ramp-down loading, the compressive strain demands remained at approximately -0.003 to -0.0025 at Pos. D for the east flange (Figure H-5), whereas for the west flange edge, the values decreased to -0.001 gradually (Figure H-6) at the 1.2Θy hinge rotation load step. The higher compressive strain demands measured at the east flange edge LVDTs during the ramp-down loading compared to the west flange edge LVDTs were consistent with the greater level of damage observed at the east flange edge during the ramp-down loading (Figure 5-15).

Figure 5-56 shows the effect of OOP loading on the compressive strains measured both at the flange edges and flange-web corners using the Layers 1, 2, and 3 LVDTs. For all three layers, an

increase in compressive strains ranging by factors of 1.5 to 2.0 was observed at the flange edge (the same behavior was observed for CW-2 and CW-3). However, for the flange-web corner LVDTs, OOP loading did not result in much higher compressive strains; for Layer 1 and Layer 2 LVDTs, the strain values were almost the same for both of the flanges, whereas for Layer 3, approximately 15% increase in compressive strains was observed. The flange edge and flange-web corner compressive strains were compared in Figure 5-57 during in-plane-only ramp-up loading (Pos. A and D). The compressive strains were higher at the flange-web corners for all three layers; with values of -0.0046 and -0.0051 for the west and east flange-web corners (Layer 1), respectively. The higher compressive strains measured at the flange-web corners during the ramp-up loading were consistent with the observation that damage occurred earlier in the WLP at the flange-web corners than at the flange edges. At Layer 2 flange-web corner LVDTs, compressive strains of -0.0043 and -0.0036 were observed at the west and east flange corners, respectively. The higher compressive strain demands measured at the west flange Layer 2 LVDTs relative to the east flange Layer 2 LVDTs were consistent with the greater extent of concrete spalling at the west flange corner (up to 22 in. above the footing) relative to the east flange corner (up to 7 in. above the footing, Figure 5-14). Figure 5-57d shows a comparison of the tensile strains at Layer 3 flange edge and flange-web corner LVDTs; for the west flange, the tensile strains were similar. However, for the east flange, the tensile strains at the flange-web corners were more than twice the values determined from flange edge LVDT.

Figures 5-58, 5-59, and 5-60 show axial strain profiles along the length of the wall determined using the Group 2 LVDTs (Figure 5-21). Similar to CW-2 and CW-3, instead of using the strain distributions given in these figures, a neutral axis depth of 13 in. was assumed to estimate the concrete strains at the flange edges and flange-web corners. The corner LVDTs were approximately

1.25 in. and 1.0 in. away from the concrete surface for the west and the east flange Layer 1 corner LVDTs, respectively. Therefore, the concrete strain can be estimated as 0.91 and 0.93 of the values for the Layer 1 west and east flange-web corner LVDT strains, which resulted in strain value of -0.0042 and -0.0047, respectively. The flange edge LVDTs were approximately 3.5 in. and 2.75 in. away from the concrete surface for the west and the east flange edges, respectively. Therefore, the concrete strain can be estimated as 0.79 and 0.83 of the Layer 1 west and east flange edge LVDT strains, which resulted in strain values of -0.0028 and -0.0026, respectively.

These values given above were comparable to the ones estimated for CW-3 (-0.0028 and -0.0031, respectively). Therefore, it can be concluded that for the walls that did not sustain significant damage during the WLP (i.e., CW-3 and CW-4), the maximum compressive strains measured at the base of the flange edges were around -0.003 during the in-plane loading ($P = 0.1A_g f'_c$). The approach used to estimate the compressive strains at the concrete surfaces under in-plane-only loading was also used for biaxial loading. The actual biaxial neutral axis depth that occurred during the experiments was not calculated, the values used are shown on Figure 2-9 and Figure 2-10, i.e., c_b=15.1 in. for CW-3 and c_b=18.9 in. for CW-4. These values were calculated using the commercial software CSICol under monotonic biaxial loading, and it should be noted here that the actual values would be different during the experiments because of the cyclic loading and some damage that occurred at the flange edges. Nevertheless, when the c_b values of 15.1 in. and 18.9 in. were used, the concrete strains were estimated to be around 0.80 of the LVDT strains, which resulted in maximum compressive strains of -0.0043 for CW-3 ($P = 0.05A_g f'_c$ at Pos. E) and -0.0047 for CW-4 ($P = 0.075A_g f'_c$ at Pos. B).

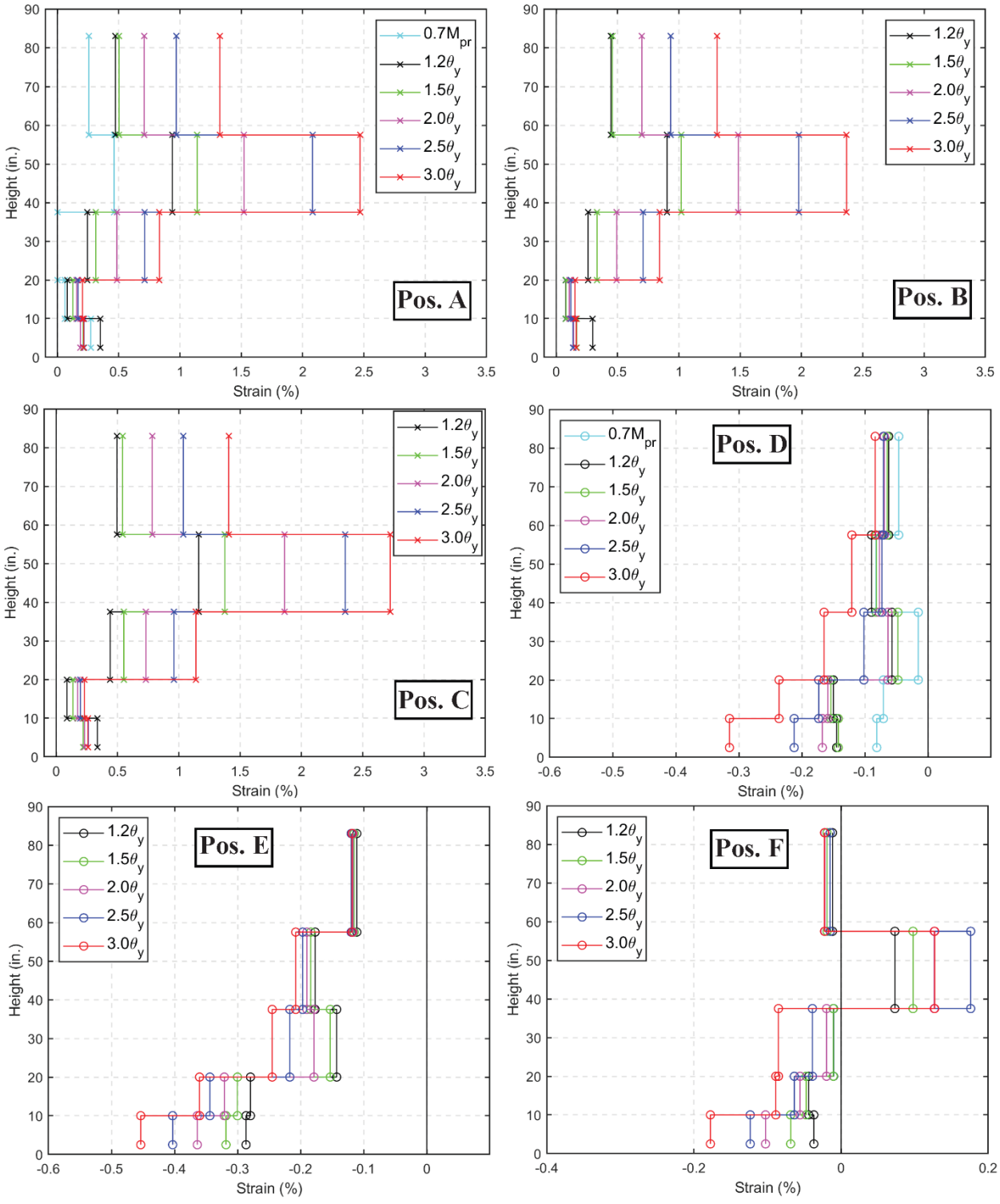

Figure 5-54: Axial strain profiles along the height of the edge of the East flange at different loading positions during the ramp-up loading of WLP, CW-4

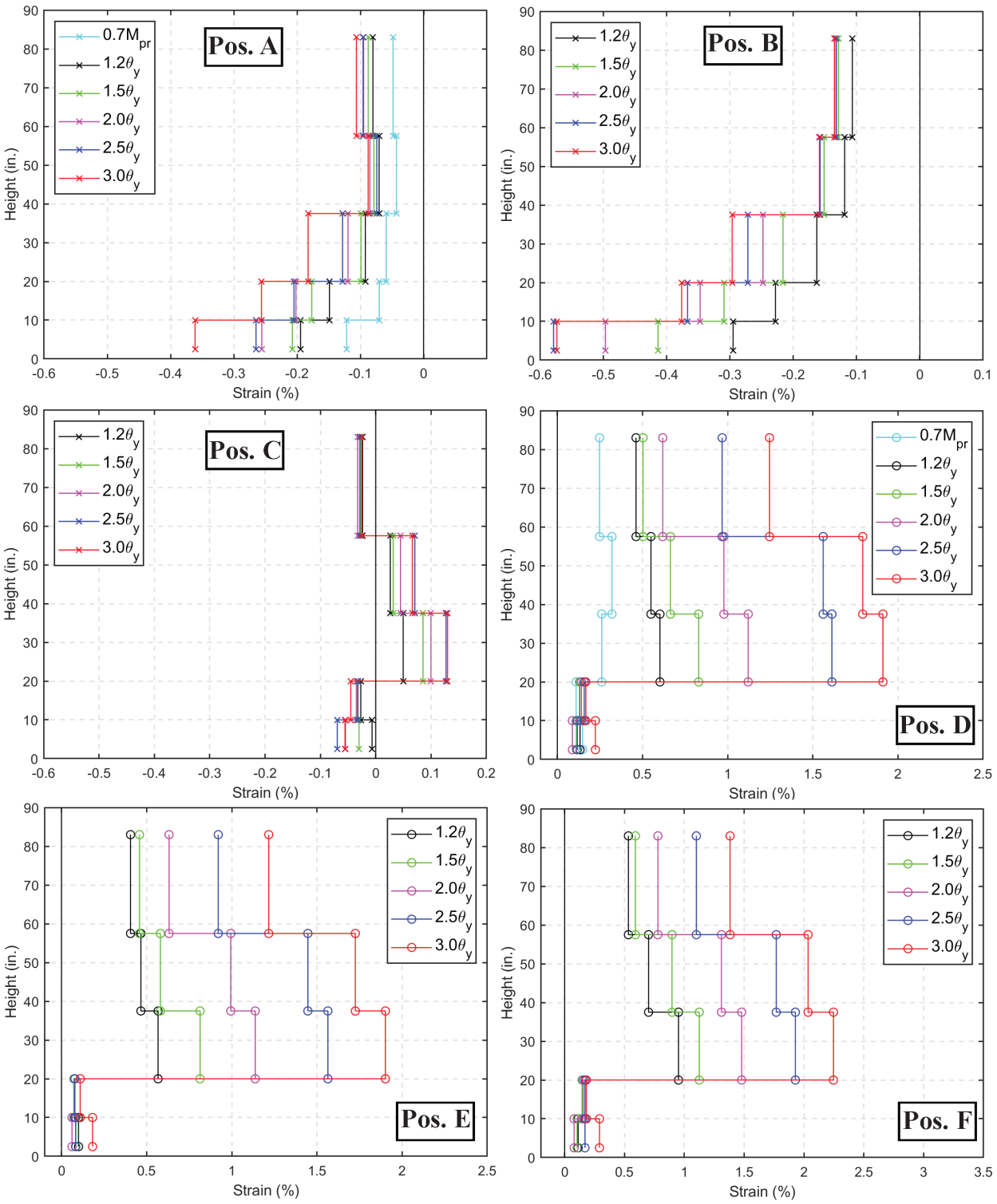

Figure 5-55: Axial strain profiles along the height of the edge of the West flange at different loading positions during the ramp-up loading of WLP, CW-4

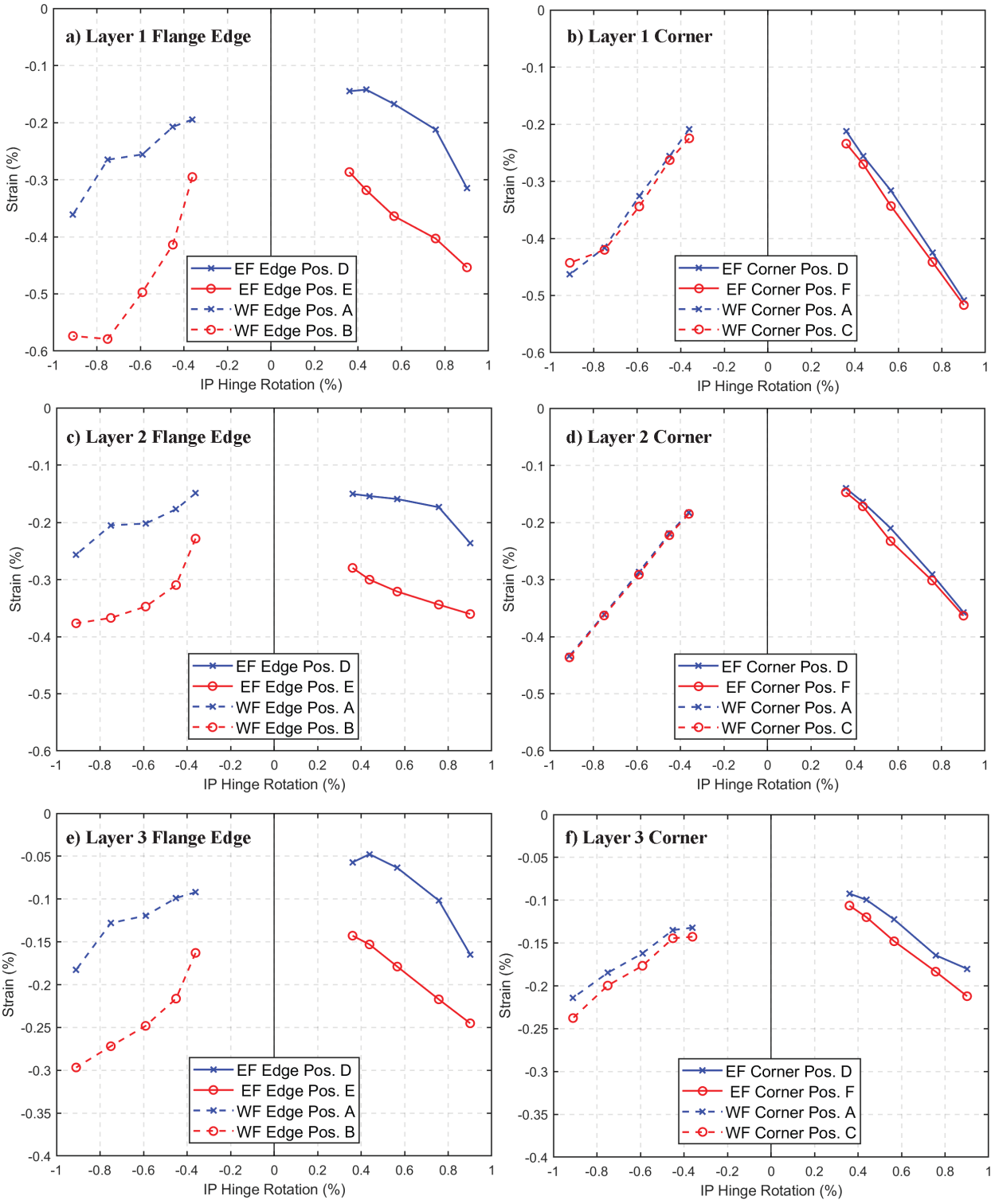

Figure 5-56: Comparison of compressive strains at different loading positions during the ramp-up loading of WLP, CW-4

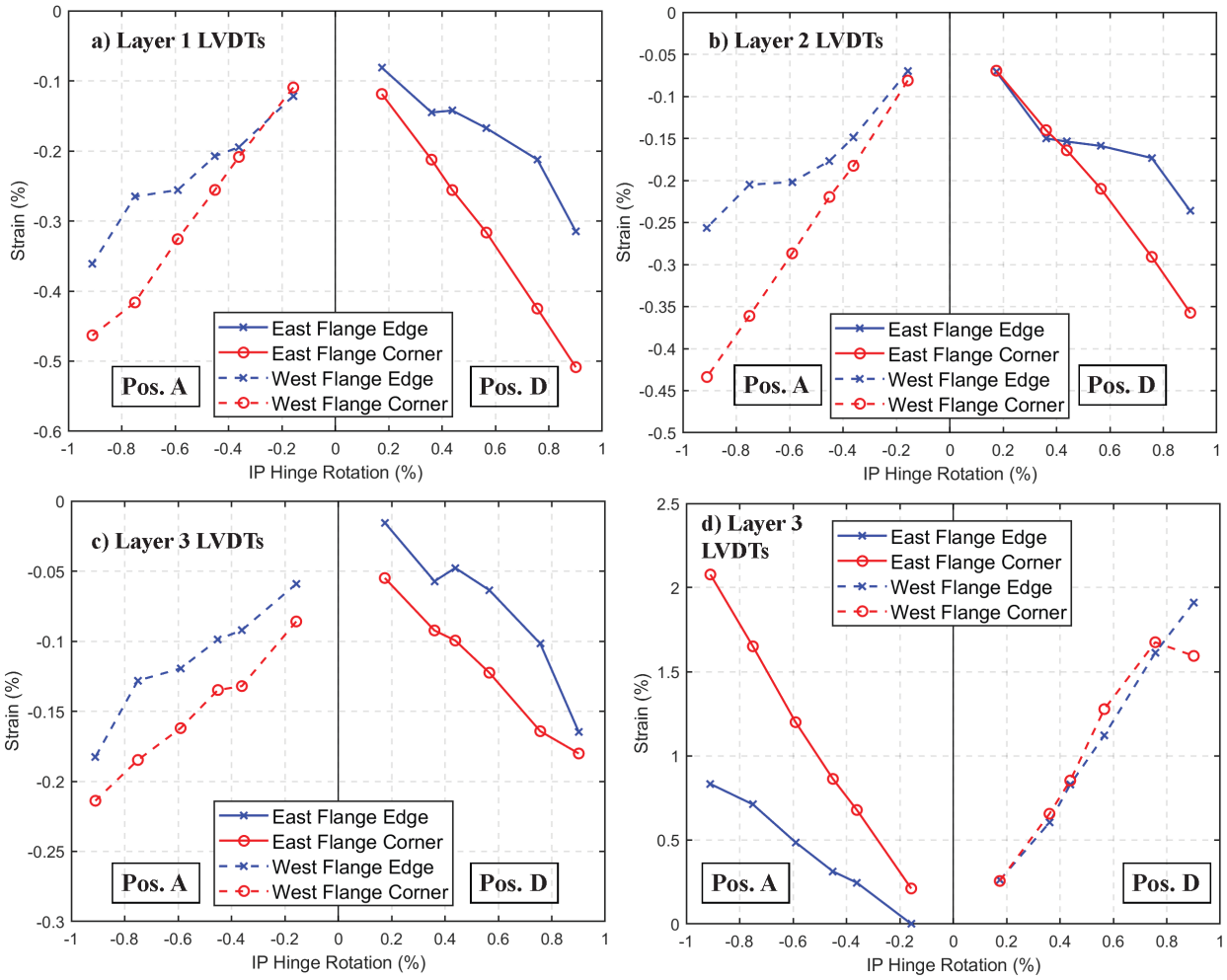

Figure 5-57: Comparison of strains at the flange edges and flange-web corners during the ramp-up loading of WLP, CW-4

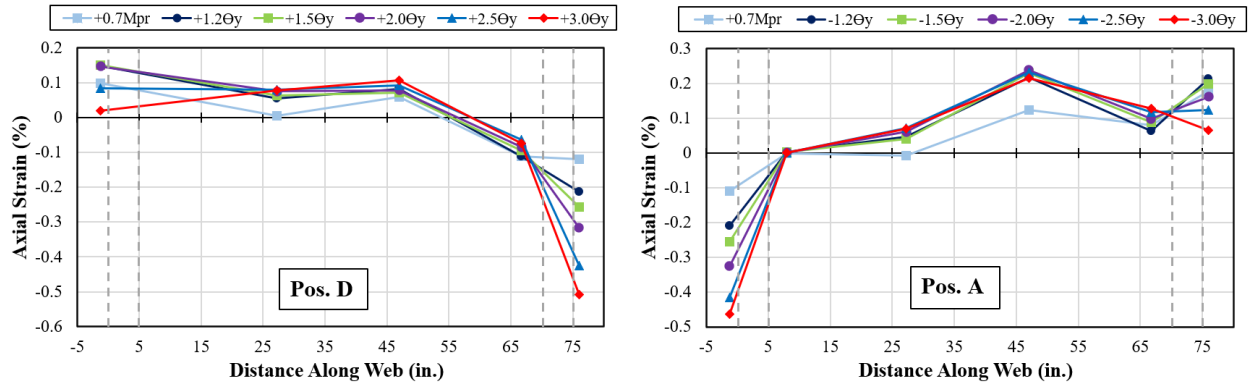

Figure 5-58: Axial strain profiles obtained from Layer 1 LVDTs (Group 2), CW-4

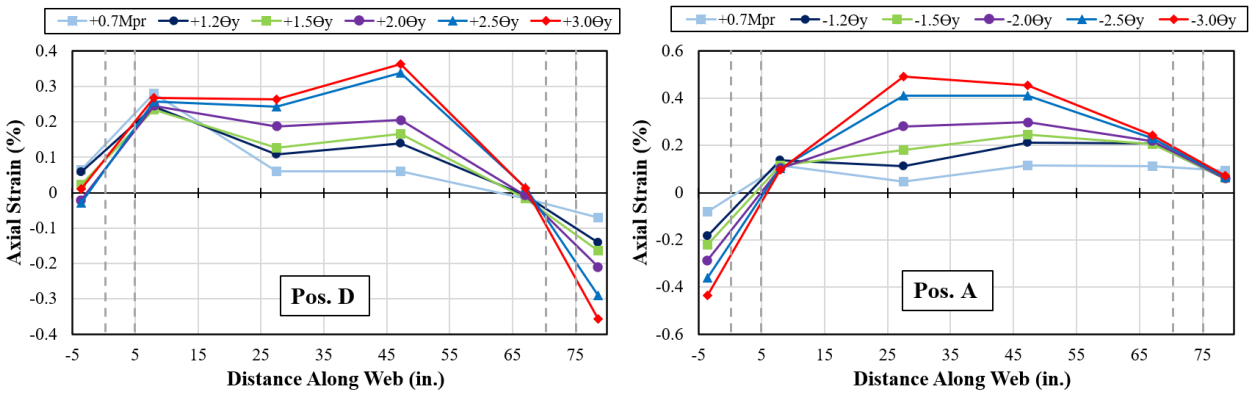

Figure 5-59: Axial strain profiles obtained from Layer 2 LVDTs (Group 2), CW-4

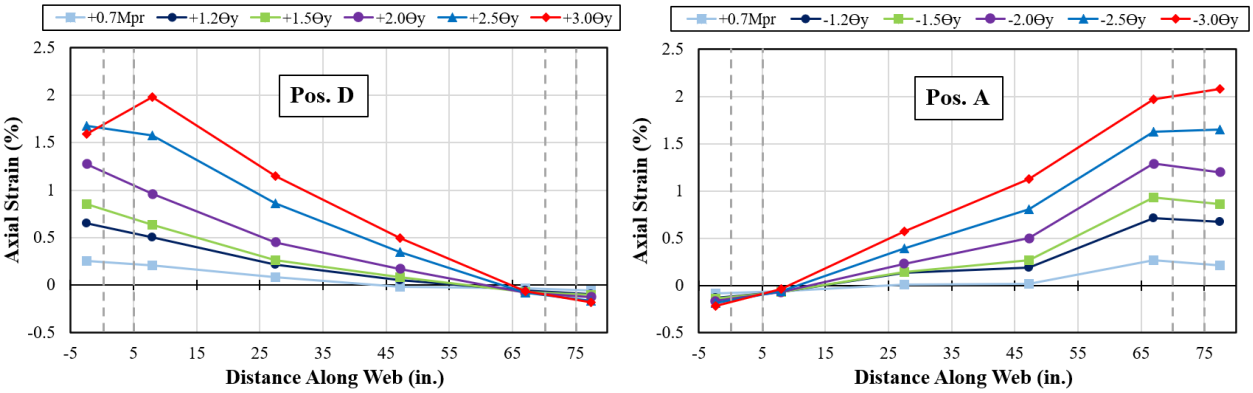

Figure 5-60: Axial strain profiles obtained from Layer 3 LVDTs (Group 2), CW-4

5.4 Lateral Stiffness

The effective flexural stiffness values (EI_{eff}) of the specimens were calculated using Equations 3.5 and 3.6 based on the free-body diagram shown in Figure 3-25 using the average rotations measured over the plastic hinge length ($L_p=l_w/2$). Similar to CW-1, two sets of calculations were done: 1) including the rotations due to the slip/extension deformations that occurred at the wall-footing interface, and 2) neglecting the slip/extension rotation, which was calculated using the LVDTs attached at the interface, at the four corners of the specimens. Figure 5-61 shows the EI_{eff} values normalized with the E_cI_g, where E_c was calculated using the ACI 318-19 provisions (Equation 2.8)

for CW-2, CW-3, and CW-4. When the rotations due to slip/extension deformations were included in the calculations, the effective flexural stiffness values at cracking were $0.59E_cI_g$ and $0.68E_cI_g$ for CW-2, $0.47E_cI_g$ and $0.60E_cI_g$ for CW-3, and $0.80E_cI_g$ and $0.72E_cI_g$ for CW-4 for positive and negative IP loading, respectively. Stiffness values, calculated at first yield of the outer layer flange longitudinal reinforcement ($\approx 0.7M_{pr,IN}$), were determined to be $0.24E_cI_g$ and $0.24E_cI_g$ for CW-2, $0.31E_cI_g$ and $0.31E_cI_g$ for CW-3, and $0.29E_cI_g$ and $0.32E_cI_g$ for CW-4 in the positive and negative IP loading, respectively. The normalized effective flexural stiffness values of the walls calculated, including the slip/extension deformations, were also plotted together in Figure 5-61. When the slip/extension deformations were excluded from the calculations, EI_{eff} values at the first yield increased to $0.41E_cI_g$ and $0.33E_cI_g$ for CW-2, $0.44E_cI_g$ and $0.43E_cI_g$ for CW-3, and $0.49E_cI_g$ and $0.57E_cI_g$ for CW-4 in the positive and negative IP loading, respectively.

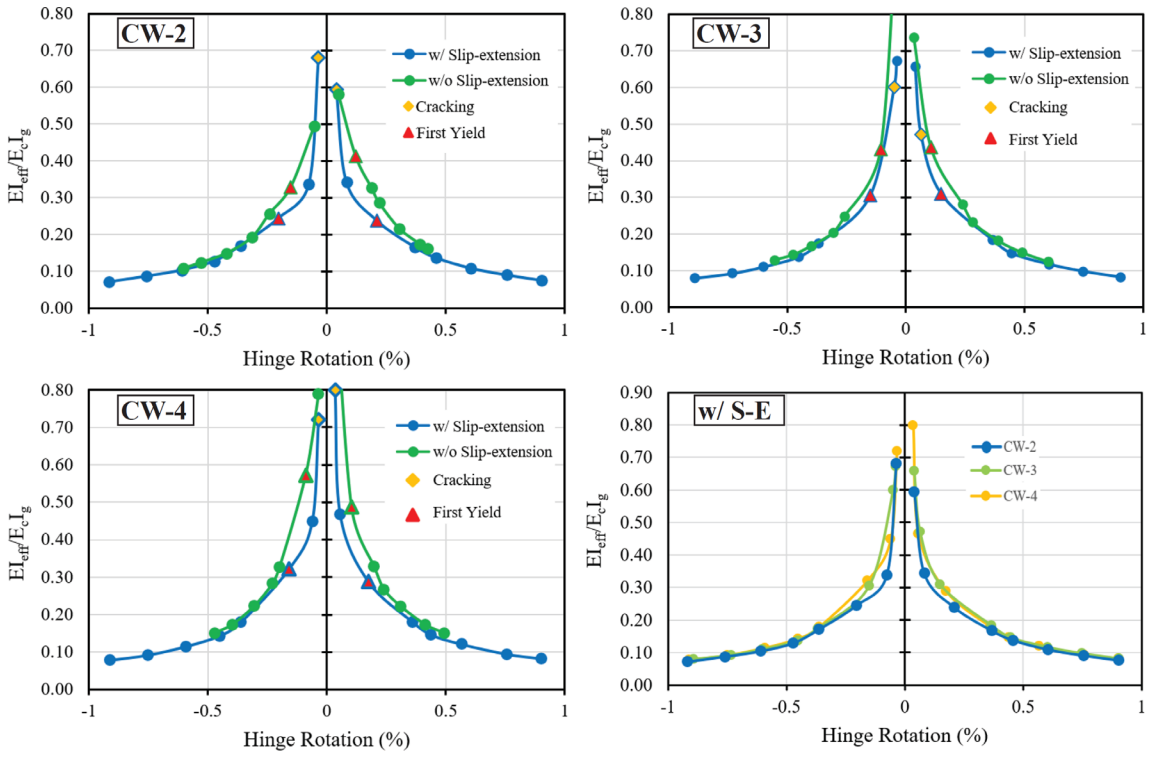

Figure 5-61: Normalized effective flexural stiffnesses (EI_{eff}/E_cI_g)

5.5 Vertical Growth

Vertical growth at the top of the walls was calculated using the column of LVDTs attached to the east and west flange edges of the specimens (Figure 2-25) are shown in Figures 5-62, 5-63, and 5-64 for CW-2, CW-3, and CW-4, respectively. The maximum vertical growth was measured was around 0.5 in. and 0.62 in. for both CW-2 and CW-3 for IP and IP + OOP loading, respectively, at the maximum hinge rotation demands (±0.9%). For CW-4, the vertical growth was higher than CW-2 and CW-3, which was consistent with the observation that higher drift ratios were reached for CW-4 under the same hinge rotation demands (Table 5-3). At maximum in-plane hinge rotation demands, the maximum vertical growth for CW-4 was around 0.6 in., and it increased to 0.72 in. and 0.79 in. for positive and negative IP loading, respectively, after applying the negative OOP moment demands.

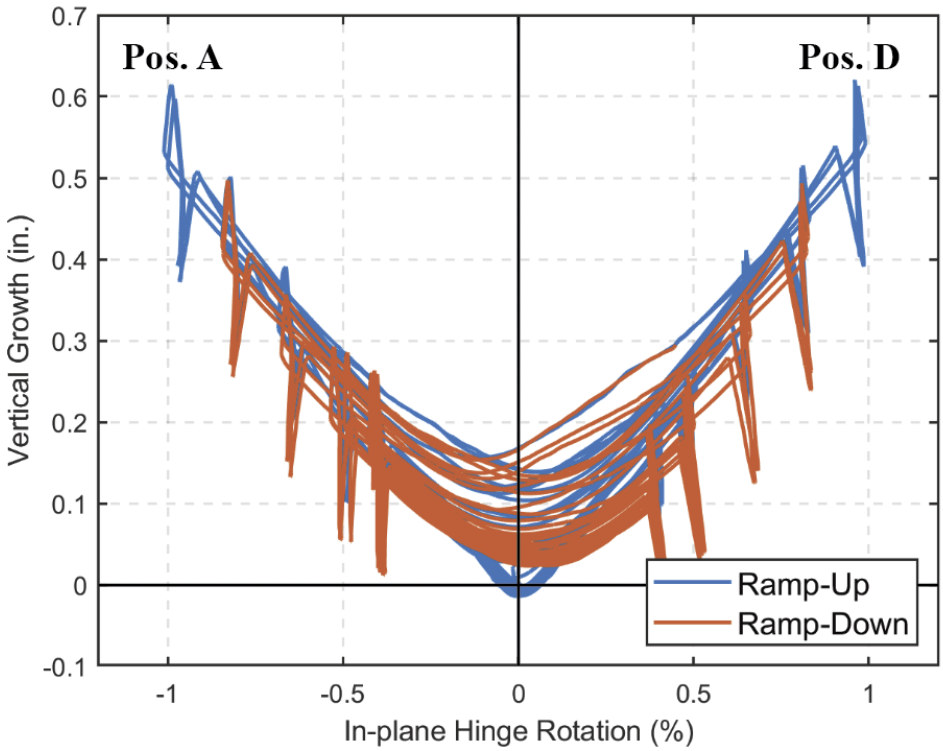

Figure 5-62: IP hinge rotation-vertical growth response of CW-2 during the WLP

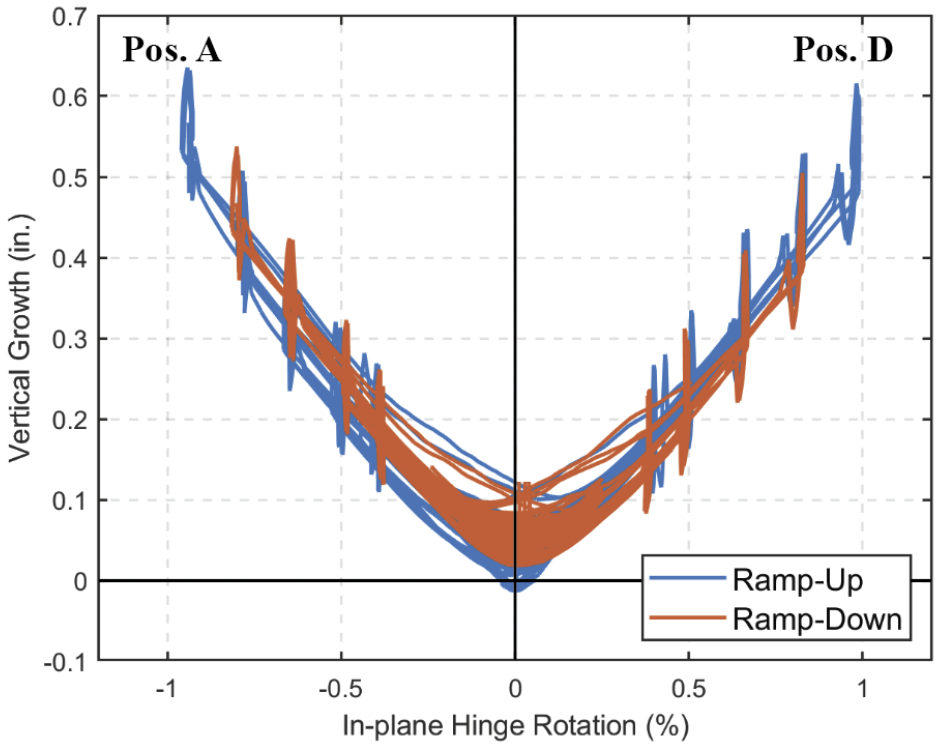

Figure 5-63: IP hinge rotation-vertical growth response of CW-3 during the WLP

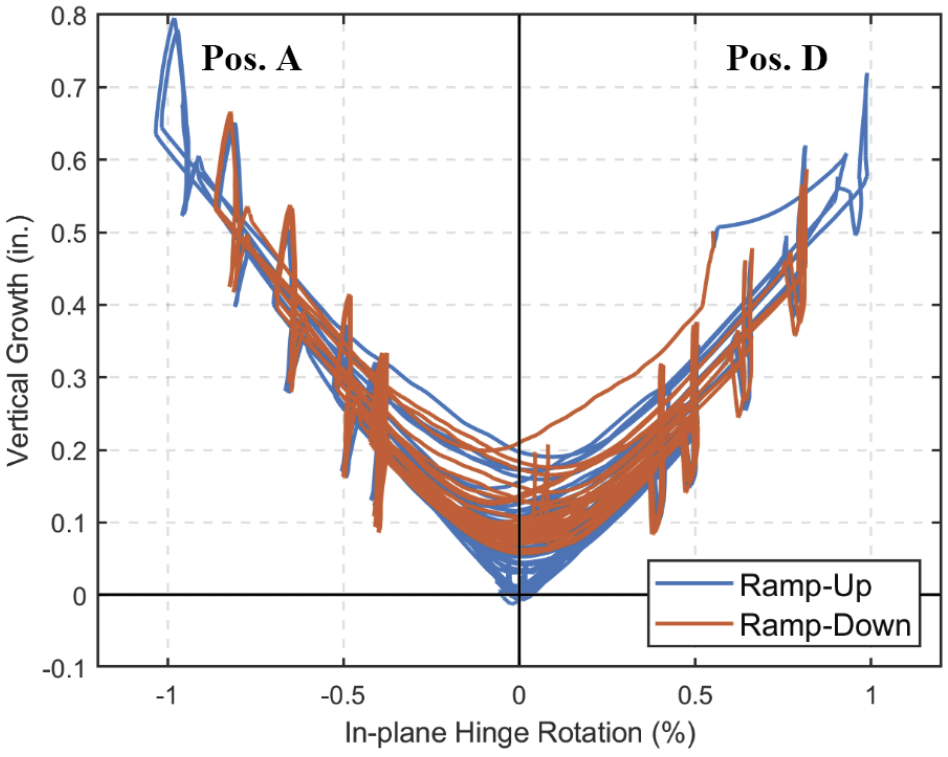

Figure 5-64: IP hinge rotation-vertical growth response of CW-4 during the WLP

5.6 Impact of Lap Splices

Lower curvature values (Section 5.3.2) were calculated within the splice regions (L_s=20 in.) because lower tensile strains were recorded in these regions (see Layers 1 and 2, Section 5.3.5). The spliced longitudinal reinforcement strengthened/stiffened the splice region such that inelastic curvatures were concentrated above the splice region. Therefore, the assumed plastic hinge length was extended by the length of the splices, i.e., $L_p = l_w/2 + L_s$ = 37.5 in. + 20 in. = 57.5 in. The rotations over the modified hinge length were calculated by using the LVDTs attached to Layer 4 (37.5-57.5 in.) at the edges of the flanges along with the control sensors used for the hinge rotation calculations. The calculated values are given in Table 5-4 for all three walls at different load steps for the ramp-up and ramp-down loading of the WLP. The base moment-hinge rotation responses are plotted in Figures 5-65, 5-66, and 5-67 for CW-2, CW-3, and CW-4, respectively, and compared with the base moment-hinge rotation responses calculated with $L_p = l_w/2$. The rotation ductility values shown in these figures were calculated based on the calculated effective yield hinge rotation values of 0.34% for CW-2 and 0.28% for CW-3 and CW-4 (the details are given in Appendix F). The analytical predictions were also plotted in these figures, and they matched the experimental results well. For the analytical predictions, the splices were not considered; therefore, the longer hinge region resulted in higher rotation values than the experimental ones. However, since the slip/extension deformations increased the hinge rotation in the experiment, the analytical predictions and the experimental results matched well.

The extended hinge region increased the maximum rotation demands to +1.26% from +0.90% (40% increase) for CW-2 and CW-3 and to +1.35% (50% increase) for CW-4 in the positive direction. The maximum hinge rotation demands in the negative direction increased to -1.31% (45% increase), -1.10% (22% increase), and -1.38% (53% increase) for CW-2, CW-3, and CW-4,

respectively. The comparison of the extended hinge rotation responses of the walls during the ramp-up loading of the WLP (Figure 5-68) shows that the responses were very similar in the positive direction. However, some variations were observed in the negative direction (the west flange was under compression), i.e., CW-4 had the highest, and CW-3 had the lowest hinge rotations at the maximum demands, possibly due to the greater level of damage that was observed above the wall-foundation interface at the west flange edge for CW-4 and the lack of observed damage at the west flange edge for CW-3.

The rotation ductility values (μ_Θ) calculated using the extended hinge region were similar to the displacement ductility values (μ_Δ, Figure 5-28) calculated at the top of the wall. At the maximum rotation or displacement demands, μ_Θ values of 3.7, 4.5, and 4.8 were computed for positive in-plane loading, and values of 3.8, 3.9, and 4.9 were computed for negative in-plane loading direction. Whereas μ_Δ values of 4.0, 4.1, and 4.8 were computed for positive in-plane loading, and 4.4, 3.8, and 5.2 were computed for negative in-plane loading for CW-2, CW-3, and CW-4, respectively. These values were summarized in Table 5-5.

Table 5-4: In-plane hinge rotation demands calculated with $L_p=l_w/2+L_s$

Load Step		Hinge rotation, $L_p=l_w/2$ $\Theta_{Lp,IP}$ (%)	Hinge rotation, $L_p=l_w/2+L_s$ (%)		
		CW-2-3-4	CW-2	CW-3	CW-4
Pos. Dir (Pos. D)	$0.4M_{pr}$	+0.05	+0.09	+0.05	+0.05
	$0.7M_{pr}$	+0.16	+0.30	+0.19	+0.23
	$1.2\Theta_y$	+0.36	+0.52	+0.47	+0.47
	$1.5\Theta_y$	+0.45	+0.60	+0.58	+0.60
	$2.0\Theta_y$	+0.60	+0.84	+0.80	+0.85
	$2.5\Theta_y$	+0.75	+1.05	+1.05	+1.10
	$3.0\Theta_y$	+0.90	+1.26	+1.26	+1.35
Neg. Dir (Pos. A)	$0.4M_{pr}$	-0.06	-0.09	-0.06	-0.07
	$0.7M_{pr}$	-0.16	-0.30	-0.19	-0.26
	$1.2\Theta_y$	-0.36	-0.54	-0.45	-0.56
	$1.5\Theta_y$	-0.45	-0.65	-0.53	-0.69
	$2.0\Theta_y$	-0.60	-0.85	-0.68	-0.88
	$2.5\Theta_y$	-0.75	-1.07	-0.89	-1.15
	$3.0\Theta_y$	-0.90	-1.31	-1.10	-1.38

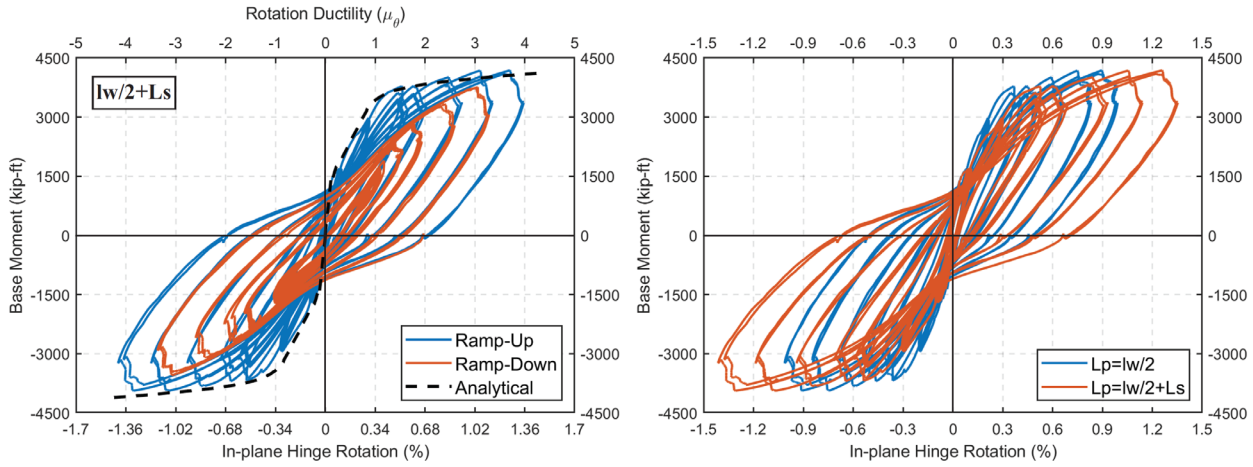

Figure 5-65: IP Base moment-hinge rotation (L_p=l_w/2+L_s) response of CW-2 during the WLP

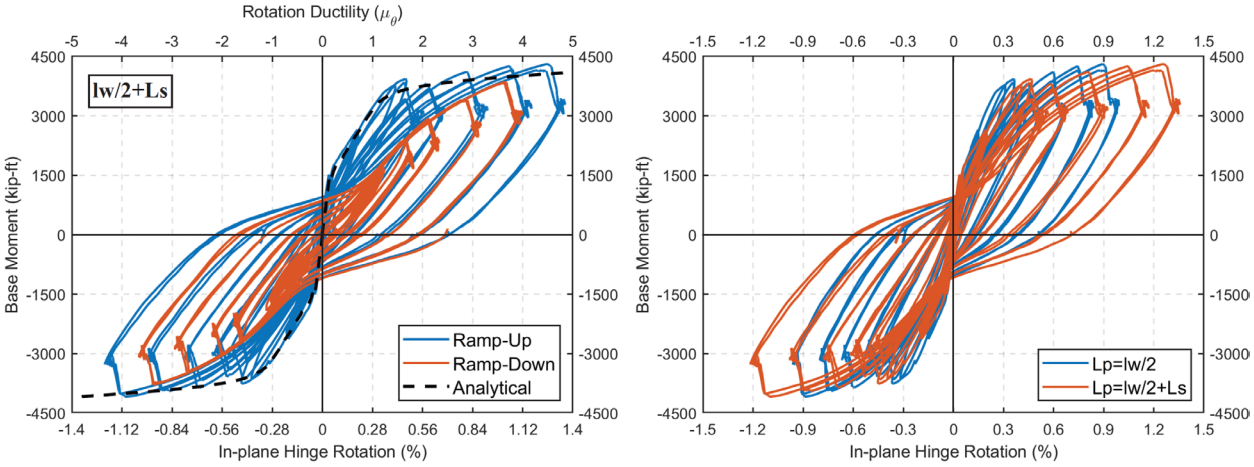

Figure 5-66: IP Base moment-hinge rotation (L_p=l_w/2+L_s) response of CW-3 during the WLP

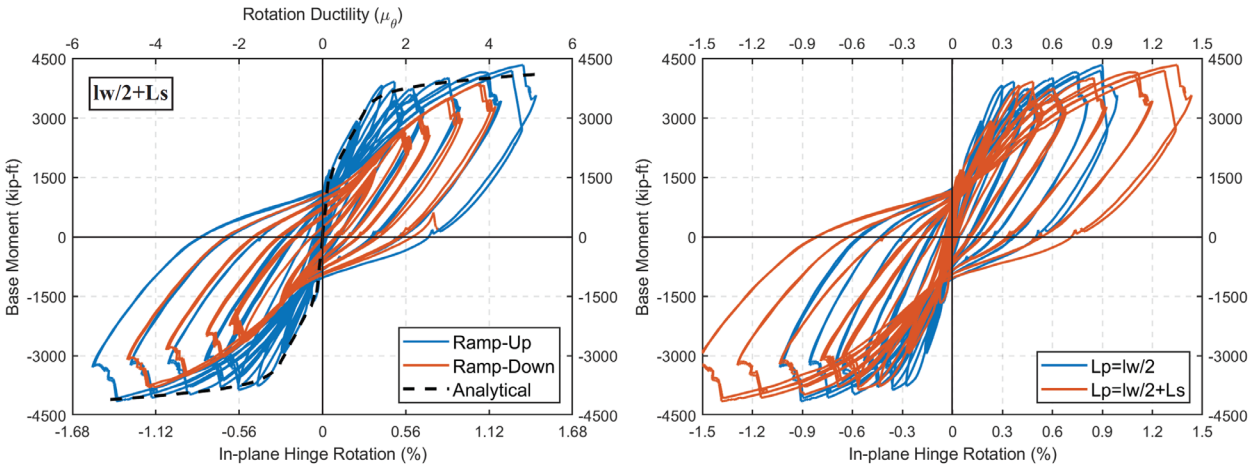

Figure 5-67: IP Base moment-hinge rotation (L_p=l_w/2+L_s) response of CW-4 during the WLP

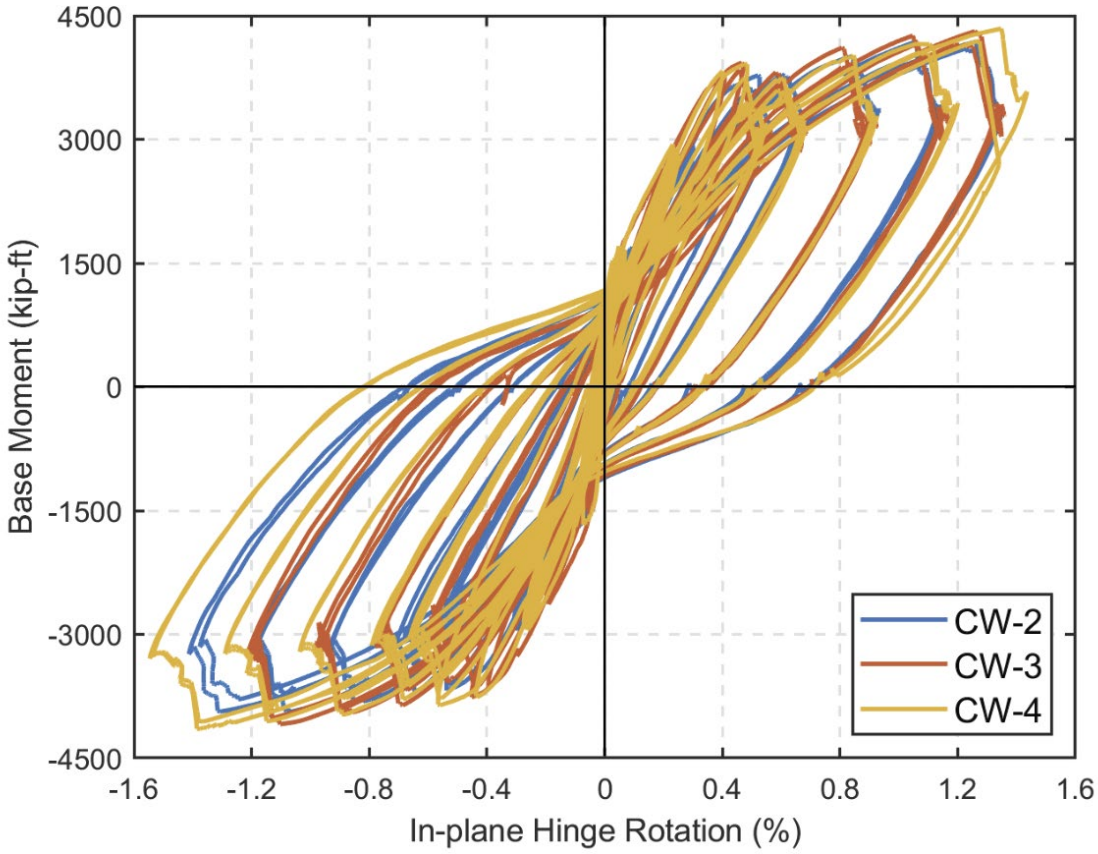

Figure 5-68: Comparison of IP base moment-hinge rotation (L_p=l_w/2+L_s) responses during the ramp-up loading of WLP

Table 5-5: Comparison of rotation and displacement ductilities at the maximum demands of WLP

Wall	Load Step	Rotation ductility ($L_p=l_w/2$)	Rotation ductility ($L_p=l_w/2+L_s$)	Displacement ductility (at the top of the wall)
CW-2	$+3.0\Theta_y$	3.6	3.7	4.0
	$-3.0\Theta_y$	3.6	3.8	4.4
CW-3	$+3.0\Theta_y$	3.6	4.5	4.1
	$-3.0\Theta_y$	3.6	3.9	3.8
CW-4	$+3.0\Theta_y$	3.6	4.8	4.8
	$-3.0\Theta_y$	3.6	4.9	5.2

5.7 Summary of Wind Test Results

The tests conducted on the specimens with the higher longitudinal reinforcement ratio (ρ_l=1.5%) highlighted the importance of the level of axial load applied during biaxial loading and the amount of confinement provided at the flange edges. Since the highest level of axial load was applied to CW-2 ($0.10A_g f'_c$) when the flange edges were under compression and the least amount of confinement was provided, more significant damage (concrete crushing, longitudinal reinforcement buckling) was observed that produced greater strength loss in the out-of-plane direction (0.66 times the peak moment demand). Less damage was observed for CW-3 and CW-4 relative to CW-2 (for similar loading history), with CW-3 displaying the least amount of damage (less cover spalling and no observed longitudinal rebar buckling) than was observed for CW-4 ($0.075A_g f'_c$) due to the lower axial load during OOP loading ($0.05A_g f'_c$). The ramp-down loading affected all the walls similarly and produced additional damage (i.e., concrete spalling, concrete crushing, and rebar buckling).

The in-plane base moment-hinge rotation responses were very similar for all walls. No strength loss was observed for CW-3 and CW-4, whereas approximately 12% strength loss was observed for CW-2 during the inelastic ramp-down cycles. The out-of-plane base moment-hinge rotation responses, on the other hand, were different, especially in the +y direction (when flange edges were under compression). While stiffness degradation and strength loss (0.66 times the peak moment demand) were observed for CW-2 in the +y direction, only stiffness degradation was observed for CW-4. No strength loss or stiffness degradation was observed for CW-3 in the +y direction. When the flange-web corners were under compression (-y direction), all specimens showed stiffness degradation. Since the plastic hinge rotations were controlled during testing,

different drift ratios (calculated at the top of the walls) were measured with maximum values of 1.75%, 1.64%, and 2.10% for CW-2, CW-3, and CW-4 at the peak moment demands.

The average effective stiffness values of CW-2, CW-3, and CW-4 at first yield were calculated as $0.28E_cI_g$ and $0.32E_cI_g$ for E_c based on ACI 318-19 (Equation 2.8) and ACI 363R-10 provisions (Equation 2.9), respectively. The effective stiffness values of the test specimens were also calculated using the ACI 369.1-22 (2022) provisions which are based on using a large wall database (Abdullah, 2019). Based on the axial load ratio applied to the specimens ($0.1A_gf'_c$), the ACI 369.1-22 proposed effective stiffness value was found to be $0.29E_cI_g$ if E_c was based on ACI 363R-10. The experimental stiffness values were higher than the proposed ACI 369.1-22 value, possibly because the wall database consisted of mainly rectangular walls and no C-shaped wall tests were included in the database or due to uncertainty in the value of E_c.

The highest tensile strains ranged from 0.015 to 0.025 and were measured above the splice regions, whereas the highest compressive strains were measured just above the wall-footing interface (Layer 1, 10 in.). For CW-3 and CW-4, where no concrete core crushing was observed during the WLP, the maximum compressive strains at the flange edges were around -0.003. However, for CW-2, a higher maximum compressive strain value of around -0.005 was measured during ramp-up loading at the maximum hinge rotation demand of 0.9% due to the extensive damage that occurred at the flange edges. The maximum compressive strain value at the flange edge increased to approximately -0.012 during the ramp-down cycles. Application of OOP moments affected compressive strains measured at the flange edges more than the compressive strains measured at the flange-web corners or tensile strains. With the application of OOP moments, the maximum compressive strains at the flange edges increased from approximately -0.003 to values around -

0.0043 and -0.0047 for CW-3 and CW-4, respectively. The difference in values between CW-3 and CW-4 was due to the different levels of axial load applied during the biaxial loading (0.05 versus $0.075A_g f'_c$).

6. Experimental Seismic Test Results and Discussion (CW-2, CW-3 and CW-4)

6.1 General

After the completion of the WLP, a seismic loading protocol (SLP) was applied to all of the test specimens. The intent of applying the SLP was to establish the deformation at strength loss for each test specimen and to identify failure modes. Table 6-1 and Table 6-2 summarize the applied in-plane base moment and hinge rotation demands for CW-2, CW-3, and CW-4, respectively. For CW-2, the SLP shown in Figure 2-40 was applied. The in-plane hinge rotation demand of ±1.35% was selected for CW-2 to apply a rotation ductility of 4.5 (calculated with $\Theta_{y,IP}$ of 0.3%). A more detailed analysis after the tests (Appendix F) showed that the effective yield rotation was 0.25% ($\Theta_{y,IP,exp}$); therefore, CW-2 was actually pushed to $\pm 5.4\Theta_{y,IP,exp}$ hinge rotation demands with failure observed during the first cycle. For CW-3, a similar SLP was used (Figure 2-40). After applying three cycles at ±1.35% IP hinge rotation demands ($\pm 5.4\Theta_{y,IP,exp}$), the wall was pushed in the negative IP direction to -1.85% IP hinge rotation demands ($-7.4\Theta_{y,IP,exp}$) when failure was observed. For CW-4, an SLP that was similar to the WLP was selected, i.e., both IP and OOP loading with $0.5M_{pr,OOP+y}$ and $0.5M_{pr,OOP-y}$ applied (Figure 2-41). The CW-4 SLP included two cycles of IP hinge rotation demands at ±0.6% ($\pm 2.4\Theta_{y,IP,exp}$) and ±0.9% ($\pm 3.6\Theta_{y,IP,exp}$), followed by one cycle at ±1.35% ($\pm 5.4\Theta_{y,IP,exp}$) prior to observed failure. The difference between the WLP and the SLP applied to CW-4 was the axial load demand applied during the biaxial loading, i.e., for the WLP, the axial load was decreased from $0.10A_g f'_c$ to $0.075A_g f'_c$ during the positive OOP load application, whereas for the SLP, the axial load was kept constant at $0.10A_g f'_c$. The higher OOP axial load was used to examine if, with improved flange edge detailing, the wall could withstand the higher axial load without observed strength loss (i.e., essentially an extension of the WLP).

Table 6-1: Applied base moment and hinge rotation demands for CW-2 and CW-3 during the SLP

Wall	Type of loading	# of cycles	Base moment, $M_{b,IP}$ (k-ft), -IP dir.	Base moment, $M_{b,IP}$ (k-ft), +IP dir.	Hinge rotation, $\Theta_{Lp,IP}$ (%)	$\Theta_{Lp,IP}/\Theta_{y,exp}$
CW-2	IP only	1	-3517	+3021	±1.35%	$\pm 5.4\Theta_{y,IP,exp}$
CW-3	IP only	3	-4221	+4556	±1.35%	$\pm 5.4\Theta_{y,IP,exp}$
		Half cycle	-4413	-	-1.85%	$-7.4\Theta_{y,IP,exp}$

Table 6-2: Applied IP base moment and hinge rotation demands for CW-4 during the SLP

Wall	Type of Loading	# of cycles	Base moment, $M_{b,IP}$ (k-ft), -IP dir.	Base moment, $M_{b,IP}$ (k-ft), +IP dir.	Hinge rotation, $\Theta_{Lp,IP}$ (%)	$\Theta_{Lp,IP}/\Theta_{y,exp}$
CW-4	Biaxial*	2	-3477	+3545	±0.6%	$\pm 2.4\Theta_{y,IP,exp}$
		2	-3782	+4081	±0.9%	$\pm 3.6\Theta_{y,IP,exp}$
		1	-3938	+4071	±1.35%	$\pm 5.4\Theta_{y,IP,exp}$

* Half of OOP probable moment capacities were applied ($0.5M_{pr,OOP+y}$ and $0.5M_{pr,OOP-y}$)
Axial load was kept constant at $0.1A_g f'_c$ during the whole loading procedure

6.2 Observed Damage

6.2.1 CW-2

Modest strength degradation (≈10% strength loss from peak strength) was observed for CW-2 at the peak rotation demand of -1.35%. It is noted that no strength loss was observed for CW-3 at -1.35% IP hinge rotation demands; therefore, relative to CW-3, a 16% strength loss was observed for CW-2. The maximum positive base moment value of 3519 k-ft was observed for CW-2 in the positive IP direction at +0.94% rotation during the first cycle to +1.35% IP hinge rotation demands.

At +1.35% rotation demands, the base moment reduced to +3022 k-ft or 0.67 times the base moment recorded for CW-3 (+4556 k-ft) at +1.35% rotation demands. When +1.35% hinge rotation demand was reached, a sudden failure occurred, and the base moment dropped to +914 k-ft (0.20 times the base moment recorded for CW-3), and the axial load decreased by 60% to 200 kips ($0.04A_g f'_c$). The strength loss occurred due to core concrete crushing and longitudinal reinforcement buckling at the base of the east flange (Figure 6-1). The shortening of the east flange due to the observed damage then led to a diagonal tension failure within the wall web, with a large diagonal crack forming between the top-west corner of the web to the bottom-east corner of the web through the entire wall thickness (Figure 6-2 and Figure 6-3). Additionally, some concrete crushing (mostly on the outer surface, Figure 6-4) was observed at the base of the west flange, which was consistent with the strength loss observed at -1.35% hinge rotation demands (when the west flange was under compression).

Figure 6-1: Damage state of the east flange after the completion of testing, CW-2

Figure 6-2: Outside surface of the web after the completion of testing, CW-2

Figure 6-3: Inside surface of the wall after the completion of testing, CW-2

Figure 6-4: Damage state of the west flange after the completion of testing, CW-2

6.2.2 CW-3

Three cycles at ±1.35% IP hinge rotation demands were applied to CW-3 successfully with only minor strength loss observed (at the 3rd cycle) due to buckling of longitudinal reinforcement at the west flange corner approximately 22 in. above the footing (right above the spliced region, Figure 6-5). Subsequently, the specimen was loaded in the negative direction to -1.85% IP hinge rotation demand (west flange in compression) with no observed strength loss. However, during unloading from the -1.85% rotation demands, -1.24% IP rotation demands, concrete crushing, and longitudinal bar buckling were observed on the inside web face adjacent to the east flange between 40 and 52 in. above the footing(Figure 6-6); base moment demands were still negative (-565 k-ft) when this damage was observed. As loading continued, at approximately +190 k-ft base moment demands (-0.7% rotation), out-of-plane instability of the east flange was observed roughly 57 in. above the footing (Figure 6-7 and Figure 6-8) and the test was stopped. Some cover spalling was observed at the base of the west flange edge; however, no concrete crushing or longitudinal bar buckling was observed (Figure 6-9). No additional damage was observed at the base of the east flange edge or at the flange-web corner.

Figure 6-5: Buckling of the west flange corner bar above the spliced region, after three cycles at ±1.35% IP hinge rotation demands, CW-3

Figure 6-6: Bar buckling and concrete crushing at around 40 in to 52 in. above the footing on the inner surface of the web, after the completion of testing, CW-3

Figure 6-7: Damage state of the east flange after the completion of testing, CW-3

Figure 6-8: Damage state of the web after the completion of testing, CW-3

Figure 6-9: Damage state of the west flange after the completion of testing, CW-3

6.2.3 CW-4

The longitudinal bar that buckled during the WLP (at the base of the west flange edge, Figure 5-13) ruptured during the unloading part of the first cycle to -0.6% rotation demand. Application of two cycles at ±0.9% IP hinge rotation demands did not result in any additional damage at the west flange (edge or the corner). However, longitudinal bar rupture was observed during these cycles at the base of the east flange edge (the inner layer of flange longitudinal rebar) with some additional concrete crushing at the base of the east flange corner (Figure 6-10). At -1.35% IP rotation demand, the base moment value of 0.94 times the value recorded for CW-3, some concrete crushing at the base of the west flange (Figure 6-11), and buckling of longitudinal reinforcement at the corner of the west flange were observed. Subsequently, at +1.35% IP rotation demand, the base moment was 0.88 times the base moment recorded for CW-3 at this rotation demand. During the application of the positive OOP bending moment to Pos. E (east flange edge was under compression), a maximum OOP base moment of approximately +500 k-ft ($0.37M_{pr,OOP+y}$) was reached. Therefore, the intended moment demands of $0.5M_{pr,OOP+y}$ could not be applied, and the test was stopped (to allow for possible repair and retesting). Concrete crushing was observed at the base of the edge flange, and either bar buckling or bar fracture occurred for almost all the longitudinal reinforcement of the east flange (Figure 6-12 and Figure 6-13).

Figure 6-10: East flange edge (left) and east flange corner (right) after the two cycles applied at ±0.9% IP hinge rotation demands, CW-4

Figure 6-11: West flange edge (left) and west flange corner (right) after the completion of testing, CW-4

Figure 6-12: East flange outer surface (left) and inner surface (right) after the completion of testing, CW-4

Figure 6-13: Outer surface of the web after the completion of testing, CW-4

6.3 Load-Deformation Responses

6.3.1 Base Moment-Hinge Rotation Responses

Figure 6-14 shows the base moment-hinge rotation, calculated over a plastic hinge length of $l_w/2$ using the control sensors shown in Figure 2-26 and Figure 2-27, for test specimens CW-2, CW-3, and CW-4 during the WLP and SLP. Figure 6-15 shows OOP base moment versus OOP hinge rotation relation for CW-4. The dashed line in Figure 6-15 represents the behavior during loading where east flange concrete crushing at the near-constant base moment was observed. The failure points in Figure 6-14 represent the point where either a sudden strength loss (CW-2, the base moment decreased to 0.25 times the maximum value recorded), the out-of-plane instability of the east flange (CW-3), or 34% strength loss in the OOP direction (CW-4) was observed.

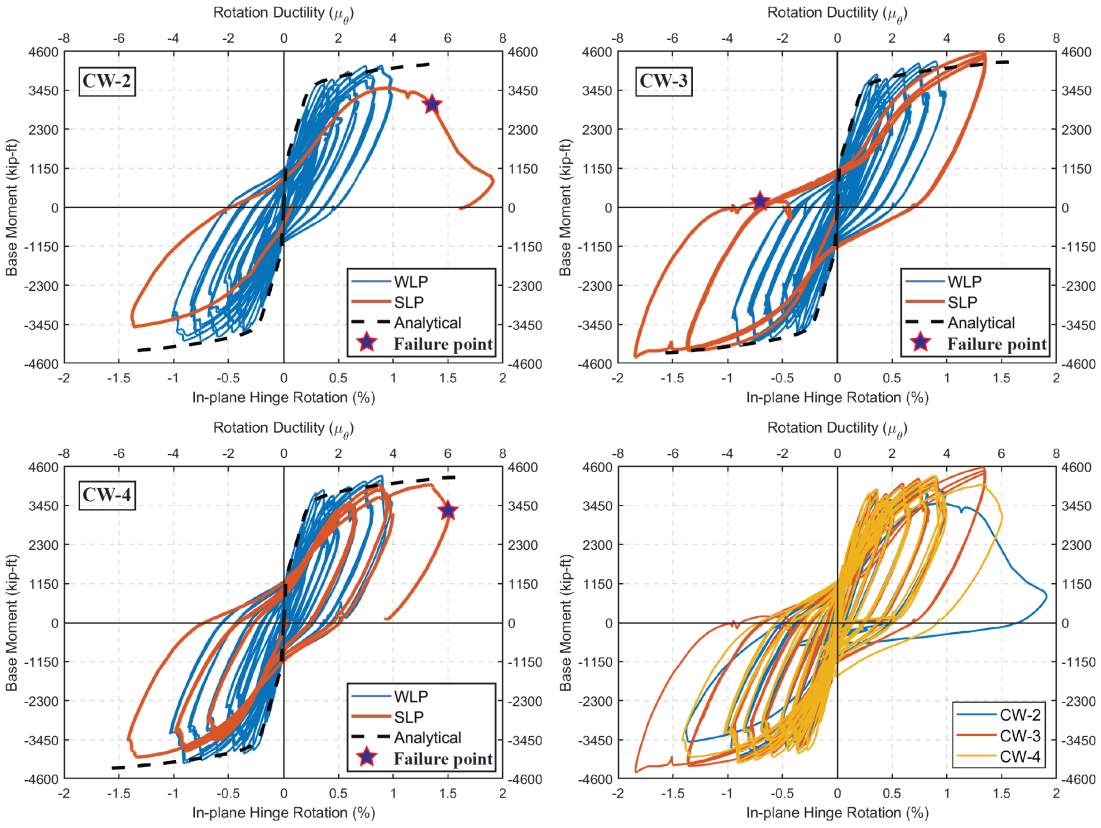

Figure 6-14: IP Base moment-hinge rotation responses of CW-2, CW-3, and CW-4

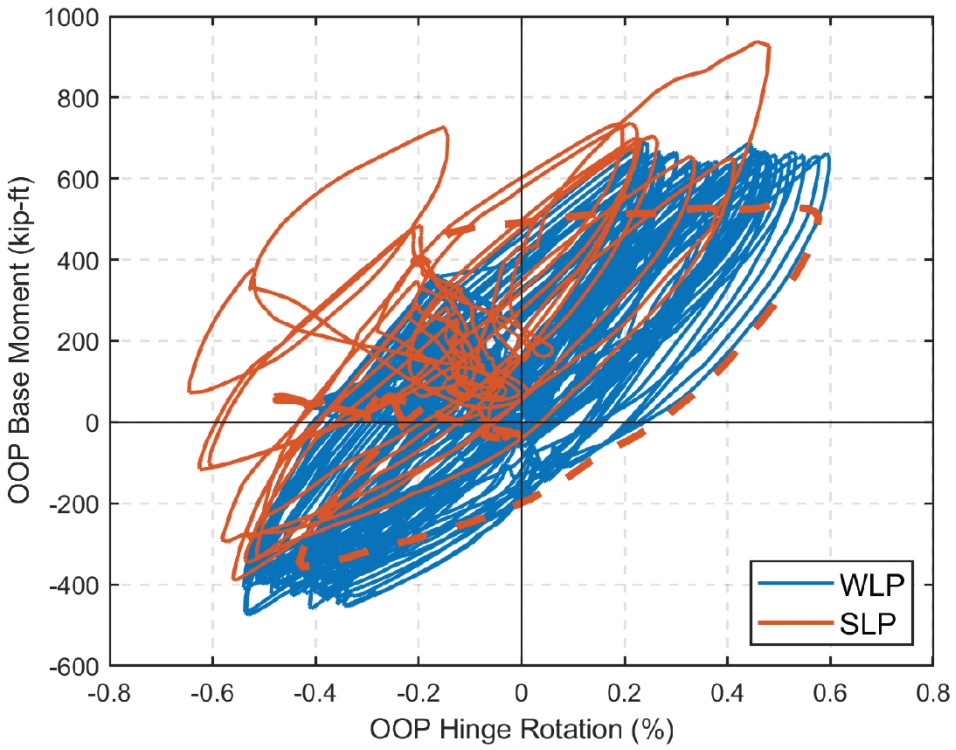

Figure 6-15: OOP Base moment-hinge rotation response of CW-4

6.3.2 Moment-Curvature Responses

The moment-curvature responses of CW-2, calculated at different layers (Figure G-1) using Group 2 LVDTs (Figure 5-21), are shown in Figure 6-16 during both the WLP and SLP. For Layers 3, 4, and 5, the curvature demands at ±1.35% IP hinge rotation demands were almost one-half of those observed during the maximum hinge rotation demands of WLP (±0.9%). For Layer 2, the curvature demands for the SLP were the same as the maximum values calculated during the WLP. However, curvature values increased for Layer 1, at positive IP rotation demands, when a curvature ductility of almost 6 was achieved.

Figure 6-17 and Figure 6-18 present moment-curvature responses for CW-3 with curvature values calculated using both the Group 1 and 2 LVDTs for Layers 1 and 2 and Group 1 LVDTs for Layers 3, 4, and 5. were used. The highest curvature demands were calculated for Layer 1 (2-10 in.) in the negative direction (east flange was under tension), with curvature ductilities of 4 and 5 calculated using the Group 1 and 2 LVDTs, respectively. Although the tensile strains were lower for Layer 1 during the WLP, after some damage that occurred at the base of the east flange, especially after the ±1.35% hinge rotation demands, the bottom half of the splice region experienced high tensile and compressive strain demands. Since the damage was mainly concentrated at the base of the flange edges, the curvatures calculated at Layer 2 (10-20 in.) using the Group 1 LVDTs were low. The highest curvatures were calculated at Layer 3 (20-37 in., above the splice region). At the last cycle before failure (at -1.85% rotation demands), a maximum curvature ductility of 9.5 was observed at this layer.

Figures 6-19 and 6-20 show the moment-curvature responses of CW-4. Similar to CW-2, since the damage was mainly concentrated at the base of the flanges, lower curvature demands were observed for Layers 3, 4, and 5 during the SLP than for the WLP. At the maximum rotation demands of ±1.35%, the curvature demands at Layers 1 and 2 were higher, with curvature ductility of approximately 2.0 and 1.5, respectively. In general, the analytical prediction of the monotonic moment-curvature responses (Appendix F) matched the experimental results well.

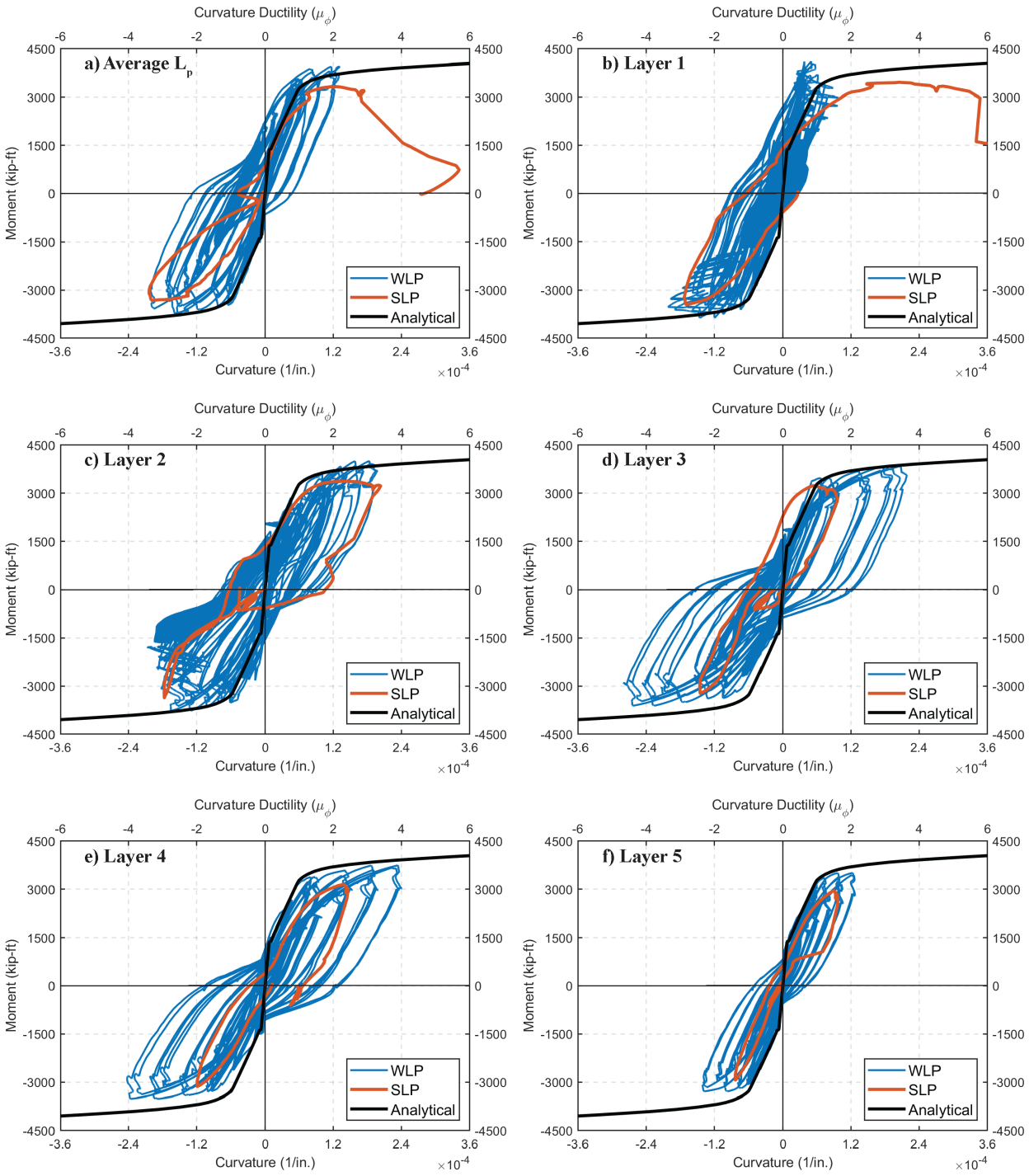

Figure 6-16: Moment-curvature responses of CW-2

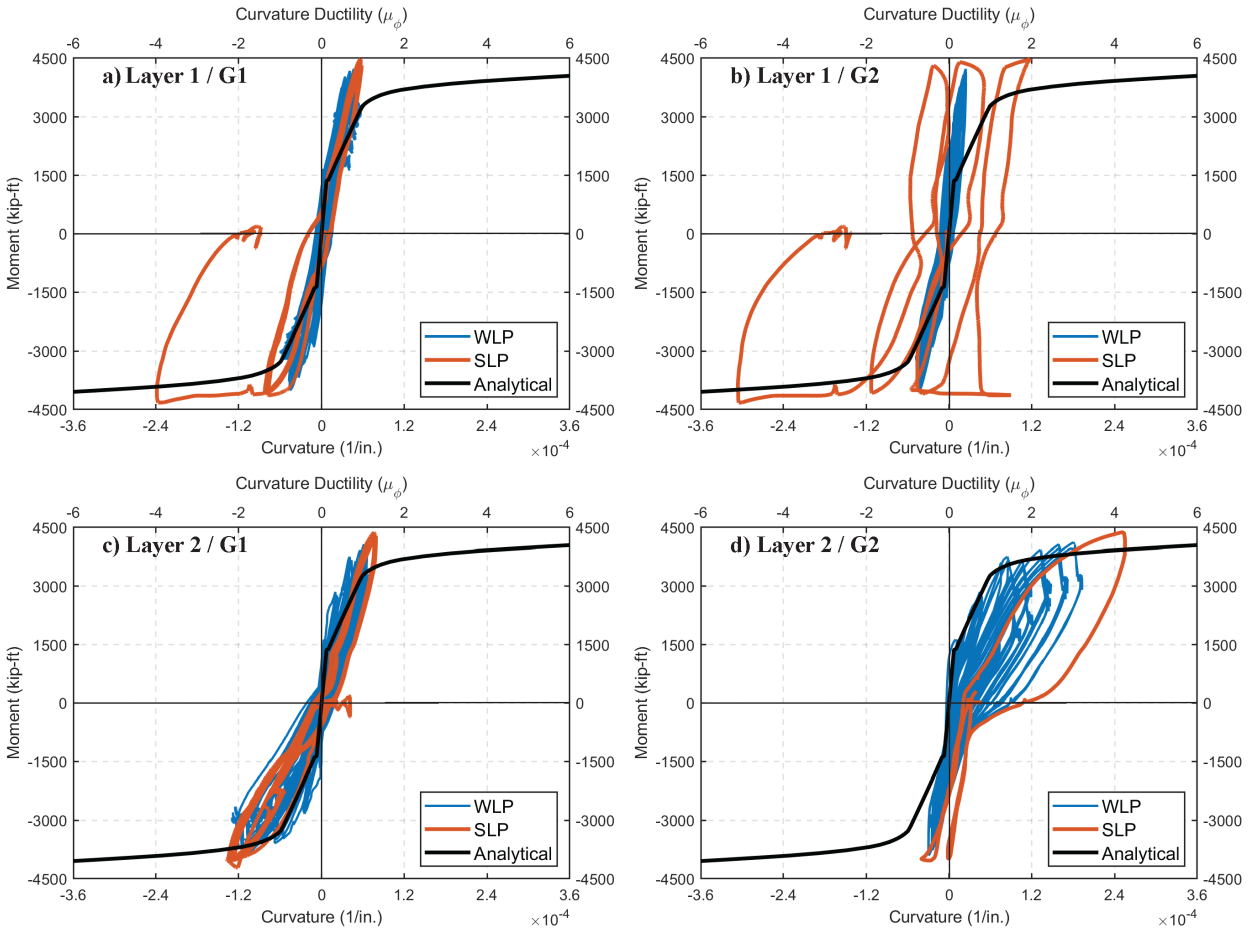

Figure 6-17: Moment-curvature responses at Layers 1 and 2 of CW-3

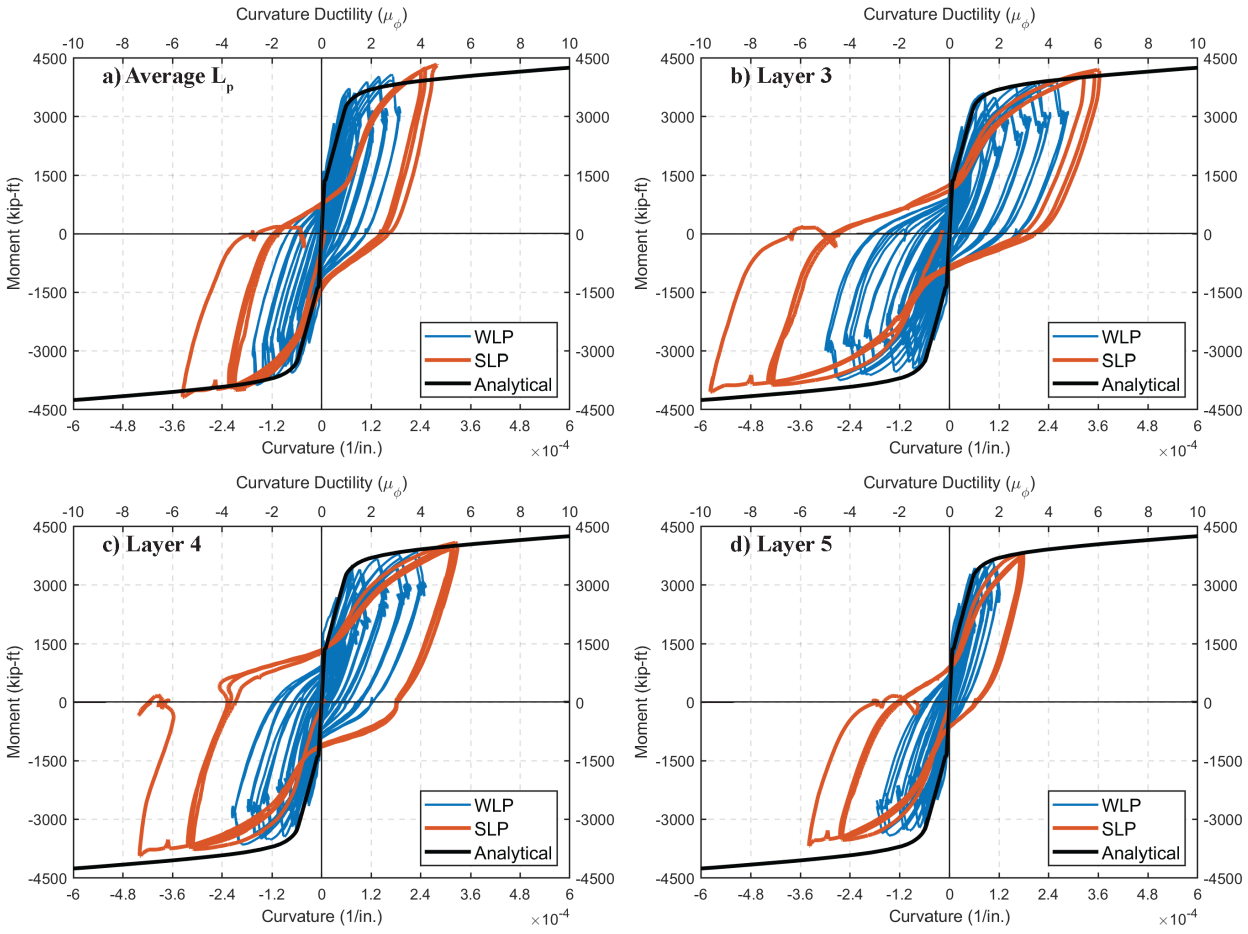

Figure 6-18: Moment-curvature responses at L_p and Layers 3, 4, and 5 of CW-3

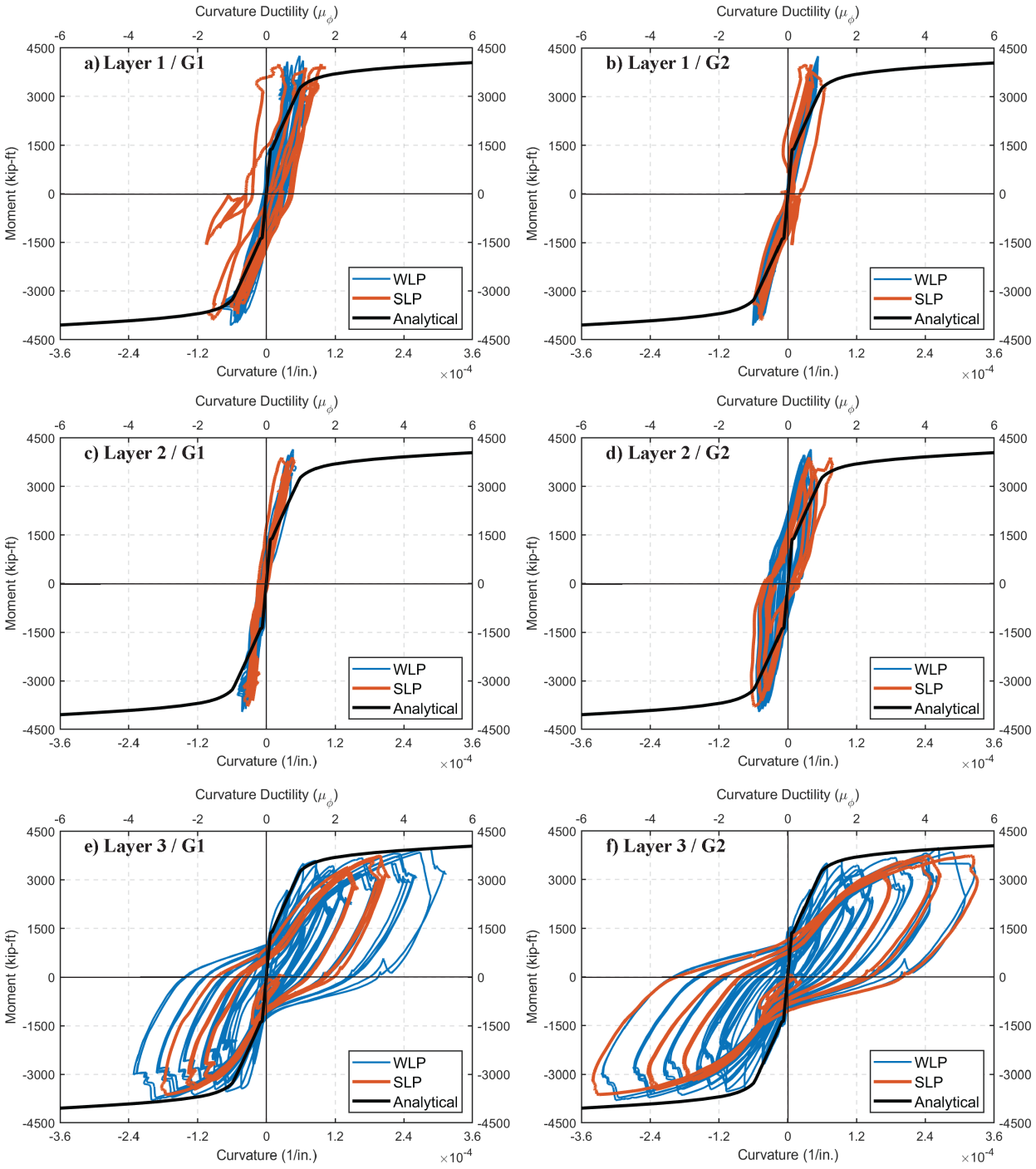

Figure 6-19: Moment-curvature responses at Layers 1, 2, and 3 of CW-4

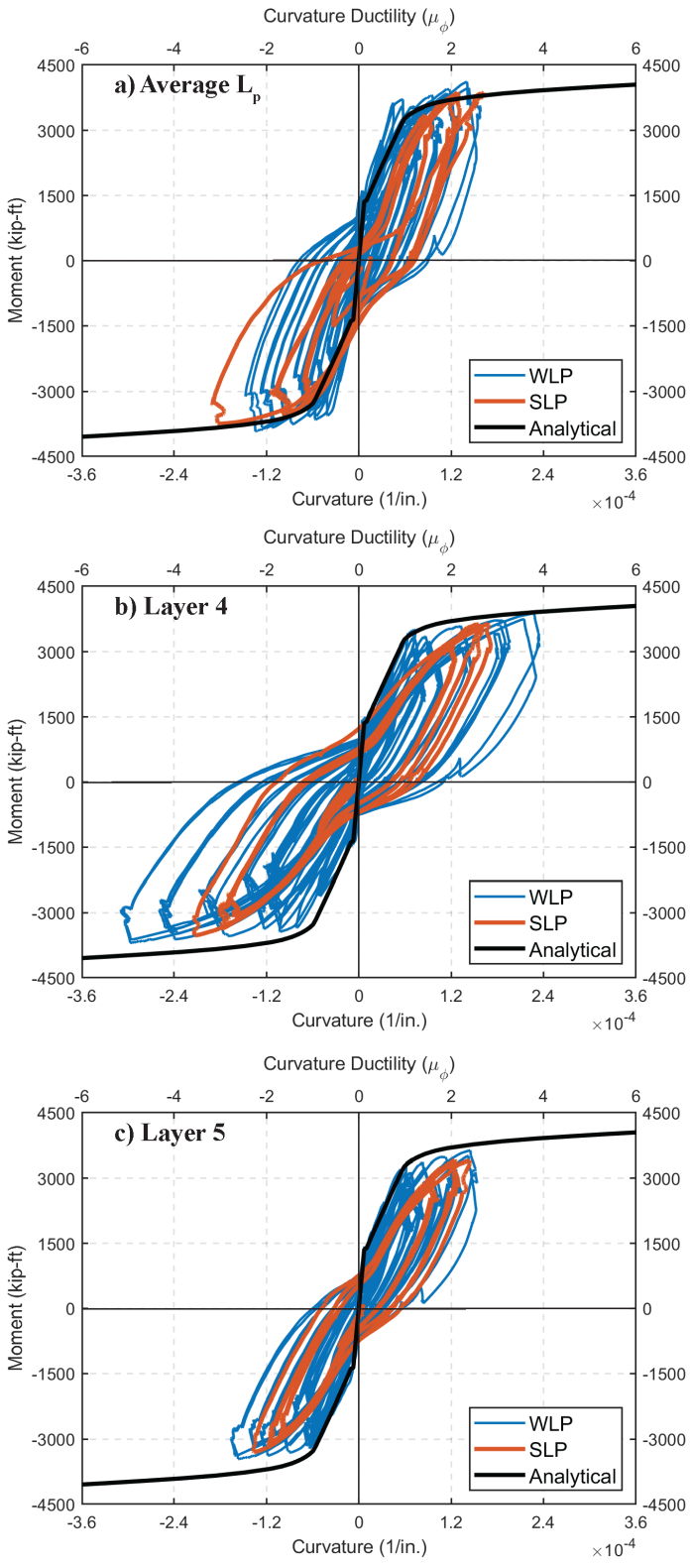

Figure 6-20: Moment-curvature responses at L_p, and Layers 4 and 5 of CW-4

6.3.3 Base Shear-Lateral Displacement Responses

Figure 6-21 shows the base shear-drift ratio responses for CW-2, CW-3, and CW-4 calculated during the WLP and the SLP. The drift ratios represent the average (lateral) drift ratio calculated using the two LVDTs attached to the northeast and northwest corners of the top block. The values recorded from the two LVDTs were very similar for all the walls; therefore, only the average drift ratio obtained from the two LVDTs is provided. For CW-2, the maximum drift ratio observed in the negative direction was the same as that observed during the WLP. On the other hand, smaller drift ratios were achieved in the positive direction, i.e., 1.45% for the SLP and 1.6% for the WLP. Although higher hinge rotations were applied during the SLP compared to the WLP, the same or lower drift ratios were achieved because lower curvature demands occurred at Layers 2 through 5 LVDTs (10-88 in., Figure 6-16).

For CW-3, drift ratios of 2.44% and -2.66% were measured at the first cycle of +1.35% and -1.35% IP hinge rotation demands, respectively. At -1.85% rotation demand, a drift ratio of -3.30% was observed. The drift ratios did not decrease during unloading (from the last cycle) because the LVDT strokes were reached, which prevented the LVDTs from measuring any changes in displacements after this point.

The drift ratios measured during the SLP for CW-4 were lower than the values measured at the same hinge rotation demands during the WLP. For example, at -0.9% hinge rotation demands, drift ratios of -2.1% and -1.75% were measured for WLP and the SLP, respectively. Similar behavior also was observed in the positive direction, except there was less difference in the peak drift values. The reason for the lower drift ratios observed during the SLP was because of the damage that occurred during the WLP, especially at the east flange edge (Section 6.2.3). At the maximum

rotation demands of ±1.35% (during the SLP), the drift ratio of 2.4% was achieved in both directions. Figure 6-22 shows the OOP base moment-hinge rotation response of CW-4. Lower drift ratios were observed in the negative OOP direction (flange edges were under tension) during the SLP compared to the WLP because of the damage that occurred at the edges of the flanges due to buckled and/or ruptured longitudinal reinforcement at the flange edges. The dashed line in Figure 6-22 represents the last cycle in which the failure occurred (loading to Pos. E from Pos. D), where about a 60% strength loss was observed.

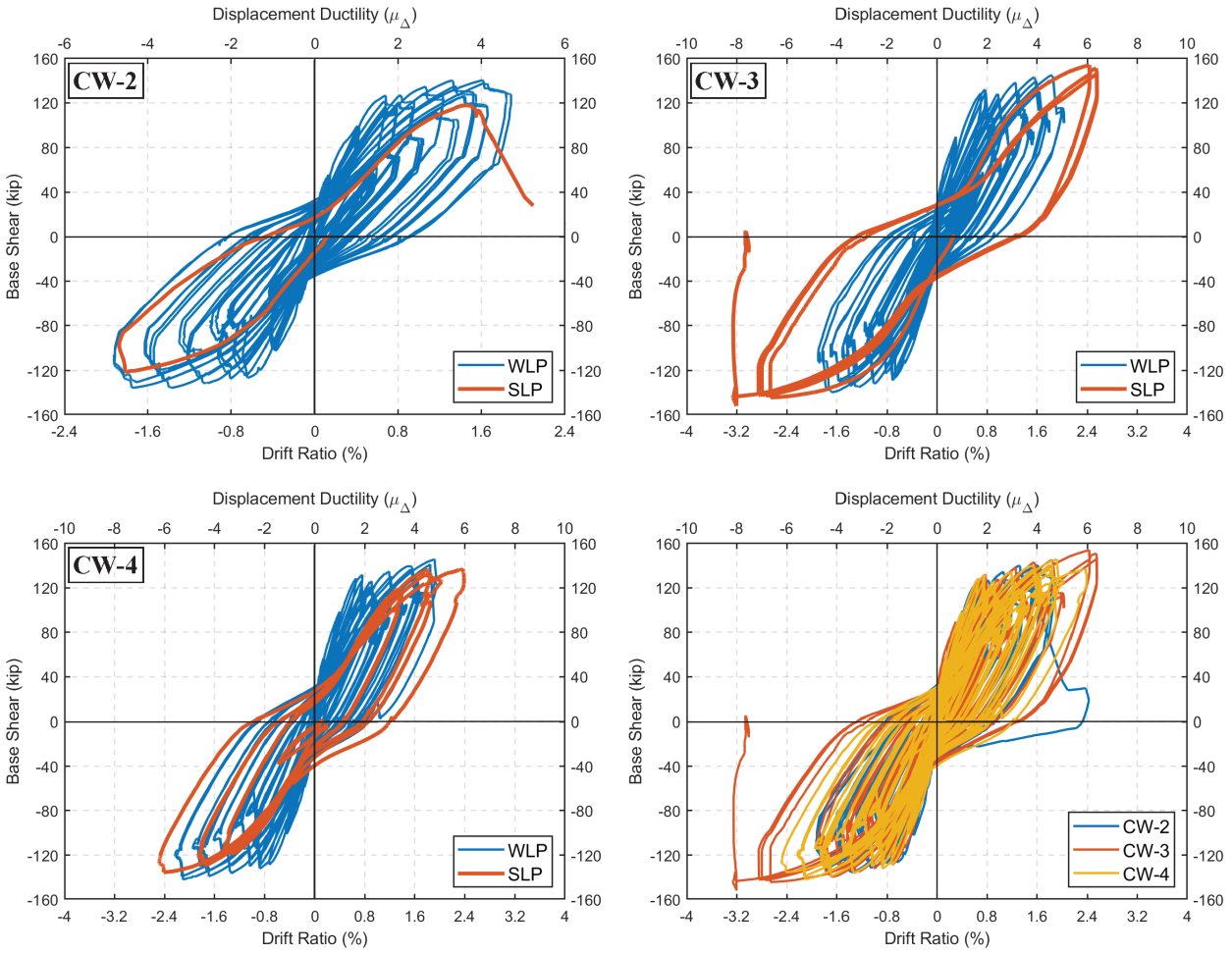

Figure 6-21: IP Base shear-drift ratio responses of CW-2, CW-3, and CW-4

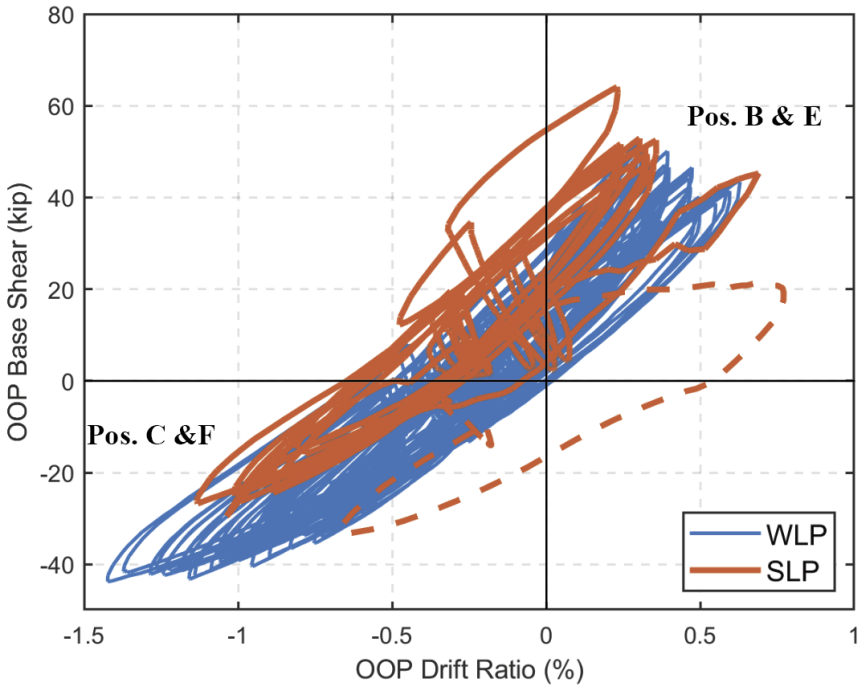

Figure 6-22: OOP Base shear-drift ratio response CW-4

The total in-plane lateral displacement (δ_{tot}) of the walls can be expressed as the sum of the flexural and shear deformations over the wall height (Equation 3.3). Figure 6-24 shows the contributions of different deformations to the total lateral displacement measured at the top of CW-2. In the positive direction, an increase was observed in the contributions of the flexural and slip/extension deformations, whereas the contribution of the shear deformations decreased from approximately 40% to 25%. In the negative direction, on the other hand, the contributions of the flexural and the slip/extension deformations were found to be decreasing, resulting in an increase from around 40% to 50% in the percent contribution of shear deformation calculated using Equation G.18. Figure 6-23 shows the drift ratios calculated at the top of CW-3 due to flexure ($\delta_{f,wall}$), slip/extension ($\delta_{f,slip}$), and shear deformations ($\delta_{s,wall}$) calculated using Equation G.18 and Equation G.19. Also, the percent contributions of these deformations to the total displacement at the top of the wall are given in Figure 6-25. On average, of both directions, the flexural

deformations contributed to approximately 48%, slip/extensions deformations contributed to approximately 14%, and the shear deformations contributed approximately 35% to the total lateral displacements at the maximum drift ratios. Approximately 3% of the total lateral displacement was due to the shear sliding at the wall-footing interface and sliding of the footing at the footing-strong floor interface. In general, for CW-4, at the maximum rotation demands of the SLP (±1.35%), an increase was observed for the contributions of the flexural deformations, i.e., from approximately 40% to 60%, resulting in a decrease in the shear and slip/extension deformation contributions (Figure 6-26).

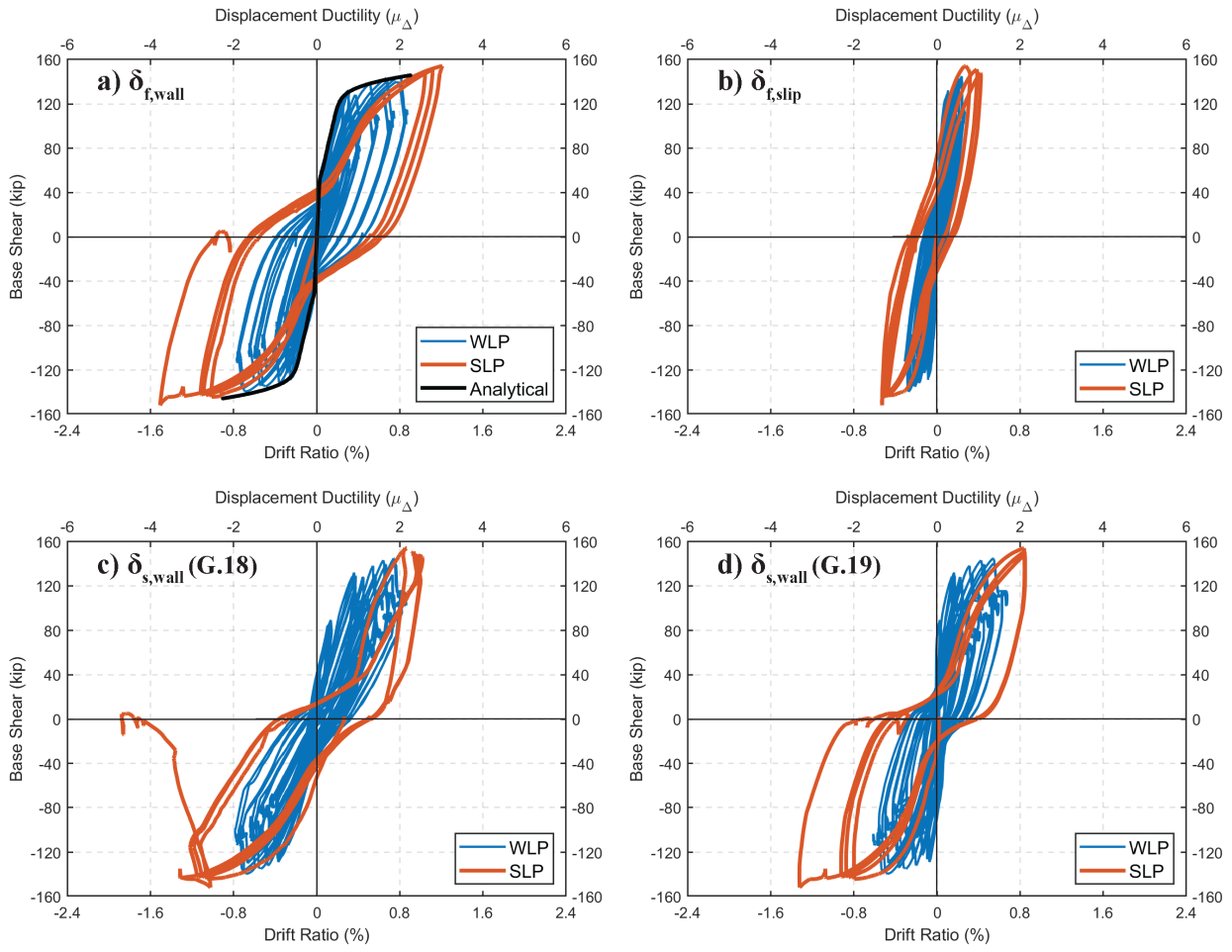

Figure 6-23: Different components of in-plane base shear-drift ratio response of CW-3

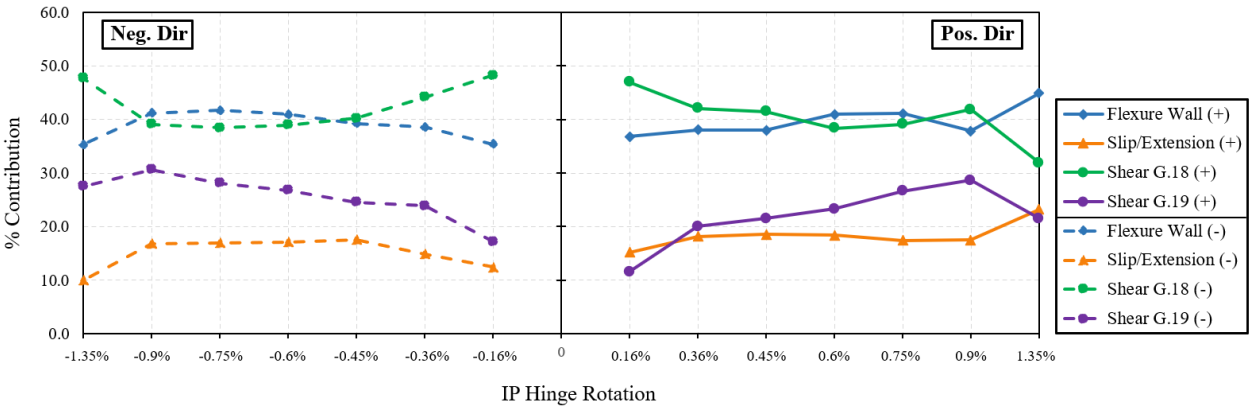

Figure 6-24: Contributions of different components to the drift ratios at the top of CW-2

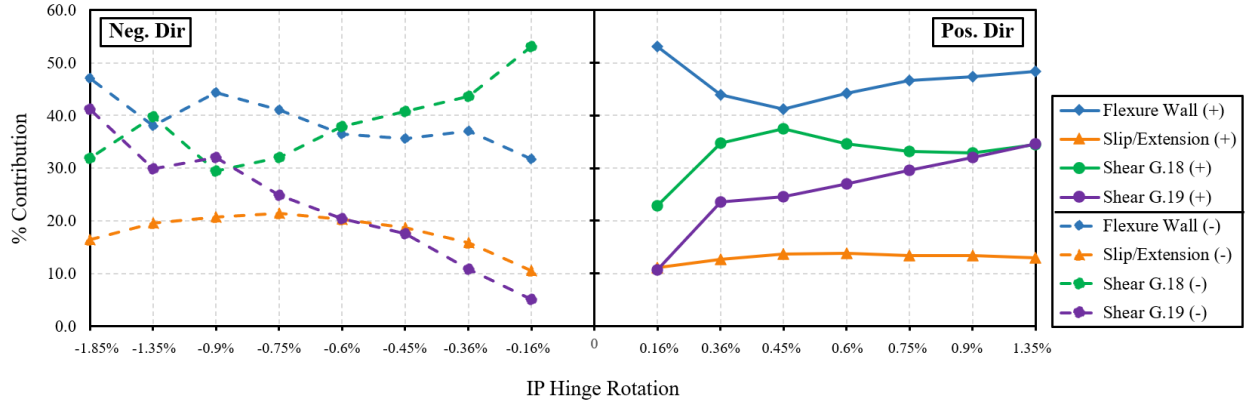

Figure 6-25: Contributions of different components to the drift ratios at the top of CW-3

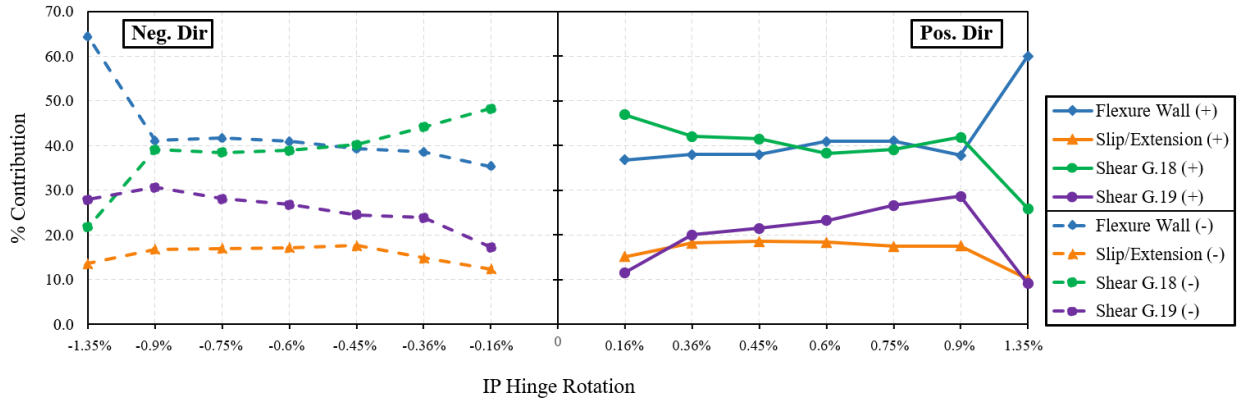

Figure 6-26: Contributions of different components to the drift ratios at the top of CW-4

6.3.4 Local Responses

The compressive and the tensile strains measured using Layers 2 through 5 LVDTs of CW-2 were lower than the strain measurements taken during the WLP, consistent with the lower curvatures observed at these layers during the SLP (Figure 6-16). Therefore, the distribution of the LVDT strains along the flange edges is not shown here for the SLP cycles. However, higher compressive strains were measured at the west flange edge for the Layer 1 LVDTs; LVDT strains versus the IP hinge rotation responses are shown in Figure 6-27. A maximum compressive strain of -0.0068 was measured at the maximum rotation demand (-0.9%) of the WLP; whereas a maximum compressive strain value of -0.0097 at -1.35% hinge rotation demand of the SLP. Due to damage at the base of the east flange edge, the values recorded at Layer 1 east flange LVDT were unreliable.

Figure 6-28 shows the reinforcement strains recorded using the strain gauges attached to the east flange U-bars (Figure 2-30). The strain gauge attached to the east flange edge U-bar yielded during the ramp-down loading of the WLP, whereas the U-bars at the east flange-web corner did not yield during the WLP. During the SLP, an increase was observed in the strains at the flange-web corner U-bars, and yielding was observed in the strain gauge attached crosstie in the web (parallel to the flange length) after strength loss started.

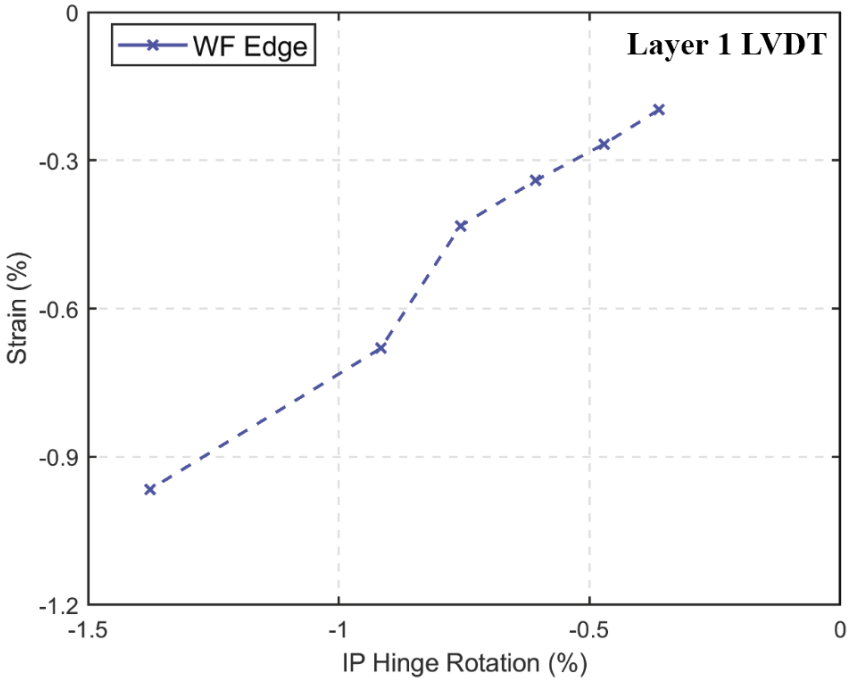

Figure 6-27: IP Hinge Rotation-LVDT strain response, West flange edge Layer 1 LVDT CW-2

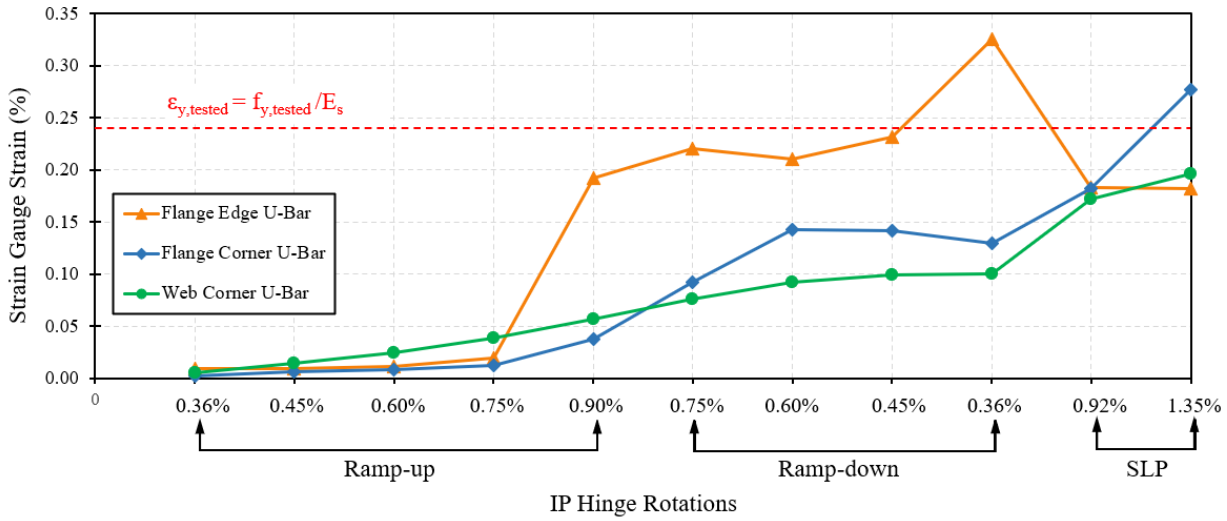

Figure 6-28: IP Hinge Rotation-Strain gauge strain response, East flange U-bars, CW-2

Figure 6-29 and Figure 6-30 show the axial strain profiles of CW-3 measured along the height of the east and west flange edges, respectively, during the ramp-up loading of the WLP and the SLP.

The highest tensile strain (0.037) was measured at the east flange edge Layer 3 LVDT (above the splice region). Similar compressive strains, values of -0.0063 and -0.0058 for the west and the east flanges, respectively, were measured at ±1.35% hinge rotation demands (at the base of the wall; Layer 1 LVDTs). During the last cycle at -1.85% hinge rotation demands, the compressive strain value increased to -0.021 at the base of the west flange edge. Figure 6-31 compares the compressive strains measured at the flange edges and flange-web corners at Layers 1 and 2. In general, the flange edge and flange-web corner strains were similar unless significant damage was observed at the LVDT anchor points.

Figure 6-32 and Figure 6-33 show the strains recorded at the strain gauges attached to hoops, cross-ties, and U-bars 5 in. above the footing (within the splice region, Figure 2-31) at the east and west flanges of CW-3, respectively. In general, higher strains were recorded when the flanges were under tension than compression. This is likely because, when the flanges were under tension, the transverse reinforcement around the spliced longitudinal reinforcement was resisting splitting forces developed due to bond-slip behavior.

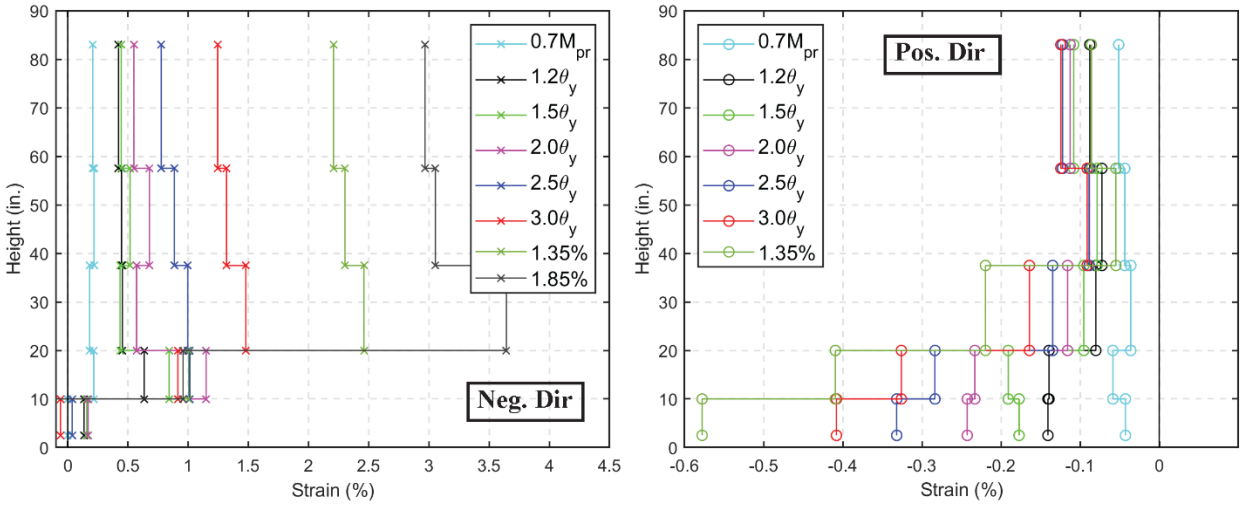

Figure 6-29: Axial strain profiles along the height of the edge of the East flange during the ramp-up loading of WLP and SLP, CW-3

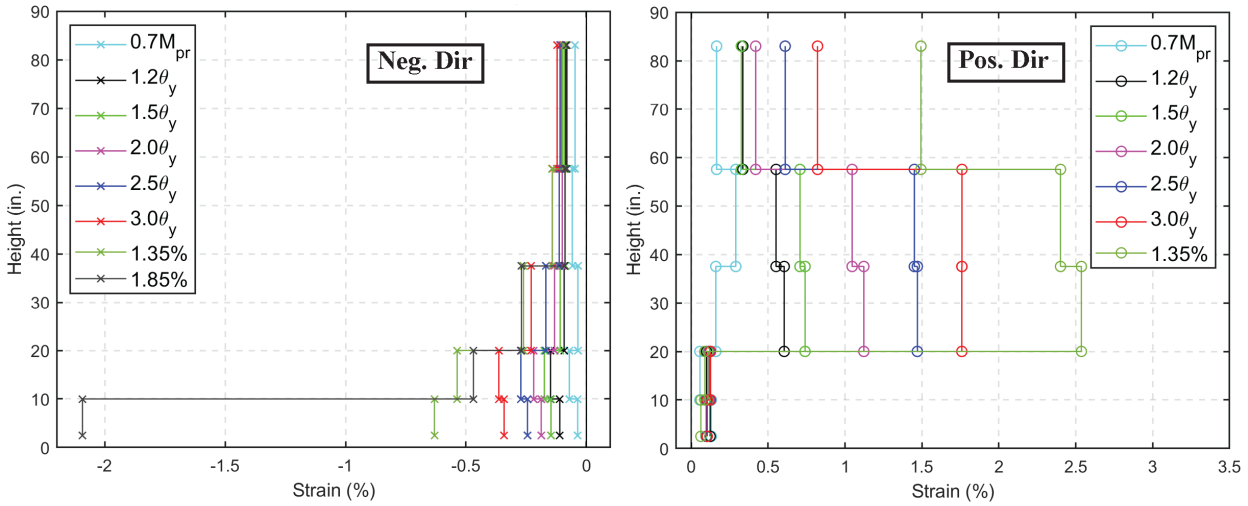

Figure 6-30: Axial strain profiles along the height of the edge of the West flange during the ramp-up loading of WLP and SLP, CW-3

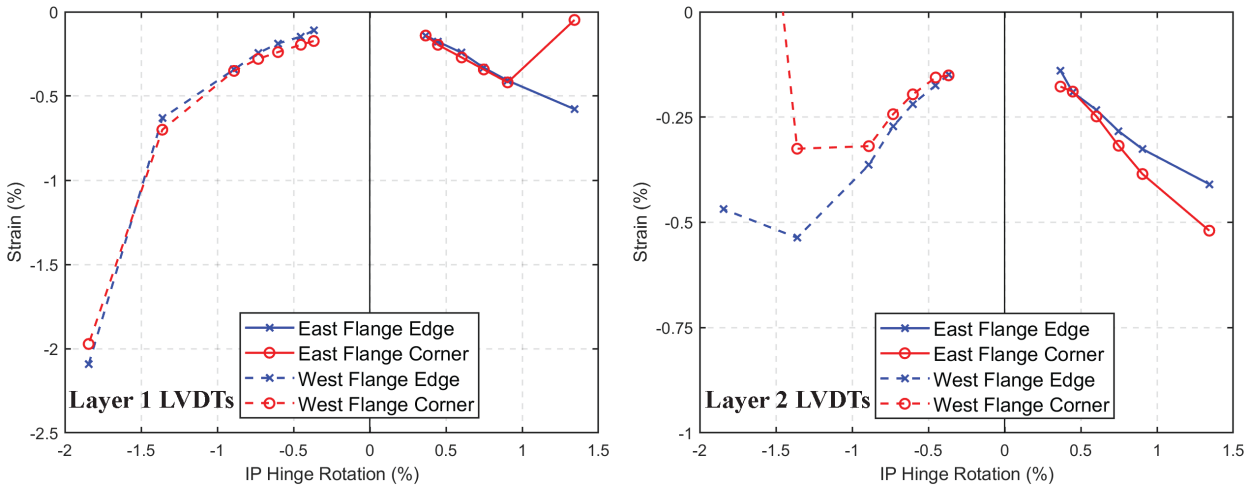

Figure 6-31: Comparison of compressive strains at the flange edges and corners during the ramp-up loading of WLP and SLP for the first- and second-layer LVDTs, CW-3

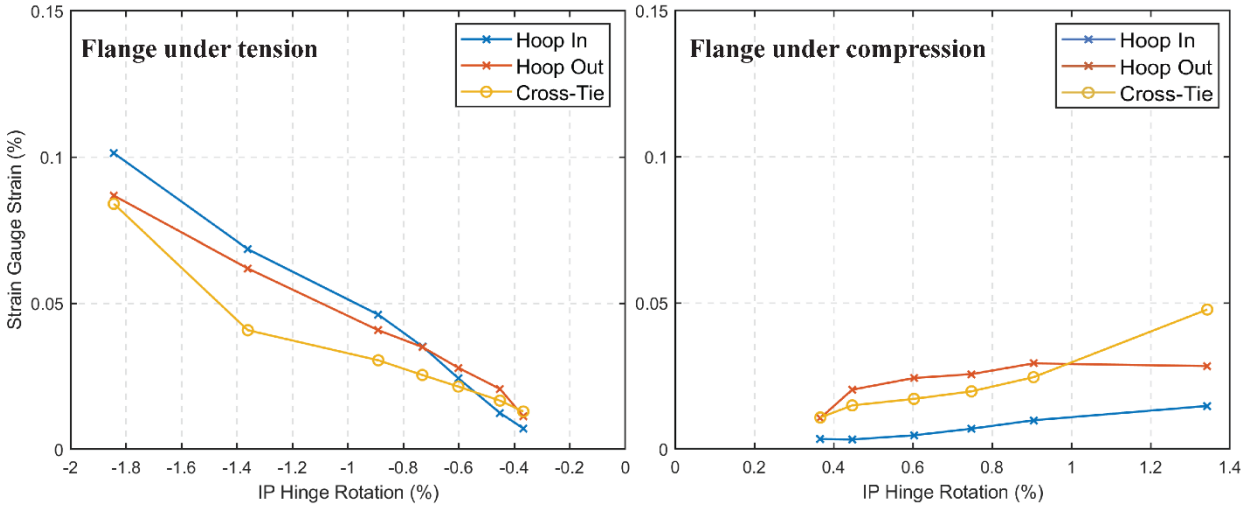

Figure 6-32: East flange transverse reinforcement strain gauge strains, CW-3

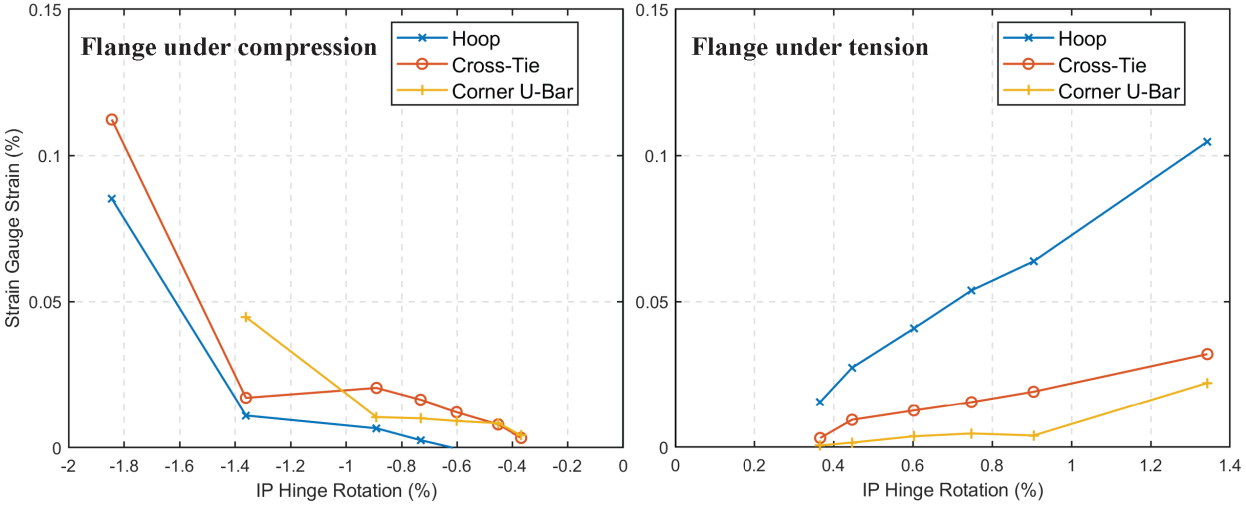

Figure 6-33: West flange transverse reinforcement strain gauge strains, CW-3

Figure 6-34 shows the compressive strains measured at Layer 1 LVDTs of CW-4 during the in-plane ramp-up loading of the WLP and the SLP. At the same rotation demands, ±0.6% and ±0.9%, the values recorded during SLP were found to be lower, except for the east flange edge LVDT. Because of the damage that occurred during the WLP at the base of the east flange edge, compressive strain demands were higher during the SLP. At ±1.35% rotation demands, similar

compressive strains were measured at the east and west flange corners, -0.0047 and -0.0049, respectively, whereas, at the west flange edge, the maximum compressive strain value was -0.0053. After the two biaxial cycles at +0.9% rotation demands, the east flange edge LVDT was not functioning properly due to the concrete crushing observed at the base of the east flange edge.

Figure 6-35 and Figure 6-36 show the effect of biaxial loading on CW-4 by comparing the compressive strains for in-plane loading (Pos. A and D) and for biaxial loading for the flange-web corners (Pos. C and F) and flange edges (Pos. B and E). Measured peak compressive strains during OOP loading were 22% (west flange) and 62% (east flange) higher that at the flange-web corners. The maximum compressive strain value measured at Pos. B (IP + OOP) for the west flange edge at -1.35% rotation demand was -0.0061, a 15% increase from Pos. A (IP). After 0.9% IP hinge rotation demands, due to concrete crushing, the values recorded at the east flange edge Layer 1 LVDT were not reliable. Figures 6-37 and 6-38 show the in-plane rotation-strain gauge strain responses for the strain gauges attached to the hoops, cross-ties, and U-bars of the east and west flanges of CW-4 (Figure 2-32), respectively. In general, similar to CW-3, the strain gauges had higher strain demands when the flanges were under tension than compression. Since these gauges were affixed to transverse reinforcement located inside the splice region (5 in. above the footing), when the flanges were under tension, the higher strains were likely due to the transverse reinforcement resisting splitting forces developed due to bond-slip behavior. The strain gauge attached to the inside surface of the hoop that was located at the east flange edge (Hoop In, Figure 6-37) showed yielding during biaxial loading at -0.9% IP hinge rotation demands at loading Pos. F (east flange edge was under tension). The same strain gauge and the one attached to the cross-tie at the edge of the east flange (Figure 2-32) showed yielding when the east flange was under

compression after the completion of the cycles at +0.9% IP hinge rotation demands. The strain gauges attached to the west flange transverse reinforcement did not show any yielding.

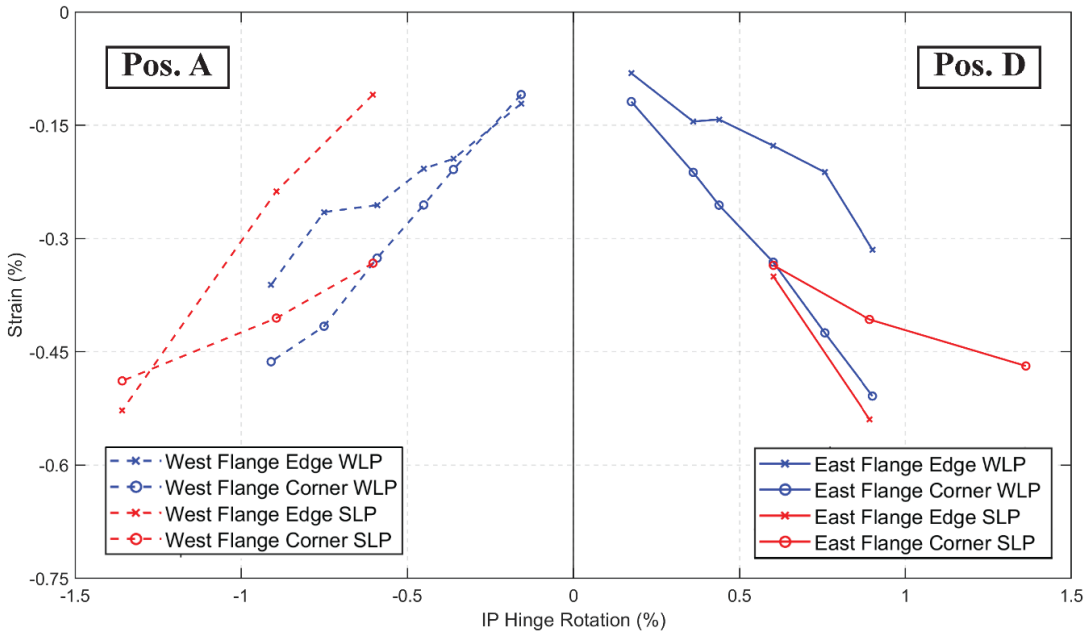

Figure 6-34: Comparison of compressive strains at the flange edges and corners during the ramp-up loading of WLP and SLP for the Layer 1 LVDTs, CW-4

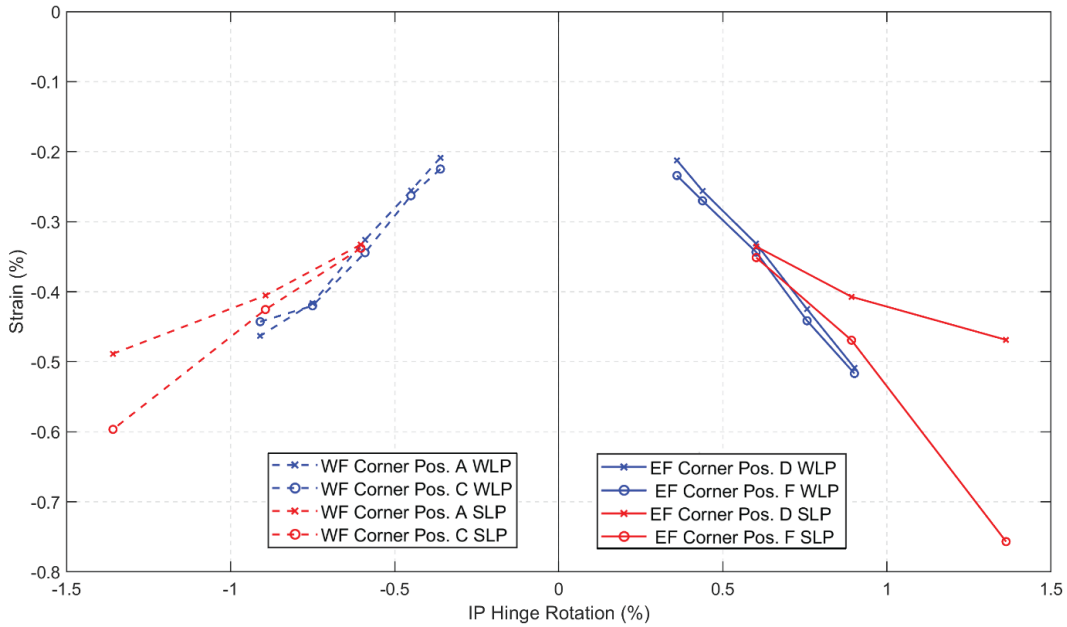

Figure 6-35: Comparison of compressive strains at the corners at different loading positions during the ramp-up loading of WLP and SLP for the Layer 1 LVDTs, CW-4

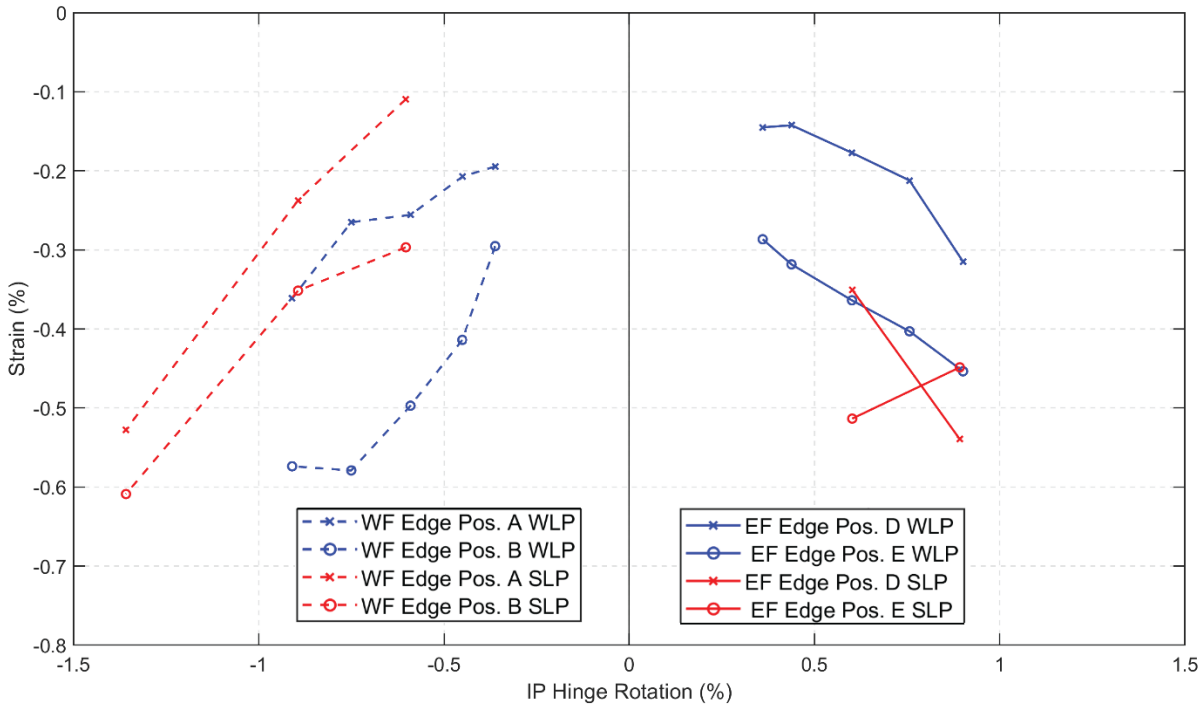

Figure 6-36: Comparison of compressive strains at the flange edges at different loading positions during the ramp-up loading of WLP and SLP for the Layer 1 LVDTs, CW-4

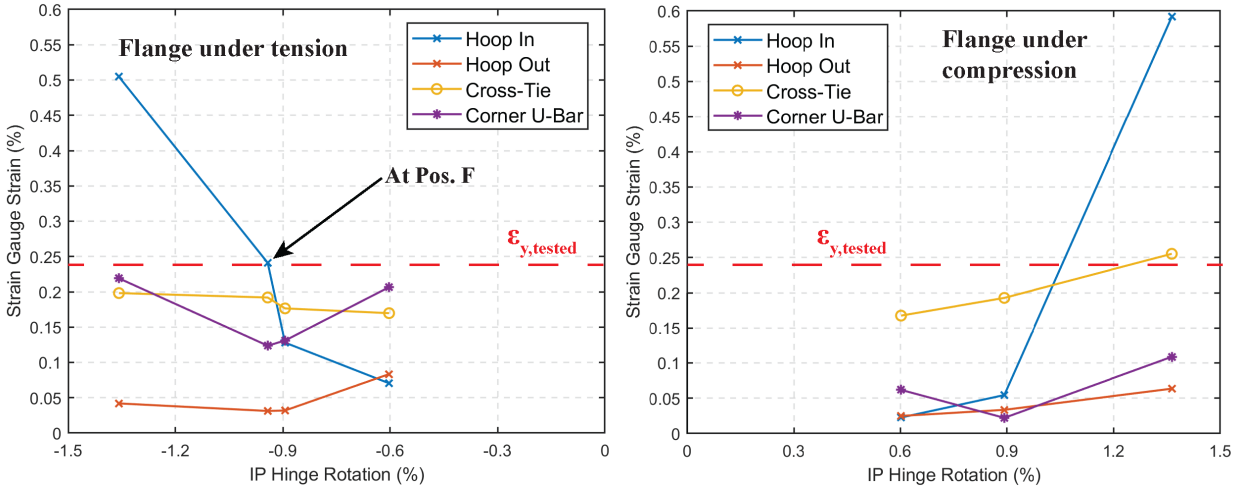

Figure 6-37: East flange transverse reinforcement strain gauge strains, CW-4

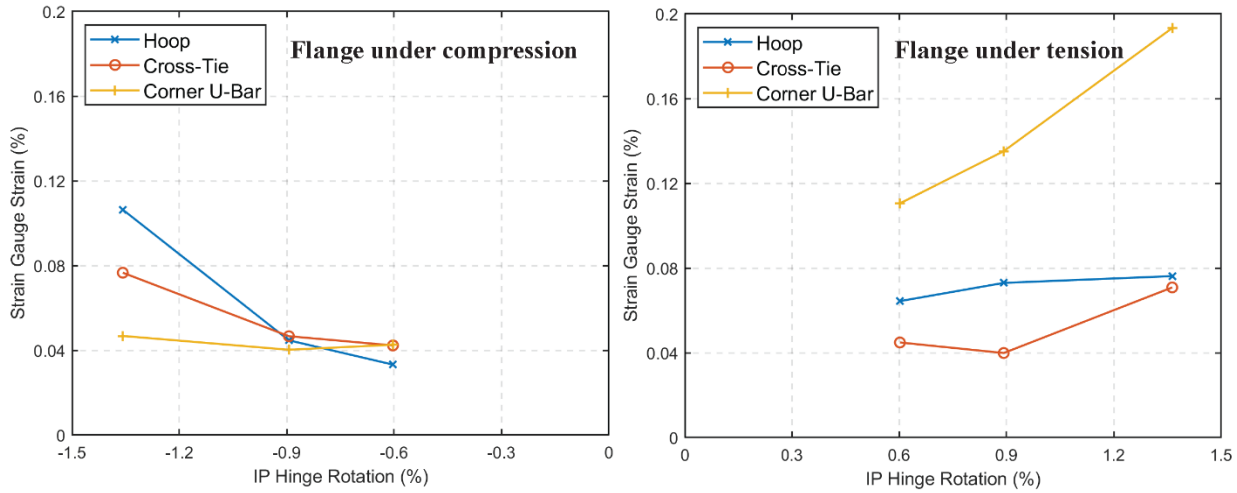

Figure 6-38: West flange transverse reinforcement strain gauge strains, CW-4

6.4 Vertical Growth

The vertical growth during the SLP calculated at the flange edges (Figure 6-37) for negative loading was similar to the values during the in-plane loading of WLP (0.5 in.) for CW-2. However, in the positive direction, due to concrete crushing at the base of the east flange, the vertical growth was lower (0.24 in.) during the SLP than during the WLP. For CW-3, at maximum hinge rotation demand of -1.85%, the vertical growth was 1.1 in., whereas at +1.35% rotation demand, vertical growth was around 0.7 in. (Figure 6-38). For CW-4, similar to the curvatures and the strains, the vertical growth was also smaller at the same rotation demands (±0.6% and ±0.9%) during the SLP compared to WLP (Figure 6-39). At the maximum hinge rotation demands of ±1.35%, the vertical growth was 0.65 in. and 0.55 in. in the negative and positive directions, respectively.

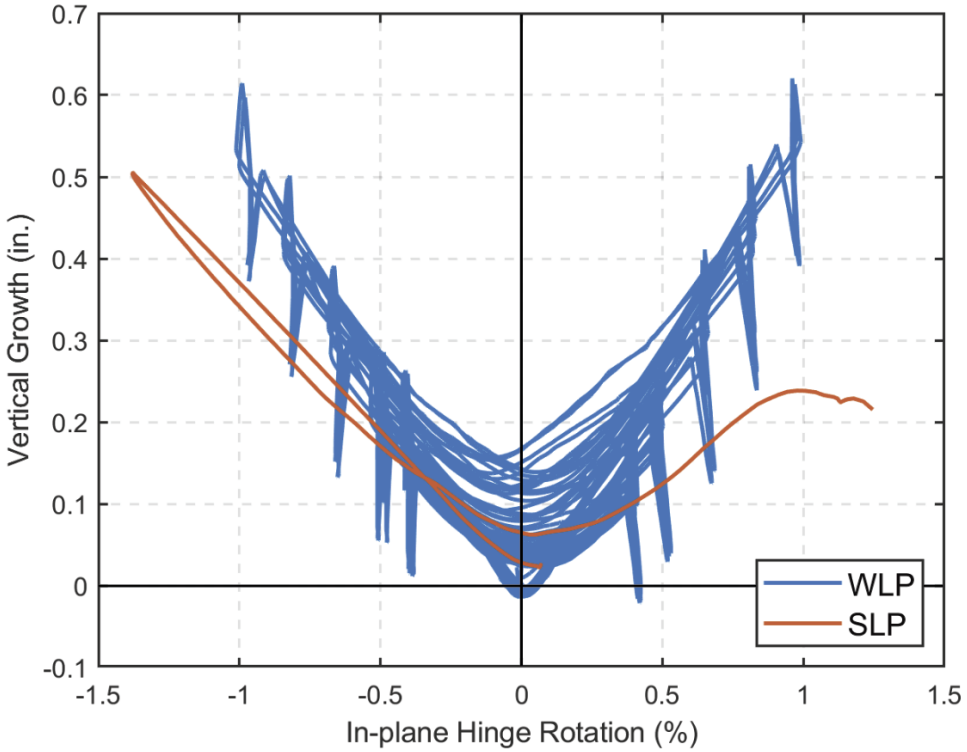

Figure 6-39: IP hinge rotation-vertical growth response of CW-2

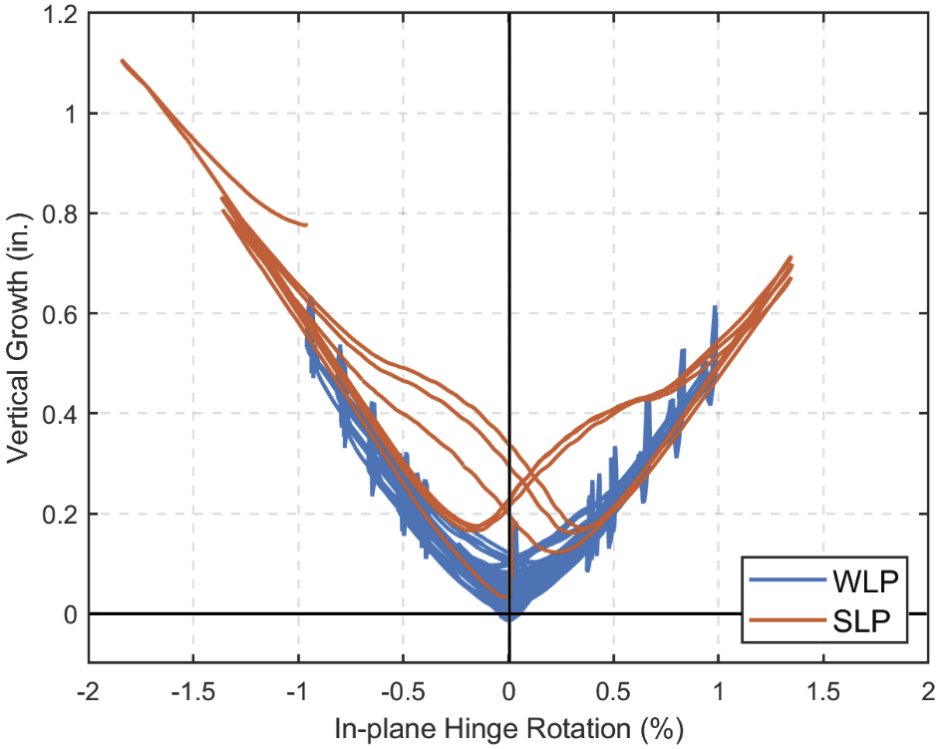

Figure 6-40: IP hinge rotation-vertical growth response of CW-3

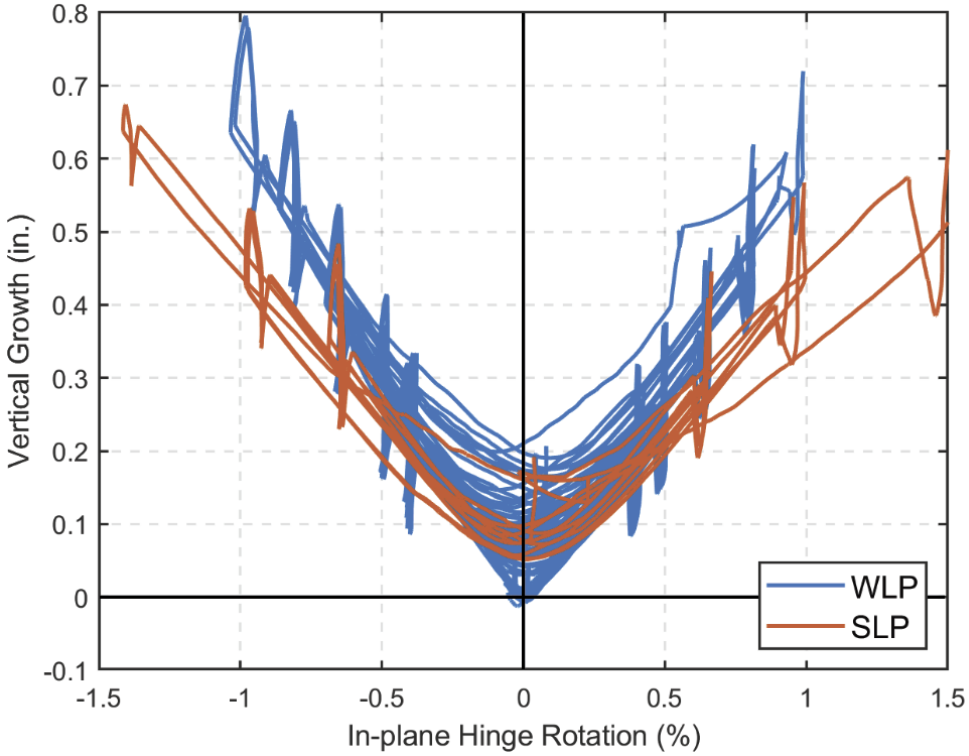

Figure 6-41: IP hinge rotation-vertical growth response of CW-4

6.5 Impact of Lap Splices

The base moment-hinge rotation responses of the walls calculated using an extended plastic hinge length ($L_p=l_w/2+L_s$=57.5 in., Section 5.6) are shown in Figure 6-40, where the star symbols represent the point where the failure occurred. The failure point represents the point where either a sudden strength loss (CW-2, the base moment decreased to 0.25 times the maximum value recorded), the out-of-plane instability of the east flange (CW-3), or 34% strength loss in the OOP direction (CW-4) was observed. The average of the negative and positive hinge rotation demands at the peak demands of the SLP are given in Table 6-3 and also compared to the hinge rotations calculated using $L_p=l_w/2$ (37.5 in.). With the extended hinge length, at the maximum rotation demands of SLP, hinge rotations of 2.39% and 1.76% were calculated for CW-3 and CW-4, and

corresponding rotational ductility ratios were 8.5 and 6.3, respectively. For CW-2, although the rotation demands were higher (1.6%) for $L_p=l_w/2+L_s$ versus using $L_p=l_w/2$ (1.35%), the curvature ductility ratio was lower with the extended hinge length (4.7 versus 5.4). This happened because rotation demands for the 20 in. (L_s) above $l_w/2$ (calculated using the Layer 4 LVDTs, 37.5-57.5 in.) were higher compared to the rotation demands at Layer 4 during SLP.

Table 6-3:Average hinge rotation demands for CW-2, CW-3, and CW-4 at the maximum rotation demands of WLP and SLP

Wall	Loading Protocol	$L_p=l_w/2$		$L_p=l_w/2+L_s$	
		Hinge rotation	Rotation Ductility	Hinge rotation	Rotation Ductility
CW-2	WLP	0.90%	3.6	1.29%	3.8
	SLP	1.35%	5.4	1.60%	4.7
CW-3	WLP	0.90%	3.6	1.18%	4.2
	SLP	1.85%	7.4	2.39%	8.5
CW-4	WLP	0.90%	3.6	1.37%	4.9
	SLP	1.35%	5.4	1.76%	6.3

Note: Values represent the average ones from the positive and the negative in-plane loading directions

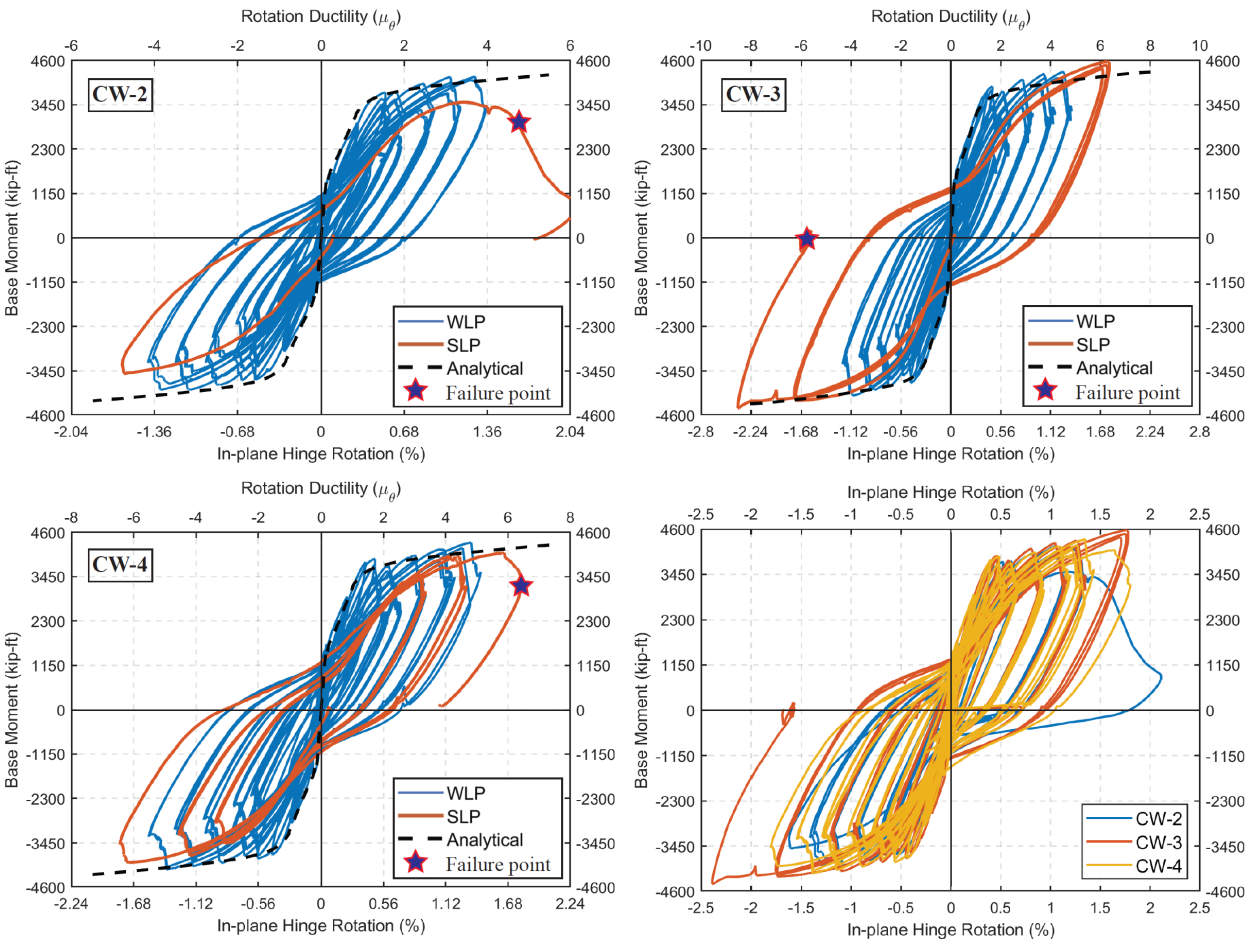

Figure 6-42: In-plane moment-hinge rotation ($L_p=l_w/2+L_s$) of CW-2-3-4 under WLP and SLP

6.6 Summary of Seismic Test Results

The seismic loading protocols were applied to the test specimens after the application of the wind loading protocols to assess the residual strengths and deformation capacities of the walls after extreme wind events. For the wall with significant damage observed during the WLP at the flanges at the wall-footing interface (CW-2) resulting in significant strength loss (0.66 times the $0.5M_{pr,OOP+y}$) during positive OOP loading (flange edges were under compression), one cycle was applied during the SLP. The in-plane plastic hinge rotation capacity of the CW-2 was measured to be 1.35% and 1.6% calculated using $L_p=l_w/2$ and $L_p=l_w/2+L_s$, respectively. Base moment values of 0.84 and 0.67 times the base moment values observed for CW-3 at 1.35% rotation demands ($L_p=l_w/2$) were recorded for CW-2. For the wall with no significant damage observed during the WLP (CW-3), the maximum in-plane hinge rotation capacity of 1.85% and 2.39% were calculated using $L_p=l_w/2$ and $L_p=l_w/2+L_s$, respectively. Given the fact that the failure of CW-3 was due to out-of-plane instability of the east flange at approximately 50 in. above the footing, corresponding to the top of the first story for a full-scale wall, higher hinge rotation capacity is expected in a real building since the floor slab would support wall and prevent the OOP instability failure. The biaxial SLP applied to CW-4 showed that the in-plane hinge rotation capacity of the test specimen under high axial load demands ($P=0.1A_gf'_c$) and under biaxial loading is 1.35% and 1.76% calculated using $L_p=l_w/2$ and $L_p=l_w/2+L_s$, respectively.

The yield moment strength, M_{yE}, and the ultimate moment strength, M_{ultE}, per ACI 369.1-22 were calculated and compared with the effective yield moment ($M_{y,eff}$, Appendix F) and the maximum base moment observed during the experiments. According to ACI 369.1-22, M_{yE} is calculated using ACI 318-19 provisions (at $\varepsilon_c = 0.003$) with the expected material properties and $M_{ultE} = 1.15M_{yE}$. The calculations resulted in M_{yE} = 4087 kip-ft, which is 1.1 times the $M_{y,eff}$ (3700 k-ft). The

maximum in-plane base moment values (CW-3) were +4577 kip-ft ($0.97M_{ultE}$) and -4400 kip-ft ($0.94M_{ultE}$) in the positive and negative directions, respectively. The coefficient of variation given in ACI 369.1-22 for M_y and M_n are 0.14 and 0.15; therefore, the test values are within one standard deviation of the mean values given by ACI 369.1-22. The deformation capacity of the test specimens using the ACI 369.1-22 provisions for nonconforming walls (d_{nl}), defined as the walls with minimum ratio of provided-to-required (per ACI 318-19 Section 18.10.6.4) area of boundary transverse reinforcement $A_{sh,provided}/A_{sh,required} < 0.7$, was calculated as 2.1%. This value was found to be higher than the maximum hinge rotation observed for CW-2; 1.35% and 1.60% calculated using $L_p=l_w/2$ and $L_p=l_w/2+L_s$, respectively. Hinge rotation demands closer to the value predicted using ACI 369.1-22 (2.1%) were observed for CW-3 before the out-of-plane instability of the east flange was observed; 1.85% and 2.39% calculated using $L_p=l_w/2$ and $L_p=l_w/2+L_s$, respectively.

7. Analytical Modeling of the Test Specimens

7.1 General

This chapter focuses on the analytical models used to predict the behavior of the C-shaped walls under the wind and seismic loading protocols using complex nonlinear reinforced concrete wall models. To this end, the open-source structural engineering software called OpenSees (McKenna et al., 2000) was used. The C-shaped structural walls were modeled using the three-dimensional, four-node macroscopic model element called MVLEM-3D (Kolozvari et al., 2021). The MVLEM-3D is an extension of the two-dimensional, two-node Multiple-Vertical-Element Model (MVLEM, Orakcal et al., 2004; Vulcano, 1992; Vulcano et al., 1988). The in-plane behavior (axial, bending, and shear) of the MVLEM are represented by the six in-plane degrees of freedom (DOFs) defined at the centerline nodes of the MVLEM (Figure 7-1). The axial and bending behaviors are governed by the axial strain history of *m* fibers and the constitutive concrete and reinforcement models assigned to these fibers. The plane section assumptions are enforced using the two rigid beams located at the top and bottom of the elements, and the relative rotations of the rigid beams occur around the model centerline at a height of *c* times *h* from the bottom rigid beam (Figure 7-1). The shear behavior is modeled using a horizontal spring located at the same point *(ch)*. More details regarding the 2-node MVLEM can be found in (Orakcal et al., 2004).

MVLEM-3D was defined by using three degrees of freedom (DOFs) at each node of the model, with each DOF including horizontal and vertical translational DOFs and one rotational DOF; therefore, each element includes 12 in-plane DOFs. On the other hand, the out-of-plane behavior is modeled using a four-node Kirchhoff plate finite element formulation. Two rotational and one translational DOF are assigned at each corner (Figure 7-2b). The element deformations in the OOP

direction are assumed to be small compared to IP ones, and linear-elastic behavior is assigned to the plate. The combination of the IP and OOP DOFs resulted in a four-node model with a total of 24 DOFs for the MVLEM-3D element (Figure 7-2). More information regarding the model and implementation of the model in OpenSees can be found in (Kolozvari et al., 2021).

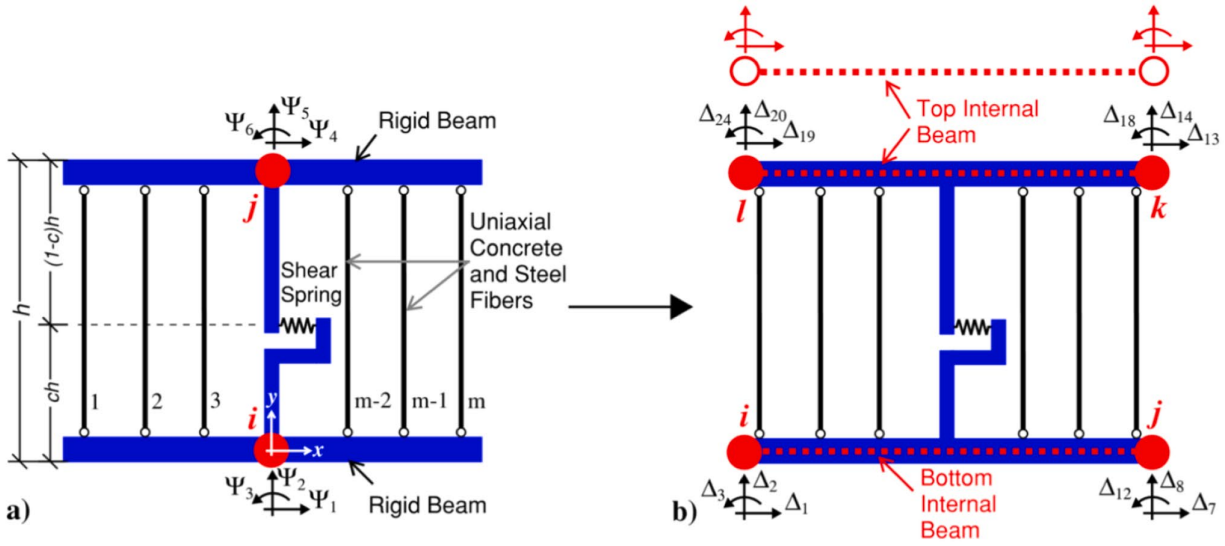

Figure 7-1: Transformation of a) 2-node MVLEM to b) 4-node MVLEM (Kolozvari et al., 2021)

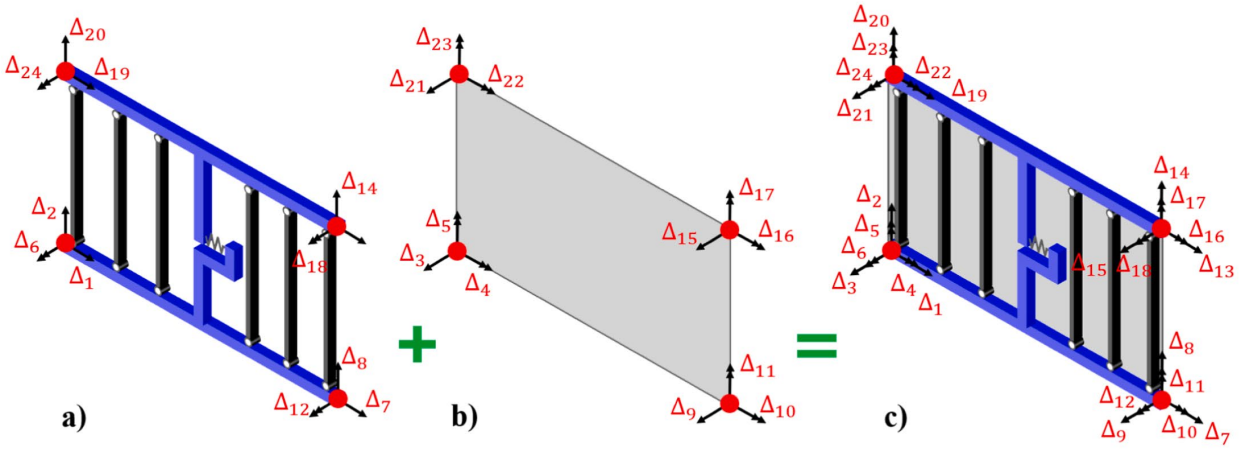

Figure 7-2: Formulation of MVLEM-3D (Kolozvari et al., 2021)

7.2 Model Description

Two different models were developed to predict the experimental behavior, i.e., a simple model and a more detailed model. The difference between these models was the number of MVLEM-3D elements used for the flanges and the web of the C-shaped walls. In the "simple" model, one MVLEM-3D element was assigned to the flanges and the web of the walls. The thickness of the elements was 5 in. in accordance with the thickness of the flange and web. Figure 7-3 shows the first layer elements (as an example). A more detailed model was also created to better estimate the tensile and compressive strains. Five 1 in. thick MVLEM-3D elements were used for the flanges and the webs of the wall segments. Each element was connected with rigid links at the flange edges and the flange-web corners (Figure 7-4). The use of five elements through the wall thickness was selected to achieve improved predictions of the magnitude of the compressive strain values within the compression zone, which likely would improve the potential to predict post-peak compression strains, and thus, strength loss.

A total of 9 and 16 fibers were used for the flanges and the web, respectively, for both models. The discretization of the fibers was based on the distribution of the longitudinal reinforcement and to model the differences in the compressive stress-strain behavior of concrete due to variations in the amount and distribution of transverse reinforcement (i.e., confinement, Section 7.3). The discretization of CW-2 is shown in Figure 7-5. The vertical discretization of the models was done in a way to enable consistent comparison between model strains and strains measured using different layers of LVDTs used in the tests (Figure 2-24 and Figure G-1). Since the test specimens were subjected to moment and shear at the top of the walls (Section 2.4), the resulting shear-span-ratios (SSR) in the in-plane and out-of-plane directions were 4.72 and 5.75, respectively, for CW-2, CW-3, and CW-4. The SSR value in the OOP direction for CW-1 was 4.80. These SSR values

resulted in effective heights of 354 in. in the IP and 173 in. in the OOP (144 in. for CW-1) directions. The IP and OOP lateral loads were applied at these effective heights in the models developed to result in the same shear-span ratios for the tests and the models. A rigid structure was modeled above the wall height (88 in.) for the application of IP and OOP lateral loads (Figure 7-6). Similar to the experimental program, the IP shear was applied as a single point that is located at the center of the mass of the C-walls. The OOP shear was applied at two different locations: the southeast and southwest corners of the web (Figure 7-6). During the experiments, the horizontal actuators used for the OOP load application (Actuators 4 and 5, Figure 2-22) were also used to prevent the specimens from twisting. Similarly, a translational spring with a high stiffness value was used in the y-direction and assigned to the nodes where the OOP load application occurred in the model to prevent torsion. In the experiments, the IP hinge rotations were held constant during the OOP load application. A translation spring in the x-direction was used at the point of the IP load application in the model to create the same loading condition. A high stiffness assigned to this spring prevented the wall from moving in the IP direction during the biaxial loading.

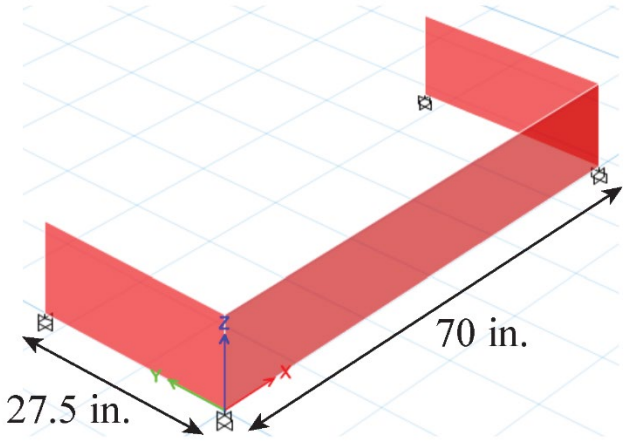

Figure 7-3: Single MVLEM-3D element assigned to the flanges and the web (Simple model)

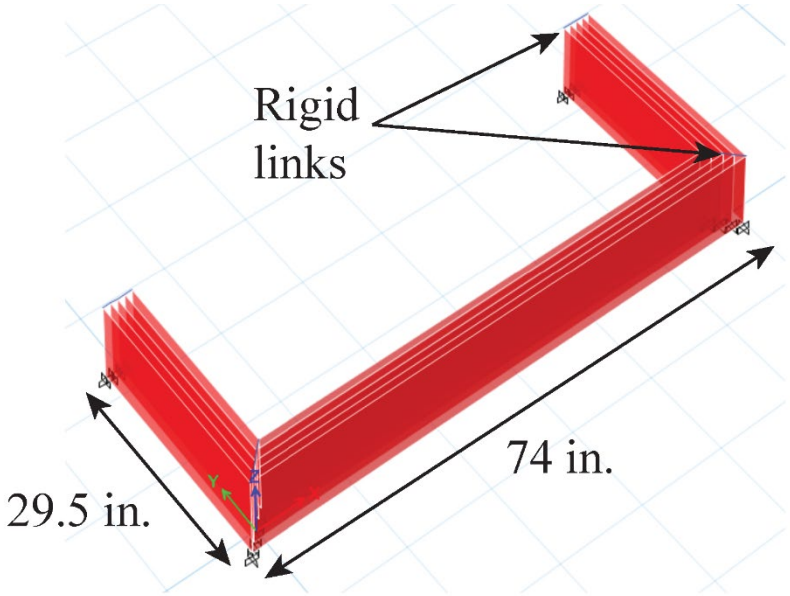

Figure 7-4: Five MVLEM-3D elements assigned to the flanges and the web (Detailed model)

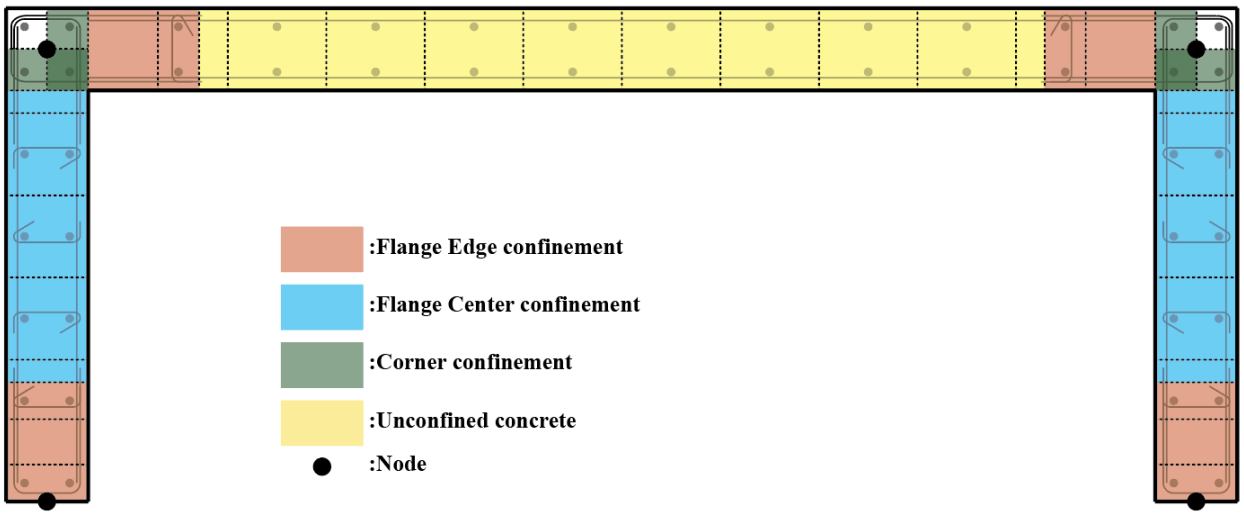

Figure 7-5: Model discretization, CW-2

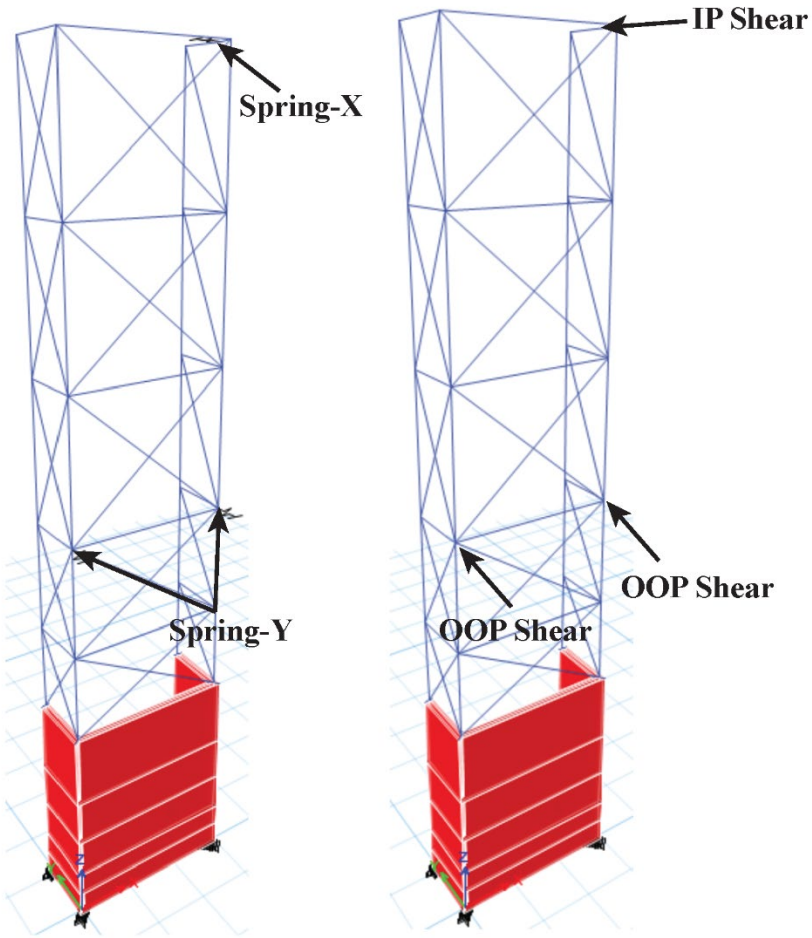

Figure 7-6: Elevation view, location of load application points, and the translational springs

7.3 Material Properties

7.3.1 Concrete

Different concrete constitutive material models were used for different walls. For RCW-1 (instead of CW-1, model results were compared with RCW-1 due to the higher stiffness and base moment values measured for CW-1, Section 4.3.1), the ConcreteCM concrete model (Kolozvari et al., 2015) was used. This model uses the uniaxial hysteretic constitutive model developed by (Chang and Mander, 1994). The ConcreteCM model was used for RCW-1 due to its ability to better capture the pinching behavior of the RC walls, which was more dominant for RCW-1 than for the other

walls. For CW-2, CW-3, and CW-4, the Concrete02 model (Yassin, 1994) was used because of its relatively simple and numerically efficient formulation. The unconfined and confined concrete compression envelope of the models were calibrated using the mathematical models developed by Saatcioglu and Razvi (1992) and Razvi and Saatcioglu (1999), respectively. As shown in Figure 7-5, the unconfined concrete properties were used for the fibers located in the web of the walls, where no crossties were provided. Depending on the transverse reinforcement used (e.g., U-bars, cross-ties, or hoops), different confined concrete properties were assigned to different fibers for the other parts of the walls (Figure 7-5). The material regularization techniques developed by Pugh et al. (2015) were applied to the unconfined and confined concrete properties to create mesh-independent models. Pugh et al. (2015) showed that with regularized material properties, different models with different vertical mesh refinement can result in the same displacement capacity, whereas without regularized material properties, the initiation of strength loss occurs at lower displacement values, and a more rapid loss was observed for the models with smaller vertical elements height (more refined mesh). The stress-strain relationships for the confined concrete (corner confinement) of CW-1 with and without regularization are given in Figure 7-7 as an example.

A sensitivity study was conducted to see the effect of material regularization on CW-1. The detailed model explained in Section 7.2 was used for the sensitivity study. Figure 7-8 shows the base moment-hinge rotation responses of CW-1 with and without material regularization. Since no strength loss or failure was observed during the applied cyclic loading, the same responses were observed from both models. However, under monotonic loading, while the failure occurred at 4.6% rotation demand for the un-regularized model, it occurred at 3.7% for the regularized model,

showing that material regularization only affects the rotation/displacement capacity and the post-strength-loss behavior.

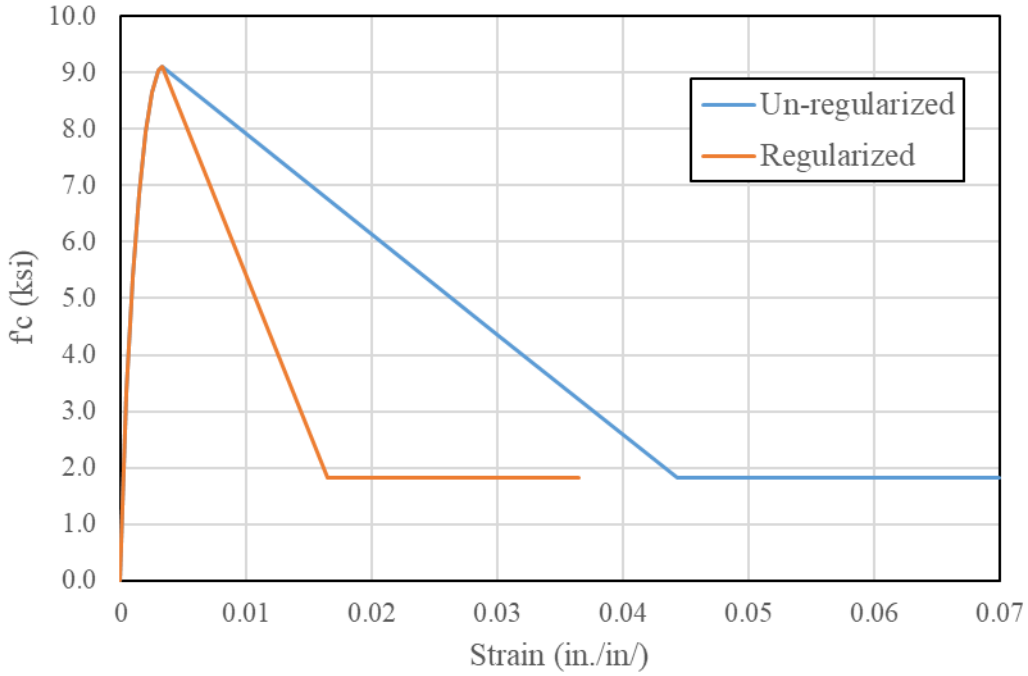

Figure 7-7: Un-regularized and regularized stress-strain relationships for corner confinement of CW-1

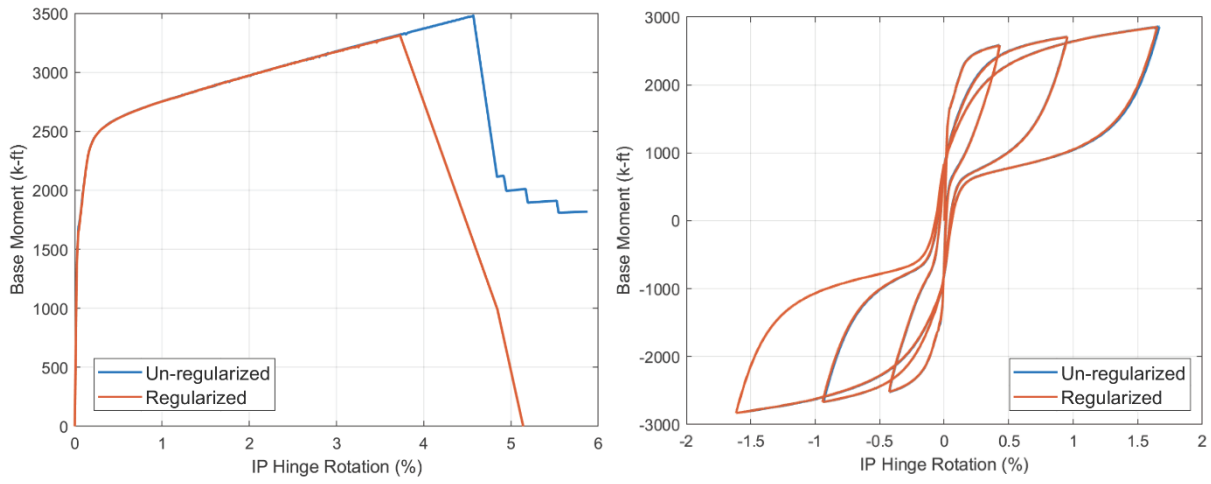

Figure 7-8: Effect of material regularization on monotonic (left) and cyclic (right) base moment-hinge rotation response of CW-1

7.3.2 Reinforcement

The behavior of the steel reinforcement was modeled using the SteelMPF model (Kolozvari et al., 2015), which represents the uniaxial constitutive nonlinear hysteretic material model developed by Menegotto and Pinto (1973) and Filippou et al. (1983). The model was calibrated using the coupon test results conducted in #3 Grade 60 (Figure 7-9) and #4 Grade 80 (Figure 7-10) reinforcement used for the longitudinal reinforcement of CW-1 and CW-2-3-4. The post-yield strain hardening stiffness of the models was selected accordingly to match the response of tested reinforcement reasonably well for the tensile strains less than 4%, which was the maximum tensile strain observed during the tests with the exception of CW-1 Layer 1 LVDTs measuring approximately 5% tensile strains at the maximum rotation demands (Figure 4-19).

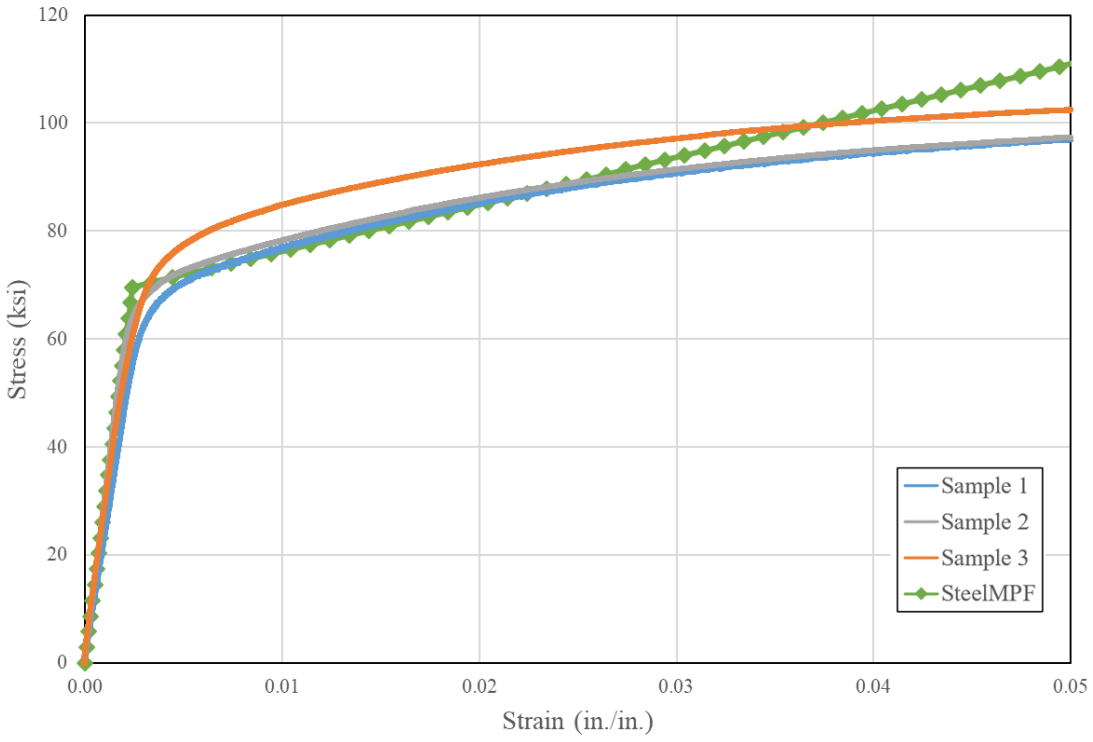

Figure 7-9: Reinforcement stress-strain relationships for #3 Grade 60 bars

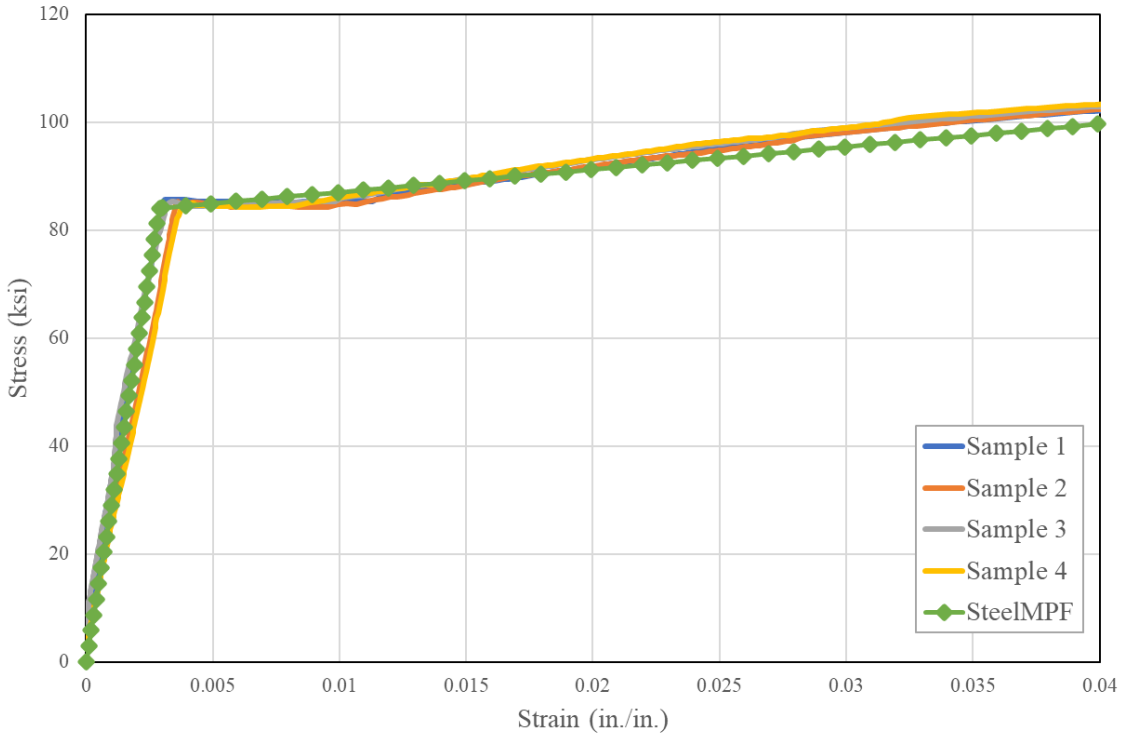

Figure 7-10: Reinforcement stress-strain relationships for #4 Grade 80 bars

7.3.3 Shear Behavior

The in-plane shear behavior of the MVLEM-3D was represented by assigning a linear elastic shear force-deformation relationship to the shear spring of the element (Figure 7-1). Sensitivity studies were conducted by Kolozvari et al. (2021) to estimate the effective shear stiffness of the shear spring. Different flanged walls (T-shaped or U-shaped) tested by Thomsen and Wallace (2004), Beyer et al. (2008), and Constantin (2016) were modeled, and the model results were compared with the experimental results. Based on the sensitivity study results, a shear stiffness of $0.025G$ (G is the shear modulus of concrete) was suggested by Kolozvari et al. (2021) for flanged walls. The concrete shear modulus for C-shaped walls was calculated using $G = E_c/(2(1+\nu))$, where E_c was calculated using Equation 2.9 and the Poisson's ratio (ν) was taken as 0.25.

7.4 Effect of Model Detailing

A pushover analysis was done to compare the "simple" and "detailed" models explained in Section 7.2. CW-2 was used for the comparison, and material regularization was done for both models; therefore, the only difference was the number of MVLEM elements used in the flanges and the web. Figure 7-11 shows the pushover analysis results for the base moment-rotation responses and also the fiber compressive strains measured at the flange-web corner fibers. As can be seen from this figure, the moment-rotation responses of the models were the same. However, a significant difference was observed in the fiber strains. The compressive strains were 2.09 times higher for the detailed model than the simple model at 2% hinge rotation demands. A comparison of the model results with the experimental results showed that the simple model significantly underestimated the compressive strains (Section 7.6.3). Therefore, the detailed model was used for the predictions of C-shaped walls under the wind and seismic loading protocols.

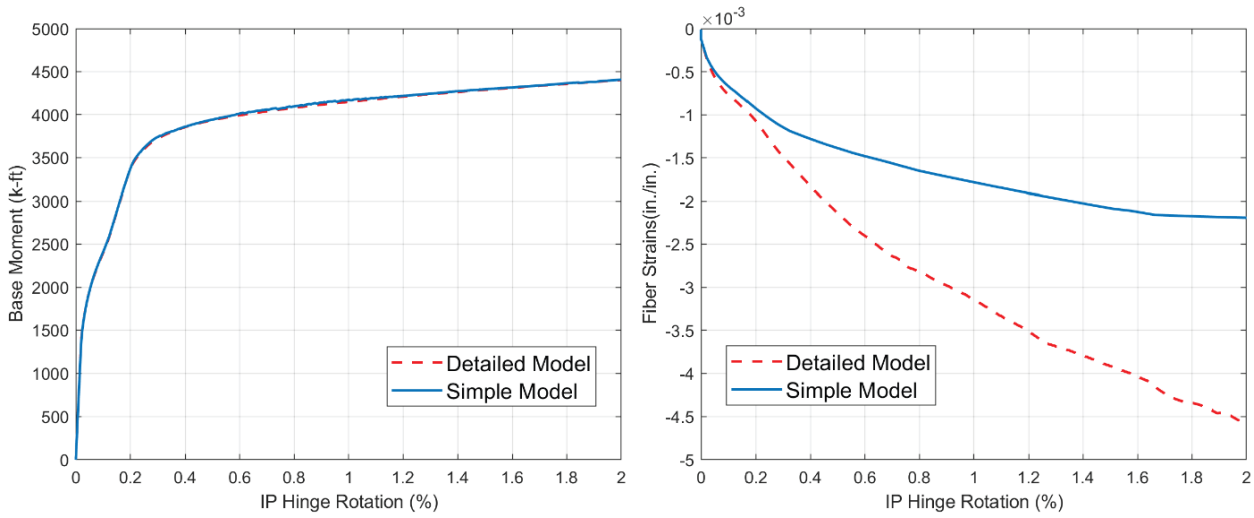

Figure 7-11: Effect of model detailing on base moment-hinge rotation response (left) and fiber compressive strains (right)

7.5 Model Results (RCW-1)

7.5.1 General

This section focuses on the model results of RCW-1. The stroke capacity of hydraulic jacks was reached for CW-1 during the experiments, which resulted in an increase in stiffness and the observed base moment/shear values (Section 4.3.1). Also, there was significant variation in the axial load applied to CW-1, whereas, for RCW-1, less variation in axial load occurred and held essentially constant at $0.1A_g f'_c$ (Section 4.4). Because of these reasons, the model results were compared to the experimental results of RCW-1. Figure 7-12 shows the wind loading protocol used in the model. This loading protocol represented a uniaxial version of the biaxial WLP used for CW-1. The same in-plane base moment and rotation demands were used; however, no biaxial loading (OOP bending moments) and ramp-down loading were applied to RCW-1 and in the model. Given that the biaxial WLP used for CW-1 did not result in any damage, high residual rotation, or strain demands during the testing of CW-1, the uniaxial loading protocol used in the model was found to be sufficient. After the application of WLP shown in Figure 7-12, the seismic loading protocol shown in Figure 2-39 was applied in the model. The same SLP was used for CW-1 and RCW-1 during the experiments.

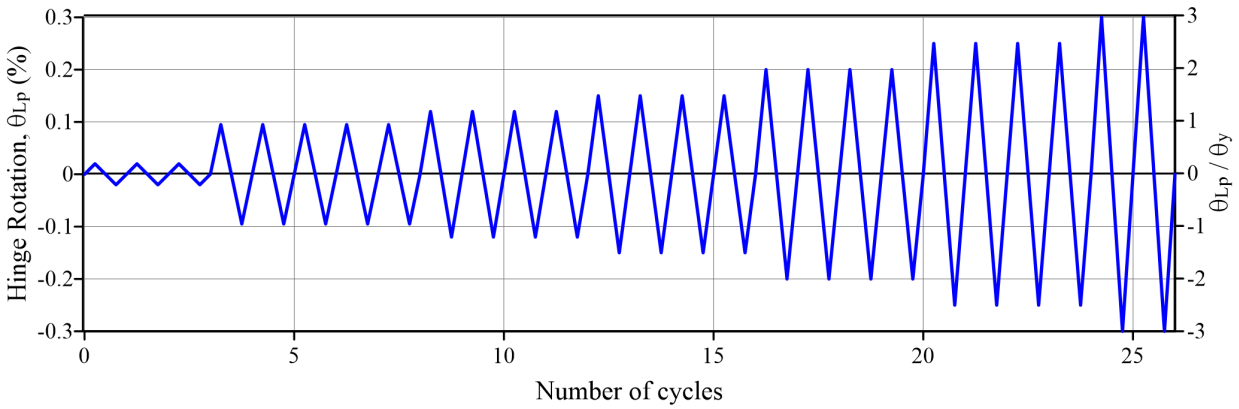

Figure 7-12: The wind loading protocol applied to RCW-1 in the model

7.5.2 Base Moment-Hinge Rotation Response

The hinge rotations in the model were calculated in an equivalent way to the experiments. The vertical displacements of the nodes located at the four corners of the C-wall (at h=L_p=37.5 in.) using the outer layer MVLEM-3D elements of the east and west flanges were used (Figure 7-13). The displacement values of the flange edge and flange-web corner nodes of the same flange were averaged for the rotation calculation.

$$\theta_{Lp,IP} = \frac{\frac{\delta_{NW} + \delta_{SW}}{2} - \frac{\delta_{NE} + \delta_{SE}}{2}}{L_w} \tag{7.1}$$

where δ_{NW}, δ_{SW}, δ_{NE}, and δ_{SE} are the vertical displacements of the nodes shown in Figure 7-13, and L_w is the horizontal distance between the west and the east node (74 in.).

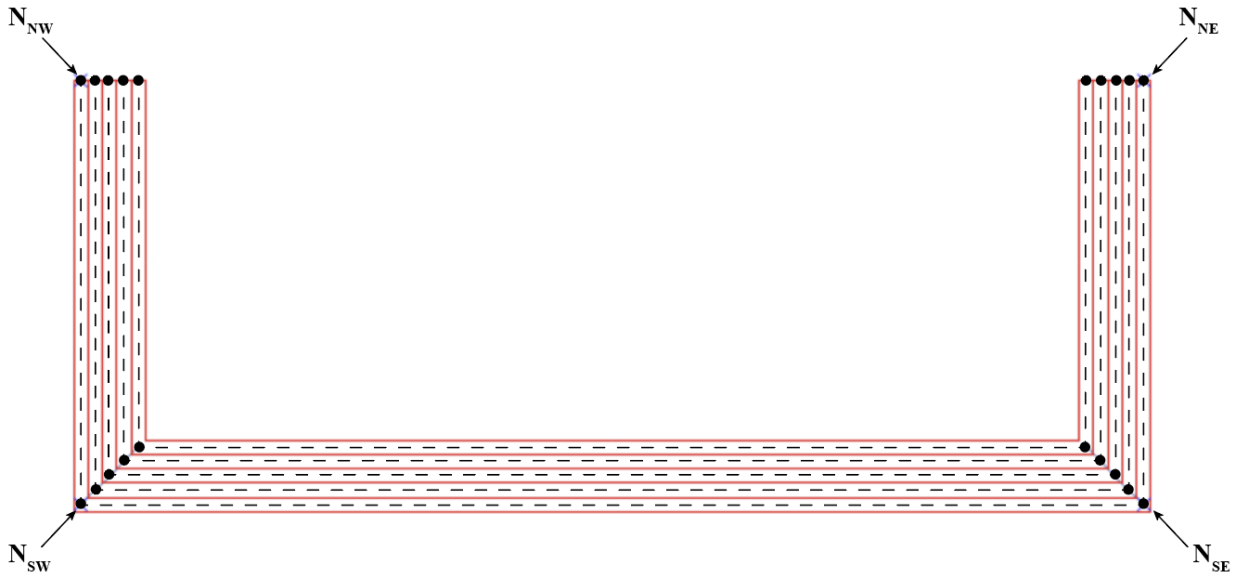

Figure 7-13: MVLEM nodes used for the calculation of hinge rotations

Figure 7-14 shows the comparison of base moment-hinge rotation responses from the tests and the model. The model predicted the strength of the specimen very well, i.e., the base moment values were approximately the same at various hinge rotation demands. The initial stiffness and the effective yield rotations were also found to be similar for the model and the test. For RCW-1, the stiffness at first yield was calculated to be $0.36E_cI_g$ ($0.35E_cI_g$ for CW-1) using Equation 3.6, and in the model, the stiffness value was calculated as $0.45E_cI_g$. The difference between the model and the experimental stiffness can be explained by the fact that the slip/extension deformations were not included in the model, resulting in lower hinge rotation and higher stiffness values. The pinching behavior of RCW-1 was also reasonably predicted by the model, except for the second cycle at ±1.5% hinge rotation demands, where the axial load was not kept constant during the experiments to see the effect of axial load variation in the pinching behavior. In the experiment, axial load values as low as $0.05A_gf'_c$ were observed during the unloading portion of the cycle, which resulted in higher residual rotations at zero loads, whereas, in the model, the axial load was kept constant at $0.1A_gf'_c$.

RCW-1 failed due to longitudinal bar buckling and concrete crushing above the splice region in the experiments with approximately 45% strength loss observed during the first cycle to 2% hinge rotation (when 2% rotation was reached). After the application of two cycles at ±2% hinge rotation demands in the model, no strength loss or failure was observed. It should be noted that neither the splice regions nor bar buckling behavior were considered in the model; therefore, the model did not predict the failure. Buckling of longitudinal reinforcement can be incorporated in the model using the (ε_p^*) approach explained in Appendix A. However, the ε_p^* models predicted the initiation of bar buckling above the splice region at around 2.7% ε_p^* strain demands (Table A-3), whereas

approximately 4% and 5.5% ε_p^* strain demands were measured for RCW-1 and CW-1, respectively, before the failure was observed, suggesting that the ε_p^* strain model might be overly conservative for predicting strength loss of modestly detailed C-shaped walls.

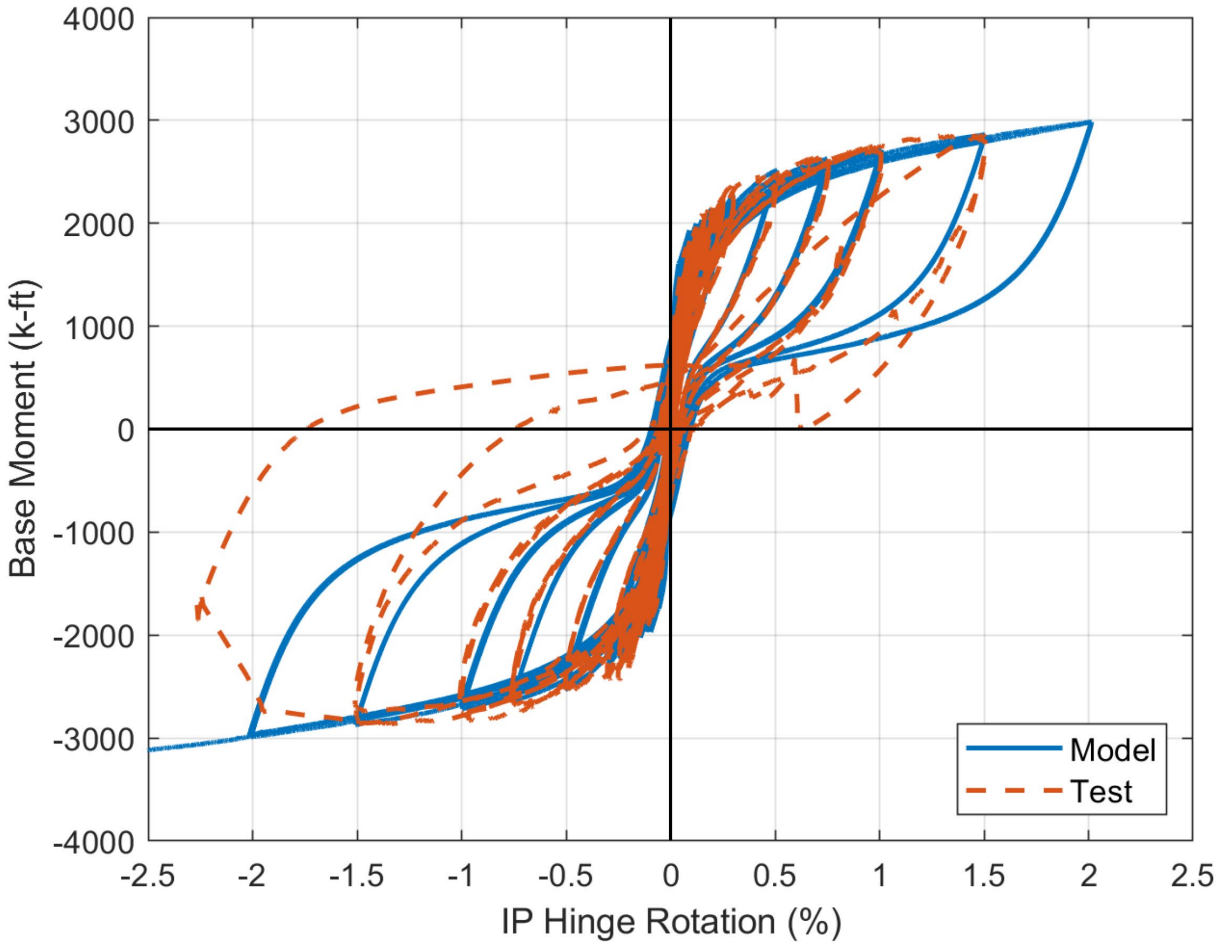

Figure 7-14: Base moment-hinge rotation responses of RCW-1

7.5.3 Axial Strains

Figure 7-15 shows a comparison of tensile and compressive strains measured during the tests (CW-1 and RCW-1) and obtained from the model. The model strains represent the fiber strains at the outer layer east flange MVLEM element and at the fiber closest to the flange edge. The test strains represent the strains estimated at the concrete surface using the Layer 1 east flange edge LVDTs. Since the LVDTs were a couple of inches away from the concrete surface (approximately 4 in.), depending on the neutral axis depth, the surface compressive strains can be overestimated by a factor as high as 2.0 from the LVDT readings. Therefore, the neutral axis depths at different hinge rotations were calculated using the experimental data and the model results. Given the neutral axis depth, the strains at the concrete surface were estimated. The comparisons show that, for hinge rotations less than -1.5%, the model tensile strains were higher than the experimental strains (CW-1), as high as 1.48 times the experimental strains at -0.5%, and as low as 1.13 times the experimental strains at -1.5% hinge rotation demands. However, at the maximum hinge rotation demands, the peak tensile strain values were very close (the model strain was 0.95 times the experimental strain). The compressive stains, on the other hand, were underestimated in the model. At the maximum rotation demands of 2%, the experimental strains were estimated as -0.39%, whereas the model strains were around -0.25%. It should be noted here that it is common for MVLEM to underpredict the compressive strains of the flanged walls (Kolozvari et al., 2021).

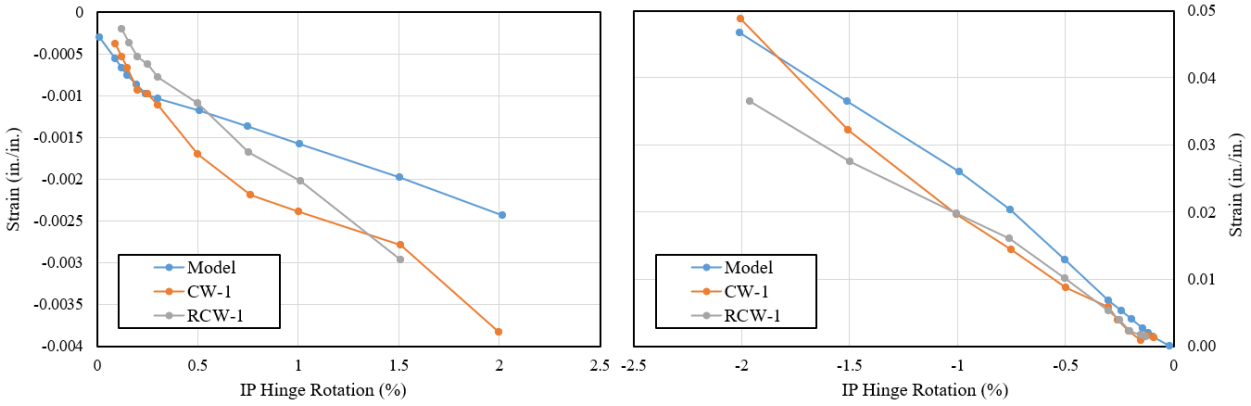

Figure 7-15: Comparison of compressive and tensile strains

7.6 Model Results (CW-2)

7.6.1 General

Figure 7-16 shows the wind loading protocol applied to the model of CW-2. The applied WLP was representative of the one used during the experiments; i.e., the same base moment or hinge rotation demands used in the tests were applied in the model but fewer cycles were applied (especially for the lower demand cycles). The cycles shown in red in Figure 7-16 indicated the biaxial cycles applied to the model. The out-of-plane demands applied to the model were the same OOP hinge rotation demands applied to CW-2 during the testing. The ramp-down loading was not applied in the model because strength loss was observed during the ramp-up loading in the OOP direction, which was not observed in the test. As mentioned in Section 5.3.4, because of the torsion observed during the in-plane loading in the experiments, lower tensile and compressive strains were observed at the flange edges, possibly delaying strength loss due to concrete crushing at the east flange edge and resulting in strength loss during the ramp-down loading. However, in the model, the torsional response of the wall was restrained; therefore, strength loss due to concrete crushing occurred during the ramp-up loading.

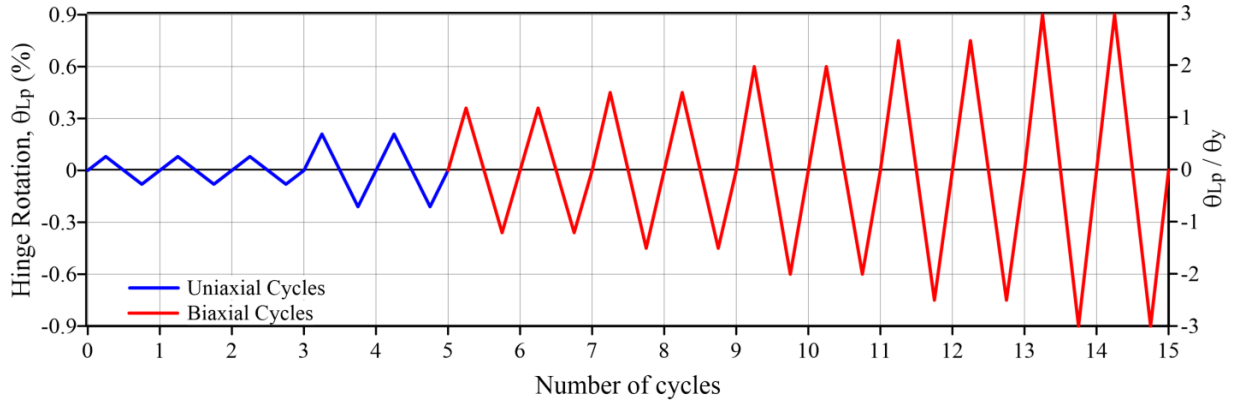

Figure 7-16: The wind loading protocol applied to CW-2 in the model

7.6.2 Base Moment-Hinge Rotation Response

Figure 7-17 shows the comparison of the in-plane base moment-hinge rotation responses from the model and the experiment. The comparison shows that the model can predict the in-plane stiffness, strength, unloading behavior, and displacement capacity of CW-2 reasonably well. The effective lateral stiffness at first yield was calculated as $0.24E_cI_g$ using the experimental results, and $0.31E_cI_g$ using the model results. The difference can be explained due to slip/extension deformations that were not included in the model. The model predicted the base moment capacity of CW-2 in the negative IP direction very well; at maximum WLP rotation demands (-0.9%), the model results were only 4% smaller than the experimental results. On the other hand, in the positive direction, the difference was higher for the inelastic cycles. At 0.9% rotation demands, the model underpredicted the base moment by approximately 10%. During the application of WLP (Figure 7-16), similar to the experimental behavior, stiffness degradation and strength loss were observed in the positive OOP direction (flange edges were under compression, Figure 7-18). At the second cycle of 0.9% IP rotation demands, significant strength loss (approximately 80%) was observed in the OOP base moment capacity due to concrete crushing in the east flange edge. The same behavior

was observed during the experiments (Section 5.3.1). While the strength loss was more gradual during the ramp-down cycles during the tests, it was more abrupt in the model. The same SLP used during testing was applied in the model after the WLP, i.e., one cycle to ±1.35% IP hinge rotation demands. The base moment at -1.35% rotation demand was the same as the experimental value. The slope of the reloading curve to +1.35% was also very well predicted. Strength loss was observed in the experiments starting from 0.95% rotations, and the failure occurred at 1.35% rotations, whereas the failure occurred at 1.15% rotation demands without prior strength loss in the model.

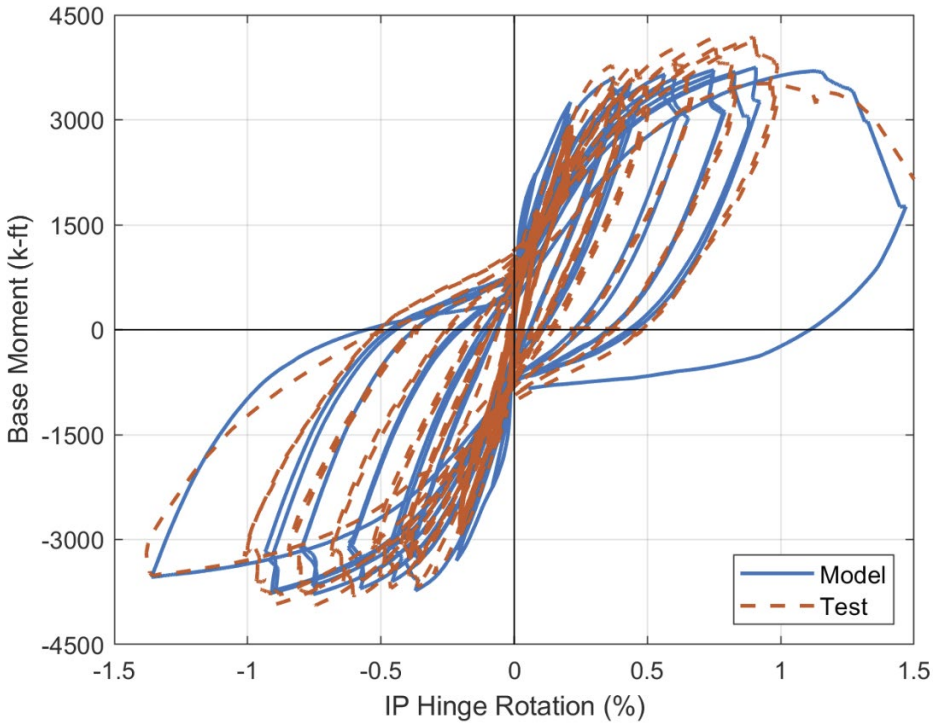

Figure 7-17: IP base moment-hinge rotation responses of CW-2

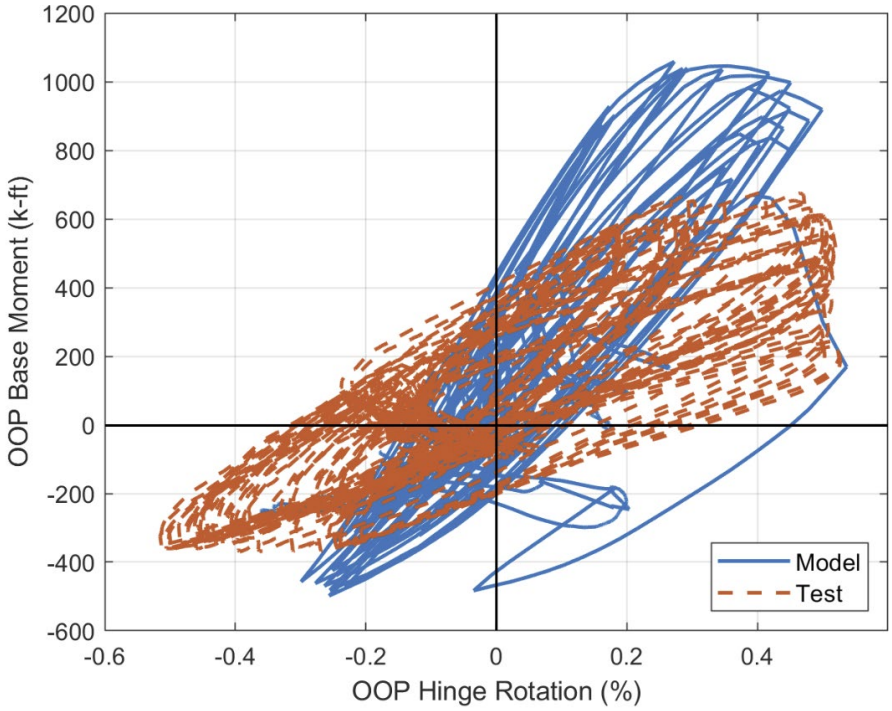

Figure 7-18: OOP base moment-hinge rotation responses of CW-2

Although the model predicted the in-plane behavior of CW-2 well, the out-of-plane base moment-hinge rotation responses differed for the model and the test results. The difference was attributed to the fact that, while some torsion was observed during the test (Figure 5-38), it was restrained in the model. A sensitivity study was conducted to see the effect of torsion on the IP and OOP moment-rotation responses of CW-2. A model with lower stiffness values assigned to the springs used to prevent the wall from twisting was created, and the WLP and SLP were applied. Figure 7-19 shows the moment-rotation responses of the model and compares them with the experimental results. The OOP moment-rotation response was better predicted when the wall was allowed to twist. The OOP stiffness and the moment demands were more comparable with the test results, especially in the negative direction, than the model with restrained torsion. However, the compressive strains were significantly lower (close to zero) at the flange edges because of the

torsion. Therefore, concrete crushing at the flange edges during the OOP bending was not predicted with this model, which resulted in a different in-plane moment-rotation response during the SLP. Given that the in-plane response of the wall is better predicted if the torsion in the models is restrained, twisting was prevented for CW-3 and CW-4. The comparisons suggest that improved modeling or torsional behavior (use of a more sophisticated model) might be needed to improve the predictions (Tura et al., 2024). However, the goal of the modeling studies presented herein were focused on approaches that more likely could be used by engineers applying Performance-Based Wind Design for actual projects, which typically involve large models with many DOFs.

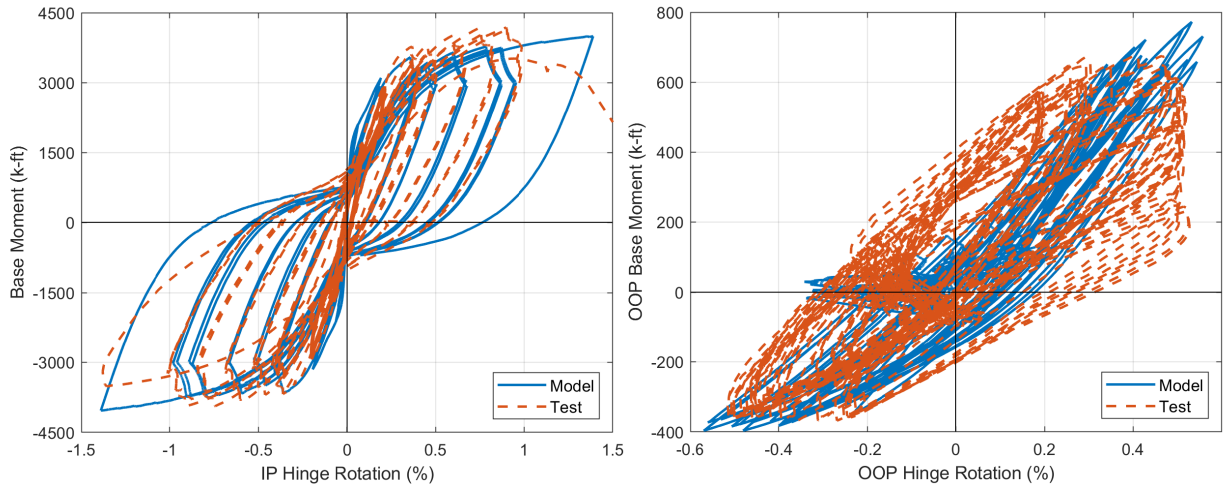

Figure 7-19: IP and OOP base moment-hinge rotation responses for the model without torsional restraints

7.6.3 Axial Strains

Figures 7-20 and 7-21 show a comparison of the compressive and tensile strains, respectively, measured at in-plane loading positions and after the application of OOP moments for the model (with restrained torsion) and the experiment. The model strains were measured at the flange edge fibers of the outer layer MVLEM-3D elements at the base of the wall (Layer 1), whereas the experimental strains at the concrete surface were estimated using the flange edge Layer 1 LVDTs. Since the LVDTs at the splice regions measured very low tensile strains, the strains measured above the splice region were compared with the model results. The model predictions for compressive strains at lower-level hinge rotation demands (0.6% and less) were lower than the experimental strains (approximately 20% to 30% lower). However, at higher rotation demands, the model strains matched the experimental strains very well. At the maximum rotation demands for in-plane loading (-1.35%), the model predicted compressive strain demands within 10% of the test results. The model results were also very close to the experimental values after the application of OOP moments (Pos. B), which shows that more detailed nonlinear models can predict the compressive strain demands under complex loading protocols very well.

The tensile strains above the splice region (the highest tensile strains were measured here during testing) are compared in Figure 7-21. The model tensile strains were found to be lower than the experimental strains; 0.58 and 0.53 times the experimental strains at the maximum hinge rotation demands at Pos. A and Pos. C, respectively. The experimental tensile strains at the flange edges were lower mainly because of the torsion observed during the tests, resulting in higher tensile strains at the flange edges compared to the model where the torsional behavior of the wall was restrained.

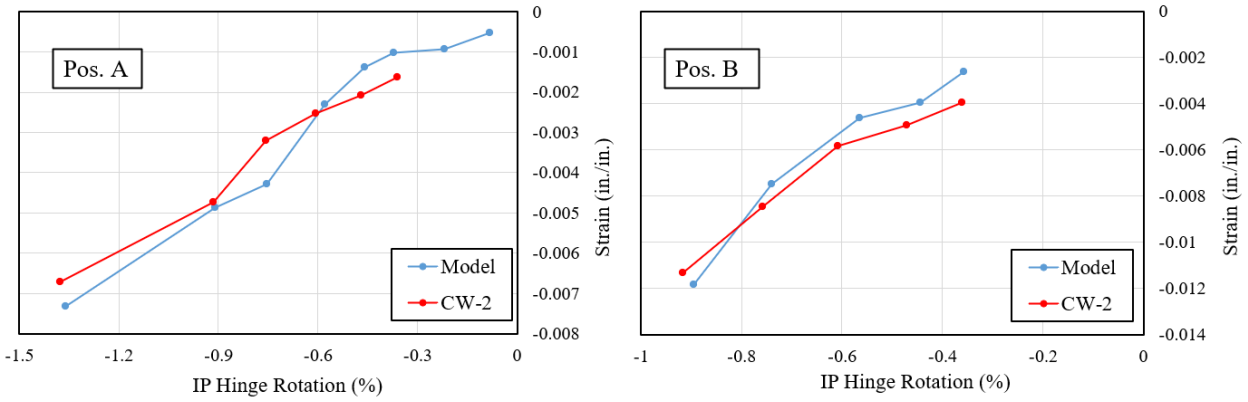

Figure 7-20: Comparison of compressive strains at the flange edges

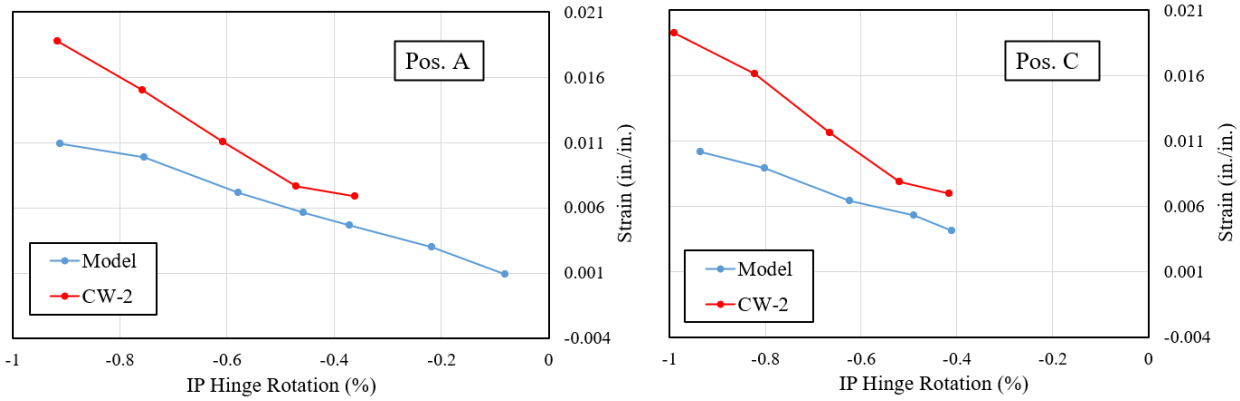

Figure 7-21: Comparison of tensile strains at the flange edges

7.7 Model Results (CW-3)

7.7.1 General

The same wind loading protocol that was applied to CW-2 (Figure 7-16) was also used for CW-3. The differences between the two models were the amount of applied axial load during the biaxial loading (when the flange edges were under compression, $0.1A_g f'_c$ for CW-2 and $0.05A_g f'_c$ for CW-3), and the stress-strain behavior of the flange edge concrete (i.e., concrete confinement, Figure 7-5); U-bars were used for CW-2, whereas, hoops were used for CW-3. After the WLP, the same SLP that was used during the tests (Figure 2-40) was applied in the model.

7.7.2 Base Moment-Hinge Rotation Response

Figure 7-22 shows the in-plane base moment-hinge rotation responses from the experiment and the model results and indicates that the results are very similar. The effective lateral stiffness at first yield was calculated as $0.31E_cI_g$ and $0.35E_cI_g$ for the experimental and test results, respectively. . The base moment demands from the model results were symmetric, i.e., the same values were observed in the positive and negative directions. However, for the experimental values, the base moment demands were higher in the positive direction, resulting in 9% lower demands for the model compared to the experimental values at the maximum positive hinge rotation demands. The model and the experimental base moment values were very similar in the negative direction. Similar to the experimental behavior, no strength loss was observed in the OOP direction during the biaxial cycles of the WLP (Figure 7-23) prior to the observed failure due to out-of-plane instability of the east flange after the unloading part of the half cycle to -1.85% IP hinge rotation demands during the experiments. However, since out-of-plane instability behavior

was not considered in the model, the failure was not predicted by the model. After one cycle to ±1.85% hinge rotation demands, no strength loss was observed in the model.

The maximum reinforcement tensile strain (ε_{sm}) to maintain lateral stability of RC walls was calculated using the recommendations of (Paulay & Priestly, 1993).

$$\varepsilon_{sm} \leq 8\beta \left(\frac{b}{l_o}\right)^2 \xi_c \tag{7.2}$$

where β is the ratio of transverse effective depth (d) to wall thickness (b) and l_o is the buckled length of the wall, which can be taken as the plastic hinge length of the wall (L_p). (Paulay & Priestly, 1993) recommended the L_p to be calculated as:

$$L_p = (0.2 + 0.044A_r)l_w \tag{7.3}$$

where A_r is the aspect ratio of the wall (h_w/l_w). The eccentricity ratio of ξ_c in Equation 7.2 can be calculated as:

$$\xi_c = 0.5(1 + 2.35m - \sqrt{5.53m^2 + 4.70m}) \tag{7.4}$$

where $m = \rho f_y/f'_c$ and ρ is the longitudinal reinforcement ratio in the region of the wall where buckling is being considered. The ε_{sm} was also calculated using the recommendations of (Chai & Elayer, 1999).

$$\varepsilon_{sm} = \frac{\pi^2}{2}\left(\frac{b}{l_o}\right)^2 \xi_c + 3\varepsilon_y \tag{7.5}$$

Table 7-1 shows the comparison of ε_{sm} values calculated using Pauley and Priestly (1993) and Chai and Elayer (1999) with L_p values calculated using Equation 7.3 and $L_p=l_w/2$. Comparison of the ε_{sm} values from Table 7-1 with maximum tensile strain measured for CW-3 during the SLP at the east flange edge Layer 4 LVDT (the region of the wall where global buckling was observed), $\varepsilon_{t,max}$ = 3% (Figure 6-29), indicate that the ε_{sm} values significantly overestimated the maximum tensile

strains if L_p is calculated using Equation 7.3. The maximum tensile strains were closer to the experimental values with $L_p=l_w/2$; however, they were underestimated for both approaches, i.e., ε_{sm} = 2.3% and 2.6% calculated with Equations 7.2 and 7.5, respectively. However, it is noted that the Pauley and Priestly (1993) model was developed based on tests of rectangular wall cross sections where peak tensile strains only occur at the extreme fiber, whereas for C-shaped wall flanges subjected to in-plane loading, nearly uniform, large tensile strains occur over the entire flange width.

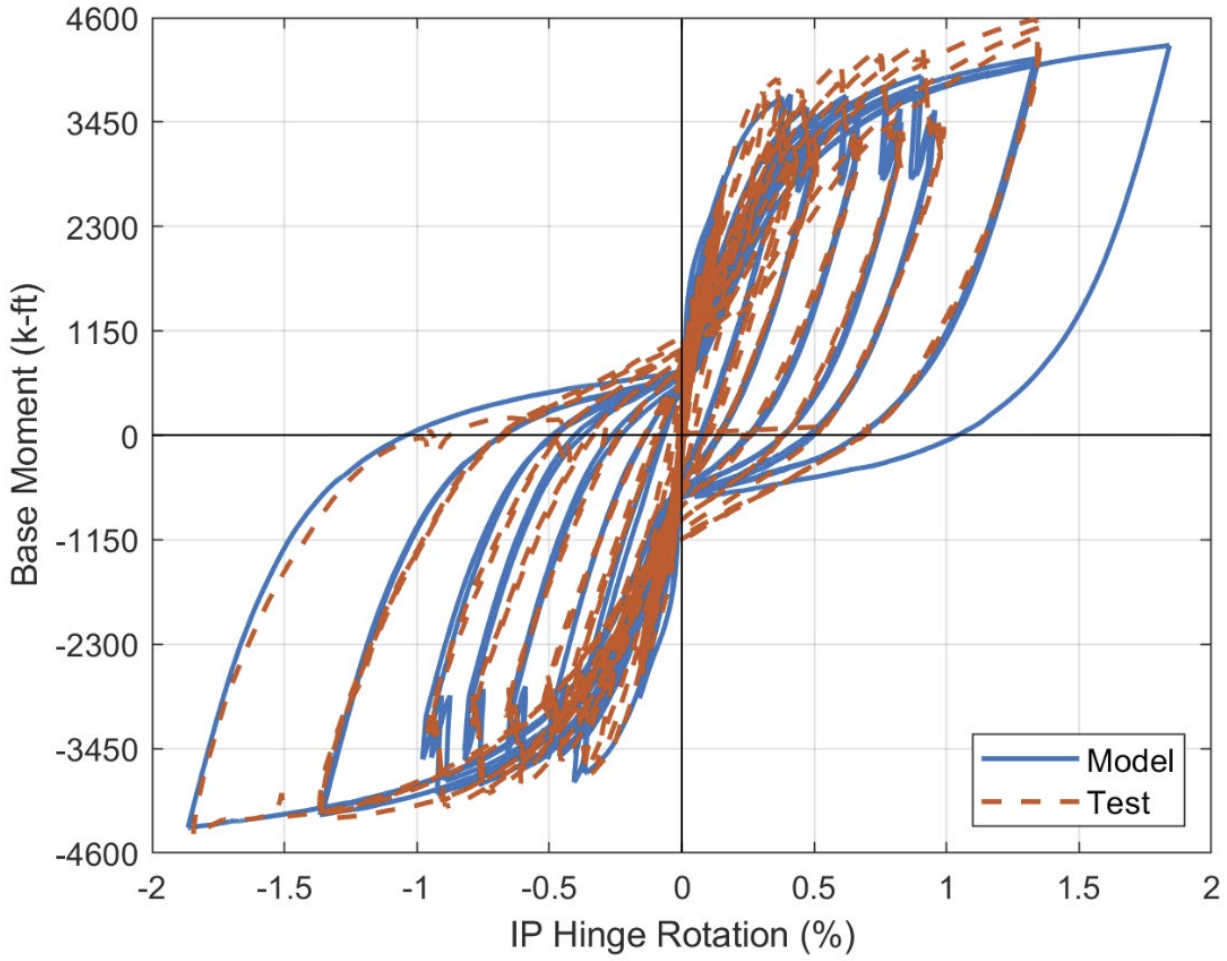

Figure 7-22: IP base moment-hinge rotation responses of CW-3

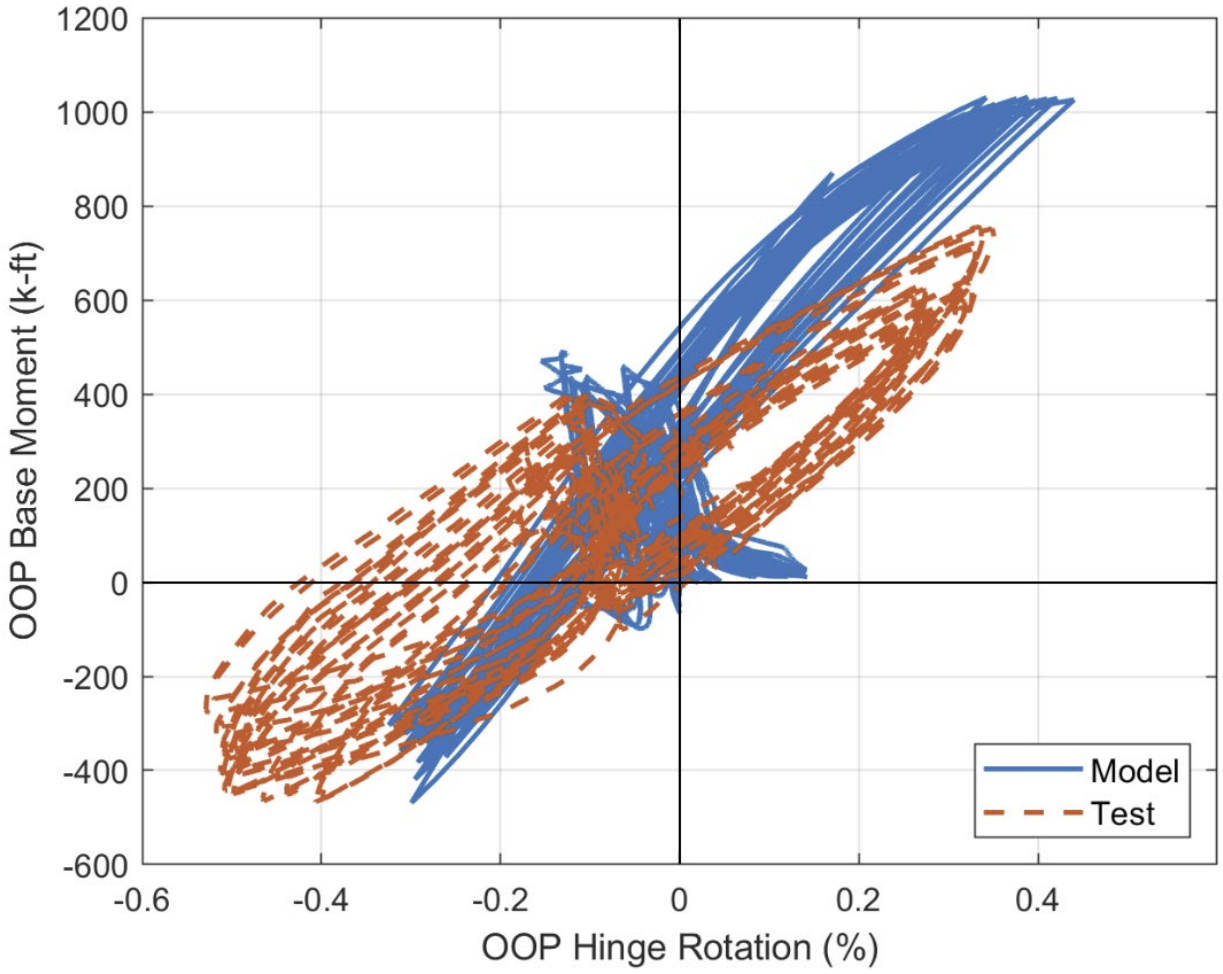

Figure 7-23: OOP base moment-hinge rotation responses of CW-3

Table 7-1: Maximum tensile strains (ε_{sm}) based on Paulay and Priestly (1993) and Chai and Elayer (1999)

	Paulay and Priestly (1993)	Chai and Elayer (1999)
L_p = 19 in. (Eq. 7.3)	0.090	0.076
L_p = 37.5 in. (l_w/2)	0.023	0.026

7.7.3 Axial Strains

Figures 7-24 through 7-27 show a comparison of the compressive strains at the flange edges and flange-web corners under the in-plane loading only (Pos. A and D) and after the application of OOP demands (Pos. B, E, C, and F). The model results show the strains measured at the outer layer flange MVLEM-3D elements and at the fibers representing the positions where the LVDTs were attached to the specimen during the tests, e.g., the corner LVDTs were attached approximately 5 to 7 in. north of the flange-web corners (Figure 2-28). The experimental strains at the concrete surfaces were estimated using the Layer 1 LVDTs and predicted neutral axis depths. The comparisons show that, in general, the model results matched the experimental values very well, especially during the in-plane loading. After the application of OOP moments, the model strain values are larger than the experimental strain values for the west flange edges. This was because of the significant amount of torsion observed in the test when the west flange was under compression, resulting in lower compressive strains than the model where torsion was restrained. Tensile strains (at the flange edges) were also compared (Figure 7-28) from the model and test results. The highest strains were measured above the splice region during testing; therefore, for direct comparison, the model tensile strains above the splice region are shown in Figure 7-28. The comparison revealed that the model strains were lower than the experimental strains; 0.7 and 0.5 times the experimental strains at the maximum positive (+1.35%) and negative (-1.85%) hinge rotation demands. The experimental tensile strains were higher, possibly because of the torsion, which increased the tensile strains at the flange edges.

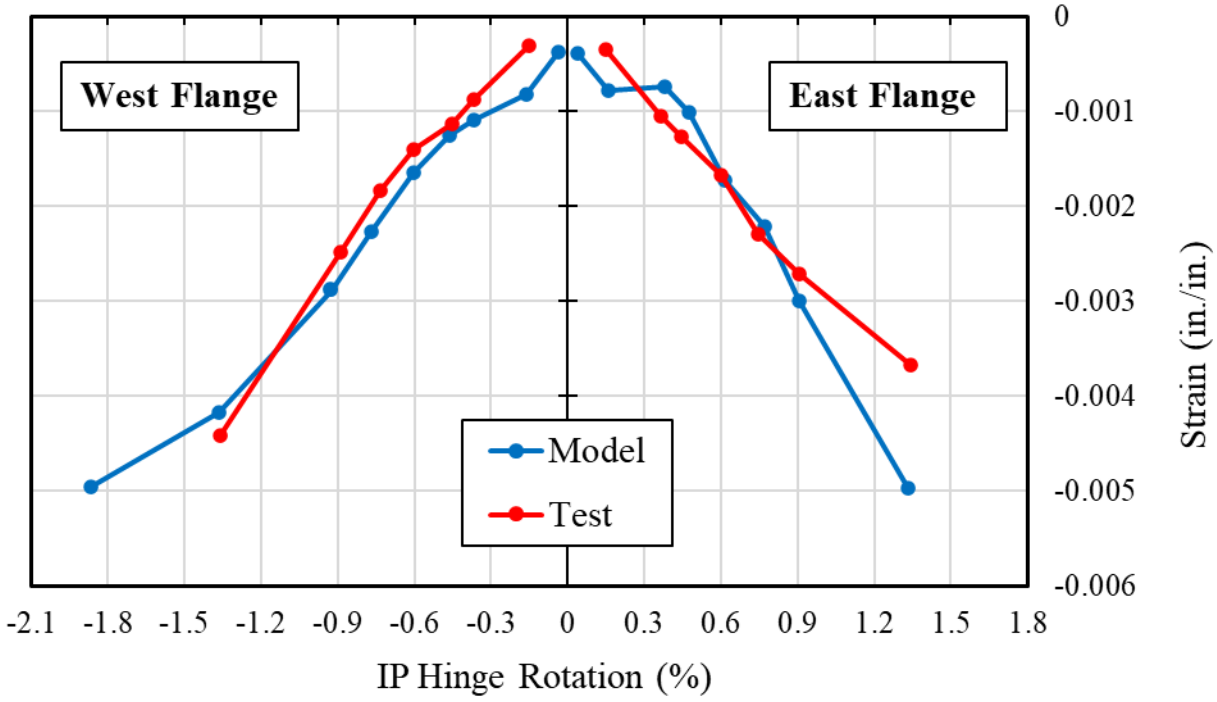

Figure 7-24: Comparison of compressive strains at the flange edges (Pos. A and D)

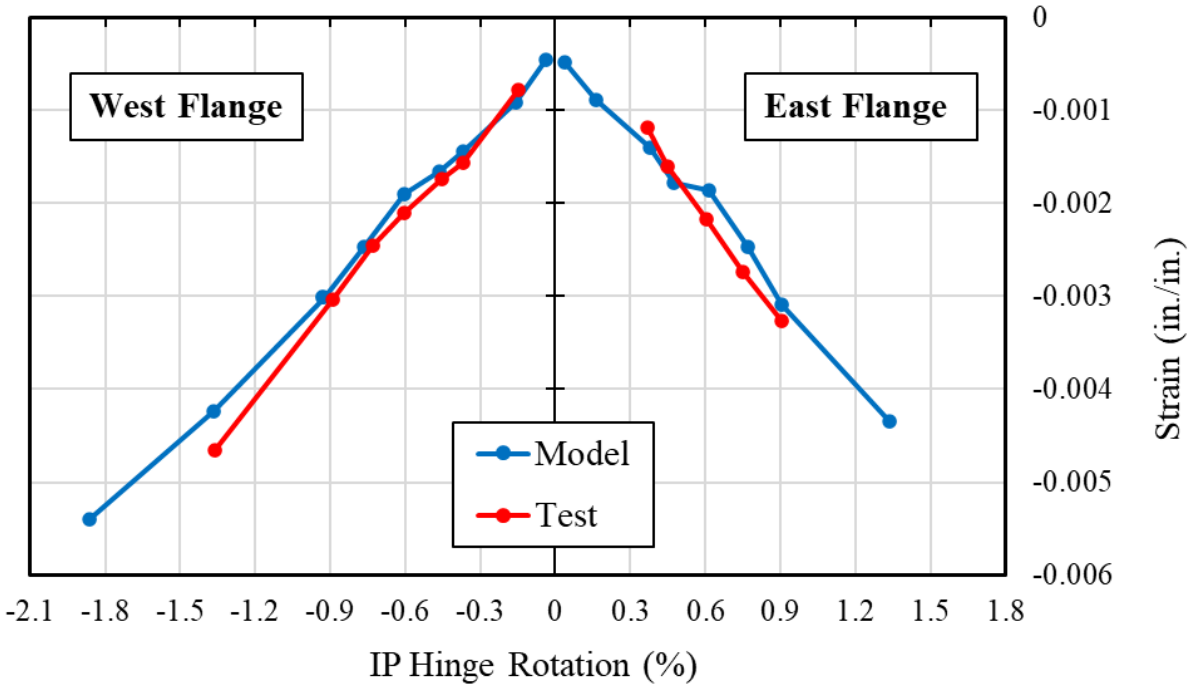

Figure 7-25: Comparison of compressive strains at the flange-web corners (Pos. A and D)

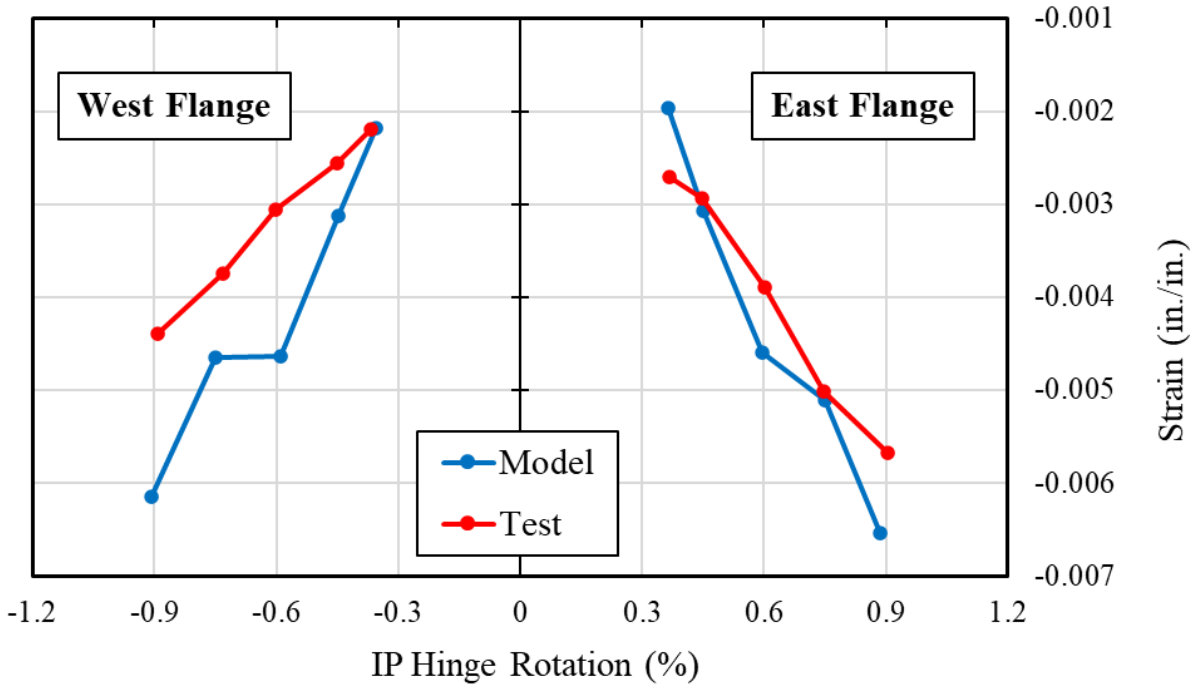

Figure 7-26: Comparison of compressive strains at the flange edges (Pos. B and E)

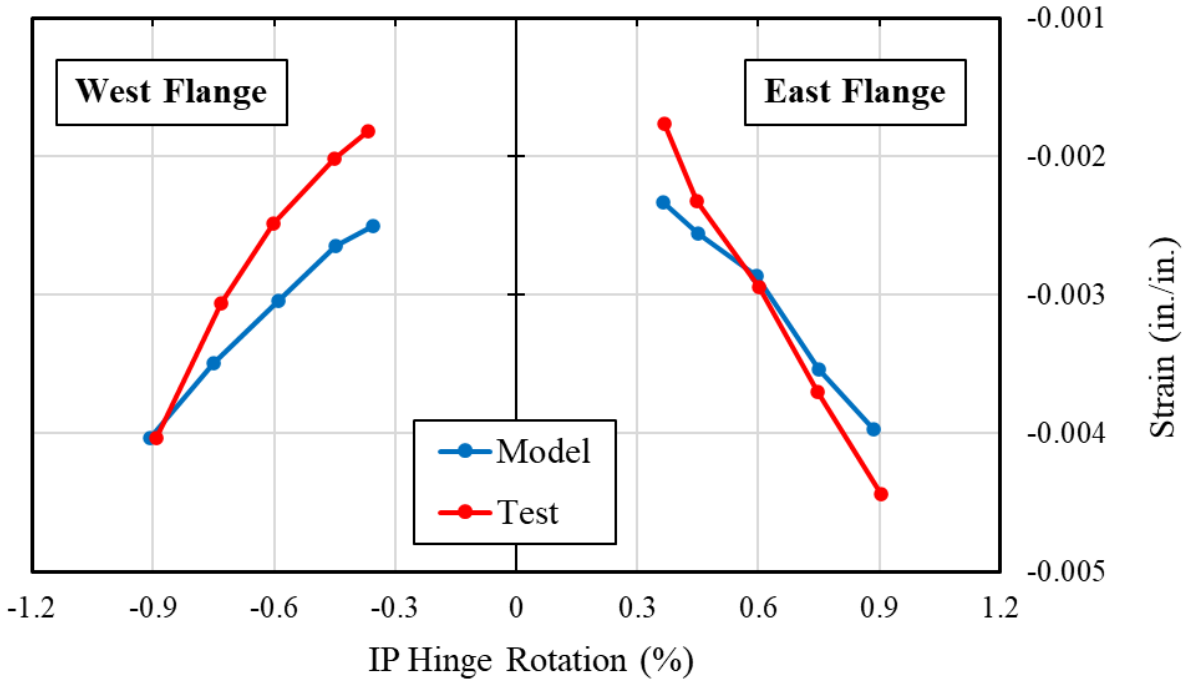

Figure 7-27: Comparison of compressive strains at the flange-web corners (Pos. C and F)

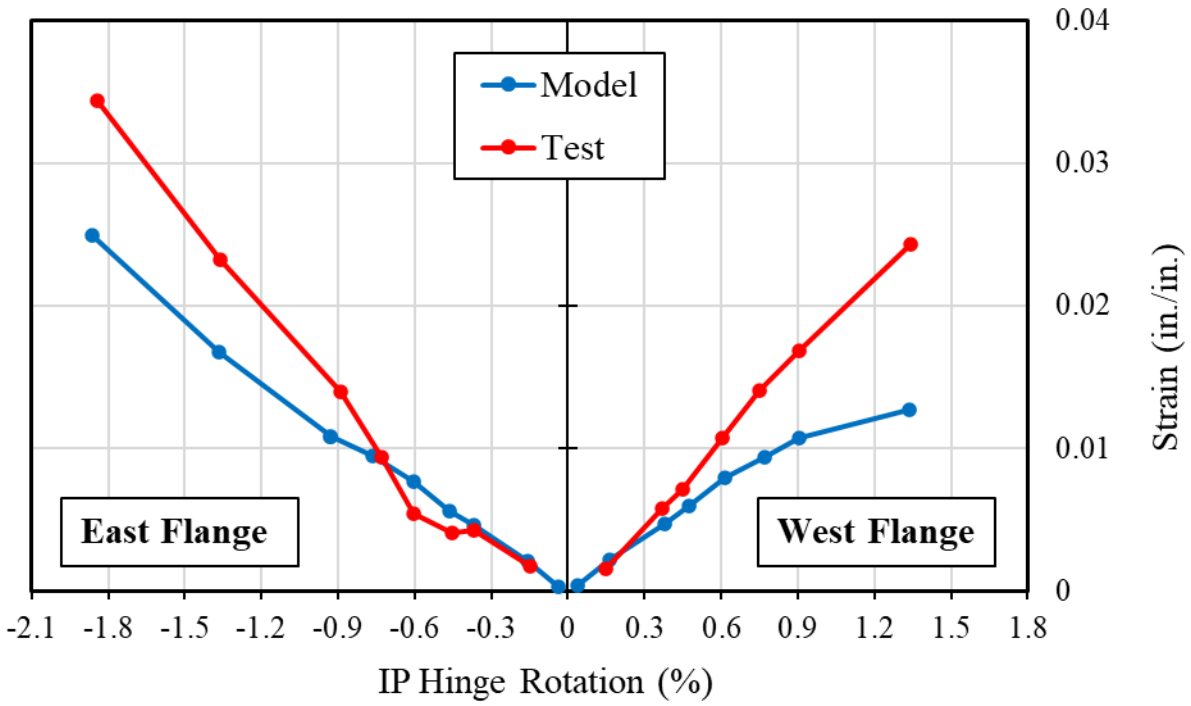

Figure 7-28: Comparison of tensile strains at the flange edges (Pos. A and D)

7.8 Model Results (CW-4)

7.8.1 General

The WLP shown in Figure 7-16 was applied to the model of CW-4. The axial loading during the OOP loading, which was held constant at $0.1A_g f'_c$ for CW-2 and $0.05A_g f'_c$ for CW-3, was decreased to $0.075A_g f'_c$ for CW-4 when flange edges were under compression. After the WLP, the SLP consisted of applying two biaxial cycles at $2.0\Theta_y$ and $3.0\Theta_y$, and one biaxial cycle at $4.5\Theta_y$ (Figure 2-41). However, as opposed to WLP, the axial load during the application of OOP loading was not decreased but held constant at $0.1A_g f'_c$.

7.8.2 Base Moment-Hinge Rotation Responses

Figure 7-29 shows the comparison of the in-plane base moment-hinge rotation responses calculated using the model and the experimental results. The model predicted the strength, stiffness, and pinching behavior of the CW-4 very well. The effective lateral stiffness at first yield calculated using the model results, $0.31E_cI_g$ and $0.33E_cI_g$ in the positive and negative directions, were very similar to the experimental values, $0.29E_cI_g$ and $0.32E_cI_g$ in the positive and negative directions, respectively. The base moment at the maximum hinge rotation demands during the WLP (±0.9%) for the model were also very similar to the experimental results, i.e., 0.93 and 0.99 times the experimental values at the positive and negative directions, respectively. Similar to the experimental results, no strength loss was observed during the WLP. During the SLP, at the same rotation demands as applied during the WLP, the model base moment values were also similar to the values observed during testing, i.e., at ±0.9% rotation demands of the SLP, the model base moment values were 0.92 and 0.99 times the experimental values. At the 1.35% rotation demands of the SLP, very similar to the experimental results, the model base moment values were 0.86 and 0.94 times the values recorded for CW-3. Figure 7-30 shows the out-of-plane base moment-hinge

rotation responses of the model and the experiment. The last cycles in the OOP direction applied at +1.35% IP hinge rotation demands are shown with black dashed lines in Figure 7-30. During testing, at the last cycle, the maximum OOP base moment was approximately 0.8 times the base moment values applied in previous cycles. In the model, a maximum OOP base moment value of 0.64 times the maximum OOP base moment value applied previously was observed before sudden strength loss occurred due to concrete crushing at the east flange edge, which resulted in base moment values 0.35 times the maximum value recorded. Although the strength loss was more abrupt in the model compared to the experiment, the model was able to capture the concrete crushing at the same in-plane hinge rotation demands (+1.35%) as the experimental demands.

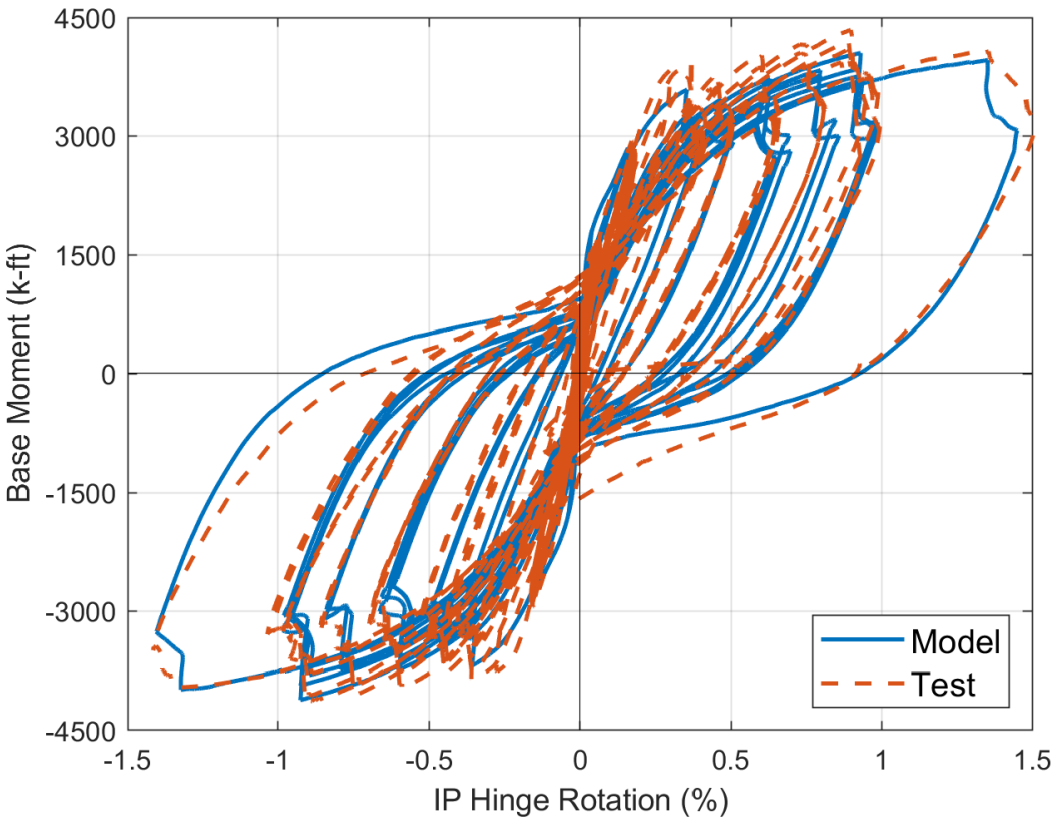

Figure 7-29: Comparison IP base moment-hinge rotation responses

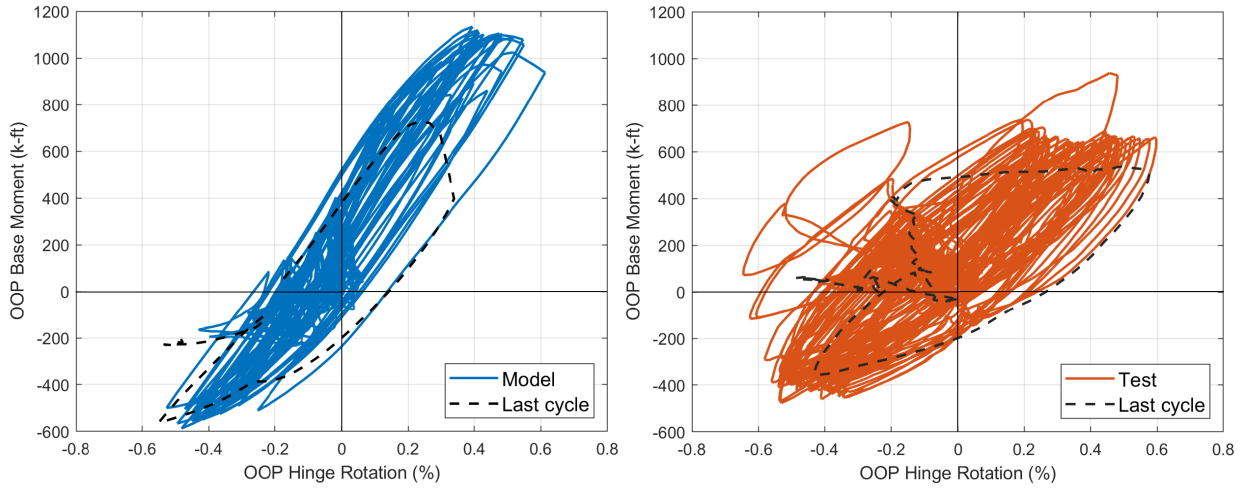

Figure 7-30: Comparison OOP base moment-hinge rotation responses

7.8.3 Axial Strains

Figures 7-31 through 7-34 show a comparison of the compressive strains at the flange edges and flange-web corners under in-plane loading only (Pos. A and D) and after the application of OOP demands (Pos. B, E, C, and F). The model results show the strains measured at the outer layer flange MVLEM-3D elements and at the fibers representing the positions where the LVDTs were attached to the specimen during the tests. The experimental strains at the concrete surfaces were estimated using the Layer 1 LVDTs and predicted neutral axis depths. In general, the model strain predictions were lower than the experimental values, except for the east flange edge at Pos. E, where the model results were higher. The model and experimental values were closest at the maximum WLP hinge rotation demands (±0.9%). At hinge rotation demands higher than ±0.9% rotation demands, i.e., at ±1.35% rotation demands of the SLP, the model predictions were higher than the experimental values. Figure 7-35 shows the tensile strains from the model and the experimental results at the flange edges at Pos. A and D. The comparison of the model and experimental results showed different behavior for the east and west flanges. For the east flange,

the model results were as high as 1.83 times and as low as 1.33 times the experimental results, whereas, for the west flange, the model results were lower; approximately 0.8 times at the lower level rotation demands (less than 0.75%) and 0.6 times the experimental values at the higher level demands. The differences between the flange edge tensile strains in the experimental results might be due to different torsional behaviors observed for different flanges, i.e., when the east flange was under tension, high positive OOP rotations (0.7%) were calculated for the east flange which decreased the tensile strains at the east flange edge, whereas, the OOP rotations were closer to zero for the west flange when the west flange was under tension (Figure 5-40a).

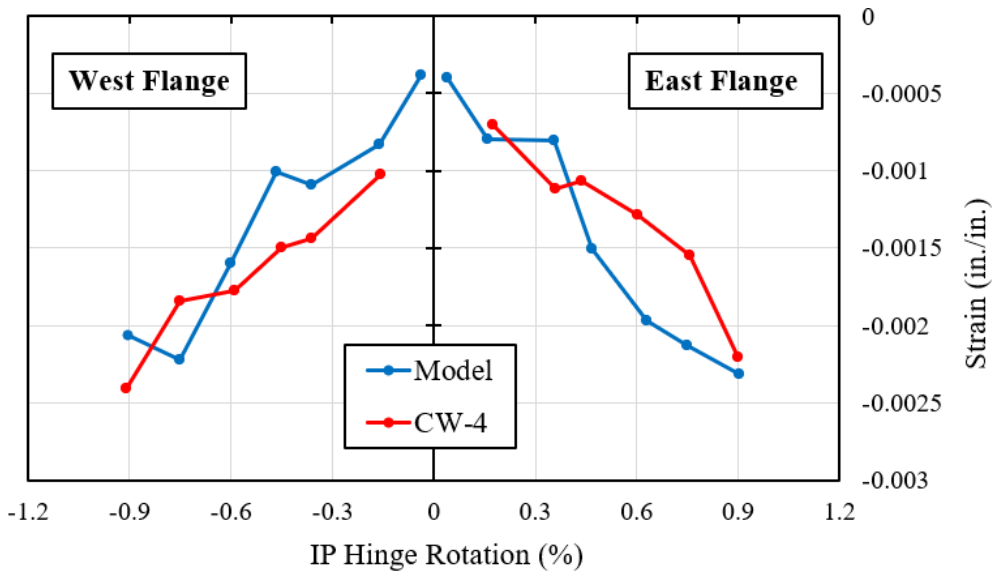

Figure 7-31: Comparison of compressive strains at the flange edges (Pos. A and D)

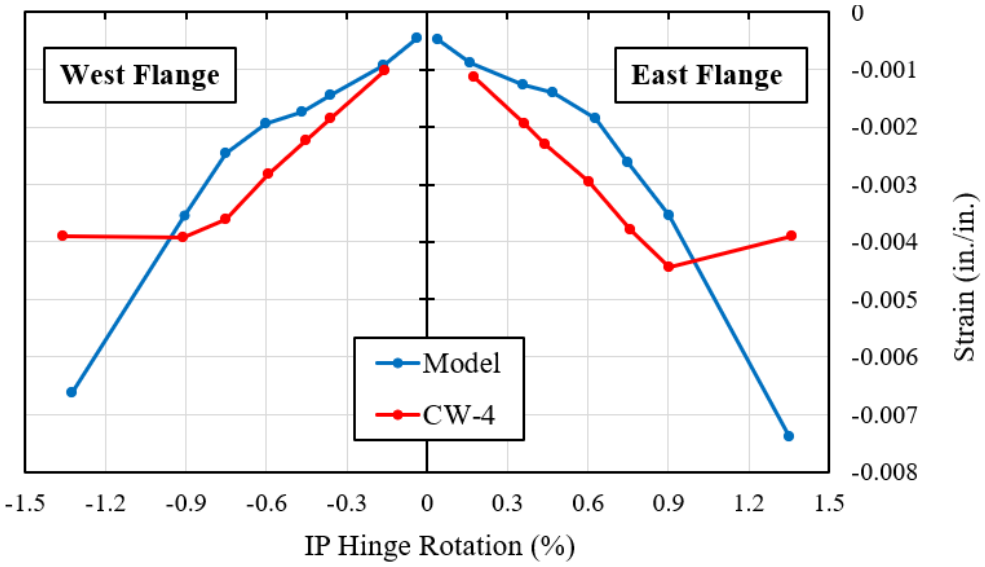

Figure 7-32: Comparison of compressive strains at the flange-web corners (Pos. A and D)

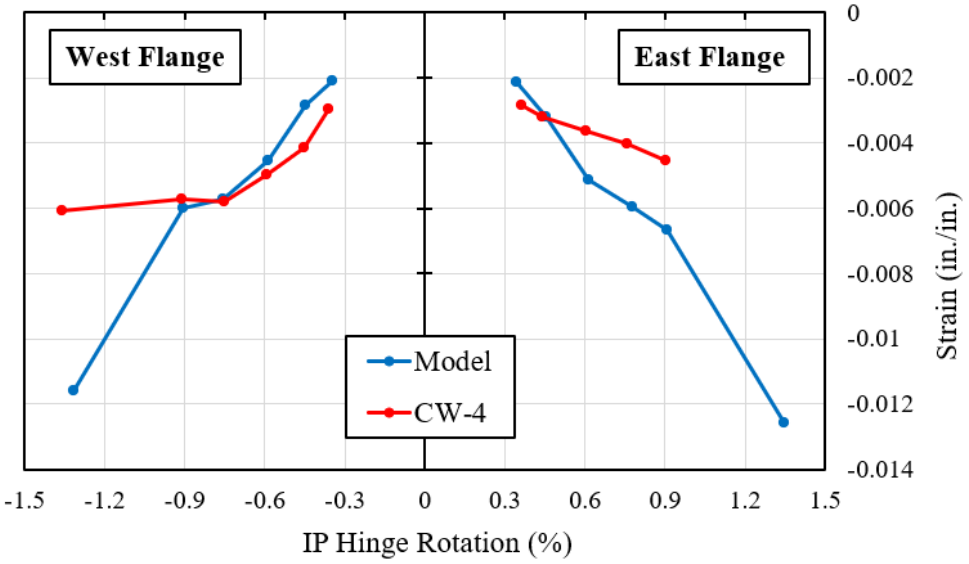

Figure 7-33: Comparison of compressive strains at the flange edges (Pos. B and E)

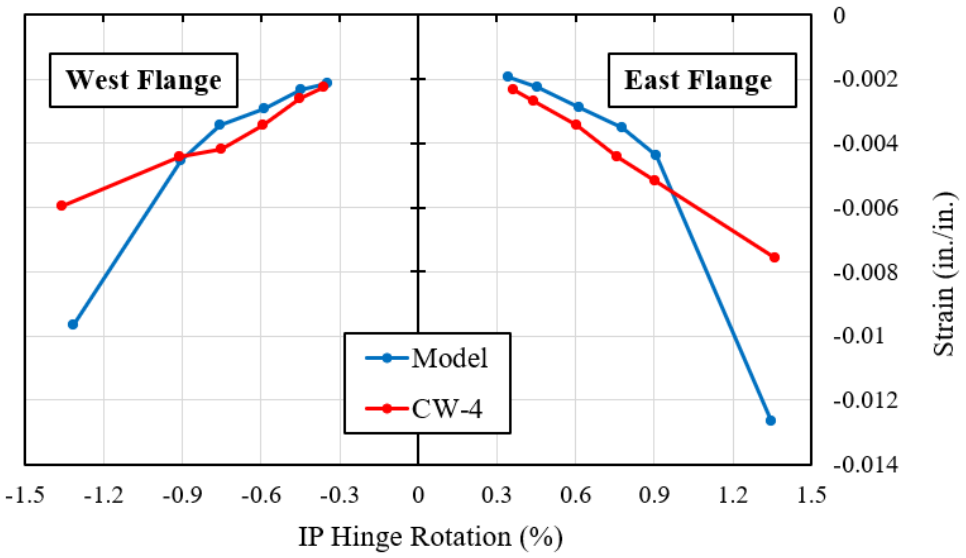

Figure 7-34: Comparison of compressive strains at the flange-web corners (Pos. C and F)

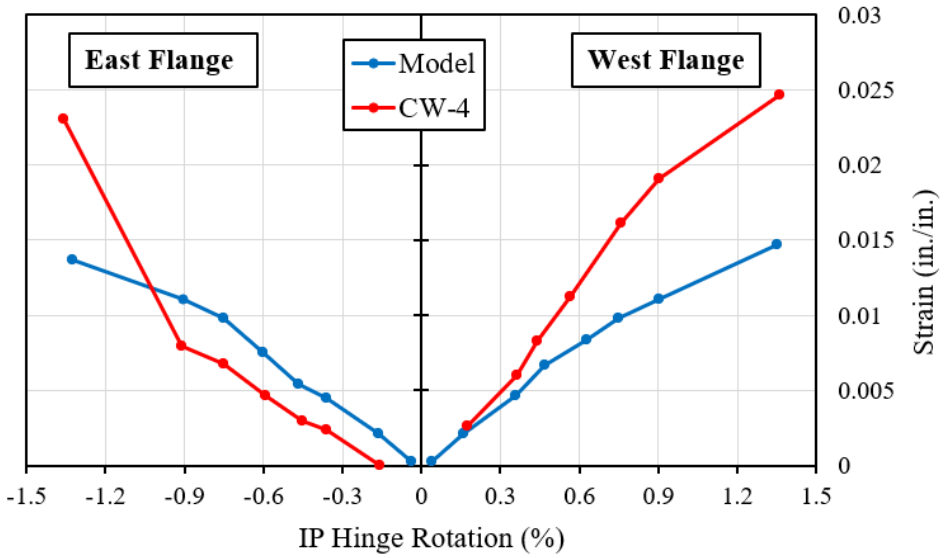

Figure 7-35: Comparison of tensile strains at the flange edges (Pos. A and D)

8. Summary and Conclusions

Four approximately one-third-scaled C-shaped walls were tested in two phases to investigate the behavior of the ordinary reinforced concrete structural walls under wind loading protocols. For the Phase-I walls, the longitudinal reinforcement ratio (ρ_l) was varied. Given the large range of ρ_l values observed from the actual buildings designed and constructed in the high-wind zones in the United States, a ρ_l value of 0.75% was chosen for the first wall (CW-1) to represent the walls with low-to-moderate reinforcement ratios, whereas, for the second wall (CW-2), a ρ_l value of 1.5% was chosen to represent the walls with moderate-to-high longitudinal reinforcement ratios. Grade 60 #3 bars were used for the longitudinal reinforcement of CW-1, and Grade 80 #4 bars were used for CW-2; therefore, the $A_s f_y$ value for CW-2 was 2.67 times that for CW-1. Since the test walls represented buildings designed in low seismic zones, the detailing of the walls was based on Chapter 11 provisions of ACI 318-19 (Ordinary walls) instead of Chapter 18 provisions (Special walls). The review of the drawings from actual buildings showed that the C-shaped walls of these buildings had uniform distribution of longitudinal reinforcement, and U-bars at wall edges and corners that overlap with wall horizontal web reinforcement. Given that lap splices are commonly used at critical sections of Ordinary walls, lap splices were also used in the test specimens. The design of the lap splices were based on T-beams tested under wind loading protocols (Unal et al., 2024 and Halim, 2024). Phase-II walls (CW-3 and CW-4) had the same cross-section dimensions as CW-1 and CW-2 and the same amount of longitudinal reinforcement as CW-2 (1.5%). The test variables for CW-3 and CW-4 were the amount of confinement provided at the flange edges and the amount of axial load applied during the biaxial wind loading protocol. Instead of U-bars at wall flange edges, CW-3 had a hoop that confined the first two layers of vertical reinforcement over an assumed upper bound plastic hinge length at the flange edges. A longer hoop was used for CW-4

to confine the first three layers of vertical reinforcement at the flange edges. An axial load of $0.1A_g f'_c$ was used for all walls during the in-plane loading. For Phase-I walls, the axial load was held constant at $0.1A_g f'_c$ during the biaxial loading. However, for Phase-II walls, during the biaxial loading, when the flange edges were under compression, axial load was decreased to $0.05A_g f'_c$ and $0.075A_g f'_c$ for CW-3 and CW-4, respectively, to account for the variation in axial load due to the presence of coupling beams. Based on the experimental results of the Phase-I and Phase-II tests, the following observations and conclusions are made:

1. The wall with the lower longitudinal reinforcement ratio (CW-1, ρ_l=0.75%) sustained no damage (e.g., concrete spalling, concrete crushing, rebar buckling, or rebar rupture) during the WLP. The residual flexural crack widths were very small (around 0.1 mm).
2. The effective lateral stiffness at first yield was found to be $0.40E_cI_g$ for CW-1, which was higher than the value calculated using ACI 369.1-22 provisions ($0.29E_cI_g$).
3. CW-1 failed at 2% hinge rotation demands (rotational ductility of 20) during the SLP due to buckling of longitudinal reinforcement and concrete crushing at the west flange above the spliced region. The rotation capacity of 2% was also calculated using the ACI 369.1-22 provisions. The maximum drift ratio measured at the top of the walls, representing approximately second-story drift ratios of a cantilever wall, was 2.78% during the SLP (displacement ductility of 18.5).
4. The failure of CW-1 at a very high rotational ductility demand ($20\Theta_y$) and the fact that no damage was observed during WLP suggest that moderate inelasticity during extreme wind events for Ordinary walls with low-to-moderate longitudinal reinforcement ratios can be allowed. However, given that the failure of CW-1 was due to longitudinal reinforcement

buckling above the splice regions, the level of axial load and the spacing of the horizontal reinforcement must be carefully considered.

5. The walls with higher longitudinal reinforcement ratios (CW-2, CW-3, and CW-4) damage at the flange-web corners was limited to cover spalling during the WLP, i.e., no core concrete crushing or bar buckling was observed. However, depending on the level of axial load applied during the biaxial loading and the amount of confinement provided, more damage was observed at the flange edges compared to the corners. For CW-2, where the axial load was kept constant at $0.1A_g f'_c$ during biaxial loading and U-bars were used with crossties to provide confinement, the damage was significant at the flange edges during the WLP (including ramp-down loading). At the base of the east flange, approximately 23% of the total length of the flange sustained substantial concrete crushing, and longitudinal bar buckling was observed above the footing-wall interface for the extreme layer flange edge longitudinal reinforcement.
6. The variation of axial load during biaxial loading (when the flange edges were under compression) resulted in less damage for Phase-II walls during the WLP. For CW-4, where the axial load was decreased to $0.075A_g f'_c$, cover spalling and bar buckling were observed above the wall-footing interface of the west flange edge, and cover spalling, bar buckling, and bar fracture were observed above the wall-footing interface of the east flange edge. No core concrete crushing was observed. Since even lower axial loads were applied during the biaxial loading when the flange edges were under compression for CW-3 ($P=0.05A_g f'_c$), less damage was observed than for CW-2 and CW-4. Only cover spalling was observed at the base of the east flange edge after the completion of the WLP for CW-3.

7. For the walls with higher longitudinal reinforcement ratios (CW-2, CW-3, and CW-4), the inelastic ramp-down loading of the WLP had a significant effect on the damage observed in these walls. Although some damage was observed during the ramp-up loading (only for CW-2 and CW-4), most of the damage occurred during the inelastic ramp-down loading. The elastic ramp-down cycles did not result in additional damage for CW-3 and CW-4. However, for CW-2, the 500 force-controlled cycles at $0.4M_{pr}$ demands did increase the damage observed at the base of the east flange edge.
8. The overlapping of longitudinal reinforcement over the splice region along with the tighter spacing of transverse reinforcement used over the splice region resulted in a stiffer (and stronger) splice region than the upper part of the walls. Accordingly, the damage was concentrated primarily right at the wall-footing interfaces and above the splice regions. The lower tensile strains measured in the splice regions resulted in lower curvatures/rotations than measured immediately above the splices. Therefore, the assumed plastic hinge length was increased by the splice length ($L_p=l_w/2+L_s$). The maximum rotation demand applied during the WLP was found to be higher than $3.0\Theta y$ when the hinge rotations were recalculated using $L_p=l_w/2+L_s$. Rotational ductilities of 3.8, 4.2, and 4.9 were applied at the maximum rotation demands of WLP for CW-2, CW-3, and CW-4.
9. Given the high rotational ductility demands of 4.2 and 4.9 applied during WLP for CW-3 and CW-4 and that the observed damage was limited, modest inelasticity can be allowed for Ordinary walls with higher longitudinal reinforcement ratios (ρ_l=1.5%) depending on the axial load level for biaxial loading when the flange edges are under compression and the level of detailing provided at the flange edges. Given that the detailed analytical models presented in Chapter 7 reasonably predict the compressive strains and, therefore, the

concrete crushing due to high compressive strains, similar models can be used to predict the behavior of walls with different configurations and different levels of axial loads.

10. The average effective lateral stiffness value for CW-2, CW-3, and CW-4 at first yield was found to be similar to the value calculated using the ACI 369.1-22 provisions; $0.32E_cI_g$ versus $0.29E_cI_g$.
11. Due to the extensive damage observed during the WLP, the base moment values for CW-2 were approximately 0.67 times the base moment values recorded for CW-3 at the maximum hinge rotation demands of the SLP before a sudden failure occurred. The failure of CW-2 occurred at 1.60% hinge rotation demands (calculated using $L_p=l_w/2+L_s$) due to concrete crushing, longitudinal bar buckling, and bar rupture of the damaged east flange during the SLP. No strength loss was observed for CW-3 during the SLP prior to flange out-of-plane instability. Maximum hinge rotation demands (calculated using $L_p=l_w/2+L_s$) of 2.39% and maximum drift ratios of 3.30% were observed. The failure of CW-3 was due to the out-of-plane instability of the east flange, which occurred at around 57 in. above the footing. It should be noted that the location of the failure represents approximately the top of the first floor in a real building at which the floor slab would be connected to the core wall; therefore, the restraint of the floor slab would likely restrain the out-of-plane instability until higher rotation demands were applied. Therefore, the test results likely represent a lower-bound rotational/displacement capacity of CW-3 given conditions in actual buildings.
12. Given that the damage at the end of the WLP was similar for CW-3 and CW-4, instead of using an in-plane seismic loading protocol similar to the one applied to CW-3, a SLP with a biaxial loading protocol that was similar to the WLP of CW-2 (constant axial load of

$0.1A_g f'_c$) was applied to CW-4. Application of biaxial loading with high in-plane hinge rotation demands (2 cycles at around $3.0\Theta_y$ and 2 cycles at around $4.0\Theta_y$, calculated using $L_p=l_w/2+L_s$) under high axial loads ($0.1A_g f'_c$) did not result in a significant damage or strength loss for CW-4; therefore, the moderate confinement provided at the flange edges was effective. The failure occurred due to concrete crushing and bar buckling/rupture during the biaxial cycle at 1.76% in-plane hinge rotation demands (calculated using $L_p=l_w/2+L_s$) or 2.4% drift ratios when the east flange edge was under compression. The results indicate that the deformation capacity of CW-4 under biaxial loading with high in-plane rotation demands and higher axial load is around 6 times the yield rotation.

13. The plastic hinge rotation capacities were found to be 2.1% for CW-2, CW-3, and CW-4, calculated using the ACI 369.1-22 provisions. While lower hinge rotation demands than 2.1% were reached for the wall that was extensively damaged during the WLP (CW-2, 1.60%) and the wall that experienced significant strength loss during the biaxial SLP in the OOP direction (CW-4, 1.76%), higher rotation demands were observed for the wall that did not experience any significant damage or strength loss during the WLP, and an uniaxial SLP was applied (CW-3, 2.39%).
14. The analytical models created using MVLEM-3D showed that the behavior of C-shaped walls (both global and local) under complex loading protocols can reasonably be predicted. The model results matched the stiffness, moment capacities, and pinching behavior of the walls well. For CW-2, strength loss and failure due to concrete crushing were also predicted. For CW-1 and CW-3, since the bar buckling and out-of-plane instability mechanisms were not modeled, the model did not predict the displacement capacity of these walls. The ε_p^* models for the predictions of bar buckling, and Paulay and Priestly

(1993) and Chai and Elayer (1999) models for the prediction of the out-of-plane instability underestimated the tensile strains that the failure was observed during testing.

Appendix A. Bar Buckling Models (ε_p^* models)

The ε_p^* models developed by Rodriguez et al. (1999), Moyer and Kowalsky (2003), Hilson et al. (2014), Motter et al. (2018), and Rodriguez and Iñiguez (2019) provide a relationship between the spacing of the transverse bars around the longitudinal reinforcement and the critical strains (ε_p^*) at the onset of buckling of the longitudinal rebars. The ε_p^* values were calculated as follows, where a slight variation was made by Rodriguez and Iñiguez (2019) compared to the one proposed by Rodriguez et al. (1999).

$$\varepsilon_p^* = \varepsilon_o - \varepsilon_{sc} \; (Rodriguez\ et\ al., 1999) \tag{A.1}$$

$$\varepsilon_p^* = \varepsilon_{st} - \varepsilon_{sc} \; (Rodriguez\ and\ Iniguez, 2019) \tag{A.2}$$

where ε_o is the axial strains at zero loading after reversal from tension, and ε_{st} and ε_{sc} are the peak tensile and compressive strain demands during a cycle.

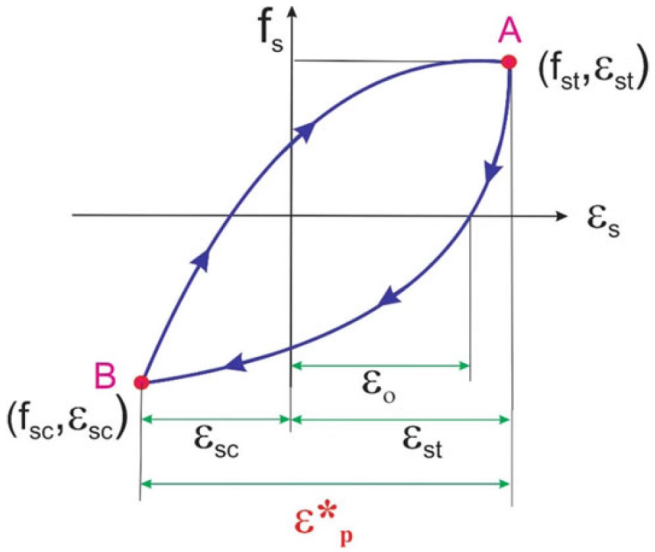

Figure A-1: Definition of ε_p^* (Rodriguez and Iñiguez 2019)

Figure A-2 shows the relationship between the ε_p^* value and the ratio of the transverse reinforcement spacing (s) to the diameter of the longitudinal reinforcement (d_b). The figure

includes the relationships developed by Rodriguez et al. (1999) and Moyer and Kowalsky (2003), and also the test data from Hilson et al. (2014) and Motter et al. (2018). Based on this, Motter et al. (2018) proposed the following for the estimation of ε_p^* given s/d_b.

$$\varepsilon_p^* = 0.03 - 0.00167\left(\frac{s}{d_b} - 6\right) \; for \; 6 \le \frac{s}{d_b} \le 16$$
$$\varepsilon_p^* = 0.09 - 0.015\left(\frac{s}{d_b} - 2\right) \; for \; \frac{s}{d_b} \le 6 \tag{A.3}$$

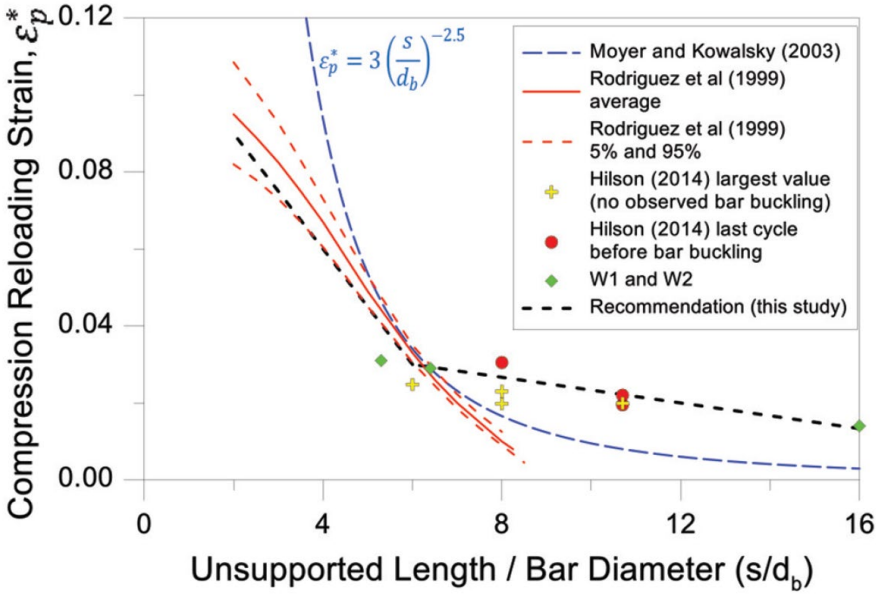

Figure A-2: ε_p^* versus s/d_b (Motter et al. 2018)

A similar relationship developed by Rodriguez and Iñiguez (2019) that uses different column and wall experimental results found in the literature, is given below and shown in Figure A-3.

$$0.02 \le \varepsilon_p^* = \frac{11 - s/d_b}{150} \le 0.06 \tag{A.4}$$

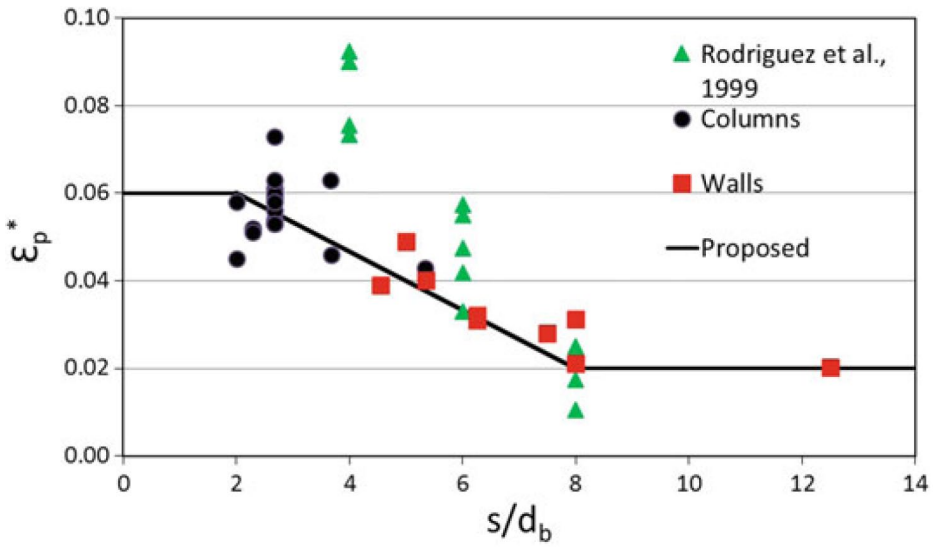

Figure A-3: ε_p^* versus s/d$_b$ (Rodriguez and Iñiguez, 2019)

Using Equations A.3 and A.4, the critical strains at the onset of bar buckling were calculated and shown in Table A-1 for CW-1 and CW-2 with 6 in. spacing of transverse reinforcement above the spliced region. While for CW-2, the ε_p^* value was found to be 0.02 for both using the Equation A.3 and A.4, for CW-1, it was 0.013 with Equation A.3 and 0.02 with Equation A.4. For the calculation of the rotations at the onset of bar buckling with s=6 in. a ε_p^* value of 0.013 was used for CW-1 to consider the worst-case scenario.

Table A-1: ε_p^* values for CW-1 and CW-2 with 6 in. spacing of transverse reinforcement above L_s

	CW-1	CW-2
Longitudinal bar diameter (d_b)	0.375 in.	0.5 in.
Spacing above L_s (s)	6 in.	6 in.
s/d_b	16	12
ε_p^* (Motter et al. 2018)	0.013	0.02
ε_p^* (Rodriguez and Iñiguez, 2019)	0.02	0.02

Analytical analysis of the test walls under monotonic loading using the expected material properties (Section 2.3) was done to estimate the moment and rotation values when the rebar strains of the outer layers of the wall flange longitudinal reinforcement reached the ε_p^* values above the spliced region. Table A-2 shows the calculated values where the moment above the spliced region was estimated to reach the given ε_p^* values at that region. Using the shear span ratios given in Section 2.2.3, the base moment and the corresponding base curvature were also calculated. The hinge rotations were calculated using a similar approach shown in Figure F-5, which resulted in 0.61% and 0.96%, respectively, for CW-1 and CW-2-3-4. These results were compared with the predicted yield rotations due to flexural (Appendix F) and due to the effect of rebar slip/extension (Appendix G). The total predicted analytical yield rotations (flexural + slip, $\Theta_{y,t,a} = \Theta_{y,f,a} + \Theta_{y,s,a}$) were found to be 0.14% and 0.25% for CW-1 and CW-2-3-4, respectively. Therefore, a failure due to bar buckling above the spliced region was expected at approximately $4.4\Theta_y$ and $3.8\Theta_y$ for CW-1 and CW-2-3-4, respectively. Although these rotation demands were higher than the maximum demand of the WLP, i.e., $3\Theta_y$, the expressions developed for the ε_p^* models were based on test

results where the specimens were subjected to seismic loading protocols. Since the C-shaped test specimens were subjected to wind loading protocols where the number of cycles is significantly higher compared to seismic protocols, the spacing of the transverse reinforcement above the spliced region was decreased to 3 in. to prevent a premature failure due to bar buckling. Table A-3 shows the calculations with s = 3 in. above the spliced region.

Table A-2: Expected moment and rotation demands at the onset of bar buckling above spliced region with s = 6 in.

	CW-1	CW-2
ε_p^* (Motter et al. 2018)	0.013 in./in.	0.02 in./in.
Moment above L_s, M_{Ls}	2383 k-ft	3959 k-ft
Tensile strains above L_s, $\varepsilon_{st,Ls}$	0.012 in./in.	0.018 in./in.
Compressive strains above L_s, $\varepsilon_{sc,Ls}$	-0.001 in./in.	-0.002 in./in.
Moment at the base, M_{base}	2453 k-ft	4110 k-ft
In-plane hinge rotation, $\Theta_{IP,LP}$	0.61%	0.96%

Table A-3: Expected moment and rotation demands at the onset of bar buckling above spliced region with s = 3 in.

	CW-1	CW-2
Longitudinal bar diameter (d_b)	0.375 in.	0.5 in.
Spacing above L_s (s)	3 in.	3 in.
s/d_b	8	6
ε_p^* (Motter et al. 2018)	0.027	0.030
Moment above L_s, M_{Ls}	2521 k-ft	4087 k-ft
Tensile strains above L_s, $\varepsilon_{st,Ls}$	0.025 in./in.	0.027 in./in.
Compressive strains above L_s, $\varepsilon_{sc,Ls}$	-0.002 in./in.	-0.003 in./in.
Moment at the base, M_{base}	2595 k-ft	4345 k-ft
In-plane hinge rotation, $\Theta_{IP,LP}$	1.1%	2.3%

Appendix B. Development Length Calculations

Development length (ACI 318-19 Section 25.4.2.4)

$$l_d = \left[\frac{3}{40}\frac{f_y}{\lambda\sqrt{f_c'}}\frac{\Psi_t\Psi_e\Psi_s\Psi_g}{\left(\frac{c_b + K_{tr}}{d_b}\right)}\right]d_l$$

$$K_{tr} = \frac{40A_{tr}}{sn}$$

- CW-1 Wall Vertical Reinforcement

  $f_y = 60\ ksi$

  $f_c' = 8\ ksi\ (expected)$

  $d_l = 3/8"\ (\#3); d_t = 2/8"\ (\#2)$

  $\Psi_t = 1.0;\ \Psi_e = 1.0;\ \Psi_s = 0.8;\ \Psi_g = 1.0$

  $\lambda = 1.0$

  $t_w = t_f = 5"$

  $c_c = 3/8"$ (clear cover to the transverse reinforcement)

  $c_{b,1} = c_c + d_t + \frac{d_l}{2}$

  (distance from the center of the spliced reinforcement to the nearest concrete surface)

  $c_{b,2} = (t_f - 2 * (c_{b,1}))/2$ (one-half of the center-to-center spacing between longitudinal reinforcement)

  $c_b = \min(c_{b,1}, c_{b,2})$

  $c_b = \min(0.813\ in., 1.688\ in.)$

  $c_b = 0.813\ in.$

$$K_{tr} = \frac{40 \times 2 \times \pi \times \frac{0.25^2}{4}}{2\ in. \times 2} = 0.98$$

$$\frac{c_b + K_{tr}}{d_b} = \frac{0.813" + 0.98}{\frac{3}{8}"} = 4.8 \geq 2.5$$

$$l_d = \left[\frac{3}{40}\frac{60000\ psi}{1.0 \times \sqrt{8000\ psi}}\frac{1.0 \times 1.0 \times 0.8 \times 1.0}{(2.5)}\right]\frac{3}{8} = 6.04\ in.$$

$$l_{s,CW1} = 1.25 \times 1.3 \times l_d = 9.8\ in$$

- <u>CW-2 Wall Vertical Reinforcement</u>

$f_y = 80\ ksi$

$f_c' = 8\ ksi\ (expected)$

$d_l = 4/8"\ (\#4); d_t = 2/8"\ (\#2)$

$\Psi_t = 1.0;\ \Psi_e = 1.0;\ \Psi_s = 0.8;\ \Psi_g = 1.15$

$\lambda = 1.0$

$t_w = t_f = 5"$

$c_c = 5/8"$ (clear cover to the transverse reinforcement)

$c_{b,1} = c_c + d_t + \frac{d_l}{2}$ (distance from the center of the spliced reinforcement to the nearest concrete surface)

$c_{b,2} = (t_f - 2 * (c_{b,1}))/2$ (one-half of the center-to-center spacing between longitudinal reinforcement)

$c_b = \min(c_{b,1}, c_{b,2})$

$c_b = \min(1.125\ in.,1.375\ in.)$

$c_b = 1.125\ in.$

$$K_{tr} = \frac{40 \times 2 \times \pi \times \frac{0.25^2}{4}}{2\ in. \times 2} = 0.98$$

$$\frac{c_b + K_{tr}}{d_b} = \frac{1.125" + 0.98}{\frac{4}{8}"} = 4.2 \geq 2.5$$

$$l_d = \left[\frac{3}{40}\frac{80000\ psi}{1.0 \times \sqrt{8000\ psi}}\frac{1.0 \times 1.0 \times 0.8 \times 1.15}{(2.5)}\right]\frac{4}{8} = 12.34\ in.$$

$$l_{s,CW2} = 1.25 \times 1.3 \times l_d = 20.1\ in$$

- <u>CW-1 Wall Overlapping U-bars</u>

  $f_y = 60\ ksi$

  $f_c' = 8\ ksi\ (expected)$

  $d_t = 2/8"\ (\#2)$

  $\Psi_t = 1.3;\ \Psi_e = 1.0;\ \Psi_s = 0.8;\ \Psi_g = 1.0$

  $\lambda = 1.0$

  $t_w = t_f = 5"$

  $c_c = 3/8"$ (clear cover to the transverse reinforcement)

  $c_{b,1} = c_c + \frac{d_t}{2}$ (distance from the center of the spliced reinforcement to the nearest concrete surface)

  $c_{b,2} = (t_f - 2 * (c_{b,1}))/2$ (one-half of the center-to-center spacing between longitudinal reinforcement)

  $c_b = \min(c_{b,1}, c_{b,2})$

  $c_b = \min(0.5\ in.,2\ in.)$

  $c_b = 0.5\ in.$

$K_{tr} = 0$

$$\frac{c_b + K_{tr}}{d_b} = \frac{0.5" + 0}{\frac{2}{8}"} = 2.0 \leq 2.5$$

$$l_d = \left[\frac{3}{40}\frac{60000\ psi}{1.0 \times \sqrt{8000\ psi}}\frac{1.3 \times 1.0 \times 0.8 \times 1.0}{(2.0)}\right]\frac{2}{8} = 6.54\ in.$$

$l_{s,CW1,Ubars} = 1.3 \times l_d = 8.5\ in$

- CW-2 Wall Overlapping U-bars

$f_y = 60\ ksi$

$f_c' = 8\ ksi\ (expected)$

$d_t = 2/8"\ (\#2)$

$\Psi_t = 1.3;\ \Psi_e = 1.0;\ \Psi_s = 0.8;\ \Psi_g = 1.0$

$\lambda = 1.0$

$t_w = t_f = 5"$

$c_c = 5/8"$ (clear cover to the transverse reinforcement)

$c_{b,1} = c_c + \frac{d_t}{2}$ (distance from the center of the spliced reinforcement to the nearest concrete surface)

$c_{b,2} = (t_f - 2 * (c_{b,1}))/2$ (one-half of the center-to-center spacing between longitudinal reinforcement)

$c_b = \min(c_{b,1}, c_{b,2})$

$c_b = \min(0.75\ in.,1.75\ in.)$

$c_b = 0.75\ in.$

$K_{tr} = 0$

$$\frac{c_b + K_{tr}}{d_b} = \frac{0.75" + 0}{\frac{2}{8}"} = 3.0 \geq 2.5$$

$$l_d = \left[\frac{3}{40}\frac{60000\ psi}{1.0 \times \sqrt{8000\ psi}}\frac{1.3 \times 1.0 \times 0.8 \times 1.0}{(2.5)}\right]\frac{2}{8} = 5.23\ in.$$

$$l_{s\,,CW2,Ubars} = 1.3 \times l_d = 6.8\ in$$

Development length of standard hooks (ACI 318-19 Section 25.4.3)

$$l_{dh} = \left[\frac{f_y}{\lambda\sqrt{f_c'}}\frac{\Psi_e\Psi_r\Psi_o\Psi_c}{55}\right]d_l^{1.5}$$

- <u>CW-1 Wall Starter Reinforcement (Anchored into the footing with standard hooks)</u>

  $f_y = 60\ ksi$

  $f_c' = 8\ ksi\ (expected)$

  $d_l = 3/8"\ (\#3)$

  $\Psi_e = 1.0;\ \Psi_r = 1.6;\ \Psi_o = 1.0;\ \Psi_v = 1.0$

  $\lambda = 1.0$

  $$l_{dh,CW1} = \left[\frac{60000\ psi}{1.0 \times \sqrt{8000\ psi}}\frac{1.0 \times 1.6 \times 1.0 \times 1.0}{55}\right]\left(\frac{3}{8}\right)^{1.5} = 4.5\ in.$$

- <u>CW-2 Wall Starter Reinforcement (Anchored into the footing with standard hooks)</u>

  $f_y = 80\ ksi$

  $f_c' = 8\ ksi\ (expected)$

  $d_l = 4/8"\ (\#4)$

  $\Psi_e = 1.0;\ \Psi_r = 1.6;\ \Psi_o = 1.0;\ \Psi_v = 1.0$

$\lambda = 1.0$

$$l_{dh,CW2} = \left[\frac{80000\ psi}{1.0 \times \sqrt{8000\ psi}} \frac{1.0 \times 1.6 \times 1.0 \times 1.0}{55}\right]\left(\frac{4}{8}\right)^{1.5} = 9.2\ in.$$

Appendix C. Footing and Top Cap Details

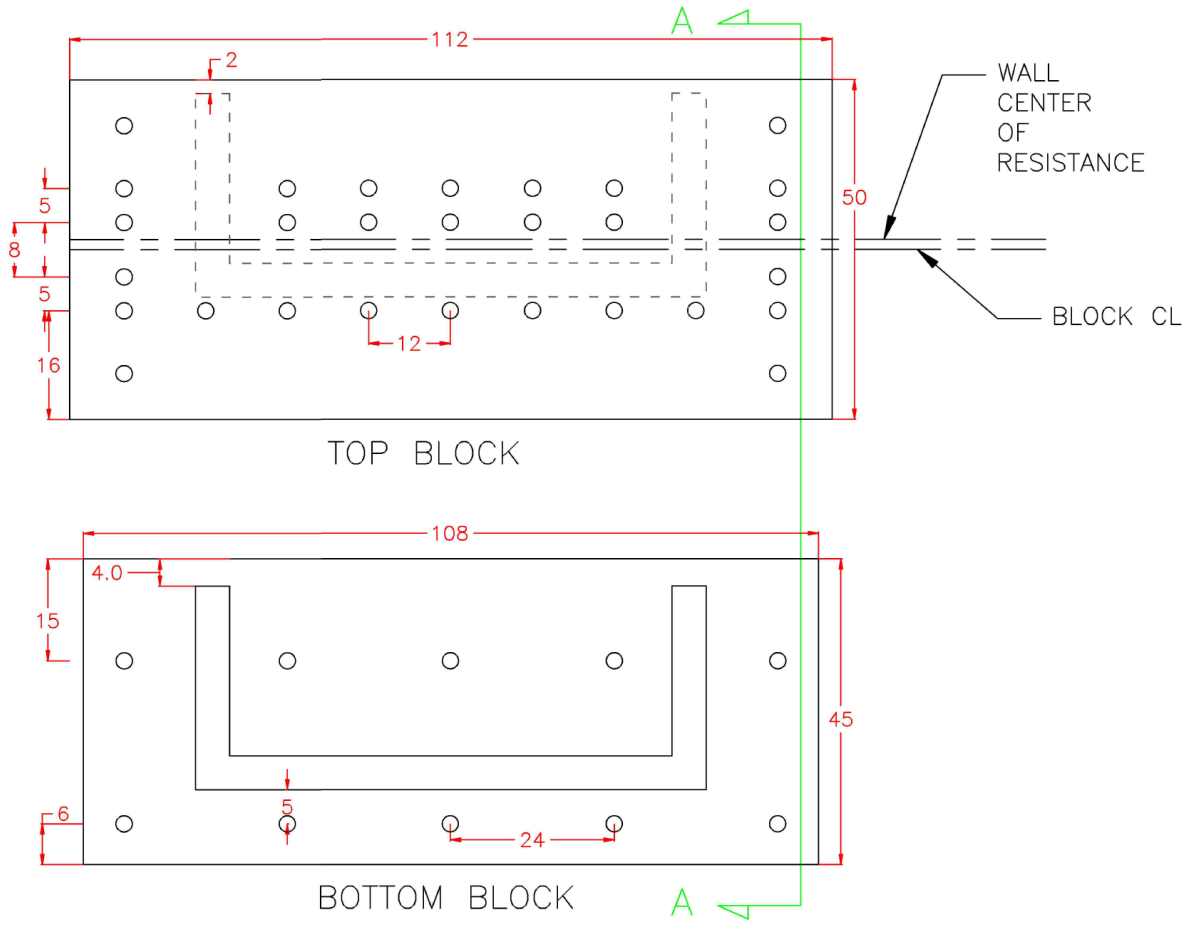

Figure C-1: Cross-sectional dimensions and the locations of the PVC pipes

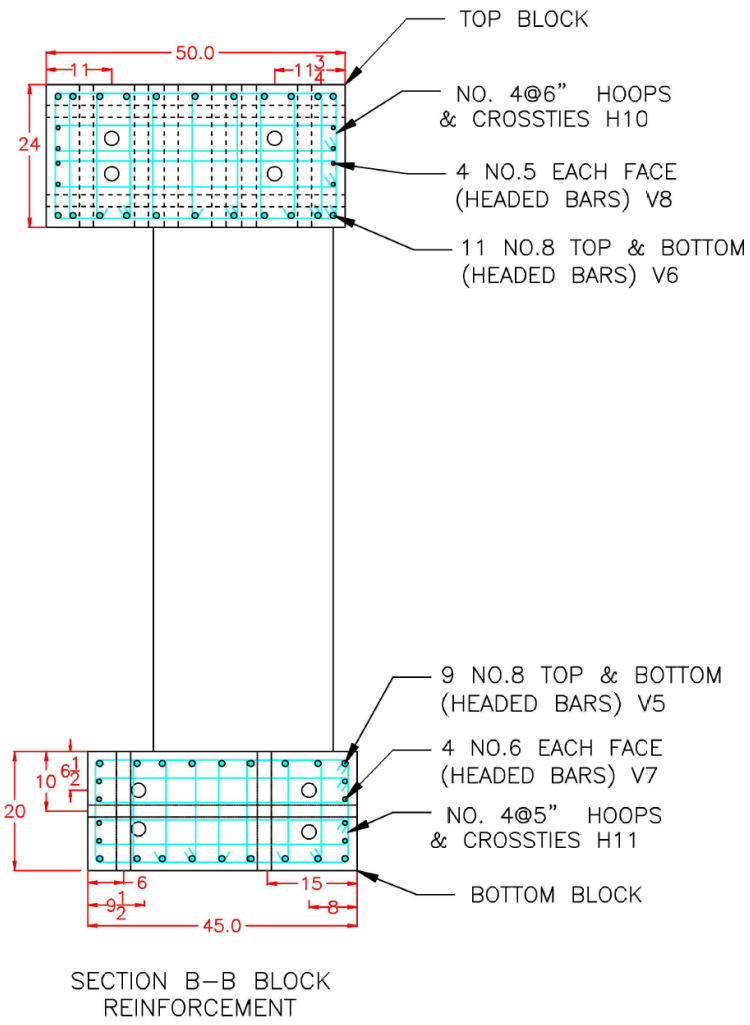

Figure C-2: Blocks Longitudinal and Transverse Reinforcements

Appendix D. Fabrication of Test Specimens

- Phase-I Walls

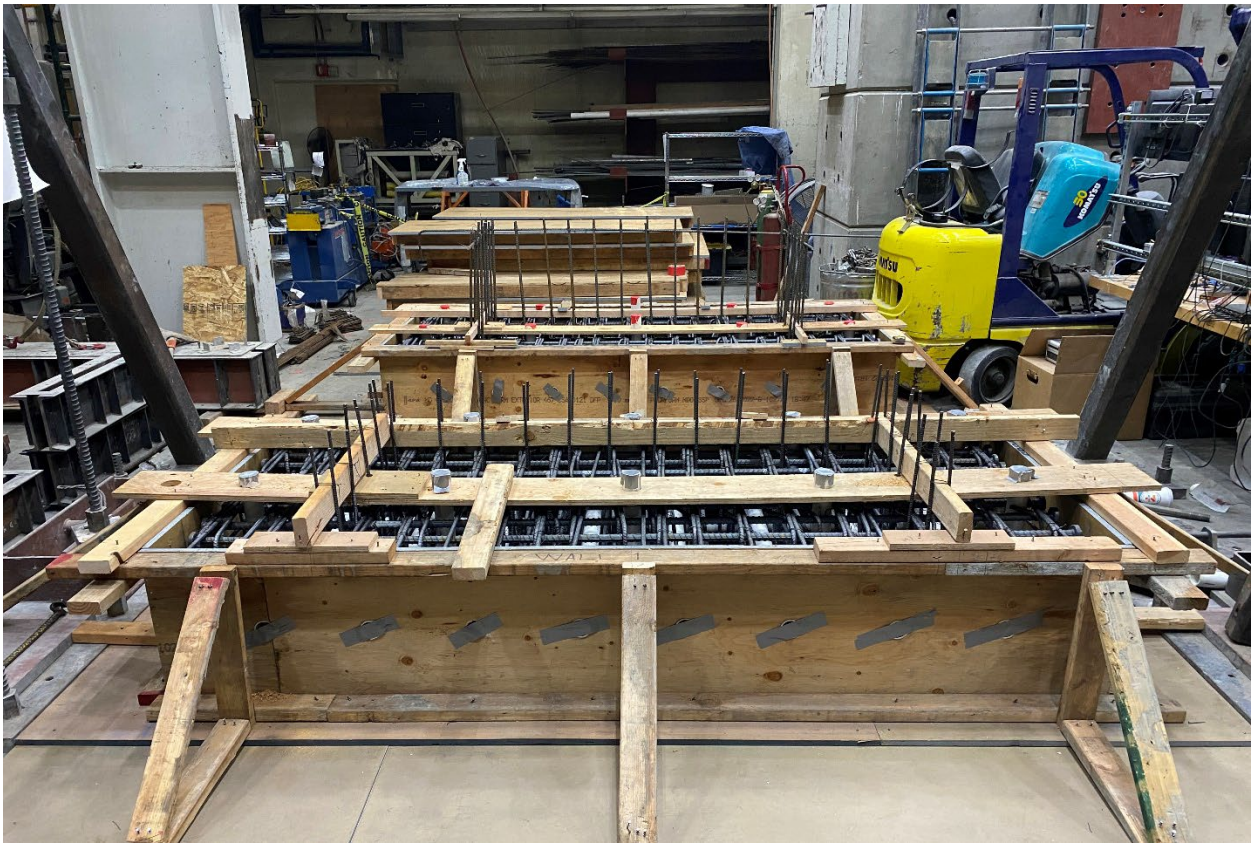

Figure D-1: Footing formwork, (Bottom) CW-1, (Top) CW-2

Figure D-2: CW-2 Footing rebar cage with the starter bars

Figure D-3: CW-1 Rebar Cage

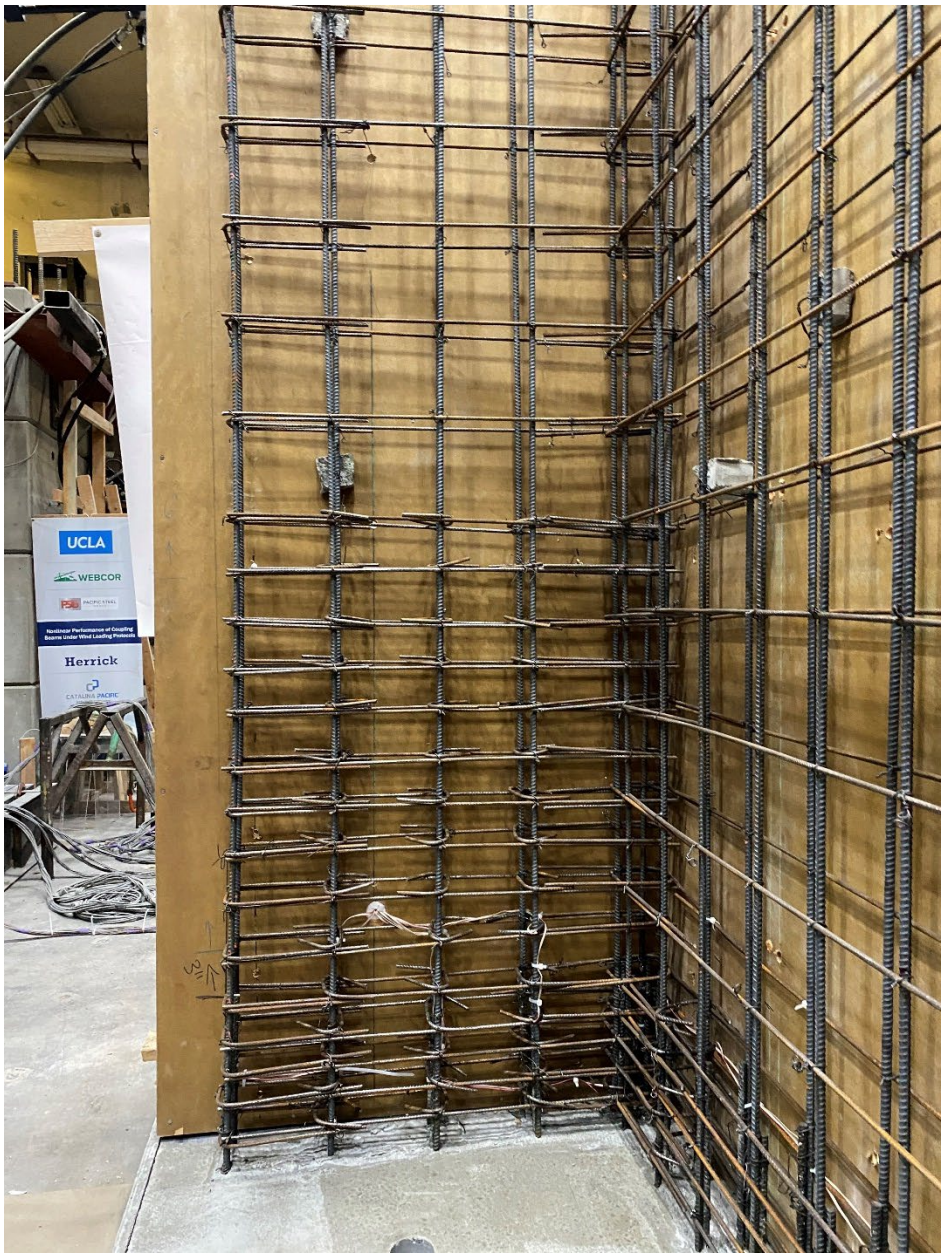

Figure D-4: CW-1 Flange reinforcement

Figure D-5: CW-1 Flange reinforcement close-up

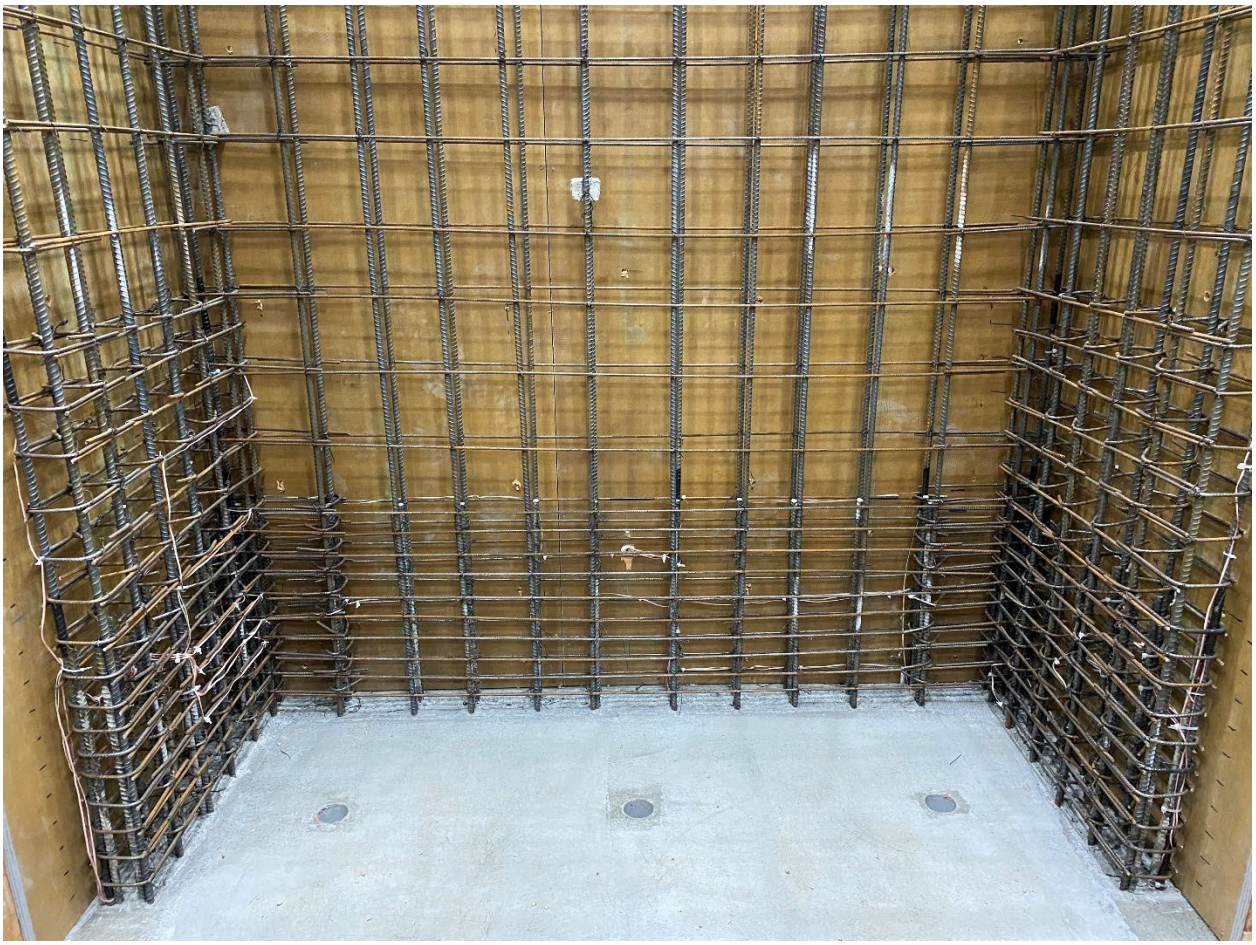

Figure D-6: CW-2 rebar cage

Figure D-7: CW-2 flange reinforcement

Figure D-8: Top cap formwork and reinforcement cages

- Phase-II Walls:

Figure D-9: Phase-II footing formwork and reinforcement cages

Figure D-10: CW-3 Reinforcement cage

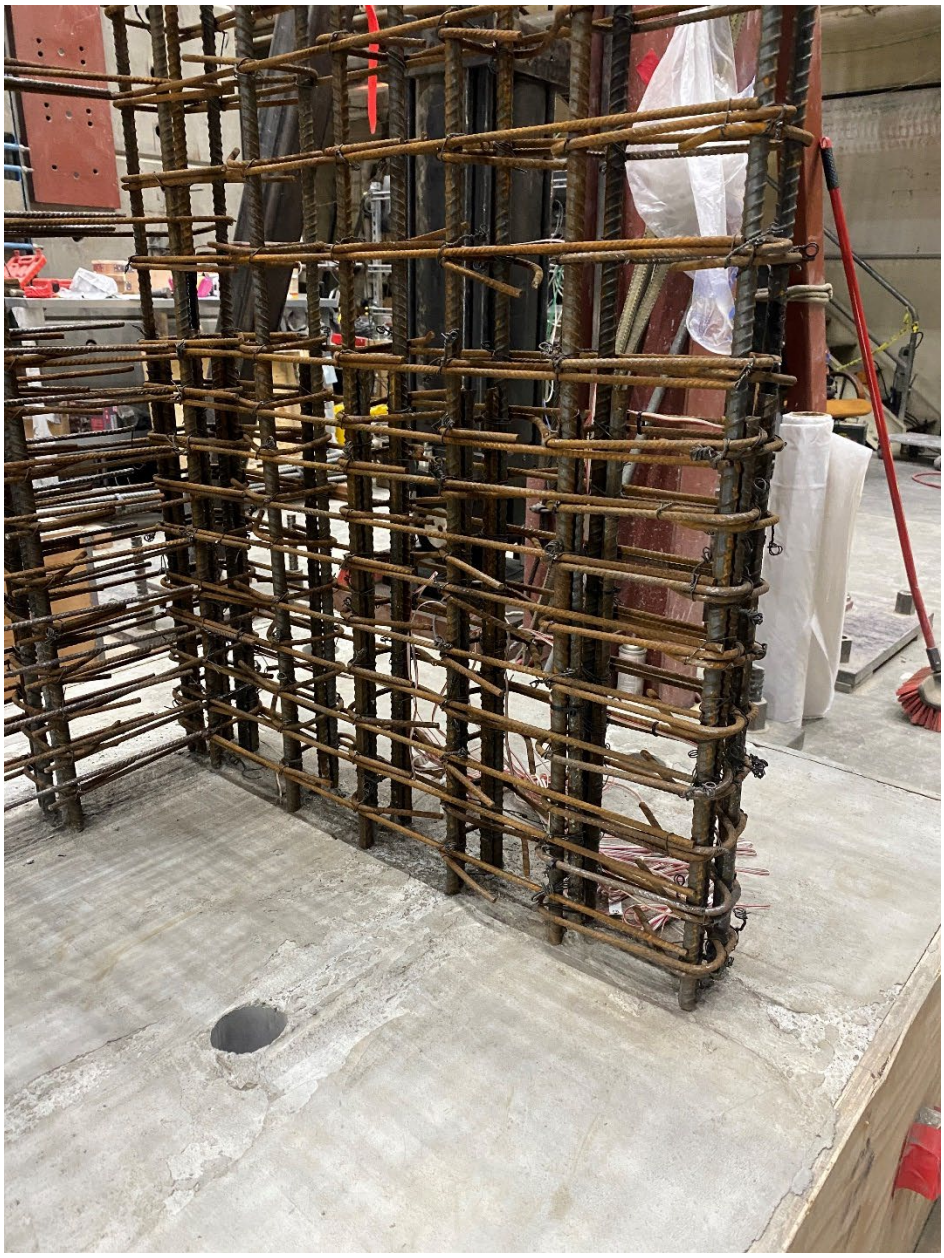

Figure D-11: CW-3 flange reinforcement close-up

Figure D-12: Phase-II wall formwork

Appendix E. Concrete Mix Design

CALPORTLAND®

Concrete Mix Submittal

Submittal Information

Submittal Name	99594 - BEAMS UNDER WIND LOAD
Date Submitted	12/06/2021
Customer	COD - UCLA COLLEGE OF ENGINEERING
Project Name	99594 - BEAMS UNDER WIND LOAD
Project Location	UCLA
Use	BEAMS UNDER WIND LOAD TEST

Mix Information

Mix ID	40E2S86
Mix Name	0.40 W/C 6000 PSI 3/8" ADVA
Compressive Strength (f'c)	6000 psi @ 28 Days
Aggregate Nominal Size	3/8" (9.5mm)
Air Entrained	☐

Mix Properties

Slump	8" ± 1"	**Sack Content**	10.2	94 lb/sack	**Total Mass**	3982	lb
Air	1%	**Total Water**	42.8	gal	**Total Volume**	26.99	ft3
W/CM Ratio	0.37	**Water/Sack**	4.2	gal	**Unit Weight**	147.6	lb/ft3

Group	Material Description	Supplier	Specific Gravity	Mass lb	Volume ft3
Cement	TYPE II/V		3.15	961	4.889
Aggregate	SAN GABRIEL VALLEY / IRWINDALE 3/8" GRAVEL 3/8" G	SAN GABRIEL VALLEY / IRWINDALE	2.64	1061	6.441
	SAN GABRIEL VALLEY / IRWINDALE WASHED CONCRETE SAND WCS	SAN GABRIEL VALLEY / IRWINDALE	2.65	1599	9.670
Water	WATER		1	357	5.721
Admixture	GRACE ADVA SUP Dosage: 38.4 fl oz/yd3 Range: fl oz/yd3		1		
	Low Range Water Reducer WRDA 64 Dosage: 28.9 fl oz/yd3 Range: fl oz/yd3	GCP APPLIED TECHNOLOGIES	1		
Air	Air				0.270

Mix Notes

WRDA 64 - Dosage Range: 2.0 - 5.0 ozs/cwt
ADVA 195 - Dosage Range: 2.0 - 10.0 ozs/cwt
RECOVER - Dosage Range: 0.0 - 6.0 ozs/cwt

Submittal Notes

Note: This mix should be approved by the project's structural engineer or architect. Mix designed for CalPortland only. No substitutions or alternations may be made. Approval of this mix design carries the inclusion of CalPortland on the distribution list for all concrete test results.

Sincerely,

Name/Title Brandon Coble / Quality Control Manager

Contact Brandon Coble
Phone 626-691-2411
Email bcoble@calportland.com

REGISTERED PROFESSIONAL ENGINEER DAVID R. HATTAWAY C 84395 EXP. 09/30/23 CIVIL STATE OF CALIFORNIA

Digitally signed by David Hattaway
Reason: I am approving this document
Date: 2021.12.02 15:12:34-08'00'

CALPORTLAND®

Combined Aggregate Blend Report

Mix ID	40E2S86	**Nominal Max Size**	3/8" (9.5mm)
Mix Name	0.40 W/C 6000 PSI 3/8" ADVA	**Aggregate Volume**	16.1
Design Strength (f'c)	6000 psi @ 28 Days	**Coarse Aggregate %**	40.0
Specification		**Fine Aggregate %**	60.0

		% Passing Gradations	
	Aggregate Type	Coarse	Fine
	% Contribution	40.0	60.0

Sieve/Test	Spec	Result	3/8" G	WCS
1/2" (12.5mm)		100.0	100.0	100.0
3/8" (9.5mm)		95.6	89.0	100.0
#4 (4.75mm)		64.6	16.0	97.0
#8 (2.36mm)		51.8	5.0	83.0
#16 (1.18mm)		40.8	3.0	66.0
#30 (.6mm)		26.8	2.4	43.0
#50 (.3mm)		10.9	1.8	17.0
#100 (.15mm)		2.9	1.2	4.0
#200 (75µm)		1.08	0.60	1.40

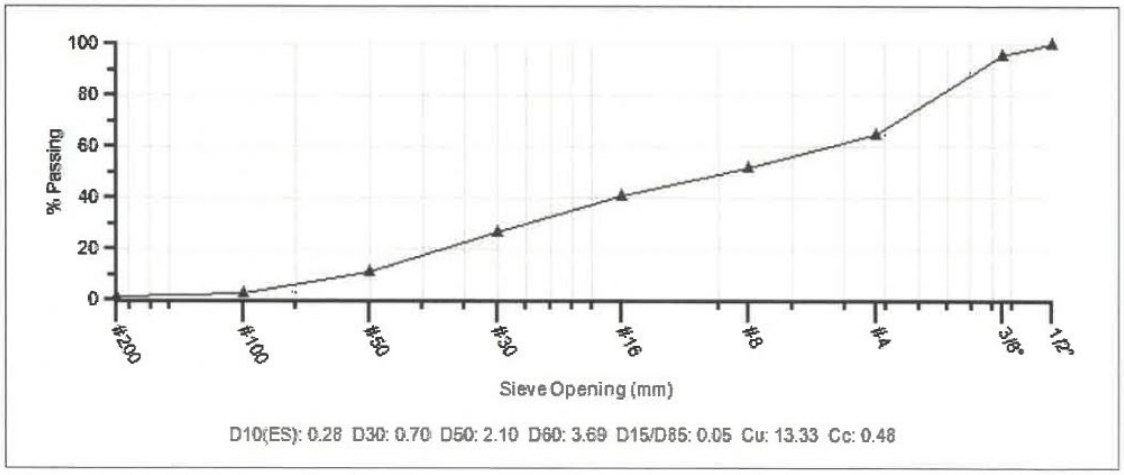

D10(ES): 0.28 D30: 0.70 D50: 2.10 D60: 3.69 D15/D85: 0.05 Cu: 13.33 Cc: 0.48

CATALINA PACIFIC
A CALPORTLAND Company

TRIAL BATCH RESULTS

Mix Design: 40E2S86

Proportioning: California Building Code

Water/Cementitious Ratio: 0.37

Ingredients		Cu Yd Weights	Specific Gravities	Absolute Volume (Cu Ft)
Cement Type II/V		961 lbs	3.15	4.89
Water (Design)		357.3 lbs	1.00	5.73
W C Sand Orca		1599 lbs	2.65	9.67
3/8" Gravel Durbin		1061 lbs	2.64	6.44
Entrapped Air	1.0%			0.27
Admixtures:				27.00
WRDA 64		25.7 ozs		
ADVA 195		34.2 ozs		

TESTING RESULTS (ASTM C 192)

Date Cast:	May 6, 2019	Plastic Unit Weight:	142.2 pcf
Slump:	9.00"	Air Content:	4.1%
Temperature:	66°/64°		

COMPRESSIVE STRENGTH RESULTS (ASTM) C 39)

Number	3 Days	7 Days	28 Days	56 Days
1	5430 psi	6490 psi	7880 psi	8430 psi
2	5400 psi	6430 psi	7770 psi	8360 psi
3	5340 psi	6210 psi	7690 psi	8240 psi
Average	5390 psi	6380 psi	7780 psi	8340 psi

DRYING SHRINKAGE RESULTS (ASTM C 157 as modified by SEAOC)

Prism Size (ASTM C490): 4" x 4" x 11" (gage length = 10" ± 0.10")

Total Age (Days)	Air Dry Age (Days)	Shrinkage Percentage
7	0	0.000
14	7	0.029
21	14	0.036
28	21	0.040
35	28	0.048

Vulcan
Materials Company
Western Division

Contractor: ***CalPortland Company*** November 5, 2021

Project: ***Various***

Plant: ***Vulcan Materials / Durbin (SMARA# 91-19-0023)***

Material: ***3/8" Pea Gravel (ASTM #8)***
Product Code: ***28092***

This is to certify that Vulcan Materials Company, Western Division, **Durbin**, will supply 3/8" Pea Gravel to the above listed project and that this product will conform to Table 1 and the grading limits in section 6, of ASTM designation C33 - 18, except where indicated by an asterisk *. *Due to the natural effects of segregation and the effects of post-delivery handling, Vulcan Materials Company guarantees that its material will meet the specifications in this submittal at the point of delivery only, and when sampled in accordance with ASTM D75.*

Sieve Size		ASTM C33 Table 1	Percent Passing
12.5 mm	(1/2")	100	100
9.5 mm	(3/8")	85 - 100	**83***
4.75 mm	(No. 4)	10 - 30	11
2.36 mm	(No. 8)	0 - 10	4
1.18 mm	(No. 16)	0 - 5	1
75 um	(No. 200)	0-1	0.8

Specific Gravity (SSD)	2.64
Absorption	1.1%

Table 4 - Negligible Weathering Region

	Method	Result	Spec.
Clay Lumps / Friable Particles*	C 142	0.0%	5.0 % Max.
Material Finer than #200	C 117	0.8%	1.0 % Max.
Coal and Lignite *	C 123	0.0%	1.0 % Max.
Abrasion (C) 500 rev.	C 131	30%	50 % Max.

* All other classes of concrete

Soundness	C88	2%	na

Submitted by:

Jeff Pollard
Manager Technical Services
JP/je

Southern California Quality Control Department
16009 Foothill Boulevard • Irwindale, California 91706 • Telephone (626) 856-6190 • Fax (626) 969-2918
Please Note: Not Valid if Altered

Vulcan
Materials Company
Western Division

Contractor: ***CalPortland Company***

November 5, 2021

Project: ***Various***

Plant: ***Vulcan Materials / Durbin (SMARA# 91-19-0023)***

Material: ***Washed Concrete Sand (WCS)***
Product Code: ***31822***

This is to certify that Vulcan Materials Company, Western Division, **Durbin**, will supply Washed Concrete Sand (WCS) to the above listed project and that this product will conform to Table 1 and the grading limits in section 6, of ASTM designation C33 - 18. *Due to the natural effects of segregation and the effects of post-delivery handling, Vulcan Materials Company guarantees that its material will meet the specifications in this submittal at the point of delivery only, and when sampled in accordance with ASTM D75.*

Sieve Size		ASTM C33 Section 6	Percent Passing
9.5 mm	(3/8")	100	100
4.75 mm	(No. 4)	95 - 100	96
2.36 mm	(No. 8)	80 - 100	82
1.18 mm	(No. 16)	50 - 85	66
600 um	(No. 30)	25 - 60	46
300 um	(No. 50)	5 - 30	23
150 um	(No. 100)	0 - 10	8
75 um	(No. 200)	0 - 5 [A]	2.7

Specific Gravity(SSD)	2.65
Absorption	0.9%

	Method	Result	Spec.
Fineness Modulous (F.M.)	C 136	2.8	2.3 - 3.1
Soundness	C 88	3%	10 % Max.
Organic Impurities	C 40	lighter	lighter than standard

Table 1

	Method	Result	Spec.
Clay Lumps / Friable Particles	C 142	0.0%	3.0 % Max.
Coal and Lignite *	C 123	0.0%	1.0 % Max.

* All other concrete

Submitted by:

Jeff Pollard
Manager Technical Services
JP/je

Southern California Quality Control Department
16009 Foothill Boulevard • Irwindale, California 91706 • Telephone (626) 856-6190 • Fax (626) 969-2918
Please Note: Not Valid if Altered

CALPORTLAND®

Manufacturer's Certification

Report Date: 3/8/2021

We hereby certify that CalPortland Type II/V Cement meets the standard requirements of ASTM C150 and AASHTO M85 specification for Type II and Type V cements, as well as Caltrans Standard Specification Sec. 90-1.02B(2). Reported are the average chemical and physical data for the month indicated below.

Month: February, 2021 **Riverside Type II / V Cement**

Source: Oro Grande, CA, USA

	ASTM C150 and AASHTO M85 Requirements		Analysis	IPA	Limestone
Chemical Properties	**Type II**	**Type V**	**Results**	**Analysis**	**Analysis**
Silicon dioxide (SiO_2), %	---	---	**20.5**	**11.6**	**7.5**
Aluminum oxide (Al_2O_3), max, %	6.0	---	**4.1**	**2.9**	**0.6**
Ferric oxide (Fe_2O_3), max, %	6.0	---	**3.8**	**1.5**	**0.3**
Calcium oxide (CaO), %	---	---	**63.9**	**44.6**	**50.5**
Magnesium oxide (MgO), max, %	6.0	6.0	**1.5**	**0.9**	**0.4**
Sulfur trioxide (SO_3), max, %	3.0	2.3	**2.5**	**0.2**	**0.2**
Loss on ignition (LOI), max, %	3.5	3.5	**2.6**		
Insoluble residue (IR), max, %	1.5	1.5	**1.1**		**Base**
Alkalies ($Na_2O+0.658*K_2O$), %	---	---	**0.46**		**Cement**
Tricalcium silicate (C_3S), %	---	---	**59**		**61**
Dicalcium silicate (C_2S), %	---	---	**13**		**14**
Tricalcium aluminate (C_3A), max, %	8	5	**4**		**5**
Tetracalcium aluminoferrite (C_4AF), %	---	---	**12**		**12**
$C_4AF + 2(C_3A)$, max, %	---	25	**20**		
CO_2, %	---	---	**1.4**		
Limestone addition, max, %	5.0	5.0	**3.4**		
IPA addition, max, %	5.0	5.0	**0.5**		
$CaCO_3$ in Limestone, min, %	70	70	**92**		
Physical Properties					
Air content of mortar, max, volume %	12	12	**7**		
Blaine Fineness, min, m^2/kg	260	260	**398**		
Autoclave expansion, max, %	0.80	0.80	**-0.02**		
Compressive Strength, min					
3 Day, MPa	10.0	8.0	**28.6**		
3 Day, psi	1450	1160	**4150**		
7 Day, MPa	17.0	15.0	**36.4**		
7 Day, psi	2470	2180	**5280**		
28 Day (from previous month), MPa	---	21.0	**44.0**		
28 Day (from previous month), psi	---	3050	**6380**		
Vicat Setting Time, min-max, minutes	45 - 375	45 - 375	**92**		
C1038 expansion, max, %	0.020	0.020	**0.005**		

Apparatus and methods used in this laboratory have been audited by the Cement and Concrete Reference Laboratory of the National Institute of Standards and Technology. A copy of the report detailing their findings is available upon request. Major oxides are analyzed in accordance with ASTM C114.

Note 1: ASTM C150, Table 1, Note D, It is permissible to exceed the values in the table for SO_3 content, provided it has been demonstrated by ASTM C1038 that the cement with the increased SO_3 will not develop expansion exceeding 0.020% at 14 days.

Note 2: Complies with Caltrans Specification Sec 90-1.02B(2).

Bob Sylvia

Bob Sylvia - Chief Chemist

Appendix F. Effective Plastic Hinge Yield Rotation Calculations

The effective plastic hinge yield rotations (Θ_y) were calculated using a procedure prescribed by ASCE/SEI 41-17 (2017). According to this procedure, Θ_y can be estimated by drawing a line through the origin that crosses the experimental force-displacement curve at a value of 60% of the effective yield forces/moments, $M_{y,eff}$, (Figure F-1). The effective moment values were estimated by using either the analytical moment-curvature response of the wall specimens or the experimental moment-rotation response. Although ASCE/SEI 41-17 requires to use the 60% of the effective yield forces for the estimation of the effective displacements/rotations, in ACI 374R.2-13 (2013), a value between 0.65 and 0.75 is recommended depending on the level of axial load applied to the specimen. Given the level of axial load applied to the specimens ($0.1A_g f'_c$), an α value of 0.75 was used.

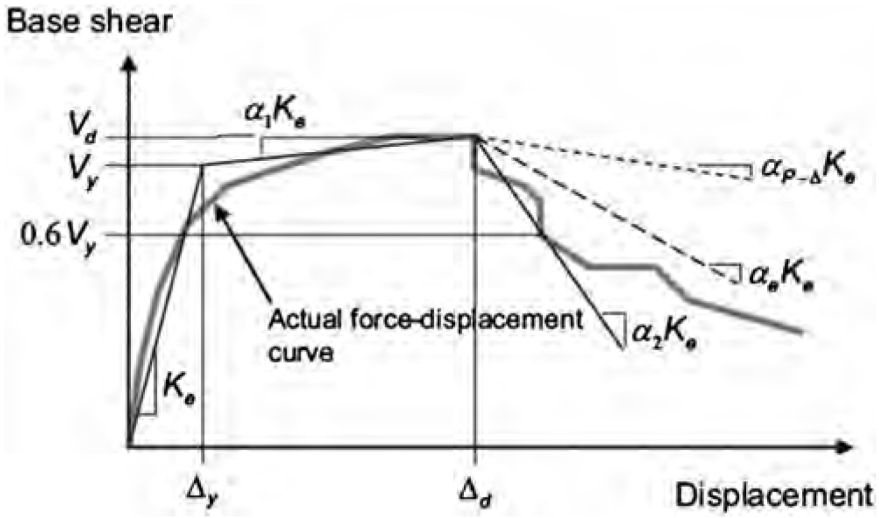

Figure F-1: Idealized force-displacement curves (ASCE/SEI 41-17, 2017)

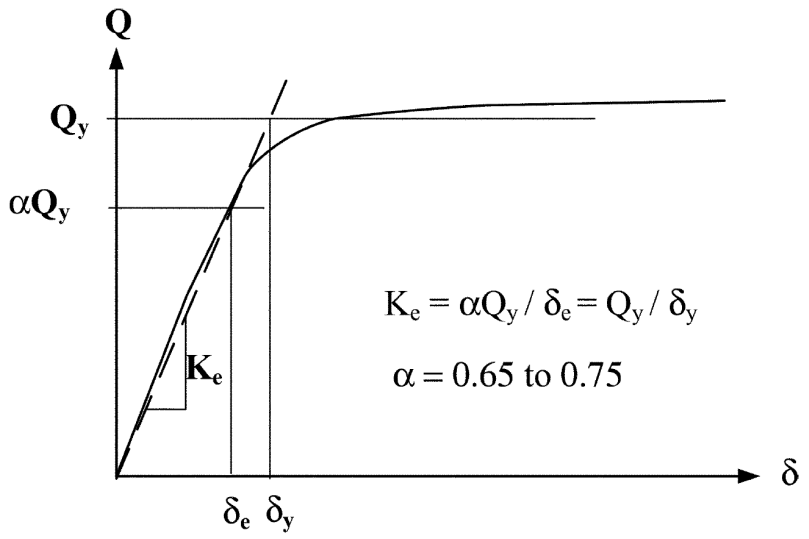

Figure F-2: Determination of effective force and displacement values (ACI 374R.2-13, 2013)

Analytical Effective Hinge Rotations ($\Theta_{y,f,a}$)

The analytical prediction of the yield hinge rotations ($\Theta_{y,f,a}$) due to flexural deformations was calculated by using the procedure mentioned above and the analytical monotonic moment-curvature analysis of the wall specimens. For the moment-curvature analysis, Figure F-3 and Figure F-4 for CW-1 and CW-2-3-4, respectively, the tested material properties (Section 2.3) was used. The effective yield hinge rotations were calculated by integrating the curvatures in the hinge region (Figure F-5). A trapezoidal curvature distribution was assumed with the curvature at the plastic hinge height (L_p) of $\phi_{Lp} = M_{Lp}/K_e$ where K_e is the effective stiffness, and M_{Lp} is the moment at L_p, which is calculated as follows,

$$M_{Lp} = M_{base} - V \times L_p$$

$$M_{Lp} = M_{y,eff} - \frac{M_{y,eff}}{SSR \times L_w} \times L_p \quad \text{(F.1)}$$

Table F-1: Effective analytical yield moment, curvature, and rotation values

	CW-1	CW-2-3-4
$M_{y,eff}$	2350 k-ft	3700 k-ft
$\phi_{y,eff}$	$3.8*10^{-5}$ 1/in.	$6.1*10^{-5}$ 1/in.
K_E	5190283 k-ft^2	5061413 k-ft^2
SSR	4.72	4.72
V	79.7 kips	125.4 kips
M_{Lp}	2101 k-ft	3308 k-ft
ϕ_{Lp}	$3.4*10^{-5}$ 1/in.	$5.5*10^{-5}$ 1/in.
$\theta_{y,f,a}$	0.13%	0.22%

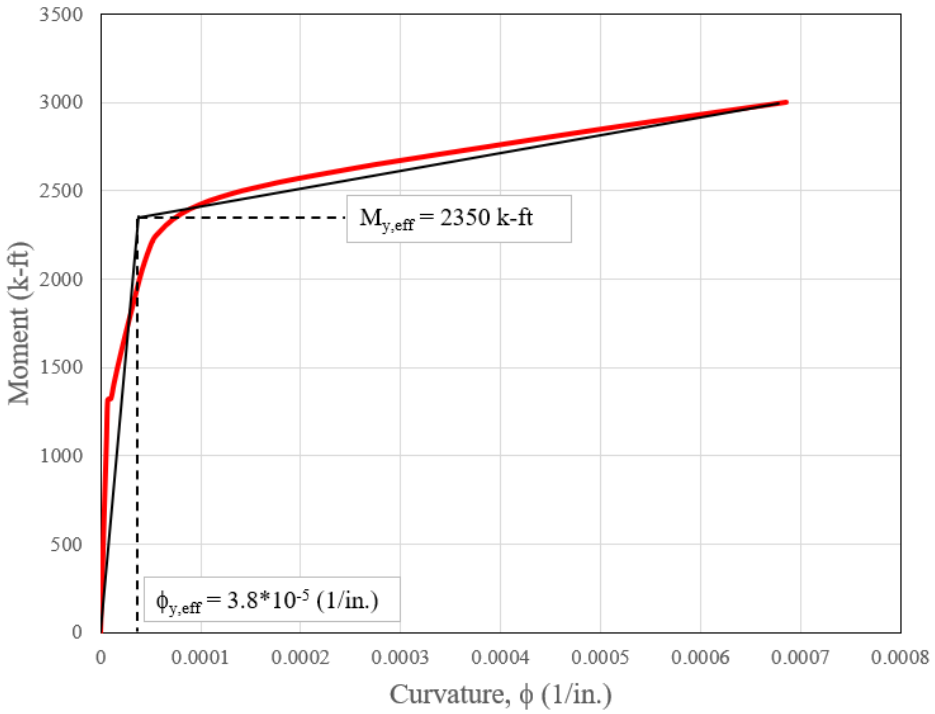

Figure F-3: Analytical moment-curvature response of CW-1 with effective yield moment and curvature values

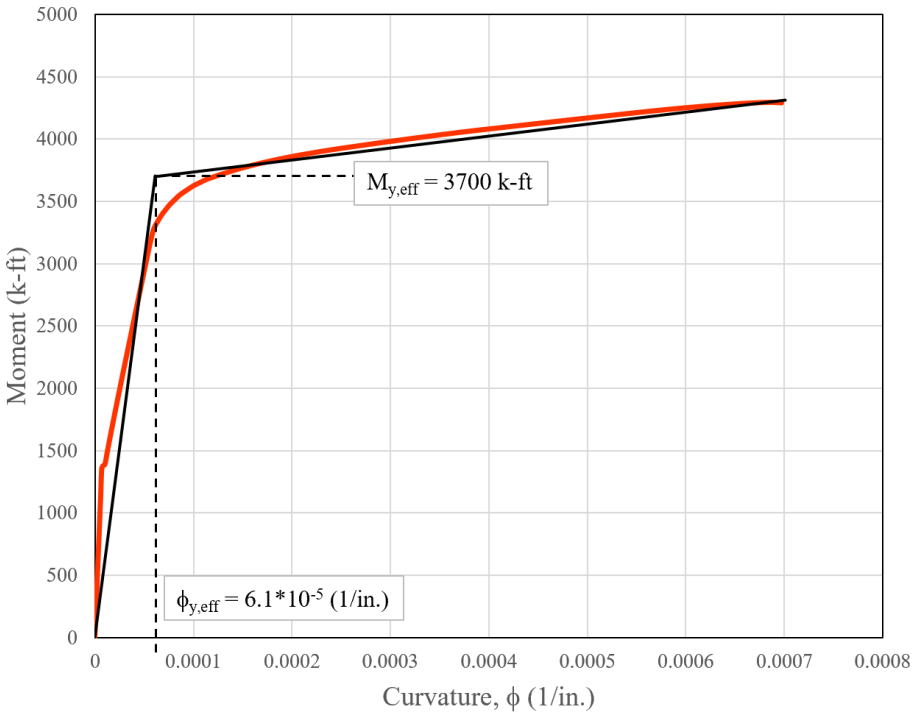

Figure F-4: Analytical moment-curvature response of CW-2-3-4 with effective yield moment and curvature values

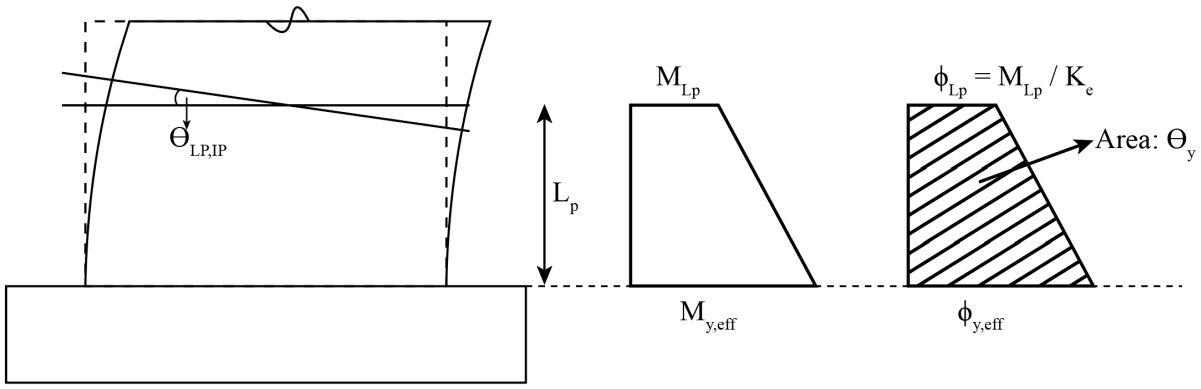

Figure F-5: Calculation of $\Theta_{y,f,a}$

Experimental Effective Hinge Rotations ($\Theta_{y,exp}$)

The experimental plastic hinge yield rotations were calculated by using the experimental base moment-plastic hinge rotation ($L_p=l_w/2$) response of the specimens. Backbone curves were created using the maximum hinge rotation and base moment values measured at different load steps. For CW-1, the moment values for the backbone after the WLP were taken from RCW-1. Using the analysis explained above and the effective yield moments given, 2350 k-ft and 3700 k-ft, $\Theta_{y,exp}$ values 0.11% and 0.25% were calculated for CW-1 (Figure F-6) and CW-2 (Figure F-7), respectively. The effective hinge yield rotations of the specimens were also calculated assuming a larger plastic hinge region ($L_p=l_w/2+L_s$). For CW-1, the effect of longer hinge region on the effective yield value was negligible. Figure F-8 shows the experimental backbone base moment-hinge rotation curve for CW-2, for which the extended hinge region increased the effective yield rotation values to -0.35% and 0.33%. The behavior of CW-3 and CW-4 were very similar to each other and stiffer than CW-2. Therefore, the effective yield rotations were found to be -0.28% and 0.27% for CW-3 and CW-4 (Figure F-9).

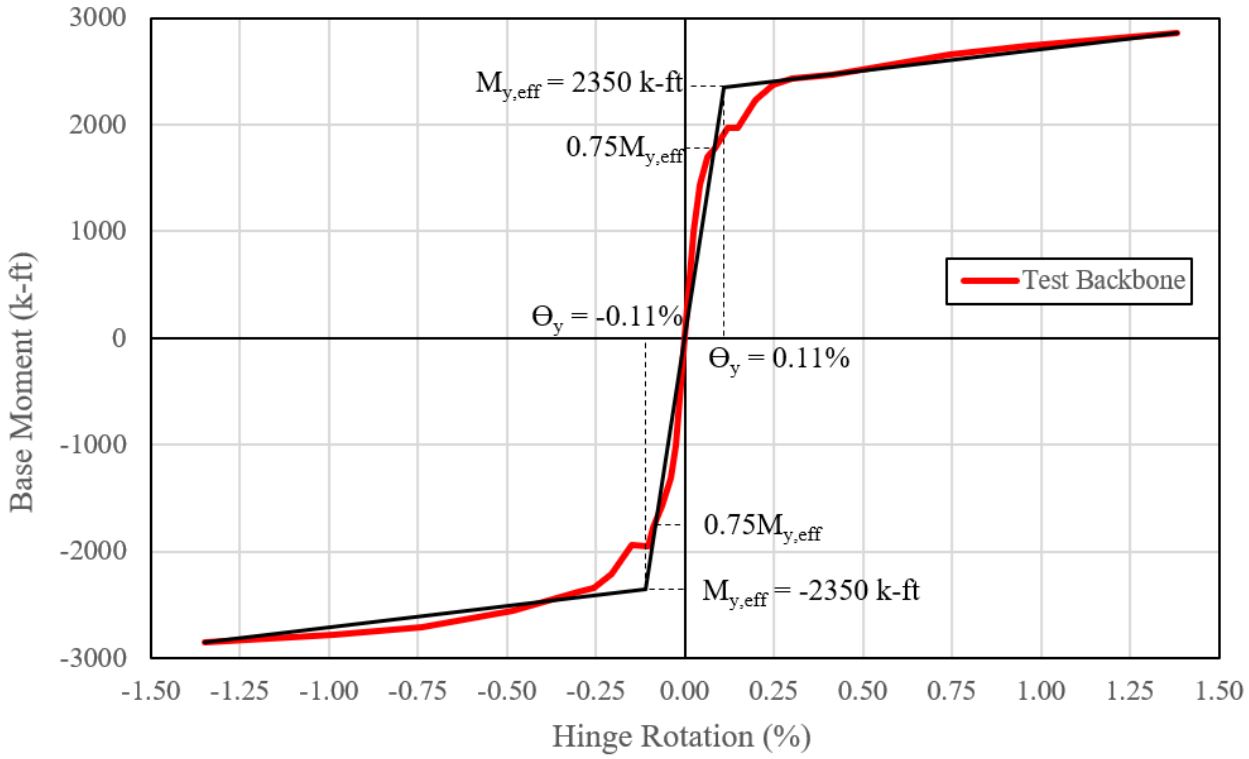

Figure F-6: Experimental plastic hinge yield rotation (L_p=l_w/2, CW-1)

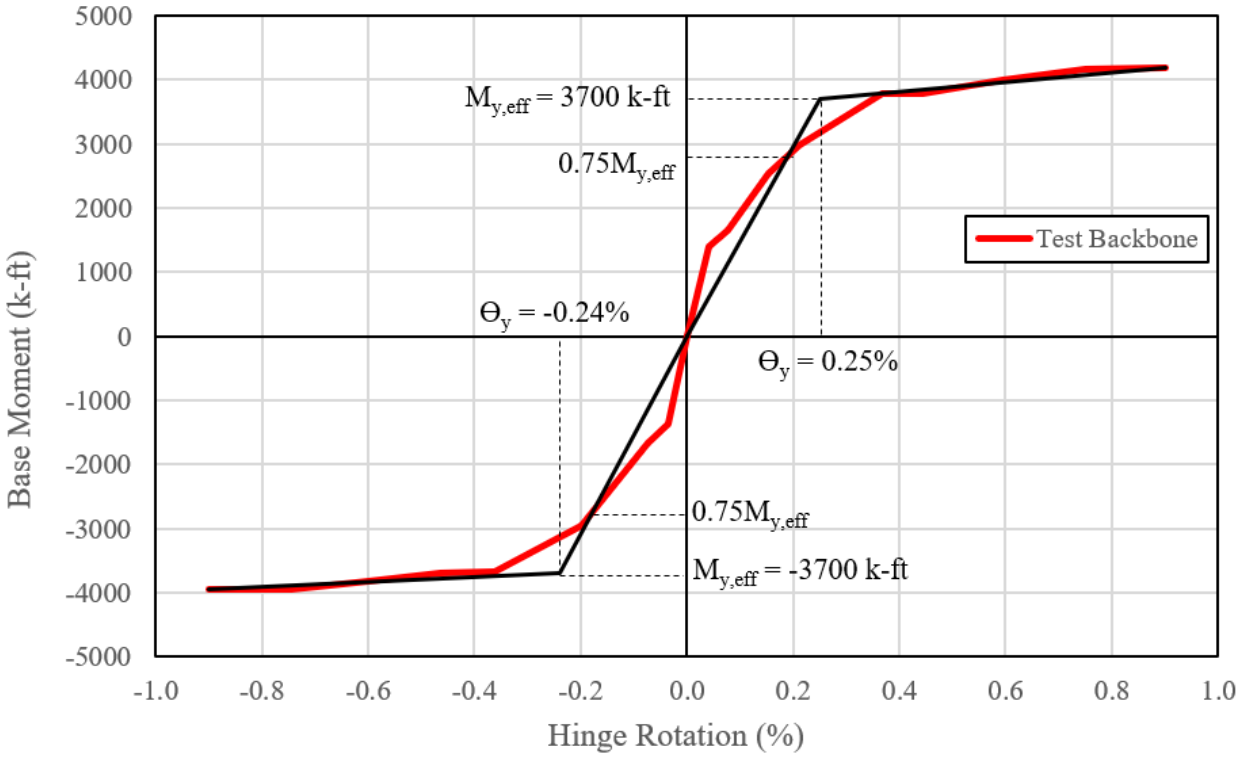

Figure F-7: Experimental plastic hinge yield rotation (L_p=l_w/2, CW-2)

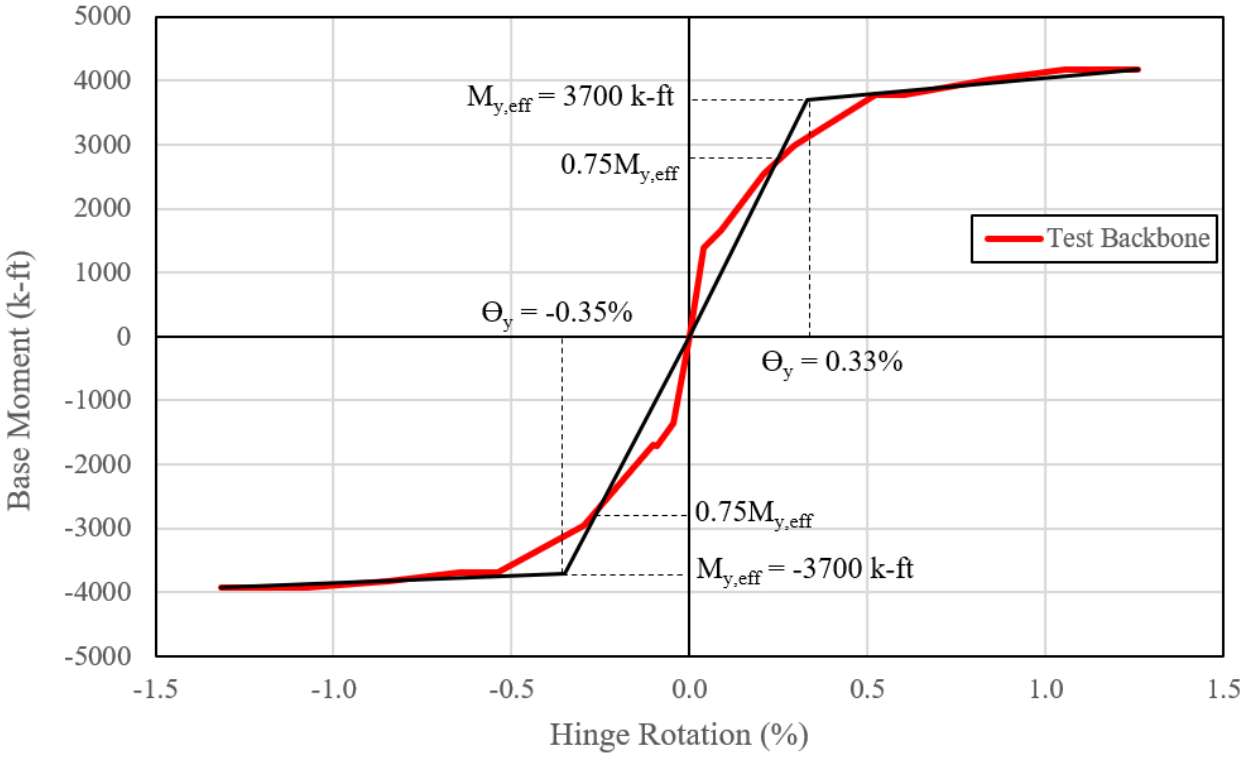

Figure F-8: Experimental plastic hinge yield rotation ($L_p=l_w/2+L_s$, CW-2)

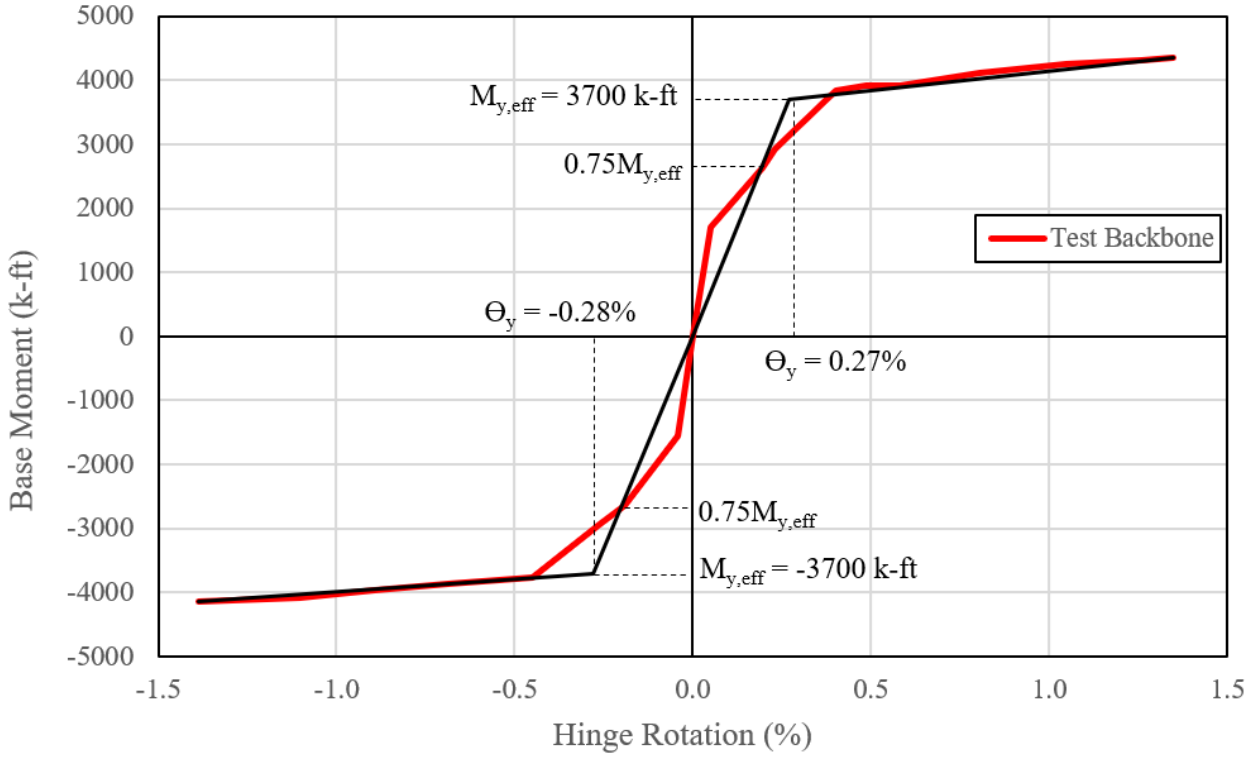

Figure F-9: Experimental plastic hinge yield rotation ($L_p=l_w/2+L_s$, CW-3-4)

Appendix G. Components of Lateral Deformation

The lateral deformations of the wall specimens can be separated into five parts. Flexural deformations include the curvature/rotation of the wall ($\delta_{f,wall}$), and the deformations due to the slip/extension at the wall-footing interface (δ_{slip}). Shear deformations include the pure translation (shear distortion) along the height of the wall ($\delta_{s,wall}$), the shear sliding along the wall footing interface ($\delta_{s,slide,wall}$), and also the shear sliding of the bottom block along the laboratory floor ($\delta_{s,slide,block}$). The last two components were measured directly using the horizontal LVDTs attached at the wall-footing interface and from a rigid frame to the bottom block respectively.

$$\delta_{tot} = \delta_{f,wall} + \delta_{f,slip} + \delta_{s,wall} + \delta_{s,slide,wall} + \delta_{s,slide,block} \quad \text{(G.1)}$$

Flexural Component ($\delta_{f,wall}$)

The lateral displacement at the top of the wall due to curvature/rotations was calculated as follows,

$$\delta_{f,wall} = \sum_{i=1}^{n} \theta_i (h_{wall} - x_i) \approx \sum_{i=1}^{n} (\phi_i h_i)(h_{wall} - x_i) \quad \text{(G.2)}$$

where θ_i is the rotation of the layer i, h_{wall} is the height of the wall, x_i is the distance from the centroid of the curvature distribution of the layer i to the footing, and h_i is the height of the layer i. θ_i was calculated as the area under the curvature distribution. Therefore, it was approximated as the curvature of the layer i (ϕ_i) times h_i. ϕ_i were measured directly using the LVDTs attached to the flanges and the web of the specimen. The centroid of the curvature distribution in a layer was assumed to be at $h_i/2$. This assumption was made due to the small height of the layers in the hinge region and the application of both the moments and shears at the top of the wall, which resulted in

a shallow moment gradient. Given the shear span ratio value of 4.72, the moment demands relative to the base moment at each layer were calculated and shown in Figure G-1.

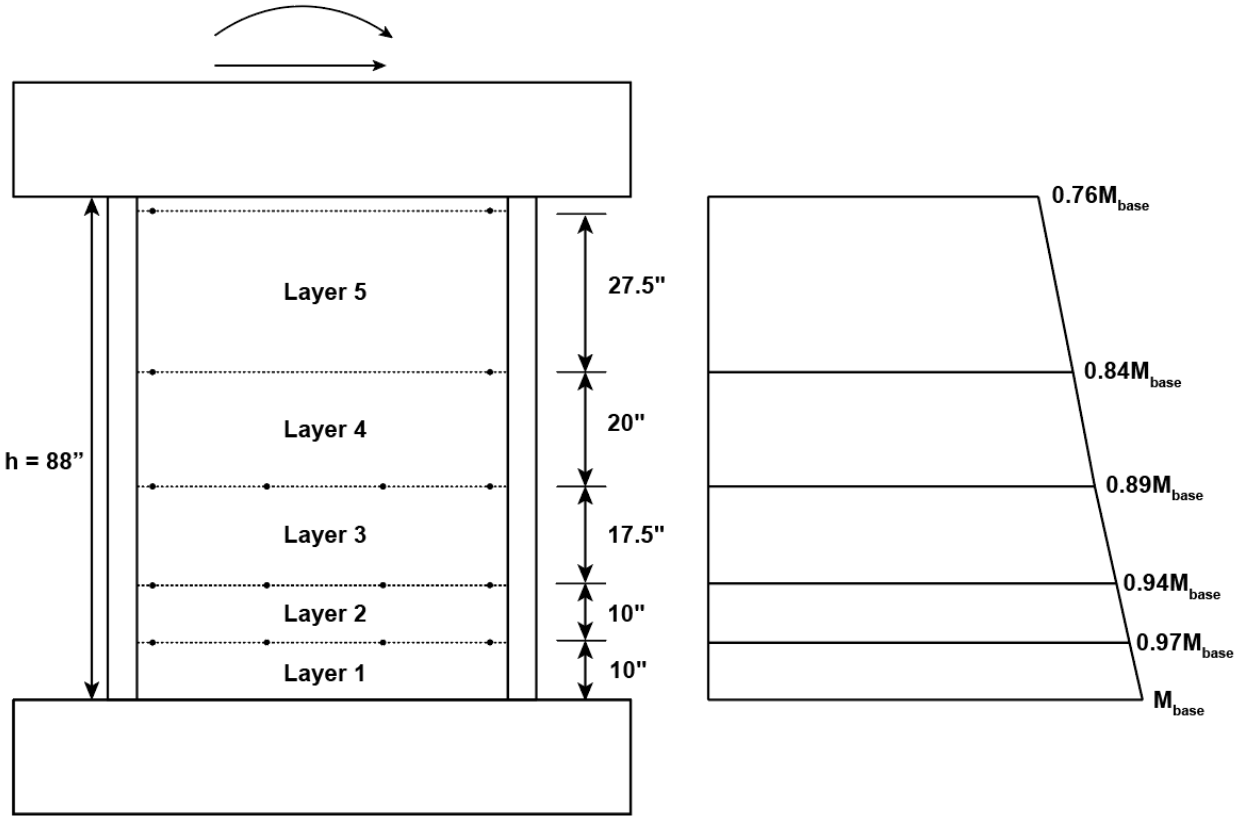

Figure G-1: Wall LVDT layers and the distribution of the moment along the height of the specimen

The lateral displacements at the top of the wall due to curvatures/rotations only were also predicted using the analytical moment-curvature responses shown in Figure F-3 and Figure F-4 for CW-1 and CW-2-3-4, respectively, and Equation G.2. Figure G-2 and Figure G-3 shows the predicted curvature distribution over the wall height at different $\phi_{y,eff}$ demands for CW-1 and CW-2-3-4, respectively. Given the distribution, the centroid of the curvature distribution for each layer was calculated. The calculations showed that, for CW-1, for Layers 1 and 2, due to the small height of

the layers, the centroid was at $h_i/2$, even at high curvature demands ($\phi_i = 25\phi_{y,eff}$). For Layers 3 and 4, it was found that the centroid starts to shift after yielding occurs at the layer. At high curvature demands ($\phi_i > 7.5\phi_{y,eff}$), the centroid was at $0.46h_i$. For Layer 5, similar to Layers 3 and 4, the centroid was found to shift around the yielding of the layer. However, unlike Layers 3 and 4, due to the bigger height of the layer, the centroid was at $0.4h_i$ when the average curvature over the layer reached twice the yield curvature ($\phi_i = 2.0\phi_{y,eff}$). For CW-2, the centroid was at $0.46h_i$ on average for all the layers. It should also be noted here that the lateral displacements due to the curvatures of Layer 5 were small compared to other layers (less than 5% of total displacement). Therefore, the centroid was assumed to be at $h_i/2$.

Given the damage state of the spliced regions for all the specimens, no significant cracking was observed, and also, using the LVDT recordings attached to the spliced region, the lateral displacements due to the curvature of the spliced region were smaller than other layers. Therefore, the analytical predictions were adjusted accordingly. For CW-1, the h_i value for Layer 1 was decreased to 2 in. (20% of L_s) from 10 in. to only account for the rotations due to the bottom 2 in. of the spliced region, where a single big crack was observed during the experiment. Also, for CW-2-3-4, the contributions from Layers 1 and 2 were adjusted by decreasing the height of the layers for the rotation calculation from 10 in. to 4 in. (20% of L_s). Figure G-4 and Figure G-5 show the analytical base shear-drift ratio prediction due to flexure for CW-1 and CW-2-3-4, respectively.

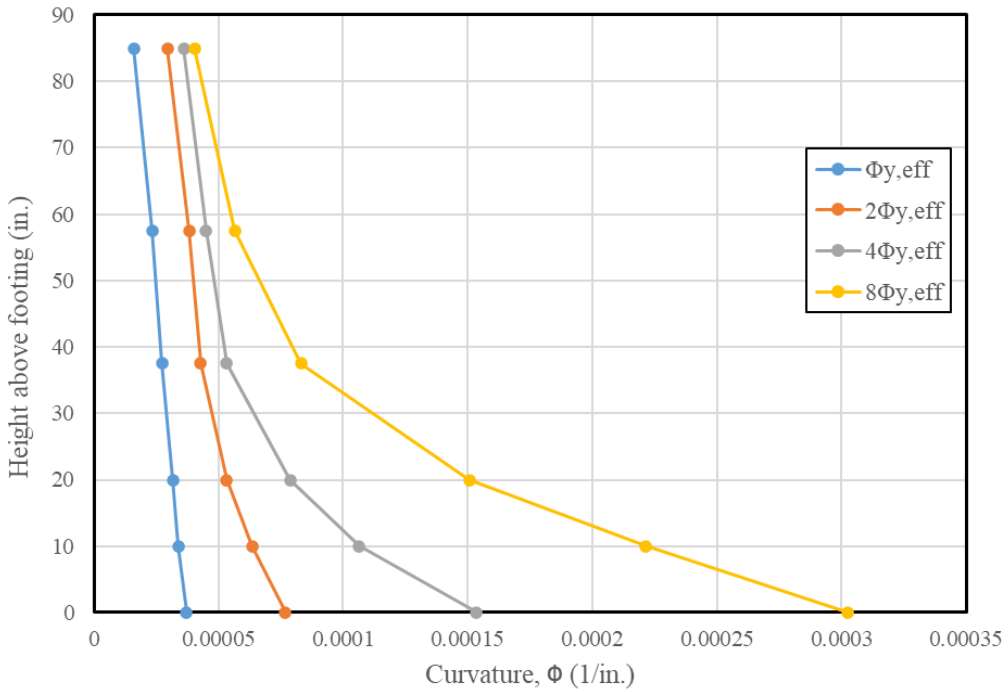

Figure G-2: Analytical curvature distribution over wall height at different $\phi_{y,eff}$ demands (CW-1)

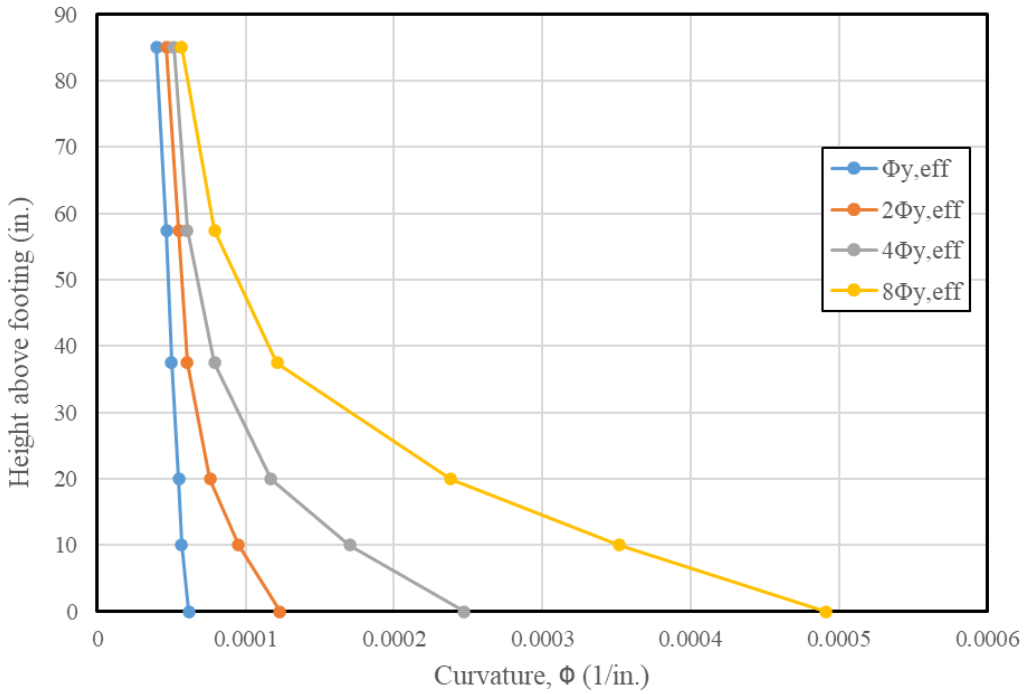

Figure G-3: Analytical curvature distribution over wall height at different $\phi_{y,eff}$ demands (CW-2-3-4)

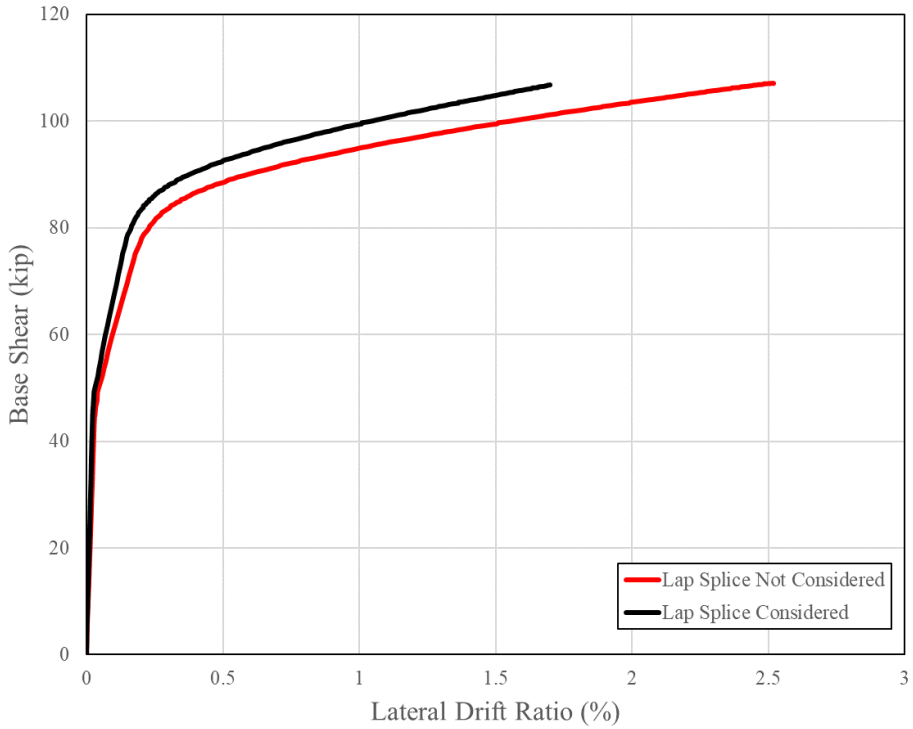

Figure G-4: Analytical shear-drift ratio response of CW-1

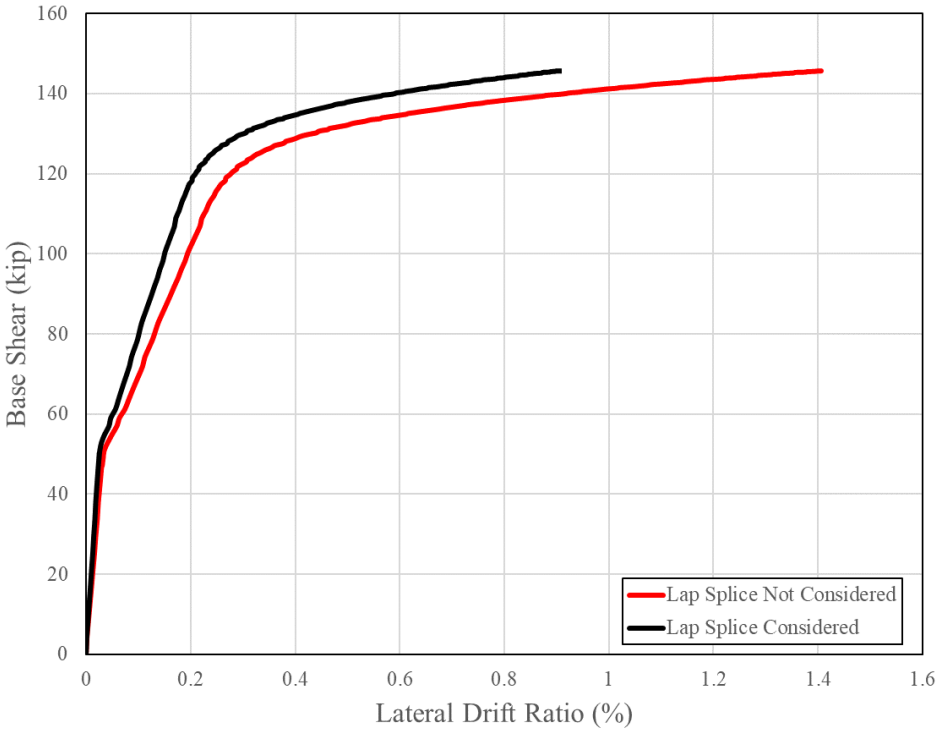

Figure G-5: Analytical shear-drift ratio response of CW-2-3-4

Slip/Extension Component ($\delta_{f,slip}$)

The base slip/extension at the wall-footing interface was measured using four corner LVDTs attached to the footing on one end and to the wall 2.5 in. above the footing. Therefore, these LVDTs recorded both the slip/extension displacements and also the flexural deformations with the 2.5 in. at the base of the wall. The contribution attributed to the slip/extension only was calculated/approximated by assuming similar curvature values for the 2 in. gauge length at the base of the wall and layer right above the splice region (Layer 2 for CW-1 and Layer 3 for CW-2-3-4). The layers inside the splice region were not used for these calculations because lower curvature values were measured in the splice region. $\delta_{f,slip}$ is calculated as follows,

$$\theta_{slip} = \frac{\frac{\delta_{NW} + \delta_{SW}}{2} - \frac{\delta_{NE} + \delta_{SE}}{2}}{L_w + \frac{l_{NW} + l_{SW}}{2} + \frac{l_{NE} + l_{SE}}{2}} \quad \text{(G.3)}$$

$$\delta_{f,slip} = [\theta_{slip} - \phi_{Layer2}(2.5")]h \text{ for CW-1} \quad \text{(G.4)}$$

$$\delta_{f,slip} = [\theta_{slip} - \phi_{Layer3}(2.5")]h \text{ for CW-2-3-4} \quad \text{(G.5)}$$

where δ_{NW}, δ_{SW}, δ_{NE}, and δ_{SE} are the displacements of the slip LVDTs, and l_{NW}, l_{SW}, l_{NE}, and l_{SE} are the distance from the concrete surface to the LVDTs attached to the northwest, southwest, northeast, and southeast corners, respectively.

The effect of the rebar slip/extension at the wall-footing interface was also calculated using the procedures developed by Alsiwat and Saatcioglu (1992), and Sezen and Setzler (2008). According to Alsiwat and Saatcioglu (1992), the contribution of rebar slip/extension to the yield rotation can be calculated using the following equations,

$$u_e = \frac{f_y \times d_b}{4 \times l_d} \; [MPa] \tag{G.6}$$

$$l_d = \frac{440 \times A_b}{3 \times d_b \times \sqrt{f_c'}} \frac{f_y}{400} \; [mm] \tag{G.7}$$

$$L_e = \frac{f_s \times d_b}{4 \times u_e} \; [mm] \tag{G.8}$$

$$u_u = (20 - \frac{d_b}{4}) \times \sqrt{\frac{f_c'}{30}} \; [MPa] \tag{G.9}$$

$$\delta_{s1} = \sqrt{\frac{30}{f_c'}} \; [mm] \tag{G.10}$$

$$\delta_s = \delta_{s1} \times \left(\frac{u_e}{u_u}\right)^{2.5} \; [mm] \tag{G.11}$$

$$\delta_{exty} = \varepsilon_y \times \frac{L_e}{2} \; [mm] \tag{G.12}$$

$$\delta_{toty} = \delta_s + \delta_{exty} \; [mm] \tag{G.13}$$

$$\theta_{y,s} = \frac{\delta_{toty}}{d - c} \; [rad] \tag{G.14}$$

where u_e represents the elastic bond stress, L_e represents the elastic region length, u_u represents the peak bond stress, and δ_{s1} represents the local slip at the peak bond stress. Also, δ_s represents the slip of the reinforcement, δ_{exty} represents the extension of the bar due to accumulation of strain along its length at yield, δ_{toty} represents the total displacement of the bar at the beam-wall interface at yield, $\theta_{@\delta toty}$ represents the rotation of the section due to the slip/extension of the bar at yield, d is the depth of the section, and c is the neutral axis depth.

Similarly, according to Sezen and Setzler (2008), the rebar slip/extension deformations and the resulting rotations at reinforcement yield can be calculated as follows,

$$slip = \frac{\varepsilon_s \times l_d}{2} \tag{G.15}$$

$$l_d = \frac{f_s \times d_b}{4 \times u_b} \tag{G.16}$$

$$\theta_{y,s} = \frac{\varepsilon_s \times f_s \times d_b}{8 \times u_b \times (d - c)} \; [rad] \tag{G.17}$$

where u_b is the uniform bond stress and a value of $12\sqrt{f_c'}$ (psi) is proposed.

For the calculation of the yield rotations due to rebar slip/extension, the tested material properties (Section 2.3) were used. Also, two sets of calculations were done. For the first, the development length of the bars was calculated using the Equations G.7 and G.16, and for the second, the development length provisions of the ACI 318-19 (see Appendix A) were used. Table G-1 summarizes the results.

Table G-1: Analytical prediction of yield rotations due to rebar slip/extension

$\theta_{y,s,a}$		CW-1	CW-2-3-4
Alsiwat and Saatcioglu (1992)	l_d (Eq. G.2)	0.017%	0.031%
	l_d (ACI 318-19)	0.014%	0.032%
Sezen and Setzler (2008)	l_d (Eq. G.11)	0.012%	0.025%
	l_d (ACI 318-19)	0.012%	0.029%

Shear Component ($\delta_{s,wall}$)

The shear deformations were calculated with two approaches. First, they are calculated using Equation G.18 which attributes any deformations not associated with flexure, slip/extension, or shear sliding to shear distortion of the wall panel. Secondly, the diagonal LVDTs attached to the inner surface of the web (Figure 2-22) was used as shown in Equation G.19 and Figure G-6. According to Massone et al., (2017), this approach does not account for the impact of the curvature distribution on the shear deformations, which might overestimate shear deformations by as much as 30%. Therefore, they recommend calculating the shear deformation by taking into account the curvature distribution if the centroid of the distribution is not at $0.5h_i$. Since for the test walls, the centroid of the curvature distribution was expected to be at $0.5h_i$ (see previous discussion), Equation G.19 was directly used.

$$\delta_{s,wall} = \delta_{tot} - \delta_{f,wall} - \delta_{f,slip} - \delta_{s,slide,wall} - \delta_{s,slide,block} \quad \text{(G.18)}$$

$$\delta_{s,wall} = \sum_{i=1}^{n} \frac{1}{2}\left(\sqrt{(d_1 + D_1)^2 - h^2} - \sqrt{(d_2 + D_2)^2 - h^2}\right) \quad \text{(G.19)}$$

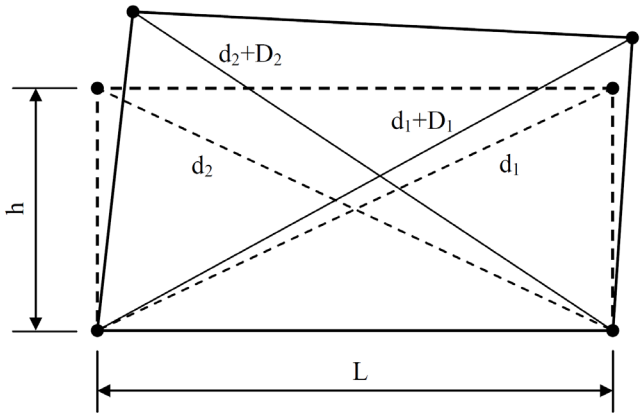

Figure G-6: Determination of shear deformations

Appendix H. Axial Strains during Ramp-down Loading of WLP

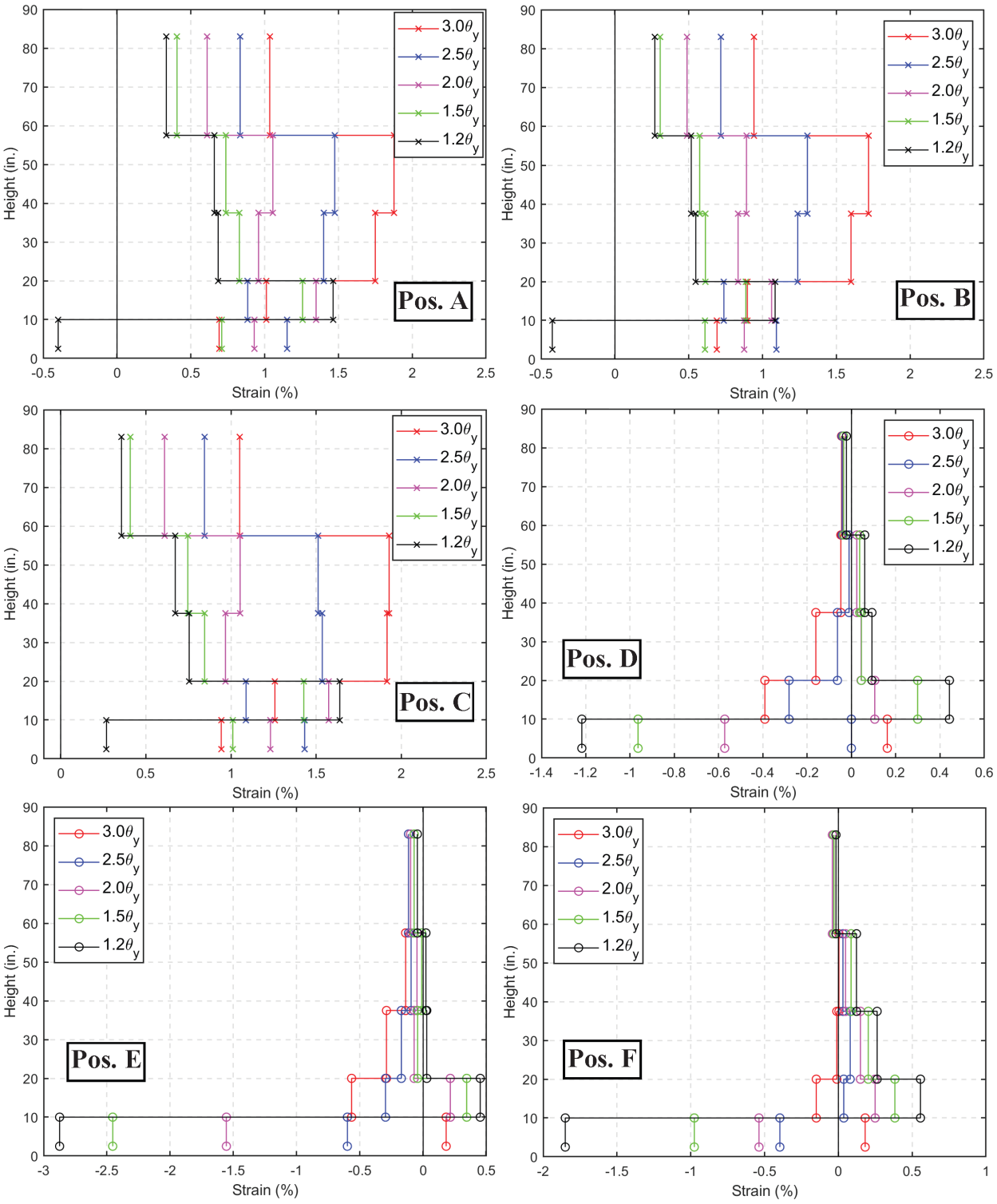

Figure H-1: Axial strain profiles along the height of the edge of the East flange at different loading positions during the ramp-down loading of WLP, CW-2

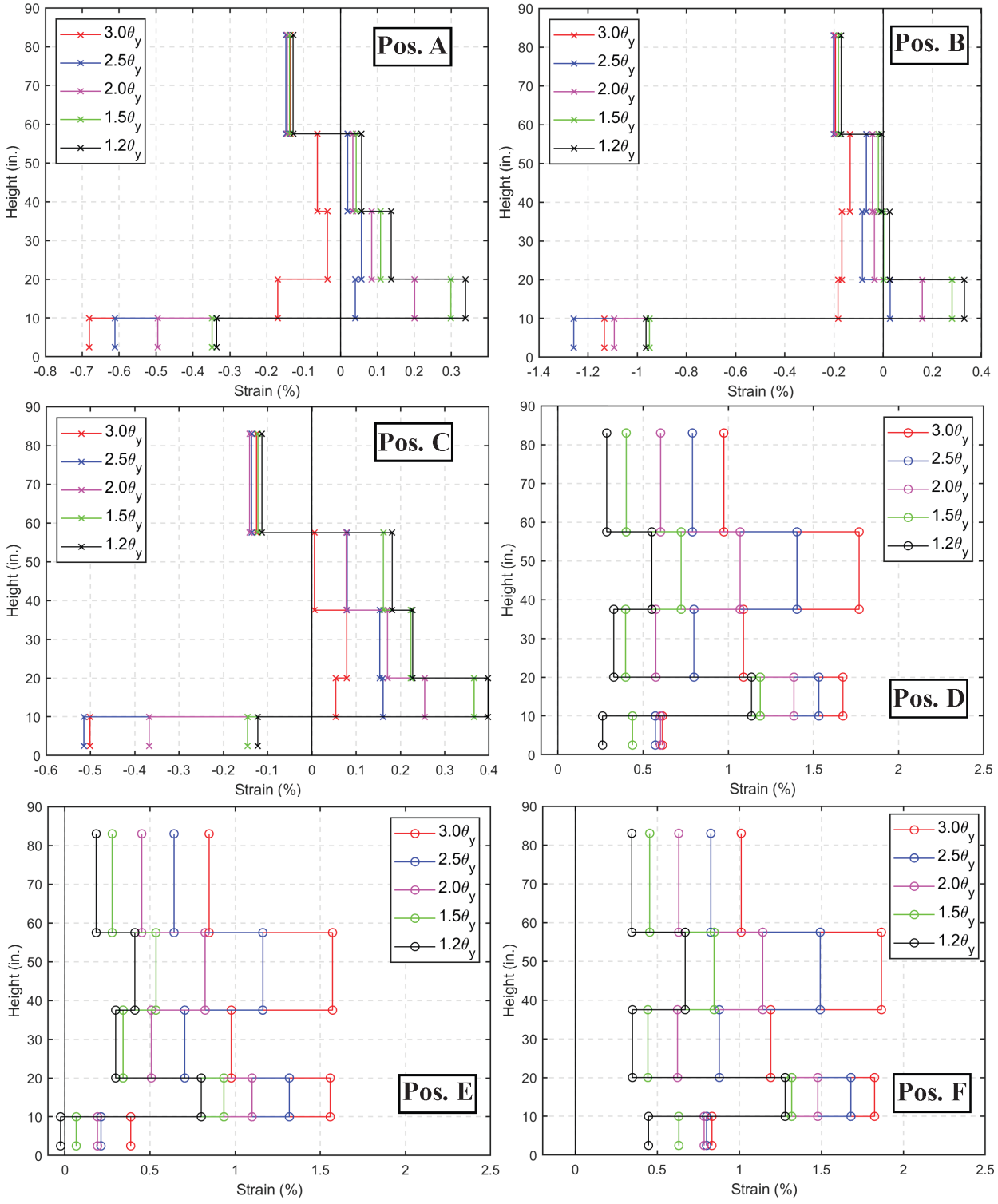

Figure H-2: Axial strain profiles along the height of the edge of the West flange at different loading positions during the ramp-down loading of WLP, CW-2

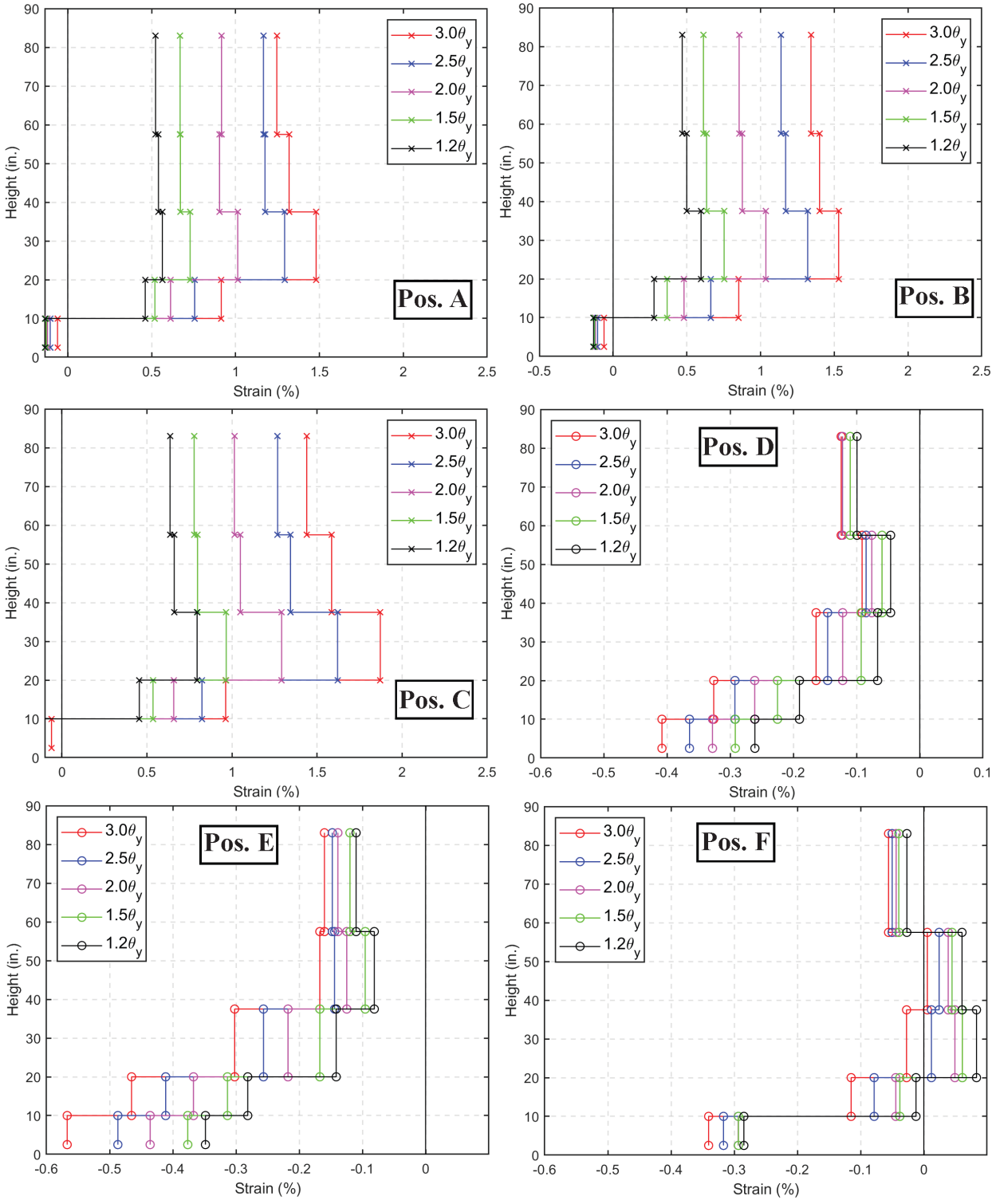

Figure H-3: Axial strain profiles along the height of the edge of the East flange at different loading positions during the ramp-down loading of WLP, CW-3

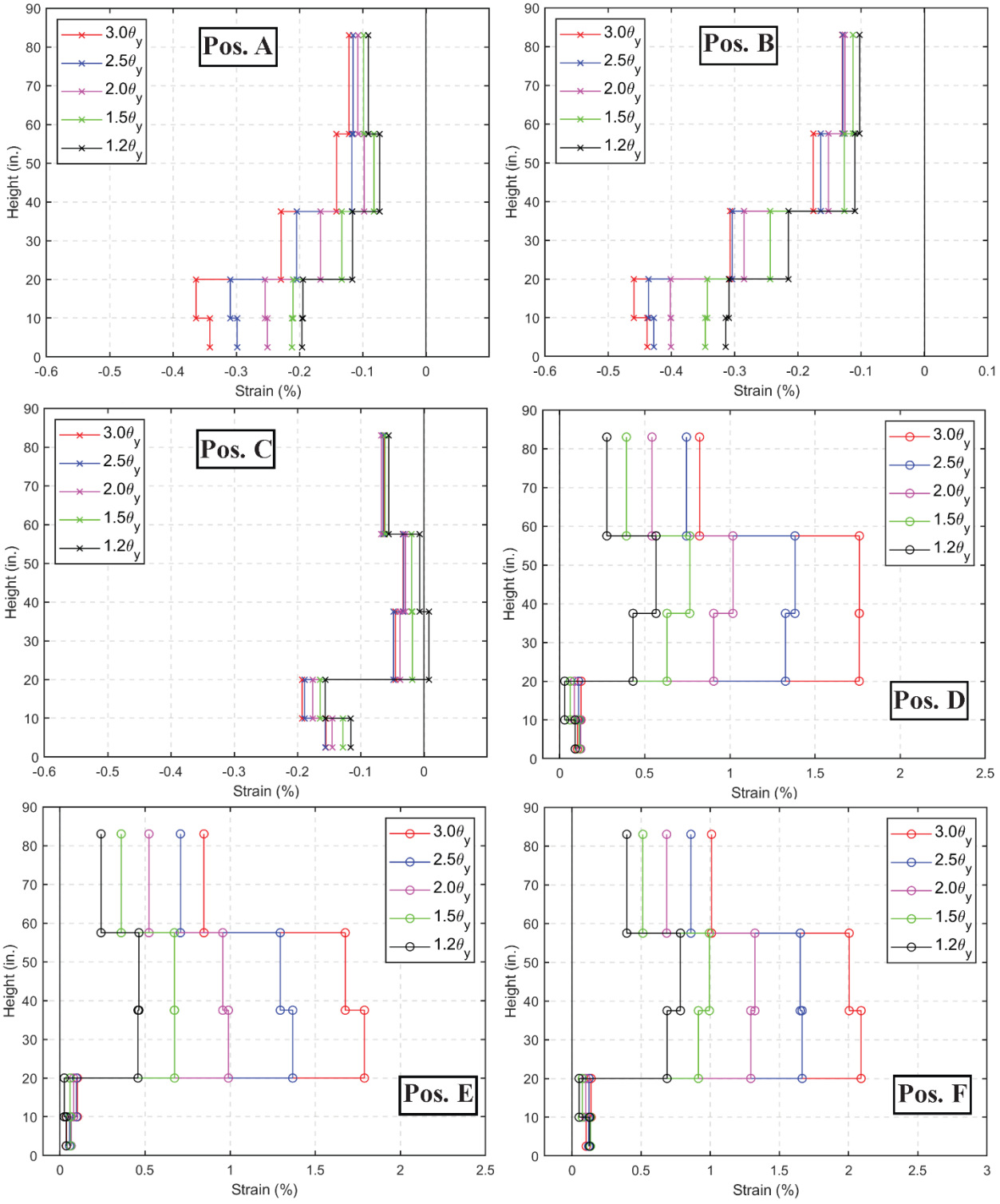

Figure H-4: Axial strain profiles along the height of the edge of the West flange at different loading positions during the ramp-down loading of WLP, CW-3

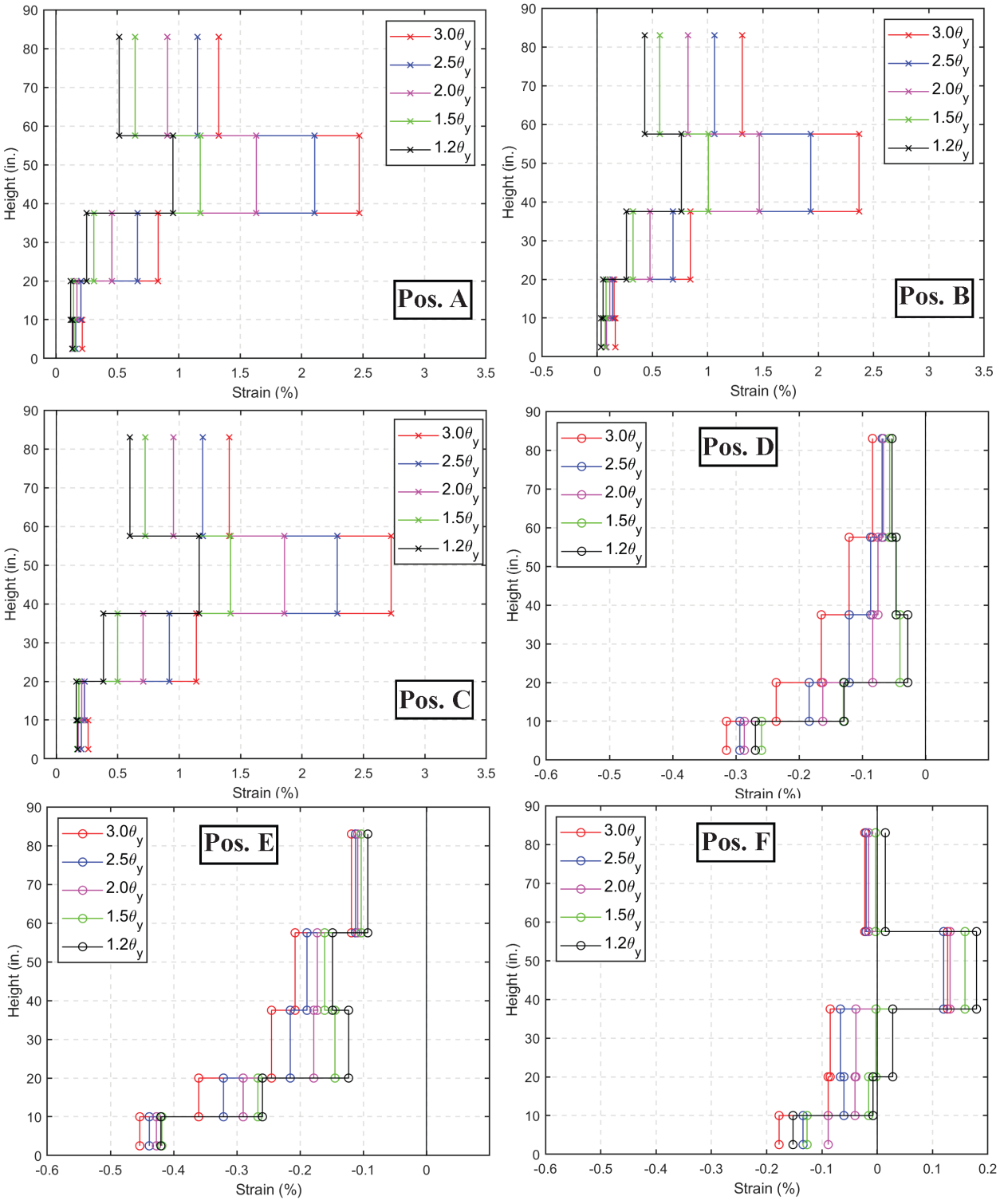

Figure H-5: Axial strain profiles along the height of the edge of the East flange at different loading positions during the ramp-down loading of WLP, CW-4

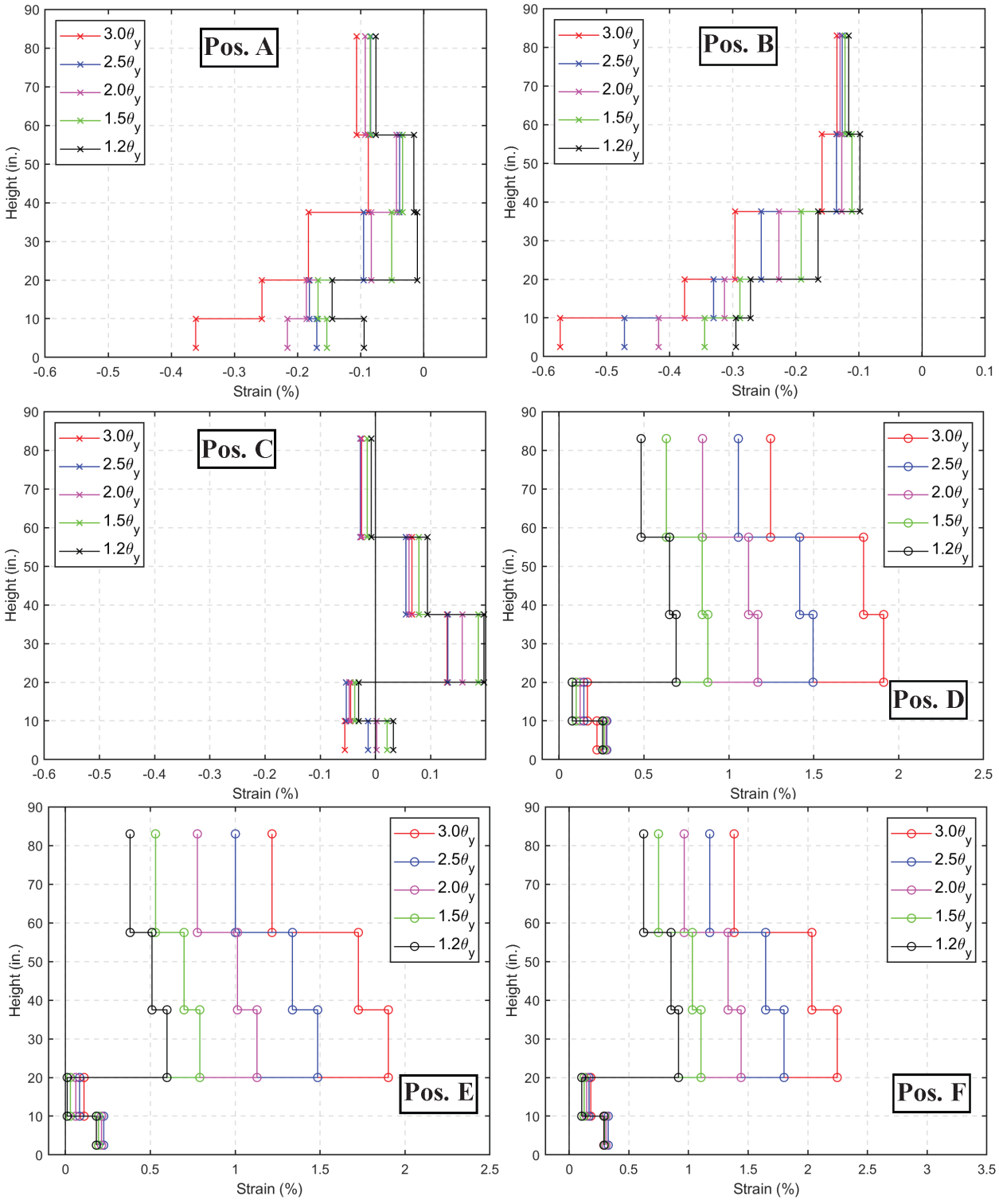

Figure H-6: Axial strain profiles along the height of the edge of the West flange at different loading positions during the ramp-down loading of WLP, CW-4

References

Abdullah, S. A. (2019). *Reinforced Concrete Structural Walls: Test Database and Modeling Parameters* [PhD dissertation]. UCLA.

Abdullah, S. A., Aswegan, K., Jaberansari, S., Klemencic, R., & Wallace, J. W. (2020). Performance of Reinforced Concrete Coupling Beams Subjected to Simulated Wind Loading. *ACI Structural Journal*, *117*(3).

Abdullah, S. A., Aswegan, K., Klemencic, R., & Wallace, J. W. (2021). Performance of Concrete Coupling Beams Subjected to Simulated Wind Loading Protocols—Phase II. *ACI Structural Journal*, *118*(3). https://doi.org/10.14359/51729356

Abdullah, S. A., Aswegan, K., Klemencic, R., & Wallace, J. W. (2022). Seismic performance of concrete coupling beams subjected to prior nonlinear wind demands. *Engineering Structures*, *268*, 114790. https://doi.org/10.1016/j.engstruct.2022.114790

Abdullah, S. A., Wallace, J. W., Aswegan, K., & Klemencic, R. (2020). *Experimental Study of Concrete Coupling Beams Subjected to Wind and Seismic Loading Protocols* (2020/01; Issue 2020/01). Department of Civil & Environmental Engineering at University of California, Los Angeles.

ACI 318-19. (2019). *Building Code Requirements for Structural Concrete and Commentary*. American Concrete Institute. https://doi.org/10.14359/51716937

ACI 363R-10. (2010). *Report on High-Strength Concrete* (p. 65). American Concrete Institute.

ACI 369.1-22. (2022). *Seismic Evaluation and Retrofit of Existing Concrete Buildings—Code and Commentary*.

ACI 374.2R-13. (2013). *Guide for Testing Reinforced Concrete Structural Elements under Slowly Applied Simulated Seismic Loads*. American Concrete Institute.

Alsiwat, J. M., & Saatcioglu, M. (1992). Reinforcement Anchorage Slip under Monotonic Loading. *Journal of Structural Engineering*, *118*(9), 2421–2438. https://doi.org/10.1061/(ASCE)0733-9445(1992)118:9(2421)

ANSI A58-1. (1972). *Building Code Requirements for Minimum Design Loads in Buildings and Other Structures*.

ASCE standard, ASCE/SEI, 41-17: Seismic Evaluation and Retrofit of Existing Buildings. (2017).

ASCE/SEI 7. (2022). *Minimum Design Loads and Associated Criteria for Buildings and Other Structures (7-22)*.

ASCE/SEI 49-21. (2021). *Wind Tunnel Testing for Buildings and Other Structures*. American Society of Civil Engineers.

ASTM A706/A706M-22. (2022). *Standard Specification for Deformed and Plain Low-Alloy Steel Bars for Concrete Reinforcement*. American Society for Testing and Materials.

ASTM C469. (2014). *Standard Test Method for Static Modulus of Elasticity and Poisson's Ratio of Concrete in Compression*. American Society for Testing and Materials.

Aswegan, K., Larsen, R., Klemencic, R., Hooper, J., & Hasselbauer, J. (2017). *Performance-Based Wind and Seismic Engineering: Benefits of Considering Multiple Hazards*. 473–484. https://doi.org/10.1061/9780784480410.039

Bernardini, E., Spence, S. M. J., & Kareem, A. (2013). A probabilistic approach for the full response estimation of tall buildings with 3D modes using the HFFB. *Structural Safety*, *44*, 91–101. https://doi.org/10.1016/j.strusafe.2013.06.002

Bernardini, E., Spence, S. M. J., Kwon, D.-K., & Kareem, A. (2015). Performance-Based Design of High-Rise Buildings for Occupant Comfort. *Journal of Structural Engineering*, *141*(10), 04014244. https://doi.org/10.1061/(ASCE)ST.1943-541X.0001223

Beyer, K., Dazio, A., & Priestley, M. J. N. (2008). Quasi-Static Cyclic Tests of Two U-Shaped Reinforced Concrete Walls. *Journal of Earthquake Engineering*, *12*(7), 1023–1053. https://doi.org/10.1080/13632460802003272

Chai, Y. H., & Elayer. (1999). Lateral Stability of Reinforced Concrete Columns under Axial Reversed Cyclic Tension and Compression. *ACI Structural Journal*, *96*(5). https://doi.org/10.14359/732

Chang, G. A., & Mander, J. B. (1994). *Seismic Energy Based Fatigue Damage Analysis of Bridge Columns. Part I, Evaluation of Seismic Capacity* (NCEER-94-0006). National Center for Earthquake Engineering Research.

Chou, T.-A., Lee, S. H., Chang, C., & Kang, T. H.-K. (2023). Reinforced Concrete Coupling Beams with Different Layouts under Seismic and Wind Loads. *ACI Structural Journal*, *120*(4), 165–178.

Ciampoli, M., Petrini, F., & Augusti, G. (2011). Performance-Based Wind Engineering: Towards a general procedure. *Structural Safety*, *33*. https://doi.org/10.1016/j.strusafe.2011.07.001

Constantin, R.-T. (2016). *Seismic behaviour and analysis of U-shaped RC walls*. Ecole Polytechnique Federale de Lausanne.

CSICol, CSI (Version 10.1.0). (n.d.). [Computer software]. Computers & Structures, INC.

FEMA 306. (1998). *Evaluation Of Earthquake Damaged Concrete and Masonry Wall Buildings*. Applied Technology Council (ATC-43 Project).

FEMA 424. (2010). *Design guide for improving school safety in earthquakes, floods, and high winds*. Federal Emergency Management Agency.

FEMA P-58. (2018). *Seismic Performance Assessment of Buildings*. Federal Emergency Management Agency.

FEMA P-695. (2009). *Quantification of Building Seismic Performance Factors*. Federal Emergency Management Agency.

Filippou, F. C., Popov, E. P., & Bertero, V. V. (1983). *Effects of Bond Deterioration on Hysteretic Behavior of Reinforced Concrete Joints* (Report EERC 83-19). Earthquake Engineering Research Center, University of California.

Halim, S. D. (2024). *Experimental Study on Lap Splice Nonlinear Fatigue Behavior under Wind-Loading Protocol* [Master of Science Thesis]. University of California, Los Angeles.

Hill, A., Forbes, J., & Motter, C. J. (2023). *Nonlinear Wind Design of Steel Reinforced Concrete (SRC) Coupling Beams* (RGA #06-19). Charles Pankow Foundation.

Hilson, C., Segura, C., & Wallace, J. (2014, July 1). *Experimental study of longitudinal reinforcement buckling in reinforced concrete structural wall boundary elements*. NCEE 2014 - 10th U.S. National Conference on Earthquake Engineering: Frontiers of Earthquake Engineering. https://doi.org/10.4231/D3CC0TT9C

Irwin, P., Denoon, R., & Scott, D. (2013). *Wind Tunnel Testing of High-Rise Buildings*. Routledge. https://doi.org/10.4324/9781315879529

Klemencic, R., Hooper, J., Larsen, R., Aswegan, K., & Hasselbauer, J. (2019). PERFORMANCE-BASED WIND DESIGN: THE PATH FORWARD. *Proceedings of the 2019 Annual Meeting of the Los Angeles Tall Buildings Structural Design Council*. ADVANCES IN STRUCTURAL DESIGN OF TALL BUILDINGS.

Kolozvari, K., Kalbasi Anaraki, K., Orakcal, K., & Wallace, J. (2021). Three-dimensional model for nonlinear analysis of slender flanged reinforced concrete walls. *Engineering Structures*, *236*, 112105. https://doi.org/10.1016/j.engstruct.2021.112105

Kolozvari, K., Orakcal, K., & Wallace, J. (2015). *Shear-Flexure Interaction Modeling for Reinforced Concrete Structural Walls and Columns under Reversed Cyclic Loading* (2015/12). Pacific Earthquake Engineering Research Center Headquarters at the University of California, Berkeley.

Larsen, R., Klemencic, R., Hooper, J., & Aswegan, K. (2016). *Engineering Objectives for Performance-Based Wind Design*. 1245–1258. https://doi.org/10.1061/9780784479742.104

Los Angeles Tall Buildings Structural Design Council (LATBSDC). (2023). *An Alternative Procedure For Seismic Analysis And Design Of Tall Buildings*.

Massone, L. M., Sayre, B. L., & Wallace, J. W. (2017). Load – Deformation responses of slender structural steel reinforced concrete walls. *Engineering Structures*, *140*, 77–88. https://doi.org/10.1016/j.engstruct.2017.02.050

McKenna, F., Fenves, G. L., Scott, M. H., & Jeremic, B. (2000). *Open system for earthquake engineering simulation* [Computer software]. Pacific Earthquake Engineering Research Center, University of California.

Menegotto, M., & Pinto, P. E. (1973). Method of analysis of cyclically loaded RC plane frames including changes in geometry and non-elastic behavior of elements under normal force and bending. *Proceedings of IABSE Symposium on Resistance and Ultimate Deform Ability of Structures Acted On by Well Defined Repeated Loads*, *11*, 15–22.

Motter, C., Abdullah, S., & Wallace, J. (2018). Reinforced Concrete Structural Walls without Special Boundary Elements. *ACI Structural Journal*, *115*, 723–733. https://doi.org/10.14359/51702043

Moyer, M. J., & Kowalsky, M. (2003). Influence of tension strain on buckling of reinforcement in concrete columns. *ACI Structural Journal*, *100*, 75–85.

Naish, D., Fry, A., Klemencic, R., & Wallace, J. (2013). Reinforced Concrete Coupling Beams-Part I: Testing. *ACI Structural Journal*, *110*, 1057–1066.

Orakcal, K., Wallace, J. W., & Conte, J. P. (2004). Flexural Modeling of Reinforced Concrete Walls- Model Attributes. *ACI Structural Journal*, *101*(5). https://doi.org/10.14359/13391

Paulay, T., & Priestly, M. J. N. (1993). Stability of Ductile Structural Walls. *ACI Structural Journal*, *90*(4). https://doi.org/10.14359/3958

Pugh, J. S., Lowes, L. N., & Lehman, D. E. (2015). Nonlinear line-element modeling of flexural reinforced concrete walls. *Engineering Structures*, *104*, 174–192. https://doi.org/10.1016/j.engstruct.2015.08.037

Razvi, S., & Saatcioglu, M. (1999). Confinement Model for High-Strength Concrete. *Journal of Structural Engineering*, *125*(3), 281–289. https://doi.org/10.1061/(ASCE)0733-9445(1999)125:3(281)

Rodriguez, M. E., Botero, J. C., & Villa, J. (1999). Cyclic Stress-Strain Behavior of Reinforcing Steel Including Effect of Buckling. *Journal of Structural Engineering*, *125*(6), 605–612. https://doi.org/10.1061/(ASCE)0733-9445(1999)125:6(605)

Rodriguez, M. E., & Iñiguez, M. (2019). Drift Capacity at Onset of Bar Buckling in RC Members Subjected to Earthquakes. In T. T. C. Hsu (Ed.), *Concrete Structures in Earthquake* (pp. 185–200). Springer. https://doi.org/10.1007/978-981-13-3278-4_12

Rodriguez Sanchez, S., Unal, M. E., Ahlberg, E., & Wallace, J. W. (2024). *Repair of a Heavily Damaged C-Shaped RC Wall.* 18th World Conference on Earthquake Engineering, Milan, Italy.

Saatcioglu, M., & Razvi, S. R. (1992). Strength and Ductility of Confined Concrete. *Journal of Structural Engineering*, *118*(6), 1590–1607. https://doi.org/10.1061/(ASCE)0733-9445(1992)118:6(1590)

Scott, D. (2023). *Advancement in Performance-Based Wind Design: Workshop Report*. National Institute of Standards and Technology. https://doi.org/10.6028/NIST.GCR.23-045-upd1

Sezen, H., & Setzler, E. J. (2008). Reinforcement Slip in Reinforced Concrete Columns. *ACI Structural Journal*, *105*, 280–289.

Smith, M., & Caracoglia, L. (2011). A Monte Carlo based method for the dynamic "fragility analysis" of tall buildings under turbulent wind loading. *Engineering Structures*, *33*, 410–420. https://doi.org/10.1016/j.engstruct.2010.10.024

Smolka, A. (2006). Natural disasters and the challenge of extreme events: Risk management from an insurance perspective. *Philosophical Transactions of the Royal Society A: Mathematical, Physical and Engineering Sciences*, *364*(1845), 2147–2165. https://doi.org/10.1098/rsta.2006.1818

Spence, S., Bernardini, E., & Kareem, A. (2015). A First Step towards a General Methodology for the Performance-Based Design of Wind-Excited Structures. *Structures Congress 2015 - Proceedings of the 2015 Structures Congress*, 1482–1493. https://doi.org/10.1061/9780784479117.127

Spence, S., Chuang, W.-C., Tabbuso, P., Bernardini, E., Kareem, A., Palizzolo, L., & Pirrotta, A. (2016). *Performance-Based Engineering of Wind-Excited Structures: A General Methodology*. 1269–1282. https://doi.org/10.1061/9780784479742.106

Spence, S. M. J., & Gioffrè, M. (2012). Large scale reliability-based design optimization of wind excited tall buildings. *Probabilistic Engineering Mechanics*, *28*, 206–215. https://doi.org/10.1016/j.probengmech.2011.08.001

Spence, S. M. J., & Kareem, A. (2014). Performance-based design and optimization of uncertain wind-excited dynamic building systems. *Engineering Structures*, *78*, 133–144. https://doi.org/10.1016/j.engstruct.2014.07.026

Thomsen, J. H., & Wallace, J. W. (2004). Displacement-Based Design of Slender Reinforced Concrete Structural Walls—Experimental Verification. *Journal of Structural Engineering*, *130*(4), Article 4. https://doi.org/10.1061/(ASCE)0733-9445(2004)130:4(618)

Tura, C., Orakcal, K., Gullu, M. F., & Ilki, A. (2024). *Nonlinear Modeling and Response Simulation Of Reinforced Concrete Walls Under Generalized Loading Conditions*. 18th World Conference on Earthquake Engineering, Milan, Italy. p.12

Unal, M. E., Wallace, J. W., Abdullah, S. A., Kim, S., & Kolozvari, K. (2024). *Testing of Lap Splices in Reinforced Concrete Beams and Structural Walls under Wind Loading Protocols*. 18th World Conference on Earthquake Engineering, Milan, Italy.

Vulcano, A. (1992). Macroscopic modeling for nonlinear analysis of RC structural walls. In *Nonlinear Seismic Analysis and Design of Reinforced Concrete Buildings* (pp. 189–198). CRC Press. https://doi.org/10.1201/9781482296662-14

Vulcano, A., Bertero, V., & Colotti, V. (1988). Analytical Modeling of R/C Structural Walls. *Proceedings of the 9th World Conference on Earthquake Engineering, Tokyo/Kyoto, Japan*, *6*.

Wallace, J. W., & Orakcal, K. (2002). ACI 318-99 Provisions for Seismic Design of Structural Walls. *ACI Structural Journal*, *99*(4), 499–508.

Yassin, M. H. M. (1994). *Nonlinear Analysis of Prestressed Concrete Structures under Monotonic and Cycling Loads* [PhD dissertation]. University of California.